CRANFIELD UNIVERSITY

CRANFIELD DEFENCE

PhD

Academic Year 2016 - 2017

JOHN DAVID REINECKE

Partitioning of Shallow Buried Near-Field Blast

Supervisor: Professor Ian Horsfall
February 2017

ABSTRACT

Buried blast continues to present a threat to military and humanitarian operations. Burying an explosive device simultaneously hides and has the potential to enhance the subsequent blast loading. Although widely published and accepted that a buried blast load consists of a number of temporally separated elements most research instruments quantify resultant load in terms of a single impulse value. Over-pressure sensors have been used to temporally research buried blast loading, however these provide only a single point measurement to a three-dimensional loading. Understanding the temporal loading from a buried blast will support the development of more effective and innovative protection systems. In recent years there have been a number of published research efforts providing new methods and results on temporal blast loading, however how these results relate to the blast loading has not been presented in the public domain.

Using a combination of computational modelling and a specifically designed scaled test rig that enabled both free-field as well as intermediate and near-field target response measurements, this research explored the quantification and the temporal phasing of a shallow-buried blast load. The target force-time response, the target side-on and face-on pressure and the target assembly displacement-time confirmed a phased free-field blast load, phased target pressure loading and a phased temporal target response. Based on published work and the computational modelling and test results from this work, three shallow buried blast load phases were identified comprising:

1. An initial soil ejecta and blast overpressure impact (Phase One);
2. Followed by gas expansion (Phase Two) and;
3. Last reflected pressure combined with afterburn (Phase Three) loading.

For this research the soil ejecta primarily contributed to the blast load as part of the first phase impact and had limited contribution thereafter. The percentage phase contribution to the total blast loading is dependent on the measurement system and its characteristics. The identified three loading phases were verified

through comparison to secondary data from both scaled and full blast load test rigs.

Keywords:

Shallow-Buried BLast, Partitioning, Temporal Phasing, Blast Load, Landmine, Scaling, Quantification,Force-Time, NIR

ACKNOWLEDGEMENTS

Professor I. Horsfall, J. Goosen, Dr. P. Walters, Dr. W. Proud, Ouma de Beer, M. Eden and F.J. Beetge

TABLE OF CONTENTS

LIST OF FIGURES

LIST OF TABLES

LIST OF ABBREVIATIONS

AEP	Allied Engineering Publication
APC	Armoured Personnel Carrier
BNC	Bayonet Neill Concelman connector
CASSPIR	Acronym of the CSIR and South African Police
CSIR	Council for Scientific and Industrial Research
DBEL	Detonics, Ballistics and Explosive Laboratory
D:H	Diameter to Height Ratio
DOB	Depth of Burial
DPSS	Defence, Peace, Safety and Security
DREV	Defence R&D Canada – Valcartier
DSTO	Defence Science and Technology Organisation
EBW	Exploding Bridgewire
EFP	Explosively Formed Projectile
EM	Electromagnetic
EOS	Equation of State
FE	Finite Element
FEA	Finite Element Analysis
FS	Full Scale
FSI	Fluid Structure Interaction
FY	Financial Year
GSS	Geometrically Similar Scaling
HBM	Hottinger Baldwin Messtechnik GmbH
ICL	Imperial College London
ICP	ICP
IED	Improvised Explosive Device
JWL	Jones-Wilkins-Lee
LLNL	Lawrence Livermore National Laboratory
LS	Landwards Sciences
LTD	Limited
LVDT	Linear Variable Displacement Transducer
MABS	Military Application of Blast and Shock
MIL	Military

NATO	North Atlantic Treaty Organisation
NEC	Net Explosive Content
NIR	Near Infrared
NSA	NATO Standardisation Agency
PASS	Personal Armour Systems Symposium
PE	Plastic Explosive
RDX	Royal Demolition eXplosive
RH	Right Hand
RHS	Right Hand Side
RSA	Republic of South Africa
RTG	Research Task Group
RTO	Research and Technology Organisation
SA	South Africa
SANDF	South African National Defence Force
SD	Standard Deviation
SI	International System of Units
SIIMA	Scientifically Instrumented Impulse Measurement Apparatus
SOD	Stand-off Distance
SODS	Stand Off Distances
SPH	Smooth Particle Hydrodynamics
STANAG	Standardisation Agreement
STD	Standard
STO	Science and Technology Organisation
TNT	Trinitrotoluene
TTL	Time To Limit
UK	United Kingdom
USA	United States of America
UXO	Unexploded Ordinance

DEFINITIONS AND TECHNICAL TERMS

Figure 1 presents the general terms and definitions defined in RSA-MIL-STD-37 Issue 3 and as used for this research.

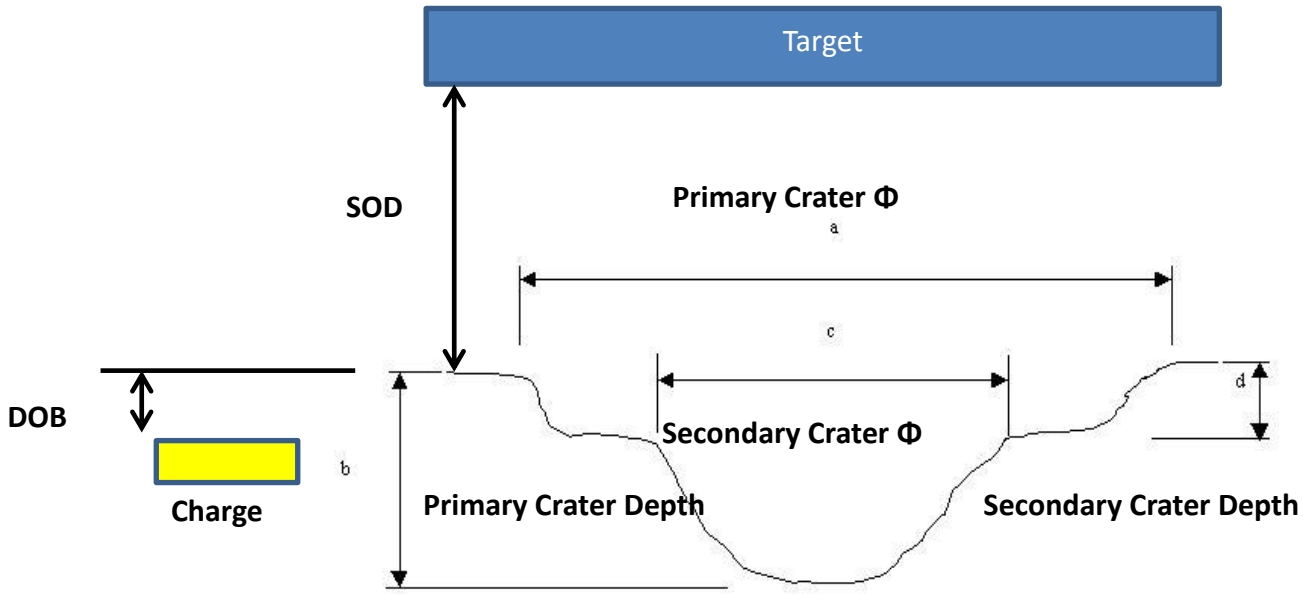

Figure 1: Buried Blast Definitions (RMSS February 2005)

DOB (Depth of Burial): The distance measured from the top of the soil to the top of the charge.

Flush buried: The top of the charge is level with the surface of the soil with the sides and bottom encased in soil.

Full scale (prototype): A cast TNT charge with a NEC of 8 kg with a D:H of 5:1 or 3:1.

Intermediate field: The surface of the soil is within 950 to 2,000 mm from the target and/or measurement point.

Near field: The surface of the soil is within 400–950 mm of the target and/or measurement point. Thus the charge is located within one to one-and–a-half times its largest characteristic length from the target. As defined by (Smith, Hetherington 1994) near field is where the scaled distance (Z) is less than 0.3 $m/kg^{1/3}$. (Held 2004) states that near field is where the scaled distance is less than or equal to 2 $m/kg^{1/3}$.

NEC (Net Explosive Content): The total explosive mass of the charge inclusive of the booster but exclusive of the detonator charge.

NIR (Near Infrared Radiation: This refers to light in wave lengths from 700 to 1,100 nm. For this work the upper end of Ultraviolet radiation wavelengths are included in this definition.

Open field: There is no reflective target above the buried explosive charge.

Scaling: Hopkinson or Similitude scaling with the full scale termed the prototype and the scaled item the model (Jones 2011a).

Shallow buried: The charge is not buried deeper than 200 mm or two-and-a-half times its vertical length. There is no published definition of shallow buried, thus this definition is proposed for the purposes of this research.

SOD (Stand-off Distance): The distance is measured from the top of the soil to the lowest point on the target.

1 Introduction

1.1 Background

Landmines and buried Improvised Explosive Devices (IEDs) are used both as offensive as well as area denial weapons. They are generally cheap, easy to place, can be difficult to detect and remain active for long periods. Since their inception and use, various active and passive technologies have been developed and used to counter the threat of these devices.

Passive protection against landmines is epitomised by the monocoque v-hull technology refined during the bush war which occurred from the 1960s to the 1980s in Southern Africa (Stiff 1986, Camp, Heitman 2014). This technology is still applied in the most successful protected vehicle systems deployed today across a range of countries from the USA to Australia. Examples of this technology are the Mechem CASSPIR MKIV, the General Dynamics (GD) Buffalo the GD / BAE Land-Systems RG-31, the Rheinmetall Dingo II and the Maxxpro. This technology provides protection against buried and side attack blast IEDs.

Although highly successful in providing protection against landmine threats, the Monocoque v-hull technology results in vehicles with a relatively high centre of gravity and concomitant particularly visible profile, which negatively affects overall tactical and strategic mobility, increases conspicuousness and reduces strategic transportability. With the advent of modern armoured steels, so-called flat-bottom hull protection systems have been developed, for example as applied in the Patria Armoured Modular Vehicle (AMV). These flat profile systems allow larger blast loads to develop and be transferred from the threat, and this results in larger local deformation and global loading, requiring additional techniques and trade-offs to ensure that survivability levels are achieved. Although partly successful in meeting protection standards, these types of protection systems require more extensive repairs and are thus expensive and technically more difficult to return to service. These systems are also more susceptible to catastrophic failure with over-match threats.

A large body of knowledge has been developed for air blast. A common thread of most of this research is that the blast load is presented as a single impulse value, either total or specific, with a peak side-on (incident) overpressure ratio using the maximum peak pressure of the shock front, rather than a dynamic force or face-on (reflected) pressure. Thus the blast load is presented as a single sum value containing the total of all the dynamic constituents. In many cases assumptions are made of a blast load, such as it being an impulsive event, to enable the impulse to be calculated.

A large number of impulse damage tables have been developed and successfully applied over many years. However, most published work identifies the presence of different constituents within the impulse load. These are normally presented as shock loading followed by a blast wind and ejecta for a buried blast load. In some cases secondary burn effects and reflected shock are noted where a near-field target is present. Limited work has been published regarding the relative contribution of these components where the authors allocate the largest contributors to the load to the ejecta and blast wind, with the shock and secondary detonation contributions generally being regarded as minimal.

Most of the blast research work done from the 1960s to the 1970s was focused primarily on nuclear and large explosive yield blasts. Much of the current research referenced on buried blast load uses either the so called ‘flyer plug’ method to comparatively estimate the blast impulse at discrete points across the loading surface or the total transferred blast load using a flyer plate (fee target) or blast pendulum (Pickering, Chung Kim Yuen et al. 2012, Braid 2002, Grujicic, B Pandurangan et al. 2007). As noted above, these methods result in singular measures of blast load in terms of impulse transferred to the target. Although there are research platforms that measure the force-time effects of blast load, these data have in most cases not been published.

In the late 1990s and early 2000s European landmine protection research was focused on using the steel pot method. This method used a wax-based explosive positioned in a steel pot and was validated according to the maximum

permanent deformation recorded (NATO Standardization Agency (NSA) 31 August 2011). The advantages of this method are that it reduces the inherent variability prevalent in buried blast loads, the mass of the vehicle can be allowed to bear against the steel pot without risk of damaging the charge and is much more comparable between test houses than prepared soil test pits. However, this type of threat loading on a vehicle is considerably different to that of a buried charge. This, combined with buried IEDs encountered in operation Enduring Freedom, has seen renewed European, Canadian and US interest and research with regard to buried blast charges and their effects.

1.2 Problem

The design of protected vehicles is based in many cases on the assumption that a buried blast load can be represented as a single discrete impulsive event. This assumption is in turn used in the development of research methods, the processing and presentation of blast loading data, computational modelling, as well as in the development of methods and theories pertaining to near-field buried blast loads and related target response, and ultimately the development of blast protection systems.

However, a near-field shallow-buried blast load is a complex event with a sequential timeline of events and interactions that generate various constituents, interacting within an unstable and changing environment that develops over time and not instantaneously nor simultaneously.

Furthermore, these constituents have different properties which transfer their loads to the blast atmosphere and if present, to the target structure at different times with different durations and different mechanisms. The presence of a near-field target affects the development of these constituents over time, increases the load transferred to the target and creates an environment that allows the formation of additional constituents, thus increasing the total blast load available and coupled into a target.

Due to the different timelines and coupling mechanisms of the blast load constituents, they can affect the dynamic response and final structural

deformation of the target. These phenomena, if characterised and quantified, can be used to incrementally improve passive and active protection systems and support the development of active landmine protection systems by identifying which phenomena occur at what time during the blast loading cycle.

However, when near-field blast loading is presented only in terms of total impulse load transferred to the target or specific impulse or impulse density, the ability to customise protection systems according to the blast load constituents is lost. The single impulse blast load value includes the effects of variables such as soil types and moisture content, diameter-to-height ratio (D:H) and depth of burial (DOB) of the charge. These variables could change the blast load constituents present as well as their morphology, thus a system that works well for deep-buried long cylindrical charges might not work for a shallow-buried pancake (right cylindrical) type blast.

The premise that the effects of shock loading are negligible and the focus of protection should be on addressing the ejecta and blast gases, which are nominally seen as the primary contributor to the total impulsive loads, has proved successful. This approach, however, ignores the possible benefits of the protection system for a blast load that is partitioned in accordance with its constituents. Lastly, it ignores the coupling time line of each constituent into the structure and how this is affected over time by the complex interactions of the soil and the near-field target in a buried near-field blast load.

1.3 Research Questions

i. What are the constituents of a near-field buried blast load?

ii. What are the temporal characteristics of the constituents of a near-field buried blast load in terms of:

    a) Start time?
    b) Duration?
    c) Quantification parameter values of each constituent over time (force, pressure, velocity, etc.)?

d) Their contribution to the total load (force) coupled into the target over time?

iii. How do these characteristics of these constituents change over time?

1.4 Research Objectives

There are four research objectives for this work. They are as follows:

i. To partition a shallow-buried near-field blast load in terms of the following constituents:

   a. Initial blast shock wave;

   b. Primary explosive gas expansion;

   c. Soil ejecta;

   d. Reflected shock waves;

   e. Secondary burn; and

   f. Other ejecta such as casing fragments.

This will be achieved through the following supporting objectives:

ii. To quantify and investigate the relative contribution to the total target-coupled blast load of each of these constituents in terms of a primary quantification measurement.

iii. To quantify the blast-loading time line for each of the identified constituents during a shallow-buried near-field blast. These data, combined with the previous quantification, will provide the morphology of each constituent relative to a common quantification parameter and time baseline.

iv. To quantify and investigate the effects of the near-field target on the morphology of the identified shallow-buried blast load constituents. It is recognised that the presence of a near field target introduces additional complexities and loading effects such as reflected shock waves, longer pressure durations, etc. This research will quantify the difference

between near-field and open-field blast loading in terms of the identified constituents and contribution to the total blast load.

1.5 Thesis Statement

A shallow-buried high explosive blast load interacting on a near-field steel target is not a discrete impulsive event but is an asynchronous amalgamation of various physical events over time. Furthermore, the morphology of these events is affected by various factors such as distance from the target, explosive mass and geometry, depth of burial, soil type and soil condition. This type of blast loading, coupled into a near-field target, can be separated into seven events. Each of these events contributes to the blast load experienced by the target and each has a different time line and method of coupling the load into the structure. The relative contribution to the load on the target of each of these events can be determined and quantified.

1.6 Delineation and Limitations

This research focuses on shallow-buried near-field blast loading as coupled into the target. Other than testing required for determining the quantity of soil ejecta expelled and the far-field buried blast pressure data to be obtained, this research focuses on a near-field full-scale (prototype) target stand-off distance (SOD) of between 400–500 mm measured from the soil surface.

The DOB for this research focuses on a prototype distance of 50 mm measured from the soil surface to the top of the charge, which is seen as typically shallow buried. This research focuses on vehicular buried mine blast threat loading and subsequent target response. Although partly applicable, this research does not directly address free-in-air blast threats.

Only buried uncased blast threat blast loads and their effects were investigated. Standard river sand was used with nominal moisture content as close as possible to NATO-specified soil parameters and granulometry (NATO Standardization Agency (NSA) 31 August 2011). The soil was un-compacted. The exclusion of casings reduced the risk of fragments striking measurement equipment and eased the measurement of the blast load constituents. However,

this precluded the quantification and investigation of the effect of the casing on the subsequent blast load. Thus steel pot type tests, explosively formed projectiles (EFPs) or shaped-charge (SC) mine threats were excluded.

The threat researched was restricted to flat right-cylindrical charges with D:H ratios of 2:1, 3:1 and 5:1. The 5:1 and 3:1 ratios were the threats of interest to South Africa and NATO respectively with regard to landmine protection evaluation. Due to initial test data (primary data) being available for scaled free-in-air blasts, the 2:1 ratio was also included.

Only cast TNT with a Pentolite 60/40 booster weighing no more than 25% of net explosive content (NEC) of the charge, PE-4 and PETN-B were used as high explosives for this research. Although progress in the development of new explosives has been made, TNT is still the primary high-explosive threat encountered during current conflicts and, as it is oxygen poor, its detonation products are more conducive to the creation and occurrence of secondary burn effects. Lastly, there is considerable published data on TNT pertaining to its detonic characteristics, which enables independent verification of the test results.

Hopkinson (also called Cube Root) (Baker 1973b) scaling for the explosive and Similitude (Jones 2011b) for the target scaling was used for this work. (Baker 1973b) notes that Hopkinson Scaling formulated in 1915, states that explosives of the same explosive and geometry detonated in the same atmosphere will generate self-similar blast waves at identical scaled distances where scaled distance (Z) is equal to the distance from the centre of the charge (R) divided by the cube root of the energy of the explosive charge (E). As the energy of the charge is directly proportional to the weight of the charge (W) these values can be interchanged leading to the common formulation $Z=R/W^{⅓}$. The scaling laws were derived through Dimensionless Analysis (Buckingham Pi Theory) (Cooper 1996a, Jones 2011a). (Baker 1973b) notes various references validating Hopkinson Scaling. These were mostly smaller charges (model) scaled from much larger charges (prototypes) as applied to nuclear blast research. Limitations of Scaling Laws are noted by (Baker 1973b) are rate dependant

effects such as viscosity in fluid or strain-rate in solids and gravity which is difficult to scale so if neglected affects results where loading and response against gravity are important. In particular for this work this is of concern for ejecta up-scaling inaccuracies.

Concomitant scaling of the target is required when scaling the explosive charge. (Baker 1973b) discussed this based on work Doering and Burhardt (1949), Brown (1957) and Baker, Ewing and Hanna (1958). The later derived law was called Replica scaling. For this work the methodology presented in (Jones 2011a) was used.

For this work the prototype (full-scale) threat is an uncased NEC eight (8) kilogram TNT charge inclusive of an eighty to one-hundred-and-twenty grams (80-120 g) gram Pentolite booster. The model was a one-seventh scale of the prototype. For one-seventh scale tests an impulse equivalent charge of PE-4 was used due to concerns about full ignition of small charges of TNT. This PE-4 charge reduced the possibility of generating secondary detonation for the model.

Only flat target plates positioned parallel with the soil surface were used to generate the near-field blast loads to be partitioned. There is a large amount of published literature on the use of simple flat plates, thus this research can be linked to and correlated with published results. With the exception of the side-on and face-on pressure data, the blast load was quantified in terms of the load coupled into the target. Effects that were too small to change the effect on the measured target response were therefore not quantified. The choice and sizing with resultant mass of the target limited the level of quantification.

1.7 Assumptions

The following assumptions have been made with respect to this work:

i. The Hopkinson and Similitude scaling laws as applied will fully replicate both proportionally and geometrically the constituents of shallow-buried near-field blast loading in accordance with the stated laws.

ii. Scaled charges of PE4 do not create conditions conducive to secondary burn or detonation.

1.8 Significance

This research quantifies the phased load contribution for shallow-buried near-field blast load events in terms of occurrence, timing, duration and the relative contribution to the total blast load for a flat non-deformable steel target. Thus blast load data are not only presented in terms of a singular amalgamated impulse value, but also in terms of a quantification measurement such as target force response or pressure over time. This insight can assist in better understanding how materials respond to blast loads and the development and validation of improved, more representative computational buried blast, load coupling and material models. It will also assist in the development of more representative and refined material characterisation methods.

A blast load time line was developed indicating when and for how long each constituent is involved in and contributes to the total blast load coupled into the target. This can be correlated with computational models assisting in the validation of these models.

The application of Hopkinson and Similitude scaling used for shallow-buried near-field blast loading was investigated with respect to the blast loading event and the blast loading time line as defined by the target response, and provided a more refined method to validate this theory. This work will assist in the enhanced application of existing protection technologies as well as the development of new protection technologies that can be applied to targets subjected to near-field shallow-buried blast loads, such as vehicles. It can assist in incrementally improving Monocoque v-hull technologies by identifying additional blast load constituents and addressing these based on the characteristics and structural coupling methods of the identified constituents.

In understanding the blast load, better methods can be used or developed to properly test or interpret protection system evaluation data. Lastly, this information is invaluable in identifying both the time line as well as the types of

active mitigation systems for protection of assets and personnel against shallow-buried near-field blast loads.

1.9 Chapter Overviews

This dissertation comprises a total of six chapters. Chapter one covers:

- An introduction to the research problem, questions, objectives and thesis statement;
- The delineation and limitations of this work, technical term definitions, assumptions and significance.

Chapter two presents the literature review as deemed by the author to be pertinent to this research. This is review is presented in terms of:

- Areas of interest,
- The buried blast process and characteristics;
- The morphology of the buried blast load and effects of quasi-constrained environment on the blast loading;
- The temporal quantification of blast loading;
- Partitioning (separating) of shallow buried blast loading components;
- Hopkinson and Geometrical Similar scaling; and
- Explosive equivalence and afterburn.

Chapter three presents the research methodology in terms of:

- The research design;
- The selected methodology;
- The data analysis;
- The method limitations and ethical considerations for this research;
- The selected methodology section that includes the description of the one-seventh scaled test rig designed and used for this work to generate the primary research data. It also includes the two secondary data test rigs whose data was utilised and the computational modelling executed and whose data was used as part of this research.

- The data analysis section presents the four sets of primary research and two sets of secondary data, how they were processed and used for this research.

Chapter four presents the processed primary and secondary data results in eight sections:

- Research Data Summary
- Modelling results;
- Shallow buried blast ejecta;
- Intermediate-field target response force-time phasing;
- Near-field target response force-time phasing
- Near Infra-Red (NIR) light emission results;
- Target assembly displacement;
- Secondary data results with scaled data comparison and verification.

Chapter five presents the analysis and discussion of the results in seven sections:

- Sections one and two present the analysis of shallow and deep buried free-field blast morphology using computational, primary and secondary data results;
- Section three covers the target force-time response including the blast-target interaction, the force-time morphology and subsequent partitioning with partitioned phased impulse;
- In section four the NIR results are discussed in terms of verifying the three loading phases and in particular possible occurrence of afterburn during shallow buried blast and within free-field and quasi-constrained blast environment. Based on literature and the analysis three shallow buried blast loading phases are proposed at the end of this section;
- Section five analyses and discusses the side and face-on pressure morphology and the partitioned phase specific impulse in terms of the proposed three blast loading phases;
- Section six discusses the differences in total and partitioned shallow buried blast loading and their phase contributions to the total quantified

load in terms of specific impulse, target response impulse and target displacement-time;

- Section seven analyses and discusses the secondary data results and compares them to the primary research results.

Chapter six concludes by summarising the research findings, discussing the problems with the work, final conclusions and suggestions for further work.

2 Literature Review

The literature reviewed and deemed pertinent for this research is presented in here in eight sections and a conclusion. These section are (1) Areas of Interest; (2) Buried Blast Processes and Characteristics; (3) Blast Load Morphology with in a Quasi-Constrained Environment; (4) Temporal Blast Load Quantification; (5) Separation of Shallow-Buried Blast –Load Events; (6) Scaling of Near-Field Blast; (7) Explosive Equivalence and (8) Afterburn.

Only reviewed published work that was directly referenced within this dissertation has been included in this chapter.

2.1 Areas of Interest

The simple buried blast landmine has been employed for many years to limit mobility of the enemy and in support of dictating the terms of battle. The landmine is both effective and cheap and thus has been and is still widely used. The landmine threat has morphed in recent conflicts into the so-called Improvised Explosive Device (IED), where conventional munitions as well as commercial and other non-conventional explosives have been employed in both the buried under-belly as well as side-attack role (NATO Standardization Agency (NSA) 23 May 2014).

The effectiveness of buried blast is due in part to its natural concealment of being buried and in part by being more detonically efficient than open-air blast (Braid 2002). A number of key parameters combine to enhance the effect and subsequent projection and duration of shallow-buried near-field blast. These parameters are explosive type, shape, the resultant placement SOD, DOB, soil type and condition, presence and shape of a near-field target (Tremblay 1998, Deshpande, McMeeking et al. 2009b).

An under-belly IED or landmine usually consists of a main charge, which in most cases is flat cylindrical in shape. The charge could have wave shaping enhancements that maximise the developed blast load due to the geometry effects. In the case of Explosively Formed Projectile (EFP) type mines a concave platter is placed on top of the main charge. This results in a slug

moving at around 1,850 ms^{-1} which accelerates ahead of the blast, penetrating the vehicle structure and allowing the subsequent blast gases to easily enter the vehicle (Baillargeon, Sirios et al. 2005).

A booster is used to initiate the main explosive charge. The booster is normally placed centrally at the bottom of the main charge. This ensures that the detonation wave is aimed upwards towards the soil surface and the target. Some mines can have more than one booster placed within the main charge, usually radially with the purpose of providing initiation of the mine if it is lifted which prevents easy removal (Canadian International Demining Centre c.a. 2001). A mechanically or electronically activated initiator utilising a small primary explosive charge is placed within the booster. When activated this device detonates, setting off the booster and subsequently the main explosive charge. All these items are housed within a casing to allow robust handling and deployment. The material can be steel or plastic. In some mines the casing or parts thereof are deliberately utilised to generate large penetrative fragments, as with an EFP. All these elements can be modified to enhance certain effects or to make the device more difficult to detect or both.

The primary research areas of interest are as follows:

i. Detonics
ii. Blast Loading
    a. Free-in-air
    b. Buried
    c. Far-field (no target present over charge and $z > 0.5$ m/$kg^{1/3}$)
    d. Near-field (target present and $z < 0.5$ m/$kg^{1/3}$)
    e. Shock physics
    f. Blast load morphology
        - Pressure (side-on)
        - Pressure (face-on)
        - Force
    g. Impact physics:

- Load coupling (Fluid Structure Interaction (FSI))
- Stress/shock wave generation and propagation
- Impulsive loading

h. Materials behaviour when subjected to high strain rate loading
   - Material behaviour
   - Materials testing

iii. Blast scaling

a. Blast load scaling

b. Structural scaling

iv. Computational modelling covering all of the above areas, but in particular:

a. Detonic models

b. Material models

c. Soil models

d. Euler/Lagrange coupling

e. Fluid Structure Interaction (FSI)

2.2 Buried Blast Process and Characteristics

Buried blast temporal phasing has been noted by Bangash (1993) and quoted by (Deshpande, McMeeking et al. 2009b); the authors list three temporal phases, namely detonation and soil interaction, expansion of gaseous detonation products and the development of soil ejecta. Following this, a buried blast loading process begins with the initiation of the explosive device, usually by some form of electrical, electronic, mechanical or combined mechanism. This initiator, usually a small primary explosive charge of a few grams, in most cases detonates a booster charge that has enough shock energy to set off the main charge. In some cases the primary charge can be detonated directly from the initiator.

The explosive type, NEC (Net Explosive Content), shape and initiation point all affect the detonation of the main charge and the subsequent blast development. The main charge can be almost any form of high- or low-order explosive; however, for landmines it is generally a high-order explosive in a flat right-

cylindrical shape. Some land mines use the charge geometry and casing as wave shapers to enhance the blast effect (Canadian International Demining Centre c.a. 2001). The detonation of the high explosive is characterised by a self-sustaining shock wave that moves radially outward from the initiation point at a high velocity with great localised pressure. As defined in (Cooper 1996a) a detonation is "*a shock wave with a rapid exothermic chemical reaction occurring just behind the shock front*". The shock front velocities are stable and asymptotically increase with increasing charge diameter when axially detonated. These velocities and pressures are characteristics of the explosives. For TNT the velocity of detonation (VOD) is 7 km/s and has a Chapman-Jouget pressure (P_{cj}) of 30 GPa (Cooper, Kurowski 1996). The Chapman-Jouget pressure (P_{cj}) is defined in detonation theory as the steady-state of the detonation products behind the detonation front. The detonation front has a higher pressure referred to as the Von Neumann spike however due to relatively short duration its effect is ignored in simple detonation models as the energy within this detonation zone is considered to be much smaller than that contained in the detonation products (Cooper 1996a). The gas expansion (rarefaction) wave behind the detonation front is also characteristic of the explosive and is affected by physical confinement and thickness of the charge with increases in both resulting in increased rarefaction wave pressure (Cooper 1996a).

Due to the flat geometry of a general landmine charge, the detonation shock wave impacts the upper surface of the charge and then runs laterally outwards along the surface of the charge at approximately the detonation velocity. For an 8 kg TNT NATO threat mine (NATO Standardization Agency (NSA) 31 August 2011), and ignoring higher detonation velocities of the booster charge, it takes a calculated 8.6 µs for the detonation shock to reach the top of the charge and 19.3 µs to reach the radial edge. It takes around 4.2 µs for the detonation wave to reach the bottom of the charge. A key characteristic is that the detonation process is not instantaneous across the surface of the explosive, but takes up to 20 µs to detonate across the entire surface.

Due to the high pressures involved, the detonation shock wave transmits large amount of energy to the surrounding soil, generating a shock wave that moves out radially as the detonation process takes place. If the charge has a flat right-cylindrical shape, the generated vertical shock wave is not planar but partially spherical in shape as the time of arrival (TOA) on the front face is not the same as discussed above. In the case of a NATO surrogate landmine, due to the position of the initiation point, the detonation shock from the booster will impact the soil on the bottom of the charge first, and for the top of the charge it will run radially outwards, arriving outer bottom edge of the charge before the detonation wave reaches the outer top edge. This leads to a detonation front that is directed upwards due to the longer detonation path dictated by the asymmetric detonation point. The initial loading transfer from the charge to the soil is temporally asymmetric when compared to spherical charges, which are initiated centrally. This will contribute to the shape and velocity of the blast front that develops and is moved towards the target.

The interaction of the detonation shock on the soil is complicated as soil is a particulate material with varying properties of granulometry, compaction, moisture content and base material. Each of these characteristics affects the development of the buried blast-load, how it evolves, the transfer of the developing blast-load to the target and the coupling of the blast into the target.

When the detonation shock wave reaches the edge of the charge it partially reflects at the interface due to the physical boundary and the impedance mismatch between the soil and undetonated explosive as well as detonated explosive products (Braid 2002). Impedance refers to the shock impedance of a material which is defined as the product of the material density and the shock velocity (Cooper 1996a). When there is an impedance mismatch between two materials the shock pressure will increase when moving from a low to a high impedance material and will reduce when going from high to a low impedance material. There is also a reflected pressure (rarefaction) wave back into the material when the shock is moving from a high to a low impedance material (Cooper 1996a). (Deshpande, McMeeking et al. 2009b), quoting Bangash 1993, note that for the detonation and soil interaction there are three interaction zones

in the soil around the detonated charge. Bangash's work was based on buried spherical charges that were centrally detonated, thus the soil zones are defined as ratios of the charge radius, Re. The effect of a flat cylindrical explosive shape on these zones was not discussed by the authors.

From Figure 2 the first zone (Zone I)is spatially defined as two to three charge radii (Re) in thickness and is characterised by a shock and load transfer that is independent of soil properties due to the extremely high detonation pressures and temperatures. The second zone (Zone II) extends outwards from three to six charge radii and is characterised by irreversible crushing and plastic deformation of the soil. The last zone (Zone III) extending from six charge radii outwards is characterised by normal elastic behaviour with deformation reversibility and soil stress wave transmission mechanisms. It is clear from these size definitions that there is great variability with regard to the effects a buried charge has on the surrounding soil.

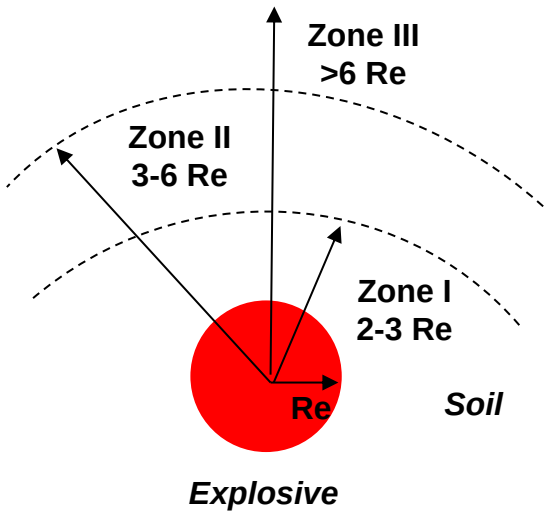

Figure 2: Bangash Soil Interaction Zones for Buried Blast (Deshpande, McMeeking et al. 2009b)

Applying this to the standard NATO 8 kilogram flat cylindrical mine threat prototype (full-scale) and one-seventh scale model charges gives the dimensional results shown in Table 1: Buried Blast Zone Characteristic (Re) **Dimensions** (Deshpande, McMeeking et al. 2009b)

For charges buried at depths shallower than 2 Re to 3 Re the soil cap loading is characterised by extremely high shock pressures and temperatures and resultant non-linear interaction. The cap loading is temporally and radially distributed from the vertical detonation axis.

Table 1: Buried Blast Zone Characteristic (Re) Dimensions (Deshpande, McMeeking et al. 2009b)

Zone Start	Characteristic Parameter	One-Seventh Model (Scaled Charge)		Prototype (Full Scale)	
		Radial Distance (mm)	Vertical Distance (mm)	Radial Distance (mm)	Vertical Distance (mm)
I	**2 Re**	36	12	270	90
II	**3 Re**	54	18	405	135
III	**6 Re**	109	36	810	270

The role and contribution to the developing blast and resultant load from the detonation-reflected shock going back into the developing blast cloud was not discussed in the reviewed references. Based on (Needham 2010) this shock continues to reflect within the high pressure and temperature detonation products of the developing blast. This phenomenon is visible in an unconstrained free-in-air blast, and it is assumed that with the boundary constraints of the containing soil, the continued reflections of the shocks will be facilitated while the blast expands in all directions. The direct contribution of these shocks to the blast load in terms of impulsive loading is minimal, but they would keep the detonation products energised through repeated interactions as the blast develops (Eridon, James. Zelenik,Tom. Bogalev, Alex. 2014). The authors note that the blast load transfer to the soil is extremely quick but does not quantify what this means. This statement appears to be based on an unreferenced assertion in the paper and states that explosives complete both pressure and change in volume work over very short distances. The authors go on to state that the motion of the soil is delayed due to its large inertia. This

work was based on tests where the charge appears to be relatively deeply buried compared to this dissertation's focus. Although no burial depth dimensions were given the hypothesis requirement of not having blast breakout was noted and is indicative of deeper buried blast. Breakout is characterised by the release of high-energy gases between the sections of the soil cap being pushed upwards, thus if not present the effects of the non-linear loading of the soil cap should not be present.

According to (Deshpande, McMeeking et al. 2009b, Braid 2002) compression, shear and Rayleigh waves are generated in the soil by the detonation. The compression and shear pressure waves generated in the soil loses amplitude exponentially, while the Rayleigh waves that move over the surface of ground also lose amplitude exponentially but at a markedly slower rate. Typically at distance of 20 radii from the charge the shear and compressive pressure wave amplitudes are only 2.5% of what they were at the explosive charge edge, whereas the amplitude of the Rayleigh wave is still 22% of its initial amplitude at the charge edge.

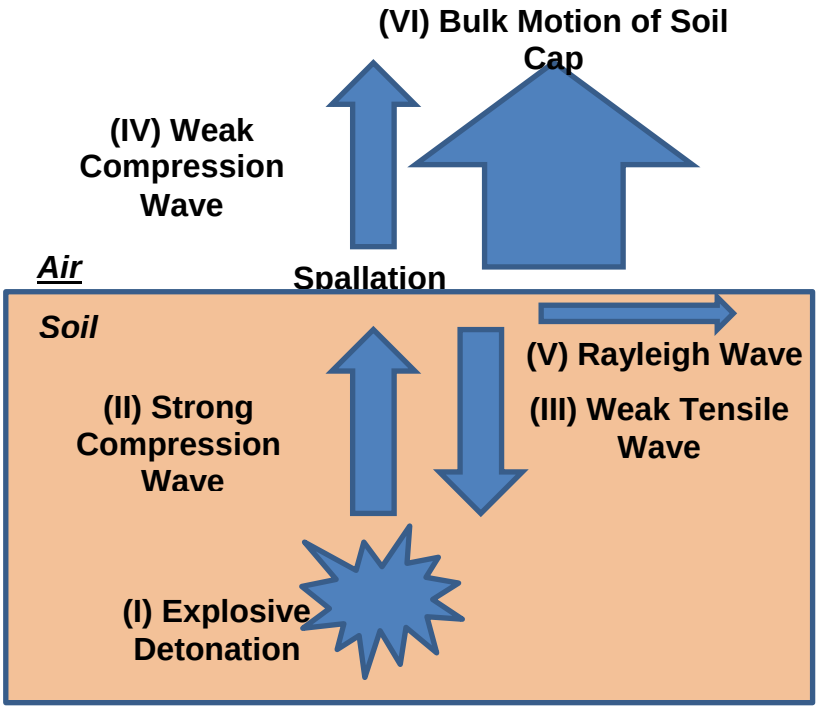

Figure 3: Deep Buried Blast Loading Process From Various References

From Figure 3, for deep-buried charges, where deep is defined as larger than Bangash's (Deshpande, McMeeking et al. 2009a) defined Zone II, on reaching the soil surface the detonation shock wave reflects at the air-soil boundary, sending a weak compression shock into the air and a tensile wave back into the soil (Deshpande, McMeeking et al. 2009b, Tremblay 1998, Braid 2002). According to (Deshpande, McMeeking et al. 2009a), referencing Bergeron, the weak reflected shock is due to the large impedance mismatch between the soil and air. This weak shock wave moves radially outwards close to the speed of sound. The shock reflection causes spalling of the soil surface and subsurface. This is to be expected as the cohesion of soil is extremely low. This is followed by the bulk motion of the soil cap and immediate surrounding surface towards the target. The velocity of this soil cap varies based on DOB from as low as 250 m/s for deeper buried charges (McDonald 2013a) to as high as 4,000 m/s for flush-buried charges (Snyman 2012, Freitas, Bigger et al. 2014). The big difference in velocity can be due to the soil interaction zones as defined in (Deshpande, McMeeking et al. 2009b) and results reported in (Freitas, Bigger et al. 2014) and (Eridon, James. Zelenik,Tom. Bogalev, Alex. 2014).

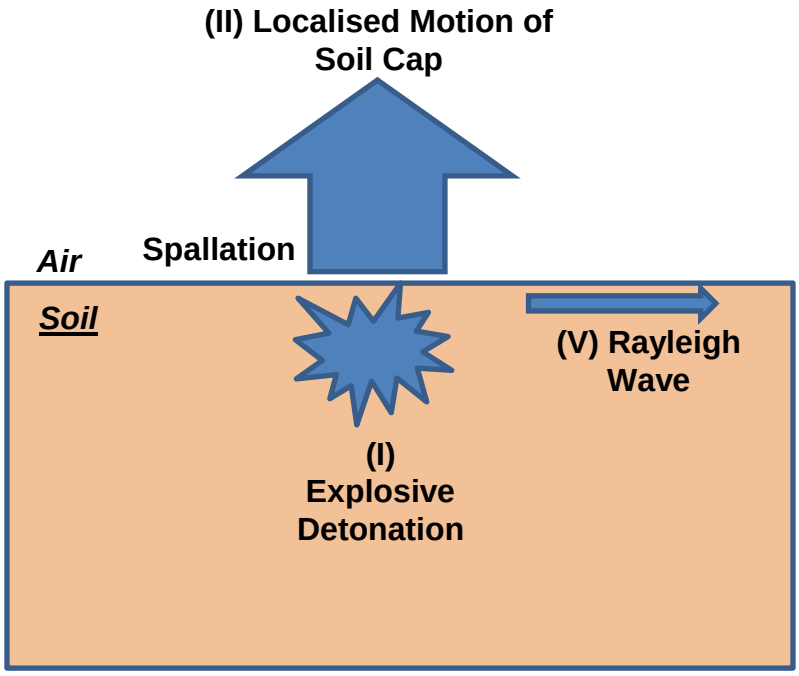

Figure 4: Shallow Buried Blast Process From Various References

From Figure 4, for shallow-buried charges the soil cap is completely overwhelmed by the initial detonation shock energy, being almost instantaneously crushed and accelerated upwards as the path of least resistance/inertia, resulting in higher blast front velocities. The thinner the soil cap the higher the resultant blast front velocities. For deeper buried charges this high-pressure crushing effect is constrained within the thicker and heavier soil cap, resulting in a much slower upwards acceleration and resultant blast front velocity.

The detonation shock both transmits into the surrounding soil as well as reflects back into the blast cloud that develops as a result of the detonation of the explosive. The strength of these shock interactions is dependent on both the explosive and the soil (Cooper 1996b). The type of explosive dictates the strength of the shock through the detonation velocity and detonation pressure, while the charge geometry governs the amount and direction of the detonation and blast energy released to the soil and towards the target. Soil moisture content, bulk density, granulometry and compaction dictate the impedance parameters which will govern the shocks reflected and transmitted by the soil and the effect on the pressure that develops after the detonation and initial blast release through the ejected soil cap.

The detonation shock reflects from the soil-air interface into the developing blast gas cloud (Braid 2002). Nothing could be found in the literature that quantifies the contribution of the loading of these gas cloud shocks to the blast load and the load coupling into a near-field target. These shocks do, however, serve to energise the detonation products (Mostert July 2015).

Based on the sub-surface of a shallow-buried charge in the upwards direction, the transmitted soil shock reflects at the nearby air-soil boundary, reflecting a tension wave back into the soil while transmitting a weak compression shock into the air (Braid 2002). The strength of the reflected shock that precedes the blast front is based on the depth of burial as soil can be seen as a granular material and thus reduces the strength of the shock (Gelfand, Silnikov 2004). In deeper buried charges the weak air shock propagates towards the target at

around the speed of sound (McDonald 2013a). The air-soil interface reflection results in break-up of the soil cap by the interface stresses generated by this process, supported by the limited tension cohesion of the soil cap.

The post-detonation pressure builds up rapidly with chemical detonation reactions, which are energised by the reflecting shock waves and constrained by the soil sides and cap (Braid 2002). The products of the detonation form a gas bubble (Ramasamy, AM Hill et al. 2009, Braid 2002, Bergeron, Coley et al. 2001, Tremblay 1998, Grujicic, Pandurangan et al. 2008) that expands in all directions, but primarily upwards due to the broken soil cap and lower inertial resistance combined with the containment of the surrounding soil. In some cases the blast gases push ahead of the soil cap forming the irregularly shaped 'fingers of fire' (Joynt 2011). These expanding gases continue upwards as a bubble at around 1,000–2,000 m/s for shallow-buried explosives (Snyman 2012) and at a slower velocity of between 250–500 m/s for deep-buried charges (McDonald 2013b).

This blast front is mostly made up the soil cap as well as possibly some surrounding soil that is entrained by the expanding high-velocity gas bubble. The soil cap accelerates and thins out as the blast front expands upwards and outwards (Deshpande, McMeeking et al. 2009b). The velocity of the soil cap is around 2,000 m/s and initially grows and then slows down quickly – for the near field the velocity is mostly constant for a large portion of the travel distance to the target. The blast cone that develops is said to vary in angle between 45–51 degrees from the centre line (Braid 2002) and is affected by soil parameters such as moisture content (Clarke, Fay et al. 2014) and granulometry (Cooper 1996b). This cone angle is reported to vary up to 120 degrees by (Ramasamy, AM Hill et al. 2009); however, it appears to have been obtained from computational models rather than empirical data.

For deeper-buried charges the blast front velocity is slower than the speed of sound and therefore the weak reflected shock wave that precedes the blast front strikes and reflects off the target and returns into the upcoming blast front (McDonald 2013a). This weak shock wave does not appear to have any effect

on the blast front, which continues upwards to strike the target with resultant force coupling taking place. As the blast loading processes are obscured, the post-impact blast load interactions are not easy to define nor are they clear.

It is thought that as the blast load front is subsonic, there are limited low-level shock load interactions between the target and the initial weak detonation shock wave, and that the blast load is primarily transferred as a high-speed impact of the ejecta front with subsequent fluid-structure coupling of the gas bubble and entrained soil (Ramasamy, AM Hill et al. 2009). Deeper-buried charges also appear to have an inversion effect whereby the soil closer to the charge is subjected to a higher energy transfer from the detonation shock and the expanding gas cloud, and these penetrate and push aside the top layer of the soil cap and then go on to strike the target. The occurrence of this effect is dependent on the DOB and the distance to the target. For closer targets this will not occur and the upper soil layer will impact first (McDonald 2013a).

For shallow-buried charges the sequence of events is similar, but the blast front velocity is much higher. The blast front speed is highly dependent on the occurrence of early gas break-out which, if it materialises, results in higher blast front velocities of around 2,000 m/s. For the DOB range of interest in this study without break-out, the blast front velocity is around 1,000 m/s (Freitas, Bigger et al. 2014, Snyman 2012). With primary wave velocities in loose soil of around 400–1,200 m/s (Mavko Unknown) the initial wave forms reach the surface at 40–250 µs after detonation. Although (Cooper, Kurowski 1996) note that the heaving of the soil only starts after the soil cap relief waves have reached the gas bubble, video analysis suggests that the soil layer starts moving with the initial weak air shock reflection, or no later than about 50 µs after the first air shock wave forms at the soil surface for scaled buried blast (McDonald 2013a). Thus for shallow-buried charges the blast front catches the air shock wave within about 10–25 µs or within 20–30 mm from the soil surface.

The blast front shape from a buried charge is not flat but is curved and is characterised by irregular and apparently random streams called jetting (breakout). The source of these jets is not definitely known and is still being

researched. One theory is that hot spots develop within the explosive during the detonation and post-detonation processes (Milne, Bradley et al. 2014). Current theories by (Milne, Bradley et al. 2014) relate this to coalescence of hotspots within the early post detonation blast development, which could be related to containment of the charge by the surrounding media.

The energy release and shape of the generated blast wave is dependent on the shape of the charge. Most fundamental theories are based on spherical charges (Kinney, Graham 1985, Baker 1973a, Cooper 1996c). For non-spherical charges such as cylinders, most initial research work has been focused on long cylindrical charges such as those found in bombs or missile warheads (Swisdak 1975, Baker 1973a). The threat focus for this work has a very small length-over-diameter (L/D) ratio varying between 0.2 and 0.5 mm (Cooper, Kurowski 1996). Work by Cook 1971 presented in (Cooper, Kurowski 1996) notes that a cylinder initiated longitudinally along its centre line will detonate initially in a spherical manner and then at some longitudinal distance reach a maximum radius of curvature and continue to propagate down the charge column with this curvature radius as the detonation front. As the diameter is increased the radius of curvature increases, moving the detonation centre (forward) point longitudinally out. However the ratio of the detonation front curvature and the charge diameter remains constant for each type of explosive. This radius of curvature ratio changes according to the explosive type; however, for the range of L/D ratios applicable to landmines (<1) all the explosive test data including TNT and RDX have the same radius of curvature (1:1). The authors note that the work done at the end of the charge in terms of a function based on the indentation of a plate, increases as the L/D increases, that is with decreasing D:H ratio. This work appears to reach a maximum at a L/D of 2. This implies that a threat with similar charge mass but a larger diameter to height ratio will result in lower work being done on the target.

(Cooper, Kurowski 1996) also note that the longer the sides of the charges the larger the losses are. (Baker 1973a), referring to work by Lindberg and Firth 1967, states that blast loads from planar charges such as sheet explosives have longer durations than spherical charges but lower initial peak

overpressures. (Baker 1973a) notes that the approximation presented is only applicable close to the blast source, and that for large target distance ratios (R) to biggest characteristic charge dimensions (L), the blast fronts become spherical and asymmetric geometry effects are reduced. This implies that for flat cylindrical charges the blast duration is longer with lower peak pressure when compared to a similar spherical charge mass.

Although not explicitly stated, these L/D data in (Baker 1973a) are assumed for free-in-air detonations and do not accommodate the effects of containment by a media such as soil. With no clear definition of the required R/L ratios, these relationships for the scaled distances being researched here are not definitive but indicate that lower peak pressure and longer durations can be expected for pancake-type charges. Typically for most land mines the small L/D ratios are normally inverse and presented as a diameter-to-height ratio (D:H).

2.3 Blast Load Morphology within a Quasi-Constrained Environment

The presence of a target over the buried blast creates a quasi-constrained environment which traps the blast between the target and the soil only allowing pressure release laterally around the target. As the blast front is moving at several times the speed of sound of the surrounding air it forms a shock front that appears to be attached to the front of the blast wave (Cullis 2001).

For a shallow-buried blast the blast front with the precursor bow wave shock moves upwards towards the target. The precursor shock impacts first and is followed by the thinned soil cap impact and then the blast wind (Deshpande, McMeeking et al. 2009b). At the same time entrained soil is fed upwards by the rapidly expanding detonation gases (Ramasamy, AM Hill et al. 2009). The shock front load will couple almost instantaneously to the target, whereas the subsequent soil and expanding gas cloud will transfer loads with respectively increasing durations as they are arrested and stagnate against the target.

The shock wave impact results in a weak reflected wave off the target back into the high-pressure gas cloud and soil behind the blast front (Proud 2014). As it is a weak shock reflection it remains a compressive wave. On reaching the crater

and soil surface another reflection occurs back upwards, with each reflection having decreasing peak overpressures (Smith, Hetherington 1994).

In addition to the normal reflected shock waves, expansion shock waves reflect off the edges of the target back into the blast ejecta cloud as the blast front progresses upwards around the target (Smith, Hetherington 1994). Although it adds to the general complexity of the near-field shallow-buried blast, the contribution to the total energy of the blast loading seen by the target from these normal and transverse reflected shocks is unknown.

The expanding gas cloud is constrained by the target and along with the soil surface creates a quasi-constrained environment that results in longer pressure duration. The near-field target stagnation surface increases the load seen by the target (Smith, Hetherington 1994). This loading is differentiated from the side-on pressure impulse and is termed reflected pressure. It is noted to be between 8 and 20 times higher than side-on pressure (Smith, Hetherington 1994, Baker 1973a). Theoretically a reflected pressure 8 times higher is predicted for strong shocks and this discrepancy with the test results is ascribed to aspects within the near field of a blast.

In addition to constraining the blast and generating higher and longer blast wind pressures, the soil is understood to have a focusing effect on the blast gases (Braid 2002), thus further increasing the average load pressure and duration seen by the target. However, the soil layer above the charge lowers the peak overpressure generated by the detonation, and the thicker the soil cap over the charge the greater the reduction in peak pressure (Uribe, Poveda et al. 2011). Conversely, the impulse increases with DOB. However, as noted by (Zakrisson, Wikman et al. 2008), increased impulse from deeper DOB does not necessarily equate to increased damage in the form of larger dynamic and permanent deformation.

For quasi-constrained blast pressure, measurements show that the pressure load appears to be phased with an initial rapidly rising peak followed by a more gradual but longer duration phase attributed to the gas pressure (Syngellakis 2013). There can also be several peaks superimposed on the so-called gas

pressure phase, and these are attributed to reflections from the initial blast over-pressure interaction with the target. This phenomenon is supported by (Smith, Hetherington 1994) who present similar pressure-time histories for constrained but vented blast loads, and they use broad assumptions to obtain simplified pressure load estimations. This phasing in the blast pressure morphology results in a phased target loading response. This phased load morphology is also present in incident (side-on) pressure time histories for free-in-air detonations.

Further work by (Held 2004, Tremblay 1998) postulated that a near-field blast load is not uniformly distributed over the target. They indicate that a maximum transferred impulse density occurs towards the centre and decreases outwards. This is supported by data from (McDonald 2013a), which indicate that areas of higher pressure can occur further out from the target centre. This was ascribed to the jetting process noted earlier. This phenomenon is not noted by (Braid 2002), who uses Trembaly's proposed blast-load equation.

The initial weak shock front impact initaites stress waves that move through and radially outwards in the target material from the impact point at the nominal speed of sound of the materials. The blast cap ejecta impacts immediately after the bow wave or precursor shock, and is pushed out laterally across the target as the expanding detonation gases push and stagnate against the target. The stress waves in the target quickly form complex reflections within the target due to the high speed of sound of steel combined with varying thicknesses of the target structural members (Grujicic, B Pandurangan et al. 2007).

If there is a near field that is partially constrained between the crater, soil surface and near-field target, conditions conducive for the formation of secondary burn will develop (Edri, Felgun et al. 2012). It is postulated that the reflected shock waves moving through the detonation gas cloud noted previously could assist with initiating secondary burn of the detonation by-products of poorly oxygenated explosives, resulting in an additional pressure increase from this reaction (Cooper 1996c, Cooper, Kurowski 1996).

2.4 Temporal Blast Load Quantification

The vast majority of research work presents blast loading in terms of impulse. Over the course of time empirical damage tables associated with impulse have been developed (Cooper, Kurowski 1996, Baker 1973a, Smith, Hetherington 1994). A variety of methods have been used to measure impulse. These include overpressure from Bikini gauges or side-on pressure gauges (pencil probes), horizontal and vertical blast pendulums as well as simple flyer plates (Held 2004, Smith, Mostert et al. 2008, Bonorchis, Nurick 2010, Zakrisson, Wikman et al. 2008). Most of the work published from the 1950s through to the 1970s and early 1980s was based on large blasts, and thus focused on over-pressure and complex shock waves derived from large equivalent blasts. From the mid-1980s the focus shifted to near-field buried blast loading and its effects and the development of suitable test rigs.

Various authors (Swisdak 1975, Tremblay 1998, Beetge 2008) have developed empirical formulae to predict near-field shallow-buried blast loading in terms of impulse. Many authors, including (Tremblay 1998), use the work by (Westine, Morris et al. 1985) based on blast plugs. These are similar to blast plates, but estimation of the transferred blast impulse is based on the jump height and/or velocity of a number of measurement plugs. This method, developed in the 1950s as part of nuclear blast research (Baker 1973a), uses several measurement plugs, which enables the blast loading variation across a surface to be relatively quantified. Unfortunately this paper is export controlled and thus cannot be critically evaluated.

Over the past 15 years there has been a large increase in research on buried blast loading and its quantification. However, very little published work could be found regarding the empirically measured morphology or temporal measurement of reflected pressure or the resultant load force-time target response. Although full-scale test rigs that measure the force-time response of a buried blast exist (Snyman, Reinecke 2006, Wasmuller 2008), most published data are for scaled blast loading. Generally, published scaled methods use piezoelectric force washers fitted behind the target (McDonald 2013a, Clarke, Rigby et al. 2015), while full-scale methods employ strain-based force load

cells. (Cheesman, Tilbury et al. 2014, Clarke, Rigby et al. 2015) developed a test rig using a matrix of target plates each mounted against force washers and employing a special damping mechanism to reduce natural frequency effects. This rig was developed for free-in-air side-blast applications. (Clarke, Rigby et al. 2015) developed a method to quantify near face-on pressure time distributed across a target face using a matrix of Hopkinson bars positioned across the target face. A Hopkinson bar is a simple steel bar measurement system that uses a strain gauge to measure the stress waves generated by a blast impact and then infer the pressure-time curve of the blast (Cooper 1996a). This method, however, relies on computational modelling to correct for stress wave dispersion effects to obtain the applied target face pressure. Although this rig also measures the global target force-time response, the data obtained have not as yet been published.

As current blast quantification devices use mechanical systems to quantify blast loading, the blast load must be considered in terms of its positive phase duration compared to the natural frequency of the quantification system. (Smith, Hetherington 1994) defined three loading types or regimes based on the product of the blast duration (t_d) and the natural frequency of the system in radians (ω). These loading types are impulsive ($t_d\omega<0.4$), dynamic ($0.4<t_d\omega<40$) and quasi-static ($t_d\omega<0.4$). Based on the US Department of Army Technical Manual (1991), these loading types can also be presented in terms of the ratio of positive phase load duration and the time taken to reach maximum displacement (t_m) as follows: impulsive $t_m/t_d > 3$, dynamic $3 > t_m/t_d > 0.1$ and quasi-static $t_m/t_d < 0.1$. This work unfortunately does not state whether the impulsive or dynamic loading response of the structure can be phased.

2.5 Separation of Shallow-Buried Blast-Load Events (Partitioning)

In line with limited published temporal target force and pressure responses, only limited data has been presented on the phasing of the blast load and the relative contribution of these phases to the total load transferred into the target. The greater proportion of the blast load has been generally ascribed to the blast

wind (Cullis 2001) but this is for free-in-air blast. Scaled blast research presented by (Fourney, Leiste et al. 2005) states that the shock loading is negligible and the blast wind only contributes around one-third of the total blast load in terms of total impulse, with the rest of the load coming from the soil ejecta. This conclusion appears to be based on the difference in impulse between flush or surface blasts and buried blasts, and thus does not evaluate the two loading mechanisms from the same test. In addition, the target plate mass is relatively great compared to the expected blast, and the video framing rate is relatively slow, thus tending to smear out the loading phases. As the transferred impulse load was calculated from the total jump height and the calculated impulse is dependent on gravity, the scaling models applied are distorted (Jones 2011a). Despite these quantification limitations, this position is supported by work done by (Freitas, Bigger et al. 2014) using side-on pressure to quantify the blast load from shallow-buried detonations.

According to (Ramasamy, AM Hill et al. 2009), the blast is also divided into two similar main components of blast and soil ejecta. Phasing of the two loading mechanisms is introduced by the authors, but the source of the data is not disclosed. They assert that the blast loading occurs first, followed by the soil ejecta which is driven by entrainment onto the crater boundary creating a hollow blast cone. The loading phase of the soil ejecta lasts from five up to ten times longer than the blast wind phase. The blast wind loading from typical landmine threats is stated to occur from 5 to 10 ms after detonation, followed shortly thereafter by the soil ejecta phase, which lasts from 50 to 100 ms, giving a total blast load duration of about 55 to 110 ms. The authors state that the detonation shock wave is reflected and attenuated by the soil cap. The process described excludes the soil cap loading as well as the effects of confinement and target reflections on the blast load transferred to the target.

(Deshpande, McMeeking et al. 2009b), quoting Bangash 1993, note three temporal phases with a buried blast as follows: detonation and soil interaction, expansion of gaseous detonation products and the development of soil ejecta, with the last two contributing most to blast loading.

2.6 Scaling of Buried Near-Field Blast

Scaling of blast loading was first ascribed to B. Hopkinson in 1915, also called Cube Root scaling (Baker 1973a), and has been extensively researched, used and expanded to accommodate different applications and uses. Hopkinson's scaling law states that: "*Self-similar blast (shock) waves are produced at identical scaled distances when two explosive charges of similar geometry and the same explosive, but of different size, are detonated in the same atmosphere*". This and related laws such as Sachs' law, are universally accepted, with much of this theory being validated under specific conditions, including for buried blast (Swisdak 1975).

The key parameter of Hopkinson scaling is scaled distance (Z) after (Baker 1973a), which is simply the ratio of the distance from the centre of the charge to a specific distance away and the cube root of the mass or the energy of the explosive charge. This dimensional parameter has the units of m/kg1/3 and is important in that as blasts with the same scaled distance will have the same blast over-pressure ratios, scaled time of arrival and scaled positive pulse duration, etc. (Cooper 1996a). For this work the scaled distance is presented in Table 2. Charges with different D:H ratios are shown, which highlight the difference of the scaled distance Z due to ratio changes on the charge dimensions and thus the distance parameter R, when maintaining other similitude scaling parameters of charge mass, DOB and SOD.

Table 2: Scaled Distance for Shallow-Buried Research Threat Test Conditions (DOB 50 mm)

Scaled Distance (Z)	DOB (mm)	SOD (mm)	D:H		
			2:1	3:1	5:1
$Z_{(500)}$ m/kg$^{1/3}$	50	500	0.305	0.298	0.291
$Z_{(1400)}$ m/kg$^{1/3}$	50	1,400	0.755	0.748	0.741

However, as noted above, most of the published blast scaling work has been done for up-scaling of charges to simulate nuclear blasts at larger scaled distances rather than down-scaling to represent small buried charges with small scaled distances.

Of as much importance as blast scaling is the concomitant scaling of the target and its response. Scaling of the target and its response, called geometric similarity or similitude scaling (Jones 2011a), was according to (Jones 2011a), first presented in 1949 by Doering and Burkhardt. These laws have been expanded to include scaling of elastic structures with small and large elastic and plastic deformation (Baker 1973a). Of importance in the case of these laws is that geometric similarity must be maintained between the prototype and model, which is termed replica scaling by (Baker 1973a). Many original scaling law formulations were derived to take differences in atmospheric conditions into account; however, as this research is based on constant atmospheric conditions, these scaling law expansions are not discussed here.

A summary of scaling relationships from various sources is presented in Appendix A. The scaling relationship for reflective (face-on) impulse was not found in any of the references reviewed and was derived by the author from principles presented in (Cooper 1996a, Jones 2011a) and verified with (Snyman 2015). These scaling parameters are based on the scaling ratio or numerical ratio between the prototype (full-scale) and the model charges. This ratio is then applied to all other structural and test condition dimensions applicable to this research. For this work the scale factor is presented as β and is equal to the prototype parameter divided by the model parameter.

Scaling of crater diameters is also presented in (Cooper 1996a), where it is noted that for surface bursts Hopkinson scaling is approximated, but does not apply to buried blasts. Alternative crater scaling parameters are also proposed in (Cooper 1996a) based on work by Baker, Westine and Dodge (1973) using empirically based correction parameters. These laws do not, however, predict other important crater geometries of importance for blast loading effects such as depth and internal profile. The crater sketches in (Cooper 1996a) are indicated for a side view, and the craters have a funnel shape with two diameters. This phenomena is not discussed here.

There are various limitations to these scaling laws (Baker 1973a, Cooper, Kurowski 1996, Jones 2011a), the main one of interest to this work being

gravity, which cannot easily be scaled. Some work with blast under scaled gravity is referred to in (Braid 2002). When similitude scaling is used gravity must be increased by the inverse of the geometric scaling factor. This would impact on experiments that are heavily influenced by gravity such as ballistic trajectories and vertical blast pendulums or flyer plates. Another practical limitation is that explosive charges cannot be scaled reliably below their critical diameters (Cooper 1996c). For TNT this varies between 3 to 12 mm (Cooper, Kurowski 1996).

2.7 Explosive Equivalence

Explosive equivalence is a general explosive concept where the output of an explosive is compared to another or baseline explosive. In many cases this baseline explosive is TNT and is presented in terms of mass equivalence. Explosive equivalence can be for a range of different blast output parameters such as specific energy, overpressure (shock), positive phase duration, impulse (specific side-on pressure), transferred/coupled impulse (Weckert, Anderson September 2006), etc. (Baker 1973a, Swisdak 1975, Cooper 1996a). These equivalence factors are not necessarily the same for each parameter and, as reported by (Swisdak 1975), do not necessarily scale according to Hopkinson's scaling rules. Equivalence is required, as one-seventh scaling of 8 kg TNT results in a TNT charge mass of 23.3 grams. Although this small charge diameter size is above the critical diameter for TNT at 36 mm for a D:H of 3:1, the difficulty of ensuring reliable ignition of the small charge without a suitable booster requires that a suitable plastic explosive be used.

2.8 Afterburn

(Edri, Felgun et al. 2012) notes that afterburning is a complex chemical process that occurs when the detonic products react with the surrounding air containing oxygen under conducive conditions. These conditions are the presence of available oxygen, mixing of the oxygen and a temperature above the ignition temperature of the reactant. The author notes that detonation occurs over microseconds, whereas afterburn is a so-called late-time process that occurs in the order of milliseconds. The author notes constrained detonation products

lose temperature much more slowly. He also notes that fuel-rich explosives have negative oxygen balance, meaning that they produce detonic products suitable for afterburn. An oxygen balance for TNT of -74% and for RDX of -22% has been calculated using Cheetah 2.0 thermo-equilibrium code by Fried et al. (1998). The authors also note that even if there is insufficient oxygen available, the products can react with the oxygen present in the detonation products to generate after-burn.

2.9 Conclusions

Although the reviewed literature supports the occurrence of phased loading from shallow-buried near-field blast, there appears to be little evidence of, or discussion on, the source of these loading phases and or the primary loading or coupling mechanism into the structure and ultimately the structural response contribution for each of these phases. Thus the influence and effect of these phases on the dynamic response or failure of the target are also not openly presented at this time. Although some authors have proposed relative contribution for each loading phase in general, these are not validated by the experimental data presented for near-field shallow-buried blast loading. There have been isolated discussions on measured results from buried blast, but no detailed analysis.

Time-resolved blast loading phases would give better resolution required for identifying loading phases, quantifying their contribution to the total blast load seen by the target as well as the evaluation of mitigation methods. Currently used empirically based blast load predictions, although extremely useful and quite accurate in terms of impulse load seen by targets, are not very useful where active mitigation or non-impulse based blast load mitigation systems need to be researched and evaluated.

3 Method

The research method implemented used an experimentally based approach supported by secondary blast test data and computational modelling to identify, isolate and quantify the postulated five sequential components of a near-field buried blast load. A purpose-built test rig was used to identify and quantify the development, load duration with and without a near-field target and the target response force of a shallow-buried blast load.

The research methodology is discussed in the first four sections; (1) Research Design, (2) Selected Methodology, (3) Analysis, (4) Limitations, (5) Ethical Considerations and (6) Method Conclusions. The selected methodology is discussed in the five subsections; (i) Research Instruments, (ii) Computational Modelling, (iii) Secondary Data Research Instruments, (iv) One-Seventh Scale Test Data and (v) Secondary Data.

3.1 Research Design

The experimental research method utilised a purpose-designed one-seventh scale Hopkinson and Similitude threat test rig. The full-scale (prototype) blast threat was defined as an 8 kg TNT charge with a D:H of 5:1, buried to a DOB of 50 mm and positioned at a near-field SOD of 500 mm and an intermediate-field SOD of 1 400 mm from a rigid circular target. The test rig was designed, built, commissioned then upgraded to measure time-resolved face-on or side-on pressure and to simultaneously record the force-time response of the target. Near-infrared (NIR) temporal intensity measurements and high-speed video of the blast were made to provide supporting data. Analytical and empirical formulae and tables were used to verify the initial total target response impulse results of the test rig.

To support the time-based scaled test results and conclusions, secondary data from two separate test rigs were used, namely one set of data from Cranfield University (McDonald 2013a) and one set from the CSIR (Snyman, Reinecke 2006). These rigs differ in size but are similar in operation as they measure the force-time response of a target to a buried blast load. This secondary data

provides verification of the partitioning derived from the one-seventh scale test charges and additional information pertaining to near-field blast loading phenomena not obtained from the primary research tests of this work. This additional data have different soils, charge shapes, DOBs, a larger range of SODs as well as full-scale TNT blast test data, thus enhancing robustness of the findings and the conclusions drawn from the primary research instrument.

To support the data analysis by providing initial quantification values for the experimental design and identification of temporal phenomena, computational modelling of the primary test was done using the commercial hydro-code Ansys Autodyn®. The modelling was restricted to two models, one for soil ejecta without a near-field target and one for side-on pressure quantification with a near-field target. No tests were done of an intermediate-distance target model.

3.2 Selected Methodology

The methodology selected is detailed in three sub-sections: Research Instruments, Data and Analysis. The sub-section Research Instruments describes the experimental tools that were used to obtain primary and secondary data. The sub-section Data lists the research data that were generated and discusses the quality of the data – its strengths and weaknesses. The Analysis sub-section presents how and with what tools the empirical and computational modelling data were analysed and what information was derived from the data set.

3.2.1 Research Instruments

The primary data were obtained from a specially designed and built scaled buried blast test rig. The secondary data were obtained from two different research instruments developed for buried blast research: one was from a master's dissertation and one from military research of buried landmine and IED blast loads. Limited computational modelling was used to evaluate the experimental design and estimate quantification parameters.

3.2.1.1 One-Seventh Scale Test Rig

The test rig developed for this work was a one-seventh scale buried blast rig. The rig was designed to be adapted to measure a variety of test parameters with or without a near-field target. The primary test rig configuration, when set for near-field blast as shown Figure 5, comprises a soil bin with a measurement assembly rigidly mounted over the centre with four arms. An instrumentation frame was placed over the middle of the assembly and measures the dynamic deflection of the measurement assembly via a displacement probe attached to the top of the measurement assembly. The test rig was weighted down by the test soil filled into the base. The SOD was varied by changing the soil level in the bin. When used to quantify soil ejecta from buried blast, the measurement assembly and attachment arms were removed and a smaller steel bin is placed inside the soil bin as shown in Figure 6. The instrumentation frame had a V deflector plate bolted onto the underside and the displacement sensor was removed and replaced with a side-on pressure probe. The scaled buried-blast test rig is further detailed in the following sub-sections.

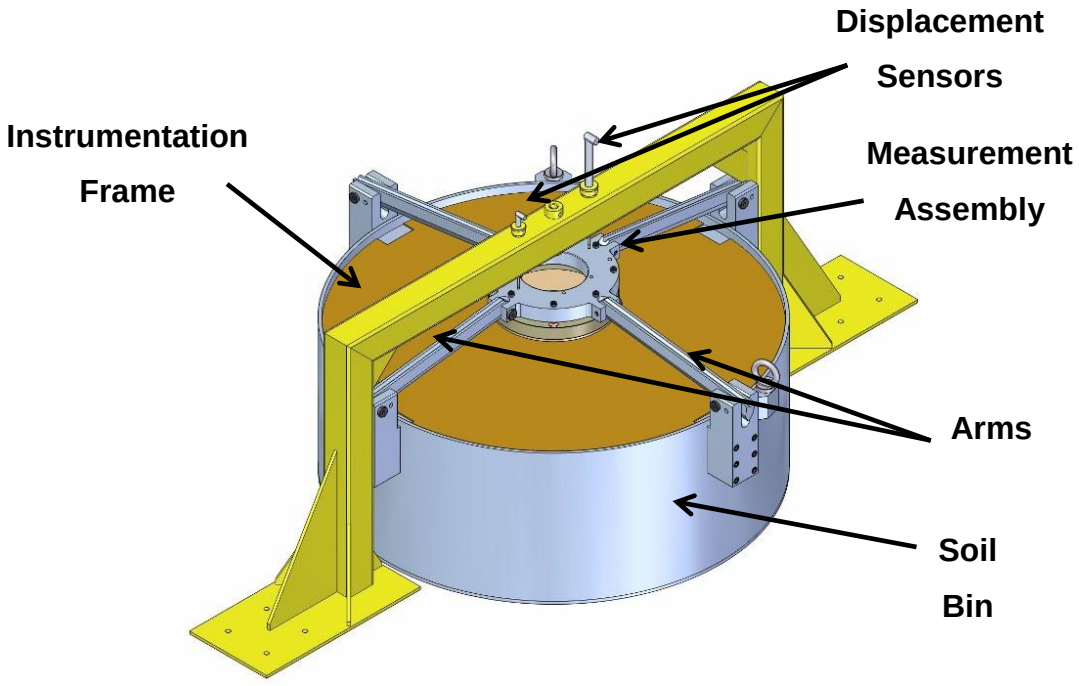

Figure 5: One-Seventh Scale Test Rig (Blast Force Response Configuration)

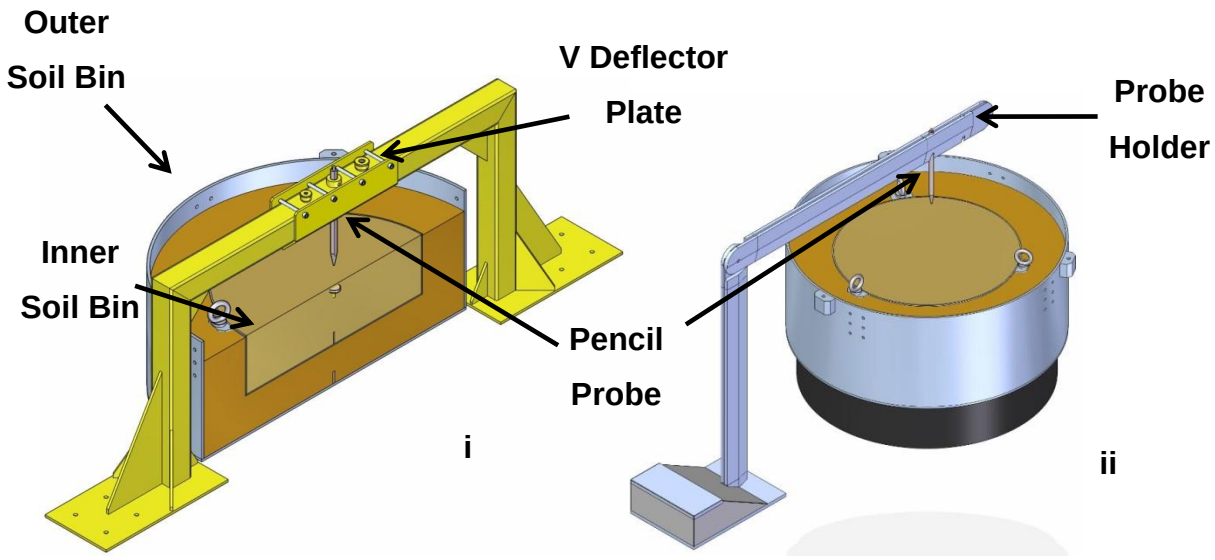

Figure 6: Soil Ejecta Commissioning i) and ii) Primary (Final) Research Ejecta Test Configurations

Figure 7 shows the one-seventh scale test rig as used for near-field target response with the face-on pressure configuration and the free-field ejecta tests.

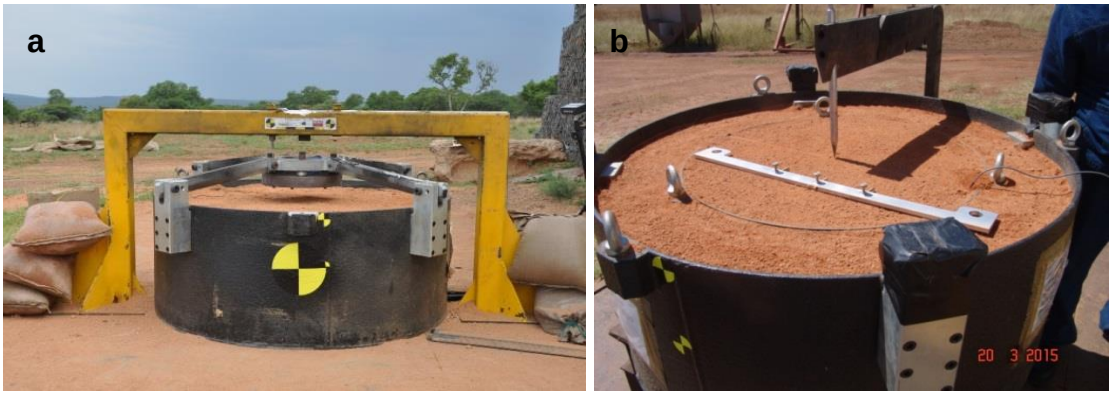

Figure 7: One-Seventh Scale Test Rig as used for a) Near-Field Target Response and b) Free-Field Ejecta Tests

3.2.1.1.1 Measurement Assembly

The measurement assembly consist of three main components bolted together. These are a constraining plate, the support ring and the target plate as shown in Figure 8. The 360 mm diameter target plate is bolted onto the supporting ring

with eight bolts, which formed the target assembly. Due to the thin target plate (10 mm), the bolt heads remain proud of the target plate face. The target assembly is bolted onto the rigidly mounted constraining plate using four equispaced through bolts with four piezoelectric force washers sandwiched between the supporting ring and the constraining plate. A threaded hole in the centre of the target plate accepts one of two threaded adapters, one for a pencil probe (side-on) and the other for a flush-fitting face-on pressure probe. For the side-on pressure measurements the pencil probe is mounted such that the side-facing sensing element is just above the front target face. For the face-on pressure the sensor is mounted with the sensing element flush with the front face of the target. The target assembly weighs 24.6 kg. The side-on pressure probe adapter weighs 1.3 kg and the face-on pressure probe holder weighs 1.3 kg.

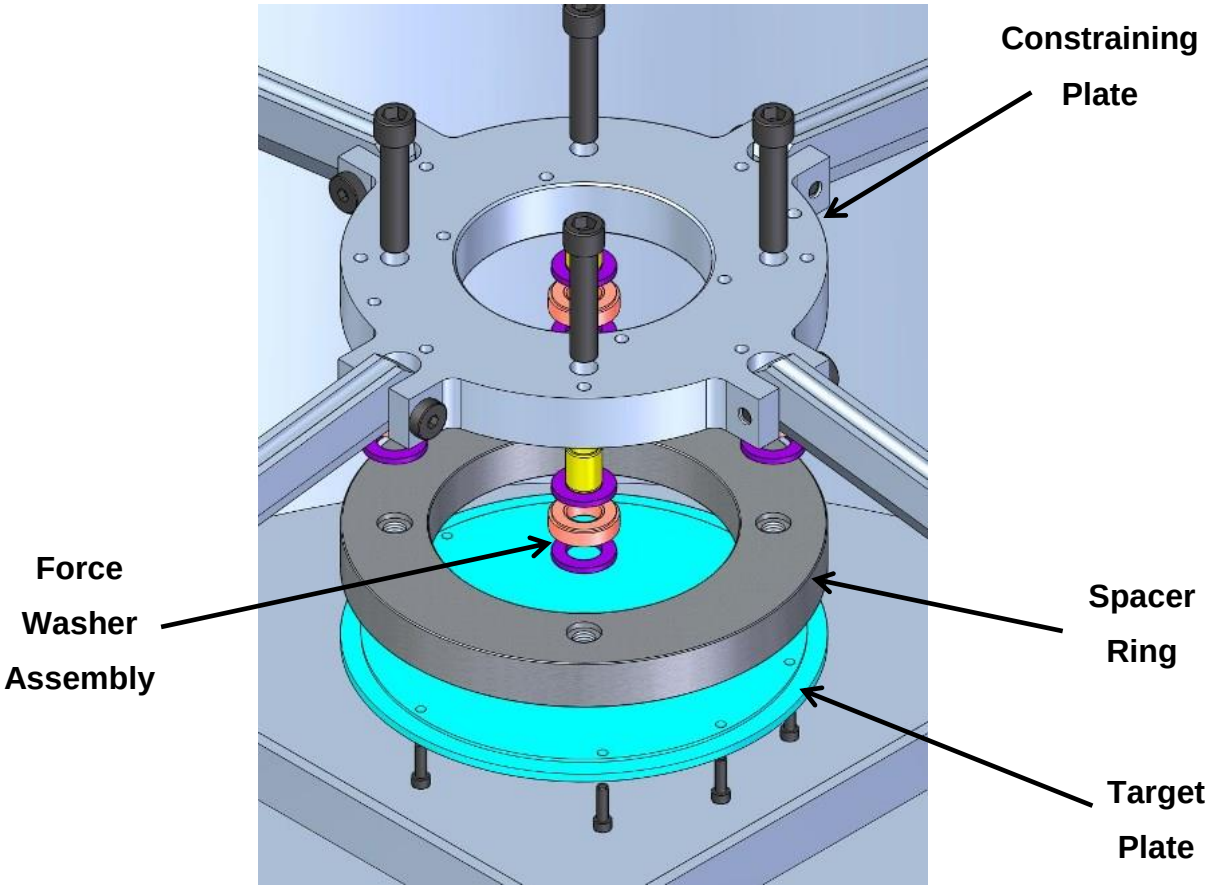

Figure 8: Measurement Assembly – Exploded Diagram

During assembly the force washers were pre-torqued to 50% of their load capacity, creating a pre-loaded stiff vertical spring-pendulum system. The method of operation for near-field tests was to bury and detonate the charge centrally to the target at the prescribed DOB and SOD. The blast propagates upwards, impacting against the target plate and pushing upwards against the target and the spacing ring, consequently pressing the force washers against the rigidly mounted constraining plate. The squeezing of the force washers by the target's response to the blast load generates an electrical output that is proportional to the force applied. In situ verification of the force washer measurement was accomplished by using a force or impulse hammer to strike the target plate, and then comparing the recorded hammer strike force-time to the net force-time response recorded by the four force washers.

3.2.1.1.2 Pressure, Displacement and NIR Sensors

The centrally mounted target sensor enables either the face-on or side-on pressure generated by the blast load against the target plate to be measured while the force washers concurrently provide the force-time response of the target assembly. These two configurations are shown in Figure 9.

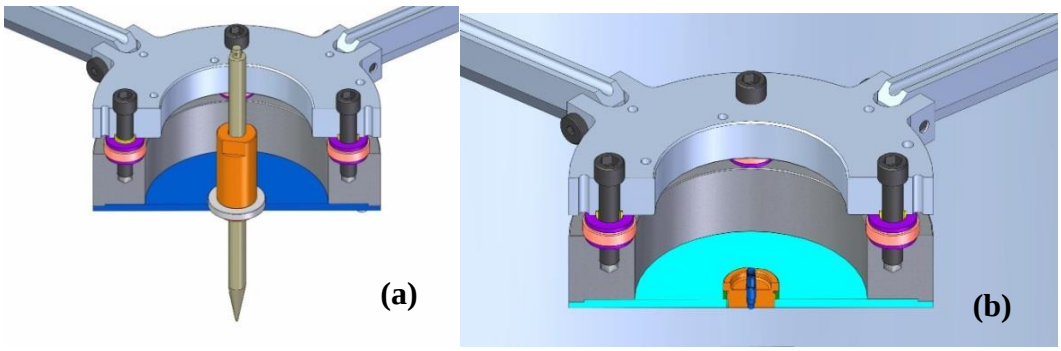

Figure 9: Side-On Pressure (a) and Face-On Pressure (b) Target Assembly Configurations

Even though the measurement head is rigidly mounted, there is still some limited dynamic motion of the system due to the blast load impact. The displacement transducer provides the limited vertical displacement morphology of the constraining plate and target assembly attached to the soil bin, which provides additional target response morphology. The NIR photodiode sensor assembly consists of four separate sensors with a mix of broadband and narrow

band wavelengths varying from 450 to 1,150 nm. It was positioned at a height of 1.5 m and angled to face the centre of the surface of the soil pit at the expected blast break-out point. This system was only used for the primary shallow-buried target response tests.

3.2.1.1.3 Signal Conditioning

With the exception of the light detector, commercially available sensors were used. Piezoelectric force washers require charge amplifiers. For the commissioning tests, HBM inline charge amplifiers with a frequency response of 10 kHz were used with 100 kN force washers. For shallow-buried tests in this research, multichannel PCB charge amplifiers with a frequency response of 100 kHz were used along with 330 kN force washers. As the charge output of these bigger force washers was larger, inline PCB 1/10th charge dividers were used for the primary research tests. PCB sensors with built-in amplifiers (ICP®) were used for both face-on and side-on pressure measurements. These sensors were powered by PCB signal conditioners with a 1 MHz frequency response. The light detector had its own built-in power supply and signal conditioning.

3.2.1.1.4 Data Acquisition and Synchronisation

With the exception of the NIR light emission all high speed data was recorded on an HBM Gen7® system operating with Perception® software using a combination of high-speed voltage and high-speed bridge boards. The data were sampled at 1 MHz with a 250 kHz Bessel anti-aliasing filter. The commissioning test data were acquired on a Graphtec field data acquisition unit and sampled at 1 MHz. The high-speed camera data were stored in the camera memory and downloaded after each test. The data recording speed was set according to the test conditions and varied between 30,000 and 40,000 frames per second. The soil ejecta scale readings were taken using an HBM SOMAT® eDAQ Lite® data acquisition unit. The NIR sensor output was captured with a Tektronix® field oscilloscope. Data acquisition of all the sensors and cameras was synchronised to start simultaneously using a trigger pulse emitted by the detonator firing unit when the charge was initiated. This synchronisation was maintained to within 15 µs between all instruments. All data recordings included

a pre-trigger signal of at least 100 µs. The EBW detonators used had a delay of 5.38 µs with a jitter of 125 ns (Risi Teledyne N/A).

3.2.1.1.5 Ejecta Test Configuration

The one-seventh scale test rig is able to quantify a buried blast load in terms of the blast front morphology (temporal velocity and shape), side-on pressure and mass of soil ejected without a near-field target. Removing the target minimises the effect of ejected soil fall back when assessing the mass of soil ejected. This test configuration is achieved by removing the complete measurement assembly and the four attachment arms and placing a smaller soil bin inside the larger soil bin. The smaller inner soil bin was placed on top of a soil layer in the larger test rig bin. Additional soil was then backfilled around the inner bin and lightly tamped up to the top of the inner soil bin sidewall. This configuration was chosen to minimise the ground wave reflections by having a medium denser than air around the inner bin, which allowed for some transmission of the soil stress waves through the sides and bottom of the inner soil bin. To obtain the ejecta mass the mass of the smaller bin was recorded before and after the blast test. The smaller bin size enables more accurate measurements of ejected soil, as percentage-wise the larger bin would have a much smaller amount of ejecta, which makes accurate measurements more difficult. To weigh the soil bin, a scale was designed and built using three calibrated precision load cells sandwiched between two wooden plates. To enable the side-on pressure to be measured in this configuration, a stand was placed over the middle of the bin with the side-on pressure probe placed centrally over the buried charge. The blast morphology was recorded using two-high speed cameras with their centre lines placed as close as possible level with the edge of the soil bin. These data, along with both the side-on pressure time at the intermediate SOD and the mass of the soil ejected, enabled the shallow-buried blast load development to be temporally quantified in terms of side-on pressure, blast front velocity and mass of soil ejecta. Although some soil ejecta fall back was evident, this was deemed to be minimal.

3.2.1.1.6 Test Soil

For soil standard Commercial River Sand was used for these tests. The soil moisture content was not controlled but was measured and recorded along with wet and dry density during the tests using a Troxler nuclear device. Due to measurement limitations the soil parameters could not be measured when placed in the steel soil bins, so they were measured from the spare soil pile prior to use. The moisture content and wet density of the test varied between 7.3% to 7.4% and 1 663 to 1 541 kg/m^{⅓}. The granulometry of the test soil was quantified and it was geometrically well scaled to NATO-specified soil (NATO Standardization Agency (NSA) 31 August 2011). The test soil was not completely replaced after each test. After all crater measurements had been taken, all discoloured (burnt) soil and the immediate crater soil was manually removed using a spade. The remaining soil was loosened with a fork. Replenishment soil from the stockpile was then added and smoothed to achieve the correct soil level. The soil was not compacted or tamped for any of the tests.

3.2.1.1.7 Test Explosives

One-seventh cube root scaling of the 8 kg TNT threat results in a mass of 23.3 g TNT. To ensure reliable ignition of the small test charges and to remove the need for a booster charge, PE4 was used as the test explosive. Applying an impulse equivalence of 1.19 (Weckert, Anderson September 2006) resulted in a PE4 equivalence mass of 19.6 gr. This was reduced to 18.6 g PE4 to accommodate the 1 g RDX of the RP-83 Exploding Bridge Wire (EBW) detonator. For practical application the charge mass was rounded up to 19 gr. This produces a prototype charge that is 162 g heavier than the specified threat level or has a 2% higher mass than the specified full-scale threat. This charge difference is deemed negligible when compared to the potential error with the equivalence factor and to the typical variability of a buried blast. This variance is also well within NATO's allowable charge mass variation of 5% for landmine test surrogate charges (NATO Standardization Agency (NSA) 31 August 2011). The commissioning tests were executed using 20 g PE4 charges and all other one-seventh scale tests were executed with 19 g PE4 charges.

To make the soft formable PE4 charge robust to handling, facilitate charge placement and maintain charge and detonator geometry during testing, the charges were hand formed and placed in machined plastic containers with a wall thickness of 1 mm. This is consistent with AEP 55 (NATO Standardization Agency (NSA) 31 August 2011) casing allowance for cast charges. The casing was designed so that the separately weighed and then formed PE4 charge would be flush with the casing side wall. The plastic casing has a small undercut in the bottom corner to lock the charge in position once formed in the casing. The casing has a 7 mm long detonator support tube machined on the bottom face to keep the detonator perpendicular to the charge face. This modification was only implemented with the primary near-field research tests. During the hand forming a Teflon-coated cavity plug was inserted through the detonator cavity to ensure that the cavity depth was no more than 6 mm into the explosive, thus ensuring that the detonator tip is inserted consistently to this depth. The detonator was inserted facing upwards resulting in the detonation of the charge towards the target. This is consistent with NATO requirements of the detonation being initiated upwards. (NATO Standardization Agency (NSA) 31 August 2011). In addition to the 51 D:H ratio, additional supporting tests were carried out with 2:1 and 3:1 D:H ratio charges.

Two dedicated positioning jigs were developed to ensure consistent DOB and central positioning of the charge for both the soil ejecta and the near-field blast tests. For the ejecta tests the centring position was taken from the inner soil bin rim, and for the near-field tests the centring position and SOD were taken from the target. These devices were used to level the soil as well as to keep the charge centrally positioned and flat with the soil surface, while the soil that was removed to accommodate the detonator firing cable and the explosive cavity was pushed back under and then over the charge. The soil was lightly tamped around the charge to achieve a level soil surface.

3.2.1.1.8 Tests Executed

To reduce experimental risk the test rig was first subjected to an initial commissioning test series, after which a number of test rig and procedural modifications were made before the final research test series was completed.

Thus the primary test data were obtained from two plate test series, the commissioning tests and then the final research or primary tests. Each of these in turn consisted of an ejecta and a target load quantification test series. For the primary research tests, where possible each test point was repeated at least three times to obtain statistical relevance for the data.

To partition the blast load, the loading was first quantified in terms of ejecta shape, velocity, side-on pressure morphology and mass of soil ejected without a near-field target present. This was followed by both intermediate and near-field target tests, and the target force-time response along with either the side-on or face-on pressure-time response were recorded, depending on the central sensor fitted. As the pencil probes required at least ten diameters of length for flow to reattach and to provide accurate pressure measurements, initial side-on pressure measurements had to be made at a SOD of 200 mm to enable the probes to be safely used. As these tests have a scaled distance (Z) of 0.78 $m/kg^{1/3}$, they fall outside the near-field definition.

For this research intermediate-field is when the target or the measurement point of discussion is placed at a distance to the charge such that the scaled distance (Z) is greater than 0.5 and less than 1.0 $m/kg^{1/3}$.

In the same context, near-field describes tests where the target or the sensor/measurement point of discussion are placed close enough to the charge centre that the scaled distance (Z) is less than 0.5 $m/kg^{1/3}$ although (Smith, Hetherington 1994) note this limit to be < 0.3 $m/kg^{1/3}$. For the research threat presented for this work this equates to a 19 g PE4 charge with a DOB of 7.2 mm and the target or sensor placed at a SOD of 200 mm from the soil for intermediate-field blast load and at 72 mm for near-field blast load.

The upper bound was arbitrarily set at 1 $m/kg^{1/3}$ as the generally smallest scaled distance available on most scaled distance blast plots generated from the 1960s to the early 1980s (Cooper 1996c).

These intermediate target SOD tests were repeated with the face-on pressure transducer to quantify the loading relationship between side-on and face on-

pressure from shallow-buried blast. The last tests carried out were the scaled near-field shallow-buried blasts (Z = 0.31 m/kg$^{1/3}$).

3.2.2 Computational Modelling

The computational modelling of both the ejecta and the near-field commissioning tests was carried out using Ansys Autodyn®. The computational modelling was based on the commissioning test assembly using a smaller target plate (290 mm), force washers (100 kN) and spacer ring at the scaled threat SOD and DOB. The purpose was to develop an engineering understanding of the blast loading morphology in terms of the measurements to be obtained during testing with and without a near-field target and to provide initial test parameter data for pressure and blast front velocities. A set of four near-field target models were developed and executed in Ansys Autodyn®. No additional models were developed of the final test rig configuration, although the test rig design changed in terms of measurement assembly size and mass as well as the introduction of an intermediate-field SOD to enable side-on pressure measurements to be taken in the field.

3.2.3 Secondary Data Research Instruments

Secondary data from two other test rigs were used for this work. These were the Cranfield blast rig (McDonald 2013a) and the Scientifically Instrumented Impulse Measurement Apparatus (SIIMA) (Snyman, Reinecke 2006). Both these rigs measured the force-time response of a target to a buried blast load. The Cranfield rig is a scaled-blast test rig which also uses piezoelectric force washers to measure the blast load, whereas SIIMA is a full-scale blast quantification rig that uses strain-based load cells.

3.2.3.1 Cranfield Blast Rig

This test rig was designed and built as part of a master's dissertation submitted to the Impact and Armour Group of Cranfield University's Shrivenham campus in the UK. The test rig consists of dual inverted truncated V frames with a 0.5 x 0.5 m, 0.03 m thick instrumented target plate weighing about 10.25 kg bolted to the two cross I-beam frames. The target plate sandwiches two force washers

between the rear face of the target and the supporting I-beam. As only two force washers were used for the global target plate response measurement, the net force-time response was estimated. The force washers were preloaded to 30% of rated capacity. Three asymmetrically placed face-on force sensors with flush-fitting measurement pins, each with a diameter of 15 mm, were embedded in the target plate. These force sensors also use piezoelectric force washers and enable discrete face-on force-time histories to be measured at the specific points across the target plate face. The force washers were mounted in an L shape with one in the centre of the plate 100 mm from the centre along the lengthwise axis of the plate and another was mounted 200 mm from the centre along the width axis of the plate. The soil was placed inside a small plastic bucket located within a larger welded steel bucket, which was placed loosely on the base plate to which the truncated V side frames were welded. In addition to measuring the force-time response of the two corner and three face-on force washers, high-speed video was taken of each blast.

3.2.3.2 Scientifically Instrumented Impulse Measurement Apparatus (SIIMA)

This was a full-scale blast measurement test rig that measures the force-time response of a blast load up to a maximum net charge of 8 kg TNT. The test rig consists of a large steel frame that is adjustable for height and is rigidly mounted to a large concrete base (150 tons). There is a soil pit in the centre of the concrete base. It has a 9,000 kg rigid box target with an exposed area of 1.2 x 1.2 m that bears against the steel frame. The target is connected to the rigid frame via polyurethane springs and load cells. When assembled it forms a sprung vertical pendulum that is pre-loaded to 50% of its force capacity prior to use and thus is similar to both the one-seventh scale and Cranfield test rigs. The load cells measure the net force-time response of the inertial mass to a buried blast load. In addition to the force-time response of each test, limited high-speed video data were also captured. For this work only the force-time response data were used directly – any high-speed video data used were as reported in (Snyman 2012).

3.2.4 One-Seventh Scale Test Data

A total of forty-two one-seventh scaled research blast tests were carried out, of which forty-one provided measurement data. Of these, ten were commissioning tests and thirty-one were primary research and supporting tests using the final one-seventh scale test rig configuration. Due to continual improvement of the method, only the last twenty-two shallow-buried blast load target tests used the final charge casing configuration with the detonator support to ensure perpendicularity of the detonator axis to the charge face. A total of eight in situ force hammer tests were done to verify the total force measurement system.

3.2.4.1 Commissioning of the Test Data

Of the eight commissioning tests, three were ejecta tests and five were near-field shallow-buried blast tests. Only in three soil ejecta tests were pressure data recorded. Two with 2:1 D:H ratio charge tests and one 5:1 D:H ratio charge test. The commissioning ejecta tests were terminated when it was determined that the initial ejecta mass measurement system was not able to accurately measure the soil ejected. Analysis of the side-on pressure also gave an unexpected pressure morphology, which led to an upgraded method being developed to hold the side-on pressure probe in such a manner as to reduce the possibility of generating the reflected pressure (i.e. artefact of the test set-up). These data gave useable crater dimension and side-on pressure data that assisted in verifying phased loading phenomena as well as enabling the research methods to be reviewed and improved.

The shallow-buried near-field tests used 100 kN force washers and a small supporting ring with a 16 mm thick target plate 290 mm in diameter. This resulted in a target assembly that weighed 9 kg and was much lighter than the final test rig target assembly, which weighed 24.6 kg. Of these tests, only two test repeats for the 5:1 and 2:1 D:H ratio charges and only one test for the 3:1 D:H ratio charge gave useable data. Due to force data corruption of the data acquisition unit, only two of the four target response force signals could be used. The net force was thus estimated by doubling the sum of the two useable force measurements. These initial force-time test results varied considerably.

This was partly due to variability in the initial set-up and methods applied in the tests and partly due to the inherent variation of buried blast loads. These results led to the improved processes used for the primary research tests. The recorded total force load exceeded the nominal measurement capacity of the load cells, resulting in modifications to the test rig to incorporate 330 kN force washers. The captured data provided good and usable initial phased force-time signal data.

3.2.4.2 Primary Research Ejecta Tests

A total of eight final ejecta tests were carried out which provided four data points for the 2:1 and two data points each for the 3:1 and 5:1 D:H ratio charges. The last two data sets were insufficient to be able to draw strong statistical conclusions; however, the data are consistent with regard to the general morphology and peak quantitative values from shallow-buried blast. The side-on pressure recorded for each test along with the high-speed imaging of the blast front provided adequate data to quantify the ejecta morphology of shallow-buried blast loads and give the required insight into the mechanisms applicable for these loading conditions.

3.2.4.3 Primary Research One-Seventh Scale Shallow-Buried Tests

A total of twenty-four shallow buried blast tests were executed, of which twenty-three provided the required target net force response measurements. Of these, twenty-two were intermediate field tests and only two were near field tests. The intermediate field tests were divided into two test series, one with the side-on pressure sensor fitted in twelve tests and one with the face-on pressure sensors fitted in nine tests. The two near-field tests were carried out with the face-on sensor fitted, only one of which provided face-on pressure data. The near-field tests were terminated when the sensor cable connector sheared due to the acceleration of the measurement head assembly. Of the twenty-two intermediate field tests, two did not record the side-on pressure. For the intermediate side-on pressure tests at least four repeats per D:H ratio were done and three repeats for each charge ratio with the face-on sensor. The

number of repeat tests carried out for the intermediate field target was sufficient to statistically draw conclusions on key blast load parameters.

To provide a robust data set and verify the repeatability of the refined test execution methodology, the fourth intermediate side-on pressure test was done on a separate test day. The fourth face-on pressure intermediate test repeats could not be done. The repeated test data corresponded well to the original data, providing confidence that variability of the test set-up had been reduced as far as possible.

Due to an interface mismatch with the original design, the high-speed displacement transducer used for these final tests could not be rigidly mounted to the rear of measurement assembly. Double-sided tape was used to attach the sensor rod to the rear of the constraining plate. This set-up provided good upward motion data, but did not provide the downward motion response for most of the tests. The few data sets did capture sufficient temporal displacement information pertaining to the damped response of the complete restrained measurement assembly. This provided information to confirm the initial phased loading response was not a system structural artefact.

These primary shallow-buried blast tests used larger-capacity force washers combined with higher frequency response signal conditioning charge amplifiers (100 kHz compared to 10 kHz used with the commissioning tests). Due to a torque wrench limitation a maximum pre-load toque of 400 Nm was applied to each load cell and the system. This proved to be insufficient to properly pre-load the force washers. Once pre-loaded the measurement assembly was subjected to a series of force-hammer tests to verify the function and accuracy. As the target assembly was inverted and surrounded by the steel soil bin and four attachment arms, it was particularly difficult to ensure that the hammer blows were perpendicular to the target plate face or consistently impacted. The hammer results confirmed that the applied pre-load torque was insufficient, which resulted in a noisy force-time response compared to the smooth phased response obtained in the commissioning tests. Despite this, the processed

primary test data corresponded in terms of duration and impulse to the commissioning tests, which gave confidence in the measurements obtained.

3.2.4.4 Modelling data

A total of five models were successfully built and run. Three models were of the shallow-buried near-field configuration with the 20 g PE4 scaled threat in D:H ratios of 2:1, 3:1 and 5:1. The second near-field 5:1 model had additional gauge points to investigate the side-venting pressure and velocities with the near-field target as well as boundary outflows, if any. A single 5:1 D:H soil ejecta model was built and run.

The models developed were limited to standard Ansys Autodyn® material parameters and were only in 2D. As no PE4 explosive parameters are available as standard in Autodyn®, C4 parameters were used. Although both are RDX-based plastic explosives, PE4 has a nominal 88% RDX, content whereas C4 has around 91% RDX, with the rest being binders and oils (Cooper 1996a). The model was coarse as only 6,500 2D elements were used. For the ejecta simulation the same soil model and node grid was used, but with the near-field target removed and a matrix of additional data points defined around the near-field model centreline. This coarseness was due to Autodyn® allowing only one biasing (grading) of the mesh which was applied around the charge, which resulted in the mesh becoming larger as the distance from the charge increased. The requirement of a minimum of two Eulerian elements to one Lagrangian element was just met for the near-field target fluid structure interaction model. The model did not fully represent the experimental set-up due to the required model simplification. The measurement assembly was modelled as a target plate attached to a rigidly held ring, thus ignoring the dynamic flexibility of the mounting arms. The arms were not included in the model. The force washers were not modelled and the force was extracted from within the ring elements. Neither the outer steel soil bin nor the inner steel soil bin was modelled. This was primarily due to the grid biasing used within Autodyn that resulted in elements that were wider at the boundaries of the modelling space than the thickeners of the bin wall.

These differences could materially affect the quantified model results; however, as the purpose of the modelling was exploratory, these differences are deemed irrelevant to the target response morphology used to partition and quantify the loading phases of a shallow-buried blast.

3.2.5 Secondary data

The secondary data used were from a series of unconnected tests using different research instruments, threats with different geometries, explosive masses and differing soils that did not geometrically scale to the primary research test requirements. Despite this variability, there are common threads – all the available data are for buried near-field blast loading and almost all the tests used flat steel targets and measured the force-time response of the target to the buried blast load. This commonality ensures that the secondary data are relevant. The CSIR data are also currently the only source of full-scale blast loading data. The variety of test methods used to obtain the secondary test data is positive as they enabled the blast load morphology and constituents to be robustly identified.

The secondary data used for this research is further described in terms of the two different research instruments providing the data. The data provided by each instrument and the limitations of each that pertain to the research focus of this work, are noted. The original test data were available and were processed by the author as required for this work.

3.2.5.1 Cranfield Blast Rig

The data from a total of six tests data were obtained, reviewed and analysed in terms of target response force-time morphology from a buried blast. These tests provided the force-time response of the target plate as well as the force-time responses of the three face-on force sensors for three different SODs and two different DOBs. The SODs were 360 mm, 230 mm and 100 mm and the DOBs were 100 and 50 mm respectively. High-speed video data were also analysed; however, the video capturing differed from test to test regarding the position of the cameras, the subject of the video and the framing rate. These tests used a spherical 160 g PE4 explosive charge, which represents a two-seventh’s

Hopkinson scale (2/7) of the threat charge based on explosive mass, with scaled distances (Z) of 0.90, 0.66, 0.42 and 0.57 m/kg$^{1/3}$ respectively. Although these scaled distances are greater than the near-field threat conditions of interest and are either smaller or larger than the intermediate threat conditions of interest, these data are still within the research range of this work. The scaled DOBs were deeper than the DOB of the research threat conditions, and the SOD was either smaller or larger. The soil used for these tests was completely dried under laboratory conditions and was not scaled to any specific soil granulometry. No granulometry was conducted on the soil used, and neither was the soil compacted. The detonation direction was upwards. Lastly, the total force-time response was measured using only two force washers, therefore the net force was estimated. Despite these limitations, these data provided relevant and useable information regarding buried blast and loading of a near-field target.

3.2.5.2 SIIMA

Although a large amount of SIIMA data was available to the author, only two specific sets of these data were directly used to support this research. These were a set of four one-half geometrically similar scaled tests using a one kilogram TNT threat at a DOB of 25 mm and a SOD of 250 mm, and a set of three full-scale eight kilogram TNT blast tests at a DOB of 50 mm and a SOD of 1,300 mm. The full-scale test set was chosen as it is closest to the intermediate scaled tests with a test SOD of 200 mm that equates to 1,400 mm at full scale. This test set gives a scaled distance (Z) of 0.69 m/kg$^{1/3}$ compared to the scaled distance (Z) of 0.79 m/kg$^{1/3}$ of the intermediate one-seventh scaled test. The data provided were the net force-time response of a rigid heavy target subjected to a shallow buried blast load. For the full-scale test the target mass scales quite well with that of the final scaled test rig configuration, where the 9,000 kg mass scales to 26.24 kg compared to the scaled test rig target assembly mass of 25.9 kg with the side-on probe fitted. At half scale the 9,000 kg target mass scales to an equivalent full-scale mass of 72,000 kg, and at one-seventh scale this is 201.9 kg.

As with the Cranfield tests, the SIIMA soil used for the half-scale tests was not scaled and had a granulometry that was considerably finer than that specified by (NATO Standardization Agency (NSA) 31 August 2011). For each of these tests loose and un-compacted soil was also used. The full-scale tests used compacted soil and controlled soil conditions. The biggest limiting factor of the SIIMA data is that the target plate size does not scale to the one-seventh scale test rig target. SIIMA's target plate is a very rigid 1.2 x 1.2 m square with an area of 2.44 m^2 as compared to the one-seventh scale test rig which has a geometrically similar full-scale circular target of 2.520 m in diameter and an area of 4.99 m^2. The one-half scale tests used a square 0.6m x 0.6m plate which is geometrically scaled to the SIIMA full-size target. Although these differences substantially affect the quantified measurements, this negative effect is limited in that buried blast varies exponentially across the target face, with the highest proportion of the load being concentrated in the centre (Tremblay 1998, Held 2004). Although limited, these data provided useable, scaled information regarding the target response force morphology to a shallow-buried blast for both near-field and intermediate-field distances.

3.3 Analysis

All captured high-speed sensor data were processed using nCODE® N11.0 Glyphworks® software. High-speed video data were analysed using Image Systems® TEMA 3D version 3.9-007 64 bit software. Processed data were transferred to Microsoft Office® Excel® for statistical analysis, tabulation of results and graphing of the extracted data. The specific analysis methods applied to each data set are summarised below.

3.3.1 Modelling

Using standard Autodyn® output functionality, the modelling results for both the near-field target and the soil ejecta were written to Excel. The data were read into Glyphworks® using a standard function which set the time base using a sampling rate of 1 MHz which corresponded to the selected modelling output writing time steps. The modelled pressure signals were zeroed using standard atmospheric pressure of 101 kPa, as selected for the mode input parameter.

The output time series pressure morphology was inspected and the phasing and related time were manually identified and extracted using the troughs to the left and right-hand side of each peak. The pressure signals were then passed through a 100 Hz high-pass four-pole Butterworth filter and then integrated to calculate the specific pressure impulse. The extracted data were transferred to Excel.

3.3.2 Commissioning Tests

The data of the target load tests recorded on the Graphtec were converted to engineering units as part of the data acquisition software set up in the recorder and were saved as a .csv file format. The recorded data were transferred from a .csv file to Glyphworks® .s3t format using standard Glyphworks® software functionality. Once converted, the data time base was set with the trigger pulse (t_0) as 0 s, and the force-time data channels split from the displacement measurements channel.

The force-time data were plotted and inspected. As the data of two of the four target response force channel for these tests was observed to be corrupted with noise, the two clean channels were summed up and multiplied by two to calculate the estimated net target force-time response. The resulting temporal signal was zeroed using the pre-trigger data signal. The signal was then passed through the standard Glyphworks® high-pass four-pole Butterworth filter to remove DC signal content and then passed through the standard integration routine to obtain the target impulse-time measurement response. The filter frequency was determined through trial and error by inspection of the resultant impulse-time response plot. The lowest possible frequency ensuring a stable integration-time result was selected and used for all test points. For the commissioning tests it was set at 15 Hz. The displacement signal was also contaminated with noise and was passed through a 1,500 Hz low-pass four-pole Butterworth filter.

3.3.3 One-Seventh Scale Ejecta Tests (Commissioning and Primary)

For both the commissioning and the primary research ejecta tests the pressure data captured by the Gen7 were recorded in the native Perception® .PNRF file

format and transferred to Glyphworks® where they were converted automatically into the Glyphworks® .s3t file format. The recorded sensor output conversion to engineering units was done within the programming of the Perception® software using the calibration values for each sensor. Using Glyphworks® all the signals were time-base corrected to ensure that the detonation initiation time (t_0) was noted as 0s. The recorded time signals were then further digitally processed as required. For integration a high-pass four-pole Butterworth band-pass filter was used to remove any DC component in the signal and any high-frequency noise. The filter frequency was determined by trial and error. The lower filter frequency was set to 10 Hz while the upper frequency was set to 450 kHz. The processed results were then plotted and the peak values extracted in Glyphworks® using standard functionality. The temporal data were manually identified and extracted as no standard functionality exists in Glyphworks® other than the peak value extraction. This introduced some subjective variability in the duration results. The extracted data were exported to Excel®.

The recorded pre- and post-test inner bin masses were manually recorded from the eDAQ data acquisition software based on observed readings taken during the tests. Screen shots of the readings were also taken for backup. These data were manually transferred to Excel® where the change in mass was calculated. This change was the mass of soil ejected. The high-speed video was viewed in TEMA 3D®. Scaling of the video images into engineering units was done using standard software functionality. Markers of known size were placed within the image prior to testing and were used to calibrate the distance. The scaling markers were placed as close as possible to the measurement plane. The primary blast front point was tracked in TEMA 3D® and the data transferred to Excel® for plotting, trend line fitting, statistical processing and tabulation of blast front velocity results.

3.3.4 One-seventh Scale Near-Field and Intermediate-Field Tests

The data captured on the Gen7® for these tests was transferred from .PNRF format to Glyphworks® .s3t file format. The engineering units were converted

within Perception®. The test data were split into force-time response, pressure and displacement measurements for independent processing. The net force was obtained by summing the four force washer signals followed by zeroing the summed signal using the pre-trigger data. A band-pass four-pole Butterworth filter was used prior to integration to ensure a stable impulse result using the same method as applied to the commissioning test data analysis to select the low band filter value. The low band was set to 40 Hz and the high band to 25 kHz. The temporal phasing of the target response force was done after integration using the net impulse-time. The pressure signals were filtered using a low-pass four-pole Butterworth filter. In some cases the filter resulted in a small DC offset that was removed by zeroing the signal after application of the filter. The displacement signal was zeroed and a 1 kHz low-pass four-pole Butterworth filter was applied to the signal before the temporal phases were manually identified, extracted and transferred to Excel®. The high-speed video was analysed by calibrating the images using markers placed as close as possible to the blast centre. The blast front was manually tracked and the displacement time data were transferred to Excel for processing. Due to the limited space, only two to three points were extracted for each test. A linear trend line was fitted and the slope taken to provide the velocity.

3.3.5 Secondary Data

Although the secondary data were similarly processed, the actual force measurement methodology and data format differed between the three test rigs. They are summarised separately. Once the net force-time data were obtained for each secondary data set, the load phases were then manually identified by visual inspection and extracted and the data were transferred to Excel®.

3.3.5.1 Cranfield Blast Rig

This data were supplied in .CSV format and converted and loaded into Glyphworks® using standard software functionality. The force readings were split into the two target force-time responses and the three face-on force time responses. The target plate net force-time response was calculated as for the commissioning test data by summing the two target response force washer

signals and multiplying the result by two. The estimated net force signal was then zeroed using the net pre-trigger data signal. The high-pass filter frequency was determined as before by trial and error and set at 20 Hz. The high-speed video was analysed in TEMA 3D®. The scaling of the data was done using the SOD between the top of the soil and the target as no calibration markers were used for these videos. The extracted data were transferred to Excel® for further processing.

3.3.5.2 SIIMA

The load cell data for each of the sixteen measurement cells were pre-processed in Glyphworks® software into software specific time series format (.s3t). These pre-processed sixteen data sets were used to calculate the net force-time response by summing each of the eight upper and lower load cell data sets and then subtracting the summed totals to calculate the net force-time response. The net force was zeroed using the net pre-trigger signal. Further processing was done as for the other test data using the high-pass four-pole Butterworth filter frequency set to 20 Hz.

3.4 Method Limitations

Blast loading in general, and buried blast in particular, is variable – it results in different initial impact points and pressure zones across the target face. The primary weakness with the pressure data is that it only measures at a discrete point at the centre of the target face and not continuously across the target. This makes the data set vulnerable to the inherent variability of buried blast loading typified by the jetting discussed previously. Certain measurements provide extraordinarily high or low measurements between tests. Furthermore, both side-on and face-on pressure could not be measured simultaneously with the one set-up. Several different tests were required with different measurement sensors and resultant changes to the target geometry and mass. This introduces differences in the measurement system between the two types of measurements.

The scalability of the phenomenology of the various quantification parameters being measured is not known (Swisdak 1975). Lastly, scaling reduces the

duration of the key measurements being obtained. To partition and quantify the blast loading phases requires extremely high sampling rates to acquire accurate temporal data. Not all the theoretical requirements for blast-load scaling can be met, in particular gravity cannot be scaled nor could the soil be scaled within the cost and time parameters of this study. Having been scaled, the durations as well as the space to execute the measurements are reduced, making accurate measurements more difficult. The target response force measurement chain has a limited frequency response of 30 kHz, resulting in a measurement resolution of around 30 µs. The scaling of the experiment results in set-up errors being amplified in accordance with the scale factor, which results in small differences from test to test obscuring actual morphological and other measurements. The test data were generated with one-seventh scale PE4 charges (19 gr), which might not create all the required detonation and blast constituents that a full-scale TNT charges will generate.

General soil parameters such as density and moisture content could not be measured in situ, nor were they specifically maintained for the one-seventh scale tests due to limitations of the equipment used. Although the bulk parameters were measured, these were of the stockpile, and slight differences would occur in the parameters measured here and as found in the test soil.

Despite these limitations, this method is feasible for investigating and researching near-field buried blast load in terms of measured pressure and force-time target response. The application of a well-thought-out geometrically similar scaled test rig design for the prototype threat and target, combined with the development and implementation of a meticulous set-up methodology, along with supporting tools and a small number of repeat tests, provided sufficient data to statistically extract useable data from which to draw conclusions regarding the blast load constituents and their relative contribution to the total blast load force-time response of a target.

3.5 Ethical Considerations

No ethical issues were identified with regard to this research. All the work used in this research has been referenced and the authors duly acknowledged. The

inherent hazards of using and testing explosives are recognised, and the research instruments and methods conformed to all the required occupational, health and safety processes and procedures of the CSIR.

3.6 Conclusions

The research method that was used to investigate blast load partitioning has been presented in terms of research design, selected methodology, research instruments, data obtained, analyses applied and limitations. The proposed method provided the required empirical and computational data for this work. The applied research design provided a robust methodology to enable blast loading to be quantified and verified in a cost-effective manner. The use of scaled test charges enabled test points to be effectively repeated, providing statistical strength to the results and conclusions obtained.

4 Results

The focus of this research is the partitioning of a shallow-buried near-field blast load using the force-time response of the target. The test methodology used a combination of computational modelling and one-seventh scale primary test data to confirm and explore the existence of phased blast load phenomena. Due to instrumentation limitations both intermediate and near-field data were obtained. To provide robustness to the data set used additional secondary data from two independent research test rigs were obtained and analysed.

The results are presented in this section were processed in accordance with the methods presented in Section 3.3 and are discussed in nine sections. These are; (1) Research Data Summary, (2) Modelling, (3) Shallow Buried Blast Ejecta, (4) Intermediate-Field Blast Load Phasing, (5) Near-Field Blast Load Phasing, (6) NIR Light Emission, (7) Target Assembly Displacement, (8) Secondary Data and (9) Scaling.

The Results summary starts with the computational modelling results for both free-field ejecta and near-field target configurations to confirm the theoretical occurrence of phasing in a shallow buried blast load and to provide initial model quantification parameters which are then compared to actual test results. Each following section presents the test results starting with the free-field ejecta discussing only key aspects and limitations or risks of each data set specifically focussing on temporal changes in the modelled and measured parameters of a shallow-buried blast. The sections follow the development of a generic buried blast load starting with the free-field blast pressure and ejecta and progressing to the target response to this blast load. To support the primary research data results obtained, secondary test data is presented along with a section on scaling laws for the extrapolation, comparison and verification of the scaled research data.

4.1 Research Data Summary

The complete research data set used for this work comprised a total of sixty-five tests of which fifty-one were primary research test data and fourteen were

secondary data sets. The primary research data set comprised four computational model tests, eleven one-seventh scale free-field ejecta tests and thirty-six were one-seventh scaled target response tests. Of these eight were commissioning tests comprising three free-field ejecta and five near-field target force response tests. Various changes and improvements were introduced after each commissioning test series. Tables 3, 4, 5 and 6 summarise the test data sets used for this work. The test quantity column refers to the number of repeat tests executed for that specific test point.

The computational model data sets listed in Table 3 comprised a single free-field and three different near-field target model results. The model charges were set at twenty grams comprising 19 grams for the test charge and an additional one gram for the detonator NEC.

Table 3: Computational Model Data Set Summary

Test Qty.	Test Key No.	Explosive	Mass (grams)	D:H	DOB (mm)	SOD (mm)
Computational Models						
Free-Field Ejecta						
1	Autodyn Run 6 5-1 Ejecta	C4	20	5:1	7.2	-
Near-Field Target						
1	Autodyn Run 1 5-1 Target	C4	20	5:1	7.2	72
1	Autodyn Run 2 3-1 Target	C4	20	3:1	7.2	72
1	Autodyn Run 3 2-1 Target	C4	20	2:1	7.2	72

The soil-ejecta data sets listed in Table 4 comprised three commissioning and eight final research tests covering a range of three charge D:H ratios.

Table 4: Primary Research Soil Ejecta Test Data Summary

Test Qty.	Test Key No.	Explosive	Mass (grams)	D:H	DOB (mm)	SOD (mm)
Ejecta Tests						
Commissioning Tests						
2	Soil Ejecta	PE4	20	2:1	7.2	221[1]
1	Soil Ejecta	PE4	20	5:1	7.2	205
Final Tests						
4	Soil Ejecta	PE4	19	2:1	7.2	200
2	Soil Ejecta	PE4	19	3:1	7.2	200
2	Soil Ejecta	PE4	19	5:1	7.2	200

The target response data set listed in Table 5 comprised five near-field commissioning, eight hammer verification, twenty-one intermediate and one near-field tests. As with the ejecta tests these covered a range of three charge D:H ratios.

Table 5: Primary Research Target Force-Time Response Data Summary

Test Qty.	Test Key No.	Explosive	Mass (grams)	D:H	DOB (mm)	SOD (mm)
Commissioning Tests Near-Field (Z=0.31 m/kg$^{1/3}$)						
2	Test 5-6	PE4	20	2:1	7.2	72
1	Test 7	PE4	20	3:1	7.2	72
2	Test 9-10	PE4	20	5:1	7.2	72
Final Tests						
Force Hammer Verification Tests						
8	Hammer Test 4	N/A	N/A	N/A	N/A	N/A
Intermediate-Field Tests (Z=0.78-0.79 m/kg$^{1/3}$)						

[1] This is distance to the centre of the pressure-sensing element

Test Qty.	Test Key No.	Explosive	Mass (grams)	D:H	DOB (mm)	SOD (mm)
4	2-1-X	PE4	19	5:1	7.2	200
4	2-2-X	PE4	19	3:1	7.2	200
4	2-3-X	PE4	19	2:1	7.2	200
3	3-1-X	PE4	19	5:1	7.2	200
3	3-2-X	PE4	19	3:1	7.2	200
3	3-3-X	PE4	19	2:1	7.2	200
Near-Field Tests (Z=0.31 m/kg$^{1/3}$)						
2	4-1-X	PE4	19	5:1	7.2	72

The commissioning tests used charges comprising 20 grams of PE4 explosive. As this equates to a full scale 8,3 kg TNT charge and is higher than the selected research prototype mass this was reduced to 19 grams PE4 for all subsequent primary research tests.

The secondary data set listed in Table 6 comprised data from two test rigs. The Cranfield rig data set consisted of six test sets covering three SODs and two DOBs all with the same spherical charge. The SIIMA test rig data consisted of eight tests at two SOD's with different but geometrically scaled DOB's and charge masses. These test charges had the same D:H ratio.

Table 6: Secondary Test Data Summary

Test Qty	Test Key No.	Explosive	Mass (grams)	D:H	DOB (mm)	SOD (mm)
Cranfield Rig Secondary Data Tests						
2	360-X	PE4	160 gr[2]	N/A	100	360
2	230-X	PE4	160 gr	N/A	100	230
1	100-X	PE4	160 gr	N/A	100	100
1	230-50-X	PE4	160 gr	N/A	50	230

[2] Charge shape is spherical

Test Qty	Test Key No.	Explosive	Mass (grams)	D:H	DOB (mm)	SOD (mm)
SIIMA Secondary Data Tests						
4	Half Scale	TNT	1,000	5:1	25	250
4	Full	TNT	8,000	5:1	50	1,300

4.2 Modelling

The modelling executed as part of this research initially focused only on predicting experimental values that could be expected during the test phase. It was noted after completion that the models exhibited phased response within the resultant pressure traces and thus were included as part of the primary research data.

The modelling results are limited to the commissioning test configuration, which had a smaller target plate (diameter of 290 mm vs. final test configuration of 360 mm diameter). The results only include near-field target side-on pressure for all three D:H test charge ratios and a single D:H 5:1 ratio free-field (no target) ejecta model with side-on pressure and does not include any intermediate-field target models. Three D:H ratios were modelled for the near-field target model, these were 5:1, 3:1 and 2:1 and only one D:H 5:1 for the free-field ejecta.

The modelling results are presentenced in three main sections as follows; (1) Free-Field Side on Pressure and Specific Impulse, (2) Near Free-Field Side-On Pressure and Specific Impulse and (3) Near-Field Side-On Pressure and Specific Impulse.

4.2.1 Free-Field (No Target) Ejecta Side-on Pressure and Specific Impulse

Modelling results for the free-field ejecta model is presented in three sections. These are (1) Side-On Pressure Morphology, (2) Intermediate-Field Side-On Pressure and (3) Specific Impulse. As the pressure morphology changes with changes in the SOD the near-field (SOD = 60 mm) and the intermediate-field (SOD = 195 mm) model blast pressure morphologies are discussed separately.

4.2.1.1 Side-On Pressure Morphology

The pressure-time morphology of the shallow-buried blast at four different SODs predicted by the computational model is presented in Figure 10. The plots show how the blast overpressure changes at each SOD. Clear evidence of blast pressure phasing in the form of two peaks is visible from 30 mm SOD onwards. The blast front at 60 mm SOD is starting to show a third pressure phase developing in the tail of the pressure pulse. A precursor bow wave shock is seen to develop at an SOD of 60 mm. This bow wave precursor is not present at the 195 mm or 30 mm SODs. Calculating the average blast front velocity by dividing the time to reach the near and then the intermediate field sensor points divided by the distance travelled gives an near-field velocity of 1,819 m/s and a intermediate-field velocity of 1,896 m/s. This implies that the blast front is still accelerating upwards at the near-field SOD and has not reached its peak velocity.

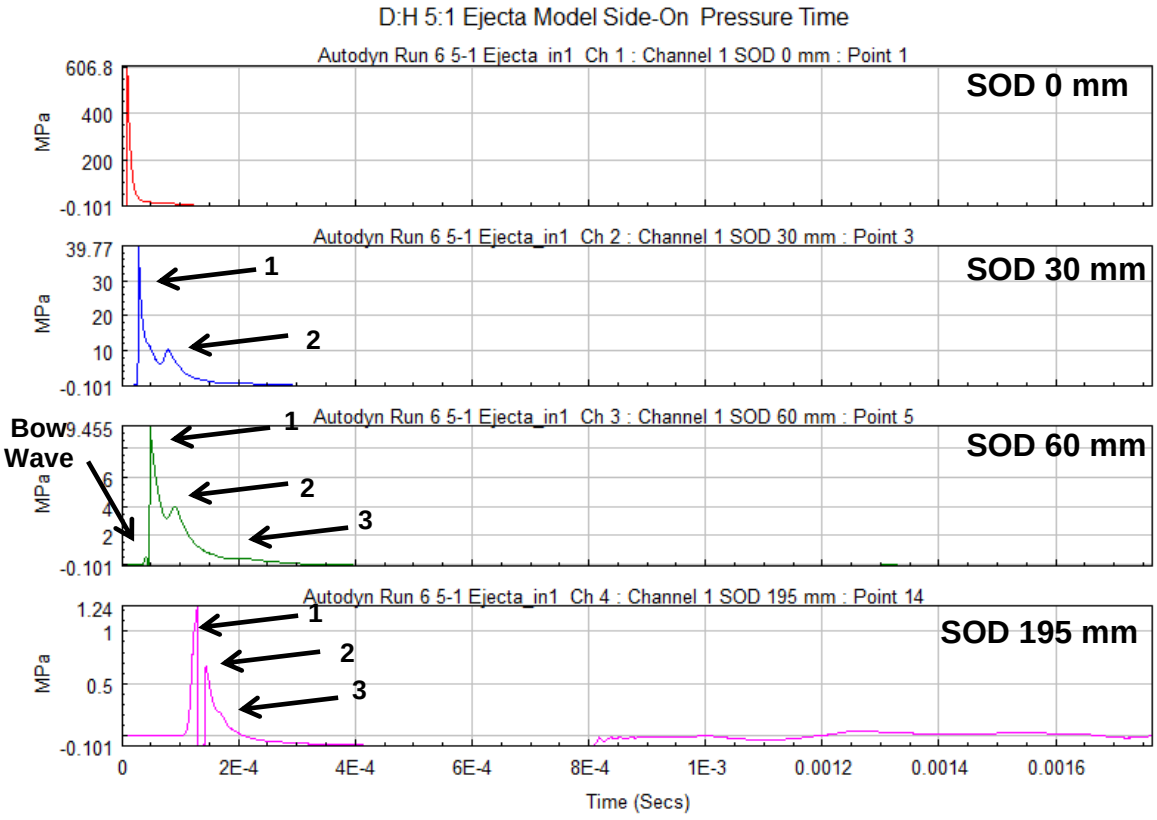

Figure 10: Shallow-Buried Blast Side-on Pressure Morphology

4.2.1.2 Intermediate-field Ejecta (No Target) Side-On Pressure

Only at 195 mm SOD does the pressure pulse exhibit the Friedlander (wave shape (Smith, Hetherington 1994) with a clear positive pressure phase followed by a negative phase, see Figure 11. At this distance the model shows that the shock wave has separated from the blast front with a steep negative inflection. The blast front is also not a strong discontinuity but is smeared with a rounded appearance. This smearing is seen from the 30 mm SOD and is understood to be due to the software introducing viscous terms to ensure energy balance is maintained (Snyman 2015). Peak model pressure of 1.24 MPa occurred at 0.139 ms after detonation. The end of the negative pressure phase at around 800 ms is characterised by a sudden pressure increase. This is thought to arise from the symmetric inflow of atmospheric air meeting near the centre of the target, creating a small pressure pulse by pushing the remaining detonation gases together.

Three pressure phases are clearly visible within the initial positive pressure period as shown in see Figure 11. A loading event or phase is determined when there is a visible change in the rate at which the pressure decreases. The initial blast overpressure (1) was determined at the first phase (Phase One). The following pressure peak (2) is the second phase (Phase Two), and the third phase (Phase Three) starts at a third pressure increase (3) and lasts until the pressure becomes negative (4). The pressure discontinuity at the end of the negative phase (5) is caused by the air replacing the vacuum caused by the detonic expansion.

As the almost instantaneous pressure decrease after the initial blast front overpressure was not observed in actual test data, the model side-on pressure plot was manually adjusted using a sine curve fit to remove the negative pressure dip. This would enable physically representative specific impulse data to be calculated from the model for comparison to the test data. This modification reduced the peak pressure from 2.24 MPa to 1.18 MPa. This is deemed acceptable. The net result is a much higher specific impulse for the modified model. The end of Phase One and beginning of Phase Two was set at

the middle of the separation gap. For actual test data this was set at the lowest point after the first peak.

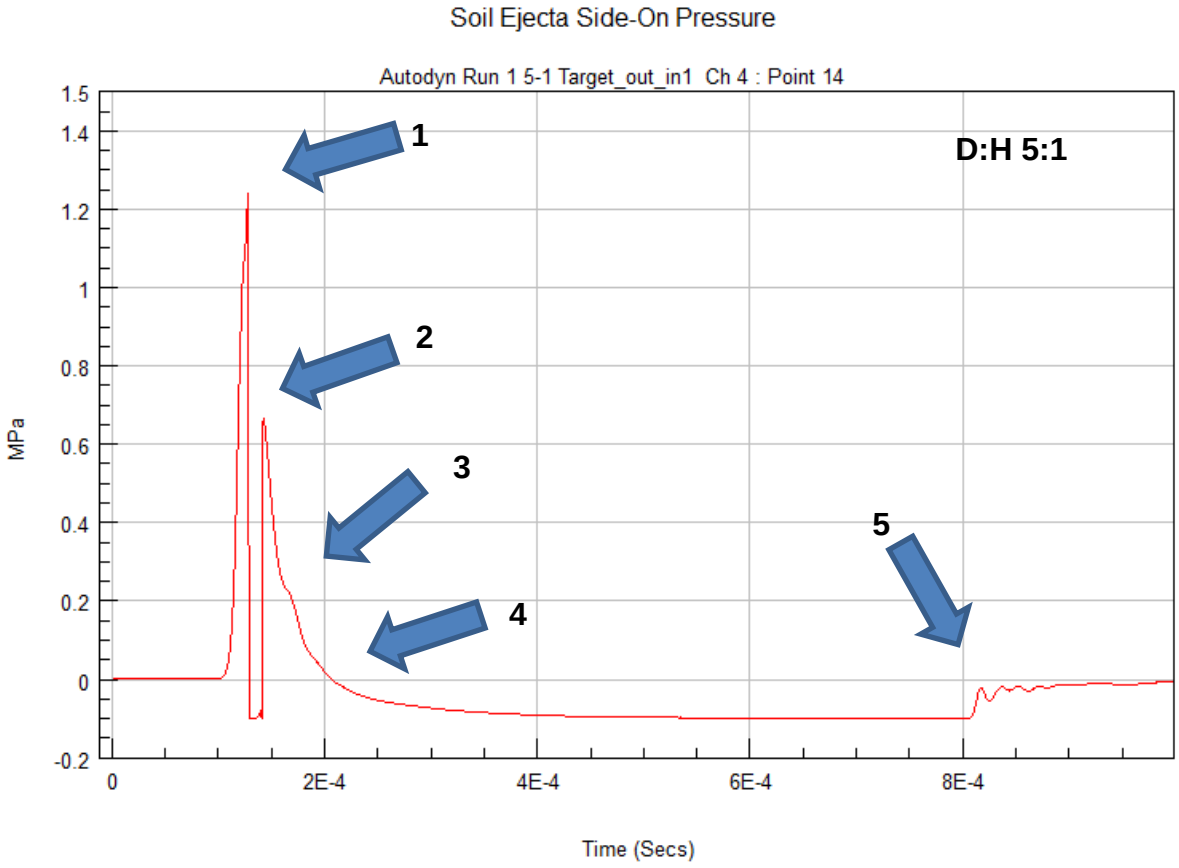

Figure 11: Partitioned Intermediate Soil Ejecta Side-On Pressure (SOD 195 mm) Phases

The peak side-on pressure and positive pressure phase duration obtained from both the initial and the modified the ejecta model for a 20 g charge with a D:H of 5:1 and at a SOD of 195 mm are 1.240 MPa and 0.206 ms and 1.187 MPa and 0.207 ms respectively. The slight difference in total positive phase durations between the modified model (MM 5:1) and the original model (M5:1) is due to the manual extraction methods used to identify the phases.

4.2.1.3 Intermediate-Field Specific Impulse

The specific impulse of the side-on pressure for the total positive pressure phase as well as each of the manually partitioned phases for both the original model 25 and 38 Pa.s. The modified model results in a total specific impulse

that is 50% higher than that of the original model. This is primarily due to the negative impulse generated by the separation gap in the original model results as well as 20 µs of additional pressure added to the curve with the manual changes implemented. The increase was temporally shared equally between the two phases.

4.2.2 Near Free-Field (No Target) Ejecta Side-on Pressure and Specific Impulse

The near-field data for a SOD of 60 mm are presented to provide model predictions pertaining to the generated blast pressure just prior to impact without a target.

4.2.2.1 Near Free-field Ejecta (No Target) Side-On Pressure Morphology

Figure 12 presents the model near-field ejecta side-on pressure time plot and the three pressure occurrences indicating phased pressure generated by the shallow buried blast are clearly visible.

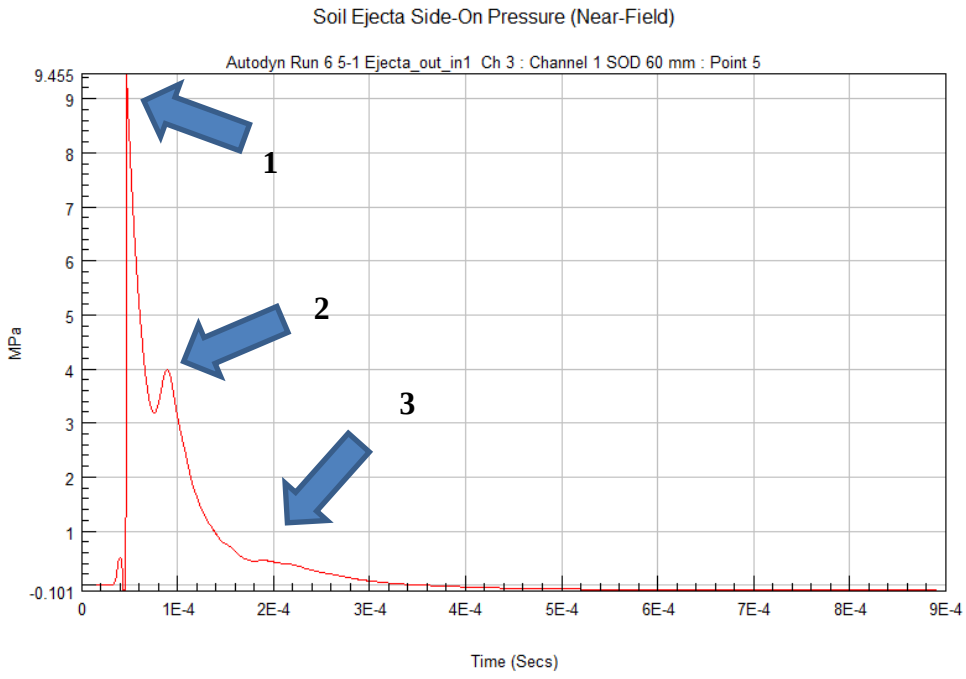

Figure 12: Partitioned Near-Field Ejecta (No Target) Side-On Pressure Time Plot

The precursor bow wave shock is considered as part of the initial loading phase. The peak pressure and the positive pressure phase duration of the

intermediate-field side-on pressure was 1.187 MPa and 0.107 ms compared to the near-field side-on model's 9.455 MPa and 0.323 ms which is more than seven times larger and the duration is three times longer.

4.2.2.2 Near Free-field Ejecta (No Target) Specific Impulse

The computational model generated total near-field (no target) phase-specific impulse of 381 Pa.s which was about ten times higher than the 38 Pa.s for the modified intermediate-field model. The bow wave shock contributes 2.85 Pa to Phase One, which is 1.56% of the impulse of the phase.

4.2.3 Near-Field (Target) Side-On Pressure and Specific Impulse

The model results of the near-field test conditions are presented in two sections as follows; (1) Side-On Pressure Morphology and (2) Specific Impulse.

4.2.3.1 Side-On Pressure Morphology

The model pressure is taken at a SOD of 65 mm as it is placed 7 mm proud of the target face. This was chosen as in the physical tests the pressure sensor diameter was 10 mm, resulting in the centre of the sensor being at least 5 mm proud of the target face, thus ensuring the closest possible correlation between the model and test geometry.

Figure 13 presents the three SOD points recorded for the second D:H 5:1 ratio model that was run to explore boundary outflow effects on the results as well as to confirm an additional 0 mm SOD point of near-field target model also indicated comparison with the soil ejecta model. As with the free-field ejecta model the at least three pressure occurrences or phases.

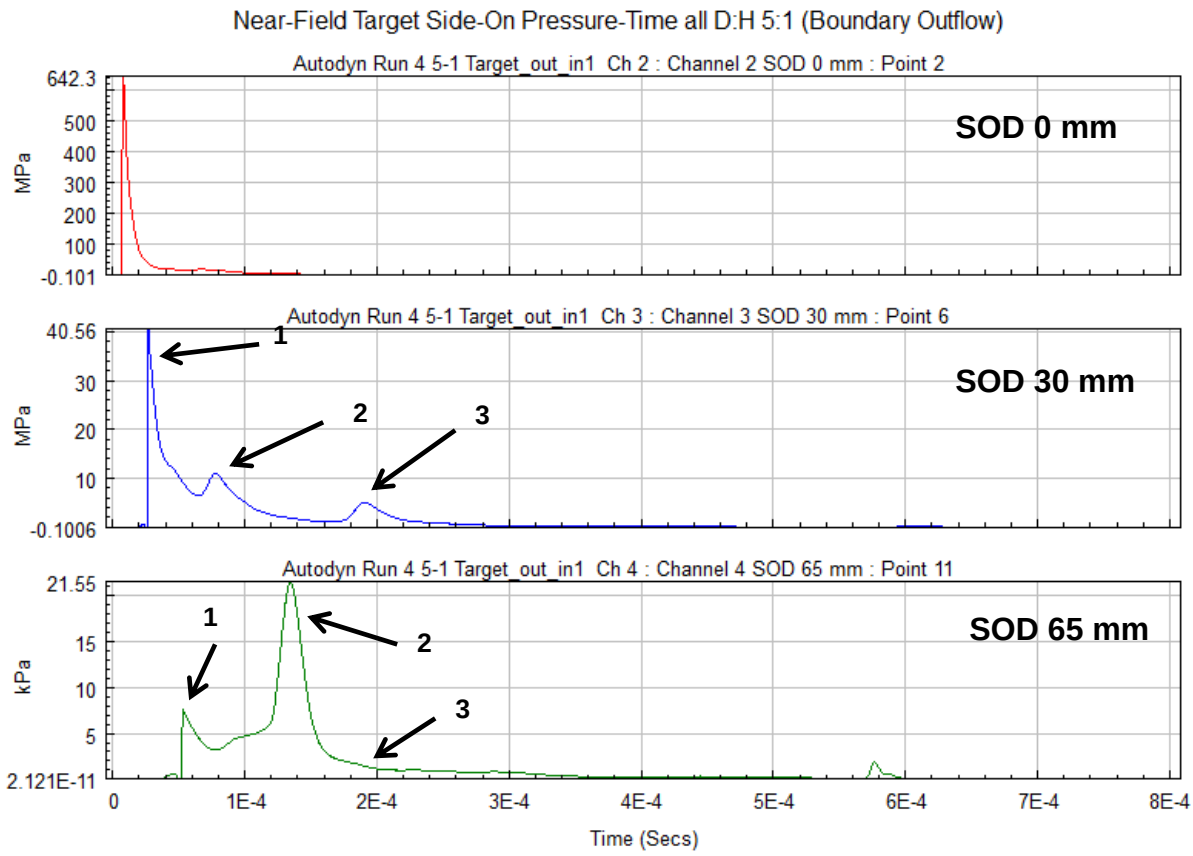

Figure 13: Near-Field Target Side-On Pressure Morphology (D:H 5:1)

The ejecta (no near-field target) model predicted a peak pressure of 606.8 MPa compared to 642.3 MPa at 0 mm SOD predicted by the near-field target model. Similarly the ejecta model predicted 39.77 MPa peak pressure compared to the 40.56 MPa peak pressure predicted by the near-field model for a 30 mm SOD. The differences are due to the variability in implicit code solvers which change the time step based on the step solution convergence. These differences reduce as the SOD increases and are considered negligible for this work. The precursor or bow wave shock seen with the ejecta model at 60 mm SOD is also visible in all the D:H near-field model pressure-time plots. A small reflection (1.8 MPa) was noted at around 0.59 ms for the 65 mm SOD.

Figure 14 presents the side-on pressure-time plots for all three D:H ratios modelled without boundary outflow just off the target facer at a SOD of 65 mm.

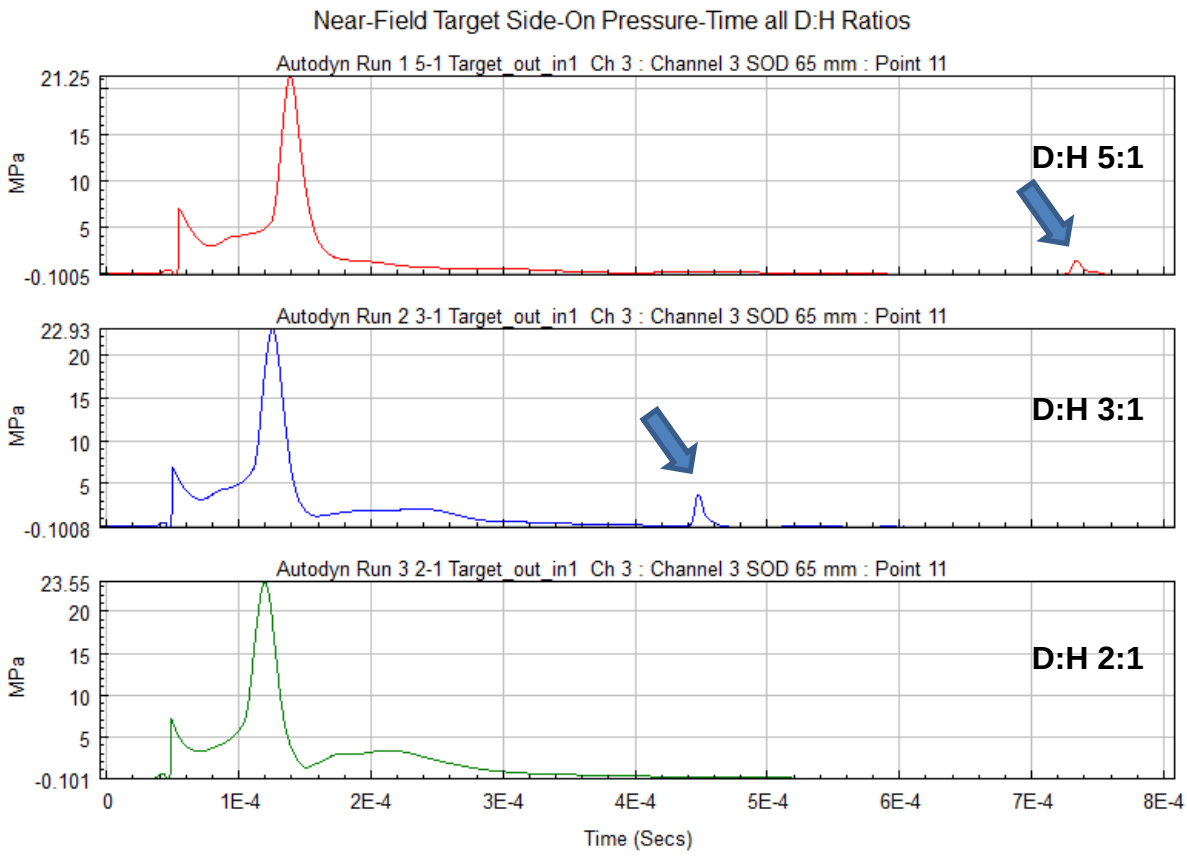

Figure 14: All Three D:H Ratio Pressure Time Plots at 65 mm SOD

The reflected pressure of D:H 5:1 is seen to occur nearly 0.1 ms later than the model with boundary outflow and appears much earlier and larger in the D:H 3:1 model. It is completely absent in the D:H 2:1 model results. Using a Rayleigh wave equation (Deshpande, McMeeking et al. 2009b, Smith, Hetherington 1994), the surface wave would only be about 4% of its initial amplitude when it reached the soil bin boundary, and thus cannot be considered the source of this reflection and it would also be present in the D:H 2:1 model results. If this small reflection was due to there being no boundary outflow the pressure phenomena would have had to move at between 1.85 and 2.6 km/s. This effect appears to be D:H ratio driven.

Again the near-field computational model provided three loading phases (see Figure 15). As previously described a loading event or phase is determined when there is a visible change in the rate at which the pressure decreases. Phase One was determined to include the bow wave shock and ends at the

next minima. Phase Two starts at the identified minima and is deemed to end at the following minima or the middle of the following bulge or pressure extension. Phase Three is regarded as having ended when the pressure becomes negative. Although this is an argument for possibly four or more phases, the partitioning was led by results from the commissioning tests presented later.

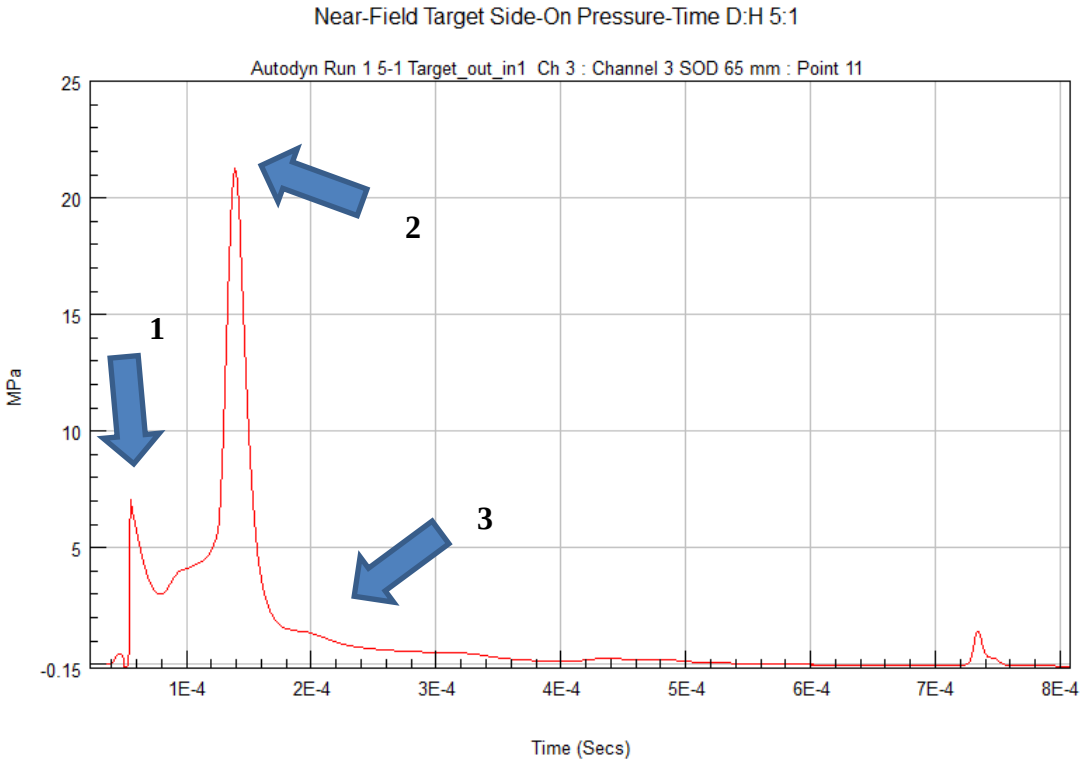

Figure 15: Near-Field Target Side-On Pressure Plot (D:H 5:1)

As the initial pressure peak was not the highest, the two peaks are presented separately as the initial and second. Initial peak side-on pressures of 7.0, 6.9 and 7.1 MPa were predicted for the 5:1, 3:1 and 2:1 DH charge ratios and for practical purposes can be considered the same. For the second peak side-on pressures of 21.3, 22.9 and 23.6 MPa were predicted for the 5:1, 3:1 and 2:1 DH ratios. These peak pressures are two times higher than the free-field side-on pressure at similar SOD's which falls within theory presented in (Smith, Hetherington 1994).

The times to reach peak pressure gave a decreasing trend as the D:H ratio decreased indicating higher gas velocities. Based on arrival times the model

predicted average blast front velocities increasing from 1,181 m/s for the 5:1 to 1,327 m/s for the 2:1 D:H ratio charge. The total positive pressure durations of between 562 µs to 541 µs were predicted by the models for the 5:1 and the 2:1 D:H ratio charges. The 3:1 D:H ratio charge gave a shorter positive duration due to a longer tail (See Figure 15). This did not affect the specific impulse results.

4.2.3.2 Specific Impulse

The computational model predicted specific side-on pressure impulse with a near-field target of 935, 1,069 and 1,183 Pa.s for the 5:1, 3:1 and 2:1 D:H ratio charges. This represents a clear increasing specific impulse with decreasing D:H ratio charges. The bow wave shock contributed 1.2 Pa.s specific impulse

4.3 Shallow-Buried Blast Ejecta (No Target) Test Results

This section confirms the presence of phased blast loading as captured by the research tests and presents the general phased blast load results of a shallow-buried threat without a near-field target present. These data include high-speed imaging, side-on pressure probe placed in the intermediate-field (SOD 195 to 200 mm), post-test crater dimensions and mass of soil ejected. As no target is present these are termed free-field ejecta tests. These results are presented in five sections as follows; (1) Visual Blast Morphology, (2) Blast Craters and Ejecta Mass, (3) Side-On Pressure-Time and (4) Specific Impulse

4.3.1 Visual Blast Morphology

Visual blast morphology refers to data that is obtained from high speed imaging. Although affected by available light, frame rates of 30,000 frames per second were achieved providing a measurement resolution of 33 µs. The video (visual) data were used to extract the morphology of a shallow buried blast in terms of shape and dimensions, ejecta and blast front velocity both vertically and horizontally. Along with pressure the blast velocity and mass of soil ejected are key elements of shallow buried blast loading. The data is presented in to sections, these are; (1) Blast Shape and (2) Blast Velocity.

4.3.1.1 Blast Shape

The high speed video revealed that a shallow buried blast develops as a tulip or spear shape. There is an early break out of light within less than 30 µs after detonation. After this the blast front grows out vertically and laterally. The vertical front growth is much faster than the sides which bulge outwards. This shape is to be expected with a centrally detonated charge as the centre will detonate first and start pushing the soil cap upwards. As the detonation wave moves laterally through the charge the rest of the soil cap is accelerated vertically in a sequentially delayed manner, resulting in the spear-shaped blast front.

The blast tip starts to open from 300-400 µs forming an inverted hollow cone as reported in (Braid 2002). Black gas is seen to escape from the opened top of the blast front indicating unreacted detonation products (Cooper 1996a). The hollow cone formation continues up to 3-4 ms after detonation and its end signalled by a slight contraction at the base of the cone (blast stem) and on the lower sides of the blast cone. The blast shape then changes as the soil at the base of the blast stem start to move laterally at a velocity of 4-5 m/s making the blast cone exterior more vertical and forming a hollow ejecta wall that is continually slowing down to around 0.5 m/s at around 120 ms after detonation. The end of the blast morphology is characterised by a heave as the blast ejecta side walls collapse outwards forming a raised lip of soil around the crater.

This two phased blast ejecta phenomena was reported by (Freitas, Bigger et al. 2014) for full-scale shallow-buried blast indicating that the scaled tests are replicating full scale blast behaviour. The two phases are termed high-speed and slow speed as defined by the ejecta velocity. The high-speed phase has initial ejecta (blast front) velocities of 1,700-2,200 m/s that slow down to around 250 m/s at the end of the high-speed phase. The slow speed phase has vertical ejecta velocities of less than 250 m/s. The high-speed phase ejecta is characterised with mostly fine power with larger clumps of ejecta emerging at around 1.5 ms after detonation.

Figure 16 presents a series of three high-speed images from a typical scaled shallow-buried blast. Frame 1 at 0.033 ms after detonation shows the blast front point at an SOD of 63 mm. This shows the tip of the developing blast front as it would be just prior to impact on a near-field target as placed for this research with a SOD of 72 mm. Frame 2 is the shape of the blast front when it reaches the sensing element in the pencil probe. Frame 3 shows the blast tip or front starting open up. No separate blast shock wave was seen in any of the shallow-buried blast tests until after the pressure probe was passed by the blast front.

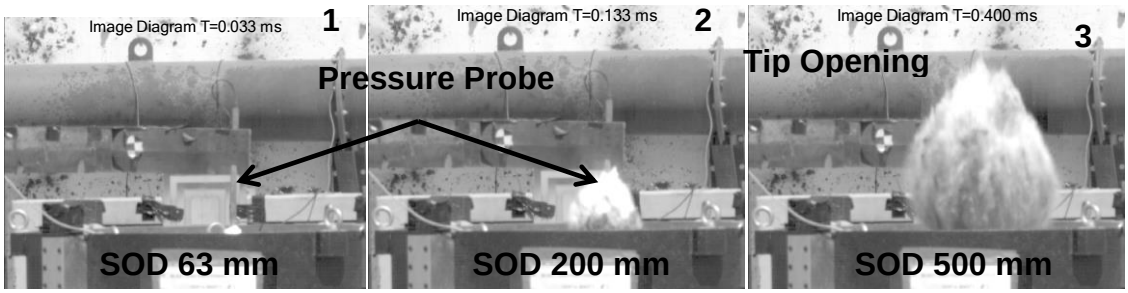

Figure 16: Sequence of High-Speed Photos showing the Blast Front Morphology for Shallow-Buried Blast

Figure 17 shows the shallow-buried blast at 4 ms and 117 ms respectively. Frame 1 shows the blast morphology at the end of the high-speed ejecta phase. Black detonation products are still visible. Frame 2 shows the end of the slow-speed ejecta phase just prior to the final heave outwards. (Freitas, Bigger et al. 2014) notes that the slow-speed ejecta phase is driven by the inertial loading of the soil.

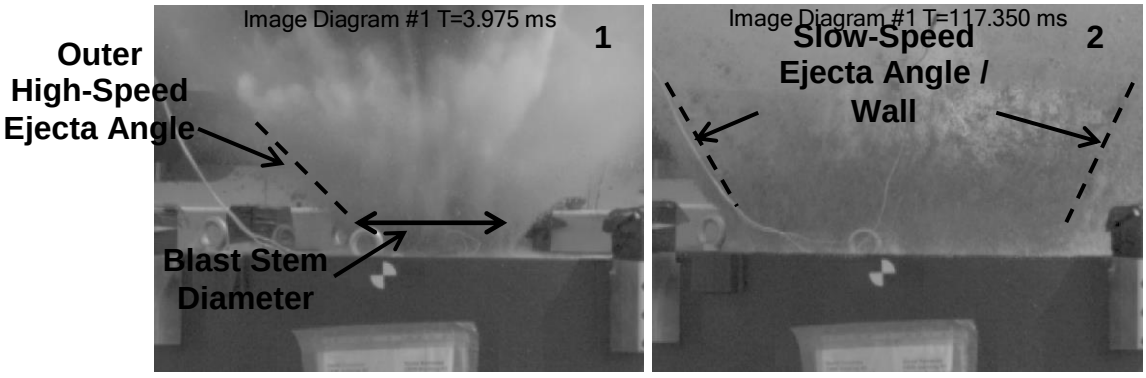

Figure 17: End of Phase One and Phase Three for Typical Shallow-Buried Blast Ejecta

Some of the high-speed videos had blast fronts that were angled to one side. Figure 18 shows a series of three frames with such an asymmetric blast front. Frame 1 shows the initial break out with a leading edge pointing to the left. This point is formed by the centrally located detonator and the cylindrical shape of the charge. Frame 2 and Frame 3 shows that this angled blast front leading point is maintained as the blast develops. This leads to the blast is impacting on the right-hand side of the sensor probe first. The pressure-sensing element is on the left-hand side. This leads to a lower peak pressure being recorded as would be the case for a vertically symmetrical blast front. For the case where the front impinging on the left-hand side first would lead to a higher initial pressure peak as well as the development of a reflected pressure pulse. The pressure probe is not designed to measure blast over pressure more than a few degrees off centre and these asymmetric conditions result in the variable side-on pressure results discussed later.

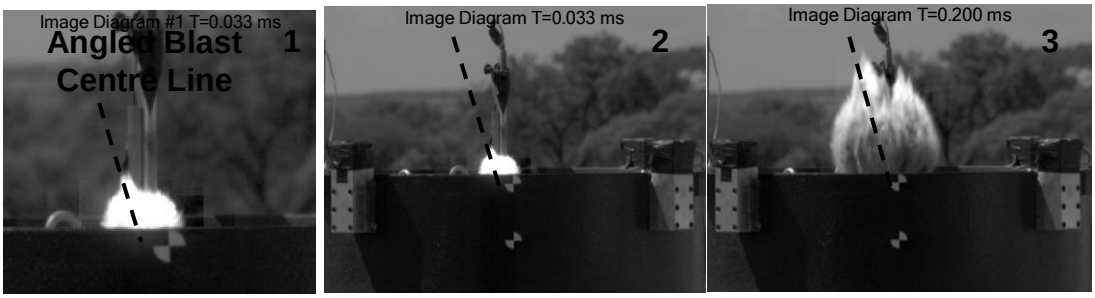

Figure 18: Sequence of High-speed Photos Showing Asymmetric Blast Front Development (Test 3-3)

4.3.1.2 Blast Front Velocity

Figure 19 and Figure 20 present a single D:H 5:1 blast front position and velocity time plot recorded by the two cameras positioned ninety degrees relative to the test rig, one in front and one on the right-hand side (RHS). These data show that a shallow-buried blast initially accelerates after detonation to a peak velocity of over 2,500 m/s at a SOD of 100 mm before decaying slowly matching the modelling results discussed in Section 4.2. This gives the parabolic displacement-time curve shown in Figure 19.

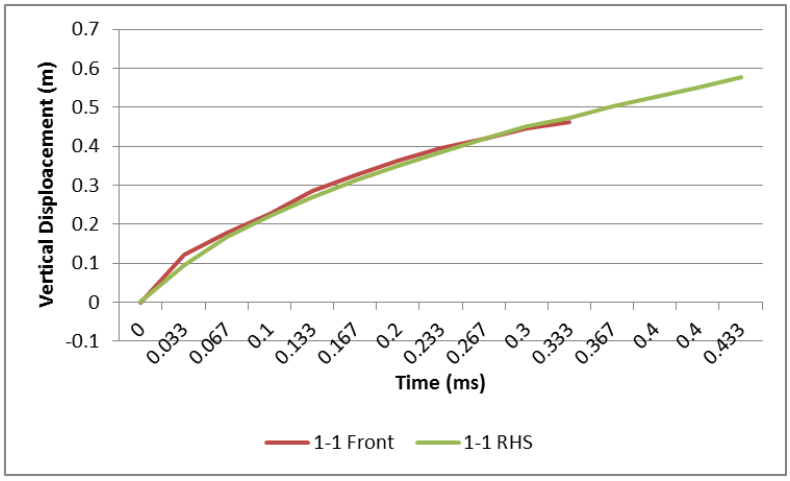

Figure 19: Blast Front Distance-Time Plot (D:H 5:1)

Although the two curves in Figure 19 follow quite closely Figure 20 shows the impact on the extracted velocity. This is due to the relatively small number of measurement points in the video.

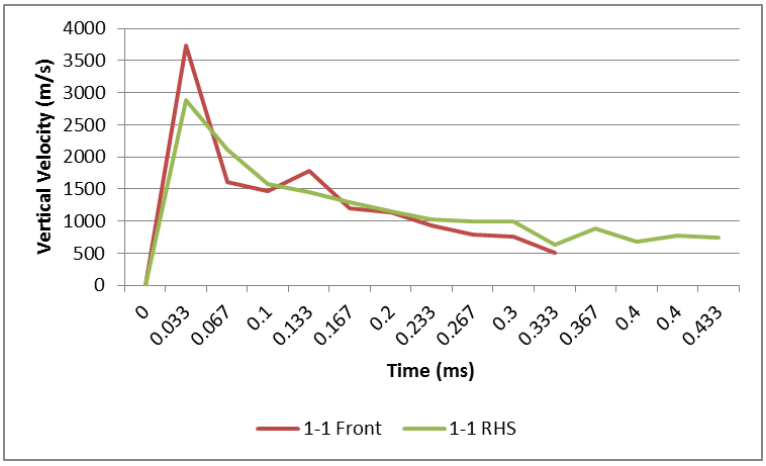

Figure 20: Blast Front Incremental Velocity-Time Plot (D:H 5:1)

Figure 21 and Figure 22 present the average velocities and calculated standard deviations for all three D:H ratio's with SODs at 72 mm and 195 mm respectively, as interpolated from the distance and velocity-time data. The experimental variability is reflected in the large standard velocity deviations recorded. From the near-field target modelling it was expected that there would be increasing blast front velocity with decreasing D:H ratios. This is not clearly evident from the 72 mm and 195 mm SOD velocity results. The large standard

deviations and the small data sets used (5 for 5:1, 2 for 3:1 and 3 for 2:1 D:H ratio charges) contribute to poor D:H ratio resolution on the blast front velocities.

There is variability between the front and right-hand side camera data. This is more apparent at the larger SODs. These differences are attributed to small experimental set-up variances between the two cameras, in particular the distance from the test target as well as the camera's angle of inclination due to the unevenness of the field test terrain. These variances, combined with the variability in the blast front angle and direction, resulted in larger differences as the blast from travel distances increased and thus the greater inconsistency at the 195 mm SOD.

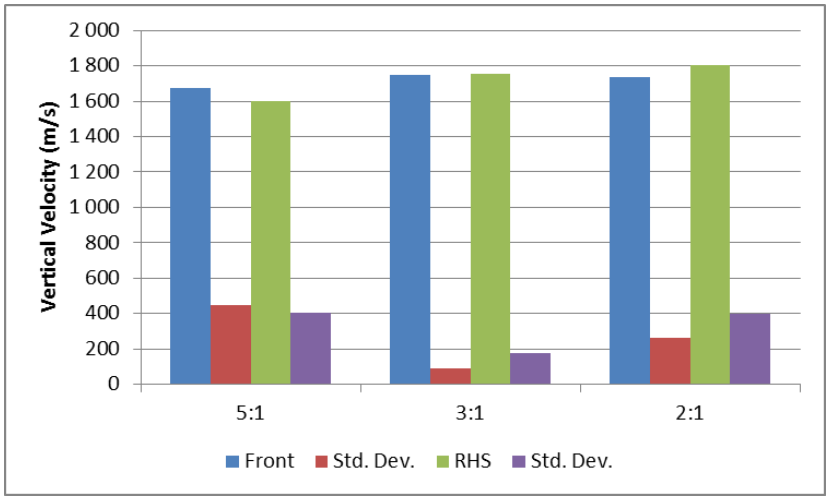

Figure 21: Camera Interpolated Blast Front Velocity at 72 mm SOD

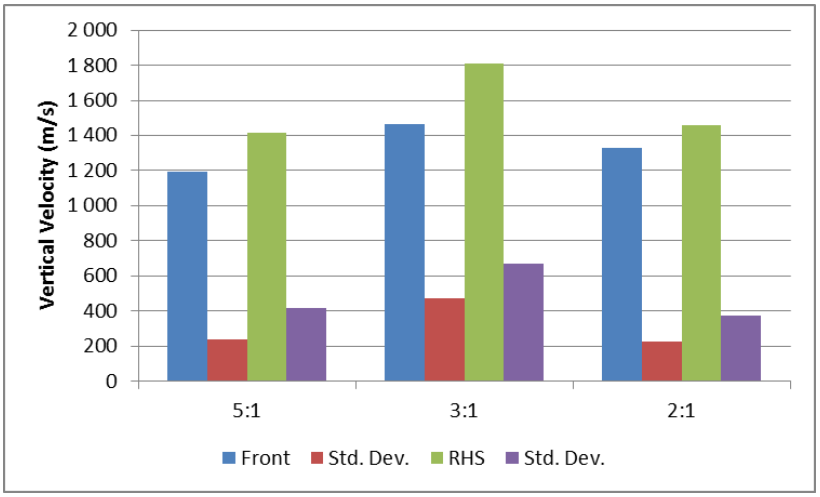

Figure 22: Camera Interpolated Blast Front Velocity at 195 mm SOD

Figure 23 presents the final averaged front and right-hand side interpolated velocities at 72 mm and 195 mm SODs. This final averaging shows the increasing blast front velocity trend with decreasing D:H charges for 72 mm SOD and only with the first two D:H ratio charges at 195 mm. This is due to a single test that gave low velocities, and when combined with the small data pool it affected the averaged velocity sufficiently to hide any trends. Although these experimental data do not provide sufficient resolution to clearly discriminate between the D:H effects, the primary focus of the research is on shallow-buried blast and these data provide useable results in this regard.

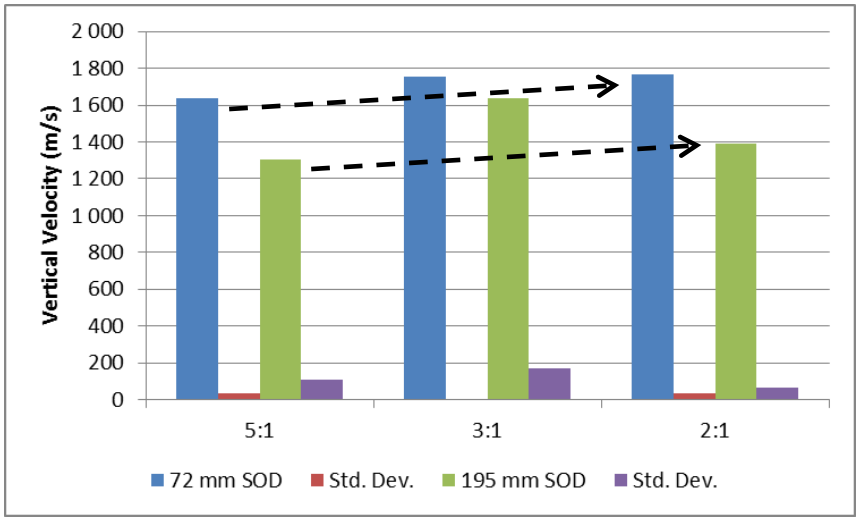

Figure 23: Final Averaged Blast Front Velocities

4.3.2 Blast Craters and Ejecta Mass

This section discusses craters measured from free-field ejecta test and presents the estimated mass of soil ejected in a typical free-field shallow-buried blast. (RMSS February 2005) notes the occurrence of two distinct craters with shallow-buried blast and a near-field target present. During the execution of the scaled free-field tests the two crater diameters were recorded. Figure 24 shows a typical test crater with soil residue from the detonation and subsequent blast (grey) and the double crater. The black line is the primary crater and the red line is the secondary crater.

Figure 24: Typical One-Seventh Scale Test Crater

Figure 25 summarises the measured crater dimensions as defined by (RMSS February 2005). With the exception of the secondary crater depth all the data for the D:H charge craters had standard deviations of less than 10% of average. The secondary depth averages had a maximum standard deviation of 20% of average. The final test free-field crater was compared to the commissioning free-field test and measured dimensions were well within the same averaged values. The commissioning data were not included in the data set as the pressure probe was positioned in a completely different holder. These results do not show any particular trends between the charge D:H ratios.

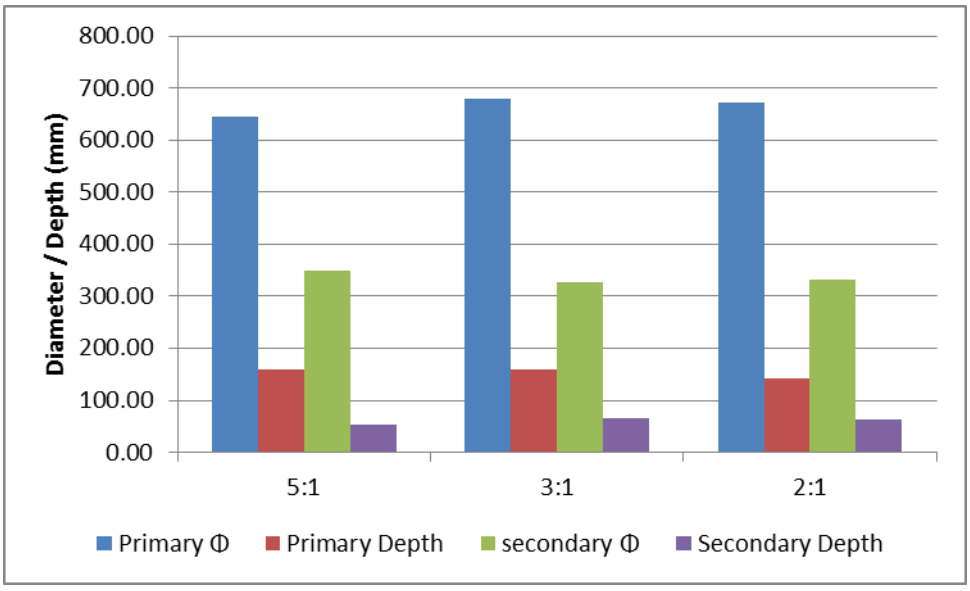

Figure 25: Free-Field Shallow-Buried Crater Dimensions (RMSS February 2005)

Figure 26 shows the blast front diameter at a SOD of 72 mm at 0.25 and 4 ms respectively for a D:H 5:1 charge test. Frame 1 shows that the initial ejected soil cap and surrounding ejected soil is smaller than the blast front, and thus will be completely captured by the 360 mm diameter near-field target. Frame two shows that at the end of the high-speed blast phase the diameter of the blast cone at 72 mm SOD is larger than the near-field target diameter at 378 mm.

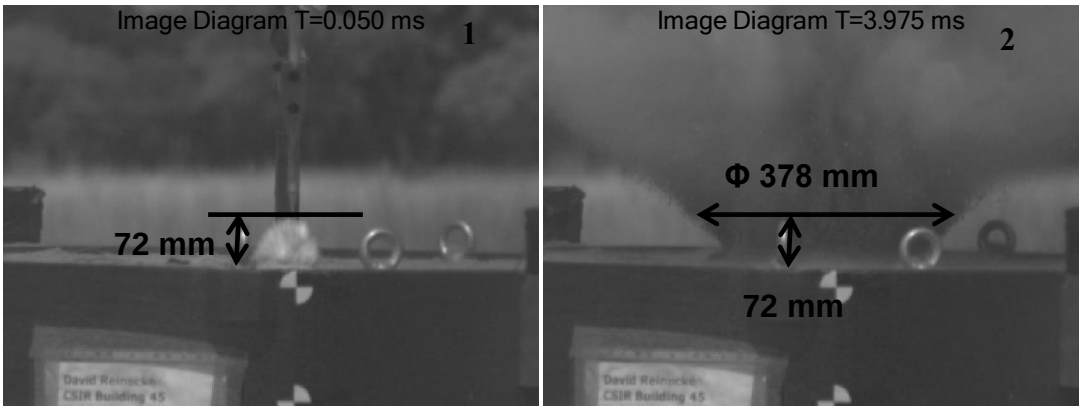

Figure 26: Ejecta Morphology at 0.025 and 4.0 ms after Detonation (D:H 5:1)

The high-speed video analysis revealed that the blast stem diameter at the end of the slow-speed ejecta phase correlated with the recorded primary crater diameter. The high-speed ejecta phase blast stem diameter correlates to two thirds the secondary crater diameter. Figure 27 shows the blast stem diameter and the crater dimension it correlates with the secondary crater diameter.

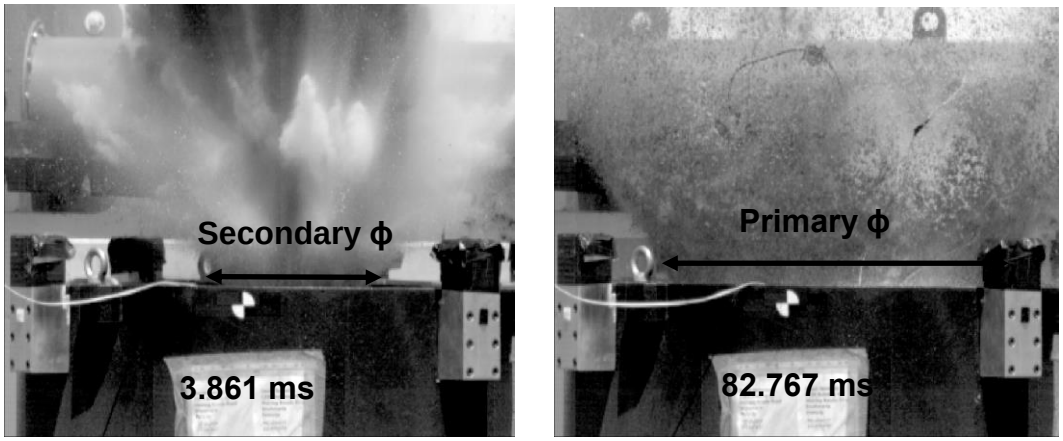

Figure 27: Blast Cone Stem Diameters at End of High and Low-Speed Ejecta Phases

Figure 28 presents the measured total soil ejecta mass and the standard deviation. No clear D:H ratio trends are visible in the data, indicating that similar masses of soil were ejected. This is attributed to the experimental variability as well as the actual differences between the D:H ratio charges being relatively small and were thus lost within the standard deviation generated by the applied methodology.

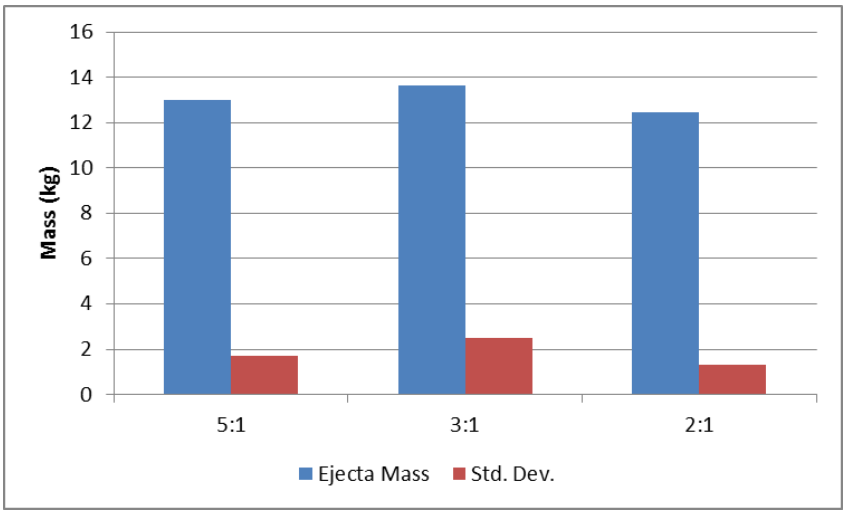

Figure 28: Ejected Soil for all D:H Ratios

The crater volume is much larger than the ejected sand volume and cannot be used as is to estimate the two ejecta phase volumes. The mass or volume ratio of the primary and secondary crater was used with the measured ejecta mass to estimate the high and slow-speed phase ejecta masses. To determine the mass of soil ejected during each shallow-buried blast phase, the crater created below the secondary crater depth is deemed to be due to crushing and compression of the soil by the detonating charge and is not ejected. This crater volume is disregarded and only the secondary crater depth is used for the ejecta volume calculations. The volume of soil ejected by the high-speed blast phase is assumed to be the volume defined by the secondary crater diameter and secondary crater depth. The volume of soil ejected during the slow-speed phase is determined by the primary crater diameter and the secondary crater depth minus the high-speed soil ejecta phase volume.

Figure 29 presents the calculated soil ejecta mass for each phase. The use of simple cylinder geometry in calculating the volume ratios is deemed sufficient for this application. The slow-speed ejecta mass is double that of the high-speed ejecta mass.

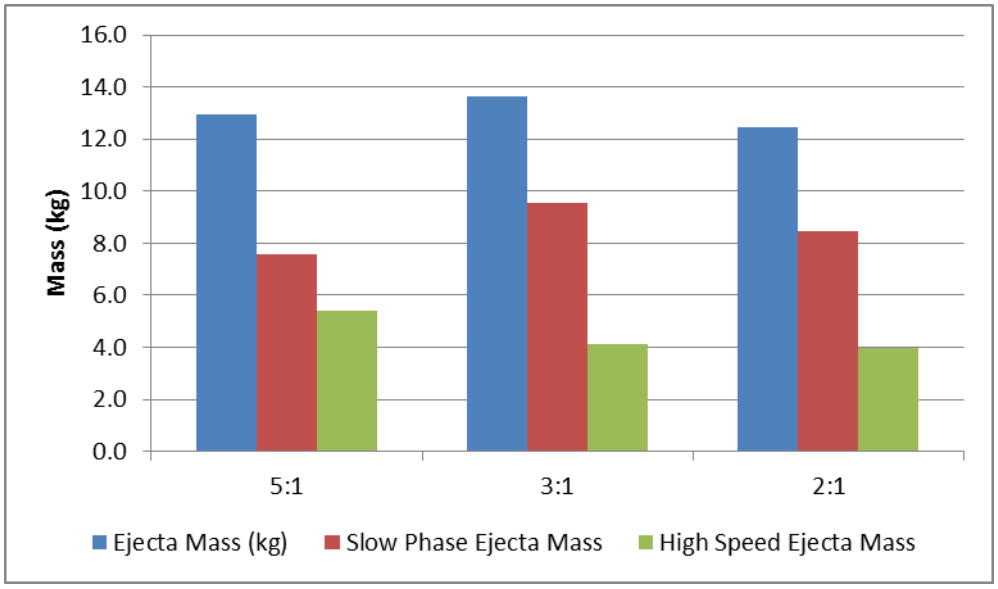

Figure 29: Averaged Total Test Ejecta and Estimated Phase Ejecta Mass

4.3.3 Side-On Pressure Morphology

Figure 30 presents the overlaid side-on intermediate-field pressure-time plots recorded for all the final free-field ejecta tests. The plots clearly show the enormous variability in the measured side-on pressure due to the experimental variability noted previously. There is also variability in the time of arrival with the same D:H test charges.

Most of the plots show a reflected pressure pulse indicating an off-vertical impact onto the pressure probe sensor. The PCB pencil probes have a flat running the length of the probe and the sensing element is placed on the flat, providing a surface that will develop reflected pressure if the blast is not perpendicular to the probe. PCB requires a deviation of no more than 5 degrees to get the best results from this type of sensor (Walters 2016). The reflected pressure is identified by a more gradual pressure rise. In some cases the

reflected pressure peak was larger than the initial blast front peak. Some test data did present the expected Friedlander pressure-time response.

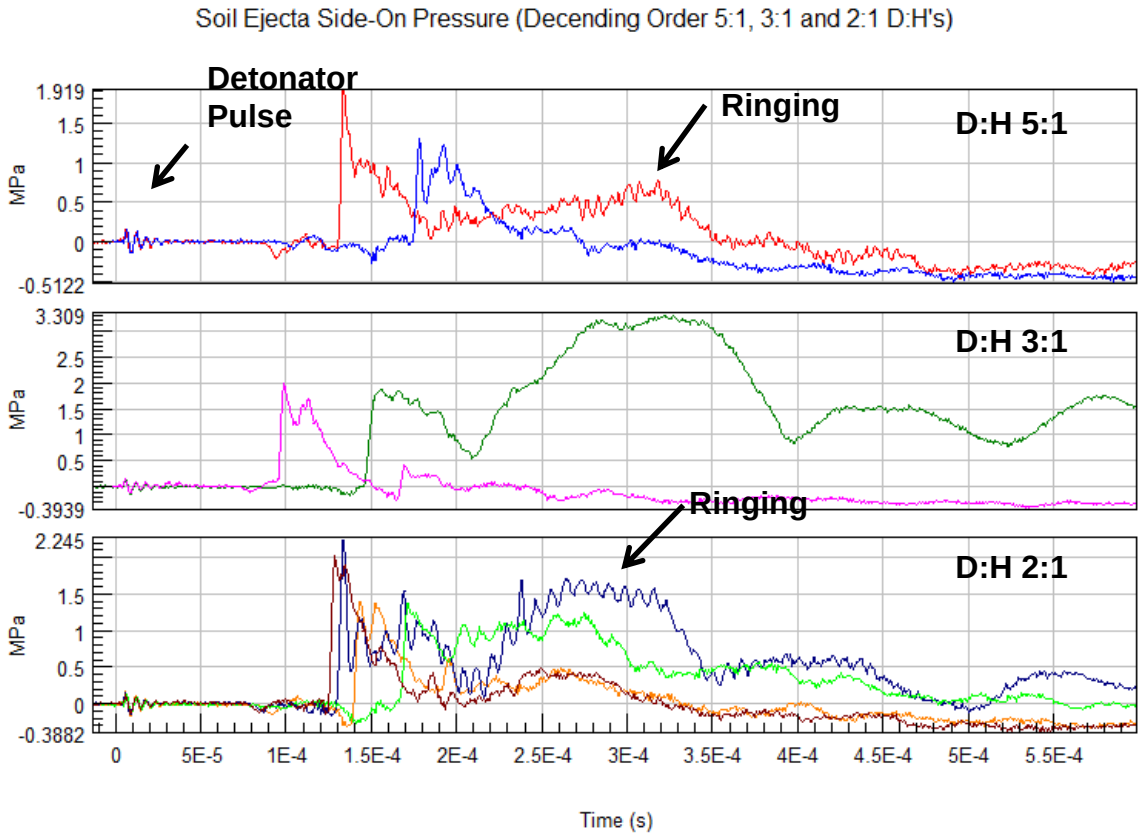

Figure 30: Final Ejecta Test Side-On Pressure-Time Plots (all Tests) D:H 5:1, 3:1 and 2:1

Most data exhibited a similar pressure-time profile as the computational model with an initial sharp peak followed by a valley and a second sharp peak before decaying slowly.

The detonator firing pulse is visible in the data at time zero. Also visible are negative and positive pressure fluctuations prior to the arrival of the blast front. These are due to electromagnetic interference from the high current and voltage firing pulse and from the ionised detonation products breaking out from the soil. No separate detached precursor shock wave is present in any of the test data. A bow wave precursor shock is present; however, it is hidden within the electromagnetic noise in some cases. Not all traces return to zero or indicate a negative pressure phase. This is due to temperature drift from heat transfer.

Ringing from ejecta impact is visible as high-frequency oscillations in the pressure traces.

Due to the large second reflected pressure peak occurring in some of the recorded test plots, the peak pressure data were extracted twice. Figure 31 and Figure 32 present the average initial and overall peak free-field pressures recorded for the final ejecta tests as well as the commissioning and computational model. Where more than one test data point was recorded the standard deviation is presented. Standard deviations of up to 25% were recoded for both initial and peak side-on pressures.

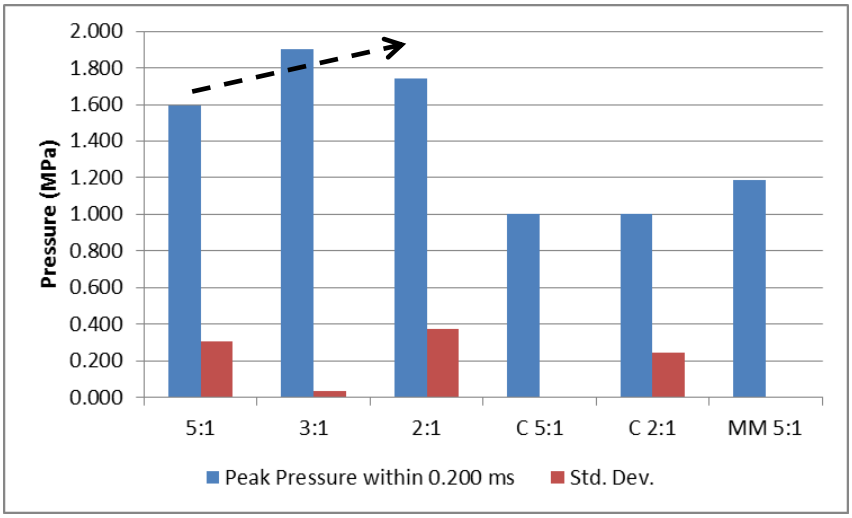

Figure 31: Free-Field Ejecta Tests Initial Average Peak Pressure

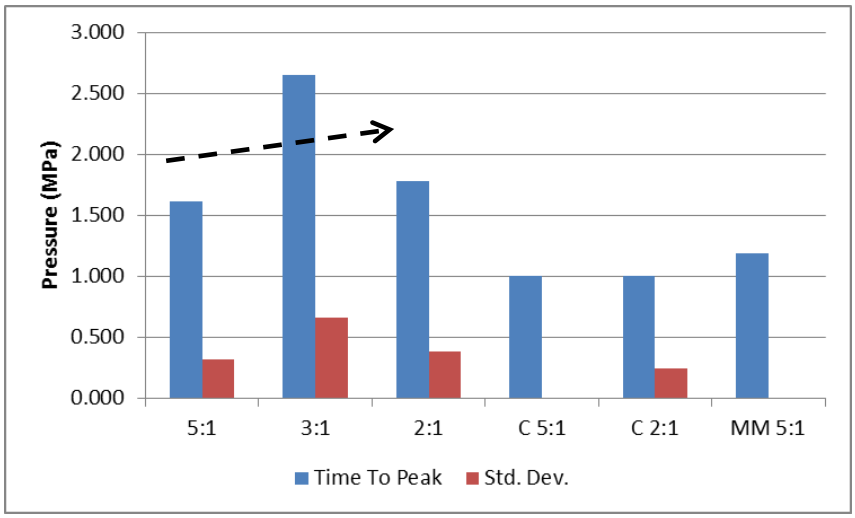

Figure 32: Free-Field Ejecta Tests Peak Pressure

Figure 33 presents the positive pressure duration and standard deviation for all D:H ratios from the final and commissioning tests as well as the ejecta computational model. A maximum standard deviation of 51% was recorded for the D:H 3:1 tests. This is due to the small test pool of only two data point of which one exhibited extremely high reflected pressure as shown in Figure 30. This was caused by angular impact of the blast on the sensor resulting in reflected pressures with attendant longer positive pressure durations as compared to a blast passing perfectly perpendicularly over the sensing element. If this single test is ignored then side-on pressure exhibits a trend of increasing side-on pressure and duration with decreasing D:H ratio for the intermediate-field.

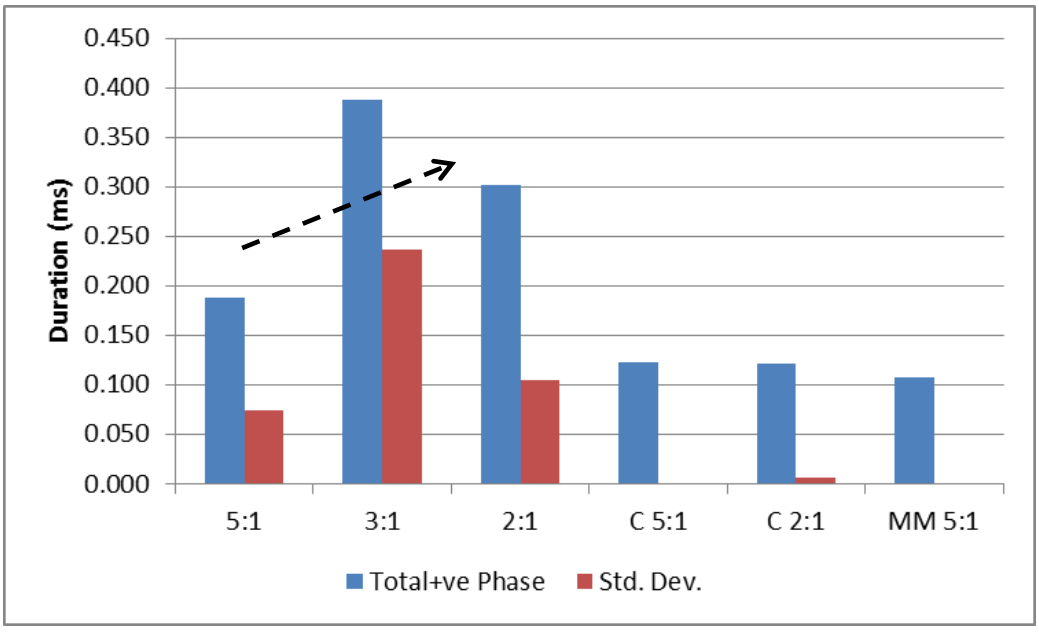

Figure 33: Free-Field Ejecta Test Average Positive Pressure Duration

Despite the variability in the side-on free-field pressure traces, each trace exhibited a phased positive-pressure profile and was partitioned accordingly into three phases using the same methodology as applied to the computational model results. Figure 34 presents the partitioned final D:H 5:1 side-on pressure traces.

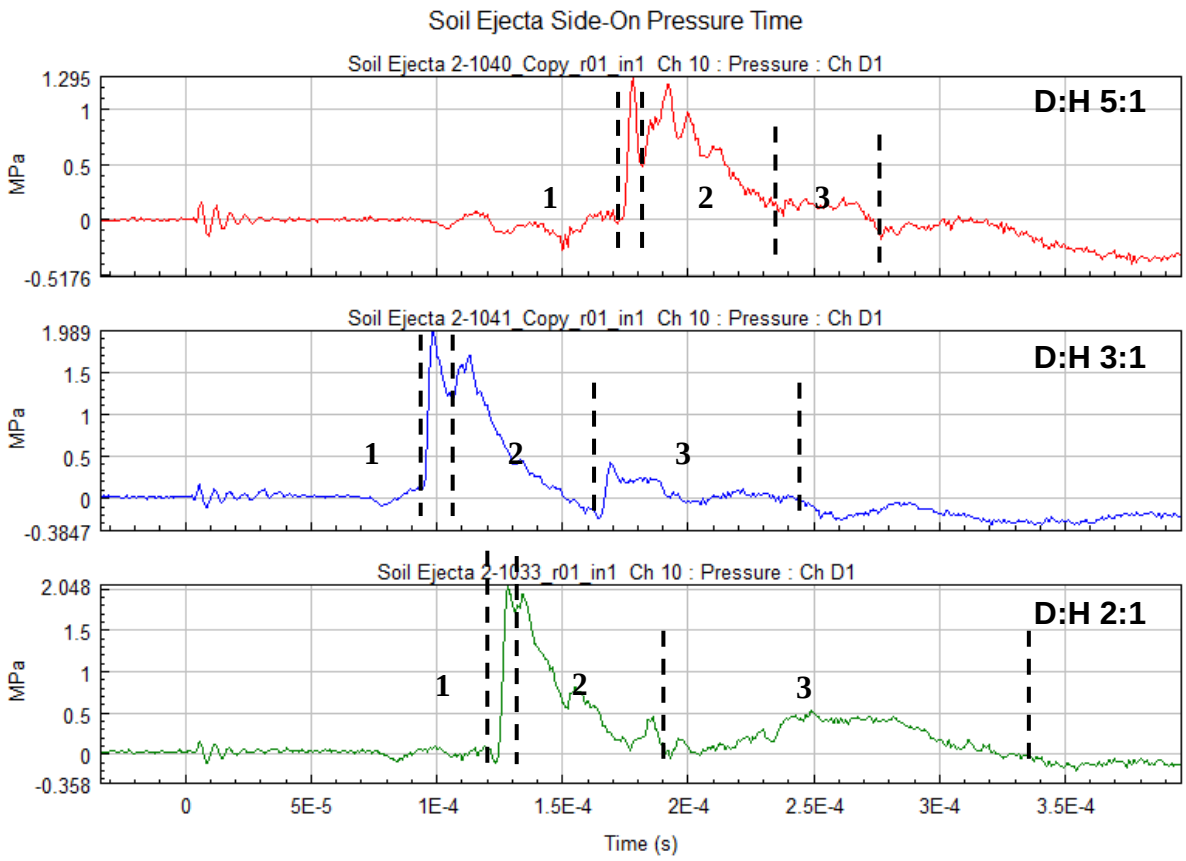

Figure 34: Final Side-on Pressure Phasing (Top to Bottom D:H 5:1, 3:1 and 2:1)

Figure 35 presents the total as well as the partitioned phase durations and Figure 36 presents the percentage contribution of each phase to the total positive pressure pulse for all tests and the computational model.

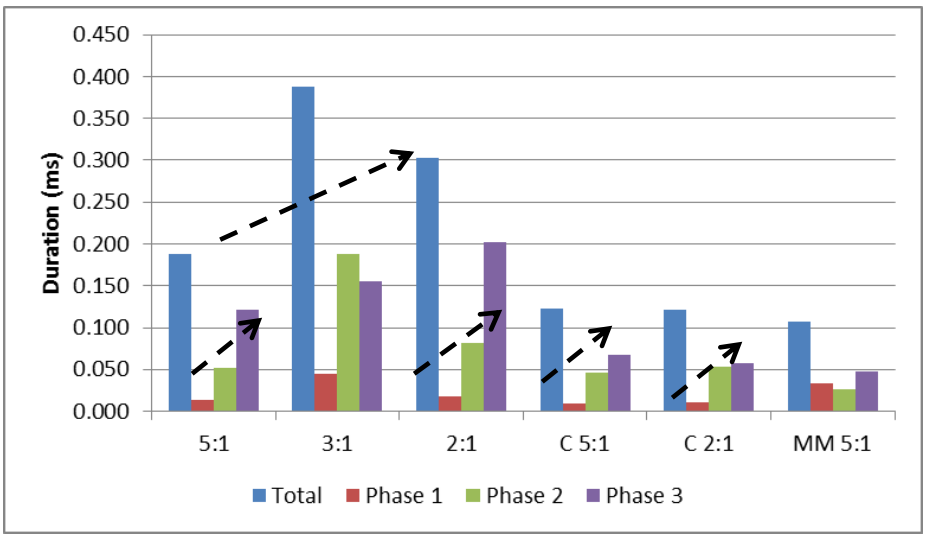

Figure 35: Free-Field Ejecta Total and Phased Durations (all D:H Ratios)

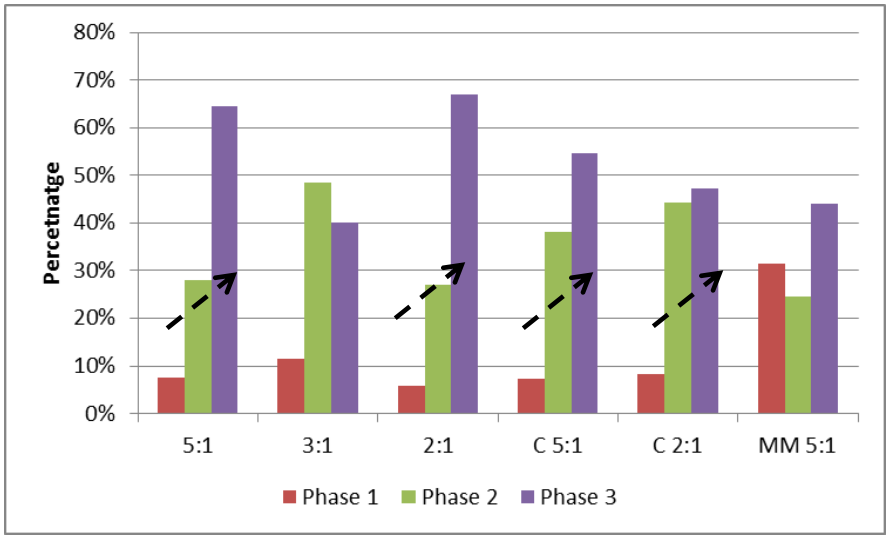

Figure 36: Ejecta Test and Model Phase Duration Contribution

Due the variability in the data no D:H ratio trends are visible. The commissioning tests correlated well with the computational model in terms of total duration but not in terms of phasing. This was due to the large wetted area of the pressure probe stand used for these initial tests, which also generated reflected pressure. However, the results indicate that the charges and detonators were better positioned relative to the sensor, resulting in a perpendicular blast wave passing over the sensor.

4.3.4 Specific Impulse

Figure 37 presents the average total specific side-on pressure free-field impulse and standard deviation and Figure 38 presents the total and partitioned phase response for the shallow buried ejecta side-on pressure tests. The peak specific impulses recorded were from 75 to 165 Pa.s. The single D:H 5:1 commissioning test correlated with the computational model in terms of total impulse but not in terms of each the partitioned phases due to the manual spline fitting used on the model as discussed in Section 4.2. The high variability of the D:H 3:1 test is again reflected in these results. If ignored then there is an increasing total and partitioned phased specific impulse trend with decreasing D:H ratios.

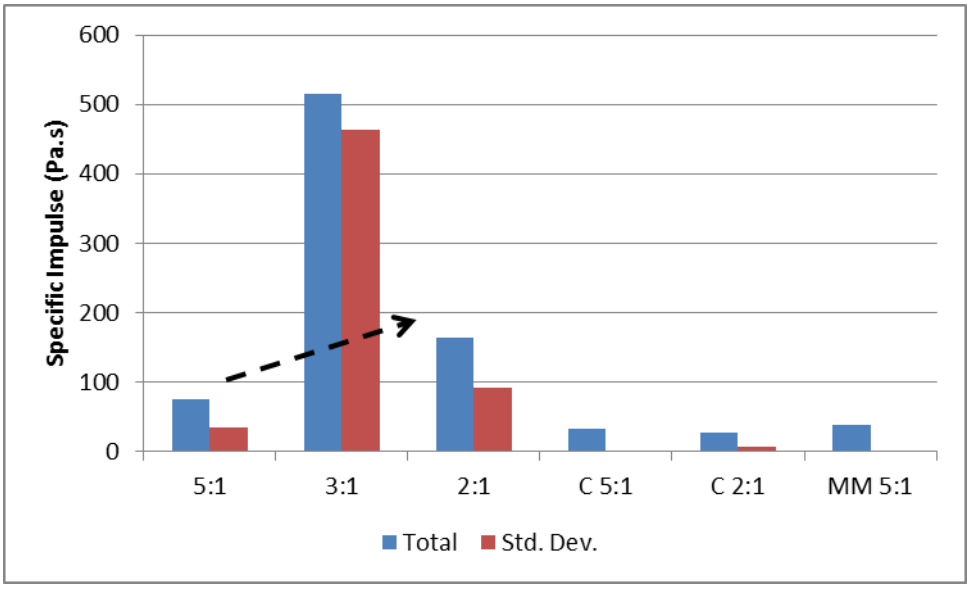

Figure 37: Free-Field Ejecta Total Side-On Pressure Specific Impulse

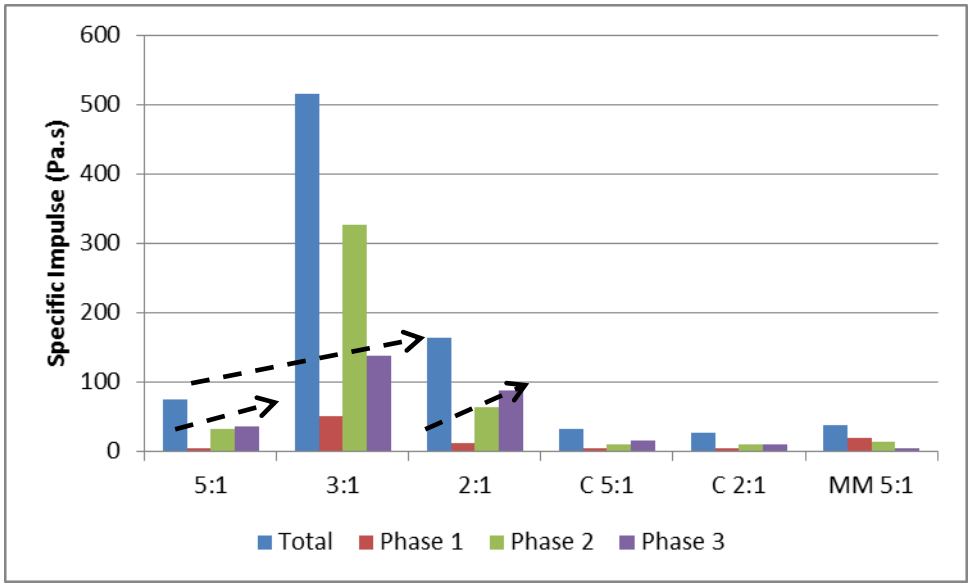

Figure 38: Total and Partitioned Phased Ejecta Test Side-On Pressure-Specific Impulse

Figure 39 presents the contribution of each partitioned phase as a percentage of the total average specific side-on pressure impulse. The modelling results predicted that Phase One would generate the highest portion of the total specific impulse followed by Phase Two and Phase Three. The test results indicate that Phase One generates the least specific impulse and Phase Three the most in two of the three test conditions. This trend is replicated in the

commissioning test data and indicates that the model does not predict the reflected pressure effects that were evident in the test results.

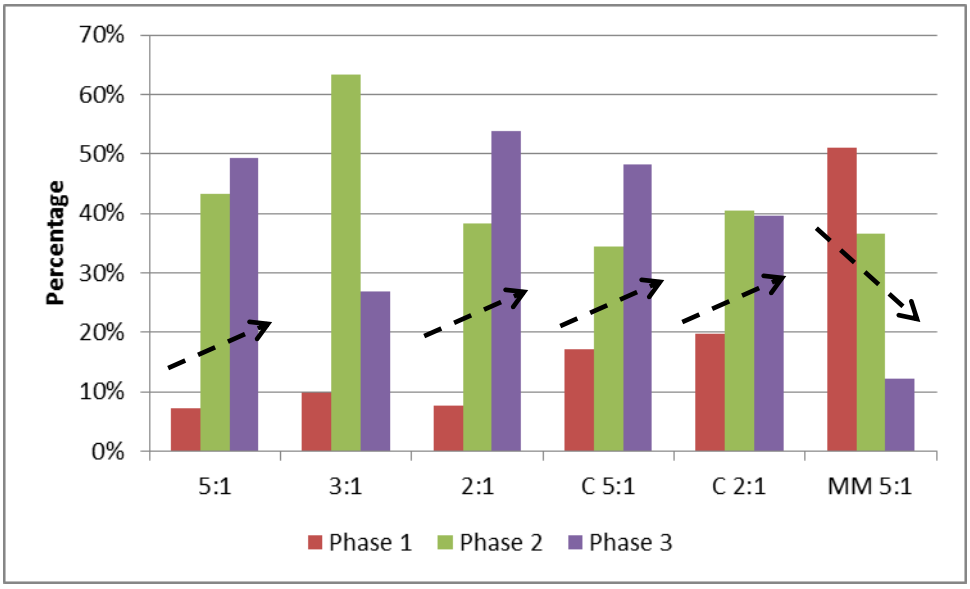

Figure 39: Free-Field Ejecta Tests Phase-Specific Impulse Contribution

4.4 Intermediate-Field Blast Load Phasing with Target

This section presents the primary research data for this work which captured by the one-seventh scale test rig for the intermediate-field SOD. This test rig captures the force-time response of a the subjected to a shallow buried blast as well as the side-on or face-on pressure depending on the configuration and the displacement of the mounted measurement assembly that includes the target plate. The light emission and high-speed imaging are also synchronously captured along with high-speed imaging of the event.

Figure 40 presents the normalised output of all measurements taken during a shallow-buried intermediate-field target blast event with side-on pressure sensor and Figure 41 presents the same normalised outputs but with the face-on pressure sensor mounted. These figures clearly show the blast loading response time line for each measurement as well as the differences between side and face-on pressure. Each of these measurements indicates temporal phasing.

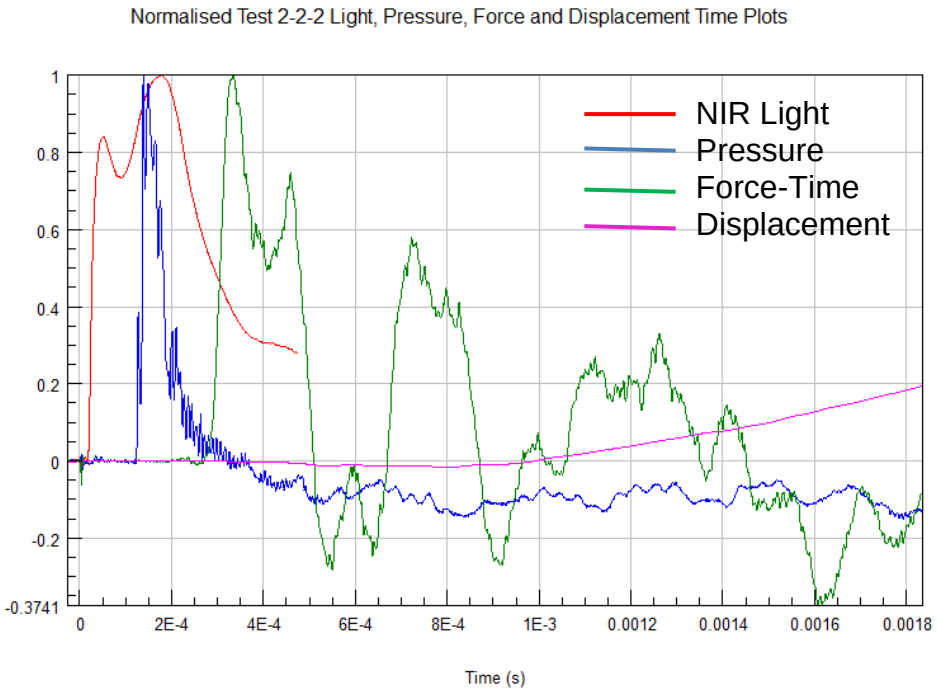

Figure 40: Combined Normalised Measurement Plot for Intermediate-Field Side-On Pressure Sensor (D:H 3:1)

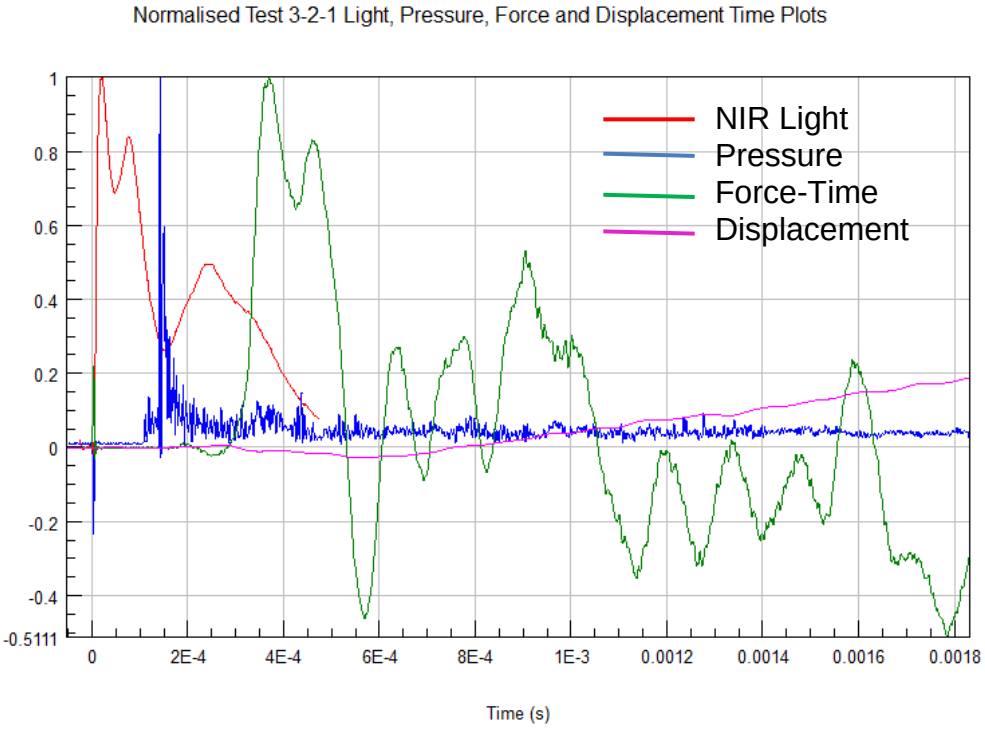

Figure 41: Combined Normalised Measurement Plot for Intermediate-Field Face-On Pressure Sensor (D:H 3:1)

The target-response test data is presented as follows; (1) Blast Front Shape, (2) Target Force-Time Response, (3) Side-On Pressure and Face-On pressure. This follows a typical blast load process by looking at the shallow buried blast development and interaction with the target followed by the overall coupled load target response. This is then followed by pressure data captured at the target interface. The target assembly displacement and NIR data is presented later in Section 4.6 and Section 4.7 as these cover both the intermediate and near-field SODs.

The data presented here represents two test configurations and three charge D:H ratios for each of these. From Table 5 these are differentiated as follows: a 2 prefix indicates the side-on and a 3 prefix indicates a face-on test configuration. A 1 suffix indicates a 5:1 test charge, a 2 suffix a D:H 3:1 ratio charge and a 3 suffix a D:H 5:1 ratio charge.

4.4.1 Blast Front Shape

Figure 42 presents a temporal sequence of high-speed images showing the development and impact of a shallow-buried intermediate target (195 mm SOD) blast load with the side-on pressure sensor mounted. The soil level is below the soil bin rim so the initial breakout is not visible.

- Frame 1 (t=0.0 ms) shows the moment of detonation.
- Frame 2 (t=0.033 ms) shows the break-out occurring with light reflected off the side of the pressure probe.
- Frame 3 (t=0.100 ms) shows the ragged asymmetric blast front starting to impact the target plate off-centre to the left of the side-on pressure probe.
- Frame 4 (t=0.133 ms) shows the front impact growing across the target face.
- Frame 5 (t= 0.300 ms) shows the blast front across the complete target face. The light emissions of the detonation products are reducing in intensity.

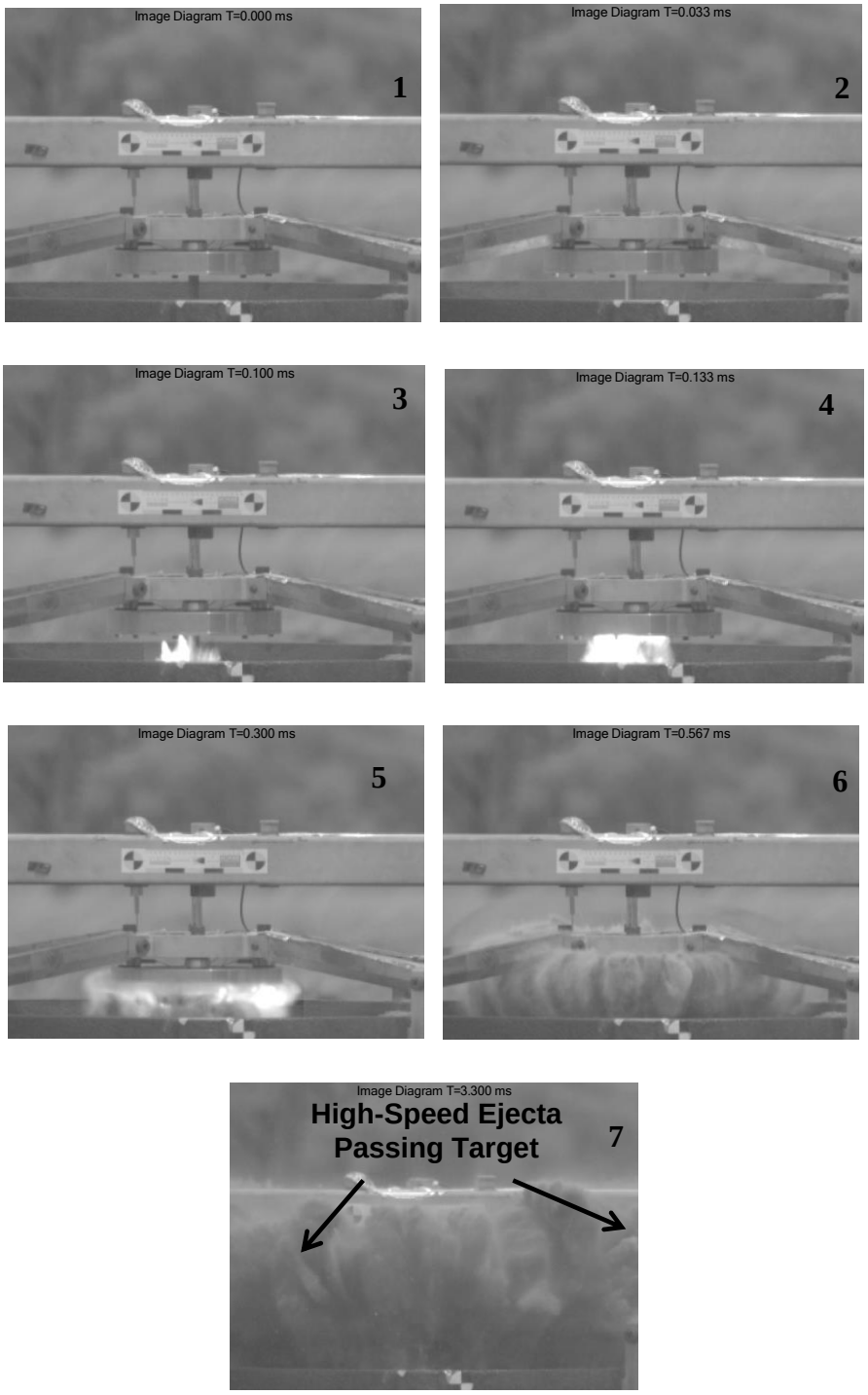

Figure 42: High-Speed Photo Sequence of Near-field Blast Front Development and Target Impact (D:H 5:1)

- Frame 6 (t=0.567 ms) shows that there is no longer high-intensity light visible and the boundary of the blast front is made up of soil ejecta and detonation gases. Based on pressure measurement results there is no

longer any substantial side-on pressure measured at the centre of the target. The blast front is starting to bulge around the target assembly. The blast resembles a pumpkin in shape at this time.

- Frame 7 (t=3.3 ms), the end of the high-speed blast phase, shows the blast ejecta completely enveloping the target plate and measurement head. The ejecta appear to be transitioning to the slow ejecta blast phase. Angled ejecta can be observed completely missing the target.

The asymmetric blast front has much less influence on the results as the target is large and both captures and smooths out the asymmetry of the blast front. The smaller the target the larger the possible effect of the blast front asymmetry on the results.

4.4.2 Target Force-Time Response

The target force-time response data is presented in four sections. These are; (1) System Verification, (2) Force-Time Phasing and Partitioning, (3) Target Force-Time Response Data and (4) Target Response Impulse. Due to the complexity in how the force-time signals were partitioned this is presented as a separate section after the system verification data. The extracted target force-time data is then presented.

4.4.2.1 System Verification

The assembled force washer system was impacted using a calibrated force hammer. Eight system verification impacts were carried out after assembly prior to the soil bin being filled with soil. The tests were difficult to carry out consistently as space was limited and the target plate was not visible as it was facing downwards. The input and measured response time net force were synchronously captured and processed.

Figure 43 presents the 40–2,500 Hz band-pass filtered, unfiltered and force-time signals of the hammer input (blue and purple traces) and the net force measurement system response (red and green traces). Most impacts initially had a slightly negative net force response; this was due to the off-centre impact

of the hammer. The ringing as a result of insufficient pre-tension is visible in both plots. The slight bulge in the hammer force trace is indicative of a double impact. The net force response is seen to start after a short delay. This is to be expected due to the inertia of the measurement plate combined with the rubber tip of the hammer.

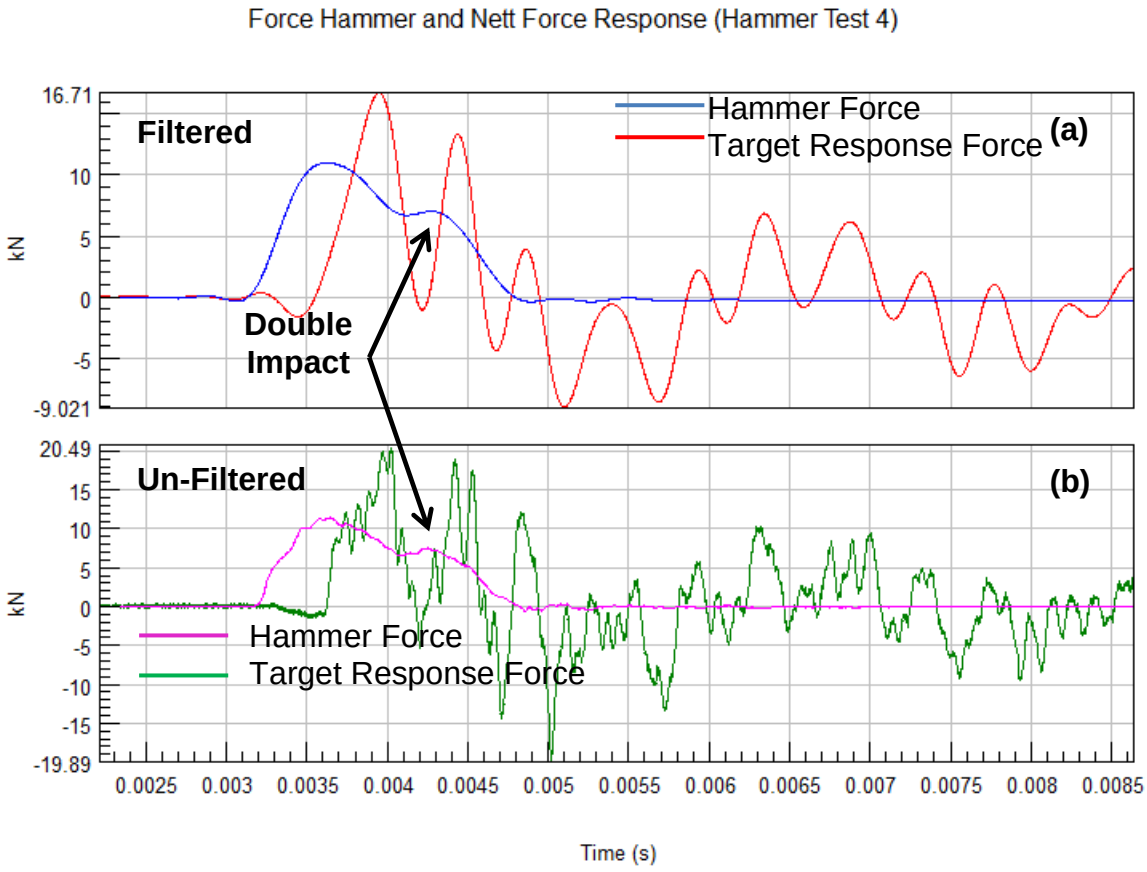

Figure 43: a) Filtered (Band-Pass 40-2,500 Hz) and b) Unfiltered Hammer and Response Net Force Measurements

Figure 44 presents the measured peak force and net force responses along with the standard deviation for all eight impacts. The net force recorded a much higher average peak force, which is due to the relatively stiff assembly combined with some system looseness from insufficient pre-tension, as well as slightly off-perpendicular impacts that can result in the applied force being reduced (a twenty-five degree off-perpendicular impact results in a 10%

reduction in applied force seen by the target compared to that measured by the hammer).

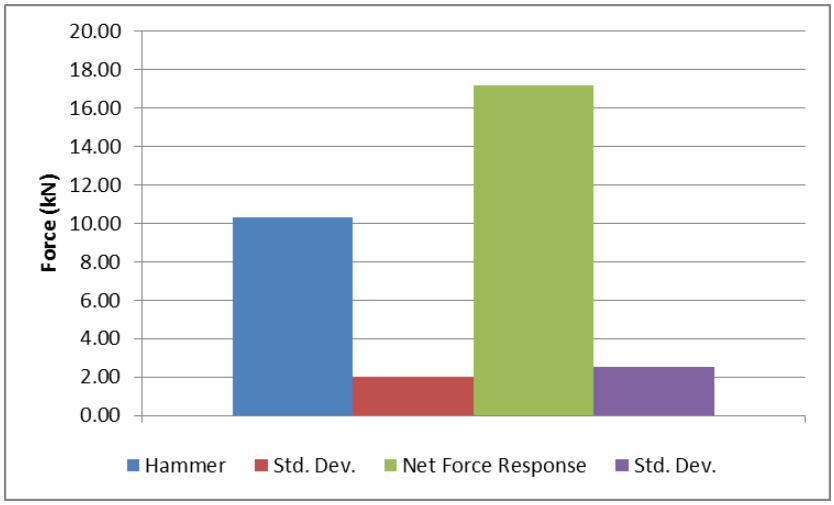

Figure 44: Peak Hammer vs. Net Force Response

Figure 45 presents the averaged positive impact force load of the hammer and the net force response of the measurement system. The hammer has a slightly longer positive duration due to the greater stiffness of the target.

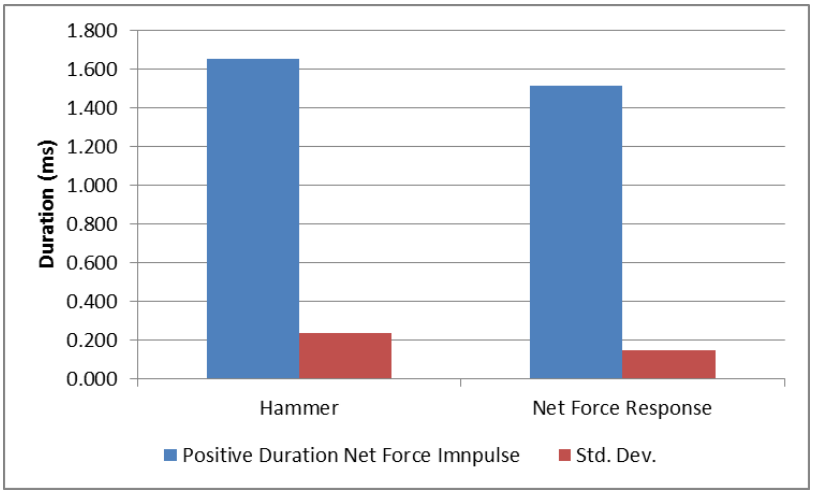

Figure 45: Verification Hammer vs. Net Response Force Positive Load Duration

Figure 47 presents the average impulse derived from the hammer and the net force response. The net force response was on average 18% lower than that of the hammer. The standard deviation was around 11% for both the hammer and net force response impulse. This difference is due to the previously mentioned

off-perpendicular impact, measurement system looseness as well as some losses from the rubber tip of the hammer. These differences are deemed acceptable for this work.

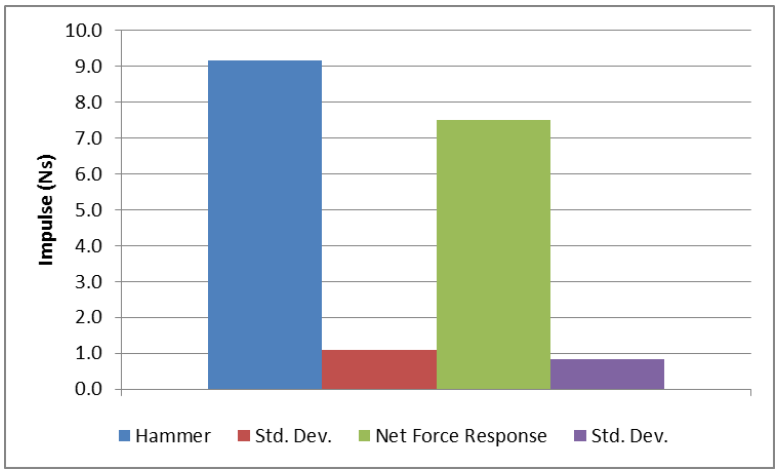

Figure 46: Hammer vs.Net Force Impulse

4.4.2.2 Force-Time Phasing and Partitioning

All temporal pressure model measurement results for shallow buried blast presented thus far have clearly exhibited three-phased response. These have been partitioned through inspection and the results presented. This methodology is not suitable to apply to the high frequency force-time response data. This section will now cover in more detail how partitioning through visual inspection as well as the more rigorous combined temporal response and impulse partitioning methodology.

Figure 47 presents the long-duration force-time target response to a shallow-buried blast measured during the commissioning tests. The response is a typical overdamped system response with an exponential decay. The area of interest is the initial positive force load phase as this represents the system's initial force response to the blast load. The force response after this initial loading phase represents the system's unforced response to the impulsive blast load.

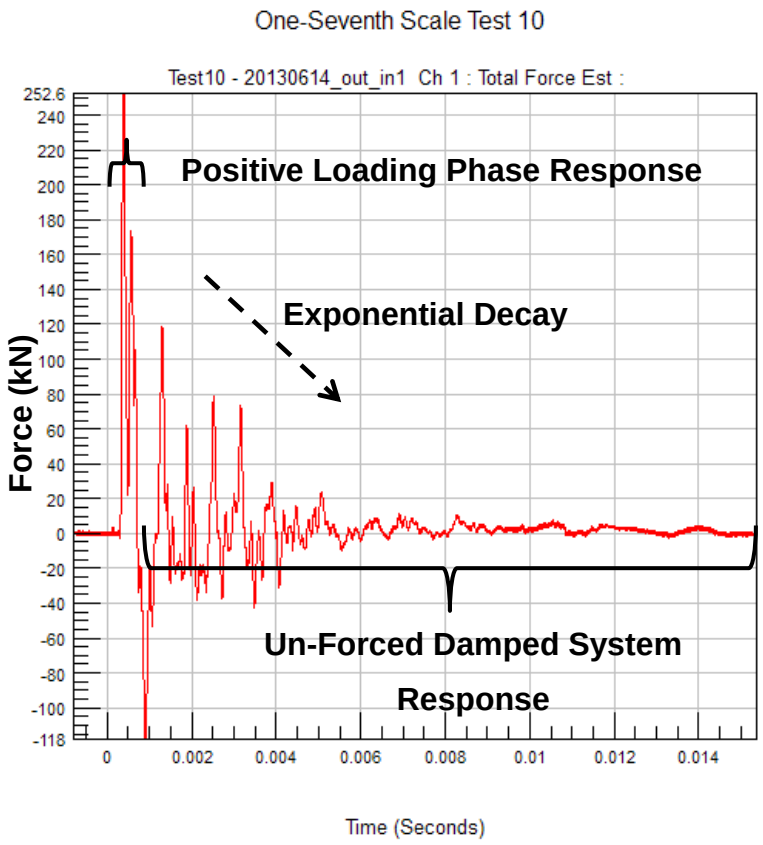

Figure 47: One-Seventh Scale Total Force-Time Plot (Long Duration)

Figure 48 presents the initial impulse loading phase force-time response of the target assembly. Inspection of the force-time response plot in Figure 48 shows three clear phases over the positive duration represented by the three peaks. Partitioning the force-time in accordance with these phases as applied to the side-on pressure plots results in the three phases shown in Figure 48.

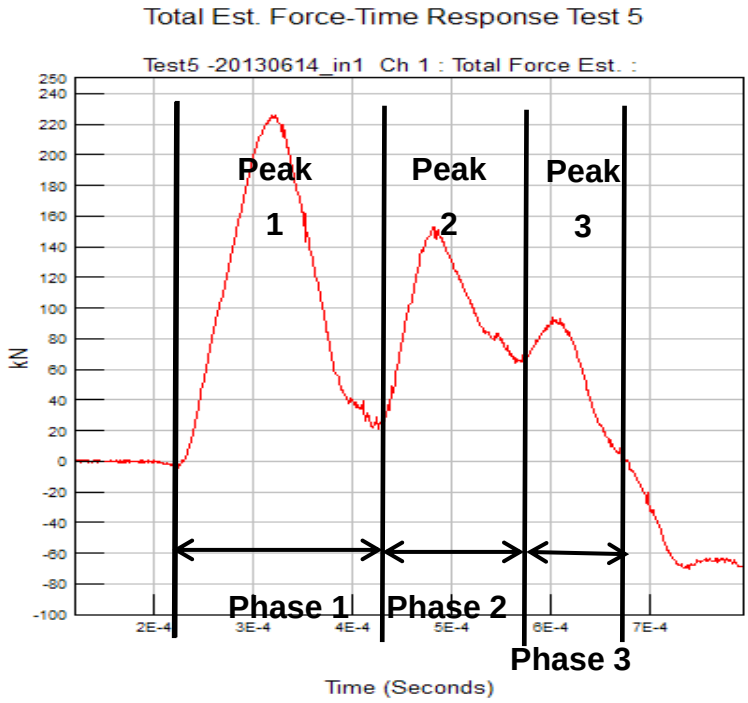

Figure 48: Partitioning of Positive Duration Force-Time plot

Figure 49 displays the target force-time response of a commissioning blast test and final near-field blast tests. The blue trace is the commissioning test result and the red plot is the final test result. The final tests, although they display three phases, show much larger valleys between the phases and have larger positive phase duration.

This is to be expected as the two test configurations differed in terms of target size (360 mm vs. 290 mm diameter), mass (24.6 kg vs. 16.5 kg) and in terms of pre-tensioning of the force washers. The commissioning data was derived from only two of the four force-washers. The final test configuration used charge amplifiers with much higher frequency response (100 kHz vs. 10 kHz) than was used for the commissioning tests. This is manifested as noise with extremely sharp peaks and valleys combined with ringing.

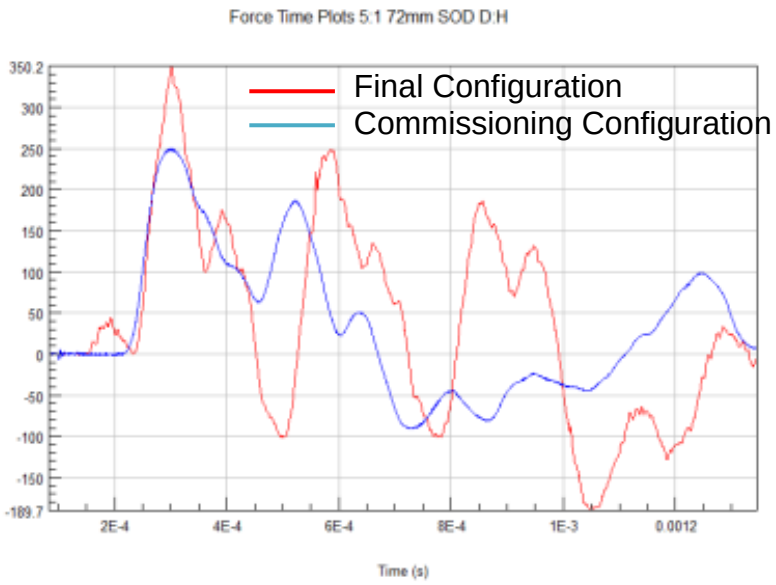

Figure 49: Commissioning and Final Test Configuration Near-Field Force-Time Response Plots (Commissioning Test 10 vs. Final Test 4-4-1 D:H 5:1)

To identify the loading phases (Partition), the impulse-time and the force-time response are plotted together and inspected. Figure 50 presents the intermediate-field target force-time response and the impulse-time plot integrated from the force-time response. The impulse time plot displays three partitioned phases. The end of the positive force loading phase is determined when maximum impulse is reached.

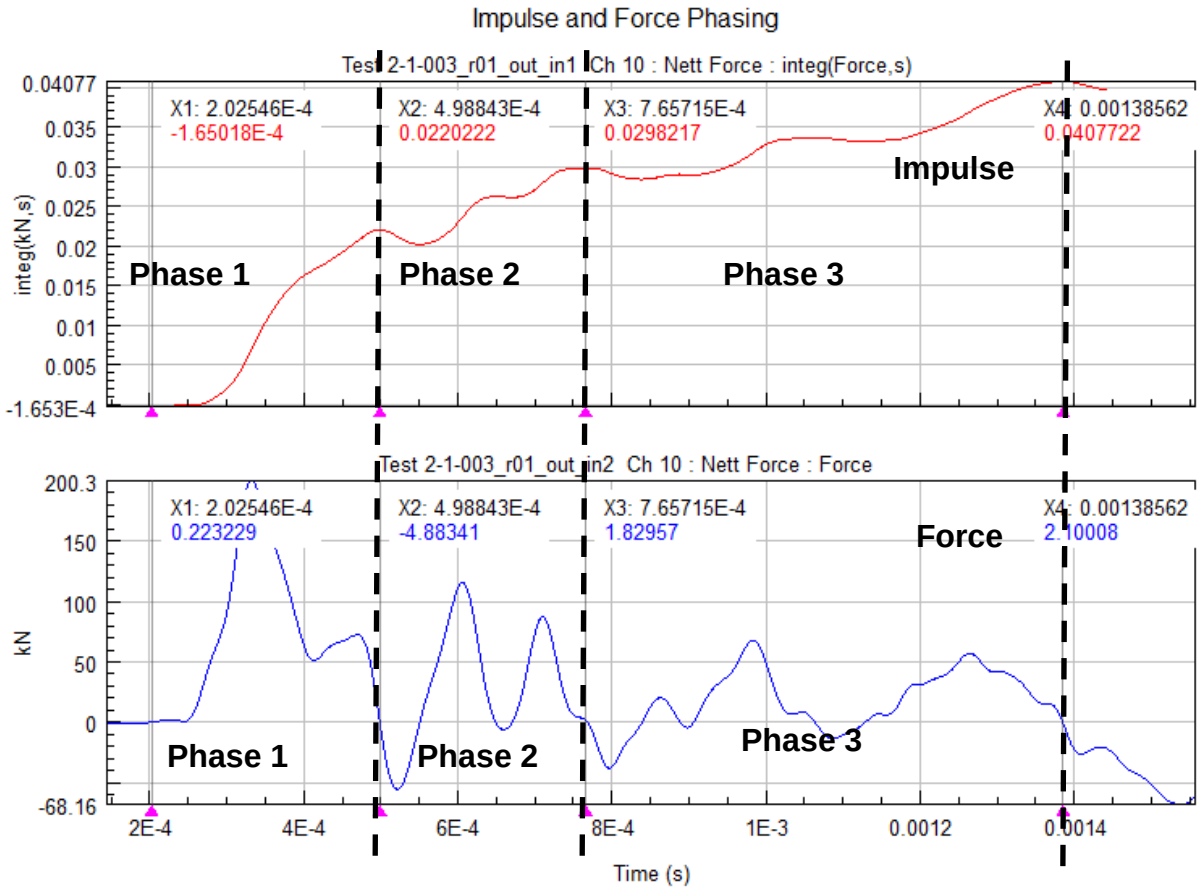

Figure 50: Final Test Intermediate-Field Force and Impulse Time Plots

4.4.2.3 Target Force-Time Response Data

Due to the noise inherent in the force-time plots, the peak force for each partitioned phase was not extracted. The peak net force for each test is shown in Figure 51. A maximum peak force standard deviation of 25% of average was recorded for the D:H 5:1 tests, while the lowest was 4% of average value achieved with the D:H 2:1 test charge. Both intermediate-field test series indicated a decrease in net peak force with a decrease in charge D:H ratio. This was much more visible with the side-on pressure probe mounted. This is due to the pressure probe extending closer to the blast by 162 mm. The smaller difference with the face-on probe configuration indicates that D:H differences smooth out as SOD increases. This is consistent with what was reported in (Baker 1973a).

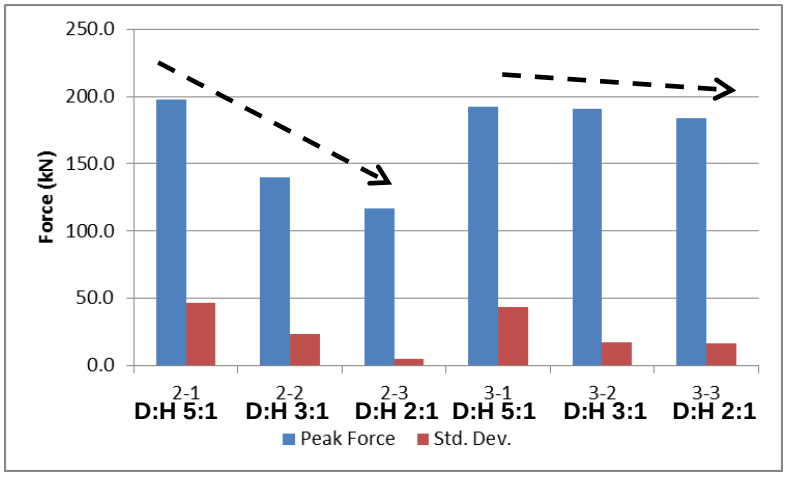

Figure 51: Peak Target Response Net Force (Intermediate Field)

Figure 52 presents the total and partitioned phase force durations for the intermediate-field side-on pressure and face-on pressure configurations.

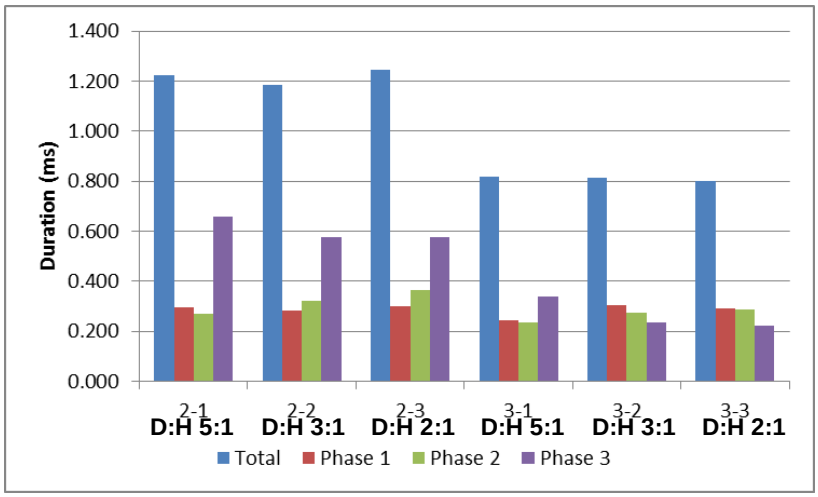

Figure 52: Intermediate-Field Total and Partitioned Phase Force Durations

The phase force durations varied from test to test, with the highest standard deviation at 30% of average value. The duration of the side-on pressure test configuration was nearly 50% shorter than that of the side-on pressure probe configuration. Although all phase force durations decreased, the largest reduction was in Phase Three, which reduced by 46%, while the other two phases durations only decreased by 17%.

4.4.2.4 Target Response Impulse

Figure 53 presents the averaged intermediate-field total impulse and standard deviation. The highest standard deviation was 12% with most at 5% or less. There is a clear decreasing trend as the D:H charge ratio decreases for both the side-on and face-on pressure sensors fitted. The face-on pressure configuration gave a higher total impulse for all D:H charge ratios despite this configuration having shorter phase force durations.

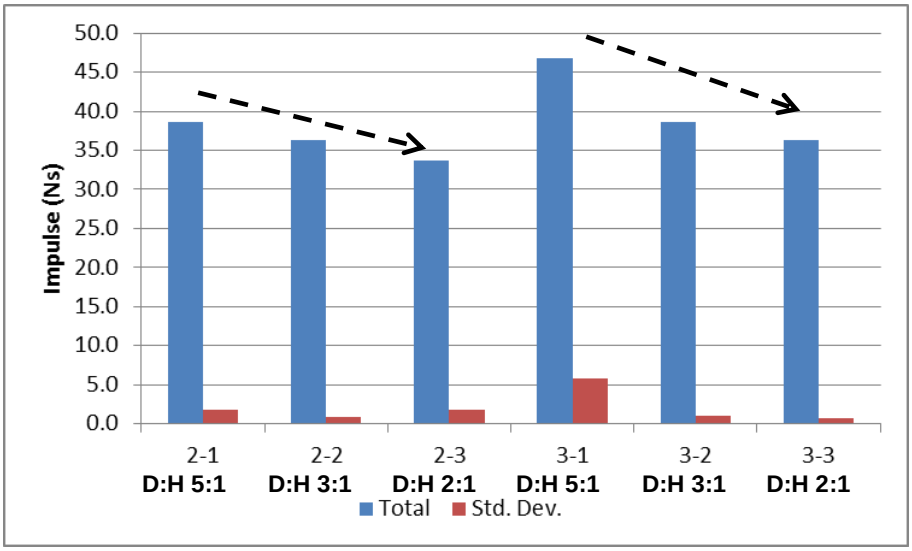

Figure 53: Intermediate-Field Total Impulse

Figure 54 presents the total and partitioned impulse per phase. The second phase appeared to give the lowest impulse in all test conditions, except for one test point with the D:H 5:1 charge and side-on pressure probe configuration.

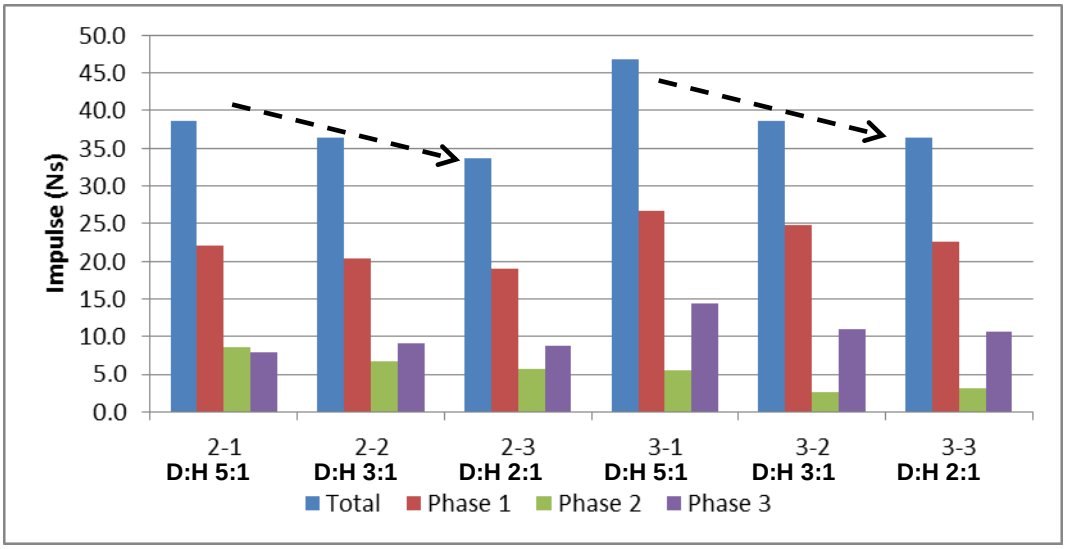

Figure 54: Intermediate-field Total and Partitioned Phase Impulse

The total increase in impulse between the two test configurations was 25% recorded with the D:H 5:1 test charge. This test point also recorded the highest standard deviation for the total impulse. The highest phased impulse standard deviation recorded was 52% of average with the Phase 3 D:H 5:1 test charge. Most phase standard deviations varied between 10 and 15% of the average value. Phase One and Phase Three impulse increased with the transfer to the face-on pressure test configurations for all D:H ratios tested. Phase Two decreased for this test configuration.

Figure 55 presents the percentage contribution of each phase to the total impulse. The percentage contribution was very similar for all tests with the exception noted for the face-on D:H 5:1 test configuration with the higher standard deviation. For the side-on configuration, the Phase Two percentage contribution decreased, while that of Phase Three remained approximately similar with decreasing D:H ratio charges. For the face-on configuration the percentage contribution of Phase Two and Phase Three seemed to remain similar between the D:H ratio charges.

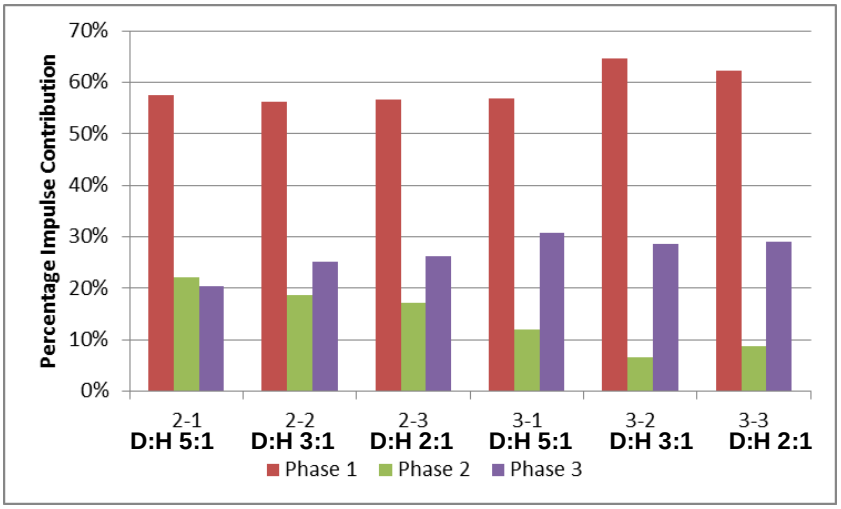

Figure 55: Average Intermediate-Field Phase Impulse Contribution

4.4.3 Side-On Pressure

Figure 56 presents the positive side-on pressure-time plots for D:H ratios 5:1, 3:1 and 2:1 that were partitioned into three phases.

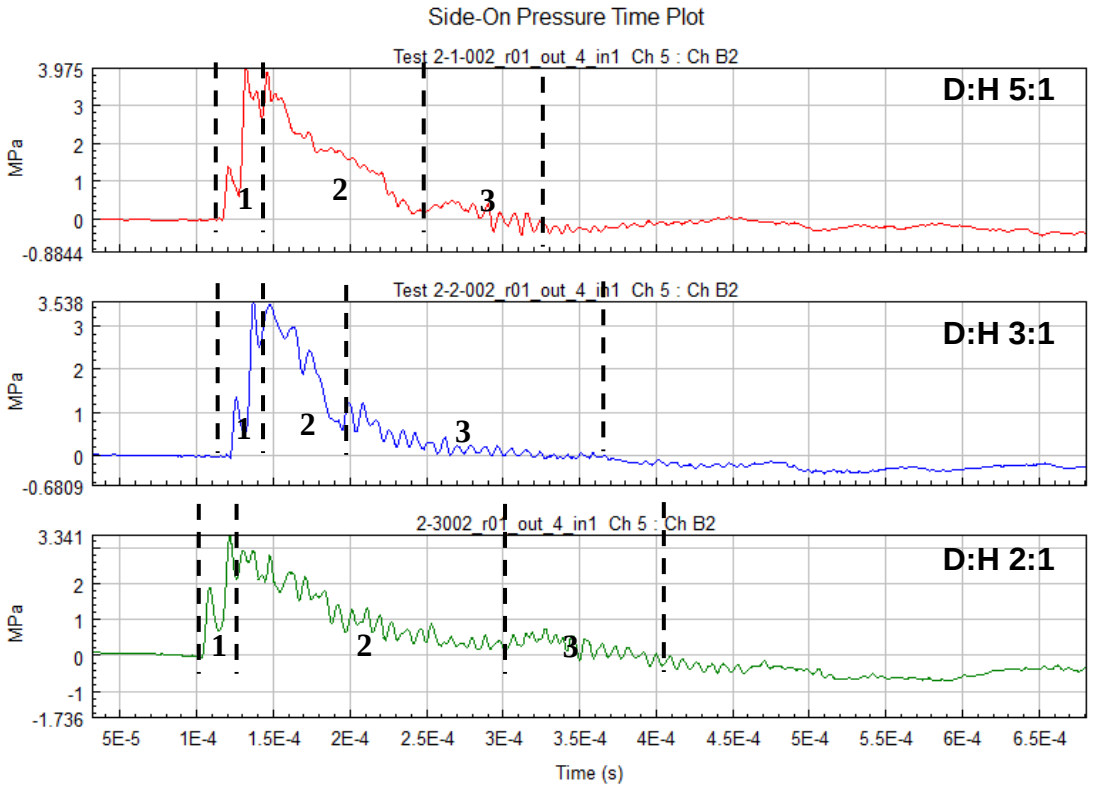

Figure 56: Intermediate-Field Partitioned Side-On Pressure-Time Phasing

The plots in Figure 55 show distinctive ringing of the signal due to the impact of the soil on the pressure probe. Each trace could be partitioned into at least three phases. The variance is mostly attributed to charge positioning errors that resulted in angled impact on the sensor element. These variances decreased as testing progressed due to improved test set-up consistency. The bow wave shock preceding the blast was visible in some traces; however, due to many off-perpendicular blasts this phenomenon was smeared or exaggerated.

Figure 57 presents the averaged side-on pressure-time response start time representing the blast front time of arrival at the sensor element. The plot shows that as the D:H ratio decreases, the blast front velocity increases.

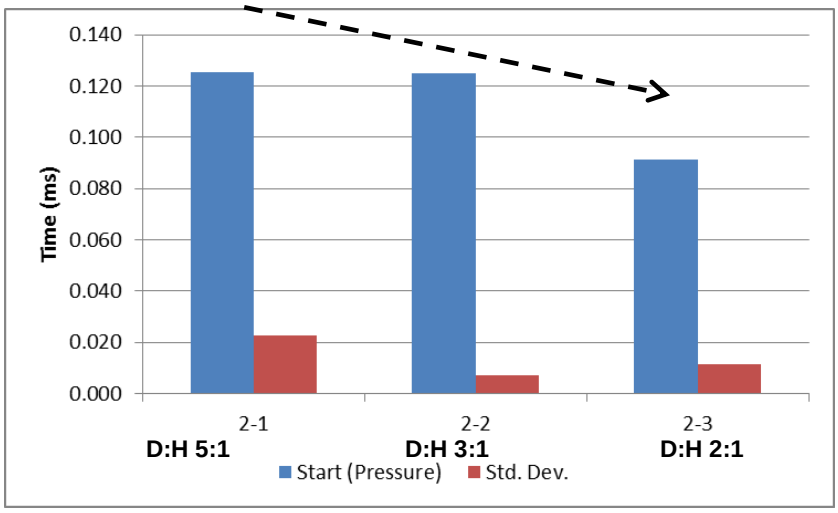

Figure 57: Intermediate-Field Side-On Pressure Trace Start Time

Figure 58 presents the averaged peak pressures recorded for each D:H ratio with the side-on pressure probe configuration and the standard deviation from the tests.

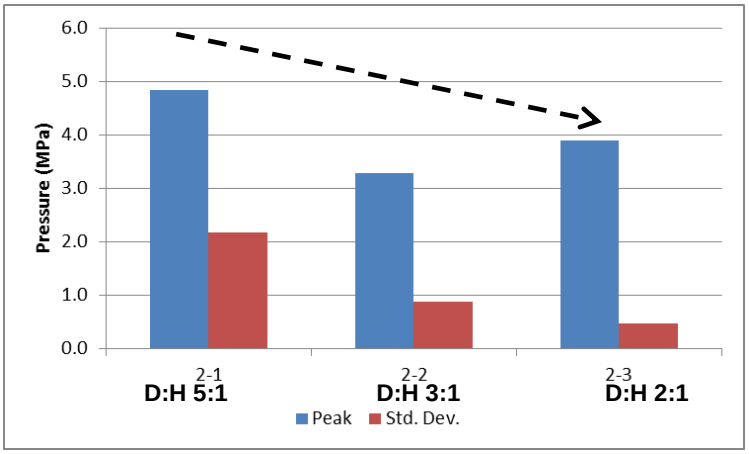

Figure 58: Intermediate-Field Average Peak Pressure (Side-On)

Figure 59 presents the averaged total and the partitioned intermediate-field side-on pressure phase durations. As the D:H ratios decrease there is an increase in total positive side-on pressure duration. The 3:1 and 2:1 D:H charge ratios indicated an increasing phase duration. The average durations of the 5:1 D:H test charge did not display any trend. This was primarily due to at least two of the traces indicating an off-perpendicular blast front, which resulted in a reflected side-on pressure measurement rather than the classic Friedlander-type pressure traces shown in Figure 56.

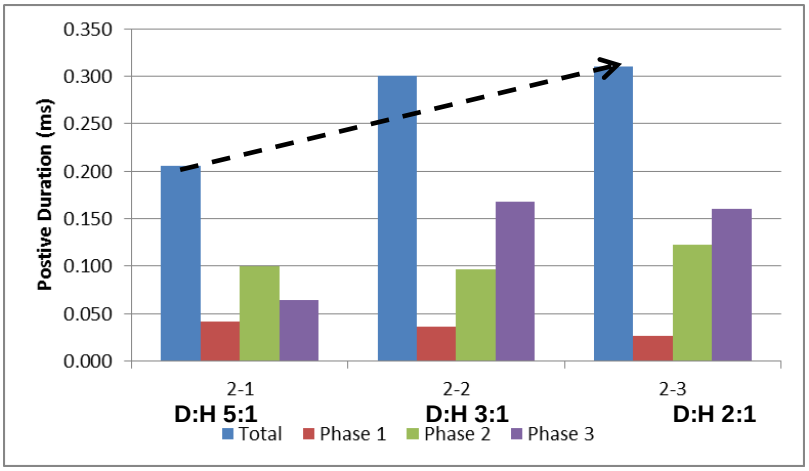

Figure 59: Average Intermediate-Field Side-On Total and Partitioned Positive Pressure Duration

Figure 60 presents the calculated total and partitioned phase-specific impulse for intermediate-field side-on pressure. There are no clear D:H trends. Overall

the highest specific impulse is Phase Two followed by Phase One and then the lowest, Phase Three. Figure 61 presents the side-on pressure-specific impulse contribution of each phase to the total specific impulse for the intermediate-field target. Although there appear to be underlying trends, no clear differences between the D:H ratios are present.

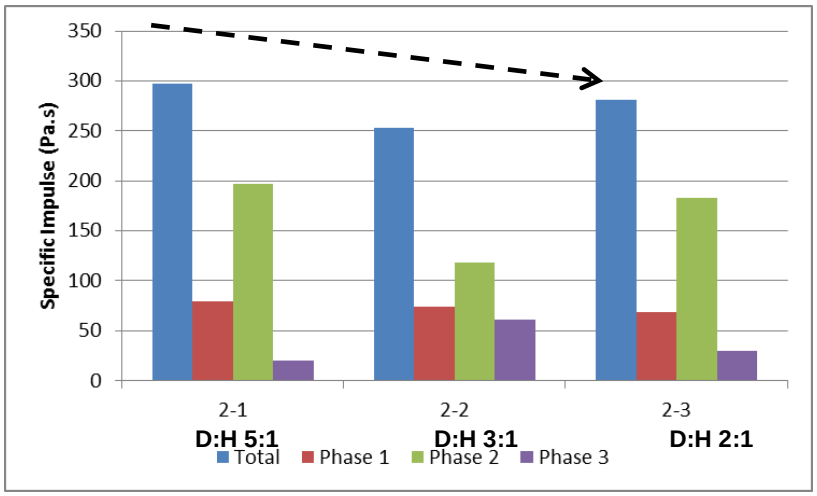

Figure 60: Intermediate-Field Partitioned Side-On Pressure-Specific Impulse

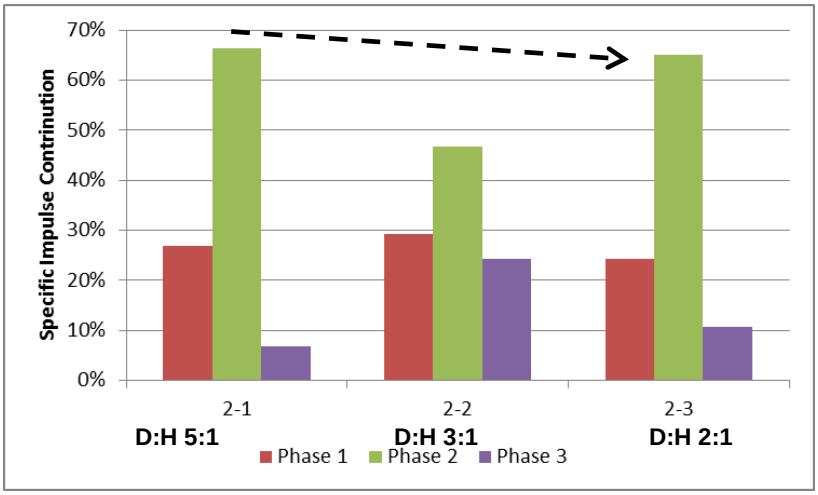

Figure 61: Intermediate-Field Side-On Pressure-Specific Impulse Contribution

4.4.4 Face-On Pressure

Figure 62 presents the intermediate-field face-on pressure-time traces for each of the D:H ratio tests. The figure shows how the traces were partitioned and phased. In most cases the end of each phase could not be identified by visual inspection and the impulse-time trace was then used to define each phase. The

results for the D:H 5:1 tests were all poor most did not have any discernible duration, with the exception of the trace shown here. The 5:1 test charge pressure traces, however, did all have a single distinct initial peak pressure value. The pressure traces show great variation in the initial pressure pulse along with ringing. This is due to numerous impacts from the soil ejecta directly onto the sensor. The bow wave shock preceding the blast front was present in most D:H 3:1 and 2:1 pressure traces.

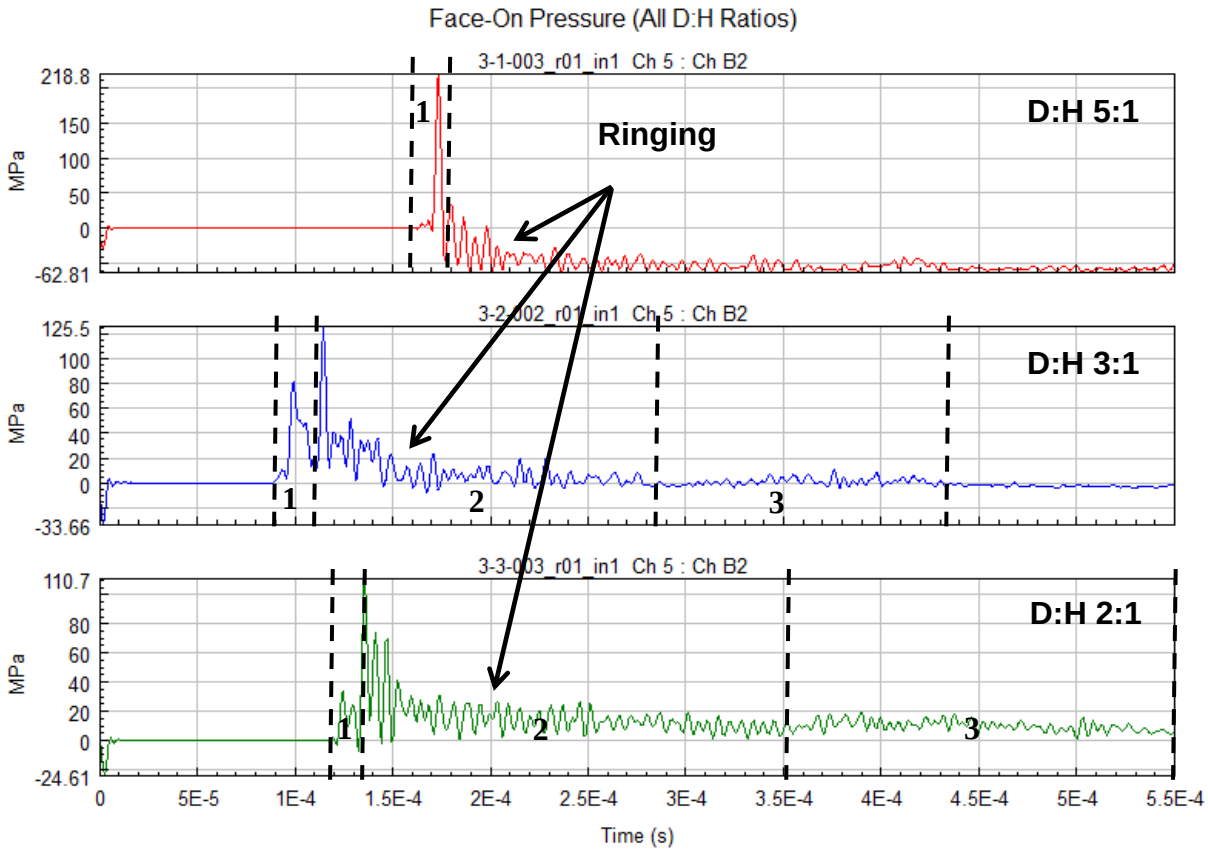

Figure 62: Near-Field Partitioned Face-On Pressure for all D:H Ratios

Figure 63 presents the pressure-time trace start times. This represents the blast front time of arrival at the sensor. The data show a decreasing trend as the D:H ratios decrease, implying that the blast front velocities increase as the D:H ratio decreases.

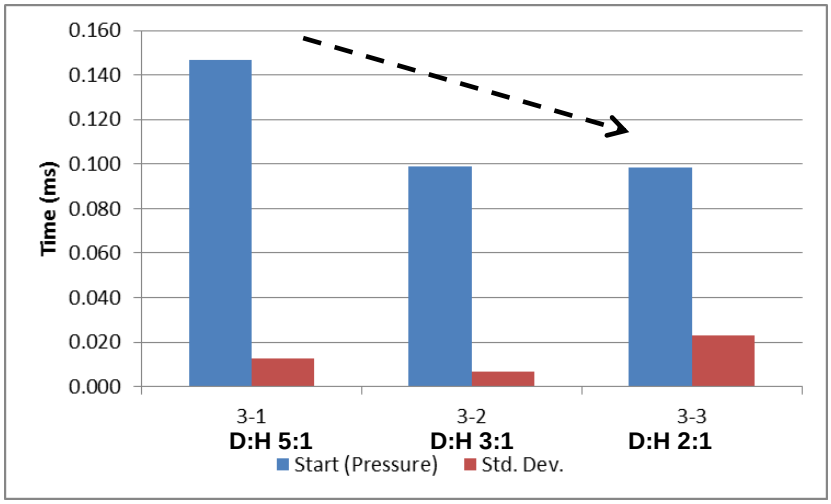

Figure 63: Intermediate-Field Pressure Pulse Start Time (Face-On)

Figure 64 presents the averaged peak intermediate-field pressure recorded for each D:H charge ratio tested. The standard deviation varied from 32% of average value all the way to 50% of average value. Despite this variation a decreasing peak pressure with decreasing D:H ratio charges trend is visible.

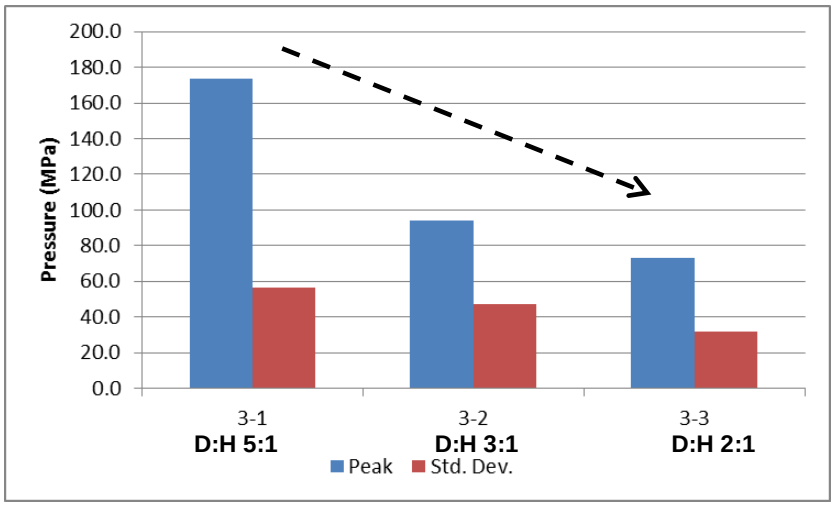

Figure 64: Intermediate and Near-Field Average Peak Pressure (Face-On)

Figure 65 presents the total and phased face-on intermediate-field positive pressure durations. The 3:1 and 2:1 data sets indicate that the initial phase is extremely short, from 14 to 23 µs on average. The D:H 3:1 charge ratio has on average a longer Phase One duration but shorter Phase Two and Phase Three durations when compared to the D:H 2:1 charge ratio. The D:H 5:1 charge test

did not produce any phased pressure traces, thus the single-duration trace that could be extracted is presented for completeness only.

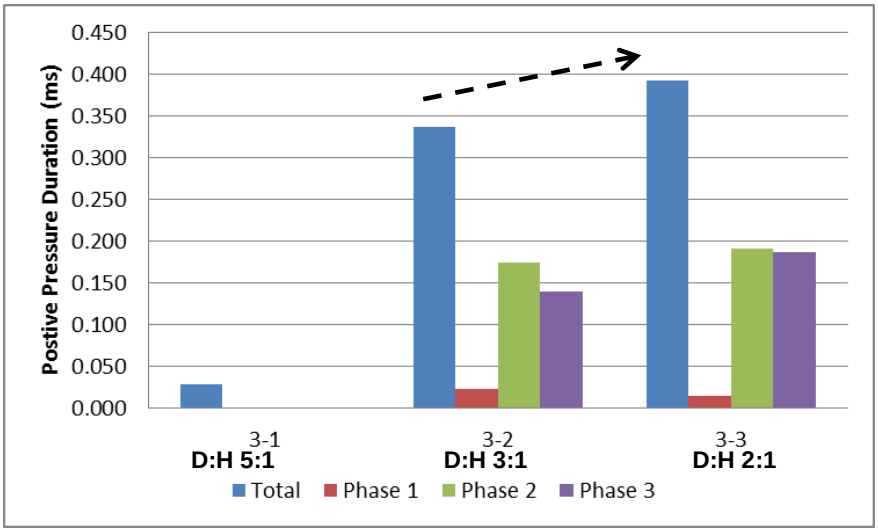

Figure 65: Intermediate-Field Total and Partitioned Positive Pressure Duration (Face-On)

Figure 66 presents the total and partitioned phase face-on pressure-specific impulse for the intermediate-field target. Figure 67 presents the phased percentage contribution to the total face-on pressure-specific impulse. Standard deviation error bars reveal large variations in specific impulse of up to 54% of average. The results indicate an increase in face-on specific impulse with decreasing D:H ratio charges.

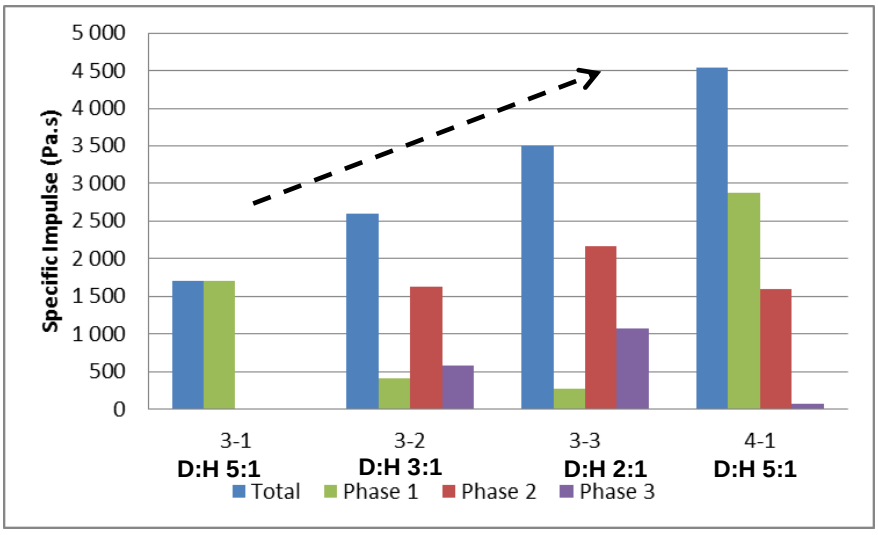

Figure 66: Intermediate-Field Phase-Specific Impulse (Face-On)

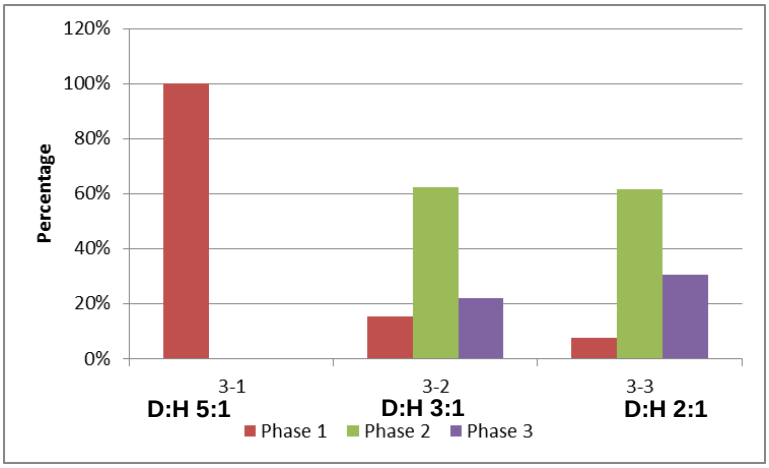

Figure 67: Pressure-Specific Impulse Phase Contribution (Face-On)

4.5 Near-Field Blast Load Phasing with Target

The near-field data is presented in this section. Figure 68 presents the normalised output of all measurements taken of a shallow-buried intermediate-field target with face-on pressure sensor in the one-seventh scaled test rig. The purple trace is the light output; the green trace is side-on/face-on pressure; the blue trace is the net force-time response and the red trace is the target measurement assembly displacement.

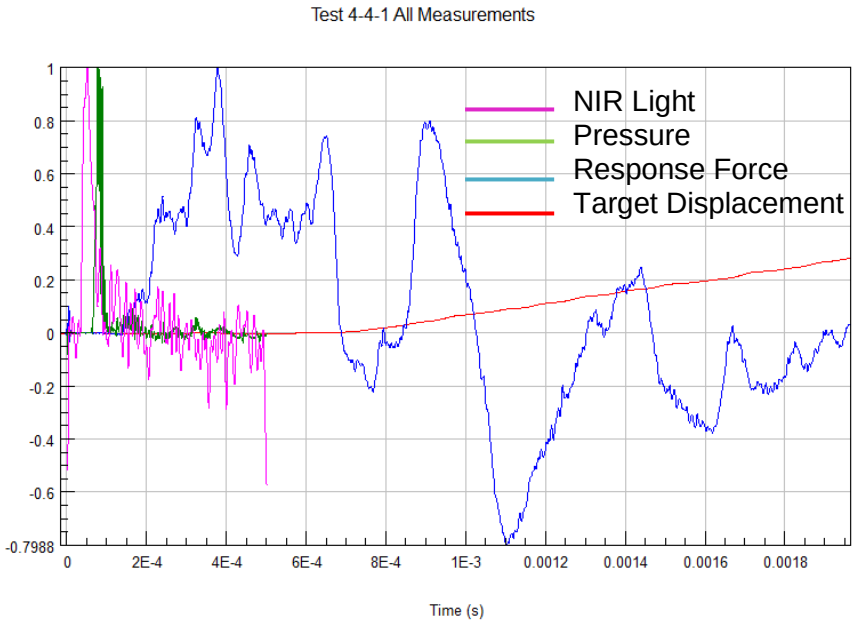

Figure 68: Combined Normalised Measurement Plot for Near-Field Face-On Pressure Test

This section presents the face-on near-field data in two sections, these are; (1) Blast Front Shape and (2) Face-On Pressure.

4.5.1 Blast Front Shape

Figure 69 presents a sequence of three high-speed images of a near-field shallow-buried blast test.

- Frame 1 is at 25 µs after initiation just as the blast front is impacting the target face. This timing corresponds to the ejecta results,
- Frame 2 is at 175 µs, which was 100 µs after peak pressure was recorded, but at the tail end of the second face-on pressure. The slightly asymmetric and off-perpendicular impact is visible in the asymmetry of the developing blast front across the target face where the left-hand side is already moving past the target edge, whereas the right-hand side is still moving towards the edge.
- Frame 3 was captured at 375 µs, which is at the end of the positive face-on pressure pulse recorded. No bright light flashes are visible, although some light noise was recorded by the IR sensors. The blast front and ejecta have formed their pumpkin shape as these blast products are pushed out by the expanding detonation gases and are sucked in over the top of the target plate by the lower pressure zones created by the target plate edge and high velocity of the blast front consisting of a combination of ejecta and blast gas products. The shock wave has not separated from the blast front at this time.

Figure 69: Near-Field Blast Front Impact Morphology

4.5.2 Face-On Pressure

Figure 70 presents the single combined face-on pressure time and specific impulse–time plot. The top plot shows the calculated impulse-time trace and the bottom plot shows the pressure-time trace on the time line. As it is difficult to partition the trace through inspection, the sepciofic impulse-time plot that was applied to the force-time phasing described previously was used. From the analysis there appears to be only one main pulse followed by two much smaller phases that appear to be measurement drift. Based on the impulse-time trace, four phases could be extracted but in this case the second phase was extended from 125 µs to 200 µs as the change in specific impulse was minimal. The large initial pressure spikes are ascribed to individual ejecta impacts combined with sensor ringing. As expected, the ringing continues after the ejecta impacts have stopped. A bow wave shock precedes the main pressure pulse.

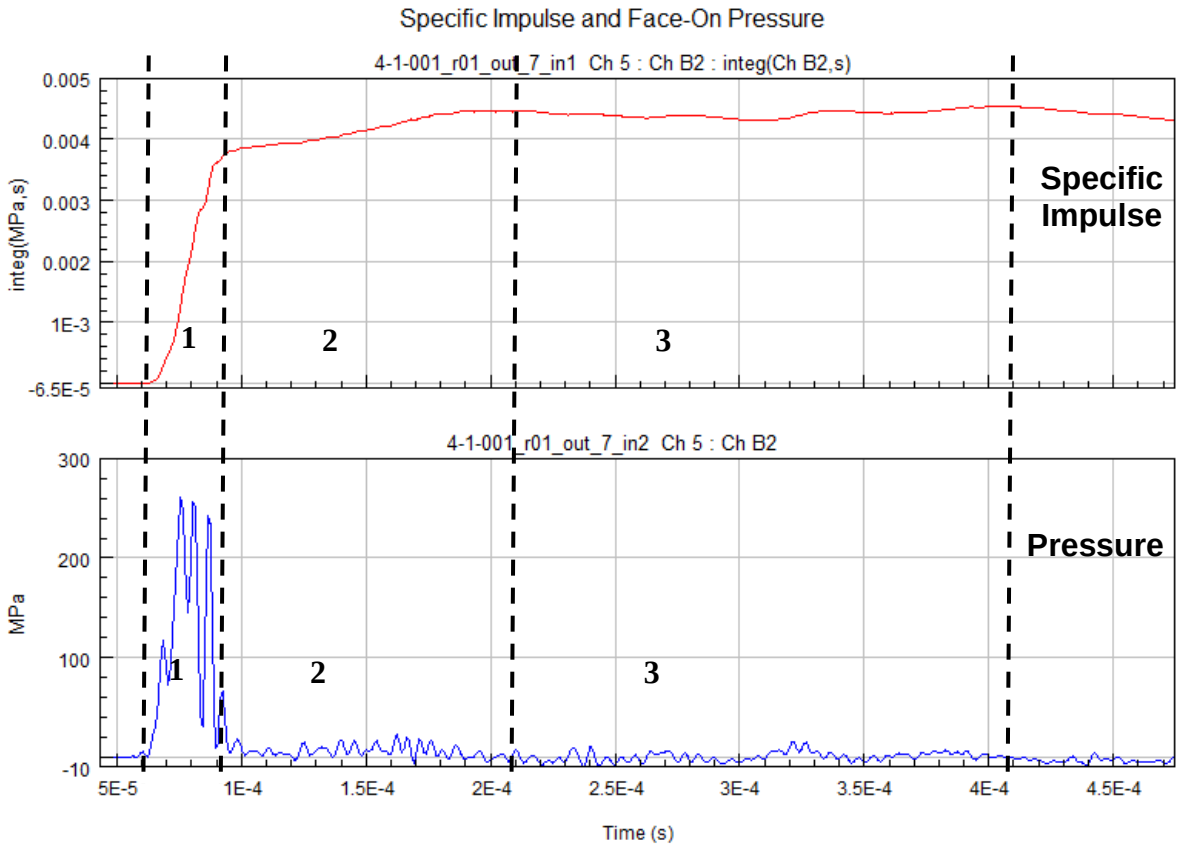

Figure 70: Near-Field Partitioned Face-On Pressure

Figure 71 presents the near-field face-on pressure trace start time and time to reach peak pressure. As expected, both are considerably shorter than the intermediate-field results.

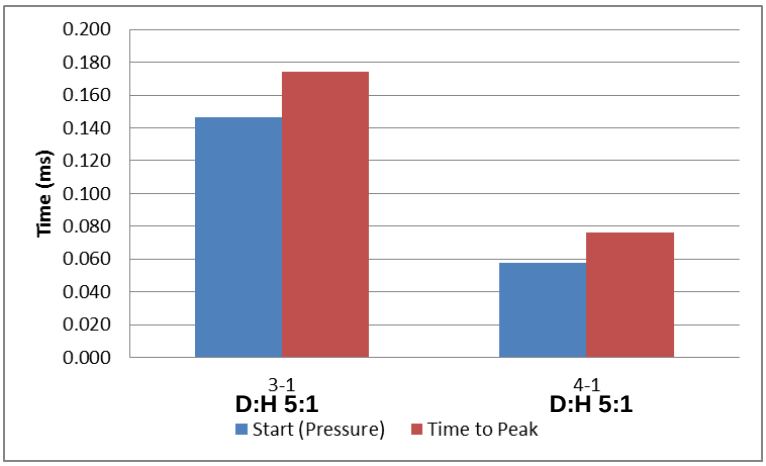

Figure 71: Near-Field Start and Time to Peak Pressure (Face-On) (D:H 5:1)

Figure 72 presents the peak face-on pressure and the standard deviations (where averages are taken) recorded for both the intermediate and near-field tests. The near-field peak pressure was 35% higher than recorded on average for the intermediate-field test.

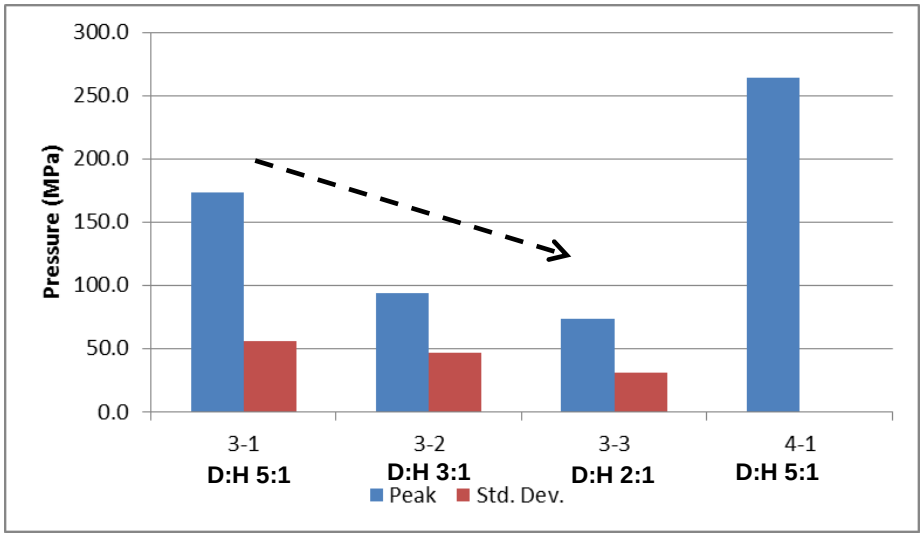

Figure 72: Averaged Intermediate and Near-Field Peak Pressure (Face-On)

Figure 73 presents the total and phased face-on intermediate and near-field positive pressure. The total, and consequently all near-field pressure phases, are of shorter duration than that of the intermediate-field target.

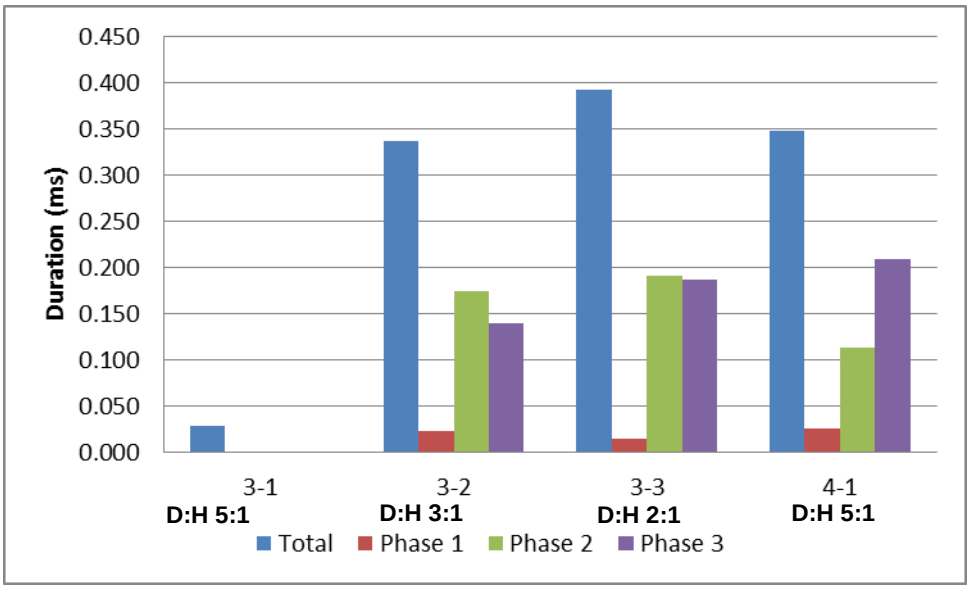

Figure 73: Total and Partitioned Face-On Pressure Positive Duration

Figure 74 presents the total and partitioned phase face-on pressure-specific impulse for both intermediate and near-field targets. Figure 75 presents the phased contribution to the total specific face-on pressure-specific impulse. The results indicate that the main contributor shifts from the second phase to the first phase when moving from intermediate to near-field test conditions. The impulse contribution from the third phase appears to disappear completely under near-field test conditions. The total specific impulse increases three-fold from intermediate to near-field test conditions. These results are, however, limited due to the fact that only one near-field pressure trace was captured.

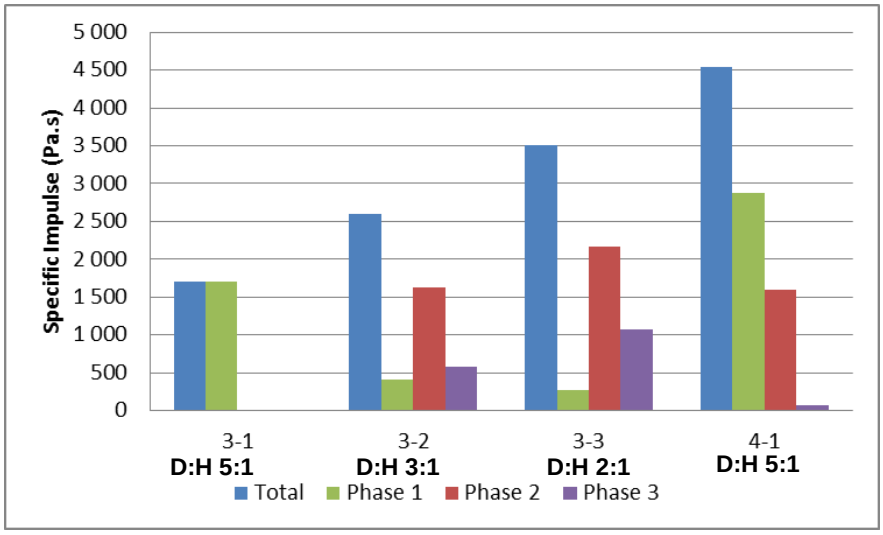

Figure 74: Intermediate-Field ace-On Pressure Specific impulse

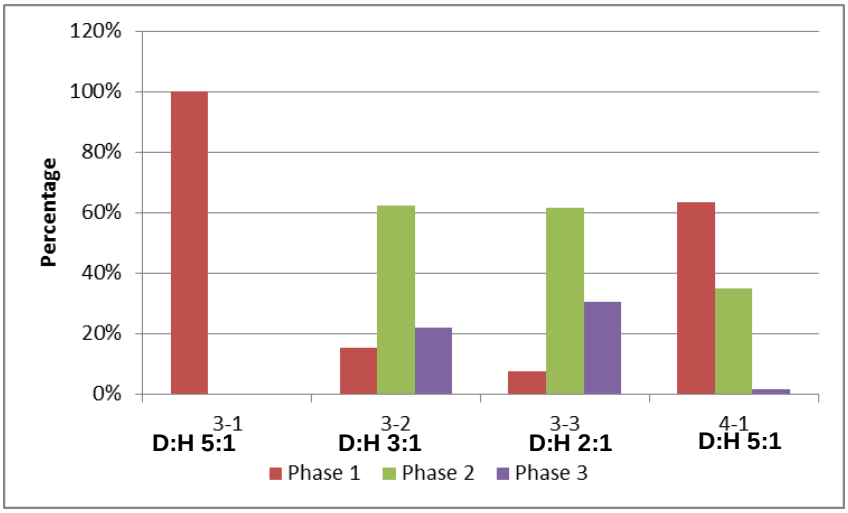

Figure 75: Intermediate-Field Pressure-Specific Impulse Phase Contribution (Face-On)

4.6 NIR Light Emission

NIR light emission was developed as an additional diagnostic tool to investigate the possibility of detecting the onset of afterburn using photodetectors. As the test methodology was not strictly controlled in terms of angle of the sensor head, there was great variability in the results, and as the detectors were not calibrated the signals were normalised rather than absolute light emission values. Not all the tests provided full captured signals. In some cases the duration was shorter than the light emission from the blast and in others the

peak outputs were larger than the settings on the data recorded (oscilloscope), resulting in cut-off signals that were discarded and are not presented here. The light sensor was only used with the final intermediate and near-field target tests.

This data is presented as follows; (1) Emission Morphology and (2) Emission Work.

4.6.1 Emission Morphology

A total of 10 useable light output traces were obtained for narrow band sensor 3 and a total of 10 for the broad band sensor. As the normalised light output peak values differed between the sensors, only the processed broad band sensor data (450-1,150 nm) are presented here. Figure 76 presents normalised output traces for a single intermediate field test captured from each sensor (D:H 3:1). The plots sequentially present the sensor outputs starting with sensor 1 at the top. Not visible in the processed data presented here is that the voltage outputs varied considerably between each sensor something reflected in the noise that is visible in the top two plots. In addition, the light outputs seemed to vary with changing ambient light conditions. It is clear from the plots that this is the phasing of the light output, allowing the output to be partitioned by simple visual inspection into at least three phases as shown in Figure 76.

The difference in normalised outputs is clear between sensor 3 and sensor 4, where sensor 3 presents a lower initial but higher second peak light emission, whereas sensor 4 has the opposite morphology. This implies that the initial light output has higher shortwave (near-ultraviolet) emissions. In sensor 3 and 4 traces an additional increase or peak appears, shown by the arrow in Figure 76. This phenomenon was not seen in all the captured test data. Rather it occurred randomly across all measurement points. It is thought to be possibly linked to atmospheric lighting or other methodology variability such as off-perpendicular charge placement.

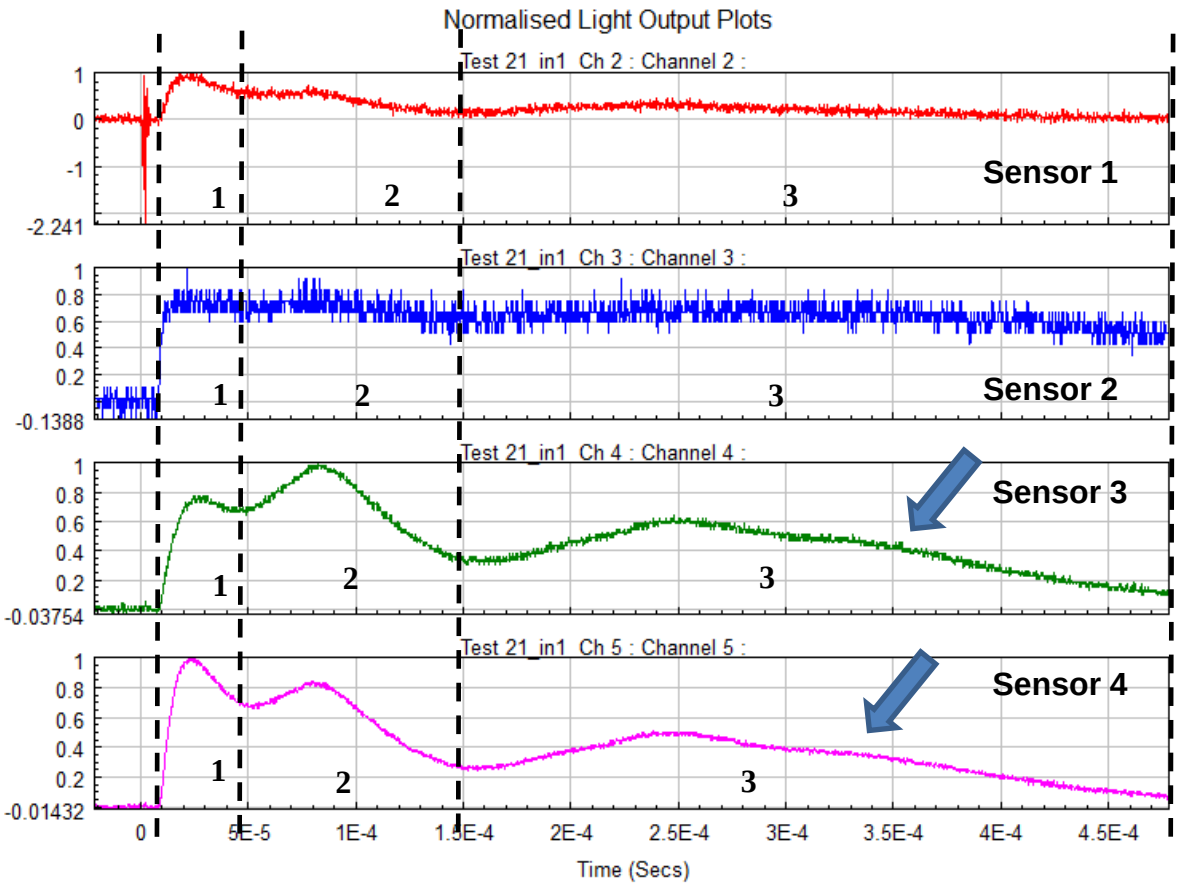

Figure 76: Partitioned Face-On Pressure Sensor Intermediate-Field Target Light Emission – all Sensors (Test 3-2-1)

According to (Gelfand, Silnikov 2004), based on silicon-germanium photo diodes (400,000– 11,000,000 nm) free-in-air D:H 1:1 TNT, RDX and a RDX wax mix similar to C4 charge detonations by the authors, the first phase is due to initial detonation products; the second phase is due to the detonation products burning in air; and the third phase is due to afterburn and occurs after detonation at around 1 to 20 ms. The one-seventh 20 g equivalent charge scales as 4/7th, thus the scaled test afterburn occurrence would be from 0.57 to 11.4 ms after detonation. The authors also note that for RDX-based explosives tested the second phase and afterburn or third phase were much lower than the explosives containing TNT. The first two phases for free-in-air blast were over by 0.2 ms. Figure 77 shows that the shallow-buried light output (radiation) levels of the duration of the first two phase's duration lasts between 0.147 and 0.462 ms. This large variation is due in part to the obscuration effects of soil ejecta

combined with experimental set-up variations in the sensors and ambient lighting.

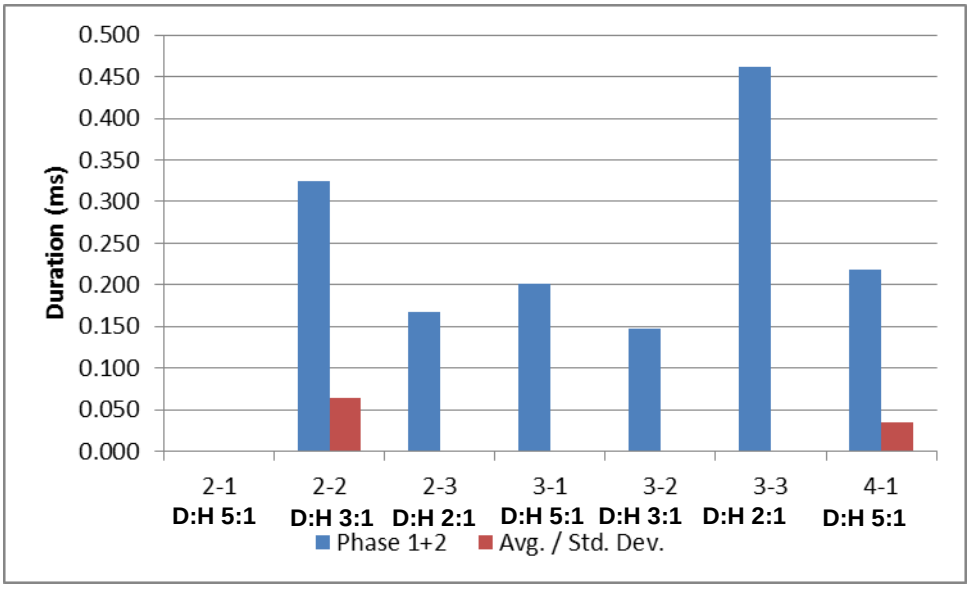

Figure 77: Normalised Summed Phase One and Phase Two Peak Radiation Output and Standard Deviation (Sensor 4)

Another difference with (Gelfand, Silnikov 2004) free-in-air results is the relatively large and distinct second phase peak recorded in these experiments. A similar large phase response was found by (Gelfand, Silnikov 2004) only with free-in-air explosives made from or containing TNT. According to the authors, this was due to soot being generated during the detonation process. As carbon has a greater radiance than the gaseous detonation products, this increases the second phase radiance output. For the RDX-based explosive blasts the radiance output declined exponentially in (Gelfand, Silnikov 2004) tests, followed by a constant shallower slope until the afterburn phase. The difference between these results could be due to the much smaller wavelengths being captured for these research tests compared to (Gelfand, Silnikov 2004) (450-1,150 nm compared to more than 0.4-1.1 mm). It is also possible that the higher radiance from the shallow-buried blast could be due to carbon being generated with the explosive interaction of the soil during the detonation process. The higher SOD would thus provide better data for light phasing as less soil is ejected for the volume spaced between the surface and the target.

The light output results indicate that for shallow-buried blast the light emitted at different wavelengths temporally responds similarly; however, the peak output values are different. Using (Gelfand, Silnikov 2004) phase explanation, shallow burial of an explosive increases the burn radiance through carbon-rich by-products and the afterburn is induced earlier and appears to be more substantial when shallow buried. Although the limited reported results from the literature appear to explain the light emission phenomena and verify afterburn effects, there are concerns that the soil ejecta, in particular at the end of the high-speed phase as well as the slow-speed phase, would hide any additional thermodynamic effects resulting in radiance increases, thus additional phases. If afterburn had been occurring later, the third peak witnessed here could have been due to other physical phenomena such as reflected pressure build-up.

Figure 78 presents the averaged or single measurement light output start time (light breakout) and time to peak one as recorded by sensor 4. There is a difference between the two radiance breakout and peak light times of the experimental pressure sensor set-ups, with the side-on pressure giving much later break-out time and time to peak. This could be due to the probe shaft and tip that extends 162 mm below the target shielding the sensors from the initial light. The variability is visible in both parameters. As noted, this is due to a number of factors, including possible experimental set-up variance as well as ambient light changes. The initial breakout and peak timing of the near-field tests was not much different from those of the intermediate face-on pressure tests.

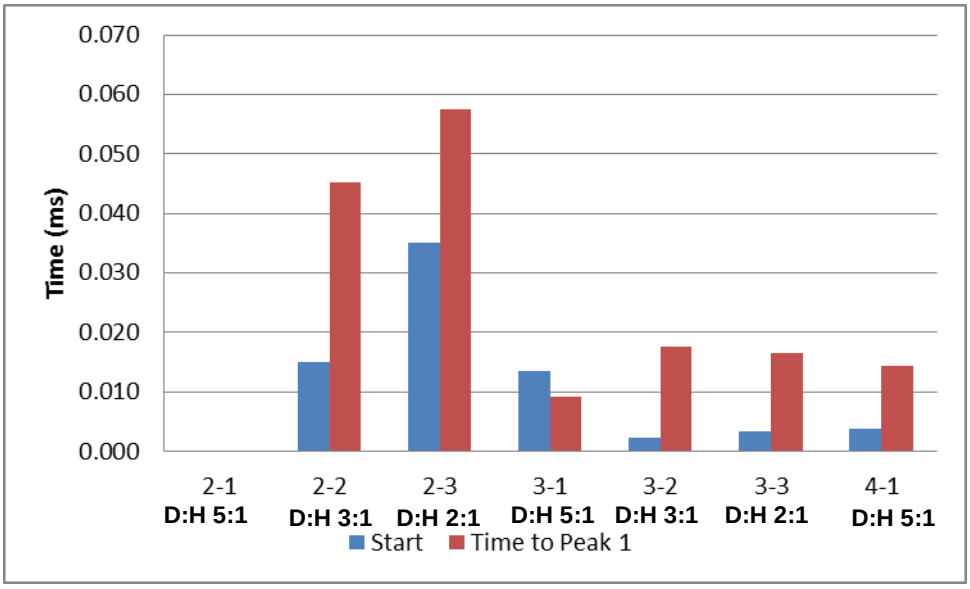

Figure 78: NIR Radiance Start Time and Time to Peak 1 (Sensor 4)

Figure 79 presents all the partitioned and averaged or single-point recorded light radiance (output) durations for sensor 4 captured during testing. No useable D:H 5:1 intermediate light emission data were captured. The total duration for the face-on pressure sensor configuration appears to be slightly longer than for the side-on pressure test configuration.

Figure 80 presents the partitioned normalised average or single peak values for each of the phases obtained from the intermediate and near-field target tests from Sensor 4. Initially it appeared that for the side-on pressure tests the second phase was larger than the first phase, whereas for the face-pressure configuration the first phase was larger than the second phase peak. This would suggest that the side-on probe would ensure that more post-detonation gaseous products are pushed out and are thus more visible. However, the 2:1 D:H face-on pressure (3-3 series) test data indicated a larger Phase Two. Why this would be different for these tests is unknown, as the narrow-band sensor 3 had three visible phases for the same test. The following near-field face-on pressure configuration test again reflected that Phase One peak was the largest. This is to be expected as this is the initial detonation breakout and should be much larger than the subsequent burn phase due to the much

smaller distance between the soil and the target (72 mm vs. 200 mm) and the much thicker soil ejecta wall which would limit light output.

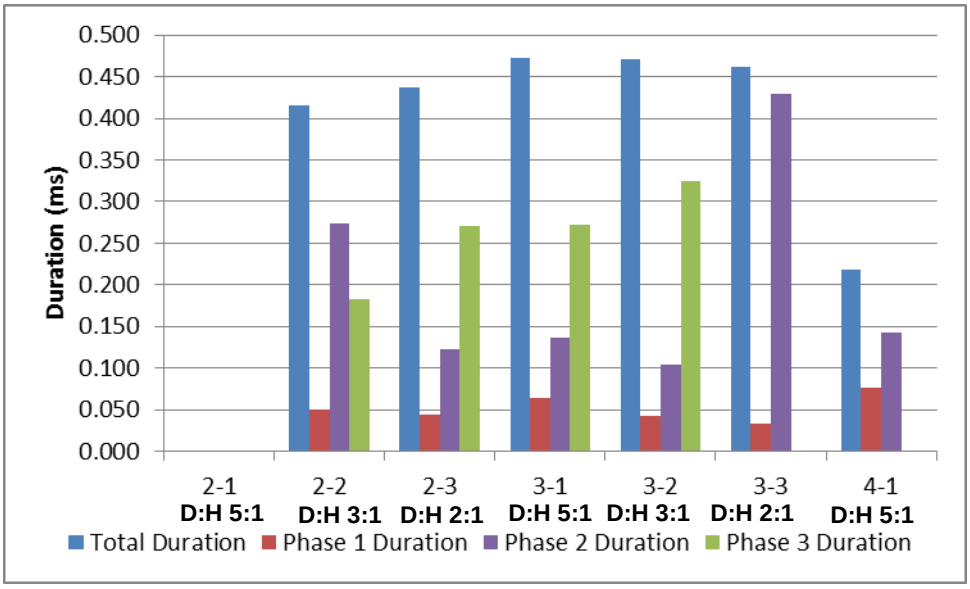

Figure 79: Total and Partitioned Light Phase Durations (Sensor 4)

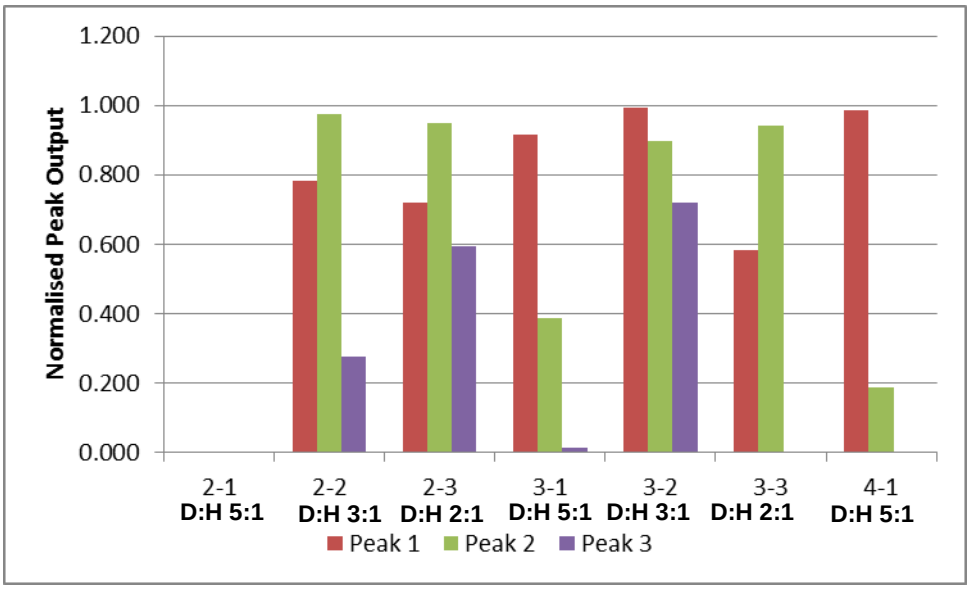

Figure 80: Total and Partitioned Phased Normalised Peak Light Output (Sensor 4)

4.6.2 Emission Work

Light emission was integrated to derive a value of the area under the curve or the work presented by the light output. This value was exceptional due to the normalisation of the signal, thus it was multiplied by a constant factor of 10^6.

The partitioned and magnified light work output is presented in Figure 81. Figure 82 presents the partitioned percentage light work contribution per phase. No clear trends are visible within this limited data set.

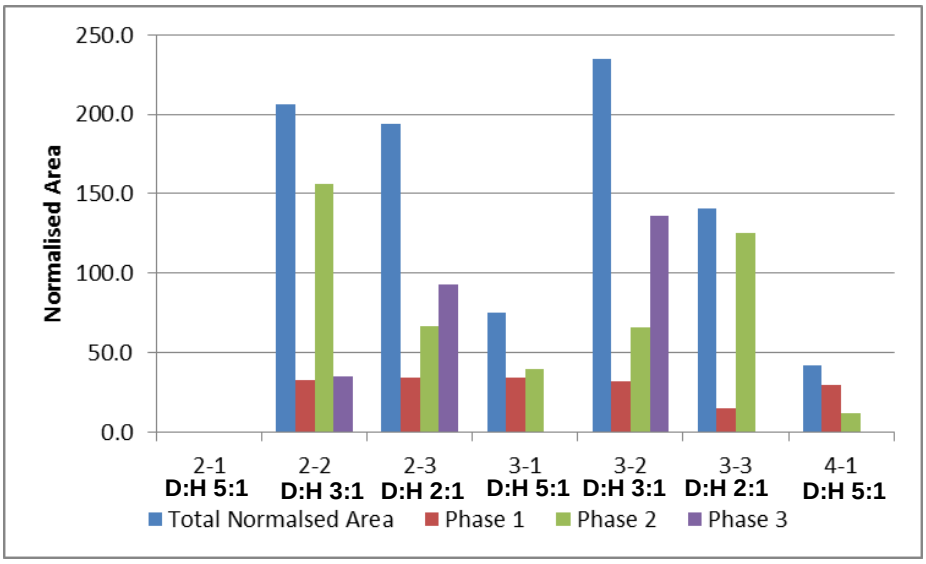

Figure 81: Partitioned Normalised Light Work (Sensor 4)

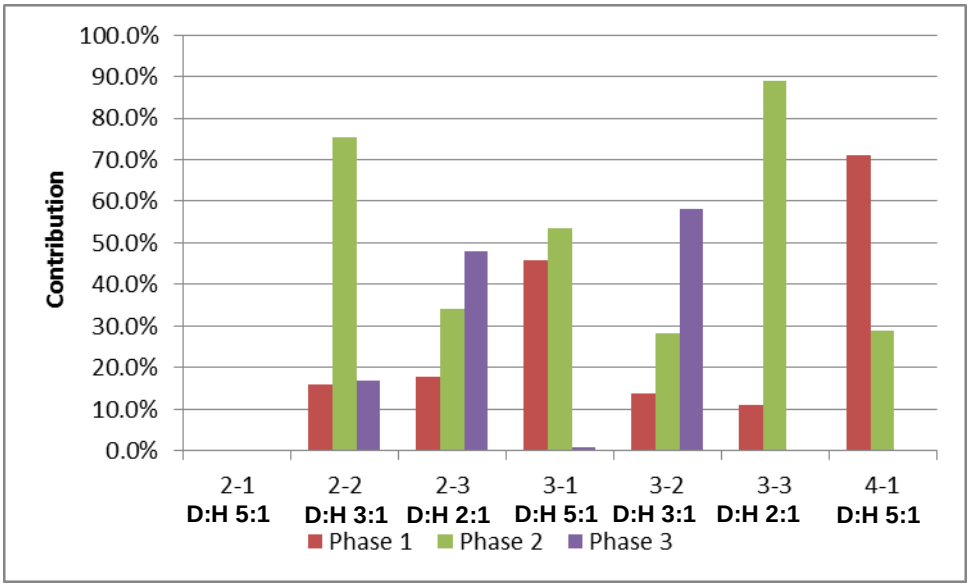

Figure 82: Partitioned Phase Percentage Contribution to Total Light Work (Sensor 4)

4.7 Target Assembly Displacement-Time

The global motion of the measurement head assembly was not intended to support the partitioning research but was also found to exhibit positive loading

phase behaviour, and was thus included as supporting data. The displacement results are in two sections, these are; (1) Morphology and (2) Integrated Deflection (Area).

4.7.1 Morphology

Figure 83 presents the full captured displacement time plots for a single D:H 5:1 test from each test configuration. From the displacement traces it is clear that the initial positive deflection characterised by phasing results from the phased loading. The plots also show that not all full cyclic traces were captured. In most cases the displacement probe detached from the head during the downwards release phase as discussed in Section 3.3. It is also clear from the full response trace for the D:H 5:1 test that it is not perfectly sinusoidal. This is due to the design of the test rig resulting in different stiffness's for the upward and downward directions.

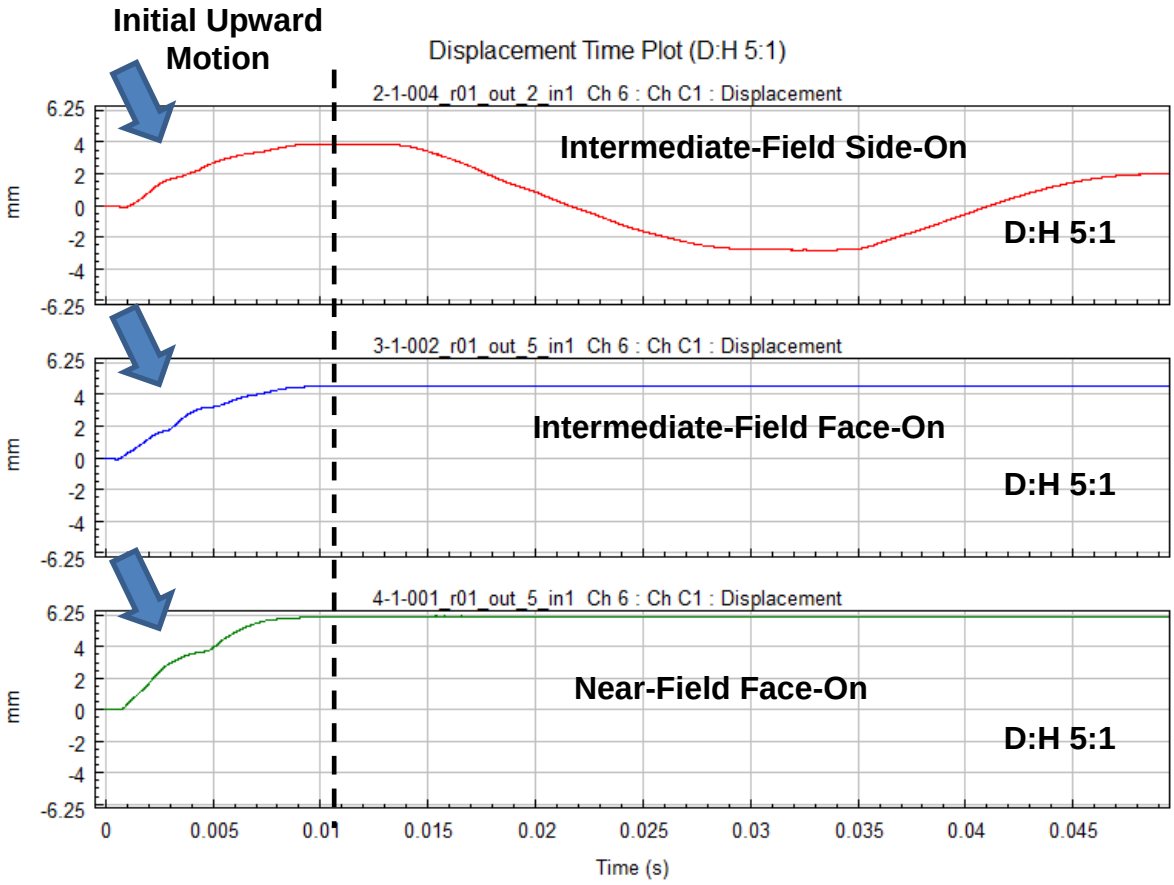

Figure 83: Displacement-Time Plot of Intermediate and Near-Field Target Side-On and Face-On Pressure Sensor

However, the focus is on the initial upwards or positive phase which was accurately captured by the sensor (see Figure 84). The end of the positive phase was set as when the peak displacement was first reached and not the middle of the defection plateau. Although not strictly correct, this is sufficient to analyse the deflection data in a comparative manner for the final intermediate and near-field target tests.

Figure 84 presents the expanded and partitioned averaged positive displacement-time plots for D:H 5:1 test charges from each test configuration. Due to the clear phasing present, the partitioning was done manually through inspection. The centre point of each inflection or displacement plateau was selected at the end of the previous phase and the start of the next phase. Figure 85 presents the displacement start time for all tests. There is a clear increasing start time with increasing D:H test charges with the face-on sensor test configuration. This trend is not quite as clear with the side-on pressure test configuration, where the D:H 3:1 had a shorter start time. As expected, the near-field test had the earliest start time. Figure 86 presents the average total and phased deflection duration. No clear trends between the D:H test charges and the derived phases are evident in the data. The side-on pressure test configuration seemed to have a shorter total deflection duration than the face-on configuration. This is not expected as the side-on test with the large probe exposed to the blast ahead of the target would be expected to give a longer loading due to the larger wetted area. The method of defining the end of last phase would result in shorter third phase duration and this will affect the results and trends present in the data.

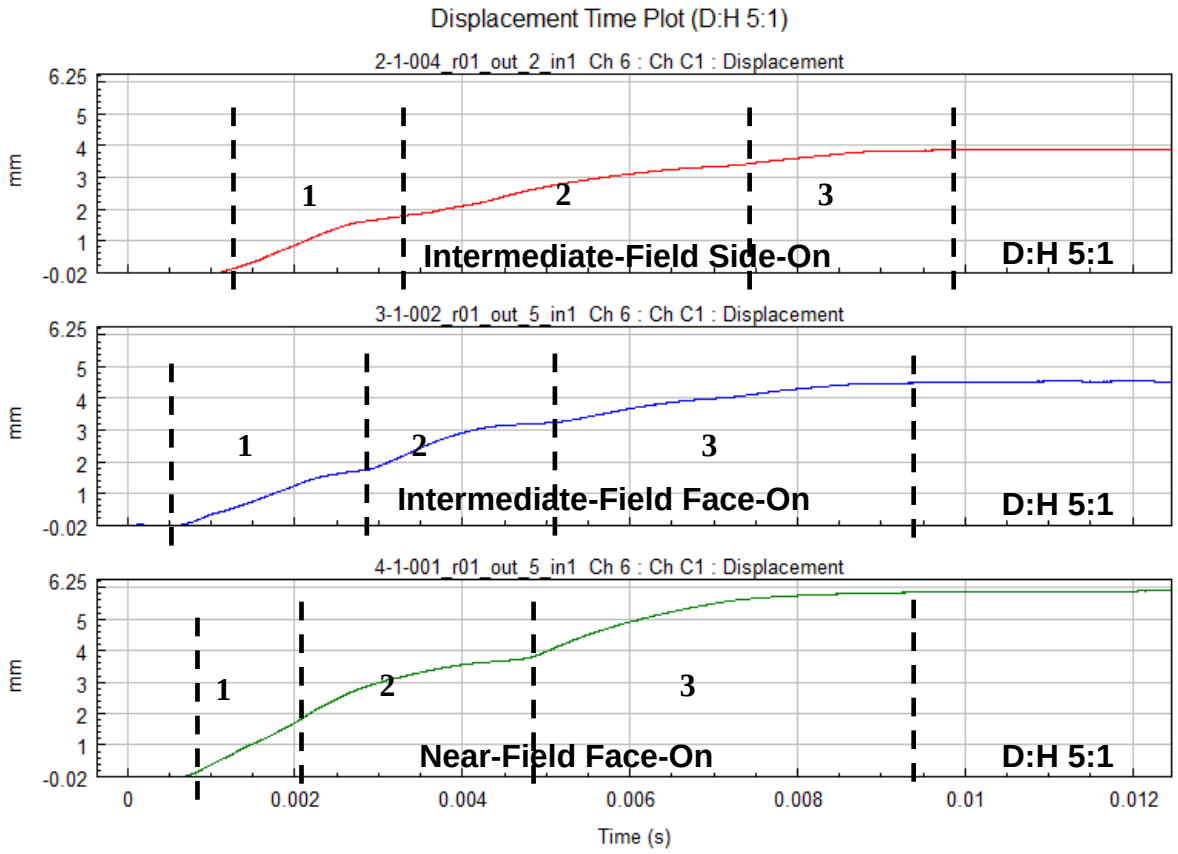

Figure 84: Measurement Assembly Displacement D:H 5:1 Side-On and Face-On Pressure Intermediate and Near-Field

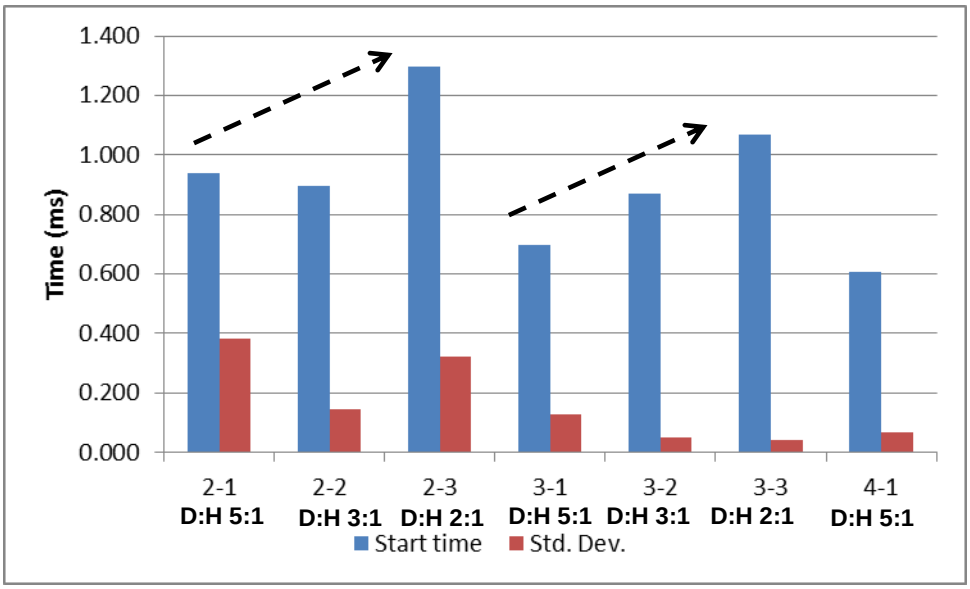

Figure 85: Averaged Displacement Start Time and Standard Deviation (All D:H)

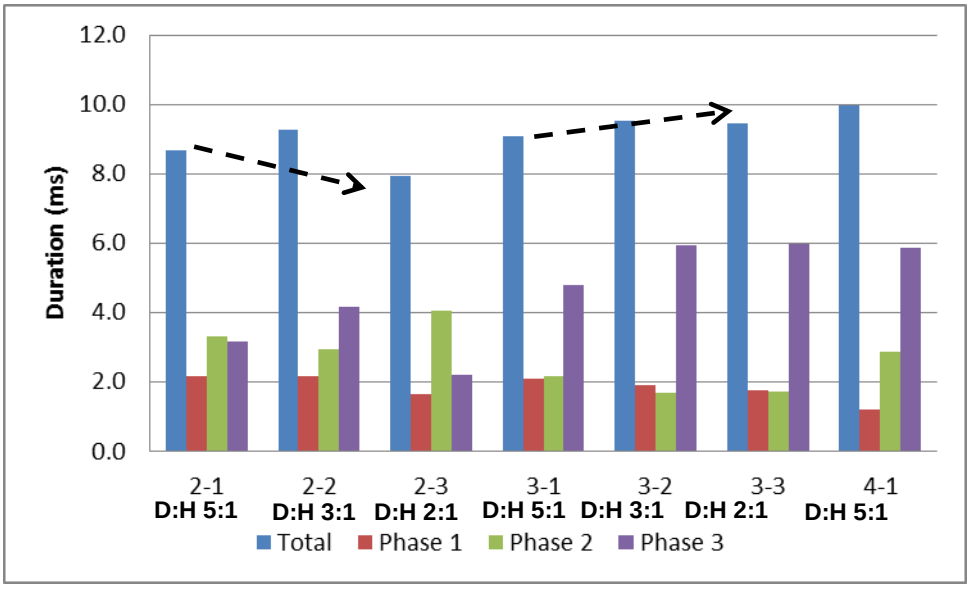

Figure 86: Total and Partitioned Average Phased Displacement Duration (All D:H)

Figure 87 presents the averaged peak displacement for each test point. There is a clear decreasing peak displacement trend with decreasing D:H ratio charges. The intermediate-field side-on test configuration gave a slightly smaller average peak deflection compared to the face-on configuration.

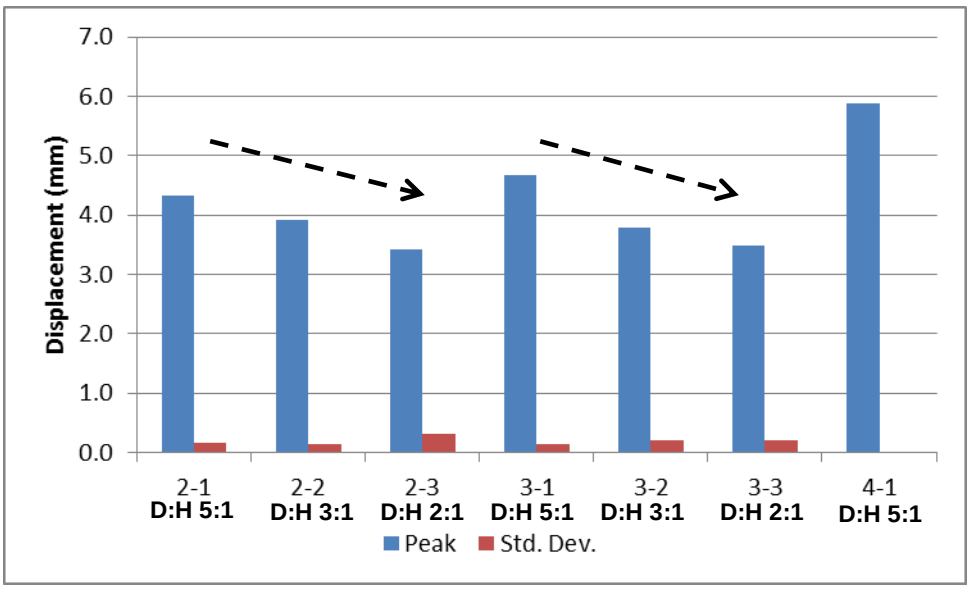

Figure 87: Measurement Assembly Peak Displacement (All D:H)

4.7.2 Integrated Deflection (Area)

The positive deflection-time phase was integrated to calculate the total and partitioned phased work. This value gives an indication of the load transferred to the target assembly. When partitioned, the phase area would be an indication of the percentage contribution of the phase. As with the light emission integration, the integrated value was very small, so it was multiplied by an arbitrary factor of 10^3. Figure 88 presents the average integrated displacement time for all intermediate and near-field tests. There is a trend of decreasing integrated displacement with decreasing D:H ratio charges with the face-on pressure configuration. This trend is not clear with the side-on pressure configuration. When looking at the test data for the 5:1 and 3:1 tests, it can be seen that each has a specific test point that varies.

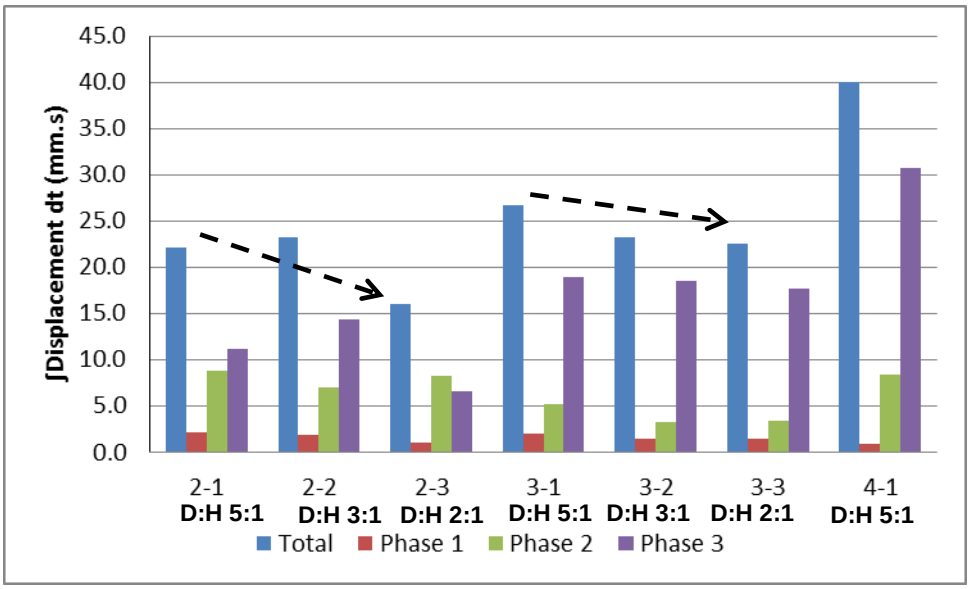

Figure 88: Total and Phased Integrated Displacement-Time (All D:H)

These test points resulted in standard deviations of 8 and 9%, but when removed they reduce to 3.5 and 2.8% of average. These revised average values then give a decreasing integrated displacement-time trend as well. This indicates that the scaling limitation in the experimental method of differentiating between the D:H ratio charges has been reached and possibly exceeded. Overall the third phase followed by the second and lastly by the first phase had the largest integrated displacement-time or area value. When moving from the

intermediate to near-field target the second and third phases increased, whereas the first phase reduces further. The side-on pressure test configuration has a consistently lower integrated displacement time, indicating a lower load transfer between the two test configurations. This is supported by the lower peak displacement observed as well.

Figure 89 presents the percentage contribution per phase to the total integrated displacement-time of the positive displacement segment. The side-pressure test configuration did not give any clear trends due to the manually extracted data variations discussed above. The intermediate-field face-on pressure test configurations gave similar percentage contributions for all D:H ratios, with the 5:1 ratio having slightly larger percentages for Phase One and Two. The near-field test configuration, however, resulted in an even lower percentage contribution from the first phase, with the second phase increasing by the same percentage and the third phase being slightly larger. This indicates that the load phase contributions change as the SOD decreases.

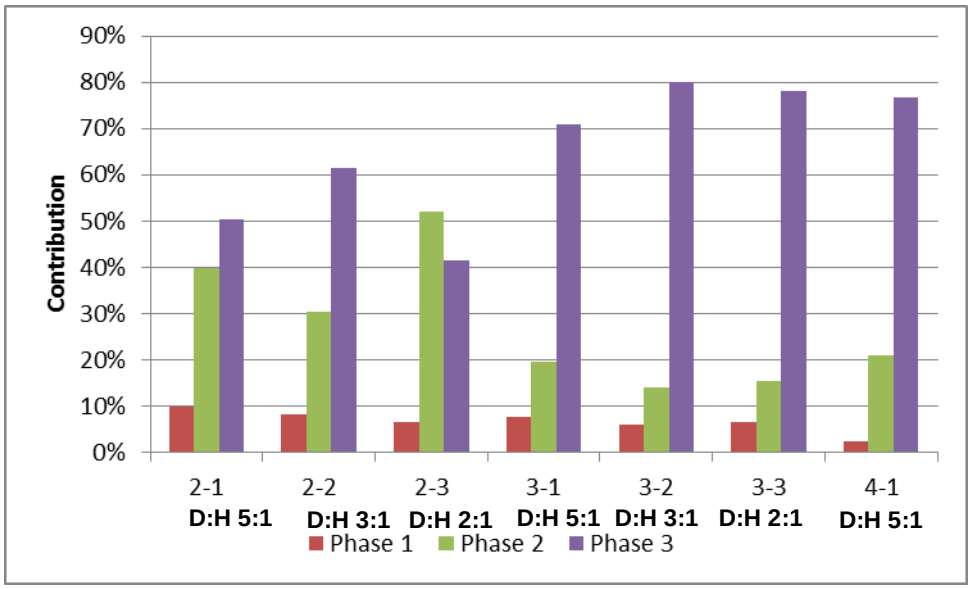

Figure 89: Partitioned Phase Percentage Contribution to Integrated Displacement-Time

4.8 Secondary Data

Processed secondary data used to support this research are presented in this section. The data presented here were processed by the author using supplied test data. These data confirm shallow buried blast load target response for larger scaled charges as well as deep buried blast tests.

4.8.1 Cranfield Blast Rig Data (McDonald 2013b)

The Cranfield (McDonald 2013b) test data comprise what are considered a combination of deep-buried and shallow-buried blast. Based on the Hopkinson scaling, the 100 mm DOB was equivalent to a full-scale (prototype) depth of 350 mm and the single 50 mm DOB was equivalent to a full-scale (prototype) DOB of 175 mm. This is consistent with Bangash as quoted by (Deshpande, McMeeking et al. 2009b) with a Cranfield test charge radius (R_c) of 29 mm. A Zone 1 or shallow-buried DOB range of between 58 to 87 mm is calculated. Thus according to Bangash, the 100 mm DOB tests are deep-buried (Zone 2), while the single 50 mm DOB test is defined as shallow buried (Zone 1). The test target SODs of 360, 230 and 100 mm scale to 1,260, 805 and 350 mm respectively.

The Cranfield tests have scaled distances (Z) of 0.90, 0.66 and 0.42 m/kg$^{1/3}$ for the deep-buried tests and 0.57 m/kg$^{1/3}$ for the shallow-buried tests. These are all larger scaled distances than the near-field scaled research threats (0.31-0.33 m/kg$^{1/3}$), but are smaller than the introduced additional intermediate scaled tests (Z=0.79-0.80 m/kg$^{1/3}$), thus providing verification of the phasing response of a target subjected to a buried blast as well as force-time morphology differences with changes in SOD and DOB.

4.8.1.1 Blast Morphology (Deep-buried)

Figure 90 presents a sequence of high-speed video images from a deep-buried (DOB 100 mm) 360 mm SOD test from Cranfield. The recorded deep-buried blast morphology follows that of current literature (Deshpande, McMeeking et al. 2009b, Ramasamy, AM Hill et al. 2009, Grujicic, B Pandurangan et al. 2007,

Fourney, Leiste et al. 2005), which proposes temporal behaviour of buried blast as follows from Figure 90:

- Frame 1 the detonation-driven shock wave reaching the soil first 47 µs after detonation, and reflecting with a weak air shock moving off towards the target.
- Frame 2 the soil spalls slightly and then starts to bulge outwards and upwards 714 µs after detonation.
- Frame 3 with large SODs the hemispherical soil cap forms and then ruptures, releasing a mixture of soil and detonation products 809 µs after detonation that continues upwards with the soil cap towards the target.
- Frame 4 and impacting the target 1,095 µs after detonation.

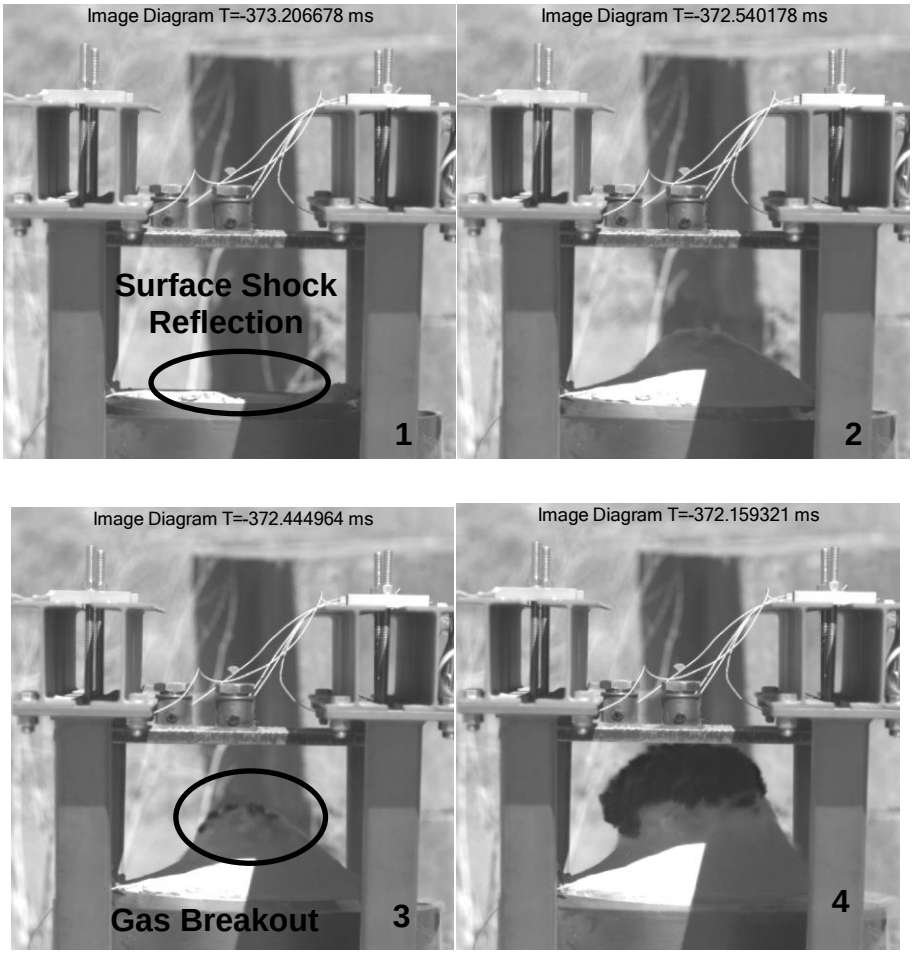

Figure 90: (McDonald) 360 mm SOD Deep-Buried Test

For this test this breakout process started at a soil cap SOD of 170 mm. The weak shock wave impacts the target and reflects back down into the oncoming blast front and disappears. No measureable target force response was seen from the air shock impact. Figure 91 presents the distance-time plot of the reflected shock front and the blast front from a Cranfield deep-buried test.

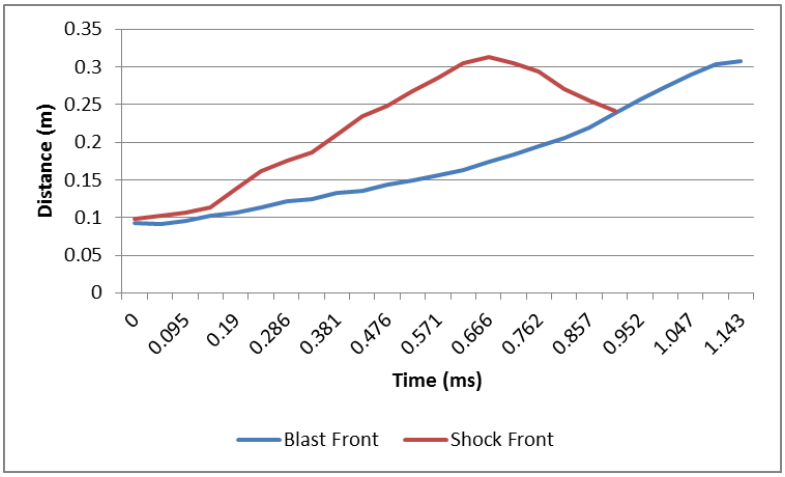

Figure 91: Deep-Buried Blast and Shock Front Displacement-Time (McDonald 2013b)

Figure 92 presents a sequence of high-speed images from a Cranfield shallow-buried test. The blast process, however, shows a similar morphology to the deep buried test as follows:

- Frame 1 a reflected soil surface shock being present,
- Frame 2 followed by gas breakout at 161 μs after the shock surface reflection,
- Frame 3 full gas breakout at 323 μs after shock surface reflection,
- Frame 4 shows the blast front growing across the target plate.

Thus other than occurring much sooner after detonation, it appears that spherical buried charges have similar blast morphologies irrespective of the depth of burial, including the appearance of a soil free-surface shock prior to bulk soil cap motion.

Figure 92: (McDonald) Shallow-Buried 230 mm SOD

This could be due to the shallow DOB being just within the Bangash zone 1 combined with the spherical charge shape resulting in an increasing DOB as one moves laterally away from the charge centre line. It could also be that the DOB is simply a deep-buried charge irrespective of the Bangash zone definitions. Using Hopkinson and Geometrically Similar Scaling, a 50 mm test DOB equates to a full-scale DOB of 173 mm. This is 75% more than that of (NATO Standardization Agency (NSA) 31 August 2011) and more than three times that specified by (RMSS February 2005), which supports this possibility. The 50 mm DOB resulted in a peak blast front velocity of 750 m/s just prior to target impact.

4.8.1.2 Target Force-Time Response Morphology

Figure 93 presents the target-force time response of all tests executed by (McDonald 2013b). The results show an asymmetric response with the upwards direction showing a series of force peaks that die over time but are not present in the negative force region. It is expected that the test set-up would be more rigid upwards as the plate bears against four I-beam members, whereas in the

downwards direction the target plate only responds against the four bolts attaching the plate. This is thought to be due to the target plate edge response.

The force washers are attached directly to the target plate, and are thus exposed to the vibrational response of the plate to the impact loading. As the plate is bent upwards the area acting against the force washer is angled upwards towards the centre, thus the outer edges will relax slightly, and when the centre of the plate moves downwards the outside edges of the target plate will compress against the force washer, thus giving a positive output and reducing the net negative force response. As the bolts are unsupported and less rigid in the downwards direction, they will also give more, thus providing a lower response force. The welded face-on force washer assembly mounts could have made the plate stiffer in the relaxation or downwards direction, and could have contributed to the noted response.

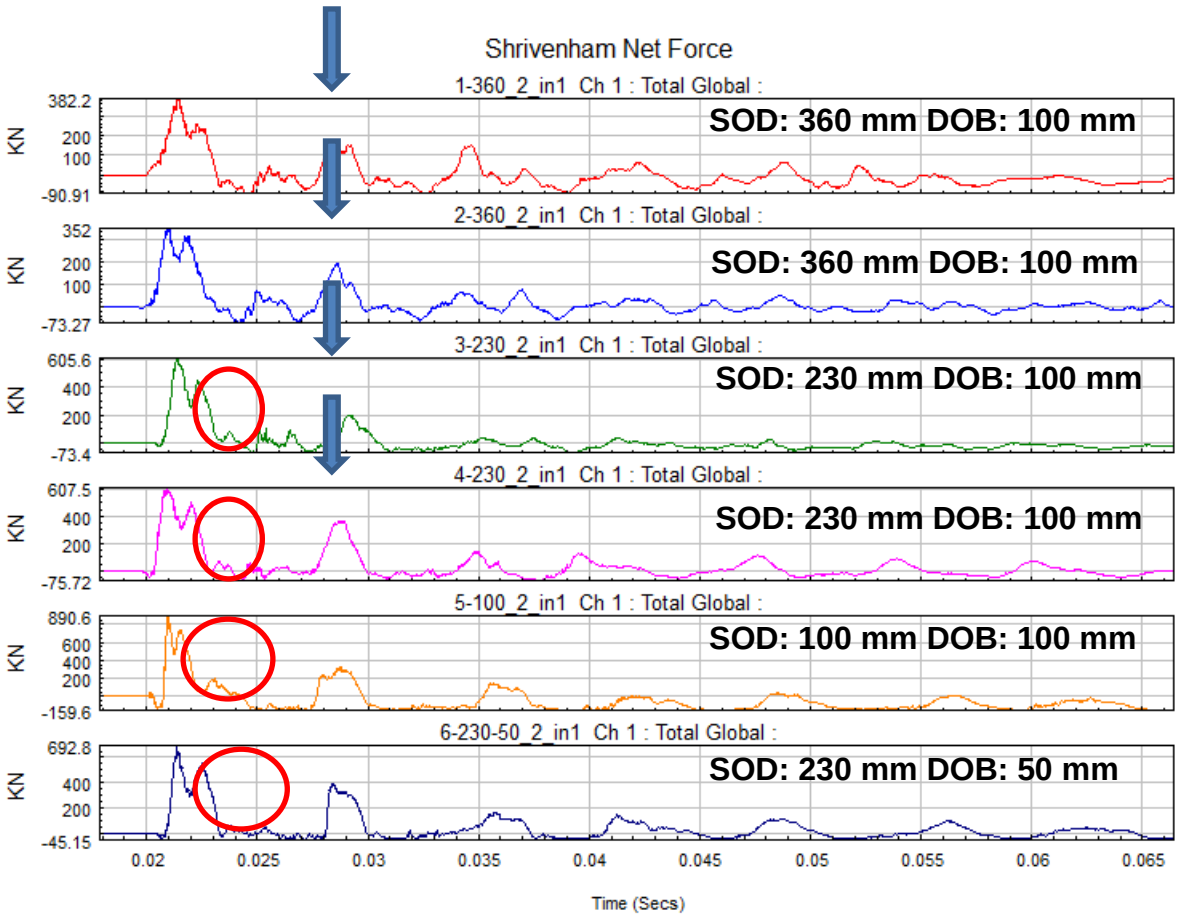

Figure 93: Cranfield Estimated Force-Time Plots (All Tests)

As these tests used only two force washers and an assumption of symmetry, any asymmetric impact would be exacerbated in the net force-time response as the measurement is doubled to obtain the total force-time response.

The positive phase indicates at least two force peaks for all tests. The larger SOD test force-time response had a smaller response peak after the positive phase prior to the main positive damped response peak (arrowed). This peak appears to reproduce for three cycles as the force response damps out. This peak reduced as the SOD decreased.

With the lowest SOD the positive loading phase response gave a third force peak (circled). This indicates that a three-phased force-time response is due to near-field target effects. This peak starts appearing with the 230 mm SOD target, both with the deep-buried and shallow-buried tests. Figure 94 shows how the Shrivenham data were partitioned into three phases. The plot shows how the third force phase manifests itself and becomes larger both in peak and duration. Also visible is the change in duration of the second force phase, which decreases as the SOD reduces.

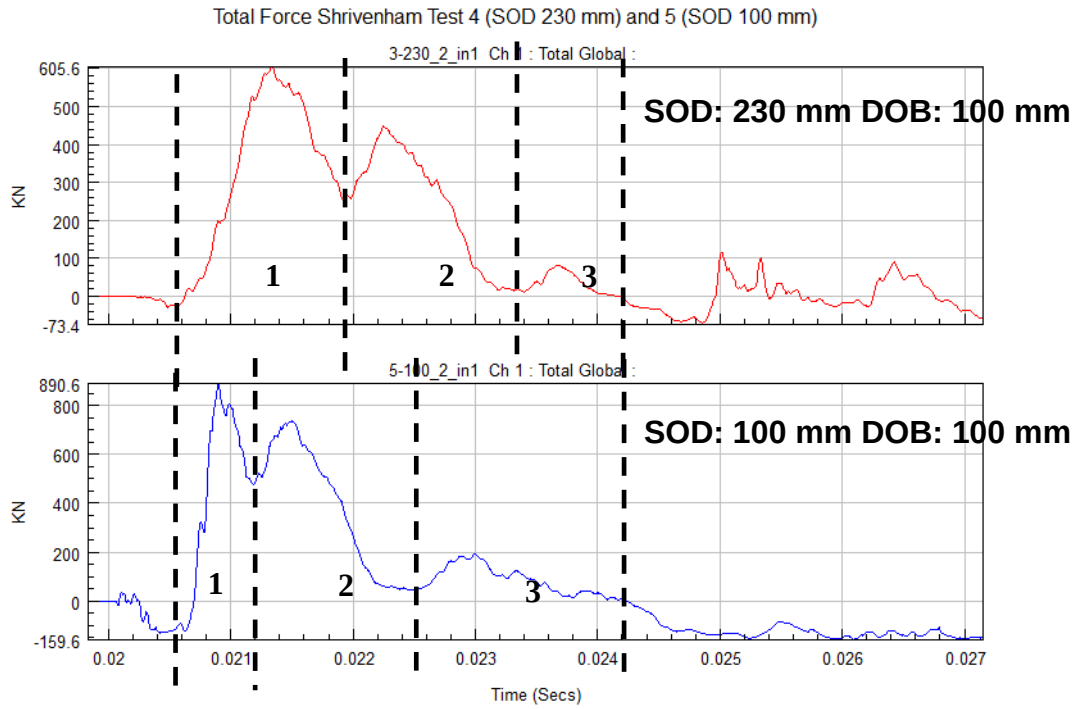

Figure 94: Partitioned Cranfield Force-Time Plot (230 and 100 mm SOD)

Figure 95 presents the averaged total and the partitioned positive phase durations for the Cranfield (McDonald) tests. The data shows clear differences in the various partitioned phases, as the SOD decreases the duration increases. The SOD also affects the partitioned phase durations with a decreasing first phase duration but increasing Phase Two and an additional Phase Three accounting for the overall increased duration. For the first two tests the first phase always has the longest duration followed by the second. The third phase has the shortest duration. Moving from 230 to 100 mm SOD with deep DOB results in the phase durations changing, with the shortest duration being Phase One and the longest being Phase Three. A shallower DOB increases both the first and second phase, but decreases the duration of the third phase. The sequence of the first phase has the longest duration, and the third phase the shortest, maintained with the shallower DOB. The averaged total durations had standard deviations of 8% and 3% of average value for the 360 and 230 mm SOD tests. The averaged duration of the partitioned phase varied by 5% for most phases except Phase Three, which varied by 15% of the average. Figure 96 presents the partitioned percentage contribution to total positive duration per phase.

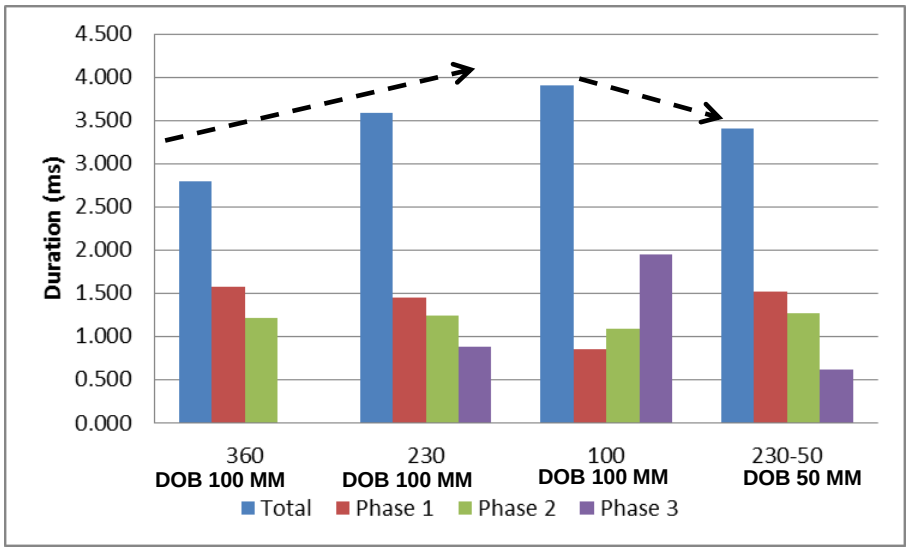

Figure 95: (McDonald) Averaged Total and Partitioned Phase Target Response Force Duration

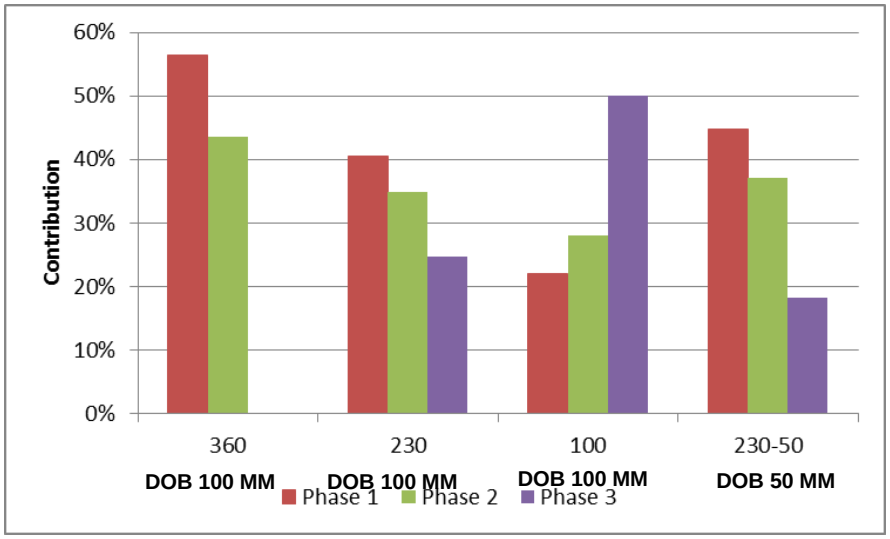

Figure 96: (McDonald) Partitioned Phase Duration Percentage Contribution

Figure 97 and Figure 98 presents the time to peak force and the peak net force respectively with the standard deviation where more than one test was carried out at a test point. The times to peak force and the peak force for the deep and shallower-buried tests were very similar despite the difference in scaled distance and DOB. This implies that the loading mechanisms are very similar, and supports the view that both tests' DOBs are equivalent to deep-buried tests. The relatively long durations overall are indicative of deep-buried blast loading.

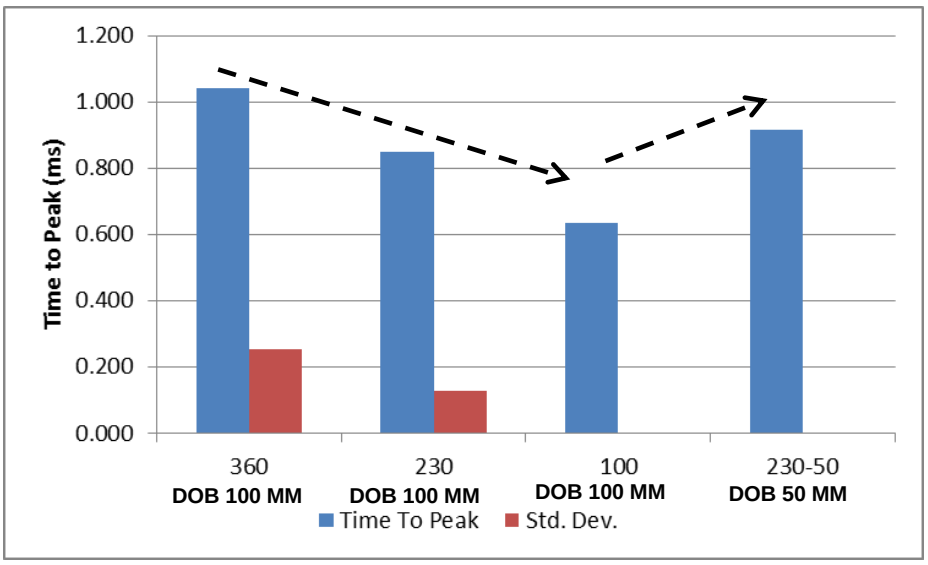

Figure 97: (McDonald) Time to Net Peak Force

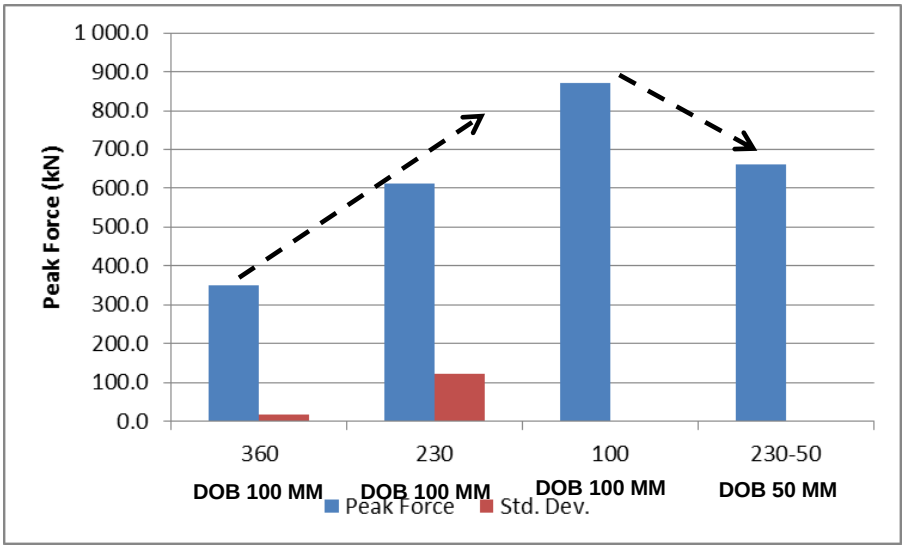

Figure 98: (McDonald) Net Peak Force

4.8.1.3 Target Response Impulse

Figure 99 presents the total and the partitioned phased impulse and Figure 100 presents the percentage impulse contribution of the phase. As expected, the impulse increases as the SOD is decreased. The data show that the total impulse contribution increase reaches a plateau at 100 m SOD. The impulse contributions for the 360 and 230 mm SODs are similar, with the first phase contributing over 50% of the total impulse and the second phase just over 40%. The third phase in the 230 mm SOD test contributes only 2% of the total impulse. Whereas the 100 mm SOD presents a different percentage contribution, with the second phase contributing over 50% of the total impulse, the first phase 28% and the third phase 17% of the total impulse. The shallower-buried charge exhibits a considerable difference in phase impulse contributions to the deeper-buried test charge, with an almost 50/50 contribution to the total impulse coupled into the target plate. The third phase contributes around minus 2% as there are a number of shallow negative phases between the two positive peaks. This is not much different to the plus 2% contribution for the deeper-buried test, but the phase contributions do differ, with the first phase contributing 57% on average of the total impulse.

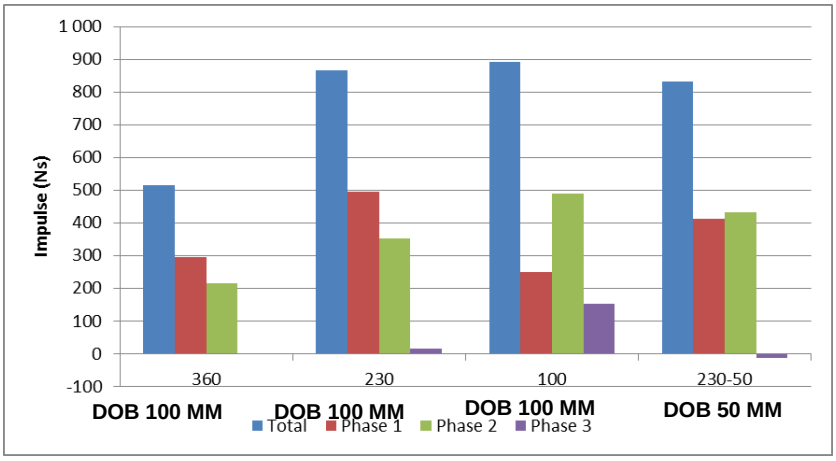

Figure 99: (McDonald) Averaged Total and Partitioned Phased Impulse

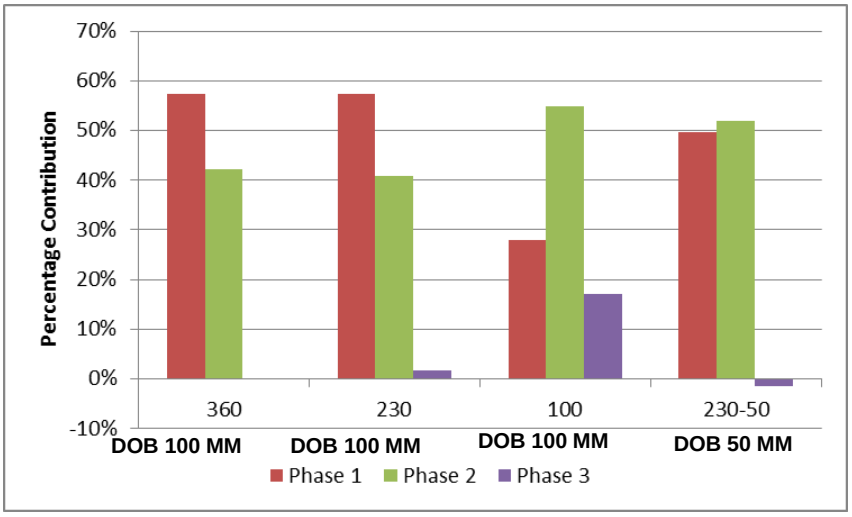

Figure 100: (McDonald) Averaged Partitioned Phased Impulse Contribution

4.8.2 SIIMA

For this work only two SIIMA data sets are presented. The first is a Geometrically Similar (GSS) one-half scaled test (1 kg TNT at a DOB of 25 mm and a SOD of 250 mm), and the second is a full-scale test at a 1,300 mm SOD. In both cases the target was not scaled to the one-seventh scale experiment in these tests. The full-scale target was 1.44 m^2 in area compared to a required full-scale value of 4.99 m^2 of the one-seventh scale target. The half-scale target was 0.36 m^2 compared to an up-scaled one-seventh target plate area of 1.25 m^2. Although this is substantial, it is well reported (Held 2004, Tremblay 1998) that the blast load is exponentially distributed over the target with the majority of

the blast in the centre portion. In the one-half scale tests the GSS target plate was attached, albeit at a higher SOD, to the 2.44 m^2 SIIMA target plate, thus some of the blow-by was captured. This difference is also further negated as the blast front is smaller than the target area. The SIIMA tests represent shallow-buried blast with scaled distances (Z) of 0.29 and 0.69 $m/kg^{1/3}$. The full-scale tests used NATO AEP-55 Edition 1 compliant soil, whereas the half-scale tests used standard loose SIIMA soil with an average measured density of 1,580 kg/m^3.

4.8.2.1 Target Force-Time Morphology

Figure 101 presents a typical heavily damped one-half near-field and full-scale intermediate-field SIIMA force-time response. The full-scale force-time trace has an initial negative peak which is lower than the second, indicating that an upward force was applied which reduced the negative net force (arrowed). This is only present in the full-scale tests and is due to loose ballast mass in the SIIMA target assembly, which, due to inertia, is still travelling upwards when the target force release occurs, resulting in an additional upward force being applied. This only occurs with large charges which have sufficient loading to accelerate the ballast mass in the target assembly.

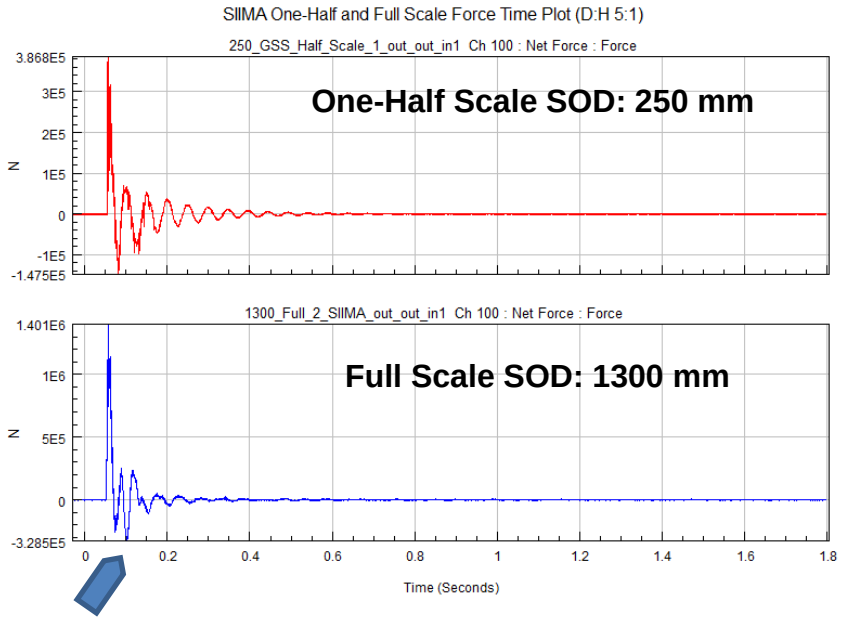

Figure 101: Force-Time Response for One-Half and Full-Scale SIIMA Tests

Figure 102 shows the partitioned positive phase of a SIIMA half-scale and full-scale test. The large number of smaller peaks is due to the force measurement system which uses sixteen load cells spatially distributed across the target assembly which are summated to obtain the next force. There is a sampling speed difference between the half-scale and full-scale test data (10 kHz vs. 50 kHz) resulting in the rough trace shown here. The positive force phase could be still be easily partitioned through inspection into three primary load phases as shown.

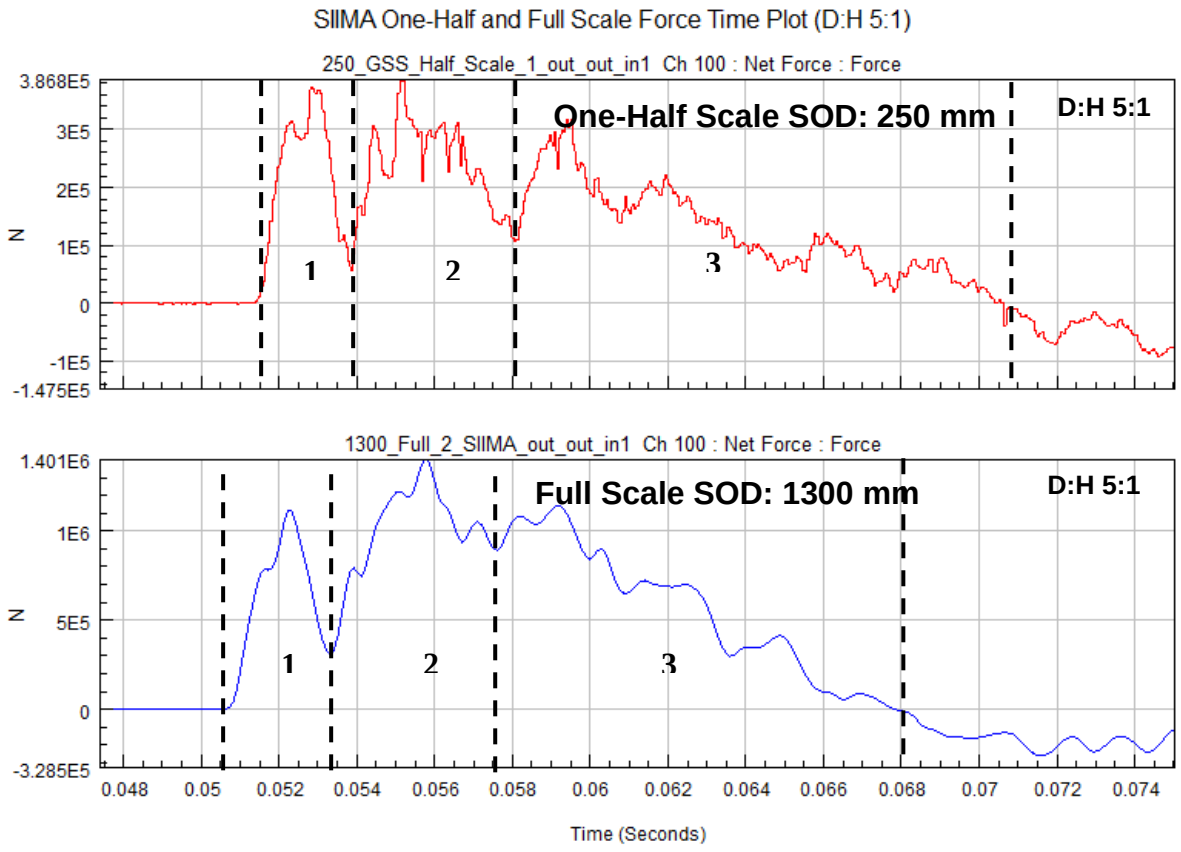

Figure 102: Partitioned Positive Force-Time Phase SIIMA One-Half and Full-Scale Tests

Figure 103 presents the peak force and standard deviation measured with SIIMA for shallow-buried near and intermediate-field half and full-scale test charges. Figure 104 presents the partitioned and phased load duration for half-scale and full-scale tests. The total positive phase duration had a standard deviation of less than 2% of the average. The phased durations all had a

standard deviation of 5% or less, with the exception of the full-scale second phase, which had a standard deviation of 25%. The overall duration of SIIMA is much longer than that of the one-seventh scale test rig, namely 17-19 ms compared to less than 1 ms. This is due to the stiffness differences between the test rigs, which results in dissimilar force-time responses. The similarity in durations between the one-half near-field and full-scale intermediate-field tests is due to target mass, which is larger than that used for the full-scale test. The system characteristics are also responsible for the relatively lower peak forces measured with SIIMA as compared to the one-seventh scale test rig, even though the charges were substantially larger.

Figure 105 presents the phased duration as a percentage of the total positive phase. These data show a different partitioned phase duration than observed with the one-seventh scale tests and most of the (McDonald 2013b) test results in that the shortest duration is Phase One and the longest Phase Three. The ratios were similar for the half and full-scale near and intermediate field, with Phase Two being twice as long as Phase One and Phase Three being two to three times as long as Phase Two. This was observed in both the SIIMA test series presented here and is ascribed to the structural differences between the two test rigs.

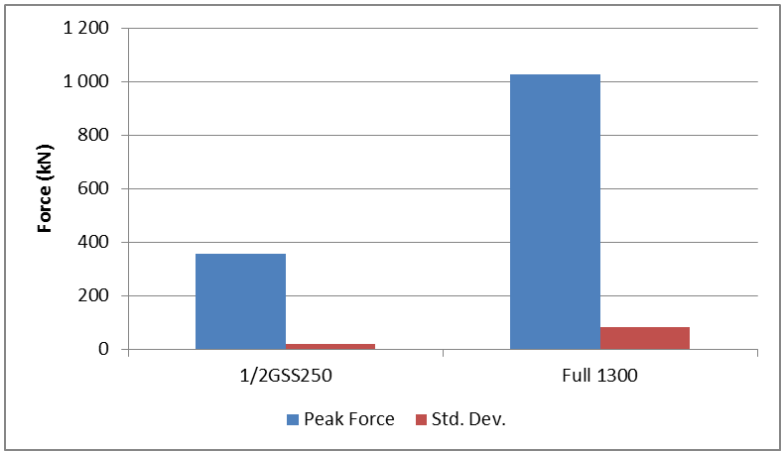

Figure 103: SIIMA Half and Full-Scale Peak Force

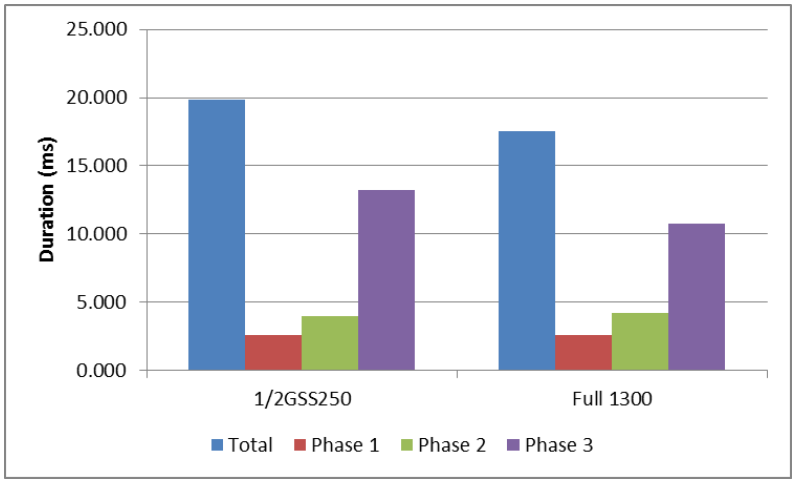

Figure 104: SIIMA Total and Partitioned Phased Response Force Duration

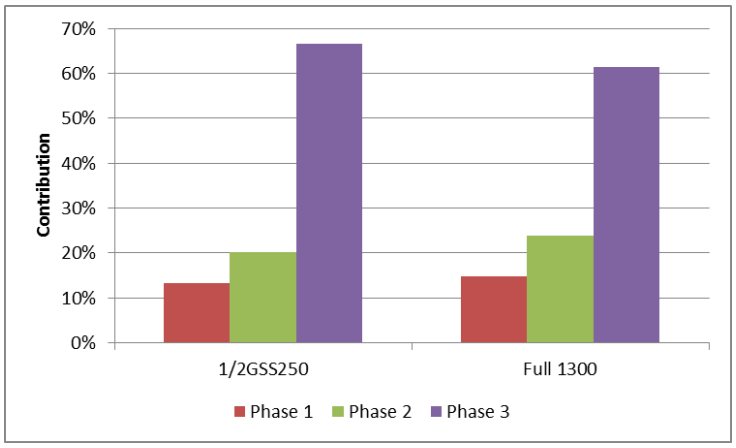

Figure 105: SIIMA Positive Load Phase Duration

4.8.2.2 Target Response Impulse

Figure 106 presents the total and the partitioned phased target response impulse to the half and full-scaled near and intermediate-field SIIMA test series. The total impulse standard deviation was less than 3% of average value, while the phase standard deviation was no more than 10% of average value. The partitioned phased impulse had the same trend as shown in the duration, with the lowest impulse being Phase One and the highest being Phase Three. The phase ratios were different from the ratios seen with duration, and there were slight differences between the half and full-scale test result phase ratios.

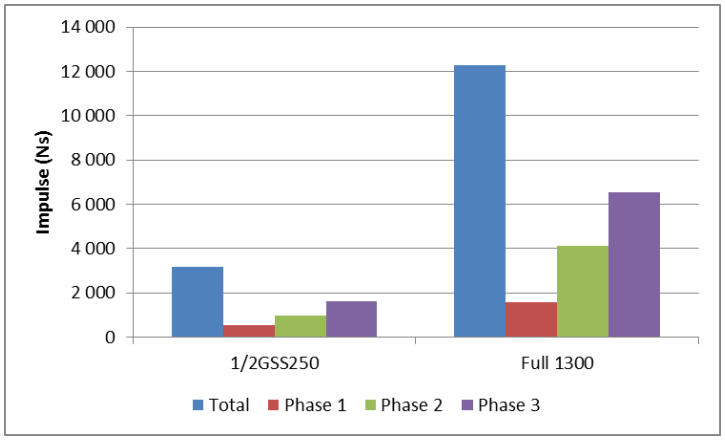

Figure 106: Partitioned SIIMA Total and Partitioned Phased Impulse

Figure 107 presents the SIIMA partitioned impulse phase contributions for both the half and full-scale near and intermediate-field test series. There is a slight decrease in the percentage contribution of Phase One and small increases in the impulse contribution of Phase Two. The Phase Three contribution remained similar.

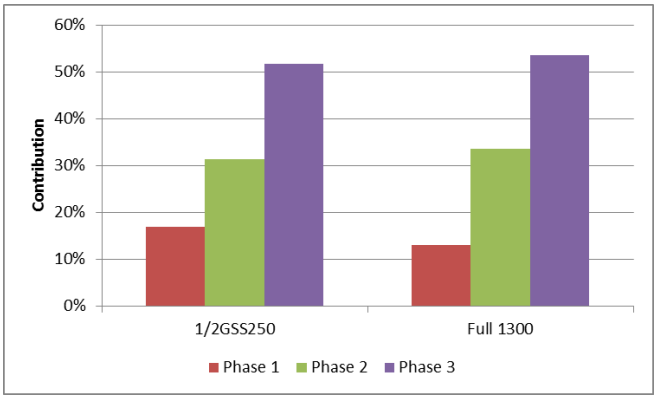

Figure 107: Partitioned SIIMA Phase Impulse Contribution

Figure 108 presents a summary of the partitioned phase impulse of all D:H 5:1 ratio test series for the one-seventh scale and SIIMA test rigs. This is the only ratio that was tested across all test conditions and on SIIMA. The differences in the phase contribution between each test condition and test rig are clearly indicated.

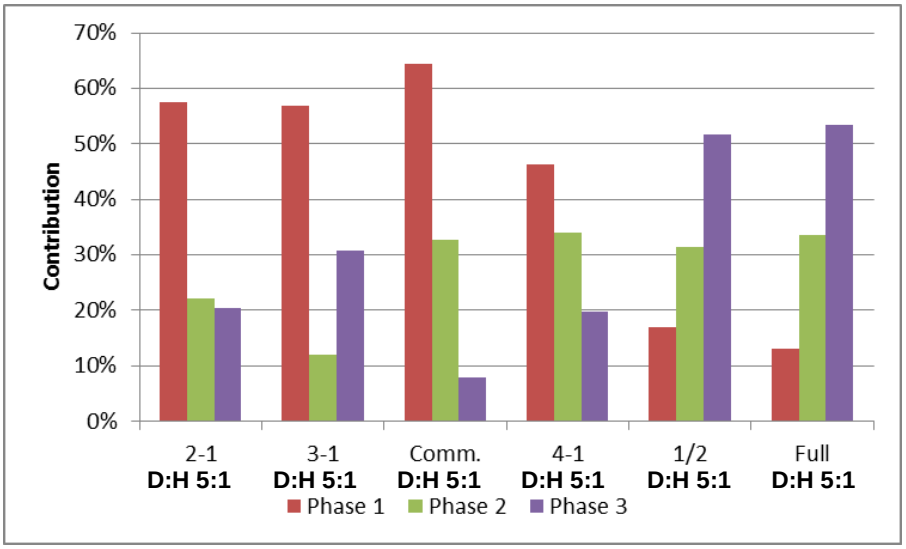

Figure 108: SIIMA and One-Seventh Scale Averaged Phase Impulse Percentage Contribution (D:H 5:1)

4.8.3 Scaling

Section 2.6 discuses blast scaling theory in terms of Hopkinson (Cube Root) and geometrically similar scaling. Using the test charge mass to the full-scale threat set for this work of 8 kg TNT and a PE4-to-TNT impulse equivalence of 1.2 (Weckert, Anderson September 2006), gives scaling factors (β) of $^{1}/_{7}$ and $^{2}/_{7}$ for the primary research charges used for this work and the McDonald's (McDonald 2013b) test data. By applying the one-seventh and one-half scaling factors, all the test data can be up-scaled and equated to the blast loading effects for a similar or full-scale (prototype charge). This enables the results from the primary research tests to be compared to the secondary data in terms of blast loading effects.

The primary value of the load secondary test data is to verify phasing of a buried blast load response of a target and has been presented in Section 4.8.1 and Section 4.8.2. Understanding how well the test data scale will provide additional confidence in applying these results to full sized threats. It assists with understanding how the secondary test rigs respond differently and assists in the analyses of the results presented in the next chapter. This section focuses on up scaling and comparing peak force and total impulse. Due to the importance of soil effects on buried blast loading the soil granulometry and

gravitational effects are presented as applicable for the primary research tests only.

4.8.3.1 Peak Force Scaling

Figure 109 presents the up-scaled (calculated prototype) peak net force for the initial one-seventh commissioning, final one-seventh scale, SIIMA half and full-scale and (McDonald 2013b) two-sevenths test results. Force scales according to scale factor to the power of two (β^2) and impulse according to scale factor to the power of three (β^3). The up-scaled data magnifies the trends previously identified and discussed.

The up-scaled and full-scale SIIMA data have much lower peak forces than either the one-seventh scale or (McDonald 2013b) test rigs. This is due to the much higher stiffness of the piezoelectric force washer rigs compared to SIIMA. Target mass also affects the force measurement and thus the up-scaled force calculated should be geometrically scaled to ensure the scale of all other parameters. The one-seventh scale target mass up-scales to 8,438 kg, which correlates well with SIIMA's target mass at 8,470 kg measured for the 1,300 mm SOD full-scale tests. However, the stiffness does vary between the two rigs. The force washer stiffness was calculated from the data sheets to be 17.24 kN/µm, and as there are four, the net stiffness is four times this value, which is much higher than that of steel. Thus force and time response will not scale.

The SIIMA one-half scale tests had a higher target mass of 10,760 kg, and thus do not scale geometrically with the full-scale tests, although done on the same test rig. McDonald's test rig target mass scales to 1,683 kg, which is the lowest and thus should have the highest full-scale force had it been shallow buried. As these tests were deep-buried, lower peak forces were recorded.

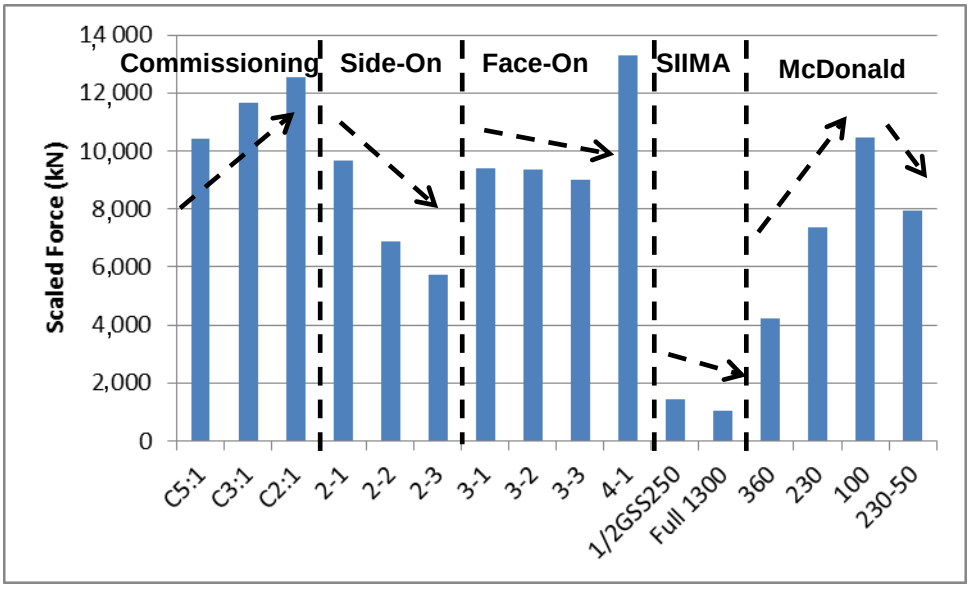

Figure 109: All Tests Peak Force Full-Scaled

4.8.3.2 Total Impulse Scaling

Figure 109 presents the Hopkinson up-scaled impulse for all tests. The trends seen and discussed in the unscaled data are visible. (McDonald 2013b) tests had up-scaled peak forces that were similar to the final one-seventh tests; however, they had higher up-scaled impulses in the deeper-buried test conditions which are now visible. The key results here are that the one-half scale and one-seventh scale near-field (Z=0.29 kg/m^3) up-scaled impulses correlate to within 4%. 25,281 Ns was obtained for the up-scaled one-seventh tests compared to 24,324 Ns for the up-scaled one-half scale tests. This occurred despite the target size differences, but as noted before, the one-half scale test target was attached to a larger target with a step. The near-field test conditions also ensured that the majority of the blast load is transferred to the geometrically smaller target.

The up-scaled impulse results of the intermediate one-seventh scale tests correlate well with the SIIMA intermediate tests considering the target size difference and higher SOD with the impulse of the side-on pressure configuration being 7% higher and the face-on pressure configuration being 23% higher. The up-scaled one-seventh impulses were 16,047 Ns and 13,220 Ns respectively, with the full-scale blast test giving 12,263 Ns. This result is still

useful as a higher one-seventh scale result is expected for the intermediate-field as the target is geometrically much smaller for the full-scale test and the larger SOD will now play a large role. The similarity of the total impulse results gives additional scaling verification of the data and serves to confirm the PE4 impulse equivalence used for TNT for the scaled tests.

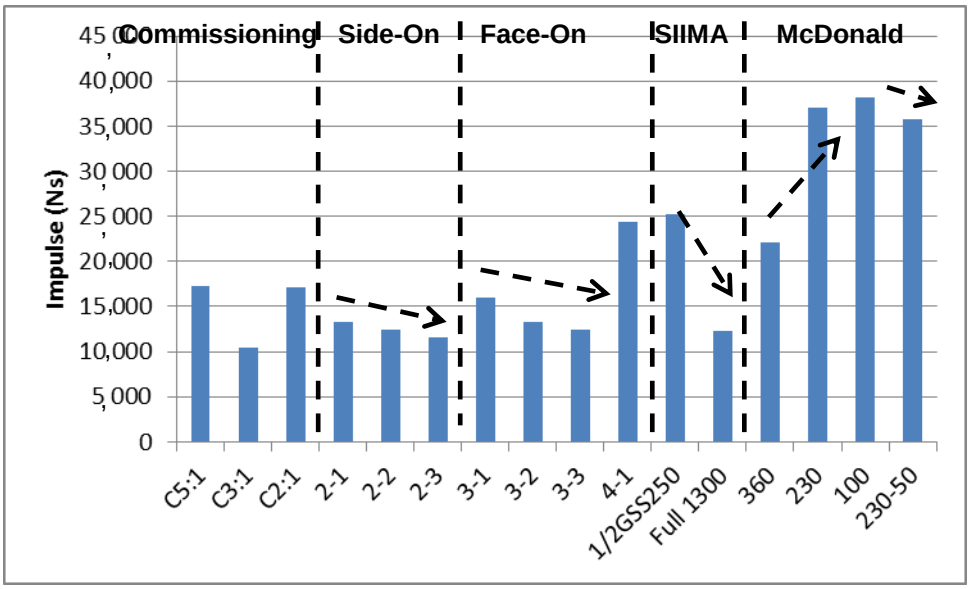

Figure 110: Total Impulse of All Tests Full Scaled

4.8.3.3 Soil

The primary research, SIIMA and McDonald tests all used different soil granulometry. The McDonald tests used dried soil while the SIIMA tests had approximately 2% moisture and the primary research tests moisture varied between 3-8% moisture. Although these differences will affect the total and phased blast loading these are deemed sufficiently small based on the total impulse scaled results comparisons.

The soil selected for the primary tests was not specifically mixed to ensure geometrically similar scaling, and commercially available river sand was used instead. The test soil granulometry was measured and the results were up-scaled from one-seventh scale to full scale.

Table 7 presents the scaled soil granulometry and the up-scaled granulometry, and for comparison purposes the current AEP55 Volume 2 Edition 2 soil

granulometry. As the scaled soil sieve sizes are in accordance with standard granulometry tests they do not up-scale to exactly the same sizes as required for full-scale soil. The data is presented in two columns with the first containing the require granulometry sieve size and the second columns the percentage of soil that passed. The first two columns present the actual primary soil results. The second two columns present the geometrically up-scaled test soil sieve size and granulometry. The last two columns present AEP-55 soil specified sieve size and granulometry. The results show acceptable scaling matching with the larger full-scale sizes being quite close and the smaller sizes less comparable. This is to be expected as the test soil is already very fine.

Table 7: Scaled Soil Granulometry and Up-Scaled Results

Test Soil Granulometry		**Geometrically Up-Scaled Test Soil**		**AEP Soil**	
Sieve Size (mm)	**% Passing**	**Sieve Size (mm)**	**% Passing**	**Sieve Size**	**% Passing**
9.5	100	-	**-**	**-**	-
6.7	99.16	**46.9**	99.16	**-**	-
4.75	98	**33.25**	98	**37.5**	100
-	**-**	**-**	-	**19**	75.99
2	76.69	**14**	76.69	**13.2**	62.37
0.85	48.13	**5.95**	48.13	**6.7**	47.18
0.425	24.37	**2.975**	24.37	**2.36**	-
0.25	14.57	**1.75**	14.57	**2**	27.9
0.15	8.94	**1.05**	8.94	**0.85**	-
0.075	5.82	**0.525**	5.82	**0.425**	18.9

4.8.3.4 Gravity Effects

Gravity was not scaled with any of the test data sets used for this work. For this research this was considered but deemed not important for blast loading events due to their extremely short in duration. Although true in terms of the pressure and force time responses that are over within 1.5 ms and the global displacement of the target assembly has completed within 10 ms. The slow speed ejecta phase that starts at about 4 ms after detonation only finishes at around 120 ms after detonation and is primarily driven by inertial loading (Eridon, James. Zelenik,Tom. Bogalev, Alex. 2014) and as such should be affected by gravitational effects and will not follow cube root scaling. This is supported by previous research that noted crater formation from blast does not scale according to Cube Root laws (Cooper 1996a). As determined from the high-speed video data in Section 4.2.1.1 the slow speed ejecta does not impact the test target thus are not important. The scaled craters however will not be directly scalable.

4.9 Chapter Summary

The modelling and test data captured as part of the research methodology have been presented and discussed. The data was presented first in terms of modelling followed by high-speed video, then side-on pressure and post-test crater and soil ejecta mass data captured without a near-field target. The primary research test data pertaining to the force-time response of a target subjected to a shallow-buried blast was then presented separately in terms of intermediate and near-field test results. Last to be presented was test data supporting the analysis of the target force-time phasing and phasing of the shallow-buried blast load covering side-on and face-on target pressure, measurement assembly displacement and NIR light emission.

The modelling data for near-field and intermediate-field ejecta results with no target over the blast were presented first, and although limited to one D:H ratio for free-field ejecta (no target) and near-field target configurations for all three D:H ratios, they confirmed the presence of at least three loading phases, as determined from side-on pressure traces.

The high-speed video analysis provided information on the physical properties of the blast front as well as confirming two ejecta phases, an initial high-speed vertical phase that ended at around 3.5 ms, followed by a low-speed primarily lateral motion ejecta phase. The two ejecta phase stem diameters corresponded to the primary (larger) and secondary (smaller) crater diameters. The high-speed analysis highlighted differences between shallow-buried and deep-buried blast in terms of blast front formation, in particular the complete overloading of the soil cap and subsequent almost instantaneous break-out effects. The data showed that the blast front was still accelerating in the near field while it was slowing down in the intermediate field SODs. It also confirmed that the low-speed ejecta diameters were larger than the target, and thus has a limited contribution to the loading. The ejecta mass results on their own could not be used to differentiate which mass was ejected in the high-speed phases and which mass was ejected in the slow-speed phases. Volume ratios of the primary and secondary craters were used to estimate the ejecta mass for the high-speed and low-speed phases. The data confirmed that the remaining soil was severely compacted and that crater dimensions are not a good indicator of ejecta mass as the mass was overestimated by 100%. The visual analyses also confirmed the hollow inverted cone ejecta reported by (Braid 2002).

The side-on free-field (no target) ejecta pressure analysis highlighted variability inherent in the test implementation, in particular tilted charges and/or off-perpendicular detonators, resulting in a reflected pressure being recorded on the pencil probe. This resulted in peak pressures and specific impulses with large standard deviations. Despite this limitation, the results confirmed that there are indeed at least three pressure phases in shallow-buried blast loads. The averaged pressure values were within the predicted ranges of the computational modelling. The test data did replicate some trends between D:H ratio charges visible in the modelling; however, due to the variability of the test results this is difficult to conclude decisively. The modelled ejecta results were also presented, which highlighted similarities and differences.

The intermediate target force-time response data provided a robust data set that confirmed the occurrence of at least three phases. Although not easily visible in the force-time plot, the phases were visually easily separated from the impulse-time plot. From the data one is able to clearly identify total and partitioned phase blast load differences due to the charge D:H ratio as well as the test configurations. Test variabilities were smoothed out with total averaged peak forces and total averaged impulse. Averaged phase parameters, however, were larger but nevertheless provided clear trends. The system measurement verification and verification results were also presented.

The time response data of the near-field target force also provided robust test data despite the limitation of only two tests of one D:H charge. The partitioned results were compared to the commissioning test data to verify the trends observed. From the data of the intermediate field results, it was possible to identify trends in both the total as well as the partitioned phase data for changes in SOD and in D:H ratios.

Target-face pressure, side-on for intermediate field and face-on for near field, were presented as sub-sections of the target force-time data. These results indicate variability in the test execution methodology as presented in the standard deviations of the average parameters; however, they still provide usable data and trends regarding phase duration of total blast load positive pressure, phasing of the blast load in terms of pressure total and specific impulse when averaged.

The NIR light emission data results were presented and support at least three load phases generated from a shallow-buried blast load in terms of light energy release. These data are compared to work previously published on free-in-air blast phasing (Gelfand, Silnikov 2004) in terms of light emission – the early onset and occurrence of afterburn is inferred.

The displacement-time results of the complete target assembly are presented and a three-phased response was verified. The data are presented in terms of peak displacement, total and phased displacement and durations and integration of displacement-time to estimate the total and phased work due to

shallow-buried blast loading as presented by the dynamic displacement of the assembly. Due to measurement limitations as the complete displacement-time signal was only captured in a few tests, the usefulness of the integrated displacement-time signal was limited. The data primarily confirm the phased blast loading from shallow-buried blast as well as how the cumulative stiffness of the target assembly affects the phased contribution to the measured target response.

The author presented and discussed processed secondary data from two other blast test rigs, providing target force-time response from larger and full-scaled shallow-buried blast (Snyman, Reinecke 2006) and from scaled deep-buried blast (McDonald 2013b). These data served to confirm blast load phasing in terms of target response force-time morphology for both shallow and deep-buried blast. The partitioned data also confirmed differences in the phasing and phase contributions between shallow and deep-buried blast. (McDonald 2013b) data further provides information on the effect of SOD on the phasing of the blast load as well as visual data on deep-buried blast morphology and how it differs from shallow-buried blast with weak reflected detonation air shocks preceding the smoothly bulging and slow soil cap blast front.

These data were up-scaled as appropriate and compared to similarly up-scaled research test data. Good correlation was achieved for shallow-buried half and full-scale data when compared to the research results. Force did not scale due to test rig differences that were not scaled, such as target assembly stiffness and mass. These differences also limited the direct scaling of phased responses with regard to time and contribution to the total load. However, they can be used for comparative analysis of threat types including shape, DOB and SOD.

The results presented will now be applied to analyse and discuss the phased force-time response of a target to shallow-buried blast as related to the primary three load phases generated by the shallow-buried threat and the target over the threat.

5 Analysis

The data presented in Section 4 is analysed and discussed to confirm, explore and describe the partitioned phasing of shallow-buried blast load in terms of the research questions posed for this work. The effects of the charge geometry in terms of D:H ratio are discussed to support and verify the phasing of shallow buried blast and subsequent target loading.

The analyses are presented in a specific sequence mimicking a typical buried blast event starting with the blast load that develops and then moving to the target response as the blast impacts and transfers loading.

Starting with the development of the blast-load from the free-field blast and ejecta results the analyses confirms and proposes three loading phases generated by a shallow-buried blast. Although the focus of this work is shallow buried blast, deep buried blast morphology analysed using secondary Cranfield (McDonald 2013b) data to quantify how these two types of buried blast differ.

The analysis then moves to the target force-time response data to explore and verify the proposed three blast-loading phases and how they manifest themselves in the target response results. To provide robustness to the phased blast-loading conclusions drawn thus far the NIR, face and side-on pressure data are each analysed and discussed separately in terms of the proposed blast-loading phases.

To address the research question of which phases contribute the most to the total blast load the specific impulse, target response impulse and target assembly displacement response are analysed and the differences discussed. The last analysis section explores and discusses the secondary data in terms of the confirmed three blast loading phases for both deep and shallow buried blast and provides robustness to the conclusions drawn in the preceding sections.

In many cases key quantified data is presented as a range of values, this is due to the inherent variability of shallow buried blast combined with test execution inconsistency noted in Section 4. Even though in some cases the variability is extremely large due to one or two test outliers the complete data set is

presented as key underlying trends are still visible within the results. Although this may appear to bring the data into question it is preferred to include the results based on all the data rather than removing these outliers. The analysis si presented in seven Sections as follows; (1) Free-Field Shallow Buried Blast, (2) Deep Buried Blast, (3) Shallow Buried Blast Near and Intermediate-Field Force-Time Blast Load Phasing, (4) Shallow Buried NIR Emission, (5) Shallow Buried Blast Load Side-On and Face-On Pressure, (6) Specific (Pressure) Impulse, Target Impulse and Displacement Response and (7) Secondary Data.

5.1 Free-Field Shallow-Buried Blast

Shallow-buried blast refers to the processes and loading mechanisms that develop when a charge is detonated in the ground with a small covering of soil. The presence of a target affects the blast load that develops, thus free-field (no target) blast load is analysed and discussed first.

For this work the DOB or overburden is considered shallow or deep-buried based on the work of Bangash (1993) and Drake and Little (1983) as reported by (Deshpande, McMeeking et al. 2009b). For shallow-buried charges this would typically be a thickness defined as Zone 1 where the soil covering is between two to three times the radius of the charge (R_c). As this work focuses on flat cylindrical (pancake) charges, R_c determined as half the thickness of the charge. For these tests R_c varied between 4.3 mm for the 5:1 and 7.4 mm for the 2:1 D:H ratio charge.

This section uses high speed video analyses, free-field side on pressure and computational modelling pressure results to confirm the presence of a three-phased loading generated by shallow buried blast.

5.1.1 Analysis

The analysis of free-field shallow buried blast is presented and discussed in three sections. These are; (1) ejecta morphology and general physical parameters as captured through high speed video, (2) free-field side-on test and computational modelling and (3) proposed three blast loading phases for shallow buried blast.

Key parameters contributing to generated blast-loads such as blast front velocity, blast stem diameter, blast cone angles and peak over pressure etc. are quantified from the test data. The analysis is concluded by proposing a three-phase shallow-buried blast loading sequence.

5.1.1.1 Shallow-Buried Blast Ejecta

High-speed imaging of the one-seventh scale shallow-buried blast developing did not reveal a leading shock wave precursor that reflected off the soil surface, but rather an almost instantaneous break-out of gases mixed with soil ejecta, see Figure 111. Figure 111 presents a sequence of four images starting at detonation initiation (0 µs) and one image every 25 µs until 75 µs after detonation initiation.

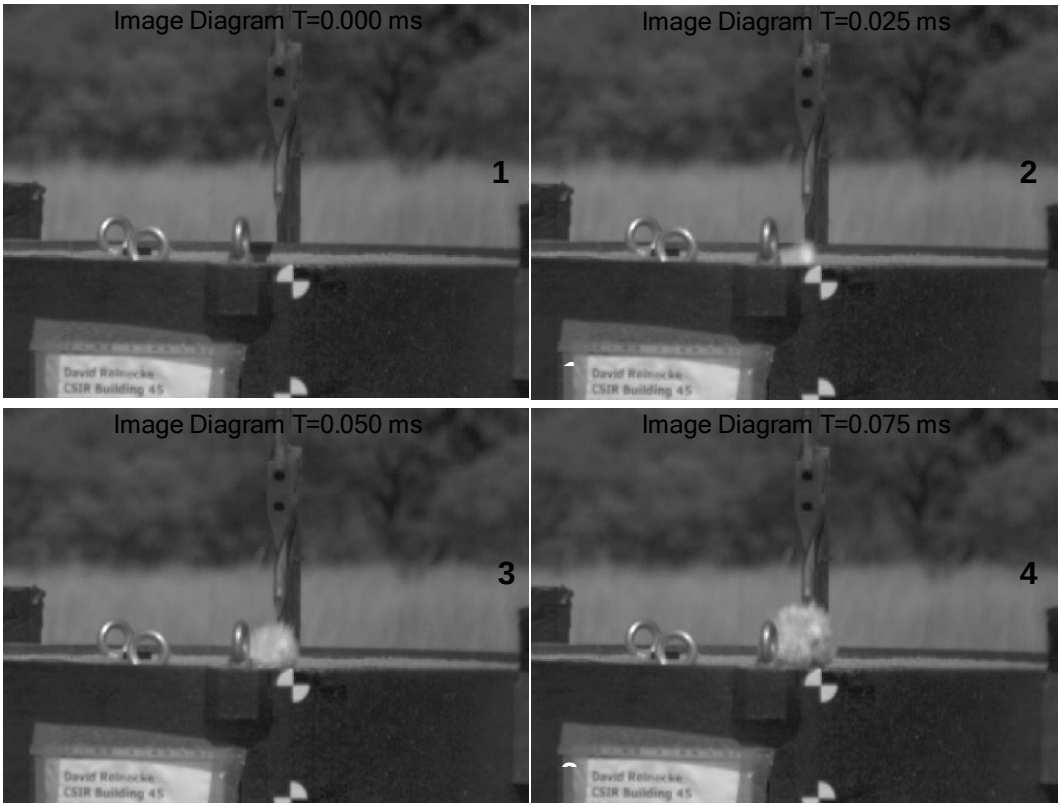

Figure 111: Initial Shallow Buried Blast Breakout Sequence (D:H 5:1)

No reflected shocks were captured by the high-speed imaging. If any surface shock reflection was generated from a buried blast it would be a weak shock as reported by (Bergeron, Coley et al. 2001). A weak shock is a compressive shock that moves at the speed of sound of the surrounding air. For these

research tests it would be in the region of 336 m/s in a standard US atmosphere (8.5 ^{o}C), and thus would be quickly consumed by the following shallow-buried blast front. Assuming a blast front moving at 1,000 or 2,000 m/s, the reflected shock would be overtaken between 11 to 26 µs or within no more than 21 to 27 mm above the soil. Thus soil-reflected shock pressure plays no role in shallow-buried blast loading. An air shock is observed detaching from the blast front at around 300 µs starting at the base and the gradually detaching upwards around the blast front. This is the bow wave expansion shock wave that detaches as the blast front velocity decreases thus it detaches at the base of the blast first where the lateral velocity is lowest and detaches last from the vertical blast front.

The blast front initially accelerates up to average peak velocities of over 2,000 m/s before gradually declining to velocities of 1,000 m/s at between 500 to 600 mm above the soil surface and 300 to 400 µs after detonation initiation. Peak velocity is achieved at a SOD of between 50 to 100 mm, see Figure 112. Figure 112 presents the averaged displacement and step-wise velocity-time multi-axis plot for a single D:H 5:1 blast front. All tests exhibited similar data trends irrespective of D:H ratio of the threat.

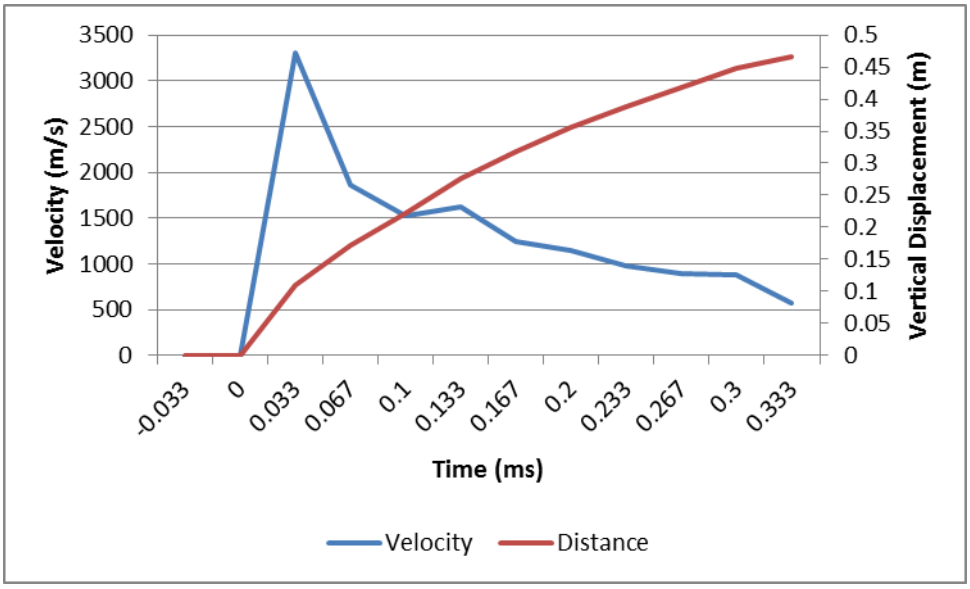

Figure 112: Average Blast Front Incremental Velocity-Time Plot (D:H 5:1 Test 1-1)

Table 8 presents the average of all interpolated and measured peak blast front velocities for each charge D:H ratio and the standard deviation. Due to the

relatively large time steps in the captured video the blast front velocity at 72 and 195 mm SOD's were calculated by interpolation. Both Table 8 and Figure 112 confirm that the blast front is still accelerating at 72 mm as it has not achieved its peak velocity by this time. The blast front is decelerating when it impacts a target placed at a SOD of 200 mm. The increasing velocity trends as the charge D:H decreases, are not clearly reflected in the D:H 2:1 averaged velocities for 195 mm SOD and maximum velocity presented in Table 8. This is due to the displacement and velocity data set being skewed by a single test.

Table 8: Averaged Blast Front Velocities

Threat D:H Ratio	Averaged Interpolated Velocity (m/s)		Averaged Maximum Velocity (m/s)
	@ 72 mm	@ 195 mm	
5:1	1,637 426	1,306 356	2,043 715
3:1	1,753 139	1,636 602	2,151 454
2:1	1,769 339	1,391 316	2,009 631

Figure 113 presents the average blast front velocities calculated from the start of the pressure sensor recording and the SOD to the probe for all free-field tests and thus are averages over a longer duration. The data starts with the final research tests for each D:H ratio in decreasing order (5:1, 3:1 and 2:1), then the commissioning tests for each D:H ratio (C5:1 and C2:1) and the single 5:1 D:H ratio free-field computational model at 195 mm and 60 mm SOD (M5:1, MM5:1 and MM5:1N). The MM5:1 refers to the modified computational model trace that removed the predicted large negative pulse or front separation between Phase One and Phase Two pressure loading thus differs slightly. The MM5:1N is the 60 mm SOD free-field position, which is based on the scaled distance (Z) of 0.28–0.29 kg/m$^{1/3}$ which this point presents. M and MM5:1 are at 195 mm. Where more than one data set per test point was available the data were

averaged and the standard deviation is presented next to the averaged peak value.

The average blast front velocities recorded during commissioning testing (1,727 m/s) were close to the predicted values (1,896 m/s). The final free-field ejecta tests showed a much lower average velocity (1,394 m/s). The side-on pressure results obtained were extremely variable and are ascribed to experimental set up variations and the tilting of the charges in particular. This result in the blast front impacting the probe at an angle and affects the blast front velocities calculated from the pressure response as well as the high speed cameras. Overall the data show a trend of increasing average blast front velocity as the D:H ratio of the charge decreases. The data also show that the model predicts that the blast front is still accelerating when it reaches the 60 mm or near-field position. This verifies what was experimentally determined.

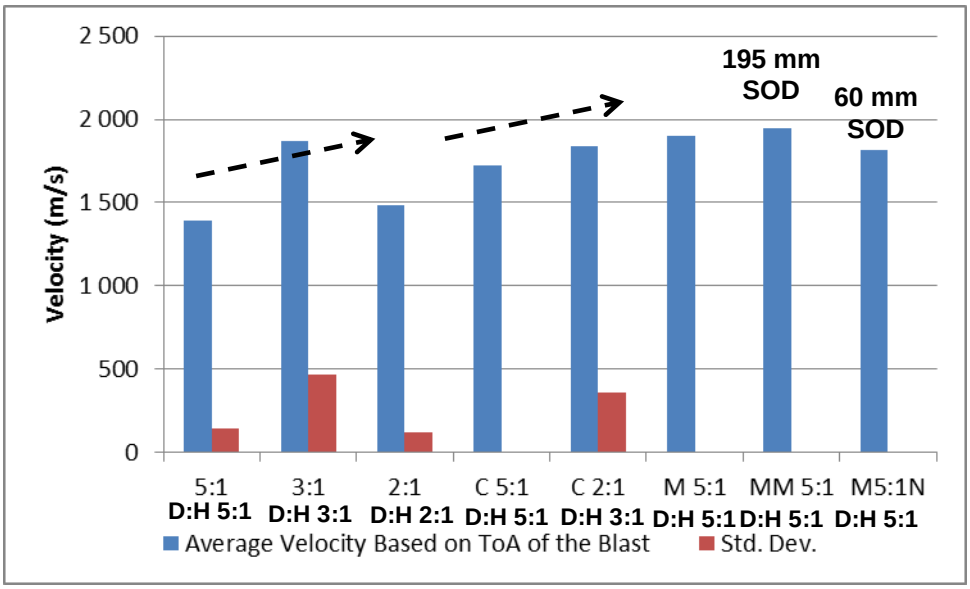

Figure 113: Average Shallow Buried Free-Field (No Target) Blast Front velocity

Figure 114 presents a sequence of six high speed images of a shallow buried blast front developing for a D:H 5:1 charge. Image 1 shows the blast front at peak velocity at a 123 mm SOD (33 µs after detonation initiation); image 2 shows the blast front at approximately 230 mm SOD with most of the visible blast front exhibiting high temperature detonation products (red arrow) and the front at 225 mm SOD (100 µs after detonation initiation).

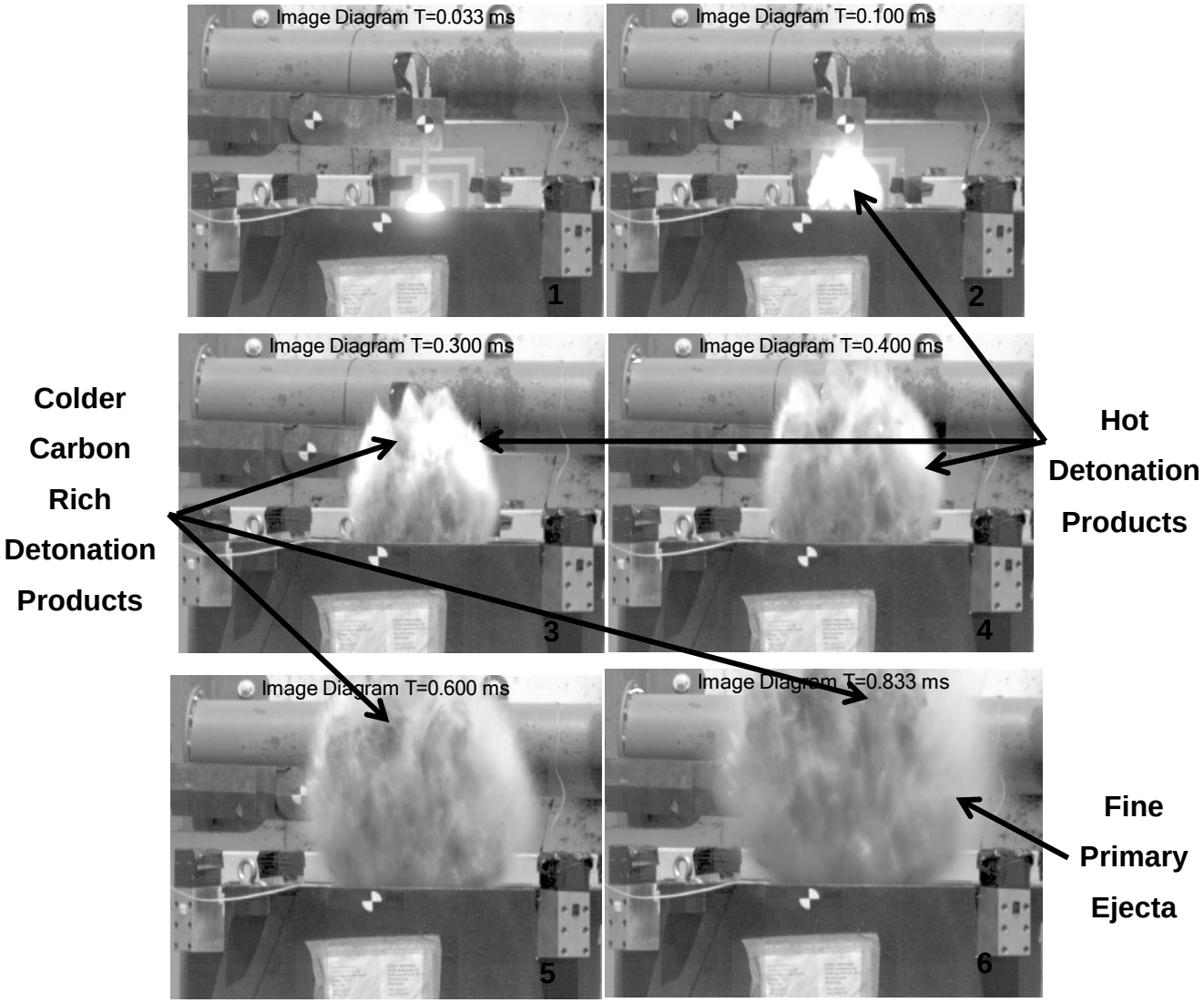

Figure 114: Blast Front Morphology Sequence (D:H5:1 Test 1-1)

Image 3 and 4 show the blast front starting to open up and the emergence of cooler black (carbon rich (Cooper 1996c)) detonation products shown by the arrows as well as the disappearance of high temperature blast gases indicated by the reduction in bright light over much of the blast front shell as shown by the red arrows (300 and 400 µs). Images 5 and 6 show no more sign of high temperature gasses and only the cooler black gases shown by the arrows (600 and 833 µs). Although discussed in Section 5.1.1.2 it is noted that on average the positive phase side-on pressure was over 427 µs after detonation initiation with a standard deviation of 160 µs.

As can be seen in Figure 114 the blast front shape was an elongated tulip, or spear, that continues to elongate and bulge outwards before the blast front

opens from 300-400 µs following detonation. When the blast front opens black detonation products start to emerge at the blast front. The sides of the initial blast front are clearly made up of a soil ejecta shell. The high-speed detonation gases are initially present over much of the blast front but reduce in temperature intensity until primarily at the top one-third of the developing blast completely disappearing at 600 µs. This is clearly seen in Figure 114 images 1 through 5.

Figure 115 presents a series of three high speed images of a shallow buried blast front morphology taken at 1.667, 2.5 and 3.3 ms after charge detonation initiation. Although the images look very similar they represent the transition from high-speed ejecta to slow-speed ejecta phases. The tulip shaped shallow buried blast front continues to expand until the inverted cone shape shown in Figure 115 image 1 is formed at around 1.67 ms after detonation initiation. The blast front maintains this blast shape with a shallow V angle of 40^{o} made up of fine dust and larger ejecta particles that are moving at velocities of 250 to 400 m/s, for the rest of the high-speed ejecta phase which ends at around 3.3 ms after detonation initiation. The centre of the inverted cone is occupied with the black detonation products that initially emerge at 300 to 400 µs after detonation initiation. The circle in all three images highlights what appears the contraction at the blast ejecta base as the blast expands using a lifting eye as reference and is seen as the precursor to the start of the slow-speed ejecta phase. This apparent contraction is simply the fine ejecta dust being lifted upwards as it is entrained by the vertically focused blast.

The larger soil particles and individual clumps of soil are being ejected at angles of between 40 and 72 degrees with the soil surface. The high-speed minimum ejecta angle reduces from an average of 42^{o} for a 5:1 to an average 41^{o} for 3:1 and an average of 34^{o} for 2:1 charge D:H ratios. There is some asymmetry prevalent in the angles due to test set up variation pertaining to the angle of the placed test charge making a definite conclusion as to the effect of D:H ratio on minimum ejecta angles as related to a single shallow DOB.

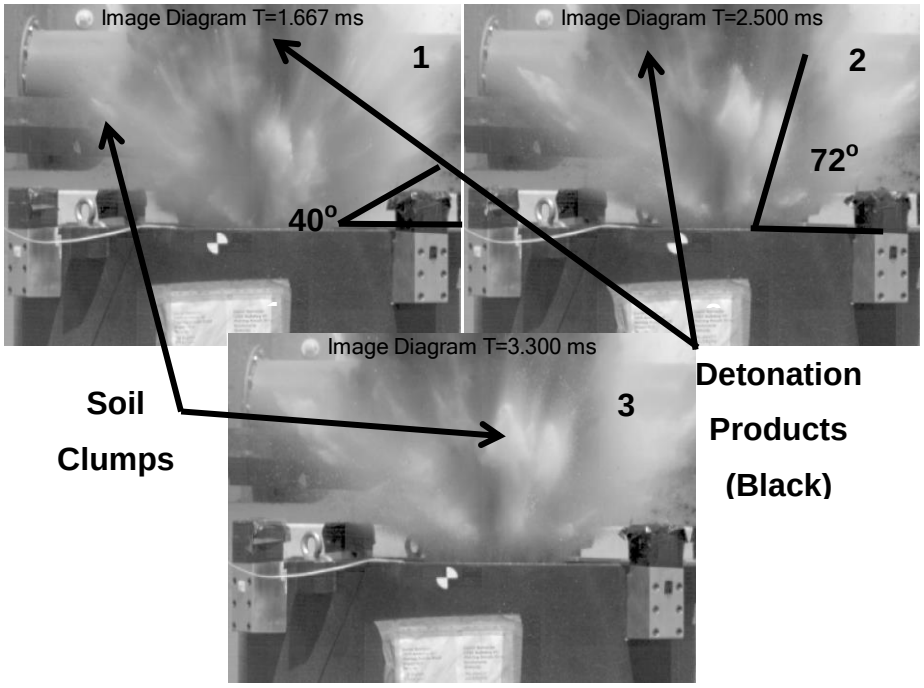

Figure 115: High-Speed Ejecta Phase End (D:H 5:1 Test 1-1)

At around 800 µs after detonation initiation (see Figure 114 image 6), the high-speed phase ejecta is characterised by large amounts of extremely fine particles and dust, this is seen as confirming the (Deshpande, McMeeking et al. 2009b) Zone 1 effects of blast pressure that completely overwhelm and crushes the soil within in $2R_c$ lengths thickness around the charge. The dust only appears later due to the opening up of the initial soil ejecta and hot detonation gases blast front as it elongates and expands.

At around 3.3 ms after detonation initiation, there is a noticeable pause in the growth at the base of the blast or the stem. This is the start of the slow-speed ejecta blast phase. The transition time is difficult to clearly determine from the high-speed images due to the initial low expansion velocity of the ejecta cone at 5 m/s as well as fine dust obscuring the base of the blast stem. The slow-speed ejecta phase ends at between 90 to 130 ms after detonation initiation.

Figure 116 presents a sequence of 6 high-speed images taken during the slow-speed ejecta phase at 4.6, 7.7, 15.1, 32.4, 107.8 and 181.1 ms after detonation initiation of a shallow buried blast with a D:H ratio of 5:1. These images were

chosen to highlight specific characteristics of the shallow buried blast slow-speed ejecta morphology.

Figure 116 frames 1 and 2 (6.6 and 7.7 ms after detonation initiation) show black detonation product gases, dust as well as larger clumps of soil being ejected. The slow lateral growth of the blast base or stem is visible using the lifting eye at the left hand side of the blast stem as reference. The stem has grown only 16 mm in 3.1 ms which is 5.1 m/s. At this time the larger soil ejecta has velocities around 40 m/s with vertical and horizontal velocity components similar at 30 m/s each.

Figure 116 frames 3 and 4 (15.7 and 32.7 ms after detonation initiation) show the ejecta stem diameter continues to grow with the literal velocity reducing to around 2.8 m/s (e.g. it moves 48 mm in 17.4 ms). The black detonation product gases have mostly disappeared and the fine ejecta dust is seen to be drifting upwards and a lot less is seen in the images. The blast ejecta is now primarily made up of larger sand particles and clumps. These are moving at a velocity of around 10 m/s with a vertical component of 9 m/s and a horizontal component of 5 m/s.

Figure 116 frames 5 and 6 (107.8 and 181.1 ms) show the end of the slow-speed ejecta phase. The ejecta cone wall starts breaking up and collapse outwards forming the raised lip on the outer edge of the large crater rim which characteristic of buried blast craters (Cooper 1996c). The ejecta cone stem lateral velocity has decreased further to around 1 m/s. The larger ejecta clumps have velocities in the order of 2.3 m/s with a horizontal component of 2 m/s and a vertical component of around 1.5 m/s.

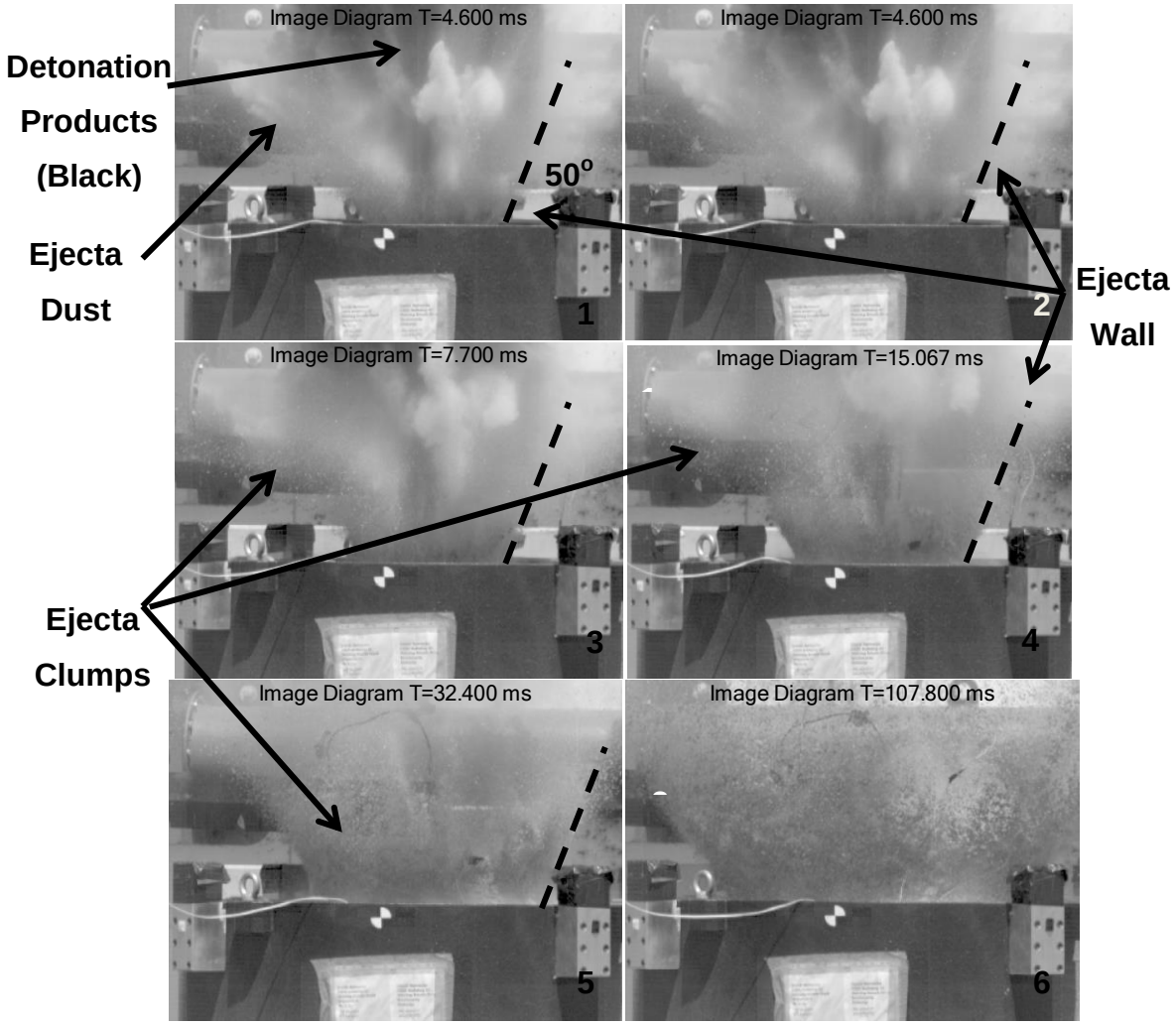

Figure 116: Shallow Buried Blast Slow-Speed Ejecta Morphology

The slow-speed phase is characterised primarily by a lateral expansion of the inverted ejecta cone base and the emergence of an ejecta wall with an angle of 50^o to the soil surface that is maintained until the soil ejecta wall breaks up and collapses to form the raised lip of the crater. The ejecta are now primarily made up of larger particles and clumps. The measured slow-speed ejecta wall angle appeared to be the same for all D:H ratios varying from a low of 49^o to a high of 57^o. It was expected that there would be some variation as the lateral charge thickness increases as the D:H ratio decreases exposing the soil to the side of the charge to a larger explosive area over which the detonation shock and the blast over-pressure work against. These effects are not clearly visible in the slow-speed ejecta data possibly due to response being inertial motion of the soil thus dominated by soil properties rather than the D:H ratio blast effects from the

detonation and subsequent blast pressure loading. It could also be a scaling limitation of the applied test method preventing sufficient resolution to measure differences as the D:H ratio changes. This is not considered important to the blast loading applied to a near-field target size as used for this work as discussed later in this section.

There is no confirmation in the high-speed images if the slow-phase ejecta are (Deshpande, McMeeking et al. 2009b) Zone 2 soil (plastically deformed or partially crushed) combined with undamaged Zone 3 soil or only Zone 3 soil. It is assumed that the initial ejecta is a combination of soil types moving from predominately Zone 1 (crushed) and Zone 2 (plastically deformed) soils through to Zone 2 and Zone 3 (elastically loaded) soils. At the end of the slow-speed ejecta phase the ejected soil will be primarily undamaged Zone 3 soil.

This two-phase shallow buried blast morphology has been observed in full-scale blasts and reported in the literature (Freitas, Bigger et al. 2014). The phase names refer to the speed of the ejecta observed during each phase. The high-speed phase has velocities peaking at over 2,000 m/s, while the slow-speed phase peaks at 250 m/s vertical velocity but are generally much slower. The initial blast shape shows that the blast is highly directional with almost no lateral blast occurring before 400 µs after detonation initiation. Angled ejecta only really manifests itself later (> 1 ms) in the form of high-speed (>250 m/s) ejecta clumps and larger particles.

This ejecta morphology corresponds to (Eridon, James. Zelenik,Tom. Bogalev, Alex. 2014) work where it is stated that explosive pressure work (pdV) is executed over a short distance. The majority of the soil ejected is due to inertial loading of the soil derived from the initial detonation and blast pressure expansion. Figure 117 and Figure 118 show a 360 mm target superimposed over a series of high-speed images from a shallow buried free-field blast with a threat D:H ratio of 5:1. The target is scaled correctly and placed at a intermediate-field SOD of 200 mm in Figure 117 and at a near-field SOD of 72 mm in Figure 118. The time steps highlight the morphology of the blast front

and a target placed above prior to detonation, at first impact with the target, the end of the high speed ejecta phase and during the slow speed ejecta phase.

Table 9 presents a summary of the average secondary (smaller) crater diameter and standard deviation as measured after each D:H charge ratio free-field ejecta test. The standard deviation is noted below the average diameter value. For most ejecta tests the soil surface was below the soil bin lip (shown as the dotted line in Figure 117 and Figure 118image 1). Thus the acute blast angle was used to estimate the blast stem diameter at the soil surface based on the soil level below the lip and the blast stem diameter measured at the lip of the soil bin. Similarly the blast diameters at the intermediate and near-field SOD of 72 and 200 mm were calculated for each test using the smallest blast angle and the calculated blast stem diameter at the soil surface. The results for each test are then averaged.

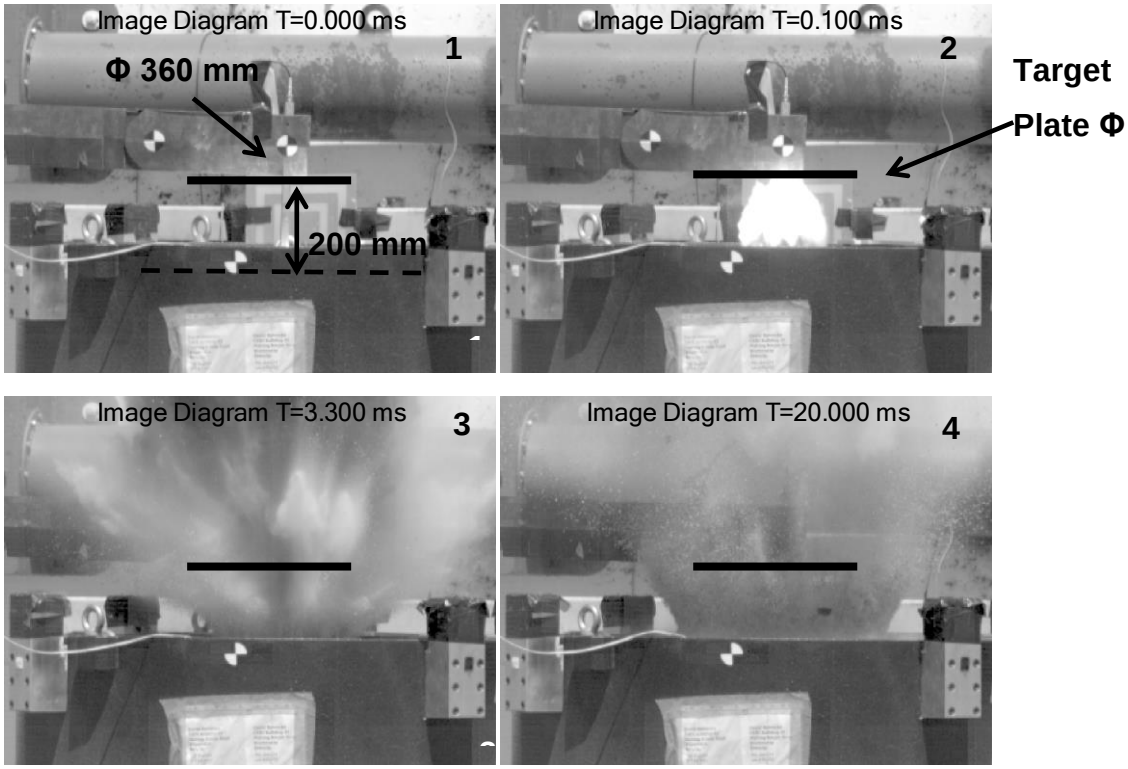

Figure 117: Soil Ejecta and Intermediate-Field Target (D:H 5:1 Test 1-1)

Figure 117 shows that for the intermediate SOD the initial blast front is fully captured by the 360 mm target plate (image 1). At the end of the high speed

ejecta phase some of the blast ejecta would miss the target. From Table 9 around 70% of the low angled blast cone at 200 mm SOD is missing the target.

Although this appears substantial load loss, as reported by (Tremblay 1998) the load contribution decreases exponentially across a target therefore this loss is not as large as the percentage area suggests. Figure 117 Image 4 shows that the slow-phase ejecta is missing the target completely thus not contributing to the blast load at all. The estimated 40^{o} blast cone diameter at the end of the high speed phase at 72 mm and 200 mm SOD's are 684 and 389 mm respectively. This indicates that on average, at both the near and intermediate-field SOD's, all the slow-speed ejecta will miss the target and not contribute to the measured blast load impulse. These data are based on free-in-air blast morphology which exclude the lateral pressure expansion loading on the sides of the blast front and ejecta caused by the target interaction which, when present, will force the soil ejecta outwards away from the target before it can impact.

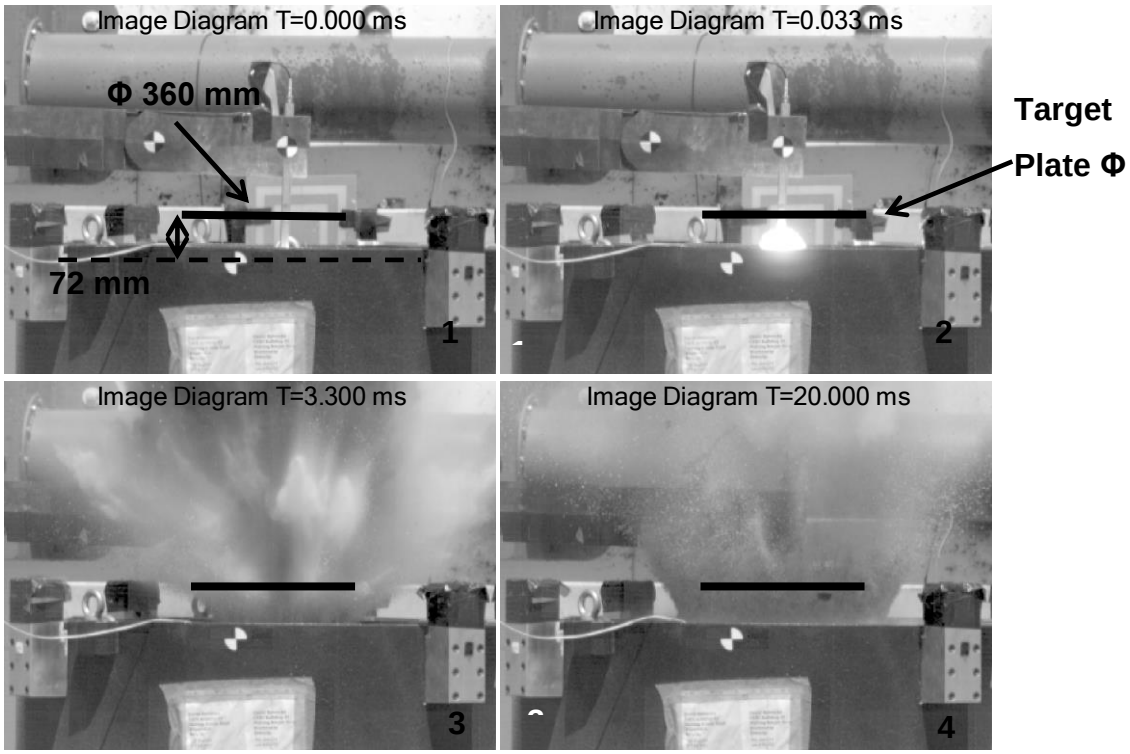

Figure 118: Soil Ejecta and Near-Field Target (D:H 5:1 Test 1-1)

The 72^{o} high-speed ejecta blast cone angle data show that after the initial soil cap ejecta being captured fully by both the intermediate and the near-field targets, only the near-field target could reasonably be impacted by later high speed ejecta whereas the intermediate-field target might only be impacted on the edge of the target. Due to the effect of the target interaction not being present no conclusion can be drawn other than to confirm that the contribution to the blast load of these later (>800-1,000 μs) soil ejecta is minimal.

Table 9: Secondary Crater vs. High-Speed Ejecta Blast Stem Diameter

Secondary Crater						
D:H	**Measured Crater**	**High-Speed Imaging Projected Blast Cone Diameter**				
	Φ (mm)	**Blast Stem Φ (mm)**	**72 mm @ 40^{o} Φ (mm)**	**200 mm @40^{o} Φ (mm)**	**72 mm @ 72^{o} Φ (mm)**	**200 mm @72^{o} Φ (mm)**
5:1	346 18	224 46	379 46	684 46	254 46	337 46
3:1	327 37	189 11	391 11	696 11	266 11	350 11
2:1	331 32	214 7	386 7	691 7	261 7	344 7

At an average of 336 mm with a standard deviation of only 30 mm across all D:H ratio charges, the measured average secondary crater diameter is larger than the high-speed ejecta phase blast stem diameter on the soil surface which, from high-speed measurements, has an overall average diameter of 205 mm with a standard deviation of 34 mm. This implies that the secondary crater also continues to grow due to inertial loading of the soil at a deeper level. This tapers off in accordance with the load profile generated by the buried blast in the surrounding soil. Thus more lateral loading is imparted in the upper soil layer which continues to grow to almost double the size of the secondary crater at an average diameter of 617 mm with a standard deviation of 28 mm as measured using high-speed imaging. The actual measured primary diameter average was 656 mm with a standard deviation of 47 mm for all D:H ratio threats. The larger

measurements will be due to how the measurements are taken bearing in mind that there is a large lip of loose ejected sand on the rim and are considered equivalent for practical purposes. These results are applicable to the soil and soil conditions used for the research tests.

Using the primary and secondary crater volume ratios and the total measured ejected soil mass of the measured free-field (no target present) shallow buried blasts to estimate the mass of soil ejected during each phase gives 4.0–5.4 kg of soil was ejected during the high-speed phase and 7.6–9.5 kg of soil was ejected on average during the slow-speed phase. If one uses the high-speed imaging high-speed blast phase blast stem diameter in lieu of the secondary crater the high-speed phase soil ejecta mass decreases between 1.3 to 1.6 kg and the slow-speed phase ejecta mass increased between 10.9 to 12.3 kg across all D:H ratios.

The estimation is based on assuming a cylinder shape of the crater, which is not the case and thus means these values are slightly overestimated. Using an average high-speed phase ejecta velocity of 250 m/s, these masses would generate an impulse of 250 Ns against a stationary target for the high-speed ejecta phase. Comparing this to the total shallow-buried blast impulse of 70 Ns recorded in the near-field test, the primary blast loading mechanism is not transferred by the soil ejecta for shallow buried blast.

5.1.1.2 Shallow-buried Blast Side-On Pressure

Figure 119 presents a single intermediate free-field (no target) side-on pressure-time plot of one of a D:H 5:1 ejecta test (blue) for a SOD of 195 mm and the plot of the unmodified computational model pressure-tome (red) for a SOD of 195 mm.

The averaged D:H 5:1 test free-field measured side-on peak pressures were 1.612 MPa and were reasonably close to the predicted side-on pressure of 1.240 MPa. The recorded average commissioning test pressures were lower at 1.004 MPa. The commissioning test side-on pressure results are lower due to the slightly higher sensor SOD (between 205 to 221 mm) that was achieved with these tests thus giving the lower test pressure values.

The start of the pressure trace, the timing of the peak pressures, the pressure decay and the timing of the end of the negative phases correlate well with the model. Although this gives confidence in the averaged results obtained, the test results consistently show a third reflected pressure (see Figure 119 arrow) that is much higher than that predicted in the model and occurs later than the predicted pressure trace. The computational model third phase pressure prediction is manifested simply as a small increase and reduction in the following rate of pressure decay, see Figure 120. This clear third phase pressure increase was seen in all, bar one, free-field ejecta tests.

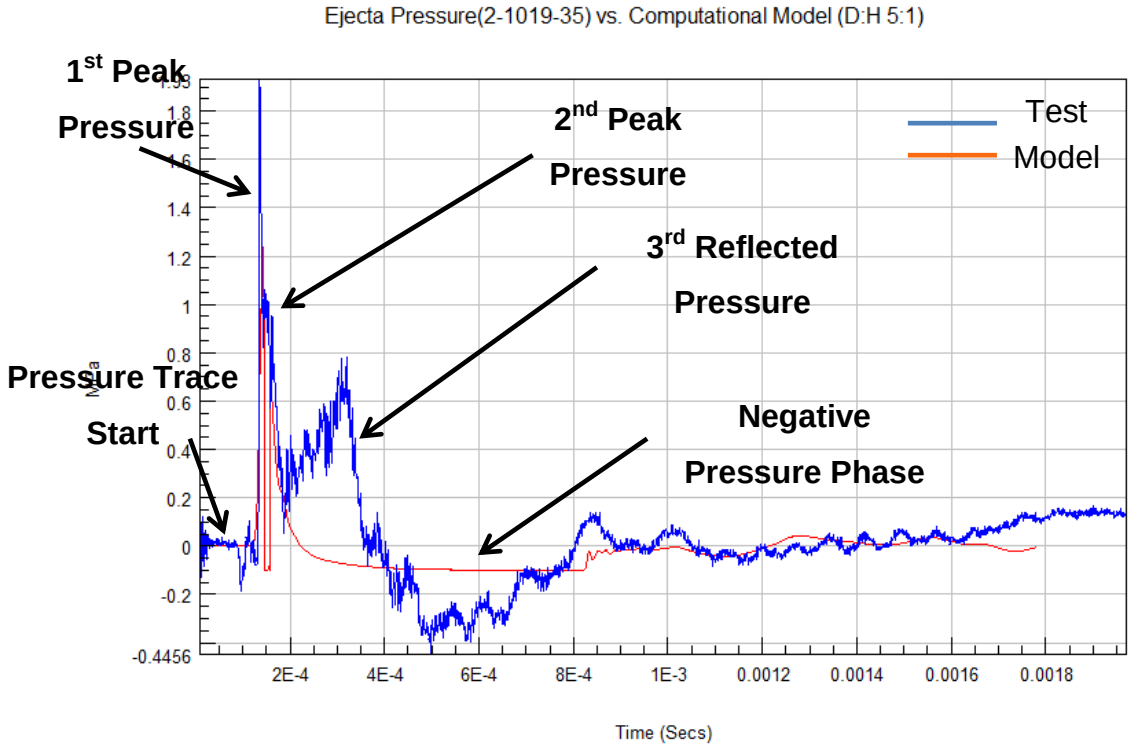

Figure 119: Intermediate-Field Computational Model and Test Pressure

In reviewing the Autodyn model pressure-time results (see Figure 120) there is a definite third pressure reflection but it is much smaller than the test results. The source of this reflection can be the soil's containment of the detonation gases and products and / or possibly from afterburn of the detonation products. The standard Autodyn JWL explosive model used for this work did not include the afterburn model. This implies that the third phase is due to reflected pressures from the soil cavity. Based on (Gelfand, Silnikov 2004) afterburn

effects were seen with 100 g cylindrical (D:H 1:2) RDX charges detonated in free-in-air conditions. Thus it can be concluded that for a quasi-constrained environment where the detonation products are confined within the soil crater afterburn will occur much more readily. This afterburn enhances the reflected pressure generated from crater constrained gases and results in the higher third phase pressure recorded in the free-field ejecta tests.

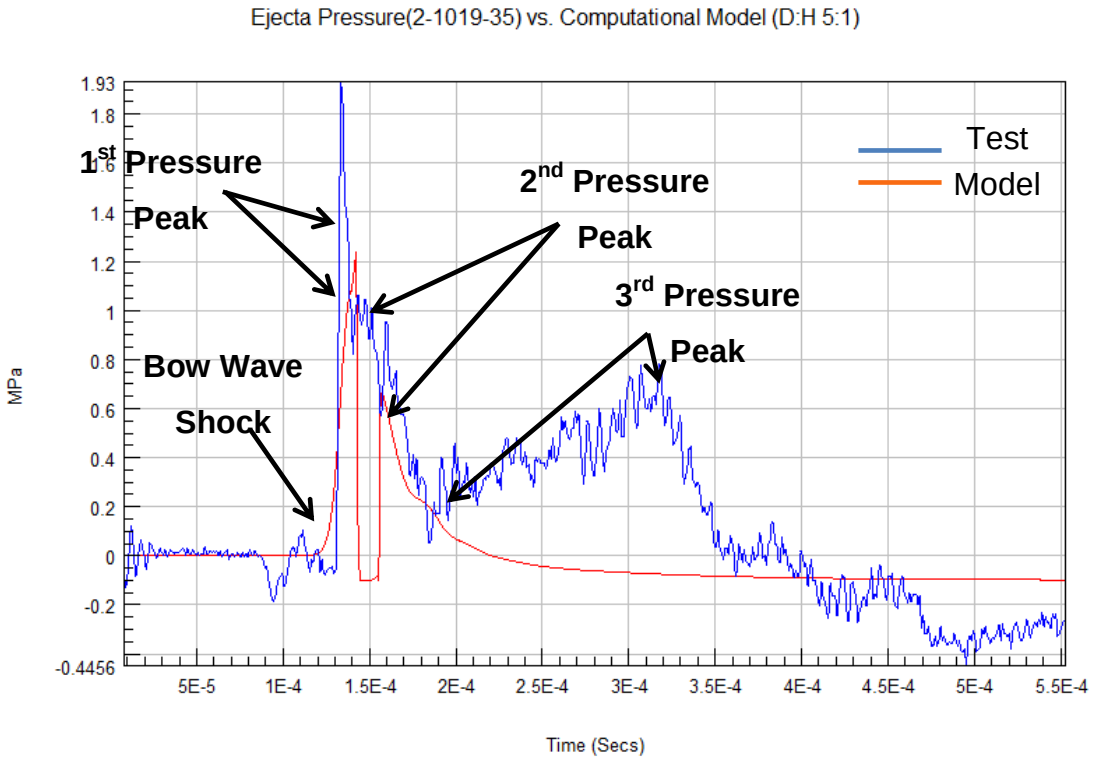

Figure 120: Phased Intermediate-Field Computational Model and Test Pressure-Time Plot (D:H 5:1) Magnified

In reviewing the modelling side-on pressure prediction of the second pressure loading phase the computational model pressures are similar or lower than the average final free-field ejecta tests.

The bow wave shock predicted was not recorded during every test due in part to EM interference from the detonation and partly due to ejecta impact causing ringing and small precursor signals. Based on modelling the precursor shock wave would only contribute around 1% of the specific pressure impulse. Thus its inclusion into the Phase One loading is deemed acceptable. In Figure 120

the model bow wave shock has been absorbed into the blast front over-pressure thus is not visible as a separate event but it is present in the test plot.

Having determined there are three primary blast load phases from the test and computational modelling side-on pressure-time traces the test data was processed by partitioning into the three phases determining the duration and load contribution in terms of specific impulse for each test.

Figure 121 summarises the total positive and partitioned phased side-on pressure durations for tests and the single computational model. The final research tests are presented first for each D:H ratio, then the commissioning tests, again for each D:H ratio and the modified computational model D:H 5:1 ratio is presented last.

The large variability in the test execution set up is directly reflected in the variability of the processed test results. The 3:1 final test average duration had a standard deviation of more than 60% of the average value due to an angled impact on the sensor This combined with a small test data pool of two tests skews the averaged results. The other D:H ratios had standard deviations that varied from 30% to a low 10% of average. The data are still useful as it indicates that on average the positive pressure phase for intermediate free-field shallow-buried blast lasts less than 380 μs and is over in less than 550 μs after detonation initiation. The end of the negative phase occurs at 850 μs after detonation initiation. The positive blast pressure is over within less than 25% of the high-speed ejecta phase duration, before the blast front has spread and is still maintaining a closed tulip shape. The computational model predicted the positive side-on pressure duration of 107 μs. The commissioning tests gave positive durations of between 121 and 125 μs, which are close to the model results. However the test set-up was different with a V shaped deflector being used rather than an aerodynamically shaped wedge. Overall this variation from the modelling results is due to misalignment in the positioning of the charge during testing with the probable occurrence of afterburn giving rise to the longer test positive pressure duration.

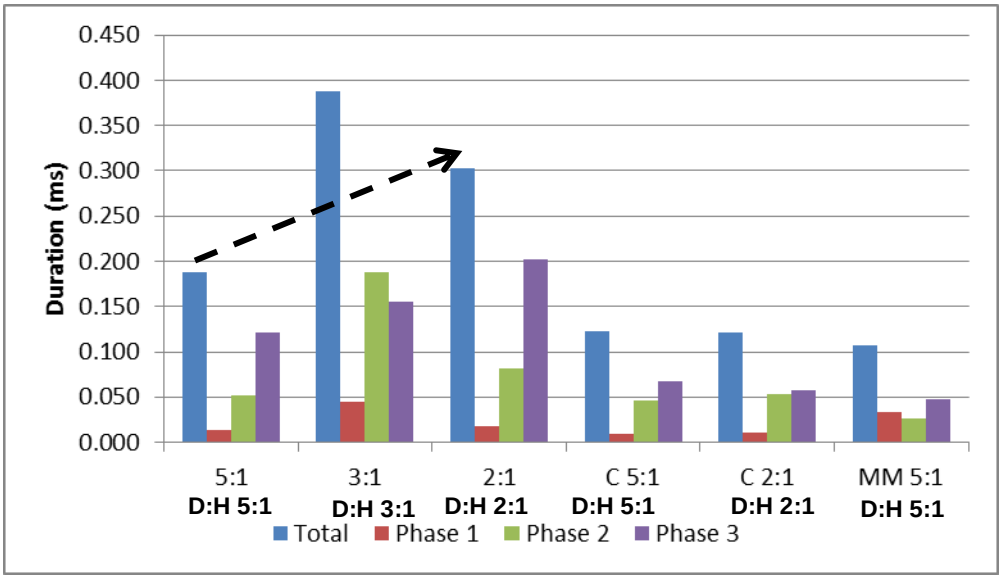

Figure 121: Average Free-Field Ejecta Test and Model Positive Pressure Duration

The variability inherent in the measured results makes it difficult to draw any clear D:H ratio duration trends. However, if one excludes the D:H 3:1 final test results and the commissioning tests as these have a different test set-up, an increasing positive pressure duration trend is clear. This would be caused by larger charge thickness as the D:H ratio decreases resulting in more gases being released laterally to be constrained and released from the crater later in the process giving rise to longer durations. Following this the partitioned phases also show increasing durations that increase from Phase One up to Phase Three. This corresponds to the morphology of the a shallow-buried blast with a front which is a short duration over-pressure event. This is followed by the detonation gas expansion which is a slower physical event and then lastly pressure reflections and afterburn, if occurring, which are slower events. The computational model does not follow this trend with the second phase being longer than the third phase. This is occurs part because the model does not accommodate afterburn effects thus does not predict the larger Phase Three pressure pulse.

Figure 122 summarises the intermediate free-field (no target) total and partitioned side-on pressure specific impulse for all tests and the single D:H 5:1 computational model. The 3:1 D:H ratio tests dominate the results. These test's

results varied enormously with standard deviations of over 80% of average. This is due to there being only two test points and one of the tests had large anomalous pressure duration generated by an angled impact on the probe sensor.

Figure 123 presents the partitioned intermediate free-field side-on pressure specific impulse contribution as a percentage of the total specific impulse. In comparing total specific impulse of the D:H 5:1 test charges the modified computational model predicted 16% more impulse than was recorded during the commissioning tests but only 50% of what was recorded during the final ejecta free-field tests. The commissioning tests SOD was at a slightly larger SOD than the predicted or the final test configuration resulting in a lower specific impulse. The final ejecta tests also had a number of reflected pressure peaks and generally recorded slightly higher side-on pressures over the positive phase. Lastly the model did not have an afterburn extension to the JWL equations and thus under predicted the Third Phase pressures.

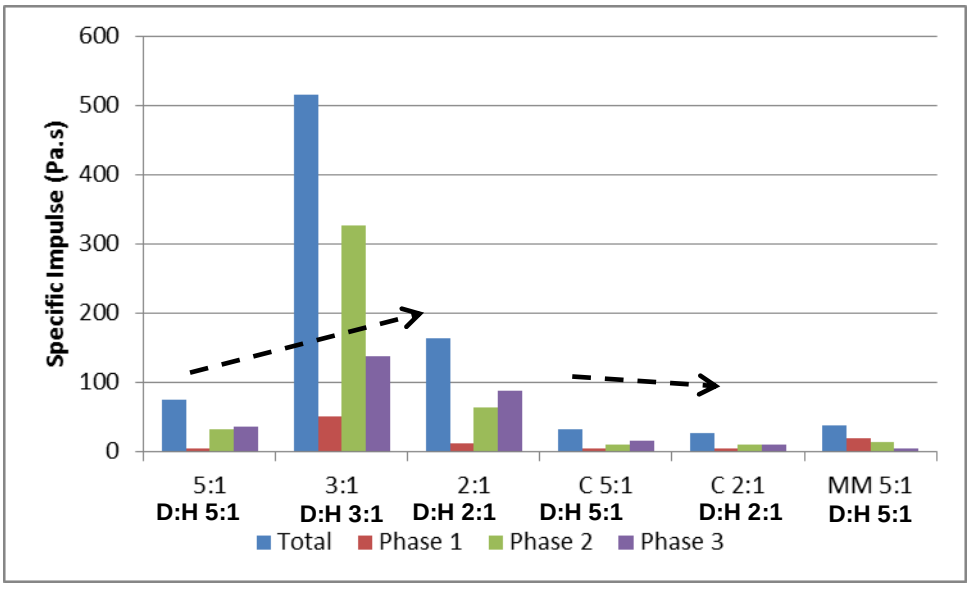

Figure 122: Free-field (No Target) Total and Partitioned Phase Side-On Pressure Specific Impulse

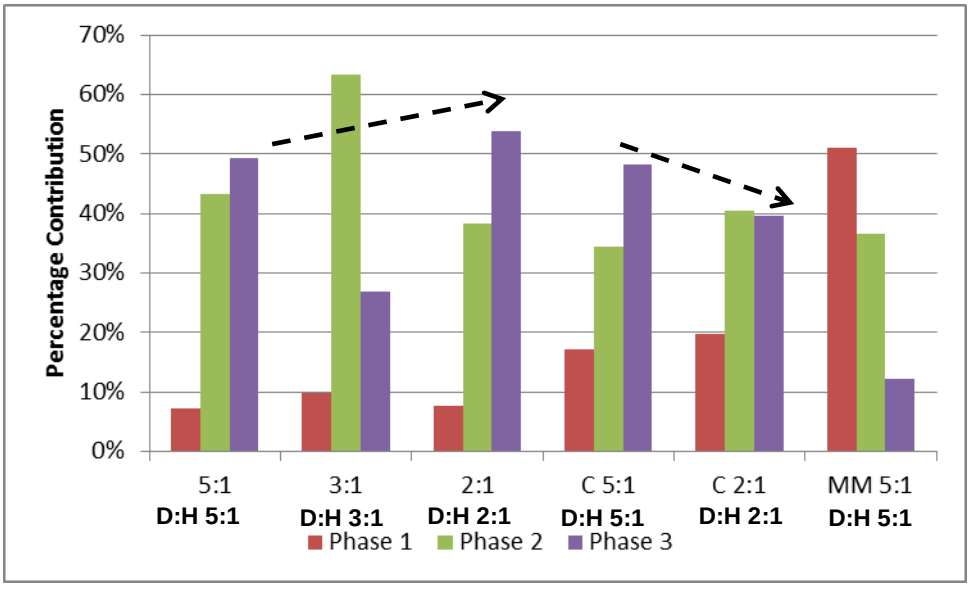

Figure 123: Partitioned Intermediate Free-Field (No Target) Specific Phase Impulse Contribution

Using the specific impulse as an indication of blast pressure loading and by excluding the averaged final ejecta 3:1 tests from the analysis, it can be stated the Third phase contributes the most to the blast pressure load whilst the first phase the least, for intermediate-field SOD's. Taking the average partitioned phase contribution across all tests, thus including all the different charge D:H ratios and test set-ups, gives the following blast load percentage contribution for each partitioned phase: Phase One: 13%, Phase Two: 39% and Phase Three 48%. Although a crude approach due to the large variations recorded with the side on pressure test, it is deemed acceptable as the large pool smooths out anomalous test results.

The modified computational model pressure-time trace predicts the opposite trend with Phase One providing 51% of the total specific-impulse and Phase Three only 12% of the blast load. This anomalous result is partly due to the computational model methodology that uses added viscous terms to balance the equations of state in the blast model (Carreira 2017, Snyman 2015) resulting in a predicted blast front that is smeared and thicker than achieved with testing. The model also predicted shock front separation at the intermediate SOD of interest (195 mm) creating a negative pressure pulse. This

was manually removed from the model by using a half-sine geometric trace to close the gap (Modified Model) to enable more representative specific impulse calculations. The partitioned Phase One end point was selected as the middle of the separation gap. It would have been better to have selected the Phase One to end when the negative pulse starts. Had this been done this would have given model predictions for total specific-impulse of 37 Pa.s and partitioned specific impulse as follows Phase One 12 Pa.s and 31% of total, Phase Two 21 Pa.s and 57% of total and Phase Three with 4 Pa.s and 11% of the total specific impulse. The difference in total model impulse in these calculations is due to small variances in the manual extraction methods and rounding off calculated values. This implies the model predicts that the Phase Two is the largest contributor to the specific impulse blast pressure loading for the intermediate field and is closer to the captured test values. Had the afterburn module been used then Phase Three would have predicted a larger phased specific impulse thus reducing Phase Two percentage contribution further and giving a result that is more comparable to the test data.

5.1.1.3 Proposed Shallow-buried Blast Load Phases

Using the presented high-speed imagery and side-on pressure trace analyses the following three sources of the pressure load phases from a shallow-buried blast load are proposed:

Phase One is the high speed blast front including the bow-wave shock created by the high speed blast front (Braid 2002). This front includes the soil cap soil and possibly a small amount soil surrounding the charge that ejected laterally and upwards with the initial blast break out following other authors models (Braid 2002, Freitas, Bigger et al. 2014, Ramasamy, AM Hill et al. 2009). This mixture forms the boundary of the expanding blast front. The overpressure front is not as strong as with a free-in-air blast as the soil cap attenuates the shock overpressure coupling (Swisdak 1975, Braid 2002). This attenuation effect is enhanced as the soil is a porous medium (Gelfand, Silnikov 2004).This phase loading is characterised by a very short load duration as the blast front thickness thins as the ejecta front expands and moves upwards.

Phase Two is the pressure loading due to the expansion of the detonation products as focused by the soil and constrained by blast front boundaries. Although there could be detonic shocks within this cloud they are not disenable in the pressure traces thus their contribution, if present, is limited to energising the detonation product cloud (Braid 2002). The pressure generated is enhanced by the soil containment of the products (Braid 2002).

Phase Three is a combination of additional pressure reflections due to the crater containment combined with after-burn. The afterburn is enhanced by the containment effects of the crater.

Phase One loading will be a typical shock or impact loading characterised by an initial almost instantaneous pressure rise followed the pressure from the expanding detonic gasses behind the front with a more gradual pressure decay, as represented by a typical Friedlander wave, that is arrested by reflected pressures from the crater and as the afterburn starts. The afterburn is characterised by a shallower more gradual pressure rise as it is not an aggressive detonic event and gives off a lower energy release over a longer period (Gelfand, Silnikov 2004). The crater confinement of some the detonic gases would assist in initiating afterburn sooner than it would under free-in-air conditions.

5.1.2 Conclusion

Shallow-buried blast front is characterised by a directional hollow tulip shape that swells rapidly upwards and initially outwards at the base. The blast front then proceeds to open at the tip to form a hollow inverted cone as reported by (Braid 2002). There are two distinct ejecta phases present in shallow-buried blast, a high-speed phase that ends at approximately 1.2 to 3.3 ms after detonation initiation followed by a slow-speed phase that ends at approximately 90-120 ms after detonation initiation.

The blast stem at the soil is established with the initial blast break out and remains constant over most of the high-speed ejecta phase duration. The end of the high-speed ejecta phase is characterised by two blast cone angles of soil

ejecta. The smaller angle is around 40^{o} and the larger angle of 72^{o}. These ejecta are formed by larger soil ejecta particles and clumps. Based on the blast stem diameter at the end of the high-speed eject phase, these ejecta angles indicate that on average only 13% of the projected blast 72^{o} cone area would impact the target at the 200 mm SOD and on average 48% of the projected 40^{o} blast cone would impact the target. Only a portion of the high-speed soil ejecta impacts the target and the proportion impacting increases as the SOD decreases.

The slow-speed ejecta phase is dominated by a wall of ejecta that moves laterally outwards slowing as it progresses and terminates with a heave outwards that results in the raised ridge of soil at the large (primary) crater lip that is widely reported in literature (Cooper 1996c). Using the high-speed ejecta blast stem diameter at the end of the high speed ejecta phase, the blast diameter of the slow speed ejecta phase is larger than the research target plate at both the intermediate and near-field. This implies that soil ejecta not forming part of the initial blast front are not important load contributors with shallow buried blast with the one-seventh scale test rig target plate used for this work. This conclusion is based on free-field ejecta blast morphology and thus should be seen as conservative. A target would create a pressure zone in the centre of the blast cone pushing the blast cone side wall ejecta outwards before they impact and load the target.

The breakout of shallow-buried blast is almost instantaneous, contains high temperature detonation gasses and follows the process defined by Bangash as reported in (Deshpande, McMeeking et al. 2009b). The blast front is still accelerating when it passes the near-field SOD (72 mm) but is decelerating when it reaches the intermediate-field of interest (200 mm).

Two craters were observed in the remaining soil, the primary (large) crater correlated with the blast stem diameter at the end of the low speed phases. The high-speed blast stem diameter was smaller than the secondary crater diameter at the end of the high-speed ejecta phase.

Although it is expected that the soil ejecta mass would vary as the charge D:H ratios varied the test method did not provide sufficient resolution to confirm this. Only the total ejecta mass could be measured thus the ejecta mass for each of the two ejecta phases was estimated using the volume ratio of the primary and secondary craters. Assuming that the secondary carter ejecta was expelled during the high-speed ejecta phase, 30-40% of the total ejecta mass or between 4.0 to 5.4 kg was ejected. Comparing the mass of soil ejected during the high-speed ejecta phase and the total impulse measured for near-field blast loading it appears that high-speed soil ejecta contributes minimally to the total blast load transferred to the target directly by the ejecta motion.

The shallow-buried blast side-on pressure test results were characterised by large variations and consequently large standard deviations. This was due to test execution variances. Shallow-buried 5:1 D:H charge intermediate free-field (no target) blast front peak side-on pressures were higher than the predicted pressures. Intermediate free-field positive side-on pressure duration was no longer than 387 μs for all tests. The measured positive phase durations were between two to three times longer than predicated by the computational model. This is partly due to the computational model not including afterburn extension to the explosive detonation model and test set up variations resulting in non-perpendicular contact with the sensor.

Both the computational model and the test side-on pressure-time traces indicated three loading phases. The pressure traces were then partitioned accordingly into the three phases. The model however predicted lower pressures for all three phases compared to the test results.

The partitioned side-on pressure total and phased specific impulse test results indicated that the intermediate free-field pressure-load contributions increased from Phase One to Phase Three. The computational model predicted the opposite trend. This was due to the method used to partition the modified model results and the absence of the afterburn extension in the explosive detonic model.

Based on the analysis of the test data the following sources are proposed for each of the three loading phases present is a free-field blast load: The first loading phase is due to the initial blast front that consists of a mixture of soil cap ejecta and blast front over-pressure combined with the preceding bow wave shock. The second loading phase is due to the expansion of detonation products as focused upwards by the surrounding soil. The Third phase is due to a complex geometrical reflection derived from the soil crater and soil surface combined with afterburn that is enhanced with the semi-confinement offered by the soil. These proposed blast load phase sources are a combination of and / or concur with those reported in the literature (Cullis 2001, Showichen 2008, Grujicic, B Pandurangan et al. 2007, Ramasamy, AM Hill et al. 2009).

5.2 Deep- Buried Blast

Secondary data in the form of high-speed video from (McDonald 2013b) that are is considered deep-buried blast, are analysed to highlight key differences with shallow-buried blast load development and target loading and in terms of the proposed three loading phases.

5.2.1 Analysis

(McDonald 2013b) tests are deemed to be deep-buried charge tests. The tests used a spherically shaped 160 g PE4 charge with an approximate diameter 58 mm with an Rc of 29 mm where R_c is the radius of the charge. Five tests had a DOB of 100 mm and one test a DOB of 50 mm. Using the Bangash Zone 1 definition for shallow-buried blast, the 100 mm DOB is larger than Zone 1 ($2R_c$ to $3R_c$) and thus meets Bangash's definitions. The 50 mm DOB is on the upper limit of the shallow-buried blast definition used by the author thus should be considered within Zone 1 and shallow buried.

Figure 124 and Figure 125 present a sequence of high-speed images from a McDonald 100 mm DOB and 230 mm SOD tests (test 3-230). The high speed image time base was not synchronised with the detonation pulse but simply set to one frame prior to the surface shock being visible. Figure 126 presents the blast front distance and velocity time plot for this test. The 100 mm DOB high

speed images clearly show a detonation shock transmits off the soil surface (see Figure 124) and preceding the blast front at an average vertical velocity of 338 m/s. After impacting the steel target the air shock reflects downwards back into the oncoming soil ejecta blast front at an average velocity of 290 m/s. The shock impact was not seen in the captured face-on force measurements and thus do not contribute to the transferred impulse.

The deep-buried blast front develops as a coherent hemispherical soil bulge as seen in images 1 and 2 in Figure 125. The bulge starts to rupture with black detonation products seen penetrating the front portion of the soil cap at around 762 µs after the shock break out and at a SOD of 103 mm. Image 3 in Figure 125 is showing the breakout has clearly manifested across the blast front in the form of black detonation products being pushed through the soil cap. The break out is at various disjointed places around the top and upper-sides of the soil bulge. There is no light flash indicating relatively low temperature of the detonic products. The gases continue to break out while the sides of the soil ejecta are pushed outwards as shown in image 4, Figure 125. The impact is led by the gasses with the sides of the soil cap and the detonation gases bulge moving laterally outwards, up and around the target edges.

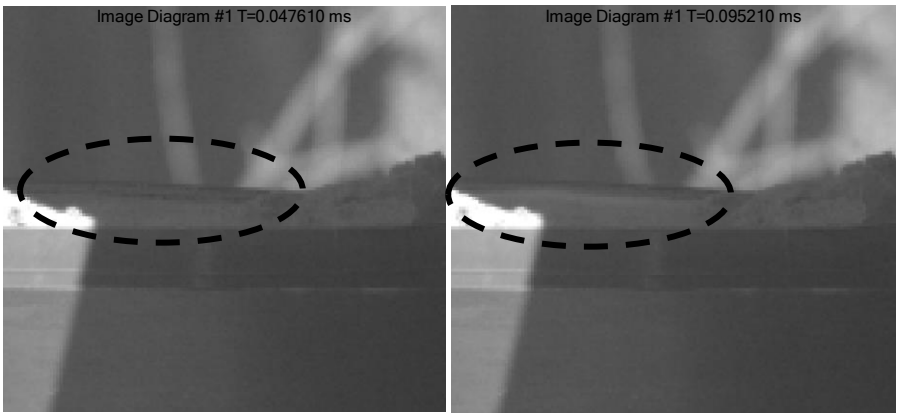

Figure 124: McDonald 100 mm DOB Surface Shock

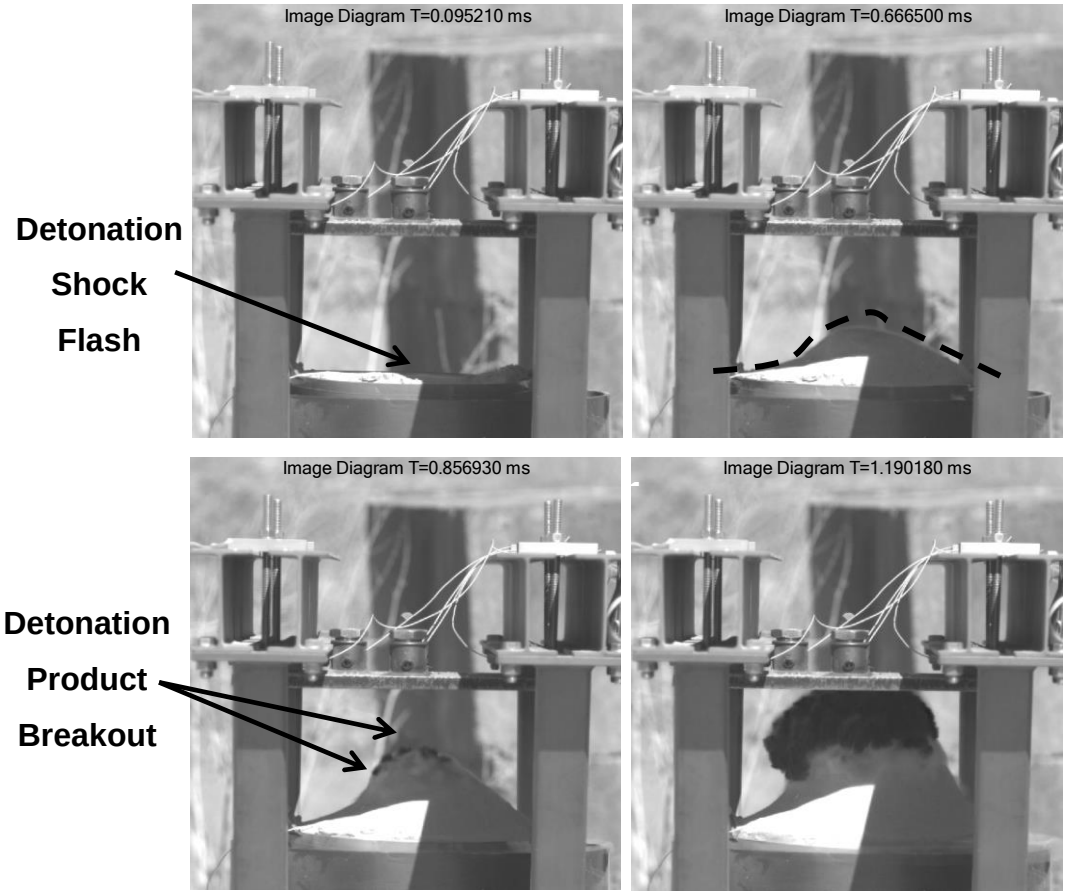

Figure 125: McDonald DOB 100 mm (>2R_c) (Test 3-230)

The blast front is asymmetric with the front bulging and expanding more on the right hand side than the left. This asymmetry manifests itself further with the detonic gas break out being more to the left hand side of the soil bulge. Possible causes are an angled detonator or non-symmetric soil covering.

Figure 126 shows the coherent soil blast front velocity initially increasing then slowing down from 286 to around 571 µs with the blast front velocity of 160 m/s. The front then starts to accelerate again with the velocity increasing at a constant rate until a peak velocity of 350 m/s is achieved at 952 µs with the front at a SOD of 164 mm. This takes place just after coherent breakout of the detonation products has occurred across the complete leading soil cap front. The blast front then decelerates achieving a velocity of 300 m/s prior impacting the target. Thus a deep-buried blast also exhibits accelerating and decelerating behaviour seen with a shallow buried blast front. The morphology of the deep-buried blast is both visibly and temporally different from shallow buried blast.

With shallow buried blast the pressure pulse is over, including the negative pressure phase, by the time this deep-buried blast front reaches peak velocity.

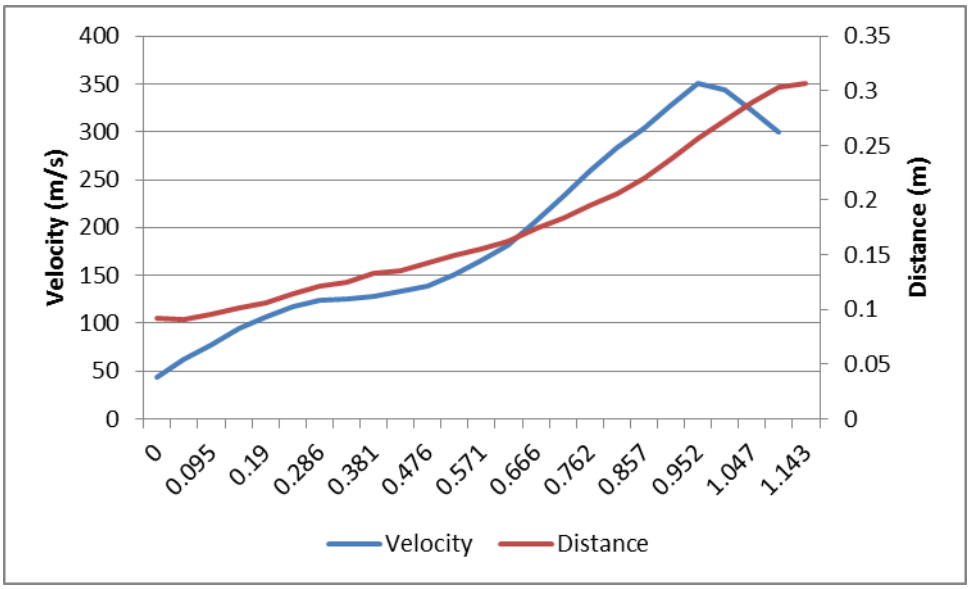

Figure 126: McDonald DOB 100 mm (>2Rc) Blast Front Displacement and Velocity Time Plot (Test 3-230)

Figure 127 and Figure 128 present a sequence of high-speed images of McDonald's 50 mm DOB test (6-230) blast front. The high speed image time base was not synchronised with the detonation pulse but simply set to one frame prior to the surface shock being visible. Figure 129 presents a plot of the blast front displacement and velocity over time.

For the 50 mm DOB (McDonald 2013b) test the blast front developed similarly to the deep-buried blast test with a surface flash indicating the arrival of the detonation shock at the soil surface, see Figure 127 and Figure 128 image 1. This surface shock appears to be stronger than with the 100 mm DOB with fine soil particles being accelerated off the surface that were not visible with the 100 mm DOB test. No reflected air-shock was visible in the captured images. The blast front starts out with a coherent soil cap which bulges symmetrically up and outwards however, the detonic gas breakout starts occurring much quicker at 322 µs and at a front displacement of only 83 mm above the soil surface. The 50 mm DOB gas break out occurs at a lower SOD but in a similar manner as

the 100 mm DOB test charge with a number of separate occurrences across the blast front leading edge.

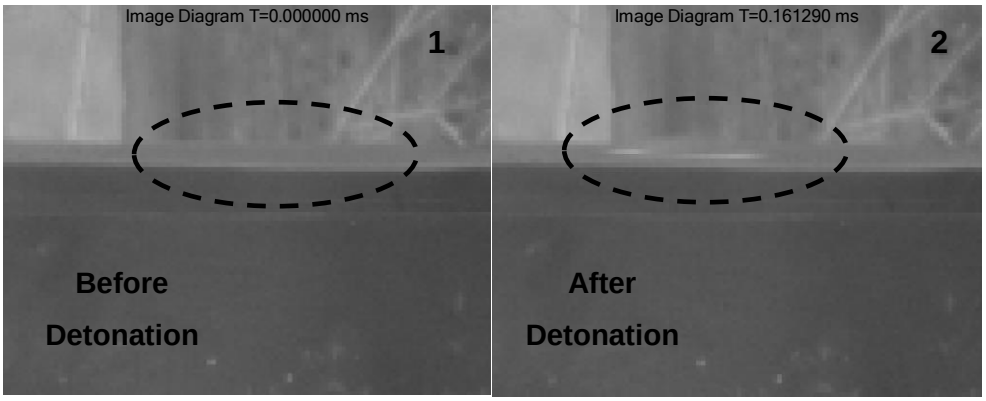

Figure 127: McDonald 50 mm DOB Surface Shock

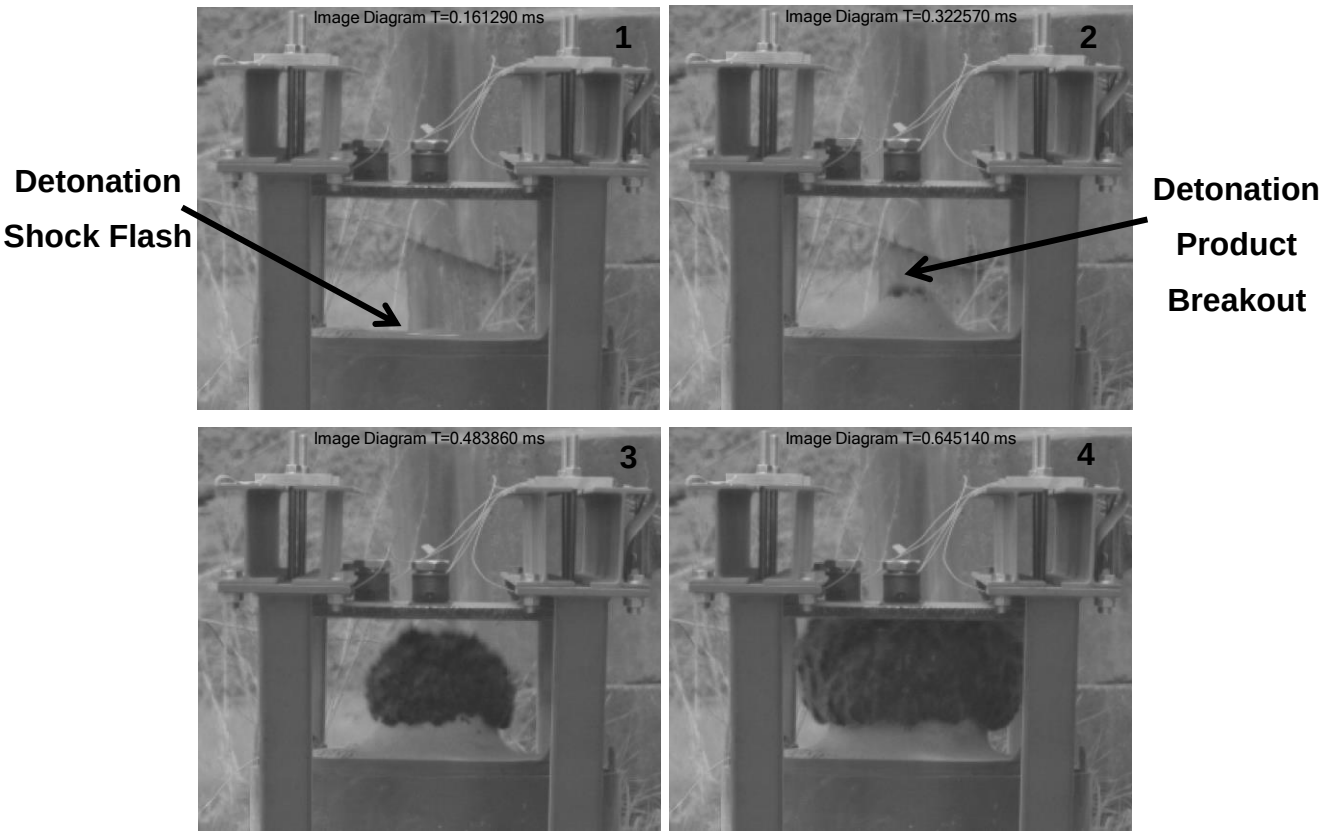

Figure 128: McDonald 50 mm DOB Test (<2R_c) (Test 6-230)

As with the 100 mm DOB test there is no light flash as was seen with the shallow-buried one-seventh scale tests indicating that the detonic reactions are completed prior to the gas break out. Thus the 50 mm DOB is behaving in a

similar manner as the deep-buried test and should also be considered a deep-buried blast test. This result is thought to be due to the detonation path of a spherical charge combined with the curved geometry of the soil cap creating on average, deep-buried conditions. It could simply be that the charge was buried deeper than 50 mm.

Figure 129 presents the blast front velocity and displacement time plot for the McDonald 50 mm DOB test (6-230). At 750 m/s the peak velocity was more than twice that of the 100 mm DOB blast peak velocity but still less than a third of a shallow buried blast's peak velocity. This is achieved at a displacement of 205 mm above the soil surface. Similarly to the 100 mm DOB the blast front starts decelerating after the detonic gas break out with the velocity increase being less rapid.

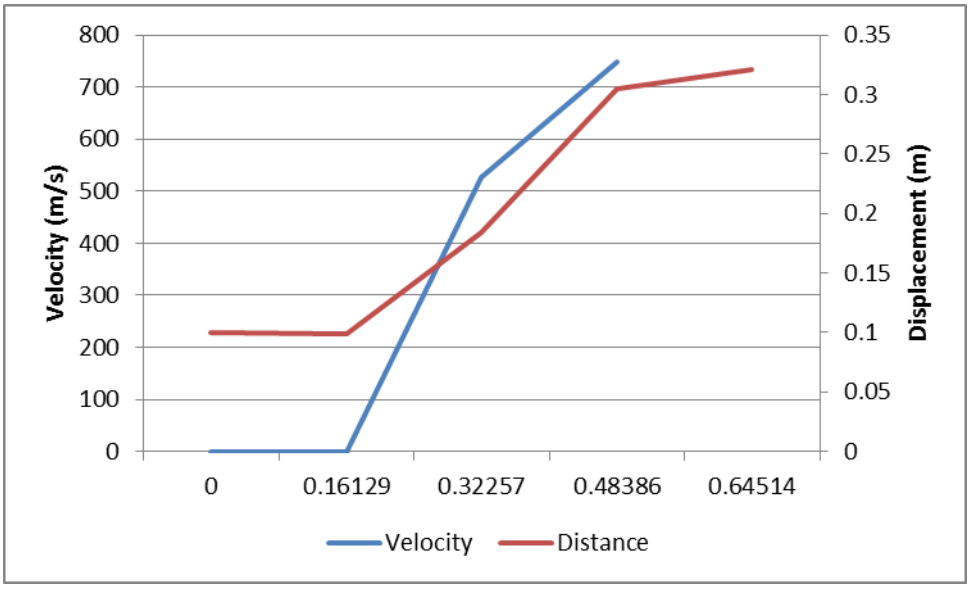

Figure 129: McDonald 50 mm DOB (<R_c) Blast Front Distance and Velocity Time Plot (Test 6-230)

Both the 100 and the 50 mm McDonald tests behave as deep-buried blast with coherent soil caps that accelerate upwards without fissures or gas leakage whereas shallow buried blast has almost instantaneous gas break out. As reported in (McDonald 2013b) these tests used hand rolled spherical PE4 charges initiated centrally with the detonator inserted from the bottom up with the detonator tip acing upwards. The would result in the detonation wave

arriving as a spherically growing detonation wave that theoretically arrives at the same time at the surrounding soil and impacts the soil perpendicular to the detonation wave front. The one-seventh scale tests were also centrally initiated but the detonation would grow radially outwards and thus run parallel with the soil cap exposing the cap to the detonation shock in a linearly spatial manner. The manner in which the detonation products from a shallow buried blast are released into the soil cap is similar to a explosively formed projectile (EFP). For shallow buried blast the soil cap is equally thick across the charge whereas for the spherical charge the soil cap thickness increases as the radial distances from the centre increases. These differences could result in the different blast front morphologies. In addition Bangash Zones could be based on fully constrained blast thus resulting in larger damage Zones as the soil is unable to vent upwards leading to thicker zone definitions than would be the case be with typical buried blast zones.

In reviewing Bangash's limit of 2-3 R_c, where R_c is the radius of the charge (Deshpande, McMeeking et al. 2009b), it is clear the Zone 1 definition is broad indicating variability in the results used by Bangash. This variability is affected by amongst other soil and explosive parameters and geometry (Cooper 1996c, Tremblay 1998). The use of charge radius as a parameter indicates that this work is based on spherical charges. The shallow-buried blast tests executed for this work used soil that had a measured moisture content of at least 3.7% up to a maximum of 8.7%. This is across all tests while (McDonald 2013b) had fine laboratory dried soil. This would result in the (McDonald 2013b) soil having much lower cohesion as well as other mechanical properties that would affect the buried blast load coupling and transfer (Braid 2002, Deshpande, McMeeking et al. 2009b, Cullis 2001, Grujicic, B Pandurangan et al. 2007).

By dividing the Zone 1 lower limit by the DOB the soil cap thickness can be presented as a percentage of the Zone 1 thickness. Thus less than 100% indicates that the soil cap falls within the lower limit of Zone 1. Furthermore the smaller the percentage the shallower the DOB is. For the one-seventh scale shallow-buried tests the DOB is less than the $2R_c$ limit for all tests with the

percentage of Bangash's Zone 1 dimension decreasing from 83% to 46% as the D:H ratio decreases from 5:1 to 2:1. This is due to the thickening of the charge height as the D:H ratio decreases. (McDonald 2013b) tests have a minimum soil cap thickness as a percentage of Bangash's Zone 1 of 86% for 50 mm DOB and 172% for 100 mm DOB. Despite the 50 mm DOB being a similar percentage of Zone 1 thickness for the shallow buried D:H 5:1 test the blast front exhibits markedly different behaviour.

In both (McDonald 2013b) tests the spherical charge blast front moved at speeds much slower than were developed with the one-seventh shallow-buried blast. Both McDonald's tests reviewed here exhibited clear separate precursor soil cap shock arrival prior to the soil cap motion. This indicates that the soil covering was thick enough to be in Bangash Zone 2 and Zone 3.

Based on the limited data the author proposes that when the blast front peak velocity is equal to or less than twice the speed of sound the threat should be considered deep-buried. This would accommodate the myriad of environmental parameters that effect the load development and transfer to the surrounding soil and focuses on one of the key physical parameters that quantifies the actual blast load definition of a buried blast.

The application of the proposed three shallow buried blast loading proposed in Section 5.1.1.3 to the (McDonald 2013b) blast test is discussed in Section 5.7.1.

5.2.2 Conclusion

Both the (McDonald 2013b) deep (DOB 100 mm) and shallower (DOB 50 mm) blast tests exhibited blast characteristics that were markedly different to shallow buried blast. These characteristics are an initial homogenous bulging of the soil followed by rupturing of the soil cap and the escaping of black cooler detonation products that move upwards. The area of soil initially affected by the developing blast is larger than with shallow buried blast. The blast front velocities are also much lower and reached later. The 100 mm DOB blast achieved blast front speeds lower than the local speed of sound with peak velocities of 350 m/s at around 850 μs. The 50 mm DOB blast reached 750 m/s at 484 μs.

The one-seventh scale shallow-buried blast tests exhibited the Zone 1 characteristic of being totally overwhelmed and crushed by the detonation and subsequent blast front. This is manifested as an early break out with high temperature gas flash mixing with the initial high speed ejecta. The shallow-buried blast front, as recorded for this work, achieved average peak blast front velocities of between 1,800-2,100 m/s across the threat D:H ratios and that were reached in around 70 μs after detonation initiation.

The use of Bangash Zones to define if a charge is shallow or deep-buried with flat cylindrical charges is not concise and is partly due to charge geometry effects on the zone thickness definition, soil conditions and the application thereof on buried blast loading on targets. Although McDonald's 50 mm DOB test and one-seventh shallow-buried tests fall within the lower Bangash Zone 1 limit and both exhibit an initially accelerating front that peaks and then decelerates there are fundamental differences in soil ejecta morphology, peak characteristic values as well as timing of events and peak values. Based on these critical differences it is proposed that both the McDonald tests are considered deep-buried blast.

There are parameters such as soil conditions and charge geometry along with DOB that could create resultant deep-buried blast effects, as defined for this work, making it difficult to use Bangash thickness limits (Zones) as is to describe if a blast is deep-buried or not. The Bangash Zone's however show potential to define shallow buried and could be refined to provide a simple single parameter for deep or shallow buried blast. Based on the two McDonald tests it is proposed that deep-buried blast be classified when the soil cap over the charge remains coherent and the peak blast front velocity is equal to or less than twice the speed of sound in the surrounding air.

5.3 Shallow-Buried Near and Intermediate-Field Force-Time Blast Load Phasing

The shallow buried blast-target interaction and the resultant target force-time response (morphology), peak force, total and partitioned force duration and impulse loading are analysed here in terms of the three proposed blast-loading

phases presented in Section 5.1.1.3. The analysis and discussion uses high-speed video, computational modelling as well as the target force-time response impulse and peak force data to quantify and confirm blast-load phasing.

5.3.1 Analysis

The analysis of the target force-time response to a shallow buried blast in terms of the three loading phases derived in Section 5.1.1.3 is presented in four sections. These are; (1) the high speed temporal analyses of the blast interaction with the target, (2) the peak forces achieved the total and partitioned target response phase duration, (3) the total and partitioned phased force-time response and (4) the total and partitioned phased impulse response.

5.3.1.1 Blast-Target Interaction

Figure 130 presents a sequence of high-speed images of a shallow buried blast front impacting and interacting with an intermediate-field (SOD 200 mm) target (side-on pressure probe configuration) for a shallow buried 5:1 blast threat. The images are synchronised to the detonation initiation firing pulse. Image 1 shows the blast front target impact at 133 µs ms after detonation initiation.

Image 2 shows the blast front as it has completed spreading across the target face and is starting to curl around the target sides at 300 µs after detonation initiation. Image 3 shows the blast ejecta side walls pushed outwards by the target pate and folding around the target of the blast at 557 µs after detonation initiation. Image 4 shows blast gasses and ejecta as deflected around the target at 3.3 ms after detonation initiation.

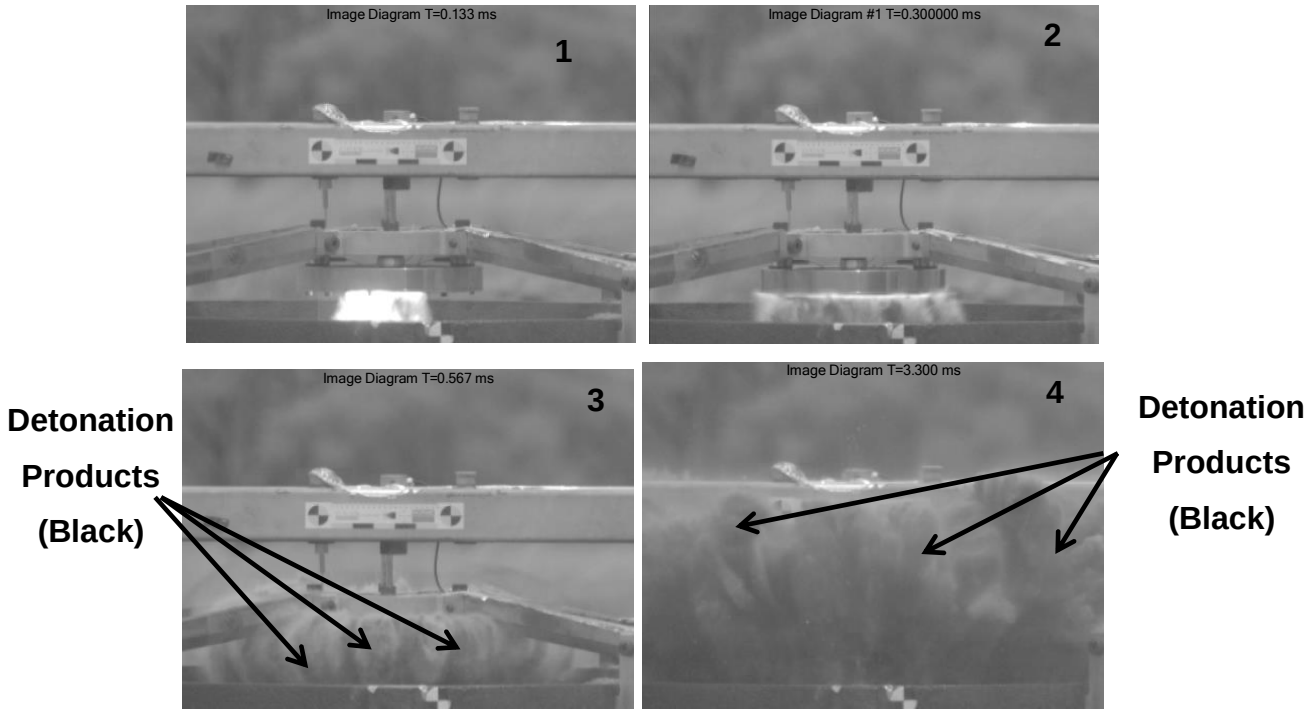

Figure 130: Shallow Buried Intermediate-Field Blast-Target Interaction (D:H 5:1)

Figure 131 presents a sequence of high-speed images of a shallow buried blast front impacting and interacting with a near-field (SOD 72 mm) target (face-on pressure probe configuration) for a shallow buried 5:1 blast threat. The images are synchronised to the detonation initiation firing pulse. Image 1 shows the blast front target impact at 25 µs after detonation initiation. Image 2 shows the blast front as it has completed spreading across the target face and is starting to curl around the target sides at 150 µs after detonation initiation. Image 3 shows the blast ejecta side walls pushed outwards by the target plate and folding around the target of the blast at 350 µs after detonation initiation. Image 4 shows blast gasses and ejecta as deflected around they target at 3.3 ms after detonation initiation.

From Figure 130 and Figure 131 a similar blast-front target interaction is seen for both the intermediate and near-field test configurations. There is an initial impact by a blast front that has a smaller diameter than the target. This is followed by a lateral expansion across the target until the edge is reached. The

blast ejecta at this time have considerable lateral motion thus they vent primarily laterally but still have a conical blast shape. The ejecta then wraps around the target due to the low pressure, as presented by (Hetherington). The main difference between the two is that the near-field interaction occurs sooner after detonation initiation due to the smaller distance to the target. The blast is then seen deflecting around the target like an air bag. The cooler black carbon rich (Cooper 1996c) detonation gas products are clearly visible at 3.3 ms after detonation initiation (Figure 130 and Figure 131 image 4). From the images it appears that the gases are present in folds found in the blast front side-walls (see image 3 in Figure 130 and Figure 131). Subjectively the near-field test appears to have less black detonation products emerging at 3.3 ms after detonation initiation than the intermediate-field test. The slower and generally larger soil ejecta “fingers” are also seen to be emerging from the blast cloud surrounding the target assembly at this time.

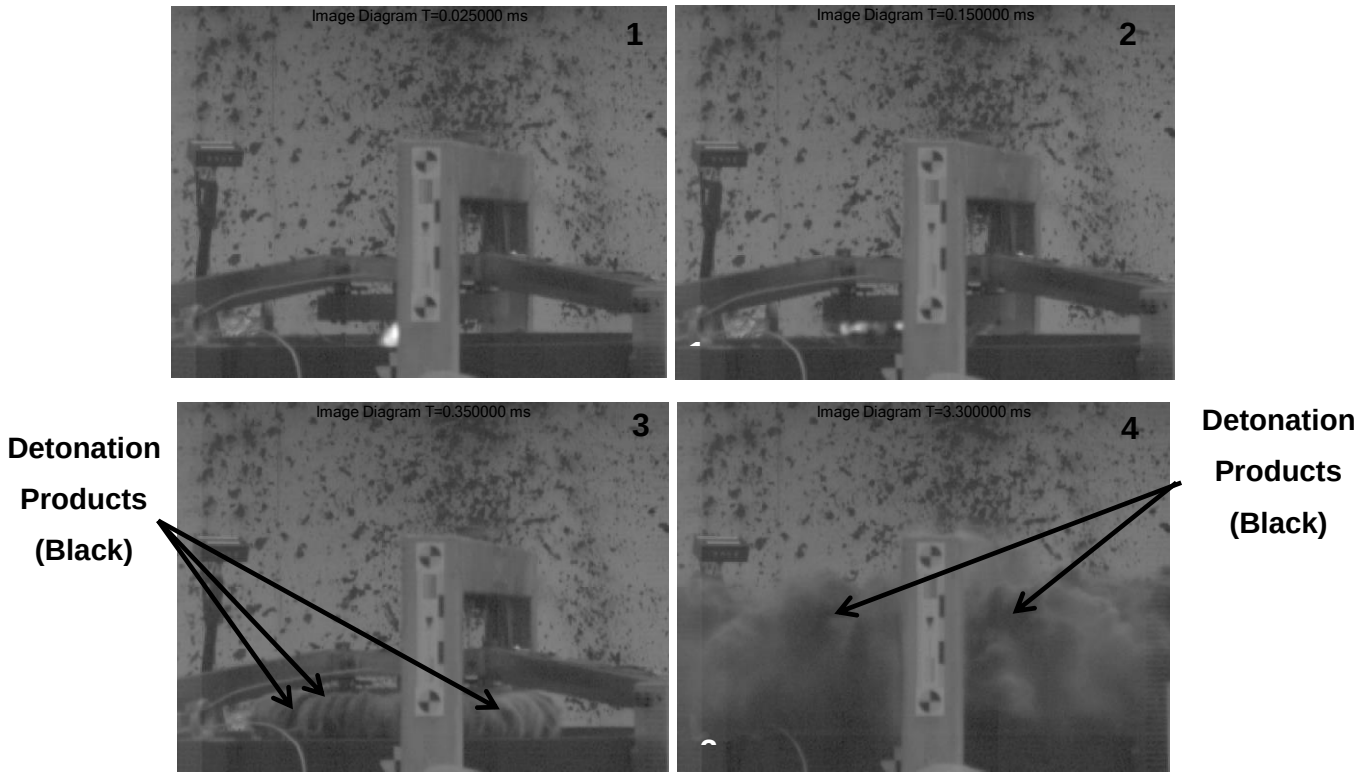

Figure 131: Shallow-Buried Near-Field Target - Blast Interaction (D:H 5:1)

Figure 132 presents a sequence of six computational modelling images of the near-field commissioning test configuration with a threat D:H ratio of 5:1. The images are an axisymmetric view of the test configuration. The target plate is 290 mm diameter as was used with the commissioning tests described in Section 3.3.1. Blue represents atmospheric air, red is the target plate attached to the small ring support that is attached rigidly in space. Light blue is the soil and green represents the explosive and detonation gasses. The soil, air and explosive are all modelled as Eulerian elements and the target assembly was modelled as Lagrangian elements. The timing starts at the initiation of the shallow buried charge.

Images 1 and 2 are of the blast front at 3 and 10 µs after initiation. The images clearly show a detonation gas bubble forming as indicated by the green centre and the thin light blue shell around the detonation products. Image 3 and 4 shows the first impact with the target at 15 µs and when the detonation gases reach the end of the target plate at 43 µs.

It must be remembered that for actual tests there is a built in initiation delay of 6 µs for the detonator to initiate (Risi Teledyne N/A) and if this is added to the model timing would give first impact at 21 µs which correlates well with test data for near-field test conditions. The model blast front reaching the edge of the target at 43 µs is much quicker than that shown in Figure 131 partly due to the target diameter being smaller at 190 mm than the test target at 360 mm. Analysis of the modelling images indicate that blast diameter of 360 mm would have been reached at 60 µs which is half the time observed during the test. This could be due to the graded mesh applied to the model with increasing mesh width from the centreline outwards. This results in elements that are 9 mm wide at the end of the target plate thus accuracy of the model will be less in this area.

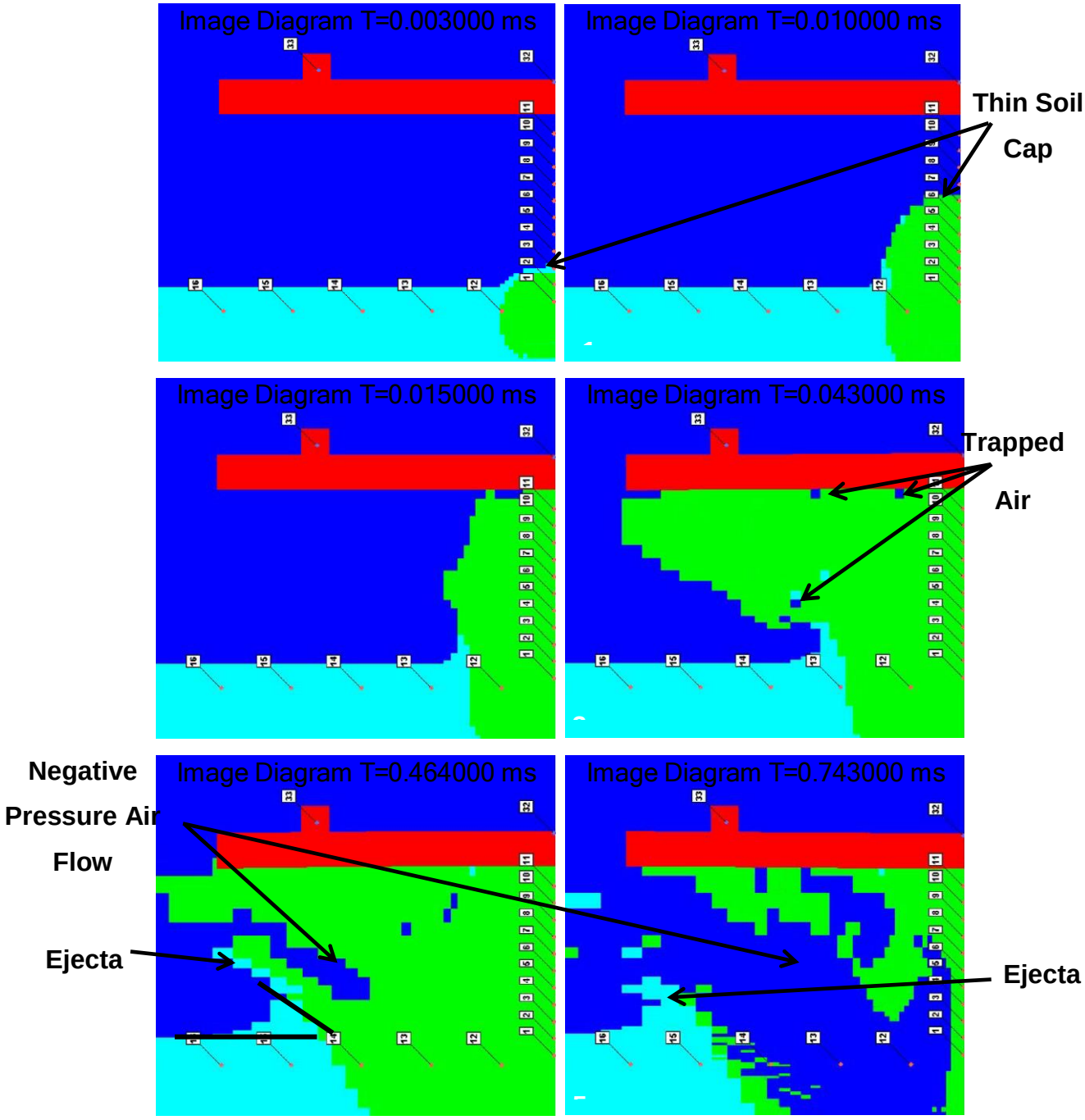

Figure 132: Computational Modelling Images Commissioning Test (D:H 5:1)

In images 3 and 4 of Figure 132 it shows that air is trapped by the blast front. This would be exacerbated in tests with a ragged blast front that is typically seen. It is important for afterburn to take place that there be oxygen for the explosive products to react with. Image 6 of Figure 132 shows air being entrained into the blast stem due to negative pressure phase at 464 µs. The image shows the ejecta side wall and the air returning into the blast zone about

two thirds of the height of the target SOD height. The onset of this air entrainment appears to start around 350 μs after detonation. Both image 5 and 6 show the blast cone angle that is formed from the shallow buried threat and the focussing effect of the surrounding soil (Braid 2002). At this time the angle from the model varies between 37^{o} and 48^{o} and depends on if the angle is measured on the outside or inside of the cone. The large element sizes generated by the graded grid in the model affect the accuracy of the blast cone angle measurement. This is nevertheless consistent what was found with the high-speed video analysis of tests. Image 6 shows the entrained air almost completely filling the blast crater at 743 μs after detonation. This is the source of the small peak that appears in the near-field target model side-on pressure trace (Figure 14). The JWL model of the explosive used in the computation does not model the detonation shock wave. This affects how the detonation products break out and the initial loading on the soil cap. These effects are exacerbated for shallow buried blast as the soil layer is thin and can be overwhelmed simply by the destination front shock pressures.

Based on the expanding bubble mechanism presented by (Braid 2002, Bergeron, Coley et al. 2001, Deshpande, McMeeking et al. 2009b) and supported by the high-speed images and computational model, the expanding blast is a hollow high pressure bubble containing expanding and reacting detonation products surrounded by soil cap and soil that initially surrounded the buried charge. The bubble pushes upwards as this is the path of least resistance. As it moves upwards it thins out the soil cap which integrates and forms part of the blast front. This then impacts the target and the growth of the blast front is driven by the expanding gas following, thus the soil ejecta on the sides is pushed outwards and around the target. The curling back of the blast front ejecta over the rear face of the target plate assembly indicates that blast ejecta does not contain heavy particles but that the ejecta is mostly made up of light particles such as expanded gases and crushed ejecta.

This process implies that other than the initial impact loading from the fractured and dispersed soil cap and some surrounding soil that is initially ejected

upwards when the charge detonates and breaks out, ejecta does not contribute to the total blast load transferred to an intermediate and near-field target as used for this work. Soil ejecta forms a flexible wall that partially constrains the expanding blast gasses and expands upwards and laterally. The ejection angle of the larger ejecta particles moving at the end of the high speed ejecta phase forming an ejecta angle without a near-field target means that with the presence of a target will push these later emerging ejecta away from the target. As discussed in Section 5.1.1.1, the slow speed ejecta diameter is close to or larger than the target thus cannot contribute to the blast load transferred to the target.

The reflected pressure created by the presence of a target above the shallow buried blast will result in the secondary crater being compressed downwards thus reducing its size on average while the primary or slower phase ejecta will be pushed outwards thus creating a larger crater. The craters measured during the intermediate and near-field tests had a clear step forming two crater diameters. A large primary crater formed on the surface and a smaller secondary crater located below the soil surface. This confirms the expected reflected pressure phase occurred as this makes the dual craters more visible when compared to the free-field ejecta craters.

5.3.1.2 Peak Target Response Force

Due to noise in the net force signal from low pre-tension of the force washers, only the total net peak force was extracted for each test and not for each partitioned phase.

Figure 133 presents the average peak target net-force response recorded for all one-seventh scale tests. The test series 2 refers to the side-on pressure test configuration and test series 3 and 4 refers to the face-on test configuration. The test charge D:H ratios follow in decreasing ratio order thus D:H 5:1 is -1 test point and D:H 3:1 is -2 test point and D:H 2:1 is -3 test point. The commissioning tests and corresponding D:H ratio of the test charge are identified directly e.g. C5:1. Test series 2 and 3 are with an intermediate-field

(SOD 200 mm) target. The commissioning tests and 4 series tests are with a near-field (SOD 72 mm) target.

The intermediate-field (200 mm SOD) one-seventh scale final tests side-on and face-on pressures test configurations peak pressures both show decreasing peak force with decreasing D:H ratios. The effect is less pronounced with the face-on configuration but is still visible in the averaged results. The side-on probe test configuration was 5% heavier than the face-on probe and this would result in a slightly lower peak force but not the large difference that was recorded. As the pencil probe extends below the target face by 167 mm towards the soil it would be expected that this test configuration would have higher peak forces and impulse due to the slightly larger wetted area and due to the longer time the blast loads the target starting with first impact on the downward extending probe.

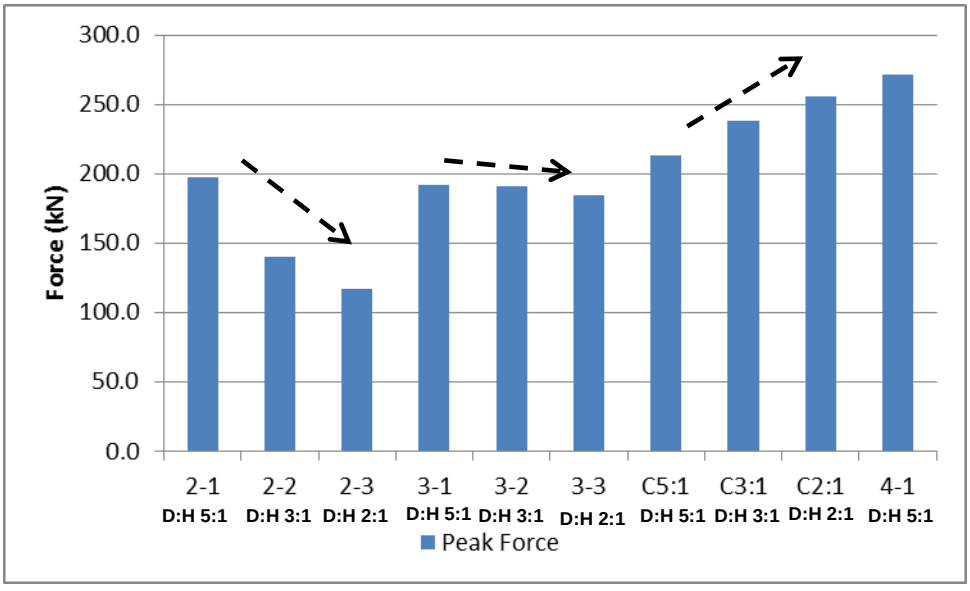

Figure 133: One-Seventh Scale Shallow Buried Blast Target Response Peak Force

These results indicate that the probe is affecting the initial loading in a different manner than was expected. In all test cases the peak force occurred during the partitioned Phase One loading. This loading in primarily the blast front impact onto the target thus the pencil probe is disturbing and deflecting the blast front. This deflection is exacerbated if the charges were not parallel with the soil

surface, the pencil probe and the target. The blast is then split by the probe and acts tangentially on the probe sides reducing the peak vertical force that the load can apply to the target. The 5:1 D:H ratio charge would be less affected as the soil cap as a ratio of the area of the pencil probe is much larger than the 3:1 and the 2:1 charges. As these charges would be placed close to centre directly under the probe the probe will, percentage wise, deflect a larger amount of the soil cap ejecta as the charge D:H ratio reduces.

The near-field commissioning tests give the opposite trend with regards to peak pressure and charge D:H ratio. Only two near-field tests were conducted for this work using the final test target configuration with a 360 mm diameter. Both tests were with a D:H 5:1 charge ratio . Thus the decreasing peak pressure with decreasing D:H ratio trend cannot be verified with the final research tests available. If the commissioning test results are accepted this trend implies that the blast load from each phase changes as the SOD changes. This could be accepted as Phase One loading consists of the soil cap and the blast front over-pressure which will differ between near and intermediate-field SOD's. The blast front velocities at 72 and 200 mm are very similar thus the soil cap contribution to the peak force loading will be similar. The difference in peak force loading between the near and intermediate-field would then be due to the blast front over-pressure differences. This implies that the blast front over-pressure increases in the near-field and then decreases in the intermediate-field as the charge D:H ratio decreases. This is counter intuitive as there is no visible difference between the near and intermediate-field that would enable the different D:H ratio blast over-pressure trend to change. It is expected that the D:H ratio that generates the highest near-field pressure will also generate the highest intermediate-field pressure.

The commissioning test pool is relatively small with no more than two tests per configuration and was executed before the test methodology was refined to improve set-up consistency. The two D:H 2:1 tests recorded peak forces of 225 and 285 kN whilst the 5:1 blast test recorded 175.6 and 250 kN directly showing the variations in the test methodology as reflected in the test results. The

commissioning test configuration also differs from the final with having a smaller target area (0.066 m^2 vs 0.102 m^2) and lighter target mass (16.5 kg vs. 24.6 kg). The commissioning tests also only captured two of the four target response load-cells and the total net force was estimated by simply doubling the sum of the two measured load cells. Any asymmetry effects in the loading would affect the accuracy of the peak net force result. This small test pool, large extreme data spread combined with measurement set-up inconsistency and target differences means no inference can reliably be made regarding the influence of D:H ratio on peak force in the near-field with these data.

In analysing the final research test's near-field results, there is only a 37% increase in peak net force from 197 to 271 kN with a 64% reduction in SOD from 200 to 72 mm with a 5:1 D:H ratio threat.

5.3.1.3 Total and Partitioned Phase Duration

Figure 134 presents all the one-seventh scale target positive force-time total and partitioned phase durations. Figure 135 presents the partitioned phase durations as a percentage of the total positive force-time duration. The intermediate-field side-on pressure test configuration total force duration (2-1, 2-2 and 2-3) is nearly 40% longer than the intermediate-field face-on pressure test configuration duration (3-1, 3-2 and 3-3). This is partly due to the larger target assembly mass with the side-on probe holder and higher target inertia. It is also has a larger wetted target area offered by the long pencil probe extending below the target towards the blast resulting in the two pressure phases following the initial impact being able to act over larger area for longer. The two pressure phases, soil focused detonic product expansion and the geometric combined with afterburn reflected pressures are not disturbed as much as the initial blast front by the probe. These pressure loads are applying loading on all surfaces they are exposed to, the target, the pencil probe, the side wall ejecta and the crater.

There are no clear intermediate-field charge D:H ratio total target-response force duration trends clearly visible in the data. The near-field commissioning tests 5:1 D:H ratio charge (C5:1) total positive force duration is on average only

50% of the final face-on pressure test configuration (series 4-1) 5:1 D:H total positive force duration. All the partitioned phase load durations are shorter by a similar ratio thus this difference is primarily due to the smaller commissioning configuration target geometry and mass. The commissioning test target area is 64% of the final test configuration target area and the mass is similarly only 67% of the final test configuration target assembly mass with resultant smaller quasi-constrained volume between the spoil and the target and lower target inertia.

Although there do not appear to be visible charge D:H ratio duration trends based on the total positive response force duration the partitioned intermediate-field phase durations show D:H ratio trends. Durations trends appear visible in the partitioned near-field commissioning tests. However, due to the variability inherent in these results combined with the limited data set (only one D:H 3:1 test), it is not practical to analyse duration trends across three D:H ratios thus are not analysed further. The near-field research test partitioned duration results for the D:H 5:1 ratio charges are discussed after the intermediate-field trends.

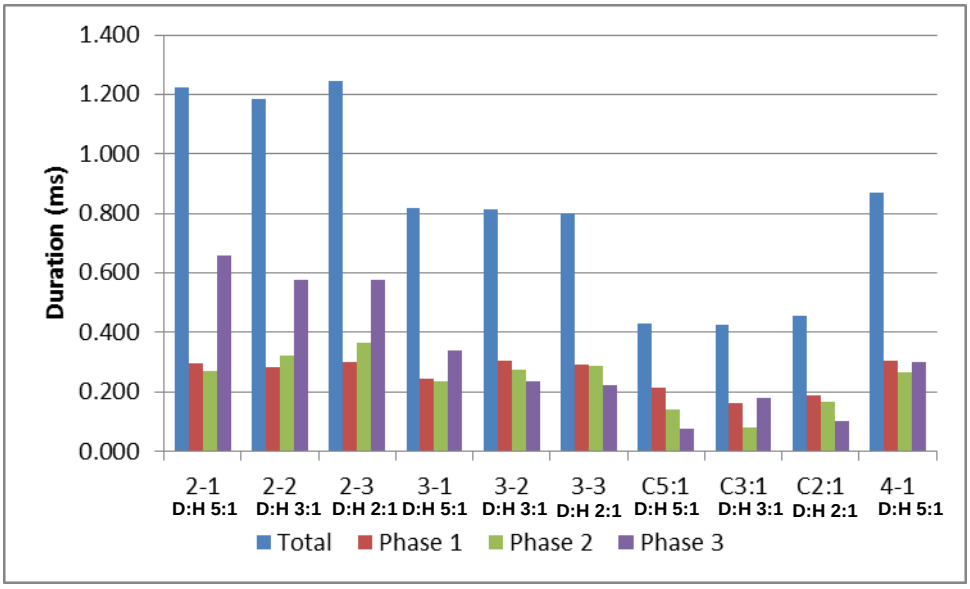

Figure 134: One-Seventh Scale Target Force-Time Response Total and Phased Durations

Partitioned intermediate-field phases One and Two averaged target response force duration trends are small and are close to the standard deviation of the

measurements. For each intermediate-field test configuration the partitioned Phase One and Phase Two durations appear similar with Phase One remaining almost constant on average and Phase Two increasing slightly as D:H ratio decreases. On average the Phase One duration is the same for both intermediate-field test configurations and vary on average by 6 µs. Partitioned Phase Two durations differ more between the two intermediate-field test configurations with the face-on pressures sensor test configuration being shorter on average by 54 µs than the side-on pressure probe configuration. This confirms the analysis above that the pencil probe extending into the blast increases the pressure loading phase duration but does not materially affect the impact loading phase (Phase One).

The clearest target force response duration trend is presented by the partitioned Phase Three, proposed to consist of afterburn combined with geometric reflections from the soil and target. This trend is clear in both the total and the partitioned data in Figure 134 with Phase Three duration being the primary duration difference between the two test configurations. On average the face-on pressure sensor test configuration Phase Three duration is 340 µs shorter when compared to the averaged side-on pressure probe configuration. Both the side-on and face-on pressure test configurations had decreasing Phase Three target response force durations as the charge D:H ratio decreased. This trend is more marked for the face-on pressure test configuration. For the side-on pressure test configuration the Phase Three duration decreased on average by 79 µs and decreased 119 µs for the face-on configuration as the charge D:H decreased from 5:1 to 2:1.

This implies that the slower afterburn and reflected pressure loading is transferred more effectively with the additional pencil probe area exposed in the SOD gap. This additional reflected surface is the same as for Phase Two however it appears that this intrusion does not influence the faster expanding detonic product load transfer as much as the slower Phase Three expansion. Afterburn is a slower process with lower peak pressures (Gelfand, Silnikov

2004, Edri, Felgun et al. 2012) thus appears to load the target longer when the pencil probe is fitted.

The increased Phase Two target response force duration indicates that as the D:H ratio of the charge decreases, the detonation gas expansion loading phase couples better into the target. This could be due to the larger volume of gases being released side-ways as the charge thickness increases with the decreasing D:H ratio. These side-ways expanded gases are then focused upwards with the Phase Two gas expansion giving rise to a longer duration simply due to the larger volume of gases available in the crater after initial detonation expansion. As the D:H ratio is decreased the amount of gasses initially expanding upwards with the fist blast expansion also decreases. This effect is not clearly evident in the Phase One force-time duration response as the soil ejecta contained in the initial expansion dominate this phase's loading.

For Phase Three The D:H ratio affects the reflected pressure and after-burn. The larger explosive face from the larger D:H ratio charge appears to generate larger reflected Phase Three pressures with the research test configuration applied for this work. This seems to be driven by the exposed explosive face area facing the target. The reduced afterburn is possibly due to reduced air mixing based on the charge face geometry as well as thicker soil side wall ejecta generated by the thicker charges reducing the amount of air that can be mixed with the detonation products. Lastly the longer Phase Two expansion could result in decreased suitable detonation products being available for afterburn. This implies that there is more efficient combustion of the explosive products during detonation of smaller D:H ratio resulting in a shorter afterburn process as the D:H ratio decreases.

As only one D:H ratio charge was tested for the near-field face-on configuration no comment can be made regarding D:H ratio partitioned phase trends for the near-field. However the changes in phase durations for the 5:1 D:H ratio charge as the SOD is reduced can be analysed. In reducing the SOD from 200 to 72 mm the total duration on average increases by 7% from 818 to 871 µs.

In reviewing the phase durations as a percentage of the total positive phase durations as shown in Figure 135the duration trends discussed above are confirmed. Both intermediate-field test configurations show the increasing Phase Two and decreasing Phase Three target-response duration with decreasing charge D:H ratios. For Phase One target response durations, the side-on test configuration the duration percentage as remained the same at 24% of the total positive phase duration but varied by 6% increasing from 30% to 36% for the face-on pressure configuration, as D:H ratio decreases.

The face-on pressure total near-field (4-1) shallow buried blast load target response force total duration is only 7% longer than the face-on pressure test configuration intermediate-field (3-1) target response force duration. Phase One duration as a percentage of the total increases by 6% and Phase Three decreases by 7% as the target SOD decreases from intermediate to near-field. Phase Two, as a percentage of the total positive force response duration, stays constant as the SOD decreases. The increase in Phase One duration would be due to the fact that the blast front has not spread much and has higher blast front pressures. The shorter Phase Three duration at the lower SOD could be due to the higher pressures giving rise to quicker more complete afterburn. Another cause could be that at the lower SOD's there is reduced mixing with air thus the required oxygen for afterburn is not sufficient with the near-field target test. It is expected that the closer location of target would increase the reflected pressure duration but this does not appear to be the case. This can only be due to the pressure releasing more quickly to the side and around the target the blast is only quasi-constrained. A larger target would ensure even longer target force response durations.

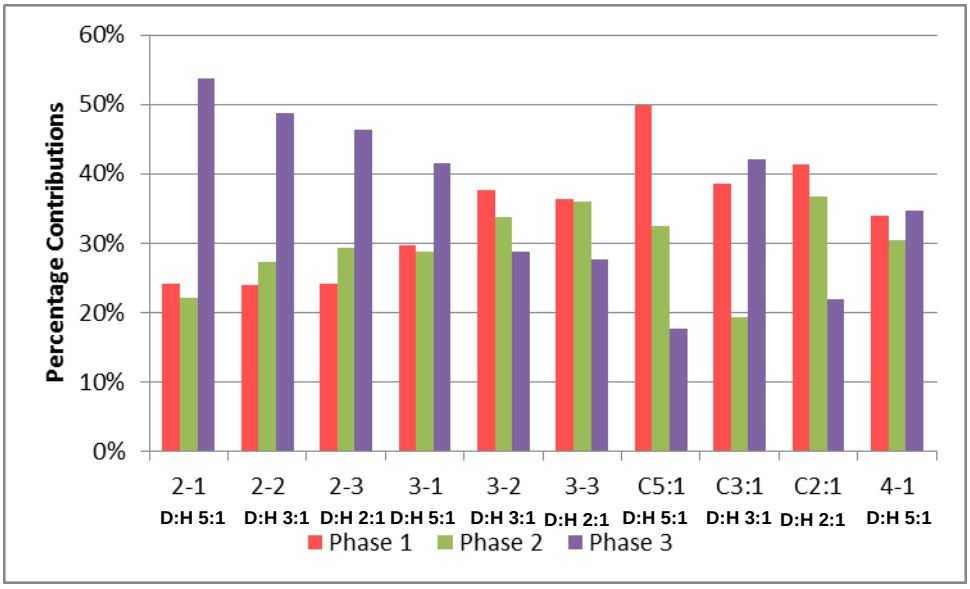

Figure 135: One-Seventh Scale Target Force-Time Response Total and Phased Duration Contributions

5.3.1.4 Total and Phased Target Response Impulse

Figure 136 presents the total and the partitioned phase target response impulse to shallow buried blast loading for all the one-seventh scale tests. Figure 137 presents the partitioned phase impulse contribution as a percentage of the total impulse load transferred to target. These data present both the intermediate-field (200 mm SOD) and near-field (72 mm) target response total and partitioned impulse. The intermediate-field tests include both the side-on and face-on pressure probe test configuration. As was seen with the partitioned force-time duration's both the total and the partitioned phase impulse results presented trends with changing D:H ratios.

In reviewing the total impulse the intermediate-field tests indicate a clear trend of decreasing total impulse with decreasing D:H irrespective of the test configuration. The near-field commissioning test data (C5:1, C3:1 and C2:1) is too variable and limited in number of tests to be able to conclude a similar trend. Only the 5:1 D:H ratio was tested (4-1) in the final near-field face-on pressure configuration. The commissioning tests (C5:1 and C2:1) have considerably lower total impulse than that was measured by the final face-on pressure near-field test configuration (4-1). This is primarily due to the difference in target size.

In reviewing the partitioned target response impulse both the intermediate-field test configurations indicate a reducing Phase One impulse with a decreasing charge D:H ratio. It is proposed in Section 5.1.1.3 that Phase One loading is primarily the blast-front mixed with the soil cap and some surrounding soil. The side-on pressure test configuration averaged lower partitioned Phase One impulses when compared to the face-on pressure test configuration at the intermediate-field SOD (200 mm). This is deemed to be due to the deflection effect of the pencil probe that extends into the blast area from the target on the initial blast front. This decreasing impulse trend with decreasing charge D:H ratio is thought to be primarily due to soil cap geometry. The soil layer reduces the shock overpressure of the blast front (Gelfand, Silnikov 2004, Ramasamy, AM Hill et al. 2009) thus following Section 5.1.1.3 for shallow buried blast, the blast front is primarily made up of the soil cap, with possibly some additional soil ejected upwards due to the detonic effects of the flat cylindrical charge shape on the surrounding soil and the reduced blast front overpressure. Assuming that the total soil cap mass is integral to the blast front and is moving at the same average speed when it impacts the target, the Phase One impulse can be said to be primarily the soil cap ejecta. Thus blast front pressure momentum is deemed negligible compared to the ejecta momentum.

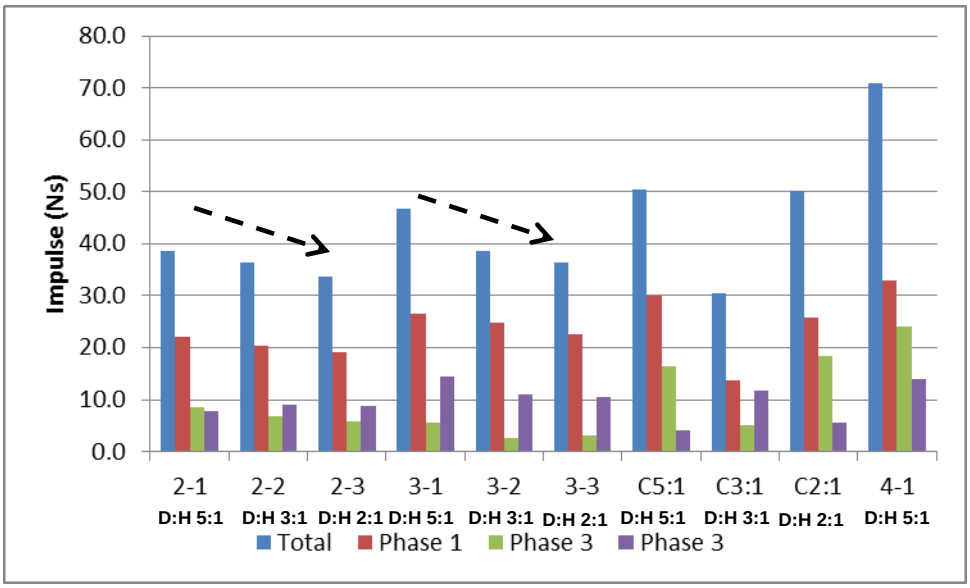

Figure 136: Total and partitioned One-Seventh Scale Target Response Force Impulse

Applying the test soil density and the charge geometry to calculate the soil cap ejecta mass and using the average blast front velocity, as determined during the free-field ejecta tests, the Phase One impulse can be approximated by multiplying the soil cap ejecta mass by the average blast front velocity. This assumes that the soil transfers all its vertical momentum to the target by coming to rest. This is deemed acceptable as the complete blast front is captured by the target plate and the target plate is rigidly held in position. As there is variation between the extracted experimental velocities the average blast front velocity was simply taken for each charge D:H ratio as captured from each camera. Average blast front velocities at the near-field 72 mm SOD were 1,632, 1,753 and 1,763 m/s and at the intermediate-field 195 mm SOD they were 1,306, 1,636 and 1,391 m/s. Standard deviations for averaged blast front velocities varied from lows of 10% to highs of 41%. The 3:1 D:H ratio tests had Standard Deviations of 10% and 26% between the two cameras.

This increasing velocity trend with decreasing charge D:H ratios was predicted by the computational model when taking the average time of arrival of the blast front. The anomalous 3:1 D:H test velocity is used as was calculated and is within the standard deviations of the average velocities. The comparatively high average D:H 3:1 ratio blast velocity is due to the small test pool of only two test data sets with a single anomalous test which recorded very high velocities.

The velocities at the 72 mm and 195 mm SOD were interpolated from the velocity time plots extracted during the high speed analysis so are not direct measurements. The 195 mm SOD is slightly lower than the actual test SOD of 200 mm. This was due to the calculations being done for the sensor centre point which was located 5 mm proud of the target thus at a SOD of 195 mm. These data show that the spread in velocities due to charge D:H changes decreases as the SOD increases. This correlates with (Baker 1973a) regarding non-spherical charge blast fronts changing to typical spherical charge blast fronts as the SOD increases. Thus the differences in blast front due to charge geometry reduce as distance from the blast increases as was seen in the extracted test data.

Using a soil density of 1,600 kg/m^3 the approximated soil cap masses of 17, 12 and 9 grams are calculated for 5:1, 3:1 and 2:1 charges. Calculating the momentum of the blast front and equating this to the impulse as the blast front is totally absorbed by the target and brought to a standstill gives the following impulses for Phase One loading: For the intermediate SOD of 195 mm 22, 20 and 13 N.s for 5:1, 3:1 and 2:1 D:H charge ratios. For the near-field SOD of 72 mm 27, 21 and 16 N.s for 5:1, 3:1 and 2:1 D:H charge ratios. At 20 Ns the intermediate-field D:H 3:1 calculated Phase One impulse is close to the 5:1 ratio impulse, this is due to the higher averaged velocity obtained during testing. If a similar percentage velocity increase, as that shown by the 2:1 and 5:1 tests between the 195 mm and 72 mm SOD's, is used to estimate the D:H 3:1 ratio blast front velocity at the intermediate-field SOD then the estimated velocity would be 1,381 m/s. This gives an intermediate-field Phase One Impulse of 16 N.s. which is more in line with expected partitioned Phase One impulse.

The measured face-on intermediate-field configuration partitioned Phase average impulses are all higher than the approximated soil cap mass and blast front impact velocity impulse for each ratio. The percentage difference between the calculated soil cap and the measured impulse increases as the D:H decreases. For the intermediate-field the recorded 5:1 ratio impulse is 17% higher, the 3:1 ratio and 20% higher than the 2:1 ratio is 42% higher than the calculated soil cap impulse. This indicates that there is additional momentum to the soil cap that forms part of the Phase One blast load. This could be due to stronger blast front over-pressure that gives rise to the higher blast front velocity. It is however proposed this impulse difference is rather due to additional soil ejected with the blast front from the boundaries of the shallow buried charge. As the D:H ratio decreases the thickness of the charge increases. This implies that the lateral losses will increase (Cooper 1996c). These lateral pressures increase the loading on the soil around the charge and lead to larger soil mass being accelerated both laterally and vertically as part of the blast front. The larger D:H ratio charges will then have less additional soil ejecta momentum added for Phase One loading than the smaller D:H ratio charges. The near-field 5:1 ratio charge gave a partitioned Phase One impulse

of 33 N.s which was 18% higher than that predicted using the soil cap ejecta mass and average blast front velocity at this SOD. This is similar to the intermediate-field results which gave 17% higher impulse than predicted, this thus supports the position that adjacent soil ejecta is responsible for the higher test Phase One impulse. As this is the same percentage impulse ratio it indicates that the same amount of mass is involved at both SOD's as momentum is a first order calculation. Had the additional momentum been due to the blast front over-pressure the increase in transferred impulse would have been much higher than a simple linear relationship as the pressures differ exponentially with SOD.

Overall the partitioned Phase Two and Three target response impulse loading decreases as the charge D:H ratio decreases. Although small and falling within the Standard Deviation of the measurements, this trend indicates that the detonic pressure loading and the combined reflected and after-burn pressure is lower as the charge D:H ratio decreases. The computational modelling side-on pressure results shows that the partitioned peak Phase Two pressure for near-field increases as charge D:H decreases. The modelling also shows that as D:H ratio decreases the Phase Two peak pressure occurs earlier. The test data shows that the target-force response for Phase Two is lower as the D:H decreases even though the peak pressure is higher and the duration is longer. Based on these data no clear reason as to why this occurs can be identified. The ejecta side-on pressure results presented in Section 5.1.1.2 indicate that the partitioned side-on and face-on Phase Two and Three positive pressure pulse durations as well as specific impulses increase as D:H ratio decreases (See Figure 121 and Figure 122).

Similarly the face-on target face pressure results presented in Section 5.5.1.2, Section 5.5.2 and Section 5.5.3 show the pressure duration and specific impulse increase as the charge D:H ratio decreases. However face-on peak pressure and side-on pressure specific impulse decrease as D:H ratio decreases. The variability of the pressure tests is also included in these results making it difficult to draw definite conclusions. As reported by (Held 2004) and

(Tremblay 1998) based on work by Westine el al., the blast load across a target varies with the highest loading occurring in the middle of the target and declining exponentially towards the edges. The test results indicate that a lower target response impulse was achieved with decreasing charge D:H ratio yet the smaller D:H ratio charges recorded higher central pressures and calculated specific impulses. Thus the rate at which the blast load varies across the target must also vary with changing D:H ratios. The lower response impulse means that the rate the pressure loading declines across the target face is much higher as the D:H ratio decreases. Thus the averaged pressure loading across the target is lower as the charge D:H ratio decreases.

In reviewing the percentage contribution effects of D:H ratio on the partitioned phases shown in Figure 137 the following is noted. The load reducing effect of the pencil probe on the intermediate side-on pressure test configuration is clear with Phase One only contributing on average 57% of the total blast loads for the side-on pressure test configuration whereas for the face-on pressure configuration the Phase One load contributes an average 64% of the total impulse.

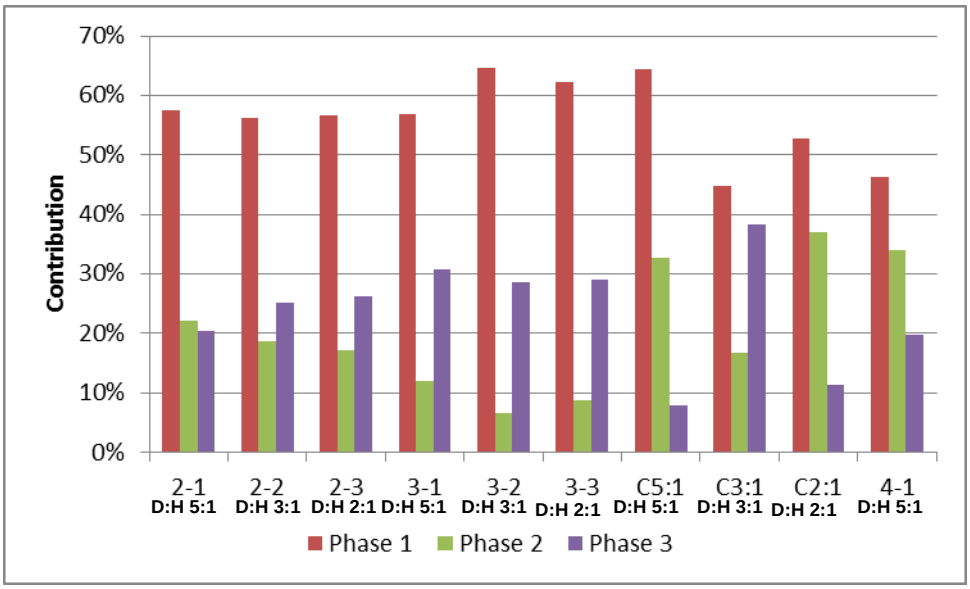

Figure 137: Partitioned One-Seventh Scale Target Phase Impulse Contribution

The partitioned phase contribution of the D:H 5:1 charge face-on test configuration as a percentage of the total impulse response load percentage's

change as SOD decreases. The face-on pressure configuration D:H 5:1 Phase One load contributes 65% of the total load for an intermediate-field target whilst for a near-field target Phase One contributes only 46% of the total target response impulse load. Phase Two and Phase Three percentage contribution increase relatively as the SOD decreases. From Section 5.1.1.3 Phase Two loading is proposed as being due to the initial detonic gas expansion and Phase Three loading is from after-burn and reflected pressure loading from the quasi constrained environment created by the soil, the crater and the target. For Phase Two loading, as noted the blast front is still accelerating when it reaches the near-field target. This means that the energy of the expanding detonation products is still high thus is still accelerating the blast front. Whereas at the intermediate target distance the blast front is decelerating implying that the detonic gas expansion is past its peak pressure. Thus at a lower SOD the load contribution from the expanding detonation gases would be higher due to the higher gas velocity and pressures. Although the D:H 5:1 charge Phase Two target response loading percentage contribution remains similar at 34% with only a 3% increase the actual impulse load contribution by Phase Two gas expansion is six fold from 5.6 Ns to 34.1 Ns.

For Phase Three loading, the closer target position for the near-field target reduces the ejecta space volume and thus improves the conditions for afterburn with a higher concentration of detonic products at a higher temperature and pressure resulting in a better afterburn, assuming sufficient air is captured with the blast front as oxygen is required (Gelfand, Silnikov 2004, Edri, Felgun et al. 2012). Additionally the reflected pressure load would also be higher due to the smaller space between the target and the soil (Smith, Hetherington 1994). However this combined load remains nearly the same at 14.4 Ns compared to 14 Ns and percentage contribution drops from 31% in the intermediate-field to 20 % in the near-field. As the reflected pressure is certain to increase within the more constrained environment the afterburn is being negatively affected by these test conditions.

The effects of target size on impulse load response are represented when comparing the near-field commissioning tests and the final near-field tests results. The commissioning tests used a target plate that was 35% smaller in area than the final test configuration and commensurately produced 28% lower impulse for the 5:1 D:H ratio shallow buried threat. Both (Tremblay 1998) and (Held 2004) reported that the blast load varies exponentially across a target, thus this is as expected. Reviewing and comparing the phase load contribution between the commissioning and final research tests it can be seen that Phase Three loading is mostly affected nearly halving in percentage load contribution as the target plate size is reduced. As the commissioning test configuration had a target assembly that was 7.4 kg lighter than the final research test target assembly thus, even though the test target configurations are similar, making direct value comparisons between the actual measured target response force and impulse are not recommended.

5.3.2 Conclusions

For shallow buried blast, soil ejecta only plays a load contributing role in the partitioned Phase One loading for this research target geometry. The detonic gases following the blast front, creating the proposed reflected pressure Phase Two loading, push the soil ejected by the short duration buried blast laterally off and around the target face after the blast front impacts the target. The blast bulges laterally and spreads across the target and then moves around the sides similar to an expanding balloon as reported by various authors (Cooper 1996c, Grujicic, B Pandurangan et al. 2007, Ramasamy, AM Hill et al. 2009, Braid 2002, Tremblay 1998).

The proposed three loading partitioned sources for Phase One, Phase Two and Phase Three loading are defined respectively as; the initial soil ejecta formed from the soil cap and small surrounding area around the charge combined with the blast front over-pressure, the initial expanding detonation products and lastly the soil and target quasi-constrained reflected pressure enhanced with afterburn. These were discussed and verified with respect to the target force-time response and impulse results obtained from the commissioning and final

research tests. The black detonation products recorded on the high speed video from the PE4 test charges confirmed there are detonation products available for afterburn (Cranfield Course 2009). The Phase One loading impulse correlated well to the soil cap plus additional surrounding soil momentum implying that the blast front overpressure gives only a minor load contribution in terms of target response force impulse.

Trends with changing charge D:H ratios were identified in both the total and the partitioned phased target force time response. Peak target response net force and total target response impulse decreases and charge D:H ratio decreases. The partitioned phased impulse also changed when either D:H ratio or SOD was changed. Partitioned Phase One, Two and Three impulse load decreased as D:H ratio decreased. As the SOD is reduced from intermediate to near-field, the relative contribution of the target response Phase One and Two decreased while that of Phase Three increased for the D:H 5:1 charge ratio. The near-field blast positive phase duration increase is less than was expected and is only 7% longer than the intermediate-field duration at 871 μs. The total near-field target response impulse generated from a shallow buried blast was 46% higher than the total impulse generated by the intermediate-field target.

The test configuration and charge geometry were noted to affect the peak target response force and duration. The test side-on pressure probe configuration affected both the peak force and the positive phase duration. This test configuration had increased target mass and thus inertia and the probe increased the wetted target area.

5.4 Shallow Buried Blast NIR Emission

NIR emission-time measurements were conducted as an additional method to determine the occurrence of afterburn with the intermediate and near-field blast tests. These measurements were seen as exploratory and were not executed with scientific vigour. This led to variability in the results making additional research findings in terms of partitioning difficult from the current data. These data were similarly processed as other data presented in this work to extract total and partitioned data. Due to fluctuations in light output in terms of sensor

output voltage the signals were normalised before processing as discussed in Section 4.6.

5.4.1 Analysis

The analysis of the NIR emission results are presented in four sections. These are; (1) NIR light emission-time trace (morphology) phasing, (2) total and partitioned light emission duration analysis and (3) normalised light emission integration results. Although the variability of the NIR emission results are such that clear total and partitioned trends cannot be clearly identified, these data are presented and analysed to look at the potential benefits of this method and to confirm afterburn as part of the third blast-loading phase.

NIR shallow buried blast light emission measurements were taken with three narrow band (870, 800 and 950 nm) centred wavelengths and a single broad band (450-1,150 nm) NIR sensors. Only the broad band (Sensor 4) is presented and discussed here with the exception of a single combined sensor plot. Due to experimental exploration a limited number of useable data sets was obtained. Where more than one data set for a test configuration was obtained the average value is used and the standard deviation is noted. As the output is simply a voltage-time plot each test result was normalised to the peak output. Due to this averaging the peak normalised values do not always equal one.

5.4.1.1 NIR Emission Morphology

Figure 138 presents a combined plot of a shallow buried blast as captured by all four NIR sensor's output voltage-time traces for an intermediate-field face-on pressure test configuration with a charge D:H 3:1. The trace duration was limited by the oscilloscope to a maximum of 3,500 points. It is thus not known if there are any additional light output events occurring later. The NIR output is a voltage record of events that release electromagnetic signals in the 450 to 1,150 nm bandwidth. These are all within the NIR spectrum. The sensors were angled downwards and were roughly aligned to the centre of the soil above the shallow buried charge. As such this data does not show light emission from the blast impact other than that reflected off the soil surface or the edges of the

target plate as the blast front expands. The difference in voltage output between the four sensors is clearly seen. Three temporal phases are clear in Sensor two, three and four outputs. They are also present in Sensor one's output and are visible when the signal is normalised.

(Gelfand, Silnikov 2004) used photo detectors and obtained similar morphological light output plots for cylindrical free-in-air charges of TNT, RDX plasticiser mix (95% RDX) and RDX. The sensors used for this work captured much longer wave lengths at 1.1 µm. The RDX plasticiser explosive is similar to and can be considered equivalent to C4 explosive based on the RDX content (Cooper 1996c). According (Gelfand, Silnikov 2004) the first peak is due to the detonation wave break out. The second peak is due the detonation products expansion. The third peak is due to afterburn effects. The third peak recorded by these authors occurred later (ca. 1 ms), was much smaller than those recorded here and the signal went almost to zero before the start of the afterburn phase.

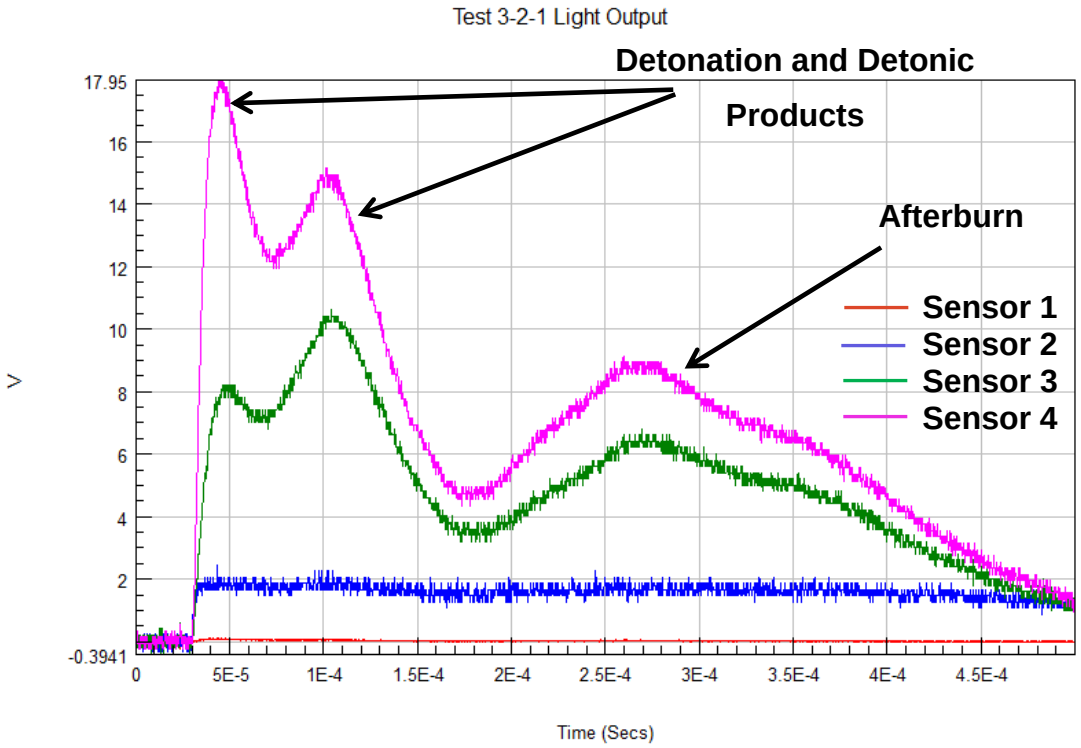

Figure 138: Sensor Voltage- Time Plot Face-On Pressure Configuration All Sensors

The (Gelfand, Silnikov 2004) TNT charges exhibited two phases whilst the RDX charges appeared to only have one initial blast phase before the onset of afterburn. The TNT tests also recorded much higher afterburn output than the RDX and RDX plasticiser tests. This as ascribed by the authors as due to the oxygen poor composition of TNT compared to RDX producing more detonation products that are suitable for afterburn.

The shallow buried blast NIR data has this same three phased light emission morphology. The primary differences are there are two clear initial phases with the RDX based PE4 explosives used and the third phase starts before the signal reduces to zero. This corresponds to the afterburn initiating earlier while there is still fairly high temperature and pressure from the detonation products expansion phase. The afterburn light output relative to peak light output is much higher than observed by (Gelfand, Silnikov 2004) for free-in-air tests. This is congruent with buried blast as the soil will constrain the gasses creating higher pressure. The target will prevent the gases from being easily dispersed creating the quasi-constrained environment (Smith, Hetherington 1994) that is rich in unreacted detonation products This creates conditions that are more conducive to afterburn than free-in-air tests executed by (Gelfand, Silnikov 2004), thus it can be expected that afterburn will be initiated earlier and be more aggressive with shallow buried blast than observed for free-in-air blasts. These quasi-constrained conditions however restrict blast front interaction with oxygen rich air to that trapped by the blast. As noted by (Edri, Felgun et al. 2012) the detonation products can still react with remaining oxygen in the detonic products to initiate afterburn.

The initial peak observed corresponds with (Gelfand, Silnikov 2004) findings. Based on Bangash's Zone 1 loading (Deshpande, McMeeking et al. 2009b) with shallow buried blast the detonation shock pressures are too high for the soil cap crushing and breaking the cap quickly thus leading to early light break out as part of the initial detonation process. This is then followed by the detonation product expansion leading to initial two-peak morphology. Both of these sequential events are expected and are present in the light output trace. The

effects of the soil cap in reducing the initial detonation NIR emission output and slightly delay the detonation gas expansion resulted in these tests producing such clear two-phased morphology for a RDX based explosive.

The last NIR emission morphology observation is that for side-on pressure the peak pressure pulse coincided with the NIR emission second light output phase whereas for face-on pressure the peak pressure occurred after the second phase NIR light peak. This is due to the loading mechanism differences with the side-on pressure being dependant on the simply measureand passing the sensor whereas for the face-on sensor the peak pressure measured is the stagnation pressure and requires time to build up. The side-on probe also provides a larger reflective surface that reflects light providing for stronger signals than would be the case for the face-on pressure sensor.

As this is a relatively new measurement technique to the Author with little published work on it, the data have a number of limitations. There is large variability in the light output signals between two similar tests. This has been ascribed to variable test set ups as this was seen as an additional measurement rather than a primary investigative tool thus insufficient diligence to ensure exact placement and alignment of the sensors for each test. The general variability in the test set up noted in the previous sections would also contribute to inconsistent results. These causes must be fully explored as aspects such as the effect of ambient light could also play a role. The limited numbers of measurement points restricted the trace lengths and many traces have not returned fully to zero thus identifying trends between test configurations and charge geometry is inconclusive with these data. The sensors are not point but rather area sensors and thus record a larger surface of light.

Despite these limitations this data does provide insight and verification of the near-field blast loading processes and thus the NIR emissions are analysed in terms of total and partitioned shallow buried blast loading as proposed in Section 5.1.1.3 and applied in Sections 5.2 and 5.3.

5.4.1.2 Total and Phased Light Emission Duration

The normalised NIR emission durations are shorter than the force and pressure-time signals as they were limited by the data acquisition to a maximum of 3,500 points. Sampling speed varied between 5 to 10 MHz. Figure 139 presents the total and partitioned phase durations extracted from Sensor 4. The total durations are longer than that observed with both face-on and side-on pressure. This is partly due to the break out occurring and being recorded before the blast front has had time to reach the sensor and partly because there are reacting products or blast ejecta activities that are releasing NIR light. As noted above many traces had not reached zero so analysis of the actual total NIR light emission durations is not possible**.**

Figure 139 shows some of the test variability noted previously, such as the intermediate-field D:H 5:1 shallow buried test (3-3) that only produced two light emission phases whereas all the other intermediate-field records show three phases. For the near-field D:H 5:1 tests (4-1) only two NIR light phases were recorded. This is due to the ejecta that develops and is pushed outwards earlier and that is thicker due to the smaller encapsulated volume, shielding the later light emissions. The overall signal voltage level was also greatly reduced for the near-field tests resulting in amplification of noise. Congruent to this the NIR emission duration for the near-field tests was half that of the intermediate-field.

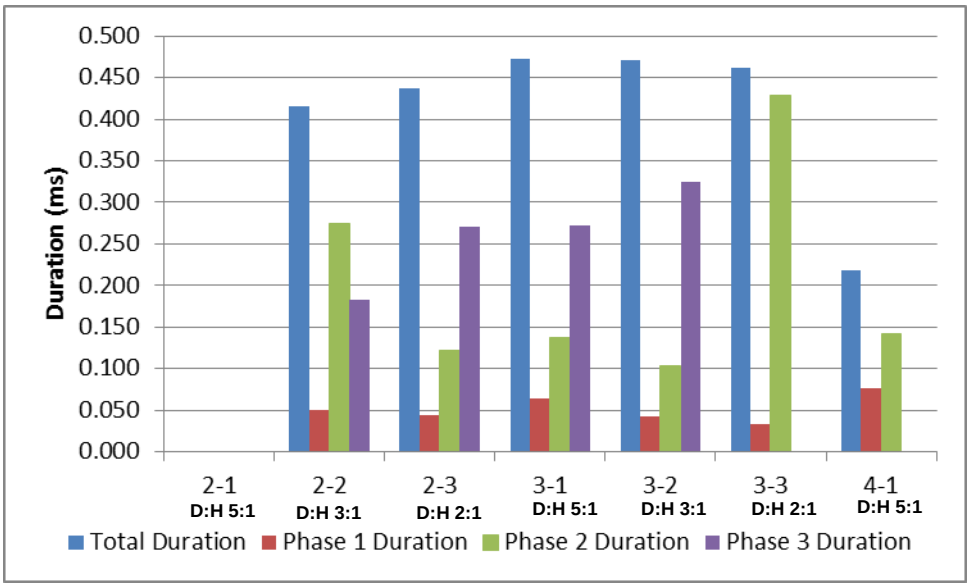

Figure 139: Total and Partitioned Light Phase Duration (Sensor 4)

5.4.1.3 Peak Light Emission

Due to the smooth signals recorded it was possible to manually identify and extract each of the normalised peaks for each of the three phases. Figure 140 presents the normalised average phase peaks for sensor.

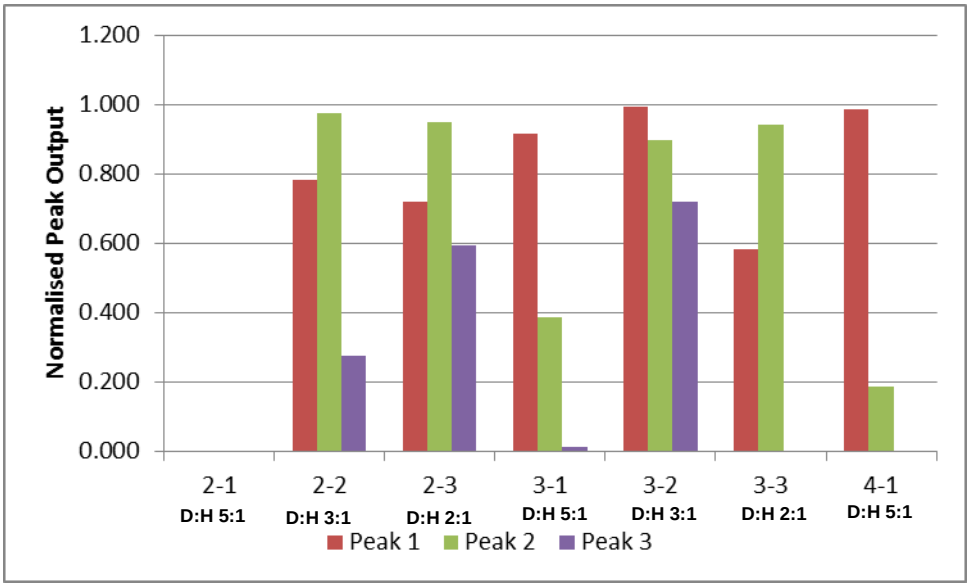

Figure 140: Averaged Normalised Peak NIR emission Output (Sensor 4)

Due to the limited number of test data sets and repeat tests it is difficult to identify conclusive trends. For the intermediate-field side-on pressure test configuration, Phase One NIR emission was lower than intermediate Phase Two NIR emission output. There were no phase trends visible with the face-on pressure test configuration. Four of the five intermediate-field Phase Two peak NIR emission outputs were similar. This indicates that the detonation product loading phase was similar for all D:H ratio charges for shallow buried blast. Thus differences in target response loading should be due to Phase One and Phase Three loading.

Where present the recorded Phase Three normalised peak was the lowest of the three phases. This supports the position that it is afterburn and not detonic shock and / or the detonation gas expansion following the shock. Ejecta formation variability can cause differences in NIR emission emissions seen by the sensor assembly, thus in some cases no Phase Three is visible or the peak emissions are reduced.

5.4.1.4 Integrated NIR emission

Figure 141 presents the total and partitioned normalised light emission area calculated by integrating the normalised light emission-time curve. Figure 142 presents the partitioned phase percentage contribution to the total light emission.

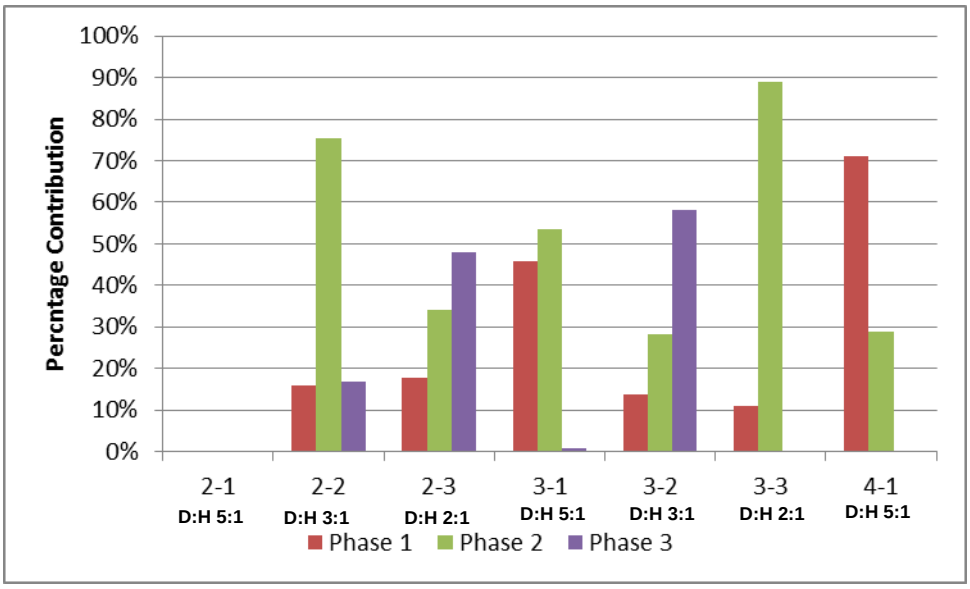

Figure 141: Averaged Normalised Light Output Total and Partitioned Area (Sensor 4)

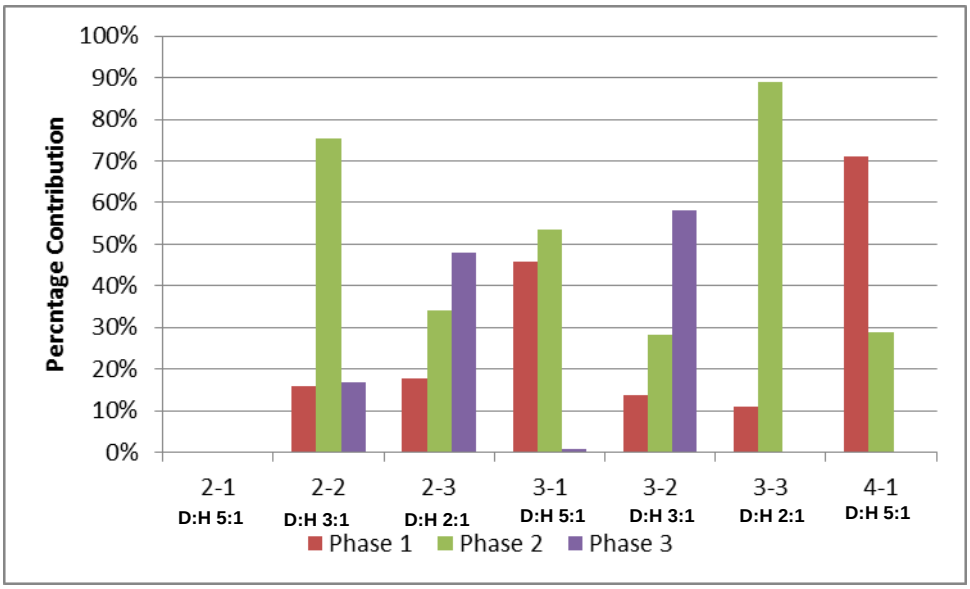

Figure 142: Partitioned Light Averaged Phased Area Contribution (Sensor 4)

These plots highlight the variability of the results and the limitation of using these data sets for near buried blast analysis where the NIR emission output is obscured by the ejecta. The data however show that the NIR emissions, if recoded consistently, should provide additional information on shallow buried blast when used at intermediate and free-field shallow buried blast.

5.4.2 Conclusion

Using the (Gelfand, Silnikov 2004) analysis of three phased explosive NIR emissions, the shallow buried blast NIR emission traces show there are three temporally separated blast phases. These phases correspond to the three shallow buried blast load phases proposed in Section 5.1.1.3. These test results, using RDX based explosives, show a clear initial two phase response compared to limited published work by (Gelfand, Silnikov 2004) that only noted a single initial peak for RDX based explosives. This is due to the research tests being shallow buried resulting in the soil cap reducing the detonation breakout intensity through masking of the light emitted and delaying the detonic gas expansion.

Based on the NIR emission results Phase One is the initial detonic breakout, Phase Two is the gas expansion and Phase Three is afterburn. The results presented in Section 5.1 and Section 5.3 confirm that the afterburn is enhanced with reflected pressure which is not directly captured by the NIR sensors. The second phase is detonic product expansion and reactions. The last phase is afterburn of the entrapped blast products.

The light emission time traces, when plotted with the side-on and face on pressure traces, indicate that side-on pressure is driven by the detonation gas pressure whereas the face-on pressure is driven by momentum of the ejecta and expanding gases. This corresponds with presented blast load theory (Smith, Hetherington 1994).

NIR emission results show there are changes in the partitioned contributions with changes in charge D:H. However due to experimental set up methodology shortcomings combined shallow-buried blast morphology variability, prevented

clear trends from being identified between the different test and threat configurations. The NIR application appears to be limited to intermediate-field shallow buried blast load and is not suitable for near-field blast load research due to light masking effects of the ejecta for the wave lengths recorded. The NIR sensors however could be used to further research and quantify shallow buried and free-in air blast.

5.5 Shallow Buried Blast Load Side-On and Face-On Pressure

To quantify the contribution of each defined loading phase the total and partitioned side and face-on pressure for both intermediate and near-field targets that were generated from shallow buried blast are analysed and discussed in terms the three blast-load phases proposed in Section 5.1.1.3.

5.5.1 Analysis

The analysis and discussion of the intermediate and near-field target pressure results in terms of the proposed three blast loading phases is presented in four sections. These are; (1) side-on pressure morphology in terms of peak and time-to peak pressure, duration and temporal phasing for the side-on and the face-on pressure, (2) total and partitioned positive phase specific impulse and (3) total and partitioned phased specific (pressure) impulse. Both computational model and test data are presented and discussed.

5.5.1.1 Side-On Pressure Morphology

Side-on test pressure in the intermediate-field is compared to side-on near-field model pressure in this section as there were no face-on pressure computational model results for the intermediate-field. There were no near-field side-on pressure tests due to technical challenges with the probe sensor as discussed in Section 0. Despite this mismatch the three phase morphology analysis and discussion is applicable and relevant irrespective of the SOD differences.

In analysing the side-on target pressure morphology data the near-field model results are compared to intermediate-field test results as it was not possible to implement side-on near-field pressure measurements for the executed tests

with the sensors available at that time. Due to the experimental variability a single 3:1 D:H ratio test pressure trace that was typical of a Friedlander (Smith, Hetherington 1994) type morphology was selected and used for this comparison. The discussion that follows is applicable to the other D:H ratio threat test as they had similar Friedlander test traces with comparable pressure-time morphology that correlate to the proposed three blast phases. Although non-spherical blast changes as SOD increases (Baker 1973a) the modelling and test results show that the near-field (72 mm SOD) target is sufficiently far away from the blast to have three distinct pressure loading phases that can be discussed in terms of the proposed three blast loading phases. As the SOD increases to the measured intermediate-field (200 mm SOD) these pressure phases will become more distinct as the physics that drive each are different.

Figure 143 Presents the normalised near-field computational model side-on pressure-time trace for the 3:1 D:H ratio threat as recorded at 65 mm SOD with the target at 72 mm SOD, thus 5 mm proud of the target face and the 3:1 D:H ratio blast test side-on pressure-time trace at a sensor SOD of 195 mm and the target at 200 mm SOD, also 5 mm proud of the target face. The plots are normalised to aid in the comparison as they were recorded at differing SODs. The model trace starts earlier as the SOD is closer. Both traces exhibit three phases with the peaks numbered 1, 2 and 3 respectively. Peak one corresponds to Phase One loading and is the blast front which is a combination of the spoil ejecta and blast over-pressure. The second peak correlated to the Phase Two loading which is due to detonic gas expansion. The third pressure peak corresponds to the quasi-constrained environment reflected pressures.

For these test results the third peak is augmented by afterburn. Three additional peaks, 4, 5 and 6, have been highlighted in the test and the modelling pressure-time traces. Peak 4 is a pressure spike that was recorded in seven of the ten side-on pressure traces captured during testing, peak 5 is the bow wave shock that appears in the model and peak 6 is a pressure artefact from the axisymmetric model set up.

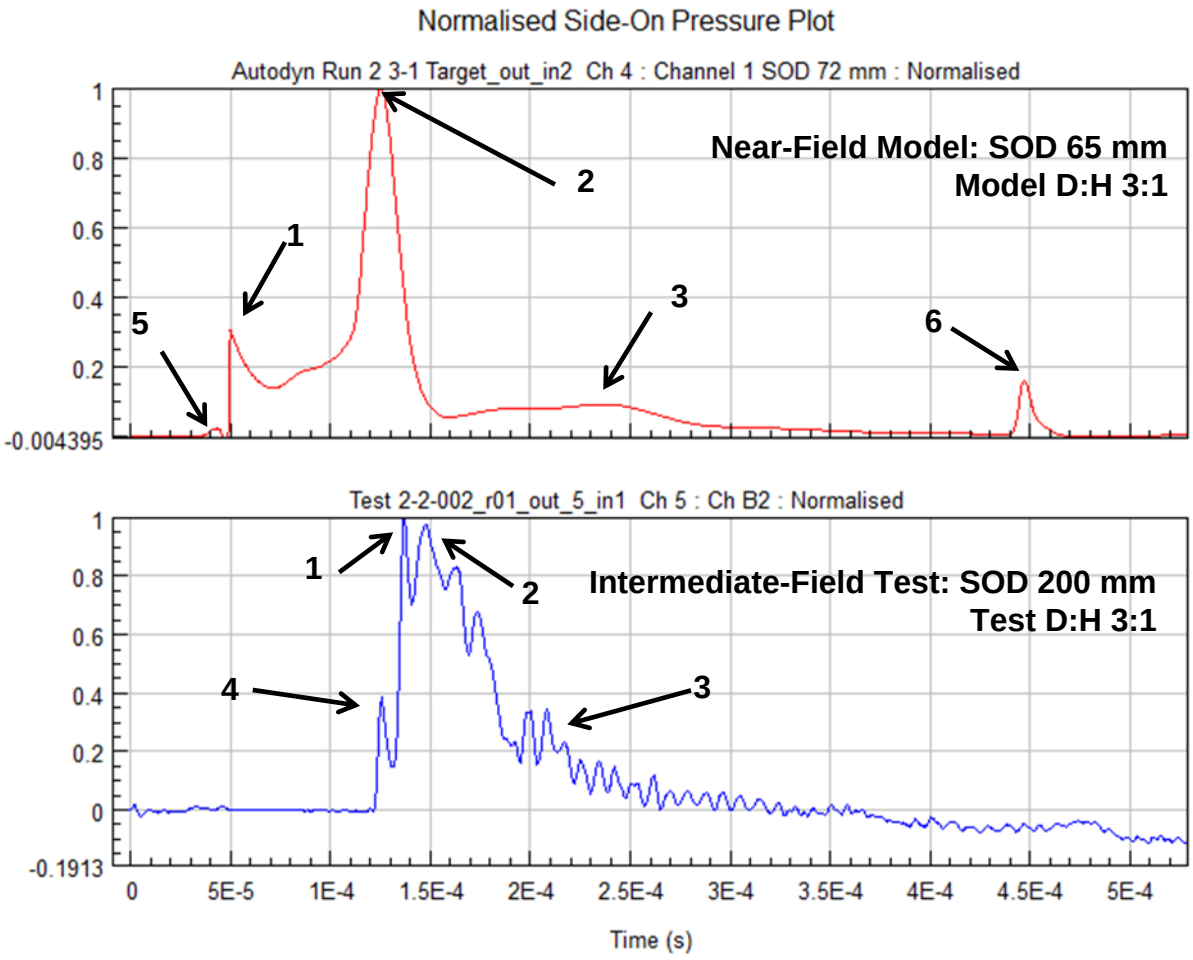

Figure 143: Near-Field Model and Intermediate-Field Target Side-On Pressure

These pressure traces are now compared in more detail in terms of the proposed three shallow buried blast loading phases:

Phase One loading is characterised by an almost vertical pressure front that is typical for blast overpressure and is seen in both the model and the test trace. This is visible in both the model and test side-on pressure traces. This phase's loading is characterised with blast over-pressure and soil cap ejecta with additional soil surrounding the charge that is ejected due to charge geometric effects. The soil ejecta will not be quantified by the side-on pressure sensor unless the blast front impact was angled. If this occurs it is manifested with much higher peak pressure followed by longer and higher phase durations. This did occur during testing due to test set up variability and in particular the flatness of the charge relative to the soil surface. The effect of this was reduced

when there is a near-field target which increases pressures due to the build up from the expanding gasses against the target, smoothing out angled blast front impact effects on the side-on pressure probe. Phase One ends with a rapid decrease in pressure that declines between 5% to 30% of the peak over-pressure. The lowest Phase One end pressures were produced by the D:H 2:1 ratio charge tests.

Phase Two loading for the model shows a decrease in pressure followed by a small rise and plateau and then only a peak which is three times higher than the first peak. The test data trace differs as there is a much sharper decrease in pressure and an almost immediate increase again to the second phase peak. The rate of increase is however less than that observed with the initial blast front and appears similar to the model. The rate of increase is higher than the rate displayed in the free-field ejecta Phase Two reflected detonic product expansion pressure. The peak pressure achieved is less than the first peak. There was only a single intermediate test side-on pressure trace that exhibited a second phase pressure that was higher than the first phase pressure peak. This was for a D:H ratio 2:1 test charge. The test second peak was also only 7% larger, whereas the model gives a peak that is three times larger. The test pressure trace has numerous small peaks superimposed on the pressure trace. This is due to ringing in the probe from soil impacts.

The model pressure trace presents the pressure build up more slowly after the first peak and is possibly linked to the JWL model and parameters used and the soil-air Eulerian model approach. Based on the free-field (ejecta) tests it was determined that at the lower SOD the soil is still accelerating and has not reached its peak velocity. This implies that the pressure behind the front would be higher and should not decline and remain low for a long period after the first blast peak before increasing again. This is mirrored in the intermediate-field test results where the side-on pressure does decline briefly after the blast front but rises again at a rate similar to the model second peak and much sooner than the model predicts. This test morphology is occurring at a higher SOD than the model where the blast front is already decreasing in velocity and the gas

expansion, with its lower density, takes longer to generate higher pressures against the target. It is expected that at lower SOD's this decline would be even less visible as the phases would not have time to temporally separate more.

Phase Three loading is proposed as being driven by a combination of pressure reflection due to the soil and target that is enhanced by the target and afterburn of the detonation products. The model does not include the after-burn effects thus should and does have lower pressures. The model predicts a rapid pressure decline from the second phase peak followed by a gradual increase and decrease occurring over a period that is longer than the combined predicted Phase One and Two loading. As afterburn is not a detonic event, the release of pressure is much slower than would be the case with a detonation or the rapid gas expansion that has high velocity gases. The gas velocity created by this slower event is much lower and is represented by the much slower pressure increase and decrease. The gradual model Phase Three pressure profile is almost like that of a traffic calming road bump. The model predicts an additional pressure spike (number 6). This origin of this peak is thought to be a reflection driven by the D:H ratio of the charge as it is only present with the 5:1 and 3:1 test charges and not the 2:1 ratio charge. The model predicted Third Phase loading pressure increases becoming larger with shorter duration as the charge D:H decreases and the spike occurs earlier before disappearing with the 2:1 D:H ratio charge. The increasing reflected pressure predicted for decreasing D:H ratio corresponds to more blast products being released laterally as the charge length increases resulting in the higher reflected pressure release after the detonic expansion. This is due to the larger volume of gasses released laterally into the crater as compared to the larger D:H ratios that release considerably less gases laterally. The last pressure spike (number 6) was not seen in any test data; however it could be hidden by the afterburn effects that are occurring with the tests. The end of Phase Three loading is the end of the positive pressure phase and is determined when the relative pressure measurement becomes negative.

Figure 144 presents the average and standard deviation of the intermediate-field blast front spike pressures (Peak 4). The blast front pressure spike (number 4) varied between a low of 0.62 and a high of 2.4 MPa. The variability in the test results prevents confirming the model predicted pressure trends however the highest average pressure was recorded by the 2:1 D:H ratio test charge and the general data averages seem to confirm there is indeed an increasing overpressure trend. The variability present in the data is evident in the standard deviations. The precursor bow-wave shock (peak 5) predicted by the model was only 0.5 MPa and was not predicted at the 195 mm model SOD. The bow-wave shock also has a much smaller gradient than that exhibited by the recorded pressure spike. This bow wave shock was not visible in the intermediate SOD test data, correlating to the free-field ejecta model side-on pressure results. This could be due to the blast front decelerating by the time it reaches the intermediate-field and the bow wave shock pressure is reduced. The predicted bow wave pressure values are considerably smaller than the pressures measured with the tests.

Broadly speaking the peak over-pressure spikes correlate to the free-field peak blast pressures which averaged from 1.612 to 2.652 MPa. Thus the spike appears to be the shallow buried blast front. The following pressure rise to peak over-pressure is extremely fast and appears as though it is part of the blast over-pressure front. This appears to be the pressure of the soil and detonic expansion gas mix attached to the rear of the blast front and due to the high velocity and the target placed just past the sensor, the combined side-on pressure reflection is equivalent to a typical blast overpressure pulse. This phenomenon could be what is presented by the computational model but the temporal split between the first blast front and the immediately following pressure is too large to be comparable. For further processing and analysis the spike was included in the Phase One blast loading. It is felt appropriate as the pressure morphology appears the same and has a much steeper gradient than the reflected pressure build up that follows the peak pressure

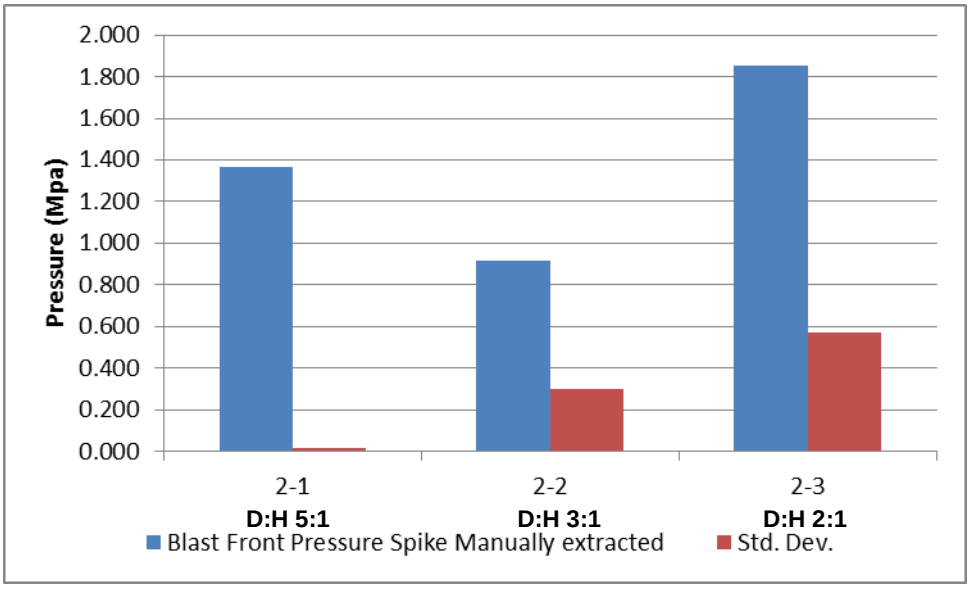

Figure 144: Average Intermediate-Field Test Blast Front Spike Pressure

5.5.1.2 Peak Pressure

Figure 145 compares the shallow buried intermediate-field target and intermediate-free-field side-on peak pressures to the free-field (ejecta) peak side on peak pressures. Test 2-1 to 2-3 are decreasing D:H ratio tests starting at 5:1 and ending at 2:1. Both the commissioning as well as final research free-field ejecta test result are presented. The final research free-field ejecta test are annotated by an E and the applicable D:H ratio. The commissioning free-field test are annotated by a C and the relevant charge D:H ratio. Included in these data is the free-field ejecta model, as modified to remove the shock front separation (see Section 4.2.1.1), result for a 5:1 D:H threat also at the intermediate-field SOD of 195 mm. The model is annotated by a MM and the relevant charge D:H ratio.

The results show that with a target over a shallow-buried blast the side-on peak pressure increases on average 2-3 times that measured without the target (free-field ejecta). Although the data is variable the target side-on pressure shows decreasing peak pressures while the free-field peak pressures show an increasing trend as the charge D:H ratio decreases. This implies that although a shallow buried smaller D:H ratio charge generates higher free-field side-on pressure the presence of a target results in the smaller D:H ratio charge actually

generating a lower peak side-on pressure. This pressure just off the face of the target is actually a reflected pressure and corresponds to the decreasing impulse load transferred to an intermediate-field target by smaller D:H ratio charges (Section 5.3.1.4).

The commissioning ejecta test peak over-pressure correlated well to the computational model but was 30% lower than the final research eject test peak pressures. This is ascribed to the variability in the test results due to the test charges not being perfectly parallel with the soil surface and relatively small test data pool, in particular for the D:H 3:1 tests which has only two test data sets.

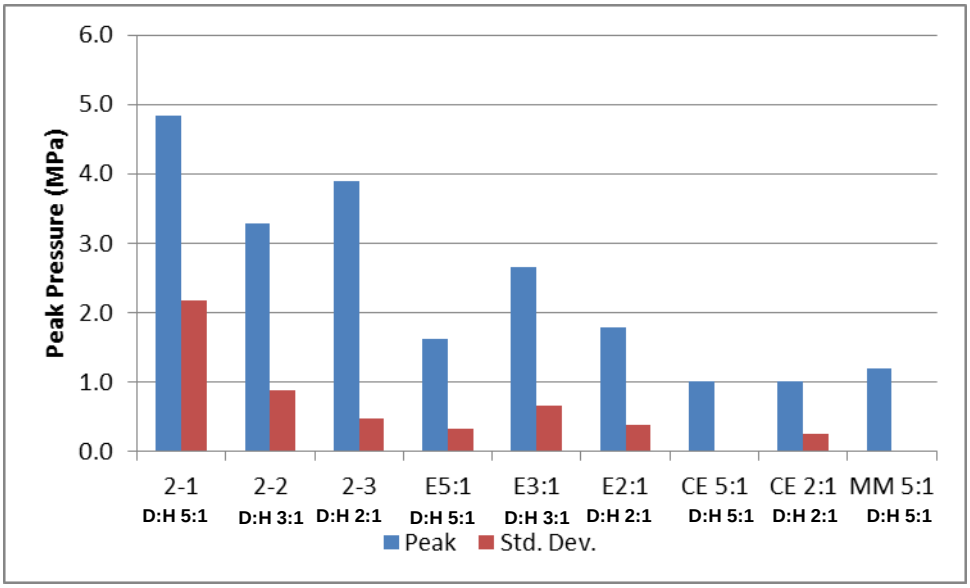

Figure 145: Side-On Pressure Peak Intermediate Field Target vs. Intermediate Free-field Ejecta and Model

Figure 146 presents the average peak pressure and standard deviation, where more than one test point was executed, for each final research shallow buried intermediate and near-field target blast test. The tests series 2 refers to the side-on pressure test configuration and test series 3 and 4 refers to the face-on test configuration. Test series 2 and 3 are with an intermediate-field (SOD 200 mm) target and test series 4 are for the near-field (SOD 72 mm) target. The test charge D:H ratios follow in decreasing ratio order thus D:H 5:1 is -1 test point and D:H 3:1 is -2 test point and D:H 2:1 is -3 test point. The pressure test

variability discussed above is clearly visible in the large standard deviation recorded for these tests.

The averaged data shows that the intermediate-field face-on pressure varies from eighteen to thirty-six times more than the equivalent charge side-on pressure as the DH ratio decreases. This ratio is higher than that predicted by (Smith, Hetherington 1994) who calculated from simplified first principles around two to eight times higher face-on (reflected) pressure. These authors did however note that for near-field blast the loading could be as high as twenty times due to gas disassociation effects not taken into account with the calculations presented. These predictions also did not take burial of the charge into account. It can be surmised that this difference in peak over-pressure ratio between side-on and face-on pressures of up to 80% more is due to burial effects and charge geometry effects.

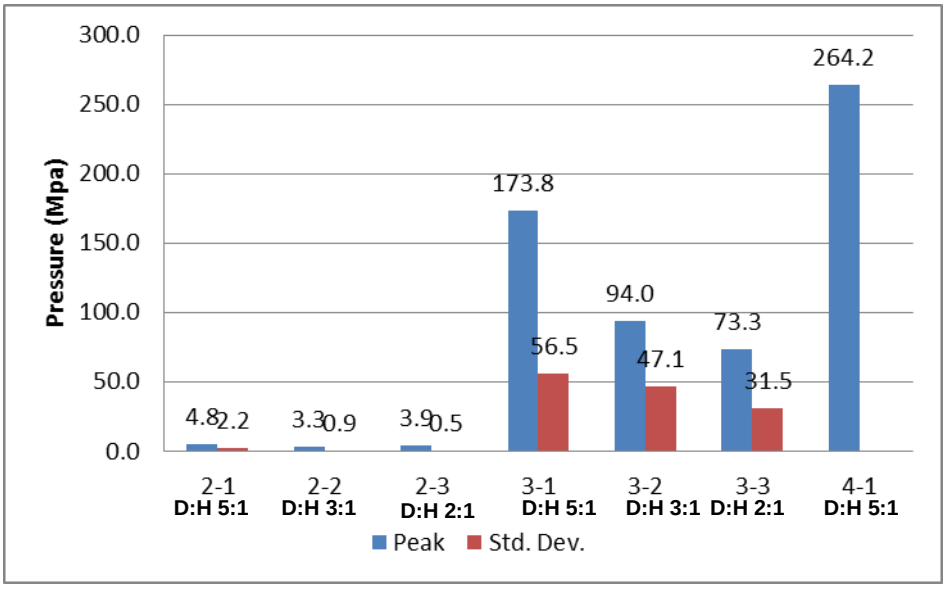

Figure 146: Peak Side and Face-On Pressure

Based on the proposed partitioned loading phases (Section 5.1.1.3), the difference in peak side-on and face-on pressure ratios will be largely due to the focussing effects of the soil on the detonation gas expansion momentum and the Phase One side-ejecta and soil cap momentum. These results illustrate the large loading increase achieved with the soil and gas momentum or dynamic motion of the blast products compared to straight gas pressure effects. Using

the single D:H 5:1 near-field face-on pressure results and converting it to side-on pressure by assuming the same ratio is applicable as was determined at the intermediate-field, a near-field side-on pressure of 6.95 MPa is estimated. This compares well with the side-on pressure model D:H 5:1 charge predicted blast front peak pressure of 7.04 MPa (Peak 1 Figure 143). Although not conclusive as this is only for a single test it does give additional confidence in the results obtained.

The face-on intermediate-field data shows a decreasing average peak pressure trend as the charge D:H ratio decreases correlating to the target response impulse results in Section 5.3.1.4. This trend is also weakly present in the average side-on peak pressure test data. This corresponds with the target response impulse discussed in Section 5.3.1.4. This same trend is present but not as clear with the side-on pressure test configuration with the 5:1 and 2:1 D:H ratio charges following this trend but with the 3:1 D:H ratio charge showing a larger decrease than the D:H 2:1 tests as was seen with the face-on tests. This tendency appears to be present in the near-field computational model results with the 3:1 D:H ratio peak initial pressure being lower than both the 5: 1 and 2:1 threats. The model however predicted that the 2:1 ratio would have slightly higher side-on pressure than the 5:1 DH ratio charge. This is not seen in the test's data and is assumed is an artefact of the implicit methods applied by Autodyn® resulting is some small variations between each solution rather than a physical trend. The three D:H ratio model's initial peak pressures varied by no more 180 kPa (3%) while the test data varied by 800 kPa (17%) between the lowest and highest first peak pressures. This trend was not seen in the target response impulse where the 3:1 D:H ratio impulse decrease fell between the 5:1 and 2:1 charge D:H ratios.

Using the approximation of the side-on pressure calculated from the pressure ratio between side-on and face-on measured in the intermediate field, decreasing the SOD from 200 to 72 mm increases the side-on pressure by 52%. As the blast front velocities are similar as 72 mm and 200 mm SOD's it is assumed that the difference in the side-on pressure is primarily due to

increased detonation product's pressure within and immediately behind the blast front rather than ejecta mass. This corresponds with the Phase Two loading increase seen in the target response impulse discussed in Section 5.3.1.4.

5.5.1.3 Time to Peak Pressure

Figure 147 presents the time to Phase One peak pressure (Peak 1) for both face-on and side-on pressures for both intermediate and the single near-field tests. Where more than one measurement was taken the averaged time to peak and the standard deviation is presented. Time-to-peak is defined as the time from initiation of the charge to the time that peak pressure is achieved. As expected the 72 mm SOD had the lowest time-to-peak at 76 µs. The intermediate-field side-on pressure time-to-peak show a clear trend with decreasing values for decreasing charge D:H ratios. The face-on pressures generally show a shorter time to peak than that achieved with the side-on pressure. This is due to the different loading mechanisms of the respective sensors. The face on loading is primarily due to impact loading of the blast front and the side-on pressure is a combination of blast front overpressure combined with a reflected pressure associated with the soil ejecta combined with and following the blast front.

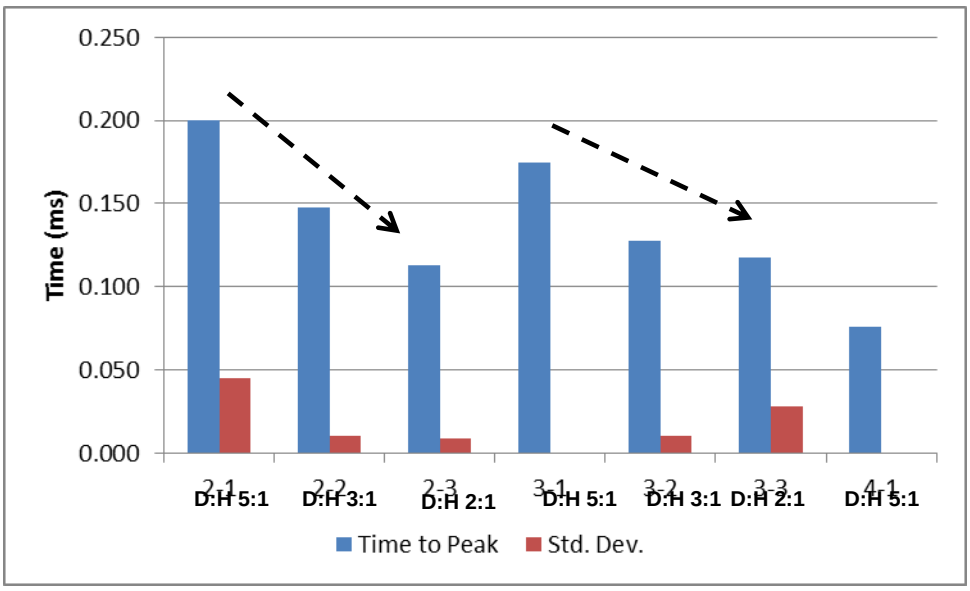

Figure 147: Time-To-Peak Pressure

The increasing velocity trend corresponds with the measured blast front velocity trends which increase with decreasing D:H ratios and with the computational modelling results (Section 5.1.1.1 and Figure 113). Figure 148 presents the averaged blast front velocity for the intermediate (2-X and 3-X) and near-field (4-X) blast tests as well as the three near-field computational models (MM-X). The blast tests and the computational models data points are presented in order of decreasing test charge D:H ratio starting at 5:1 and ending at 2:1. The model data is prefixed by an M followed by the D:H ratio of the model charge. The average velocity is based on the start time of the pressure response calculated from initiation of the test charge divided by the relevant SOD.

These data clearly show the increasing blast front velocity with decreasing D:H ratio trend noted above for both the test as well as the model results. The model data also predict a higher rate of decrease in the average velocity when moving from 3:1 to 2:1 charge ratios. This trend is replicated in the face-on-pressure average velocities but not the side-on pressure results. This trend could be from the reduced soil cap mass combined with charge geometry effects that result in higher blast front velocities. (Cooper 1996c) discusses the end effects for longer cylindrical charges in terms of the work done by the end of the cylinders based on the work by Gibbs and Popolato (1980) and Cook (1971). The work done by the pressure is defined by various means such as dents, compression and sample plate velocities and indicates that as the D:H decreases the work done by the explosive ends increases as an asymptote flattening at a D:H of 1:2 (L/D of 2 where L is the charge length and D is the charge diameter). Although this trend is not mirrored in the target force response and side-on pressure specific impulse results it is mirrored in in the face-on pressure specific impulse and in the average blast front velocities.

The near-field 5:1 D:H ratio charge average velocity at 1,242 m/s was close to the intermediate Field D:H 5:1 ratio charge face-on pressure test configuration average blast front velocity at 1,373 m/s but was lower than the average side-on D:H 5:1 test configuration which was 1,639 m/s.

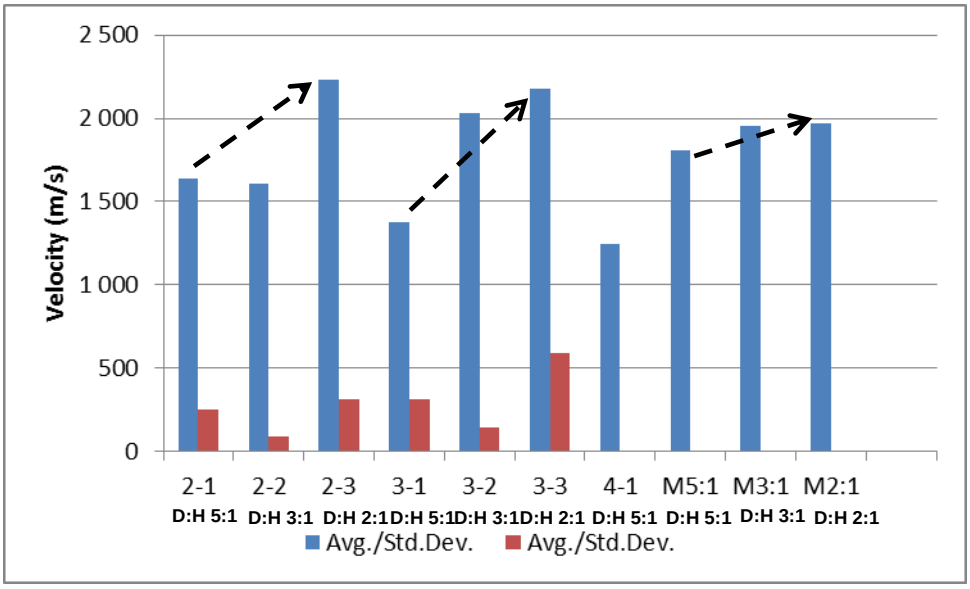

Figure 148: Calculated Average Velocity

5.5.2 Total and Partitioned Positive Phase Pressure Duration

Figure 149 presents the total and partitioned phase durations for the side-on and face-on pressure as extracted from the positive blast pressure phase. The tests series 2 refers to the side-on pressure test configuration and test series 3 and 4 refers to the face-on test configuration. The test charge D:H ratios follow in decreasing ratio order thus D:H 5:1 is the X-1 test point and D:H 3:1 is the X-2 test point and D:H 2:1 is the X-3 test point. The data also includes the single 5:1 near-field face-on pressure test data (4-1). The 5:1 D:H charge ratio intermediate-field test configuration (3-1) only had two pressure results and these pressure-time traces were anomalous to all other traces exhibiting only a single very short loading pulse. These results are deemed unusable other than for time of arrival and peak pressure. The data for the intermediate-field face-on pressure (3-1) duration is included in Figure 149 for completion. Cognisance is taken that the soil impact noise (ringing) in the sensor trace made it difficult to accurately determine the end of the positive pressure phase.

The intermediate-field side-on pressure total positive duration, which averaged between 0.208 and 0.310 ms as the D:H ratio decreased was shorter than the face-on pressure positive duration which average between 0.332 and 0.397 ms as the D:H ratio decreased. Overall the side-on pressure averaged a total

positive durations of 267 µs while the face-on averaged 287 µs for all D:H ratio test charges. This shorter side-on pressure duration is thought to be due to the pencil probe projecting into the blast field and deflecting some of the blast (Phase One soil ejecta). This correlates to the deflecting effects the probe has on the soil cap ejecta and impulse discussed in Section 5.3.1.4.

The target force-time response starts at from 0.235 to 0.310 ms after detonation initiation, thus the pressure loading is still acting on the target by the time the target starts to respond. The side-on and face-on pressure phase ends during the middle of the Phase Two force-time response of the target.

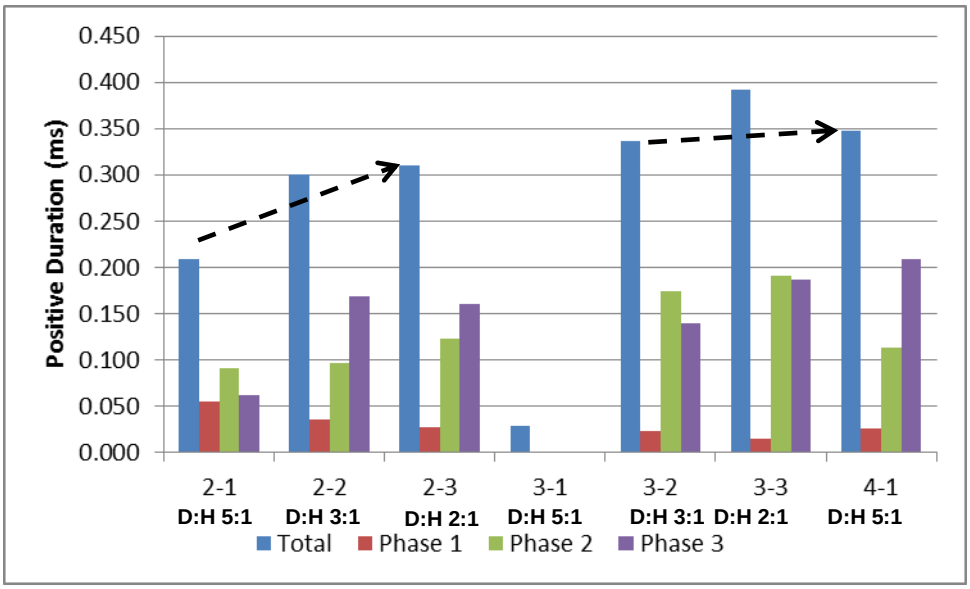

Figure 149: Total and Partitioned Phased Positive Phase Pressure Duration

The free-field ejecta test results gave an average of 0.187 to 0.387 ms total positive phase pressure duration for all D:H ratio test threats (See 5.1.1.2 Figure 121). There were test execution variables resulting in off-perpendicular blast impacts on the sensor that affected the free-field ejecta pressure measurements. These angled impacts added a reflected pressure component that increased the pressure pulse duration. These angled impacts were also present with these target tests, however the effect was smoothed out by the reflected pressure building up from the target face. This makes it difficult to extract trends regarding the effect of a target on the total positive pressure pulse duration and can only be said to appear to be around a 50% increase

from free-field conditions by ignoring data with apparent large pressure reflections.

The test data indicate increasing total positive pressure duration with decreasing D:H ratio charges, for both the side-on and face-on pressure test configurations. The total side-on positive pressure duration increases by 49% when the DH ratio decreases from 5:1 to 2:1. The total face-on pressure positive phase duration increases by 17% as the D:H ratio decreases from 5:1 to 2:1.

D:H ratio SOD from intermediate-field (200 mm SOD) to near-field (72 mm SOD) does not appear to materially increase the total positive phase face-on pressure duration. Only a single near-field face on pressure trace was captured and recorded a total face-on positive pressure pulse of 348 µs for a D:H 5:1 test charge. Averaging all the intermediate-field face-on total positive pressure durations gives a slightly longer duration at 364 µs. The longer average intermediate-field face-on pressure duration is due to the decreasing D:H ratio charges which are included in the data. For shallow buried blast this means that the closer a target is to the blast source the target loading increase is more from increased blast pressures than from containment of the blast. To achieve this, the velocity of the blast front will be much higher than that generated by the intermediate-field target configuration.

When reviewing the partitioned intermediate-field face-on pressure durations D:H ratio trends are visible in both the intermediate-field side and face-on peak and partitioned pressures. Total positive pressure duration increases as the charge D:H ratio decreases. For the partitioned phases Phase One decreases while Phase Two and Phase Three durations increase with decreasing charge D:H ratios.

This trend corresponds with the proposed loading phases and the sources of each (Section 5.1.1.3). Phase One is primarily soil cap and surrounding soil ejecta driven and thus as the D:H ratio deceases so does the ejected soil mass. Correspondingly as the D:H ratio decreases larger amounts of detonic gases are pushed laterally and constrained within the crater rather than being expelled

with the initial vertical expansion leading to longer detonic expansion phase (Phase Two). The larger volume of gases left behind provide a larger amount of products to react for afterburn and reflected pressures leading to the longer durations seen in Phase Three. For all test configurations Phase One has the shortest duration which is expected for impact loading from the blast front consisting of soil ejecta and blast over-pressure. Phase Two and Phase Three are longer duration events which is consistent with reflected gas pressure loading.

5.5.3 Total and Partitioned Specific Impulse (Pressure)

Figure 150 presents the total and the partitioned phased specific (pressure) impulse for intermediate and near-field target shallow buried blast tests and for the near-field side-on computational models. The test series 2 refers to the side-on pressure test configuration and test series 3 and 4 refers to the face-on test configuration. Test series 2 and 3 are intermediate-field target (200 mm SOD) and test series 4 is with the near-field target (72 mm SOD). The test charge D:H ratios follow in decreasing ratio order thus D:H 5:1 is X-1 test point and D:H 3:1 is X-2 test point and D:H 2:1 is -3 test point. The data also includes the single 5:1 near-field face-on pressure test data (4-1). The near-field computational modelling total and partitioned results are annotated by M and the relevant D:H ratio.

The 5:1 D:H charge ratio intermediate-field test configuration (3-1) only had two pressure results and these pressure-time traces were anomalous to all other traces exhibiting only a single very short loading pulse. This anomalous data impulse is included in Figure 150 for completion.

Figure 150 clearly illustrates the magnitude difference between side-on and face-on pressures specific impulse. On average, across all D:H ratios, the intermediate-field total face-on pressure specific impulse is eleven times the side-on pressure specific impulse. The ratio between the face and side-on pressure appears to increase as the charge D:H decreases with ten times for the 3:1 and twelve times for the 2:1 D:H ratio charges. This corresponds to the increasing total face-on pressure specific impulse recorded with decreasing D:H

ratio. The total side-on pressure specific impulse however decreases as D:H ratio decreases. This could be due to the shorter durations seen with the side-on pressure test configuration with the pencil probe deflecting some of the blast away from the target although the peak side-on pressures also were higher. The face-on pressure specific impulse trend is opposite to that seen with the target response impulse where the total impulse decreased. It also questions if face-on pressure specific impulse should be used to quantitatively determine structural loading from buried blast, whereas side-on specific impulse seems to give similar trends as to the target response load. The near-field face-on pressure specific impulse increased by 48% compared to the averaged intermediate-field face-on pressure specific impulse. This reveals the much higher pressures generated at the lower target SOD considering, as noted in Section 5.5.2, the total positive pressure duration was similar.

The partitioned intermediate-field face-on pressure phase specific impulses are similarly higher than the equivalent side-on specific (pressure) impulse. The specific impulse ratios between each of the partitioned side-on and face-on pressure phases vary as D:H ratio changes. For Phase One face-on specific impulse is five times and three times higher, for Phase Two it is fourteen and twelve times higher and for Phase Three it is nine and thirty six times higher for the 3:1 and 2:1 charge D:H ratios respectively. With the exception of Phase Three, all other partitioned phase ratios are similar between the two charge ratios with the larger 3:1 ratio charge having lager ratios. For Phase Three, there was one test that generated a very large pressure response that is three times larger than the other two D:H 2:1 results in the data pool generating the anomalously large ratio presented.

This corresponds with the blast loading proposed in Section 5.1.1.3 as follows. Phase One is primarily soil ejecta driven and is based on impact loads, thus decreases as the D:H decreases as the soil ejecta mass decreases. Phase Two specific impulse increases as D:H decreases as more gases are released laterally resulting in a longer duration detonic expansion, the focussing effect of the soil. This increase in gases released later also increases the detonic

products for afterburn as well as increased pressure reflection off the target and soil.

Overall the intermediate-field specific impulse for each partitioned phase indicates specific trends for both the side and face-on pressure with an intermediate-field target as the charge D:H ratio changes. This trend was present for both test configurations. However the contribution between the partitioned phases differed according to the test configuration. For both test configurations Phase Two was the largest phase specific impulse contributor. For the side-on pressure configuration Phase Three was the lowest specific impulse contributor but for the face-on configuration Phase One was lowest specific impulse contributor.

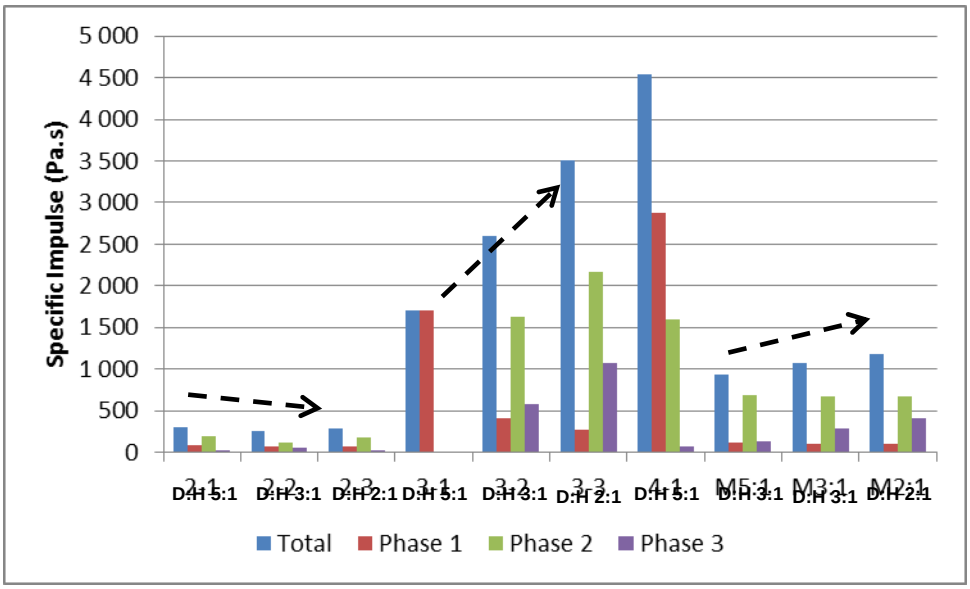

Figure 150: Total and Partitioned Phase Specific Impulse

This phase trend is not the same in the near-field where Phase One is the largest contributor followed by Phase Two and then Phase Three with the lowest. This is still congruent with the proposed loading phases and their load sources (Section 5.1.1.3). In the near-field SOD the blast front is still accelerating indicating a still expanding detonation gas bubble with resultant higher blast front over-pressure increasing the Phase One Loading. Phase Two specific impulse is similar to the intermediate-field Phase Two indicating the amount of loading transferred is the same. It was expected that this would be

higher due to the higher gas temperature, gas velocities and pressure at the lower SOD. It appears that quasi-constrained environment still enables the gasses to vent thus considerably reducing the loading transferred by Phase Three although it is the lowest specific impulse phase it is much lower than was seen at the intermediate-field at 70 Pa.s compared to the 588 Pa.s and 1,073 Pa.s recorded for the D:H 3:1 and 2:1 Phase Three specific impulse. Based on the D:H ratio trend a D:H ratio 5:1 Phase Three specific impulse at the intermediate-field target of around 350 Pa.s is expected. The much lower 70 Pa.s recorded could be due to reduced afterburn pressures based on limited oxygen despite the higher concentration of detonic products, temperature and pressures in the near-field. In this case Phase Three could primarily be the reflected pressure effect however the computational model predicted 138 Pa.s (specific impulse) for Phase Three side-on pressure. As only one near-field face-on pressure result was recorded and large signal fluctuations stemming from the soil impacts where present in the pressure trace, combined these effects could result in incorrect partitioning between the phases leading to higher and lower predictions. Additional testing is required to confirm this.

The near-field computational modelling results gave a slightly decreasing side-on pressure total specific impulse trend as the D:H ratio decreases, mirroring the intermediate-field side-on pressure total specific impulse trends. The total side-on pressure specific impulse averaged for all model charge D:H ratios was 1,062 Pa.s which is 4 times more than the intermediate-field tests total specific impulse at 277 Pa.s. This near-field and intermediate-field ratio was only 1.5 times for the measured face-on pressure specific impulse. This indicates that the blast front vertical gas and soil momentum (dynamic pressure) reduces less than the side-on pressure (static pressure). This is expected as the side-on pressure will not capture the effects of the soil ejecta.

The computational model partitioned phase specific-impulse trends had reducing Phase One and Phase Two with increasing Phase Three side-on pressure specific impulse. This mirrored the intermediate-field partitioned phase side-on pressure specific impulse phase tends. Although the 3:1 D:H ratio

charge model actually gave lower Phase One and Phase Two side-on pressure specific impulse, the general trend is accepted. These results are due to the nature of the Autodyn® hydrocode which uses variable time steps to solve the equations which gives slightly different results from each computational run. The near-field side-on pressure computational models specific impulse give a similar Phase One and Phase Two specific impulse for all D:H ratio threats but have an increasing Phase Three specific impulse.

Figure 151 presents the partitioned phase contribution to the total specific impulse for the intermediate and near-field tests and near-field computational models. These partitioned phase percentage contributions mirror the total and partitioned phase D:H ratio trends discussed previously, with decreasing Phase One and Phase Two contributions and increasing Phase Three contributions as the charge D:H ratio decreases.

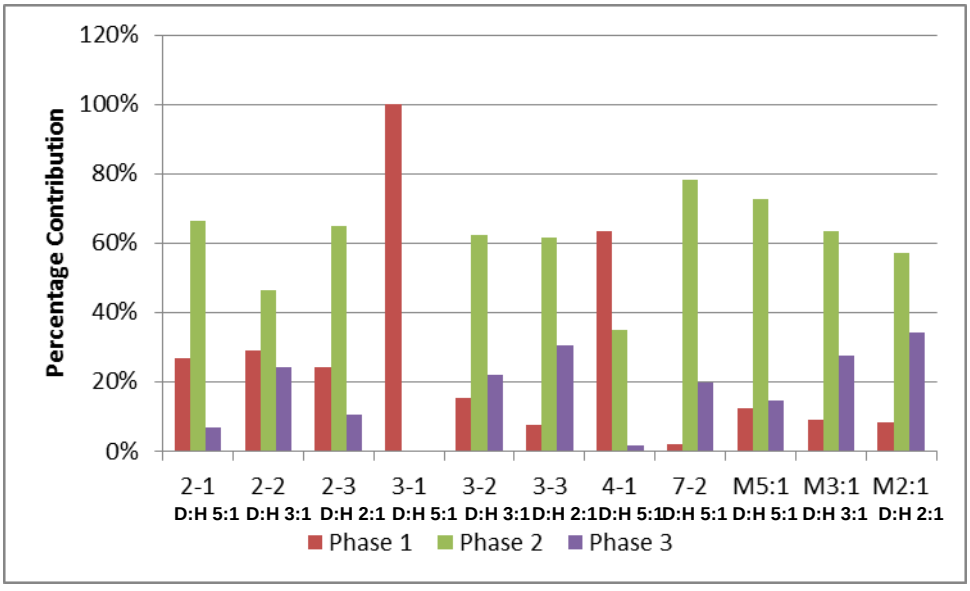

Figure 151: Partitioned Phase Specific Impulse Percentage Contribution

With the exception of the near-field face-on pressure test configuration, all intermediate-field tests and the near-field computational models ascribed the highest contribution to specific impulse to Phase Two. The intermediate-field 3:1 D:H test results appear skewed however this is due to the small data pool and large pressure variations leading to the large specific-impulse variations. As

such it is felt that the overall trends seen are valid and can be validated with additional testing.

Averaging across all intermediate-field D:H ratios the following intermediate-field target (200 mm SOD) comparison to near-field target (72 mm SOD) side-on pressure specific impulse is drawn pertaining to partitioned phase specific-impulse load contribution changes as SOD is reduced. Phase One contributed 59% of the intermediate tests total specific impulse and 10% of the computational models total specific impulse. On average Phase Two specific impulse contributed 59% of the intermediate-field tests total impulse and 64% for the near-field computational models total specific impulse. Phase Three contributed 14% of the tests total impulse and 26% of the computational models total specific impulse. For the near-field face-on pressure test configuration test with 5:1 D:H ratio charge the contribution was 63%, 35% and 2% respectively. These results are summarised in Figure 152. The A prefix refers to average across all charge D:H ratios, IF or NF refers to Intermediate of Near-Field with the M identifying the modelling results. The FO and SO suffix refers to Side of Face-On test configurations.

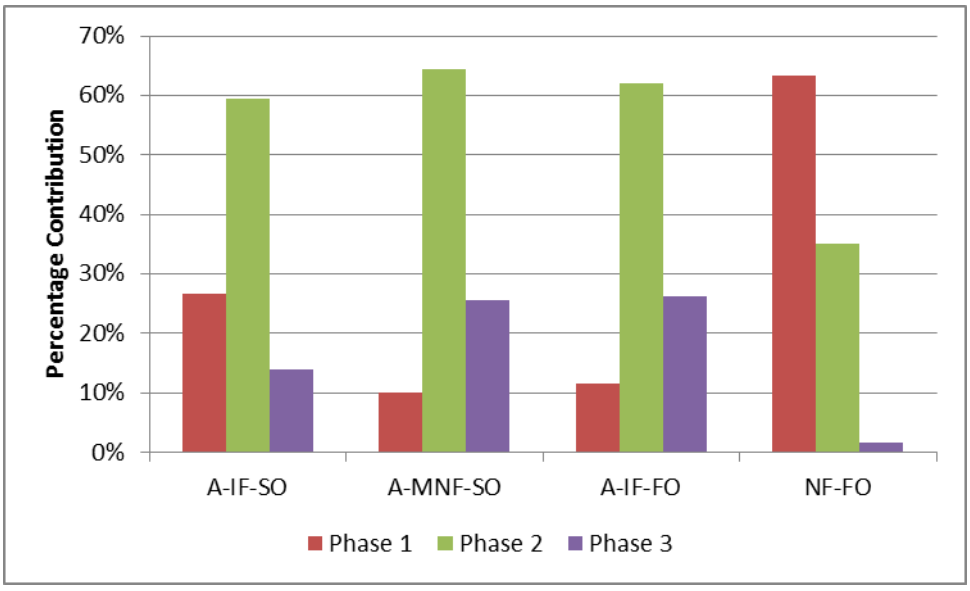

Figure 152: Partitioned Averaged Phase Specific Impulse Contribution

Figure 152 highlights the changes in the partitioned phase contributions for the side-on and face-on pressure test configurations as the SOD is reduced. For

the side-on pressure only the side-on Phase One contribution percentage decreased from 27% to 10% specific impulse load contribution as the SOD decreased. Due to the lower SOD much higher blast over-pressures are expected. This is indeed the case with the model predicting on average across all D:H ratios a peak blast front over-pressure of 7.02 MPa compared to average test measurements of 4.09 MPa. Although the actual specific impulse increases, the percentage contribution reduces due to the large percentage of the load being generated by Phase Two and Phase Three. For face-on pressure Phase One load contribution is seen to increase five-fold while Phase Two's contribution reduces by a factor two and Phase Three's contribution reduces by a factor of thirteen. Although as discussed above the intermediate-field D:H 5:1 tests are not useable for partitioning analysis and the near-field specific pressure impulse results are based on a single test, these lumped averaged results confirm that the blast load phase contributions change as the SOD is changed.

5.5.4 Conclusion

The proposed three load phases from shallow buried blast were discussed in terms of the partitioned side-on and face-on pressure from intermediate and near-field scaled blast tests and computational models. Based on available data the blast pressure morphology generated when a target is present was analysed with the intermediate-field side-on pressure test data and near-field side-on pressure computational modelling. Although for different SOD's the modelling results are comparable in terms of partitioned loading phases and enable the intermediate-field traces to be analysed and discussed in terms of the three blast loading phases proposed in Section 5.1.1.3 as follows.

The intermediate-field test side-on pressure-time traces (morphology) produced an initial smaller blast front spike that was slightly ahead of the principal blast front and was equivalent to the free-field ejecta blast front over-pressure (saw tooth profile). This generated a two part blast front. The computational model did not accurately present the pressure peak temporally with the Phase Two peak occurring much later than seen with the test results. The partitioned phase

analysis applied to the side-on pressure is equally applicable to the face-on pressure tests however the soil impacts generated noise makes it more difficult to accurately determine the phases. The proposed shallow buried three blast load phases where identified within the pressure response trace and corresponded to the loading mechanisms. For shallow buried blast these are; Phase One consisting of the soil ejecta and blast front combined with blast front over-pressure generated by the detonation shock and subsequent following initial gas expansion. Phase Two loading from detonic gas expansion following the detonation and focused by the crater. Phase Three loading derived through reflected pressure from the crater and quasi constrained conditions created by the soil surface and target augmented by afterburn. Summarised these are sequentially impact combined with blast front-high pressure, dynamic pressure and slower quasi constrained pressure increase from burn and surface reflections.

For the intermediate-field the Phase One side-on pressure traces are typically represented by a sharp pressure increase, as found with free-in-air blast over-pressure (Section 5.1.1.2). The two part pressure front has the first peak corresponding to the shallow buried blast front and the second peak over-pressure corresponding to the reflected blast front pressure generated by the target surface interacting with the blast. Phase One ends with a rapid pressure decline to between 5 to 30% of peak pressure. The Phase Two pressure profile has typically a slower rate of pressure build-up but is still higher than that seen with afterburn pressure increase. This rate of increase was visually similar to the computational model Phase Two peak rate of increase. The side-on pressure then decays more slowly than a Friedlander wave profile as expected due to the target that creates quasi constrained environment. Phase Two ends when the pressure reaches a minimum before the third pressure increase. The Phase Three loading pressure trace is a gradual pressure increase and decline that is in line with the slower energy release created by afterburn. This phase ends when the pressure goes below zero relative pressure. This is also the end of the positive pressure loading phase.

The following general conclusions are made regarding pressure trace start time, time-to-peak pressure, blast front velocity, total and partitioned phased pressure duration, peak pressure and specific (pressure) impulse.

At the intermediate-field SOD a target over the shallow buried blast increases the side-on pressure generated by a shallow buried blast by a factor of two to three depending on D:H ratio. The peak pressure analysis confirmed that the difference between the measured side-on and face on pressure for intermediate-field tests was much higher than the theoretically calculated eight times predicted by (Smith, Hetherington 1994) varying from eighteen to thirty six times depending on charge D:H ratio and averaging twenty six times across all D:H ratios. The up to 80% higher side-on to face-on (reflected) pressure ratio is due to charge geometry and burial effects. The tests indicated that the ratio of side-on and face-on (reflected) pressure changes as the test charge D:H ratio changes. For these shallow buried tests the ratio between face-on and side-on peak pressure decreased with decreasing charge ratio.

The peak over pressure and charge D:H Ratio trends were present in the test data with the intermediate-field peak side-on and face-on pressures decreasing as the D:H ratio decreased. This is opposite to the free-field ejecta tests where the side-on pressure that had an increasing peak pressure with increasing charge D:H ratio. The near-field computational modelling predicted increasing side-on pressures as D:H Ratios decreased. Unfortunately there was insufficient near-field test pressure data to confirm this trend.

The calculated average blast front velocity using the pressure trace start time and the SOD confirmed the free-field ejecta velocity trends (Section 5.1.1.1) with increasing averaged blast front velocity as the D:H ratio decreases. This increasing velocity trend was mirrored in the near-field computational modelling results.

The test results gave between 10 to 50% longer positive pressure duration, depending on the charge D:H ratio, for the face-on pressure test configuration when compared to the side-on pressure test configuration. Intuitively the intermediate-field target test configuration should have had had longer positive

pressure phase than the free-field ejecta tests. However, the test data was such that this could not be conclusively confirmed with averaged durations for free-field being similar to the averaged target positive pulse durations. The near-field face-on pressure test configuration resulted in a shorter positive phase pressure duration, than that seen with the intermediate-field face-on pressure. This implies that the near-field test conditions do not measurably increase the positive phase durations of shallow buried blast due to the quasi constrained environment allowing quick lateral reflected pressure release.

For partitioned phase durations, on average Phase One pressure had the shortest phase duration and is consistent with the loading impact loading mechanism presented by a combination of blast over-pressure and soil ejecta moving at velocities between 1,600- 2,000 m/s. Phase Two and Three pressure durations where two to four times longer than Phase One as would be expected for reflected pressure loading.

The total and partitioned face-on specific (pressure) impulse results provided an increasing specific impulse trend with decreasing D:H ratio test charges. This is contrary to what was observed with the target response force impulse. The intermediate-field side-on pressures specific impulse gave the opposite trend and correlated with the target response impulse trend with deceasing total specific impulse with decreasing charge D:H ratios. Mirroring the trends in total specific pressure impulse, the partitioned phase specific impulse contributions varied between side-on and face-on configurations and between the near and intermediate-field SOD's. Similarly these partitioned phase percentages did not correlate with the partitioned target response force-time impulse indicating that additional loading mechanisms are involved with the pressure loading and load transfer to the target that are not contained in the centrally measured pressure-specific impulse such as the load variation across the target face.

5.6 Specific (Pressure) Impulse, Target Impulse and Displacement Response as Indicators of Blast Load Contribution

One of the research questions of this work is to identify those shallow buried blast load phases that contribute the most to the blast load coupled into a structure. The research methodology followed in this work has used five measurements to quantify shallow buried blast loading for both an intermediate-field and a near-field steel target. These are, (1) target force-time response, (2) side-on and (3) face-on pressure at the target face, (4) he displacement-time of the target measurement assembly and (5) the NIR light emission during the blast loading process. As discussed briefly in Section 5.5.3, the partitioned phase load contribution percentages between target response force impulse and both the side-on and face-on specific pressure impulse for the different blast load quantification methods differ markedly.

To investigate how each of the measurement methods represents a shallow buried blast load the following four of the five load measurement methods are now compared and analysed, (1) target force-time response impulse, (2) side-on and (3) face-on pressure and (4) the integration of the target assembly deflection.

The NIR emission data is not used here due to the limited published work on the relationship between blast loading and NIR light emission and the variability in the set up application of the integration of light sensor for this work outputs resulting in a limited complete NIR response data sets.

5.6.1 Analysis

The phasing evident in the target force-time response, the side-on and face-on pressure target assembly displacement morphology has been discussed in Sections 4.4.2, 4.4.3, 4.4.4 and 4.7. Using the integration of the blast load quantification measurement as an indication the total blast load applied to or coupled into the target and the partitioned phase contribution of each of the proposed three phases to the total blast load, the results for each blast load

quantification method are compared in terms of the phase percentage contribution for each quantification method. The target force-time response, side-on and face-on pressure measurements have been analysed in Sections 5.3 and 5.5. The target assembly deflection time has not been analysed in terms of the proposed three blast loading phases (Section 5.1.1.3) and is briefly presented here.

Section 4.7 presented that theoretically the target assembly was rigidly held in position over the blast; the target assembly dynamically responded to the blast load deflecting up to 5.9 mm. The target assembly deflection-time traces mirrored both the force-time and pressure time traces, in exhibiting a three-phased morphology. The peak deflection decreased as the charge D:H ratio decreased. When partitioned the three phases also exhibited duration and load contribution trends as the D:H ratio decreased. One shortcoming with the displacement data is that the full duration at peak displacement was not captured with all tests. As discussed in Section 4.7 the positive displacement duration was taken when the measurement assembly reached peak displacement and did not take into consideration the dwell time in this position. This implies that the total and Phase Three impulses are under predicted. However the trends and results obtained with the data are applicable for comparative purposes and are accurate enough.

If the displacement-time trace is integrated the area under the curve is calculated and this gives a measure of the work or load transferred to the target measurement assembly by a shallow buried blast load. Figure 153 presents the total and partitioned averaged integrated deflection-time from all the one-seventh scale shallow buried blast tests in millimetre-seconds (mm.s). The 2 and 3 prefix indicates intermediate-field (200 mm SOD) and the 4 prefix the near-field (72 mm SOD). The suffix 1, 2 and 3 references the D:H ratios 5:1, 3:1 and 2:1 respectively. The side-on test configuration was the 2- X series tests and the face-on test configurations were the 3-X and 4-X series tests.

In reviewing Figure 153, the decreasing deflection load with decreasing charge D:H ratios trend is clearly visible. The 3-2 result is considered anomalous as

the data set is skewed by a single result that recorded a 16% greater impulse than the other 4 tests. The relatively small changes evident in the results are susceptible to data deviations due to the small scale of the tests. Similarly in general these results show the partitioned Phase One, Phase Two and Phase Three displacement load contribution decreases as charge D:H decreases. The partitioned data also show in general that the contribution of each phase is consistent with Phase One being the smallest, followed by Phase Two and lastly Phase Three. The ratio of Phase Three to the other two phases is most prevalent with the face-on pressure test configuration, Phase Three being three to six times larger than Phase Two. The only anomaly was the side-on test configuration 2-3, which on average had Phase Three load contribution smaller than Phase Two. This is ascribed to how the end of Phase Three was determined as this test series had all four tests with complete displacement-time signals and all the end points were selected consistently shorter. Although the difference is small as noted above the small variations between D:H ratios due to the scaling affects the partitioned phase trends disproportionally.

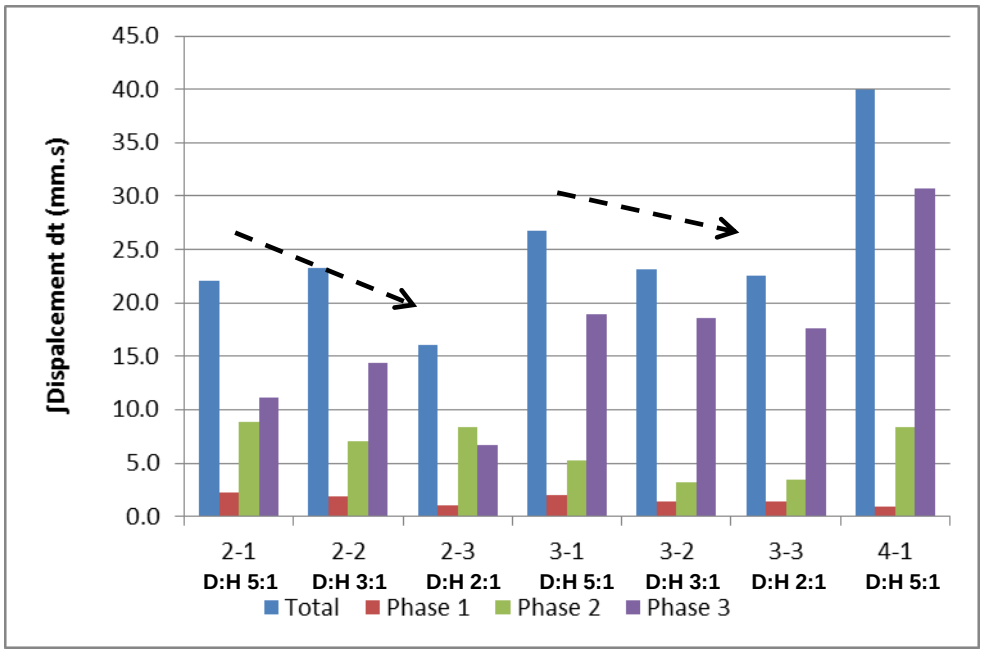

Figure 153: Total and Partitioned Phase Target Assembly Displacement Integration

As was discussed in Sections 4.4.2 and 4.7.1 the test configuration had a marked influence on the peak force and displacement and congruently the integrated force-time (impulse) and displacement-time (millimetre-seconds) target assembly displacement area thus the analysis data is presented separately for the side-on and the face-on pressure test configuration.

Figure 154 presents the partitioned phase percentage contribution from the force-time impulse, side-on specific (pressure) impulse and target assembly displacement-time integral all for the side-on pressure test configuration. The prefix 2 indicates side-on pressure test configuration and prefix 3 the face-on pressure test configuration for the intermediate-field. The near-field face-on pressure test configuration has a 4 prefix. The test charge D:H ratio 5: 1 is presented with a 1, 3:1 a 2 and 2:1 with a 3. Both these data sets include all test charge D:H ratios starting with 5:1 and decreasing to 2:1. The force-time impulse data contribution is identified by an I suffix, the specific (pressure) impulse is by a P suffix and the displacement area by a D suffix.

In reviewing Figure 154 it is seen that each measurement method presents the partitioned blast load contribution differently. For the side-on test configuration there is no correlation between the three different method's integrated and partitioned measurement phase contribution percentage. Response force-time impulse give Phase One contributing more than 50% of the total shallow buried blast load while for side-on pressure Phase Two contributes 60% to the blast pressure load while the displacement-time integral attributes more than 70% of the blast load to Phase Three.

Figure 155 presents the partitioned phase percentage contribution from the force-time impulse, specific (pressure) impulse and target assembly displacement-time area for the face-on pressure test configuration. The prefix and suffix's are the same as for Figure 154 defining target SOD and charge D:H ratios.

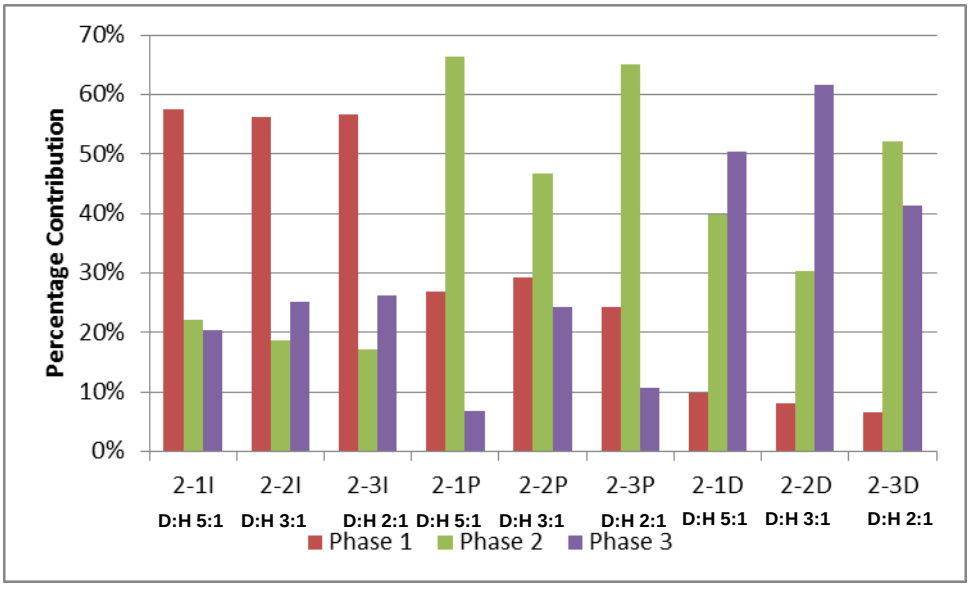

Figure 154: Partitioned Impulse, Specific (Pressure) Impulse and Integrated Displacement Area Phase Contribution (Side-On Pressure Test Configuration)

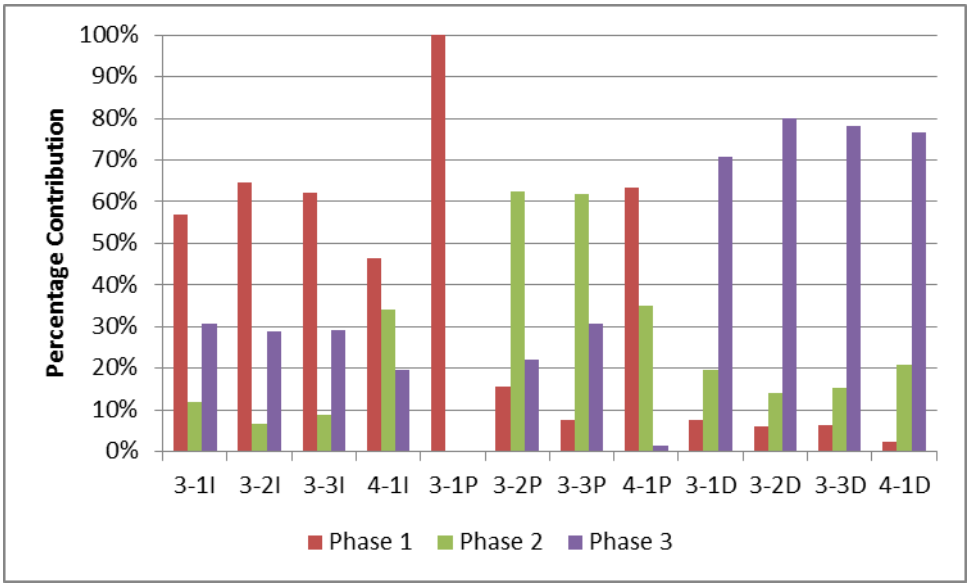

Figure 155: Partitioned Impulse, Specific (Pressure) Impulse and Displacement Area Phase Contribution (Face-On Pressure Test Configuration)

Similarly the face-on pressure test configuration results do not correlate between the different blast loading measures. As before in the intermediate-field the target force-time response impulse identifies the highest load contributor as Phase One, the face-on pressure specific impulse load contributors identifies as Phase Two as the biggest load contributor and the deflection-time integral identifies Phase Three as the biggest load contributor for shallow buried blast.

There is thus consistency with each blast load quantification method for the side-on and the face-on test configurations pertaining to the biggest partitioned load contributor phase.

There is more consistency within each of the measurement quantification grouping in terms of phase percentage contribution as the D:H ratio changes with the face-on test configuration. This is probably due to there not being a long probe extending below the target which allows any set up asymmetry to affect the load applied to and measured by the system.

These data also clearly show that the phase contribution changes when the SOD is reduced from the intermediate-field (200 mm SOD) to the near-field (72 mm SOD). For the target response force impulse the main load contributor remains Phase One however Phase Two increases to the second largest contributor. For the face-on specific pressure impulse Phase One becomes the largest contributor and looks similar to the target response force impulse. The integral of the deflection-time however maintains the same phase contribution for the near-field with small changes in the partitioned phase responses.

Overall, for these tests, the target response impulse appeared the most consistent measure across all test configurations for both the near and intermediate-field closely followed by the integral of the target assembly deflection-time. This is simply due to the fact that the relatively large target allowed for the capture of the complete load and smoothing out of the blast front variations and test set up anomalies. The least consistent was the side-on pressures specific impulse. This is due to the extremely directionally sensitive nature of pencil probes that require a no more than one degree off-perpendicular blast front impact angle to work optimally. As has been noted there was some variation in the change setup resulting in angular impacts on the probe. In addition both the side-on and face-on probes are centrally located and relatively small areas are prone to miss pressure spikes or capture pressure spikes randomly adding to the variable data sets.

To see if there were any overall trends in the partitioned phase load contributions all the charge D:H ratios were averaged. These results are

presented in Figure 156. The IF and NR prefix refers Intermediate or Near-Field. The SO and FO refers to the side or face-on test configuration. The suffix SI refers to integrated pressure-time specific impulse, I refers to integrated force-time impulse and D refers to the integrated displacement time. This table confirms that each blast load quantification method contributes blast loading differently across the partitioned phases and mirrors the trends discussed in this section.

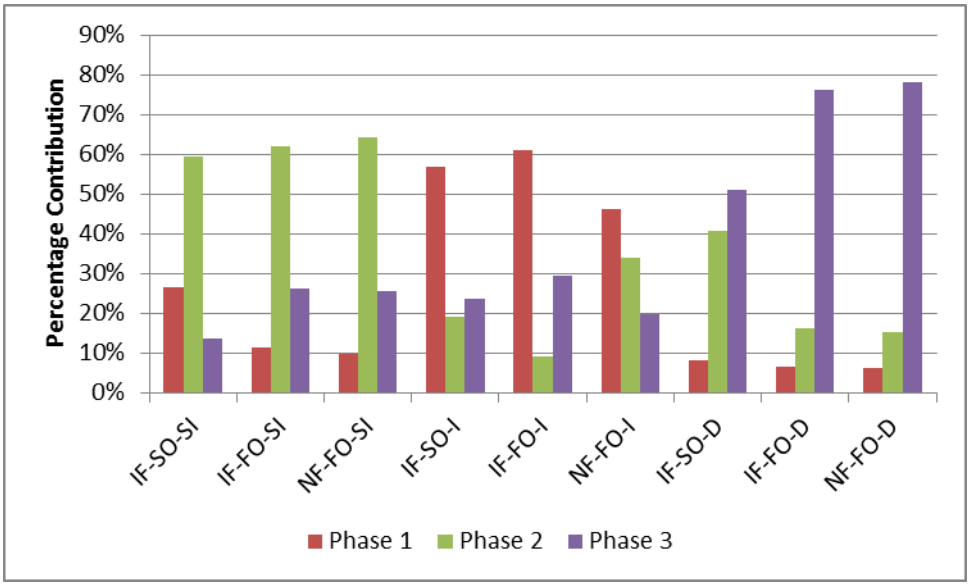

Figure 156: Averaged (All D:H Tests) Blast Load Contribution Percentage

From the above it is clear that the blast loading phase contribution to the total blast load from a shallow buried charge is dependent on the measure used. The reason is due to the measurement system structural response to the blast load. From (Smith, Hetherington 1994) there are three types of blast loading based on the target characteristics (in this case measurement system characteristics), these are impulsive, dynamic and quasi-static. The type of blast loading a target is subjected to is determined from the product of the target, or in this discussion the measurement sensor, and the blast load duration. With natural frequencies in excess of 400 kHz and blast load duration of between 0.3 to 0.4 ms the pressure sensor measurement systems, side-on and face-on, are subjected to quasi-static loading. The force-washer measurement assembly consisting of a target mass of 26.4 kg and an equivalent stiffness in excess 98 MN/m, has a

calculated natural frequency of 1,900 Hz and for the same blast duration is being subjected to dynamic loading. Calculating the natural frequency of the measurement head assembly from its displacement period gives 14 Hz and with the same blast load duration of between 0.3 and 0.4 ms the measurement head assembly is subjected to impulsive loading. This leads to the transfer function of each system and how this changes the phased short duration blast load into the measurement response that is used to quantify and analyse the blast load.

Lastly it is noted that the target response force impulse and target assembly displacement integration represent measurements of the blast load that have coupled into the target. The side-on and face-on pressures along with the NIR emissions measure the blast load acting on the target. These measurements should correlate however this correlation will and is primarily affected measurement system structural response (transfer function) that redefines how the blast load is represented by the measurement. These measurements are also affected by the test configuration; in particular the side-on pressure probe that extended into the blast and the single central measurement used for pressure that does not represent the spatial pressure variation across the target face.

5.6.2 Conclusion

This section presented and discussed the target assembly deflection-time as a measure of total and partitioned phased shallow buried blast load. The integral of the target assembly displacement-time provided a consistent measure of shallow buried blast load across all test configurations and SOD's. This integrated measure clearly reflected total and partitioned phase load differences in both the test configuration as well as the charge D:H ratio and test SOD mirroring the research findings for both target response force, side-on and face-on pressure.

Four of the five blast load quantification methods used for this work, namely target response force impulse (impulse N.s), side-on and face-on specific pressure impulse (specific impulse Pa.s) and the target deflection-time integral (displacement area mm.s), were compared in terms of the percentage load

contribution for each partitioned phase. The fifth, NIR emission, was not included due to the limited data set.

Each method of quantifying the blast load provided different phases contributing the most to the blast load in terms of that specific measure. The phase contributing the most was the same within each quantification method at a specific SOD and as the charge D:H ratio changed. As the SOD both the target response impulse and the face-on specific pressure impulse partitioned phase contributions changed. The difference in the blast load phase contribution is related to how the measurement system interacts with and measures the blast load. The system response or transfer function converts the blast load to what was presented and as each system is different the partitioned blast load contribution differed. The type of blast load applied to each measurement methods as defined by (Smith, Hetherington 1994) was determined using the product of the measured blast duration and the natural frequency of the sensor system. The displacement-time measurement is impulsive loading, the force-time response measurement is a dynamic loading and the pressure measurement is a quasi-static loading. This is discussed further in Section 5.7.1.3.

5.7 Secondary Data

To provide robustness to the developed three phased blast loading model presented by this work so far, secondary data test sets were analysed. These data sets provided test data for larger scaled as well as full scale test charges using test rigs that employ different methods to capture the temporal response of a target to buried blast. Furthermore these secondary data provide shallow and deep buried blast test data which add further strength to the three phase blast load model developed by this work. To support the analysis and discussion each of the test rig's Cube Root and Geometrically Similar scaling relationships are presented and discussed.

5.7.1 Analysis

The two secondary data sets are analysis is presented discussed in three sections. These are; (1) force-time morphology as analysed accordance with the blast loading phases proposed Section 5.1.1.3, (2) Cube Root scaling and Geometric Similarity between the primary research test rig (one-seventh scale rig) and the two secondary data test rigs (McDonald and SIIMA) and (3) the partitioned phase load contributions for the phased blast load captured by each of the three test rigs.

5.7.1.1 Force-Time Response, Total and Partitioned Positive Phase Duration

The secondary test data from the two independent blast test rigs was presented in Section 4.8. In Section 4.8.3 It was shown that PE4 one-seventh scale tests scale well in terms of total impulse for near and intermediate-field targets but the phased impulse does not scale well. It was shown that this is due to test explosive and test rig differences that do not scale between the test configurations (system stiffness and mass).

These secondary tests however all exhibited phasing in the force-time morphology. For shallow buried blast loading (SIIMA) there were three phases (Scaled Distances (Z) 0.29 and 0.69 kg/m^3). For deep-buried (McDonald 2013b) intermediate field tests there were two phases for the intermediate-field (Scaled Distance (Z) 0.90 kg/m^3), and for near-field (Scaled Distance (Z) 0.42, 0.57 and 0.66 kg/m^3) there were three force-time phases within the positive force loading.

Figure 157 presents three force-time traces (morphology), one of the one-seventh scale test rig (dynamic loading), one SIIMA full scale force-time response trace and one (McDonald 2013b) test rig force-time response trace at SOD's of 200, 1,300 and 360 mm respectively. These tests, with scaled distances (Z) of 0.79, 0.69 and 0.90 m/kg^3 and all have intermediate-field targets. They have been selected to be as representative of each other as far as is possible in terms of scaled distance within the limited test data set available for this work. An alternative data set could have been chosen using the near-field tests the data however the key analysis presented here would be

equally applicable. The partitioned phases, as identified using the methodology described in Section 4.4.2.3 and Section 4.4.2.4, are annotated 1 to 3 with phase beginning and end markers.

The one-seventh scale and SIIMA test charges have D:H ratios of 5:1 while the (McDonald 2013b) tests has a spherically shaped charge. The one-seventh scale and (McDonald 2013b) test charges were PE4 while the SIIMA test charges were TNT. All three plots are presented on the same time base (un-scaled). The SIIMA plot presents only the positive-loading force trace, the McDonald plot presents the positive phase as well as some of the systems response. Included in the McDonald plot are the partially negative response peaks that grow and merge as the SOD decreases (See Figure 157 arrows). The one-seventh scale plot is too small to show and clearly separate the positive phase loading from the un-forced system response. This is discussed in Section 4.4.2.2. Figure 158 presents a plot of the partitioned intermediate-field one-seventh scale positive force as well as initial free response of the system.

As discussed in sections 4.4.2.2, 4.8.1.2, and 4.8.2.1, all three force-time data exhibit at least three loading phases. Looking at the SIIMA force-time trace and comparing it to the expanded one-seventh force time trace (see Figure 42, Figure 43 and Figure 45 in Section 4.4.2.3) the SIIMA force-time response Phase Three loading starts at a higher level than seen with the one-seventh scale tests. This is possibly due to these tests being TNT, thus being oxygen poor (Gelfand, Silnikov 2004), generates a much larger quantity of detonic products suitable for afterburn. The result is the onset of afterburn and effects on the target appearing earlier in the process. In this case while the Phase Two loading is still relatively high with attendant higher temperatures and pressures to assist in starting the afterburn process. (McDonald 2013b) intermediate-field (360 mm SOD) test target force-time response differs from the one-seventh scale and SIIMA data in only having two clear load phases. However as discussed in Section 4.8.1.2 and arrowed in Figure 157, a third target force-time response is visible in the trace. This third response, consisting of two peaks that are mostly within the negative force-time trace at this upper end intermediate-

field SOD, increase as the SOD is decreased. Thus McDonald's tests force-time morphology response conforms to three phased loading proposed in this work. The Third Phase loading is too small at the intermediate SOD and is due primarily to reflected pressure from the quasi-constrained conditions created by the target, soil and crater for these tests. For afterburn to take place the detonic gases must be exposed to oxygen and must be of sufficient temperature. For these tests the late appearance of the blast and the shielding of the detonic products from oxygen reduce the possibility of this occurring. This would be the reason that this peak's occurrence is so closely related to lower SOD and thus is driven primarily by reflected pressures.

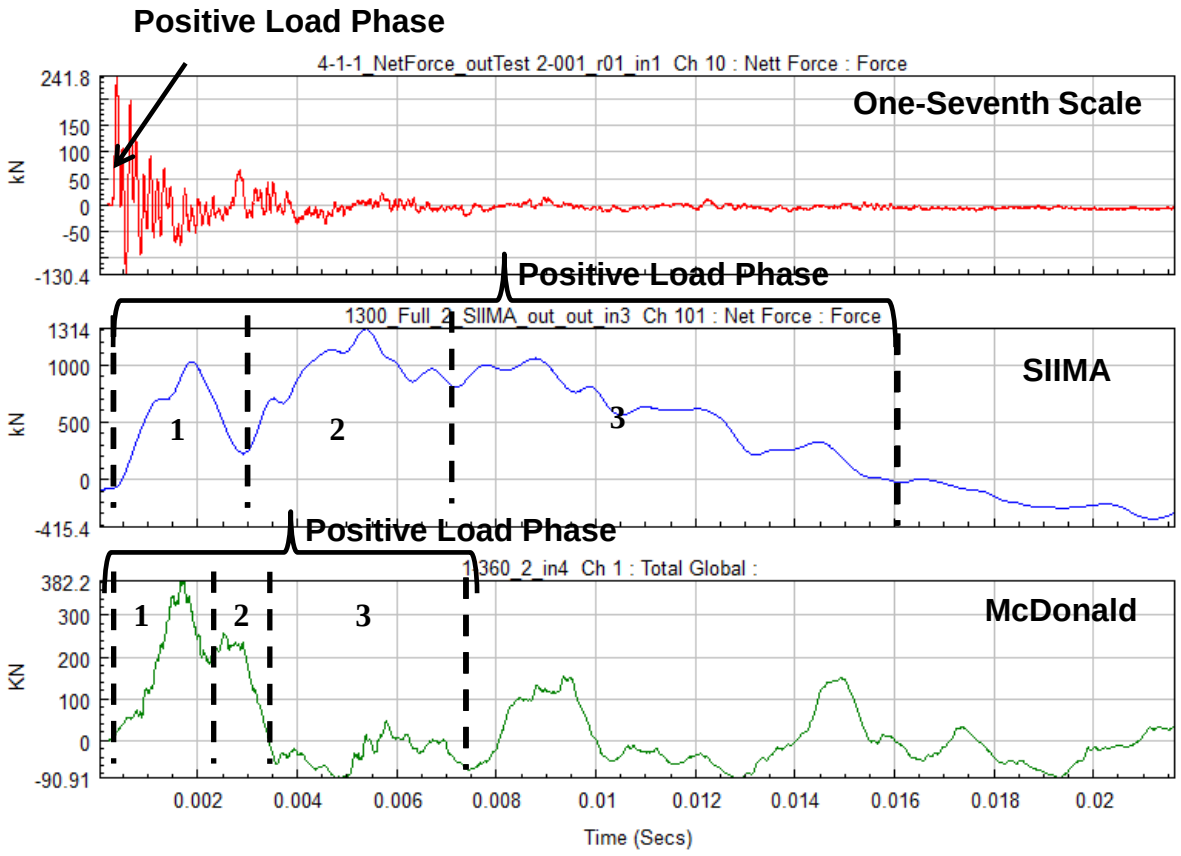

Figure 157: Force-Time Response for Each Test Rig (Intermediate-Field)

As analysed in Section 5.2, (McDonald 2013b) tests the soil cap expands hemispherically upwards and at around 200 mm SOD the soil cap start to ruptures as detonic gases push through the soil cap. This expanding gas mixed with some soil impacts the target first followed by the ensuing ruptured soil cap.

The much lower velocity is correspondingly shown in Figure 157 where the rate of change in force is much lower than seen with the one-seventh test trace. The soil cap expansion results in a sweeping type of motion of the blast front across the target as the soil cap moves radially upwards and outwards. Due to the lower blast front velocity this process is much longer than was seen with shallow buried blast load target impact. Though it is similar to the Phase One blast loading, as proposed for shallow buried blast, namely soil ejecta mixed with detonic products is at a much lower velocity. As with shallow buried blast the soil ejecta is forced outwards by the expanding detonic products but due to the much larger soil mass this process is slower and more momentum transfer from the much thicker soil cap. After the initial detonic product break out and soil cap ejecta impact the detonation product expansion takes place resulting in a second loading phase The detonic gases then start to reflect against the target, building up the Phase Two loading, as with shallow-buried blast but again much slower due to the lower gas velocities.

For SIIMA the same analyses as applicable to the one-seventh scale, as presented in Section 5.3.1.3, is applicable as these tests are shallow buried blast. In comparing SIIMA's positive phase force morphology to the one-seventh scale shown in Figure 158, it is clear that SIIMA's Phase One and Phase Two are much shorter with less defined valleys between the phases. SIIMA's duration ratio are increasing with Phase One being relatively short at 2.5 ms on average whereas Phase Three is four times longer at 10.4 ms. Comparing this to the one-seventh scale Phase Three duration that is only 1.4 times Phase One 's duration.

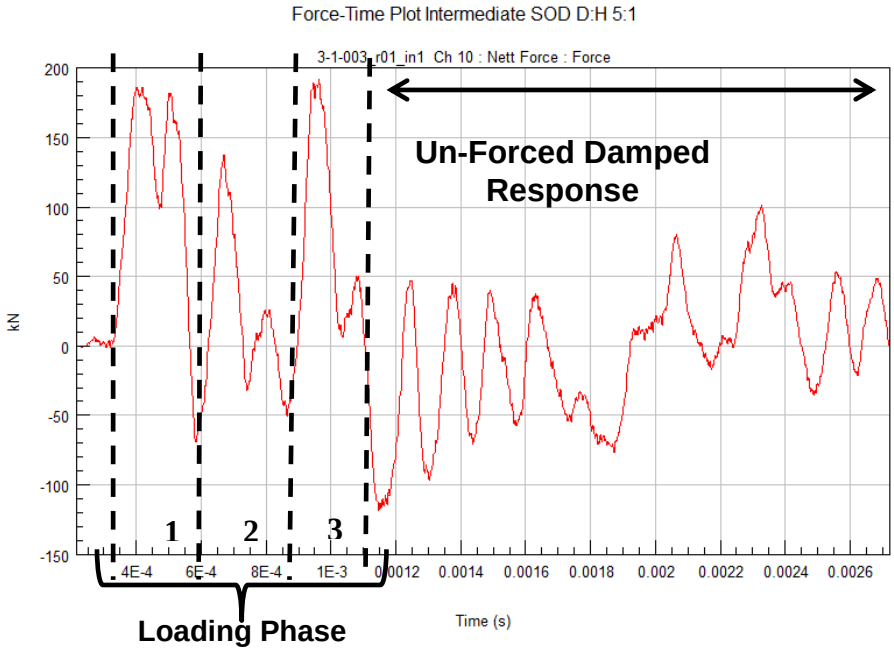

Figure 158: Intermediate-Field One-Seventh Target Force-Time Response (D:H 5:1)

Although all three test rig's target force-time response exhibited three partitioned loading phases, they differed in terms of shape and duration. For McDonald's test rig this is due to the difference in blast loading emanating from what is considered deep-buried tests for this work. For SIIMA the difference is due to key parameters that did were not or cannot be geometrically similar scaled such as stiffness and detonic parameters. This is discussed in the next section.

5.7.1.2 Geometrically Similar Scaling Comparison

As discussed in Section 4.8.3, to enable separate test's data to be compared, the test configurations should be geometrically similar scaled according to the Hopkinson (Cube Root) scaling of the charge. Table 10 presents a summary of key test rig parameters, for both the primary and secondary data sets used, and their geometrically similar up-scaled values. The Hopkinson scale factor (λ) is presented for each test data set and is based on a full-scale threat of 8 kg TNT for this work. Reviewing Table 10 there are clear differences between the one-seventh, SIIMA and (McDonald 2013b) test rigs. McDonald's test rig and the one-seventh scale test rig both use piezoelectric forced washers mounted

against rigid steel supports and would have similar vertical stiffness. The stiffness would not be equal due to size differences in the force-washers. However these two test rigs differ markedly in terms of target area (0.25 m^2 vs. 0.102m^2) shape (square vs. round) and target mass (20 kg vs. 26 kg). The mass and size differences should be compared in the geometrically similar up-scaled values. These indicate that the one-seventh scale test rig has a 67% larger target area with a mass that is effectively 5.35 times heavier.

Comparing SIIMA to the geometrically similar up-scaled one-seventh scale test rig, from Table 10 the rigs differ in terms of target shape (square vs. round) and area (2.44 m^2 vs 5.0 m^2). Target mass correlates within 1% (9,000 kg vs. 8,918 kg). The primary difference between SIIMA and the one-seventh scale test rig lies with the target mounted stiffness. SIIMA's estimated vertical stiffness is in the region of 4 MN/m compared to the one-seventh scale test rig's estimated vertical stiffness of 59.6 MN/m. geometrically similar up-scaled one-seventh test rig stiffness would be 350 MN/m.

Table 10: Geometrically Similar Scaled Test Rig Parameters

Parameter	Test Rig			
	SIIMA Full	**SIIMA Half**	**McDonald**	**One-Seventh**
Scale Factor (λ)	1	1/2	2/7	1/7
Target Mass (kg)	9,000	9,300	40	26
Scaled Mass (kg)	9,000	74,400	1,667	8,918
Target Area (m^2)	1.44	0.36	0.25	0.102
Full Scale Area (m^2)	1.44	1.44[3]	3.00	4.99
Shape	Square	Square	Square	Round

[3] The half-scale target plate was attached to the SIIMA full-scale plate thus effectively increasing the target area exposed to the near-field blast

Table 11 presents a summary of both the primary and secondary tests in terms of their Hopkinson (Cube Root) scaling. Scaled distance (Z) is included and is based on the actual test explosive used. As the threat is buried, key parameters affecting the blast load such as DOB and target SOD are also included to describe the scaled relationship between the data sets. As two SOD's were used for the primary research tests, two scaled distances are noted along with their respective SOD's. Similarly (McDonald 2013b) tests covered three SOD and two DOB's, the four scaled distances and geometrically up-scaled data are presented sequentially in Table 11. As all test scaling parameters are based on the Hopkinson scaling of the threat of interest, namely 8 kg TNT, this calculated scale factor is listed for each test rig in the first data row.

In reviewing Table 11, SIIMA's full-scale and half-scale tests correlate closest to the one-seventh scale intermediate-field and near-field tests across all parameters.

Table 11: Hopkinson (Cube-Root) and Geometrically Similar Scaling

Parameter	SIIMA Full	SIIMA Half	One-Seventh	McDonald
Scale Factor (λ)	1	1/2	1/7	2/7
TNT (gram)	8,000	1,000	-	-
PE4 (gram)	-	-	19	160
Scaled Distance Z (m/kg$^{1/3}$)	0.69	0.29	0.79 / 0.31	0.90 / 0.66 / 0.52 / 0.47
Charger D:H Ratio	5:1	5:1	5:1	Spherical
Test DOB (mm)	50	25	7.2	100 / 50
Full-Scale DOB (mm)	50	50	50	346 / 173
Test SOD (mm)	1,300	250	72	360 / 230 / 100 / 230
Full-Scale SOD (mm)	1,300	500	1 400 / 504	1 248 / 797 / 347 / 797

The main deviation is with the scaled distance of the intermediate-field with 0.69 m/.kg$^{1/3}$ for SIIMA compare to the one-seventh's 0.79 m/.kg$^{1/3}$. This is due to the

100 mm difference in SOD and that the scaled distance (Z) is based on the actual PE4 charge mass and not the impulse corrected TNT equivalent. As blast loading decreases exponentially with increasing SOD (Kinney, Graham 1985, Swisdak 1975, Cooper 1996c), the impact of the 100 mm on the blast load is deemed acceptable for initial verification of up-scaled shallow buried blast loading.

As discussed in section 4.8.3 the one-seventh scale soil up-scales well to AEP 55 (NATO Standardization Agency (NSA) 31 August 2011) soil. However the soil used for the full-scale 1,300 mm SOD test and half-scale 250 mm SOD were the same soil and do not scale to AEP 55 soil granulometry. The key difference is with the absence of large particles in the full scale soil. The largest particles present are 9.5 mm which only make up 2% of the soil. Only 7% of the soil is made up of particle larger than 6.7 mm. AEP requires at least 53% of the soil be larger than this size. It is noted in by (Cooper 1996c) that finer soil will increase impulse with buried blast. Geometrically scaling the soil give up-scaled values that are double that present for full-scale. Therefore half-scale soil correlates better with AEP 55 having large equivalent particles of 13.4 mm in diameter. The full-scale used test soil that was compacted and with controlled water content in accordance with AEP 55, whereas both the one-half scale and one-seventh scale use un-compacted soil with moisture content of between 2% to 7%. Although impulse equivalence using (Weckert, Anderson September 2006), the detonic differences between PE4 and TNT will also play a role in the scaling relationship between the one-seventh and McDonald's tests and SIIMA. It is also noted that charge shape will also play a role when therefore McDonald's tests which correlate comparably with scaled distance with one-seventh scale tests will not necessarily correlate with other scaled parameters on charge shape alone.

The one-seventh scale intermediate-field and near-field test results are now up-scaled and compared to SIIMA's intermediate-field full scale and near-field up-scaled half-scale tests results. For SIIMA no high speed ejecta images were analysed to verify blast front morphology and parameters. The three phased

loading proposed in Section 5.1.1.3 is now used to partition and analysing the total phased impulse loading comparatively between SIIMA and the one-seventh scale test results.

The first phase is the soil ejecta cap combined with the blast front over-pressure. Using the same averaged blast front velocity as was determined from the scaled ejecta tests (1 306 m/s) as velocity scales with a factor 1 and the soil cap mass for the D:H 5:1 TNT charge (6.434 kg), the intermediate-field full scale tests Phase One load should be 8,403 Ns. An average total blast load of 12,263 Ns was recorded for the SIIMA full scale intermediate-field test of which only 1,596 Ns was determined to be Phase One loading, using the integration methodology described in Section 3.2.3. As the SIIMA test used TNT which has a different (lower) velocity of detonation and consequently lower detonation pressures and velocities than RDX, the main explosive source used in PE4, this could result in lower blast front velocities and thus lower Phase One impulse. However the blast front velocity would have to be in the region of 300 m/s to generate such a low impulse.

As shown in Section 4.8.3.1, presented in Figure 105, Table 10, Table 11 and summarised in

Table 12, the total impulse load scales well between the one-seventh scale, one-half scale and full-scale charges.

Table 12 presents the actual measured averaged scaled and full scale intermediate-field total impulse results as recorded by the one-seventh scale and SIIMA test rigs. For the near-field tests the averaged one-seventh scale and one-half scale actual measured impulse from the one-seventh scale and SIIMA test rigs. These data are noted as “Recorded Test Target Response Blast Impulse”. All these data are for D:H 5:1 test charges and for the face-on pressure sensor test configuration, as applicable to the one-seventh scale test rig only. These data are then up-scaled to full scale using impulse scaling and these results are noted as “Up-Scaled Target Response Blast Impulse”. Note that as the full-scale test is the model, its scale factor is one and thus remains the same.

Table 12: SIIMA vs. One-Seventh Scale Measured Scaled and Up-Scaled (Model) Impulse

Measurement	Intermediate-field		Near-Field	
	$^1/_7{}^{th}$ Scale	Full-Scale	$^1/_7{}^{th}$ Scale	½ Scale
Recorded Test Target Response Blast Impulse (N.s)	46.8	12,263	70.9	3,160
Up-Scaled Target Response Blast Impulse (N.s)	16,047	12,263	24,324	25,281

As can be seen in

Table 12 the intermediate-field up-scaled one-seventh scale test rig generates a total equivalent full-scale blast load of 16,047 N.s at an up-scaled intermediate-field SOD of 1,400 mm compared to the averaged SIIMA full-scale test measured blast load of 12,263 N.s at an intermediate-field SOD of 1,300 mm. A higher one-seventh up-scaled impulse was calculated, even though the one-seventh scaled intermediate-field SOD up-scales to 1,400 mm, 100 mm higher than the full scale tests. This up-scaled impulse is 30% more and is attributed to the SIIMA target being geometrically smaller with only 2.44 m^2 area compared to the up-scaled one-seventh scale test rig arear of 4.99 m^2 area. The SIIMA target does not capture a geometrically similar amount of the intermediate blast load as compared to the one-seventh scale test rig, thus will comparatively record less total impulse. This smaller target area will also contribute to the lower partitioned Phase One impulse extracted from the SIIMA data and why the SIIMA result is much lower than expected.

This conclusion is supported if one looks at the averaged up-scaled D:H 5:1 side-on pressure test configuration test data. The one-seventh scale test gave an average 38.5 N.s which, if Geometrically Similar up-scaled, equates to 13,220 N.s at 1,400 mm SOD. This is much closer to the full-scale test result recorded by SIIMA and only 8% higher. As was noted in Sections 4.4.2.4 and 5.3.1.4, the face-on test configuration generated lower impulse due to the

extended pressure probe that deflected the Phase One soil cap ejecta. The extended probe resulted in an increase in Phase Two and a Decrease in Phase Three loading as well, but overall due to the soil cap deflection the total impulse was reduced by 18% from 46.2 N.s to 38.5 N.s. Looking specifically at the effect of the side-on pressure probe on the blast loading, the partitioned Phase One target impulse loading was 22.1 N.s with the side-on pressure probe and 26.6 N.s. with the face-on probe test configuration (a flat target face). This equates to a 17% reduction in partitioned Phase One impulse due to the pressure probe deflecting the Phase One blast. However the percentage reduction due to part of the blast front missing is not sufficient to reduce the partitioned Phase One impulse to the 1,596 N.s extracted from the SIIMA force-time trace. Therefore there are other factors causing the difference.

As noted there is better geometric similarity correlation with the one-seventh scale near-field tests and the SIIMA near-field half-scale tests with only the target shape and area not being Geometrically Similar. This good theoretical Geometrically Similar correlation is expected as the one-seventh scale experimental methodology was designed around an 8 kg TNT charge with a DOB of 50 mm and a near-field SOD of 500 mm. Reviewing the up-scaled near-field one-seventh and half-scale test data in

Table 12 the average one-seventh impulse of 24,324 N.s which is within 4% of the average half scale up-scaled total impulse of 25,281 N.s. due to the closeness of the near-field target resulting in most of the blast being captured by the half scale target. In addition with SIIMA the geometrically scaled target plate was mounted to the full-scale target resulting in any blast escaping the near-field target still being captured by the SIIMA measurement plate, albeit at a higher SOD. The good correlation with near-field blast indicates that for scaled testing, granulometry does not play an important role in the blast load that develops.

The total impulse full-scale intermediate-field comparison with the total up-scaled one-seventh scale intermediate-field tests provides reasonable verification of the total impulse being recorded by the one-seventh scale test rig by providing a much better than order of magnitude correlation between 20

grams of PE4 and 8 kg's of TNT, despite the Cube Root and Geometrically Similar scaling law requirements not being fully met between the two test rigs. In comparing the up-scaled near-field one-seventh and half-scale tests data, a correlation difference of less than 4% between SIIMA and the one-seventh scale provides confidence in the one-seventh test methodology and results. It offers at least one verification and validation point. It is noted that the TNT equivalence factor used for PE4 was based on impulse equivalence and the good correlation achieved both in the intermediate-field as well as the near-field bears this out by providing a robust scalable total blast impulse. These results were presented in Section 4.8.3.2, however the analysis if deep-buried vs. shallow buried blast impulse is beyond the scope of this work.

5.7.1.3 Partitioned Phased Impulse Contribution

Figure 159 presents the partitioned phase impulse contribution, based on the force-time response, for the one-seventh commissioning tests, the one-seventh final research tests for intermediate-field and near-field SOD's and both the side-on and face on test configurations, SIIMA near-field half-scale and intermediate-field full-scale and all four (McDonald 2013b) tests for deep-buried blast. Due to the effect of structural differences the partitioned phased blast loading is presented and discussed as a percentage of the total blast load rather than the extracted partitioned impulse values. The one-seventh scale commissioning tests are prefixed by a C followed by the charge D:H ratio. The one-seventh scale final research tests intermediate-field a prefixed with a 2 and 3 and the near-field with a 4 prefix. The die-one pressure test configuration has a 2 prefix while both the 3 and 4 prefixes indicate face-on pressure configuration. The D:H ratio are suffixed with a 1 for 5:1, a 2 for 3:1 and 3 for 2:1 D:H ratios. The SIIMA tests are prefixed and suffixed with the SOD in mm. The GSS indicates that the near-field tests had a Geometrically Similar scaled target. The four McDonald tests prefix to the SOD in mm. The first three had a 100 mm DOB whilst the fourth test had a 50 mm DOB.

Figure 159 presents the difference in partitioned phase load contributions for the three test rigs whose data has been used for this work. The one-seventh

scale percentage differs from SIIMA and McDonalds tests. The one-seventh scale test however are a closer match to McDonalds test data in that Phase One is the largest or close to the largest blast load contributing phase for all except the deep-buried near-field tests. This corresponds to the fact that both test rigs measure as dynamically loaded systems and have similar stiffness but the target masses are different. McDonald's partitioned near-field (100 mm SOD) phase load contributions are different from all other phased load contributions with phase contributions that are similar to side-on pressure probes. Looking at the response one might state that it is responding like a quasi-statically loaded system. This is not the case, using (Smith, Hetherington 1994) mathematical approximation of multiplying the load duration in seconds with the natural frequency of the system in radians per second ($t_d\omega$) a value of 3 s^2/radians is obtained placing the system clearly as dynamically loaded. For the one-seventh scale test rig this value is 0.52 s^2/radians which marginally a dynamically loaded system. As the blast load duration increases however this measurement system becomes strongly dynamically loaded. SIIMA's partitioned phase load contributions similarly resembles that generated by the deflection integral load quantification presented in Section 5.6.1 with Phase One contributing the smallest and Phase Three the largest to the total impulse blast load. Similarly this implies that SIIMA is an impulsively loaded measurement system. Based on (Smith, Hetherington 1994) this is indeed the case with a system value of 0.02 s^2/radians. The SIIMA tests used TNT which could have detonic effects not mirrored with PE4 that influence how the total blast load is distributed between the partitioned loading phases. The interpretation of the partitioned phased blast loading is now discussed in terms of each test rig.

The commissioning and final research test partitioned phase contributions are similar with more than 50% of the blast loading contributed by Phase One for intermediate-field loading. For the near-field this drops to 46% and is expected as the lower SOD will result in higher impulse contributions from the detonic gases as well as the reflected pressures and afterburn. The changes in Phased loading as the charge D:H ratio changes is evident. This has been discussed in Sections 4.4.2.4 and 5.3.1.4. Comparing only the 5:1 D:H ratio for intermediate-

field side-on, face-on and near-field face-on tests (C5:1, 2-1, 3-1 and 4-1 respectively), Phase One contributes the most to the shallow buried blast loading and Phase Three the least.

Reviewing McDonald's tests partitioned blast load impulse phase contributions, the first two intermediate-field tests (360 and 230 mm SOD) also allocated more than 50% of the total blast load to Phase One and the balance of the load to Phase Two. As discussed in Section 4.8.1.2, the combination of deep-buried blast and large intermediate-field SOD resulted in a negligible Phase Three contribution that is only materially emerging at the 230 mm SOD. The shallower buried (50 mm) intermediate-field blast test at 230 mm SOD had a Phase One load contribution of just under 50% of the total blast load and the balance to Phase Two with a small negative total Phase Three contribution. This is considered similar partitioned contributions as shown by the other McDonald intermediate-field tests. The shallower DOB results in less focussing of the detonation gases and when combined with higher front velocity and intermediate-field SOD the reflected pressure loading is reduced to zero. The near-field deep-buried blast load was difference to all other partitioned impulse contribution measurements with the largest impulse contributor being Phase Two. This response is a reflection of the combination of deep-buried blast loading on a near-field target. The soil cap impulse loading is expected to be lower as the soil cap is still accelerating at 100 mm SOD. The velocity was extracted to be 94 m/s at 100 mm SOD. However being closer and impact occurs before gas break out the almost all the gas's expansion load is transferred to the target being funnelled and focussed more strongly than shallow buried belts with thicker ejecta side walls giving rise to the high Phase Two loading reflected in the partitioned impulse for Phase two. The closer target combined with the deep crater would result in fairly high reflected pressures. The low blast front velocities would ensure lower lateral expansion increasing the duration that these Phase Three pressures are acting on the target. This is reflected with the reactively high Phase Three partitioned impulse. The effect of increased detonic gas expansion loading (Phase Two) due to the deeper DOB is evident across all the McDonald tests.

The two SIIMA partitioned phase impulse contributions are similar. This is expected as the measurement system is the same.

These measurement system differences result in different phases being identified as the primary load contributor. Furthermore the interpretation of how each of the phased loads interacts and loads the measurements system or target will vary according to the measurement system. It is however possible to be able to drew a link between each measurement system and the blasts load by quantifying and modelling the system response.

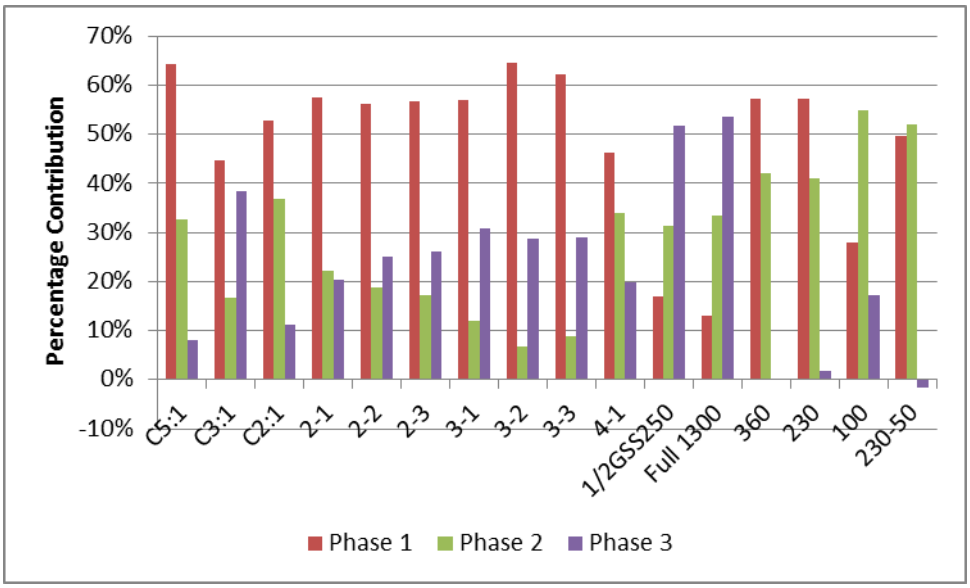

Figure 159: Partitioned Force-Time Impulse Phase Percentage Contribution

5.7.2 Conclusion

Both the secondary test data sets exhibited three phased target force-time response loading. The McDonald data clearly indicated the influence of SOD on Phase Three. The morphology of two separate test series using different tests rigs, one deep-buried with spherical PE4 charges and one shallow buried with TNT charges, was compared to the proposed three phased blast loading model for shallow buried blast developed from the one-seventh scale tests executed as part of this work. The larger TNT shallow buried blast target force-time response morphology corresponded broadly to the one-seventh scale morphology (impulsive loading) with the exception of Phase Three which was

higher in value at onset and of longer duration than the one-seventh scale Phase Three. This was ascribed in part to test explosive differences with TNT being oxygen poor thus generating more products suitable for afterburn than would be the case for the RDX based PE4 explosive used for the one-seventh scale tests and in part to the mechanical differences in the rigs. The deep-buried blast target two phase force-time response was attributed to how the blast develops and how this interacts with the target as compared to shallow buried blast. The deep-buried blast allows for better combustion of the detonation products through greater constraint by the soil cap than would be the case for shallow buried blast resulting in a much larger contribution for the gas expansion loading of Phase Two. The slower blast development results in longer duration load transfers and resultant longer force-time target response.

None of the three test rigs test configurations scaled in all aspects according to Hopkinson and Geometrically Similar scaling laws. The one-seventh scale and SIIMA half-scale tests met most scaling requirements with the exception of target size. Next closest was the intermediate-field one-seventh scale and SIIMA full scale tests with only the SOD and target size not meeting scaling requirements. McDonalds tests where not geometrically similar in being deep-buried spherical charges however some test configurations did correspond in terms of Cube Root Scaling (Scaled Distance) and provided comparable data based on total impulse. Despite the geometrically similar scaling differences McDonald's data can still be useful in comparing deep-buried blast loading with shallow-buried blast loading; however this is beyond the scope of this work.

The intermediate-field one-seventh and intermediate SIIMA full-scale correlated within 30% of total impulse whilst the one-seventh near-field and SIIMA near-field half-scale tests correlated within 4% in terms of total impulse providing good verification of the test methodology. However the partitioned phase impulse did not correlate. This was due to detonic differences between TNT and PE4 not being addressed with the equivalence scaling and the structural response difference between the test rigs. The soil did not fully scale between the various tests with the SIIMA test soil granulometry being the finest. There

was limited correlation between the half scale and one-seventh scale tests due to the fact the small scale factor with the middle to small soil particle sizes.

Using the partitioned force-time impulse phase contributions the SIIMA test rig is seen to be impulsively loaded while the Cranfield rig (McDonald 2013b) is dynamically loaded as is the one-seventh scale test rig. The different deeper buried blast phase contributions were discussed in terms of the proposed three blast loading phases (Section 5.1.1.3) for the near-field deep-buried and the shallower buried intermediate-field SOD's. It was concluded that for the near-field the soil cap was still coherent for this test condition leading to a much higher detonation and combustion products contribution due to the containment effects creating more efficient loading of the target and very high Phase Two gas product impulse loading as detonic expansion is limited (no rupture release) prior to impact. The small SOD created the most confined space of all tests resulting in Phase Three loading having a strong reflective pressure.

The mechanical differences manifested in the way the blast load is presented by each test rig. Three phases were seen in the positive force-time response traces of all three test rigs verifying a phased blast loading of a target is occurring with buried blast. These phases however did not correlate directly or through scaling laws due to the mechanical differences between the measurement systems. These are still useful data to compare loading differences between one-seventh and McDonalds to explore deep-buried blast loading. The correlation between the partitioned phase loading can be addressed through system response quantification and then applied to the recorded total and partitioned phase responses.

5.8 Chapter Summary

This chapter initially analysed and discussed the shallow-buried free-field (no target) ejecta research findings fin terms of blast front morphology and parameters of velocity, pressure and ejecta and the phasing of these parameters as the source of the target force-time response. These tests were defined as shallow buried using Bangash's (Deshpande, McMeeking et al.

2009b) Zone definition applied to the thickness of the soil cap that is Zone 1 thickness.

The ejecta analysis revealed a two phased ejecta morphology, an initial high speed ejecta phase followed by a slow speed ejecta phase. The analysis confirmed that at the intermediate-field SOD almost all of the high speed ejecta following after the soil cap will miss the target and for the near-field a substantial portion will also miss the target. Using the blast stem diameter at the start of the low speed ejecta phase it was determined that this ejecta plays no role in the shallow buried blast loading of an intermediate or near-field target. These data were used to determine blast front velocities at both the intermediate and near-field target SOD's. It was found that at 72 mm SOD the blast front is still accelerating and is decelerating by the time it reached 200 mm or the defined intermediate-field SOD.

The side-on test and computational modelling results were analysed and three loading phases were identified from the pressure-time traces. The pressure traces were partitioned and the specific impulse analysed. Although the data displayed large variations evidenced with standard deviations from 15% to 50%, general trends were visible pertaining to blast front velocities and partitioned phased blast load contributions between the phases as the D:H ratio changed. From these analyses the following three primary blast loading phases and constituents for shallow buried blast is presented as the outcome of this research:

Three primary load phases identified from the blast threat analysis were proposed as follows:

i. ***Phase One:*** Initial blast front impact consisting of bow wave shock, soil cap and adjacent soil ejecta combined blast front over-pressure and including precursor bow wave shock,
ii. ***Phase Two:*** Reflected pressure build-up of the expanding detonation products focused upwards by the soil and complimented with some high speed ejecta; and

iii. ***Phase Three:*** Reflected pressure effects due to quasi-containment of the blast between the crater, surrounding soil and the target and afterburn of the remaining detonation products contained between the soil and the target.

The Bangash Zone definitions (Deshpande, McMeeking et al. 2009b) defined the McDonald 100 mm DOB tests to be deep-buried with Zone II soil cap thickness. The McDonald tests blast morphology was analysed and compared to the shallow-buried blast results. Both the 100 mm and 50 mm DOB blasts displayed similar morphology and were markedly different to the shallow buried blast. The Bangash Zone definitions cannot be used as is defining if a blast is deep or shallow buried and an alternative method by defining this using blast front parameters was proposed.

The interaction of the shallow buried blast load with the intermediate and near-field target was analysed. Using the data obtained from the free-field ejecta tests it was determined that when a target is placed above the blast, the gas expansion following blast front over pressure would prevent any further high speed soil ejecta impacting the target. Thus only the soil cap with immediate surrounding soil entrained by the initial blast will impact the target and contribute to the shallow buried blast load. The lateral gas expansion would deflect the following high speed soil ejecta.

The analysis of the force-time response of the target plate to the blast load in terms of the proposed three loading phases and discussion followed. It was concluded, based on the target force-time response, that there are three primary load responses of a target to a shallow buried blast verifying the three load identified in the shallow buried blast free-field test data. The force and impulse-time responses were further analysed and compared with the free-field test results and three blast loading phases and constituents. There was a strong correlation that the Phase One blast load consists primarily of the initial soil cap and immediate surrounding soil ejected initially. The bow wave shock blast over pressure contributes minimally to this initial phase's loading.

The analysis indicated partitioned shallow buried blast load contribution changes as the D:H ratio changed. There were also partitioned phase load contribution trends visible when the SOD changed from intermediate to near-field conditions.

The NIR test results obtained with the target in were then analysed and discussed. These analyses also confirmed three blast loading phases based on three NIR emission phases and importantly, based on work by (Gelfand, Silnikov 2004), the occurrence of after-burn in the third load phase for shallow buried blast. The NIR emission data correlated to the constituents proposed from the force-time response analysis.

To further verify and explore the proposed three blast-loading sources, the side-on and face-on pressures and computational modelling side-on pressure were analysed and discussed. The pressure-time traces of both the computational model and test results confirmed three shallow buried blast loading phases. The analyses substantiated these phases with the proposed three loading phases and constituents. Side-on and face-on pressures were compared and results compared with literature. It was found that the ratio of side-on (incident) to face-on (reflected) pressures changed as charge D:H ratio and SOD changed. Similarly the total and partitioned specific impulse phase loading changed as the D:H ratio of the charge changed thus the results broadly speaking correlated to published data.

Four of the five blast load quantification results used for this work, namely side-on specific impulse (pressure), face-on specific impulse (pressure), target force-time response impulse and integrated target assembly displacement-time, were compared in terms of partitioned phased blast load contribution percentage. Due to the lack of set-up consistency the fifth quantification method, NIR emission integration, used for this work, was not included. The percentage contribution from each phase was seen to depend on the measurement. Each quantification method has it own partitioned phase contribution mix. The differences between the four quantification methods results were noted to be due to the unique system response of each test sensor and how it interacts with

the blast load. Using the definition proposed by (Smith, Hetherington 1994) definition the target piezoelectric force-time system is dynamically loaded; the side and face-on pressure sensors are quasi-statically loaded and complete assembly displacement measurement is impulsively loaded.

The last analysis focused on secondary data. The secondary data was analysed, compared to the one-seventh scale test data and discussed in terms the force-time response traces, Cube Root and Geometrically Similar Scaling and in terms of partitioned phased blast load contribution. The force-time response curves confirmed three target response phases however the traces differed morphologically. McDonald's and SIIMA's force time response was analysed in terms of the three proposed loading phases and their constituents. SIIMA's Phase One loading did not correlate to the soil cap blast momentum instead it was much lower. This difference is primarily attributed to the mechanical response of the SIIMA measurements system (impulsive loading). Detonic differences between PE4 and TNT are also thought to contribute to the partitioned phase loading differences. The difference between McDonald and the one-seventh scale partitioned test results is due to the different blast loading applied, deep-buried compared to shallow-buried. The difference between SIIMA and McDonalds' test traces is due to both different system responses as well as different blast test loading, that is shallow burned compared to deep-buried blast loading.

The primary and secondary test results were up-scaled using both Cube Root and Geometrically Similar scaling laws. Although some of McDonald's tests scaled relatively close with Cube Root laws (Scaled distance Z), fundamental blast load differences from deeper DOB prevented comparative total impulses being derived from the one-seventh scale test or SIIMA test data. However the data do serve as a comparative base between shallow and deep buried force-time and impulse loading with the one-seventh scale test rig as they are both dynamically loaded systems. Good correlation on total impulse was obtained between SIIMA and the one-seventh scale tests, as was expected as the one-seventh scale and SIIMA experimental designs are both based on the same

threat and similar SOD's. This scaling correlation provides verification of the one-seventh scale methodology and results obtained in terms of total impulse for shallow buried blast loading. However, the partitioned phased impulse did not correlate due to mechanical response differences in the two test rig's blast load measurement systems.

As was seen with the partitioned phased impulse loadings and the comparison of the four different blast load quantification methods, the partitioned phase load contribution does not scale between the one-seventh, McDonald's and SIIIMA tests. Using the system response definition from (Smith, Hetherington 1994) it was confirmed that McDonald's and the one-seventh scale test rig force-time response measurement system are dynamic loaded measurement system whereas SIIMA is an impulsively loaded measurement system. Correlation between the test rigs could be obtained using the mechanical system response functions to see how each system converts the phased loading into the measured response.

This chapter has presented the partitioning of shallow-buried blast loading by discussing the free-field blast ejecta in terms of blast and side-on pressure morphology confirming three loading phases are present. The constituents and sequence of the phases were proposed based on these results. A definition using Bangash affected soil zone definitions (Deshpande, McMeeking et al. 2009b) was analysed for both shallow buried blast and deep buried blast. The blast interaction and resultant target force-time response was then analysed and discussed in terms of the proposed three loading phases and a good fit was obtained. NIR emissions from shallow-buried blast load were analysed and confirmed both three loading phases and the occurrence of afterburn during Phase Three Loading. The blast load side-on and face-on pressure just off the target face was analysed and discussed in terms of the proposed three loading phases and constituents. Again a good fit was obtained. The last part of this section compared different blast load quantification measures and different (secondary data) test rigs blast quantification data, either directly or after the application of Cube Root and Geometrically Similar Scaling laws where

applicable. Although good scaled correlation was achieved between the one-seventh and SIIMA intermediate and near-field tests on total impulse, this correlation did not extend to partitioned phase loading nor its percentage contribution. The primary reason for this was structural response differences between the quantification methods and / or test rigs.

6 Conclusions

The primary focus of this work has been on the measurement, quantification and partitioning of near-field shallow-buried blast from flat cylindrical charges. The threat level was set at 8 kg TNT and a DOB of 50 mm. This equates to a NATO STANAG 4569 threat level 3. The DOB is shallower than NATO requirements, but is a more aggressive blast. A research methodology using a specifically designed one-seventh scale test rig was used to measure, quantify and then partition the positive phase blast load in terms of target force-time response.

Additional blast quantification measurements were made with side-on and face-on pressure as well as the complete measurement assembly displacement time. Due to technical limitations, additional intermediate-field target research tests were required to enable the side-on pressure measurement. NIR light emission was used to quantify shallow-buried blast in terms of emission intensity and to confirm the occurrence of afterburn. All four methods were able to partition the blast into three phases. Force-time data of secondary target response from two independent test rigs for both scaled shallow-buried and deep-buried blast were processed, partitioned and analysed with the one-seventh scale data. Computational modelling was used to predict measurement parameters and to analyse the test results obtained.

This chapter consists of a summary of the findings, a discussion of the problems, the conclusions drawn, a summary of the contributions of this research and suggestions for further work.

6.1 Summary of Findings

Although the initial focus of this work was near-field (Z = 0.29 to 0.31 m/kg$^{1/3}$), an intermediate-field SOD (Z = 0.79 to 0.81 m/kg$^{1/3}$) test series was introduced and provided the bulk of the test data analysed. A summary of the key findings is presented in terms of the free-field ejecta and deep-buried blast morphology, the NIR light emissions, target force-time response, side-on pressure, face-on pressure, complete measurement assembly displacement and secondary data.

6.1.1 Free-field Ejecta

From the free-field ejecta it was determined that the shallow-buried blast front initially accelerates before decelerating as it propagates outwards. The blast front is still accelerating in the near-field but is decelerating in the intermediate-field research SODs. The average velocity at the near-field SOD is similar to the blast front velocities at the intermediate-field SOD. Shallow-buried blast front develops into a tulip or spear shape and break-out of detonation products is observed within microseconds after detonation.

As reported by (Freitas, Bigger et al. 2014) for full-scale shallow-buried blast, two distinct phases were observed in the one-seventh scale tests. The first high-speed phase was initially dominated by crushed fine ejecta and blast overpressure. Towards the end of this phase there are 50-60 degree laterally angled ejecta fingers with larger soil ejecta particles. These larger ejecta were recorded with velocities of 250 m/s. The second phase is the low-speed phase, and this is dominated by the motion of bulk and large ejecta particles in a vertical hollow crown formation, which initially grows outwards at about 5-6 m/s and terminates with a final heave as the ejecta wall falls outwards. Just prior to this the lateral ejecta velocity is around 0.5 m/s. This second phase is driven by inertial loading of the soil by the buried charge (Eridon, James. Zelenik,Tom. Bogalev, Alex. 2014). As reported by (Braid 2002, Bergeron, Coley et al. 2001, RMSS February 2005) the blast was observed to form a hollow cone of ejecta.

Two craters were observed, and in accordance with (RMSS February 2005) the larger crater was termed the primary crater and the smaller the secondary crater. The secondary crater diameter was correlated to the blast stem diameter at the end of the high-speed ejecta phase and the primary crater. The crater at the end of the high-speed phase was similar to or larger than the target diameter. As measured, between 12.5 to 13.6 kg of soil was ejected for one-seventh scale shallow-buried blast. The volume of the complex crater was more than 100% larger than the volume of soil ejected, confirming heavy compaction of the soil. Using the volumetric relationship of the crater, it is estimated that the high-speed phase ejects on average 4.5 kg and the slow-speed phase ejects

8.5 kg of soil. This implies that the majority of the soil ejecta does not impact nor contribute to the shallow-buried blast load impulse transferred to an intermediate or near-field target.

Side-on pressure results were highly variable, with standard deviations in some cases exceeding 50% of averaged values. Most standard deviations were less than 30% of averaged values, which allowed trends to be identified and conclusions to be drawn. Due to a number of repeat tests being executed, useable averaged data were obtained. Positive-phase side-on pressure is over within less than 0.5 ms for an intermediate-field SOD.

Both test and computational modelling and test intermediate-field free-field (ejecta) side-on pressure traces (morphology) exhibited temporal phasing. Three phases were identified, and based on the analyses of the results the following stages and sources of the shallow-buried blast loading are proposed:

i- ***Phase One:*** Initial blast front impact consisting of soil cap and adjacent soil ejecta combined blast front overpressure and included the precursor bow wave shock.

ii- ***Phase Two:*** Reflected pressure build-up of the expanding detonation products focused upwards by the soil and complemented by some high-speed ejecta.

iii- ***Phase Three:*** Reflected pressure effects due to quasi-containment of the blast between the crater, surrounding soil and the target, and afterburn of the remaining detonation products contained between the soil and the target.

The computational modelling, which did not apply an afterburn model, exhibited Phase Three loading. Thus there are reflected pressure effects from the soil and the crater. This reflection will then be enhanced by afterburn if it occurs.

6.1.2 Deep-Buried Blast Morphology

No clear definition of deep-buried blast was found in the literature. Bangash (1993) and Drake and Little (1983), as reported by (Deshpande, McMeeking et

al. 2009a) was used to quantify the depth of burial in terms of charge radius or using charge thickness when applied to flat cylindrical charges. Shallow-buried blast is defined for cylindrical charges where the soil cap is no thicker than Zone 1 or one to one-and-a-half times the thickness of the charge. Deep-buried blast is when soil cap thickness is Zone 2 or larger, thus larger than one-and-a-half times the thickness of the charge for a cylindrical geometry. Zone 1 is defined by Bangash (1993) as a physical overloading of the soil due to very high detonation pressures and temperatures resulting in almost instantaneous crushing and upward ejection of the soil cap. This leads to the almost instantaneous breakout of blast detonation products and ejecta, which then coalesce to form the blast front.

The secondary data provided by (McDonald 2013b) for 100 mm DOB was deemed deep-buried according to Bangash. Deep-buried blast is characterised by a subsonic soil ejecta blast front that bulges hemispherically before rupturing at the top to allow black lower-temperature detonic gases to escape. In some cases these blast fronts were preceded by a soil cap-reflected detonation shock wave that does not materially contribute to the target loading. The (McDonald 2013b) 50 mm DOB test, although deemed to be shallow-buried, exhibited deep-buried morphology, indicating that this definition is dependent on soil conditions as well as charge geometry.

Deep-buried blast fronts also exhibit an initial acceleration to a peak velocity and then a velocity decline as the SOD increases and the blast front expands. (McDonald 2013b) deep-buried blast fronts are characterised by subsonic blast front velocities peaking at 350 m/s.

6.1.3 NIR

The normalised NIR light emission captured from the tests with intermediate and near-field targets exhibited phasing. The intermediate-field had three distinct phases which correlate to initial detonation, detonic gas expansion and afterburn based on work by (Gelfand, Silnikov 2004). This corroborates the proposed three loading phases and their constituents. The near-field results did not clearly exhibit the three-phased loading due to obscuring of the light

emission by the higher density of soil ejecta at the smaller SOD. Due to shot variations in the test set-up of the NIR sensors and emission results, the data could not be further used to quantify the blast loading in terms of light emission.

6.1.4 Target Force-Time Response

The blast front impacting the target was quickly swept across the target face and pushed the soil ejecta around the sides of the target. This confirmed that for this test configuration soil ejecta loading of the target is minimal due to the effect of the expanding detonic pressure following the blast front. For soil ejecta only the initial soil impact loading has any marked effect on the target and thus on the target force-time response.

Both the intermediate and near-field target force-time response traces exhibited three loading phases corresponding to the loading predicted from the free-field (ejecta) test analysis. The blast load in terms of target response force impulse was partitioned into the three phases proposed after the soil ejecta analyses. For both the intermediate and near-field SOD, Phase One loading contributed the most at more than 40% of the total impulse load. The lowest contribution was at the near-field test SOD. For the intermediate-field target, on average the contribution of Phase Three loading was significantly higher than that of Phase Two. For the near-field this changed with Phase Two, giving a higher contribution to the blast load than Phase Three. Therefore the contribution of the phase load changes as SOD changes.

Using the average impact velocity at the intermediate-field SOD, the soil cap mass is the primary blast load constituent for Phase One loading. For the near-field this percentage contribution was smaller due to the much stronger blast overpressure driving the blast front at the lower SOD.

The test configuration affected the force-time traces and as a result the impulse that coupled into the target. The face-on configuration recorded a 12% higher total impulse than the side-on configuration at the intermediate-field SOD. The side-on pressure probe affected the blast loading by reducing the peak force,

increasing the positive phase force duration and reducing the total impulse coupling into the target.

The commissioning near-field blast tests using a target plate that was 35% smaller produced a target force-time response impulse that was 28% lower for a 5:1 D:H shallow-buried blast threat.

6.1.5 Side-On Pressure

The side-on pressure results varied greatly with standard deviations of nearly 50% of average value for one data set due to test set-up variability, in particular charge perpendicularity with the probe and sensor. As with the free-field tests, multiple tests per configuration allowed trends to be identified. Due to the sensor being slightly proud of the target surface, the side-on pressure-time trace gave a saw tooth blast front. The initial peak pressure corresponded to the free-field (ejecta) peak blast pressure. However, for near-field the side-on pressure-time trace of the computational models correlated to the intermediate field in terms of the three loading phases. The onset of each phase occurred much quicker and at a higher pressure than was indicated by the model.

The side-on intermediate-field positive pressure duration was on average 0.267 ms. Phase One always had the shortest duration. On average, Phase Three had a longer duration than Phase Two. Quantifying the blast load in terms of specific impulse, the biggest contribution to the specific impulse blast load was Phase Two, contributing on average 59%, followed by Phase One which contributed 27% and lastly Phase Three, which contributed 14%.

The side-on pressure results correspond to the proposed blast loading phases and constituents. Phase One loading consisting of the soil cap and surrounding soil combined with blast front overpressure would have a high peak pressure but short duration. As the density of the blast front is not measured with side-on pressure, its total contribution to specific impulse will be lower. Phase Two consists of rapidly expanding, high-velocity detonation products that quickly build up reflected pressure as the gas stagnates against the target. This reflection process takes longer than the blast front impact. The Third Phase

loading is from soil and crater reflections, and is thus of much lower intensity and is augmented by afterburn, which is by definition a much lower rate of energy release process, which thus gives a much longer duration.

In comparing side-on to face-on pressure at the intermediate-field SOD, the face-on pressure is found to be 18 to 36 times greater than the side-on pressure. It decreases as the D:H ratio of the threat decreases. The presence of a target at the intermediate-field SOD increases the side-on pressure by two to three times, again decreasing as the D:H ratio of the charge decreases.

6.1.6 Face-On Pressure

As with side-on pressure, the face-on pressure results varied with standard deviations of up-to 70% of the average. This was due to direct impacts of the soil ejecta on the pressure probe surface, which resulted in unrealistic readings. The pressure-time traces contain high-frequency noise emanating from multiple direct soil impacts on the probe sensor element and surrounding steel structure. Despite the noisy signal, three loading phases could be observed for both the intermediate and near-field traces.

The positive pressure phase was on average 0.365 ms for the intermediate field and 0.348 ms for the single near-field pressure trace. The intermediate-field Phase One pressure loading had the shortest duration. Phase Two and Phase Three durations were similar, but Phase Two had a slightly longer duration. For the near-field this changed with Phase Two having a much shorter duration than Phase Three.

The contributions of the intermediate-field partitioned specific side-on pressure phase impulse were similar to the contributions of the intermediate-field SOD side-on pressure, with Phase Two contributing the most at 62% of the total specific impulse. Phase Three contributed 28% and Phase One 12% on average to the total specific impulse. For the near-field this changed to Phase One contributing the most at 63% of the total specific impulse, Phase Two 33% and Phase Three only 2%. As with the side-on pressure, these durations corresponded to the proposed three loading phases and their constituents.

6.1.7 Complete Measurement Assembly Displacement

Similarly, the complete measurement assembly exhibited three movement phases within the initial positive displacement. The test configuration had a marked effect on the side-on and face-on integrated and partitioned displacement-time results. When integrated and partitioned there was a clear difference between the side-on and face-on displacement-time area, with the face-on configuration recording 18% larger integrated displacement loading than the side-on configuration. The phased contributions were dependant on the test configuration. The side-on test configurations also affected the partitioned phase contributions. For the side-on configuration at the intermediate-field SOD, Phase One contributed the lowest displacement-time loading.

6.1.8 Secondary Data

The shallow-buried large-scale (SIIMA) and deep-buried (McDonald 2013b) secondary target-response force-time test data were analysed in terms of force-time morphology, force and impulse scaling and partitioned phase blast load contribution. The SIIMA data were obtained from one scaled near-field and one full-scale intermediate-field shallow-buried blast test series. (McDonald 2013b) test had one near-field and three different SOD intermediate-field deep-buried blast test series.

6.1.8.1 Target Force-Time Morphology Response

Both (SIIMA) and (McDonald's) data exhibited phased force-time target response. SIIMA had three phases for both the half-scale (1 kg) near-field and full-scale (8 kg) intermediate-field shallow-buried blast tests. Phase Three loading for SIIMA had a longer contributing duration, comprising on average 63% of the total positive phase force duration. This was expected, with TNT giving more robust afterburn than PE4.

(McDonald 2013b) deep-buried target force-time response traces were much longer than for shallow-buried blast and were dominated by two phases with a third appearing as the SOD was reduced. The increased DOB also affects the

occurrence of Phase Three loading as this phase was only marginally present with intermediate-field SOD and much reduced in the near-field target force-time response. In general, these phases corresponded to the Phase One, Two and Three loading. However, the constituents of these phases are different for Phase Two and Phase Three as the longer duration of the deep-buried blast development, combined with containment of the initial detonic gases, resulted in no afterburn possibly taking place and a more efficient load transfer to the soil cap. Thus the detonic gas expansion would not be a separate loading phase, but combined for the Phase Two loading. Deep-buried Phase One loading also consists of the soil cap and blast front overpressure; however, these are at much lower impact velocities and pressures and of longer duration. Due to the slower fractured rupture of the thinning soil cap, the mass of the soil impacting the target is difficult to determine for these analyses.

6.1.8.2 Scaling

Both the secondary data sets were scaled using Hopkinson Scaling and Geometrically Similar Scaling with 8 kg TNT as the full-scale (prototype) charge. (McDonald 2013b, McDonald 2013a) tests equated to a $^{2}/_{7}$th scaled blast. The SIIMA tests scaled to one-half (1 kg) for the near field and full scale (8 kg) for the intermediate field. The SIIMA one-half scale 5:1 D:H ratio near-field tests produced an average blast force-time impulse of 3,160 Ns. The one-seventh scale 5:1 D:H ratio shallow-buried blast scaled to one-half scale gave a calculated average impulse which was less than 5% different from the one-half test impulse. The intermediate field the 5:1 D:H shallow-buried blast threat of the one-seventh scale charge scaled to full gave a calculated impulse which had a 9% difference from the full-scale test data. (McDonald 2013b) intermediate and near-field tests scaled to full produced calculated impulses of 22,079, 37,083 and 38,208 Ns for intermediate and near-field deep-buried blast tests. The single shallower-buried test gave a full-scale impulse of 35,733 Ns.

6.1.8.3 Phased Blast Load Contribution

For both the intermediate and near-field partitioned shallow-buried blast the phased load contribution increased from Phase One to Phase Three. Phase

One gave the lowest contribution of 15%, Phase Two gave 32% and Phase Three gave the highest contribution of 53% of the total blast load. (McDonald 2013b) deep-buried blast test gave differing phase load contributions. The first two intermediate-field deep-buried blast tests had an averaged Phase One load contribution of 57% and the Phase Two load contribution was 43%, with no positive Phase Three loading. The intermediate-field shallower deep-buried blast test produced an equally split load between Phase One and Phase Two of 50% each. Again there was no positive Phase Three loading. The near-field deep-buried blast test produced a Phase One load contribution of 28%, a Phase Two load contribution of 55% and a Phase Three load contribution of 13%. These contributions differed from those of the shallow-buried blast load phase.

6.1.8.4 D:H Ratio/Spherical

Using Bangash's definition of Zone 1 (shallow buried) (McDonald 2013b) intermediate-field 50 mm test should have behaved as a shallow-buried blast but instead produced a deep-buried blast morphology. For these tests a hand-rolled spherical charge was used that was understood to be centrally initiated. This charge configuration appears to produce less aggressive loading on the soil than a flat cylindrical charge.

6.1.9 Blast Load Quantification

The one-seventh scaled shallow-buried blast load was quantified using five methods. These were target force-time response (impulse), side-on pressure (specific impulse), face-on pressure (specific impulse), target global displacement-time (mm.s) and normalised NIR light emission. Due to the NIR being a new experimental technique for the author, the captured data varied too much to be used for quantified trend analyses at this time. The partitioned phase load contributions vary for each quantification technique. Using the definition of loading type in terms of the natural frequency of the target response compared to the blast duration from (Smith, Hetherington 1994), where the target is seen as the quantification sensor, this difference is due to the target loading type for each of the quantification technique. For side-on and face-on pressure the loading is quasi-static, for the piezoelectrically measured target

force-time response the loading is dynamic and for the completer measurement assembly displacement the loading is impulsive. The Cranfield (McDonald 2013b) test rig is assumed to be dynamically loaded as it is constructed similarly to the one-seventh scale test rig, whereas SIIMA is impulsively loaded.

6.1.10 Charge Geometry (D:H)

The charge geometry of flat cylindrical charges affected not only the total measured blast load but also the partitioned phase contributions. For the intermediate field, as the D:H ratio decreased, the averaged total impulse, peak force and peak measurement assembly deflection decreased. The blast front velocity, however, increased as the D:H ratio decreased. The averaged side-on pressure increased as the D:H ratio decreased; however, the face-on pressure decreased as the D:H ratio decreased. These findings are summarised in Figure 160. The opposite trend was found for the specific impulse: when the D:H ratio decreased, the side-on pressure-specific impulse decreased, while the face-on pressure-specific impulse increased as the D:H ratio decreased. These findings are summarised in Figure 161. The near-field computational model predicted a side-on pressure increase as the D:H ratio decreases, which agrees with the intermediate-field test results. The force-time impulse Phase One loading was very similar between all three D:H ratios tested, thus as the D:H ratio decreases the amount of soil adjacent to the charge soil cap ejected as part of the initial blast load increases.

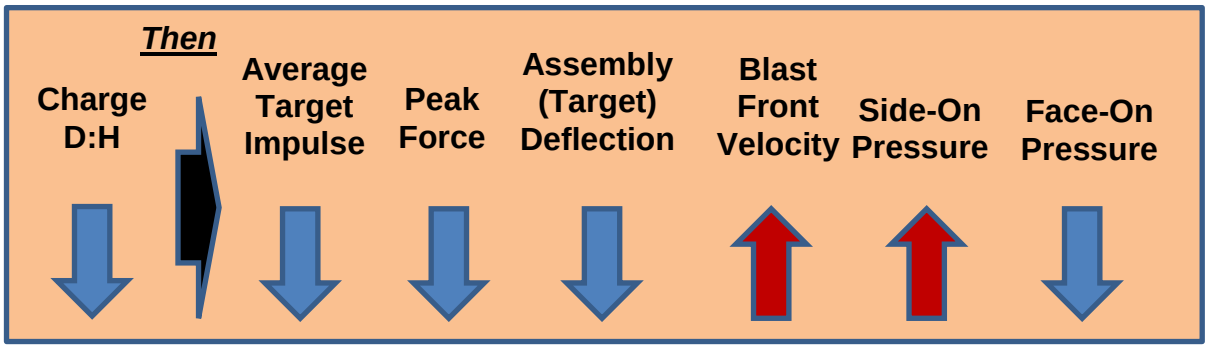

Figure 160: Intermediate Field Blast Trends

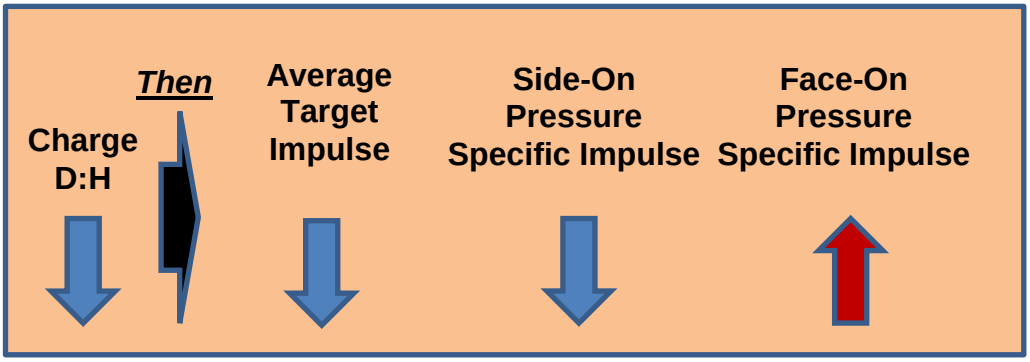

Figure 161: Intermediate Field Impulse Trends

6.1.11 Target SOD (Intermediate Field vs. Near Field)

For shallow-buried blast, as the target SOD is reduced from intermediate to near-field conditions, in addition to the total impulse increasing, the partitioned phase loading changes. The blast pressure duration remained the same for the face-on pressure test configuration at the intermediate and near-field SOD.

6.2 Discussion of Problems

The primary concerns with the test data used for this work are the variability in the results. The force-time and displacement time results were not affected. The force-time impulse provided standard deviations of no more than 12% of average for one test series, with the rest giving standard deviations of less than 5% of average. The variability was due to the small scale applied to the test charges. Although providing a properly scaled blast environment that enables the use of sensors such as flush-mounted face-on pressure sensors and pencil probes, such small-scale charges require much more detailed and refined set-up procedures. The repeatability was addressed to some degree: test repeats allowed averaged data trends to be extracted and compared, but less variable data would allow much more robust trends to be identified and conclusions to be drawn.

The majority of the test data sets are for intermediate-field test conditions and were not the initial focus of this work, which is the near field. Although limited, the near-field data did enable verification of findings and confirmed the applicability for these conditions. The intermediate-field data were, however,

most useful as they allowed for the more distinct separation of the blast load phases making their measurement and quantification easier.

The computational modelling that was done did not cover both test configuration (side-on and face-on pressure) and no face-on pressure data were extracted. This made the comparison of field tests with the model difficult and the conclusions drawn less robust.

The side-on pressure sensor required that the blast front should not vary by more than one degree from the perpendicular to the blast probe centre line (Walters 2016). This affects both the accuracy as well as adding to the variability in results seen particularly in the free-field ejecta tests. The target face side-on pressures were less affected as the target face generated a stagnation effect which reduced the measurement inaccuracy primarily to the initial blast passing the sensor prior to impact.

The partitioning of the quantification parameters all involved some degree of manual intervention, thus making the results variable and subjective to a small degree. A robust automated signal-processing method would enhance the robustness and repeatability of the partitioning quantification.

The reflection waves occurring within a detonation cloud could not be discerned in the side-on and face-on pressure traces. Thus these detonic effects are amalgamated within the blast overpressure of Phase One and the high-speed pressure contribution from Phase Two blast loading. Additional differentiation of the current three blast loading phases may be possible to identify, which is not easily done with this research methodology.

6.3 Conclusions

This work had one primary and three supportive research objectives focussed on achieving the following:

> *To partition a shallow-buried near-field blast load in terms of the following constituents: initial blast shock wave; primary explosive gas expansion;*

soil ejecta; reflected shock waves; secondary burn; and other ejecta such as casing fragments.

The following conclusions have been drawn from this work:

1. A shallow-buried blast consists of three temporally separated phases.
    - Phase One consists of the soil cap and some surrounding soil ejecta impact and blast front overpressure.
    - Phase Two loading is primarily detonic gas expansion.
    - Phase Three loading is due to pressure reflections from the crater, and when present, the near or intermediate-field target pressure reflection that is augmented by afterburn.
2. A deep-buried blast exhibits the same three phased loading. However with different constituent contributions:
    - Phase One blast loading is due to the initial blast front overpressure and ejecta impact. Impact velocity is much lower and has considerably higher ejecta mass.
    - Phase Two is dominated by detonic gas expansion supported by relatively large slow speed soil ejecta mass expansion inertia.
    - Phase Three is primarily based on reflected pressure between the soil-free surface, the crater and the target. The longer time to breakout of the gases results in shielding of the detonic gases from additional oxygen and cooler detonation gases, thus preventing afterburn.
3. Slow-speed ejecta do not contribute to the blast loading for shallow buried blast for the finite sized targets used in this work.
4. Due to the mechanics of buried blast, it is not possible to separate the constituents due to mixing. There are contributions of the preceding phases within the following phases. The transition between loading phases is not significant enough and the phases merge as the SOD is reduced.
5. Total and phased blast load contributions vary with charge geometry, DOB and SOD Changes.

6. NIR emission from a shallow buried blast exhibits temporal phasing and confirms that shallow buried blast is characterised by early detonic breakout, detonic gas expansion and afterburn.

In understanding that the Phase One followed contributes the most to shallow buried blast loading active and passive methods inserted between the bottom of the target and the soil to disrupt the soil cap and entrained ejecta will provide the most benefit for buried blast protection. A simple spike reduced the impulse loading by 25%. This understanding can also be used to relook at how existing protection methods such as external bins are positioned and used as these could inadvertently increase localised blast loading.

6.4 Summary of Contributions

The current main method of investigating and quantifying blast is a singular impulse value. Although impulse is an extremely useful and robust value that scales well, it does not necessarily equate directly to damage in terms of plastic deformation of the target for shallow-buried blast (Zakrisson, Wikman et al. 2008). A methodology has now been developed and presented to partition and quantify a shallow-buried blast in terms of the dynamic loading of a target based on its positive force-time response to the blast load it is subjected to. This phasing is a characteristic of the target geometry, the blast threat geometry, its DOB and SOD, and can be used to quantify and analyse both deeper-buried as well as free-in-air blast loading. This methodology provides a more refined method to quantify which phase is affected by the target and threat configuration. This understanding can be used to focus research on passive and active landmine protection technologies that can modify or reduce those loading phases determined to be most damaging or least desirable.

6.5 Suggestions for Further Work

To enhance this work it is recommended that additional computational modelling be done to model the intermediate-field target blast loading and target response. Additionally, the modelling of the free-field ejecta and the near and intermediate-field ejecta should be re-run using an afterburn addition to the

explosive equation-of-state model and the results compared to each other as well as to the test results. Additional analysis techniques of computational results should be applied, in particular pressure field mapping, to investigate the side-on pressure spike related to the charge D:H .

The set-up methodology, in particular the positioning of the test charge, should be further refined to reduce the test variability observed in the side-on pressure results. If possible, tests should be repeated to obtain more data to provide a more robust data set with lower standard deviations.

The NIR emission technique should be further refined to reduce variability. This includes quantification of external factors and carrying out free-in-air tests to quantify the outputs and possibly to serve as a calibration methodology.

REFERENCES

ANSYS INC., 2011. *Training Notes: Introduction to Ansys Autodyn Release 12.1.* Training Notes edn. UK: Ansys Inc.

BAILLARGEON, Y., SIRIOS, A. and MCINTOSH, G., 2005. Development of a TMRP6 Surrogate Mine, , 22nd International Symposium on Ballistics 2005, pp. 602.

BAKER, W.E., 1973a. *Explosions in air.* University of Texas Press Austin, TX.

BAKER, W.E., 1973b. *Explosions in air.* University of Texas Press.

BEETGE, F.J., 2008. *Impulse Loading of Near Field Shallow-Buried Explosions*, University of Cape Town.

BERGERON, D.M., COLEY, G.G., ROUNTREE, M.S., ANDERSON, I.B. and HARRIS, R.M., 2001. *Assement of Foot Protection Agianst Anti-perosnnel Landmine Blast Uisng Frangible Surrogate Leg.*

BONORCHIS, D. and NURICK, G.N., 2010. The analysis and simulation of welded stiffener plates subjected to localised blast loading. *International Journal of Impact Engineering,* **37**(3), pp. 260-273.

BRAID, M.P., 2002. *Experimental investigation and analysis of the effects of anti-personnel landmine blasts.*

CAMP, S. and HEITMAN, H.M., 2014. *Surviving the Ride: A Pictorial History of South African-Manufactured Mine Protected Vehicles.* 1 edn. 30 Degrees South.

CANADIAN INTERNATIONAL DEMINING CENTRE, c.a. 2001. *MIne Data Bse Program.* Computer Program Listing Landmines edn. Canada: Canadian International Demining Centre.

CARREIRA, D., 2017. *Energy balance leading to the skewness of the blast front.*

CHEESMAN, R., TILBURY, C., BRADLEY, K. and SUTTON, B., 2014. Diagnostic Techniques for Measuring Combined Blast and Debris Loading on Structures in the Near Field, *23rd Militray Aspects of Blast and Shock*, September 2014 2014.

CLARKE, S.D., FAY, S.D., TYAS, A., WARREN, J., RIGBY, S., ELGY, I. and LIVESEY, R., 2014. Repeatability of Buried Charge Testing *23rd Military Applications of Blast and Shock*, Setember 2014 2014.

CLARKE, S., RIGBY, S., FAY, S., TYAS, A., REAY, J., WARREN, J., GANT, M., LIVESEY, R. and ELGY, I., 2015. Bubble-type 'vs ' Shock-type' Loading from Buried Explosives, *Proceedings of the 16th International Symposium on Interaction of the Effects of Munitions with Structures (ISIEMS16)* 2015.

COOPER, P.W., 1996a. *Explosives Engineering.* 1 edn. USA: Wiley-VCH.

COOPER, P.W. and KUROWSKI, S.R., 1996. *Introduction to the Technology of Explosives.* Wiley-VCH.

COOPER, P.W., 1996b. *Explosives Engineering.* 1 edn. USA: Wiley-VCH.

COOPER, P.W., 1996c. *Explosives Engineering.* USA: Wiley-VCH.

CRANFIELD COURSE, 2009. *Explosive Science Advanced.* Master Training Course edn. UK: Cranfield University, Department of Applied Science, Security and Resilience.

CULLIS, I.G., 2001. Blast waves and how they interact with structures. *Journal of the Royal Army Medical Corps,* 147(1), pp. 16-26.

DESHPANDE, V., MCMEEKING, R., WADLEY, H. and EVANS, A., 2009a. Constitutive model for predicting dynamic interactions between soil ejecta and structural panels. *Journal of the Mechanics and Physics of Solids,* **57**(8), pp. 1139-1164.

DESHPANDE, V.S., MCMEEKING, R.M., WADLEY, H.N.G. and EVANS, A.G., 2009b. Constitutive Model for Predicting dynamic interactions between soil ejecta and structural panels. *Journal of the Mechanics and Physics of Solids,* 57 (2009), pp. 1139-1164.

EDRI, I., FELGUN, V.R., KARINSKI, Y.S. and YANKELEVSKY, D.Z., 2012. On Blast Pressure Analysis Due to a Partially Confined Explosion: III Aferburning Effect. *International Journal of Protective Structures,* **3**, pp. 311.

ERIDON, JAMES. ZELENIK,TOM. BOGALEV, ALEX., 2014. Blast Distribution from Buried Charges, 2014.

FOURNEY, W.L., LEISTE, U., BONENBERGER, R. and GOODINGS, D.J., 2005. Mechanism of loading on plates due to explosive detonation. *Fragblast,* 9(4), pp. 205-217.

FREITAS, C.J., BIGGER, R.P., THOMAS, J.P. and MACKIEWICZ, J.F., 2014. Threat Characterization Methodology for IED Post-Detonation Environments to Dismounted Warfighters, *PASS2014 Proceedings*, 8-12 September 2014, Cambridge UK 2014.

GELFAND, B. and SILNIKOV, M., 2004. *Explosions and Blast Control.* 1 edn. Saint Petersburg: Asterion.

GRUJICIC, M., B PANDURANGAN, B., HUANG, Y., CHEESEMAN, B.A., W N ROY, W.N. and SKAGGS, R.R., 2007. Impulse loading resulting from shallow buried explosives in water-saturated sand *IMechE Vol. 221 Part L: J. Materials: Design and Applications,* , pp. 21.

GRUJICIC, M., PANDURANGAN, B., COUTRIS, N., CHEESEMAN, B.A., ROY, W.N. and SKAGGS, R.R., 2008. Computer-simulations based development of a high strain-rate, large-deformation, high-pressure material model for STANAG 4569 sandy gravel. *Soil Dynamics and Earthquake Engineering,* 28(12), pp. 1045-1062.

HELD, M., 2004. Blast Effects with the Held Momentum Method, *21st, International symposium on ballistics* 2004.

JONES, N., 2011a. *Structural impact.* Cambridge University Press.

JONES, N., 2011b. *Structural impact.* Cambridge university press.

JOYNT, V., 2011. *Discussion on landmine blast effects.* N/A edn. N/A: N/A.

KINNEY, G.F. and GRAHAM, K.J., 1985. *Explosive shocks in air.* 2nd edn. Berlin Heidelberg: Springer-Verlag.

MAVKO, G., Unknown. *Parameters That Influence Seismic Velocity.* Training Course Notes (Chapter8 p 73) edn. USA: Stanford Rock Physics Laboratory.

MCDONALD, A.B., 2013a. *The Response and applied Pressure of Quadrangular Plates to Buried Charges*, Cranfield.

MCDONALD, A.B., 2013b. *The Response and Applied Pressure of Quadrangular Plates to Buried Charges*, Cranfield University.

MILNE, A., BRADLEY, T., KIRKPATRICK, D. and LONGBOTTOM, A., 2014. Numerical and Experimental Study of Near Field Blast Mitigation Effects in Cylindrical Geometry *23rd Militray Applications of Blast and Shock (MABS)*, 12-17 September 2014 2014.

MOSTERT, F.J., July 2015. *Discussion on initial results.*

NATO STANDARDIZATION AGENCY (NSA), 31 August 2011. *NATO Standard Allied Engineering Publication 55 (AEP-55) Volume 2: Procedures for Evaluating the Protection Levels of Armoured Vehicles for Mine Threat.* Test Standard edn. NATO.

NATO STANDARDIZATION AGENCY (NSA), 23 May 2014. *NATO Standard Allied Engineering Publication 55 (AEP-55) Volume 3 (Part I), Procedures for Evaluating the Protection Level of Armoured Vehicles – IED Threat.* Test Standard edn. NATO.

NEEDHAM, C.E., 2010. *Blast Waves.* First edn. Germany: Springer-Verlag Berlin Heidelberg.

PICKERING, E.G., CHUNG KIM YUEN, S., NURICK, G.N. and HAW, P., 2012. The response of quadrangular plates to buried charges. *International Journal of Impact Engineering,* 49(0), pp. 103-114.

PROUD, W., 2014. *Discussion on shock transmission and reflection in porous media and back into developing detonation products, blast cloud.*

RAMASAMY, A., HILL, A.M., HEPPER, A.E., BULL, A.M.J. and CLASPER, C.J., 2009. Blast Mines: Physics, Injury Mechanisms And Vehicle Protection. *Journal of the Royal Army Medical Corps December 2009,* .

RISI TELEDYNE, N/A. *RP83 EBW Detonator Technical Sheet.* N/A edn. USA: Risis Reledyne.

RMSS, February 2005. *RSA-MIL-STD-37 Issue 3 Landmine Protected Wheeled Vehicles: Design, Development and Evaluation of,* Test Standard edn. Pretoria, South Africa: South Africa.

SHOWICHEN, A., 2008. *Numerical analysis of vehicle bottom structures subjected to anti-tank mine explosions*, Cranfield University.

SMITH, P., MOSTERT, F. and SNYMAN, I., 2008. Comparison of Methods to Measure the Blast Impulse Loading of an Explsoive Charge, *24th International Symposium on Ballistics*, 22-26 September 2008 2008.

SMITH, P.D. and HETHERINGTON, J.G., 1994. *Blast and ballistic loading of structures.* CRC Press.

SNYMAN, I.M., 2015. *Personal discussion on Hopkinson (Cube-Root) and Geomyerically Similar Scaling of Force-Time impulse and derivation thereof.* N/A edn.

SNYMAN, I.M., 2012. The velocity of the expanding by-products and soil layer on top of a buried landmine *International Congress on High Speed Imagaing and Photonics 2012,* .

SNYMAN, I.M., 2009. *Blast Loading Quantification : Research Strategy, Literature Review and Experimental Design.* GLBL-AG900-09-003 Rev 1. CSIR.

SNYMAN, I.M. and REINECKE, J.D., 2006. MEASURING THE IMPULSE FROM AN EXPLOSIVE CHARGE. *Conference: Ballistics Symposium South Africa, At Denel-OTB, Bredasdorp*.

STIFF, P., 1986. *Taming the landmine.* Galago.

SWISDAK, M., 1975. Explosion Effects and Properties.Part I.Explosion Effects in Air.

SYNGELLAKIS, S., 2013. *Design Against Blast: Load Definition & Structural Response.* WIT Press.

TREMBLAY, J.E., 1998. *IMPULSE ON BLAST DEFLECTORS FROM A LANDMINE EXPLOSION.* DREV- TM - 9814. DEFENCE RESEARCH ESTABLISHMENT CENTRE DE RECHERCHES POUR LA DEFENSE.

URIBE, J., POVEDA, V. and RODRIGUEZ, J., 2011. Effect of setup parameters of landmine blast over transferred energy to rigid body: experimental and computation study, *Proceedings of the 26th International Symposium on Ballistics* 2011, pp. 187-195.

WALTERS, P., 2016. *137 Must be within plus or minus five degrees of the incoming wave to read properly (PCB Technical Note 27).*

WASMULLER, S., 2008. *CIED Conference.* Closed Military Symposium Presentation edn. Germany: IABG.

WECKERT, W. and ANDERSON, C., September 2006. *A Preliminary Comparison Between TNT and PE4 Landmines* DSTO-TN-0723. Australia: Weapons Systems Division, DSTO Defence Science and Technology Organisation.

WESTINE, P.S., MORRIS, B.L. and COX, P.A., 1985. *Development of Computer Program for Floor Plate Response for Land Mine Explosion.* TACOM Technical Report 13045. USA: TACOM.

ZAKRISSON, B., WIKMAN, B. and JOHANSSON, B., 2008. Half scale experiments with rig for measuring structural deformation and impulse transfer from land mines, *Proceedings of the 24th International Symposium on Ballistics,(September 22–26, New Orleans USA), DEStech Publications Inc* 2008, pp. 497-504.

Appendix A Scaling Research Summary

Parameter	Geometric Scale Factor for Model Equivalence	Model Parameter Scaling Equation	Comment
Distance	β	$l=\beta L$	[Jones](Jones 2011a)
Area	β^2	$a=\beta^2 A$	[Cooper]
Volume	β^3	$v=\beta$	[Cooper]
Density	1	$\rho=P$	[Jones](Jones 2011a)
Mass	β^3	$m=\beta^3 M$	[Cooper 11.2.1]
Time	β^{-1}	$t=\beta^{-1}T$	[Jones 11.2.5](Jones 2011a)
Velocity	1	$v=V$	[Jones 11.2.6]
Force	β^2	$f=\beta^2 F$	$f=ma=\beta^3 M\beta^{-1}A=\beta^2 F$ $f=pl2=P\beta^2 L^2=\beta^2 F$ [Jones 11.2.3 and 11.2.7]
Pressure	1	$p=P$	[Jones 11.2.3]
Impulse (Side-on)	β	$i=\beta I$	$i=\int pdt=\int Pdt=\int P\beta dT=\beta I$ [Baker]
Impulse (Face-on)	β^3	$i=\beta^3 I$	$i=\int fdt=\int F\beta^2 d(\beta T)=\int F\beta^3 dT=\beta^3 I$ (not in any references)
Gravity	β^3	$f_g=\beta^3 F_g$	$f_g=mg=\beta^3 Mg$ [Jones 11.3.1]
Acceleration	β^{-1}	$a=\beta^{-1}A$	$f=\beta^2 F=ma$ as $F=MA$ thus $ma=\beta^2 MA$ thus $a=\beta^2(M/m)A=\beta^2 A/\beta^3$ as $m=\beta^3 M$ (derivation not in any references however relationship is noted in [Jones] 11-2.7 for drop testing)
Wave Speed	1	$c=C$	[Jones 11.2.4](Jones 2011a)
Particle Speed (Blast Wind)	1	$u_p=284(M_x^2-1)/M_x$	Not scaled directly but calculated using equation (Kinney Graham). Remains the same [Baker]
Strain	1	$\varepsilon=\xi$	[Jones 11.2.1](Jones 2011a)
Stress	1	$\sigma=\Sigma$	[Jones 11.2.2] (key scaling requirement)
Strain Rate	β^{-1}	$\dot{\varepsilon}=\dot{\xi}/\beta$	[Jones 11.3.2]

Appendix B Research Instruments

B.1 One-Seventh Scale Test Rig

The one-seventh test rig is a dual-purpose-built scale buried-blast test rig that is able to quantify buried-blast loading in terms of soil ejecta, side-on and face-on pressure and target force-time response. Two different arrangements were used for the commissioning tests and primary research tests for both the target force-time response as well as the soil ejecta morphology configurations.

B.1.1 Commissioning Tests Configuration for Commissioning Tests

Figure 162 presents the commissioning configuration for shallow-buried near-field blast tests.

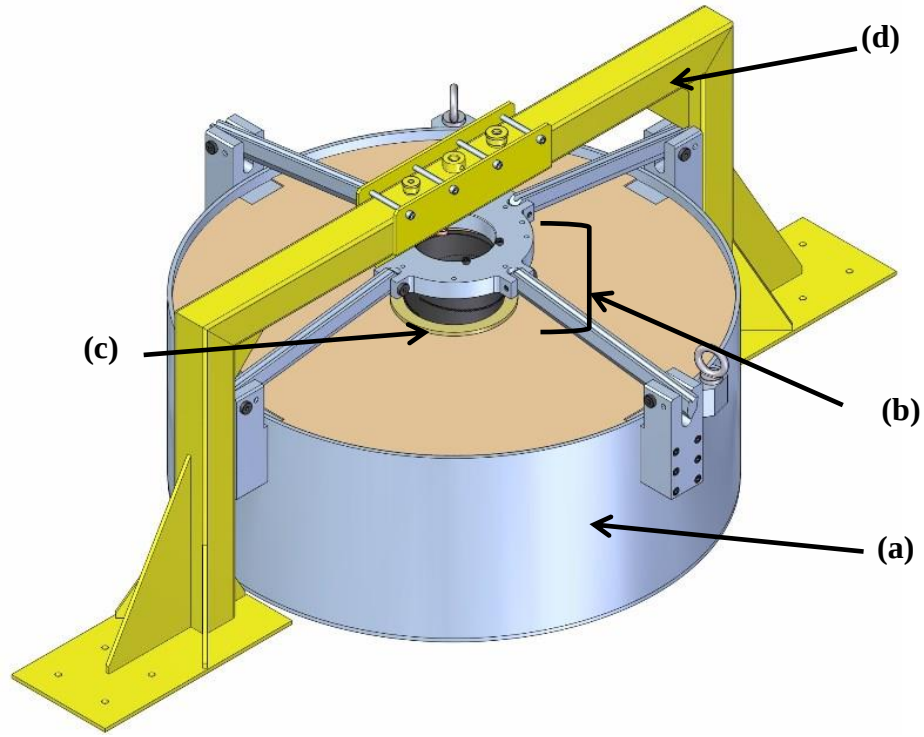

Figure 162: Commissioning Test Configuration (Small Ring and Target)

The soil bin (a) serves as the weighted base. The measurement assembly (b) consists of a small supporting ring and 290 mm diameter target plate (c) that sits proud of the external ring diameter. The instrumentation frame (d) is mounted over the measurement assembly and was used to position the LVDT (not shown) to measure the complete measurement assembly. This

measurement arrangement utilised 100 kN piezoelectric force washers. Figure 162 also shows the four mounting arms that retain the measurement assembly above the soil bin. Table 13 lists the primary measurement equipment used for the commissioning tests.

Table 13: Commissioning Instrumentation List

Description	Manufacturer	Part No	Qty.
Force washers	HBM	CFW100	4
Charge amplifiers (force washer)	HBM		4
Force washer charge amplifier BNC adapter, reset and range selector box	LS	N/A	4
Data acquisition	Graphtec	GL1100	
LVDT	HBM	-	1
LVDT	Kyowa	-	1
Combined LVDT field signal conditioner and power supply	CSIR	-	1
Side-on pressure probe (low)	PCB	137A22	2
Side-on pressure probe (high)	PCB	137A21	2
Multichannel PCB ICP signal conditioner	PCB	2482A22	4
Oscilloscope	Tektronix	T2025	2
High-speed camera	Photron	SA4	1
Weather station	Kestrel	4500	1
Firing system	Risi-Teledyne	FS-43	1

B.1.2 Primary Research Buried Blast Arrangement

Table 14 lists the main measurement instrumentation used for the primary research tests.

Table 14: Primary Research Test Instrumentation

Description	Manufacturer	Part Number	Qty.
Force washer attachment including assembly: - 1 off 10 mm thick target plate (machined) with 1 off 10 mm thick spacer ring (06119-0560-261) - 1 off spacer dummy 3 (40 mm long) - 8 off M8 cap screws - 4 off M20 cap screws (pre-tension bolts) - 4 off 330 kN nylon guide sleeves - 8 off 330 kN machined washers - 1 off 10 mm thick spacer ring (06119-0560-261)	LS	One-seventh scale blast jig dummy No. 3 / 700 kN face-on force 06119-0900-26, One-seventh blast plate – base line 06119-0560-261 and one-seventh scale blast rig 06118-0500-261	As per list
Piezoelectric force washers	HBM	CFW 330	4
Data acquisition	HBM	Gen 7	1
Charge / ICP / Voltage signal conditioner / Amplifier	PCB	482C54	2
Charge attenuators	PCB	472B03 1/50	5
ICP signal conditioner with battery power supply	PCB 482A22	482A22	1
ICP pencil pressure probe (standard tip fitted)	PCB 137A21	137A21	1
PCB pressure pencil probe holder	LS		1

Description	Manufacturer	Part Number	Qty.
Face-on pressure transducer	PCB	109B01	1
PCB 109B01 mounting threaded insert (flush) with custom wrench	LS	Pressure Holders for Sensor 109B01/134A24 Rev 1)	1
Oscilloscope	Tektronix	2024	2
New optical diode sensor assembly	LS	N/A	1
LIVM (Low-Impedance Voltage Mode) Impulse hammer	Dytran	5802A	1
Single channel ICP sensor signal conditioner	PCB	480C02	1
Displacement transducer	K Systems		1
High-speed camera	Photron	SA-4	2
Firing system	*Risi-Teledyne*	*FS-43*	1

Figure 163 shows the assembly of the target and force washers and Figure 164 shows the force washer assembly. The 10 mm thick target plate (b) is bolted onto the supporting ring (c) using eight M8 bolts (a) forming the target assembly. The bolt heads remain proud of the target face. The target assembly is then bolted to the retaining plate (f) using four M20 bolts (g) that thread through the head into the target assembly. The bolts are threaded through the force washer assembly (d) which consists of a nylon sleeve (h), two hardened ground steel washers (i) and the force washer (j) (see Figure 164). The nylon sleeve fits through the force washer with minimal friction and mates into machined recesses in the retaining plate and the supporting ring. Its purpose is to centre the force washer. The two recesses are deep enough not to compress the nylon sleeve. The two washers are each placed at the top and bottom of the force washer and serve as flat non-deforming surfaces for the force washer to bear against. The slip fit of the nylon sleeve ensures a clean load path from the

supporting ring through the force washers onto the retaining plate. The four retaining arms hold the measurement assembly in place (e).

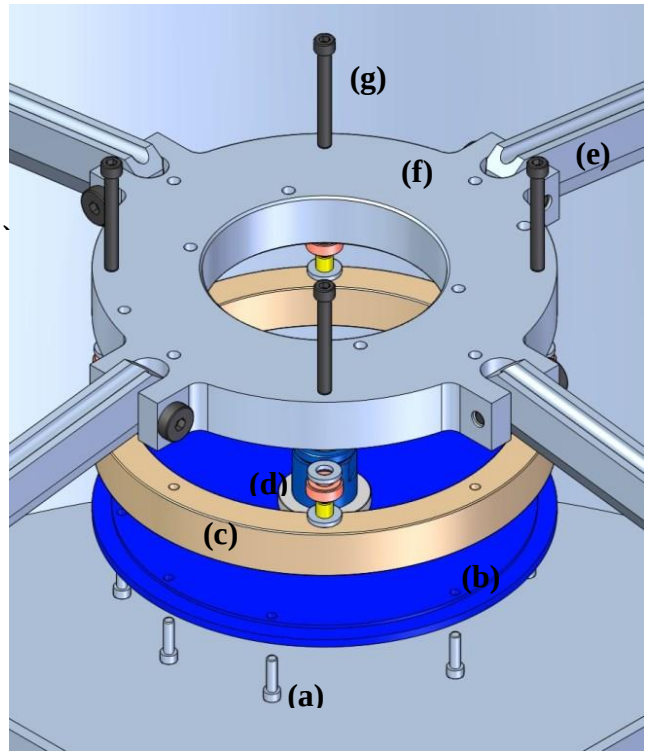

Figure 163: Measurement Assembly 100 kN Force Washers

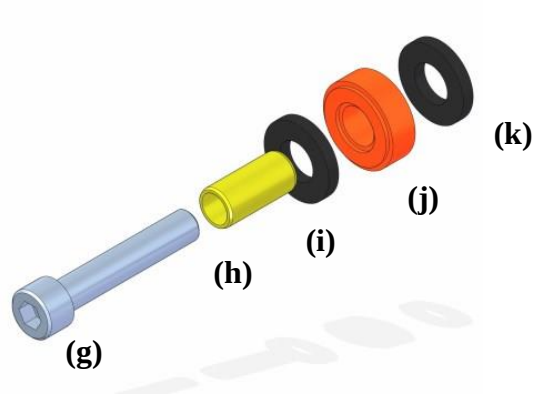

Figure 164: Force Washer Assembly

B.1.3 Commissioning Test and Primary Research Test Soil Ejecta Configuration

Figure 165 (a) presents the commissioning soil ejecta test configuration, while Figure 165 (b) shows the primary research test soil ejecta configuration. In Figure 165 the inner soil bin (a) is clearly visible showing the surrounding soil. The side-on pressure probe (b) is shown mounted on the instrumentation frame

(c) with the V-deflector plate (d). For the primary (final research) tests a streamlined pressure probe holder (e) was placed over the centre of the inner soil bin. To accommodate the change in height of the sensor the soil bin assembly was placed on a steel spacer (f).

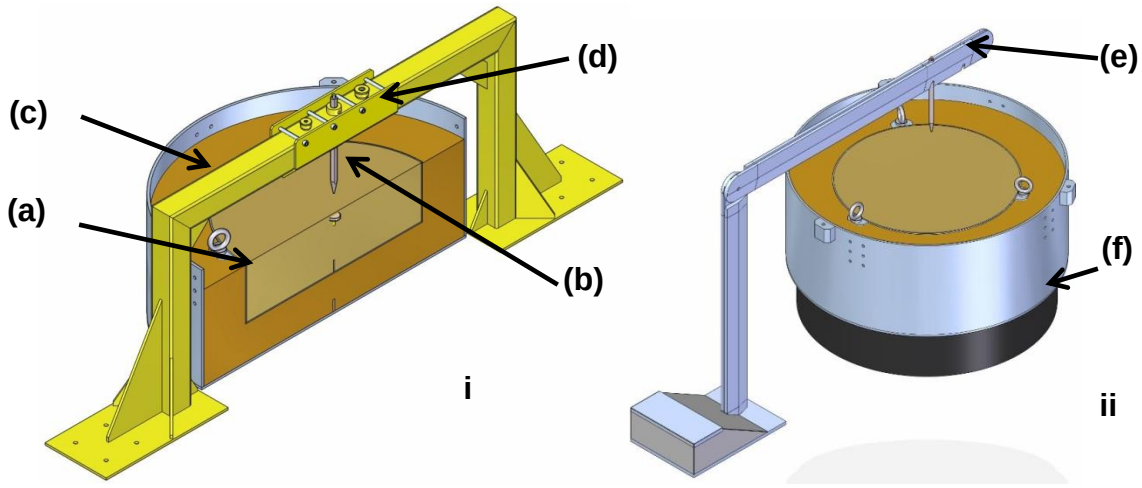

Figure 165: Soil Ejecta i) Commissioning and ii) Primary Research Configuration

Table 15: Ejecta Commissioning and Primary (Final) Research Test Instrumentation

Description	Manufacturer	Part Number	Quantity
6.9 MPa pencil probe	PCB	137A21	2
3.5 MPa pencil probe	PCB	137A22	2
Data acquisition	HBM	Gen7	1
4-Channel ICP signal conditioner	PCB	482C16	1
SA4 camera systems with laptops, lenses (fixed and zoom) and stands	Photron	SA-4	2
1,000 kg in-line load cell with shackles for use with the crane	Load Cell Services	-	1
Scale assembly	CSIR	06120-0100-261	1
Somat eDAQ Lite®	HBM		1

B.1.4 Supporting Equipment

Figure 166 shows the hand-form charge with the detonator forming tool inserted (a). The tool is removed to allow the detonator (b) to be inserted to the same depth. The detonator support (d) that ensures that the detonator remains perpendicular to the charge face is also shown, along with the small undercut used to lock the charge in the casing (d).

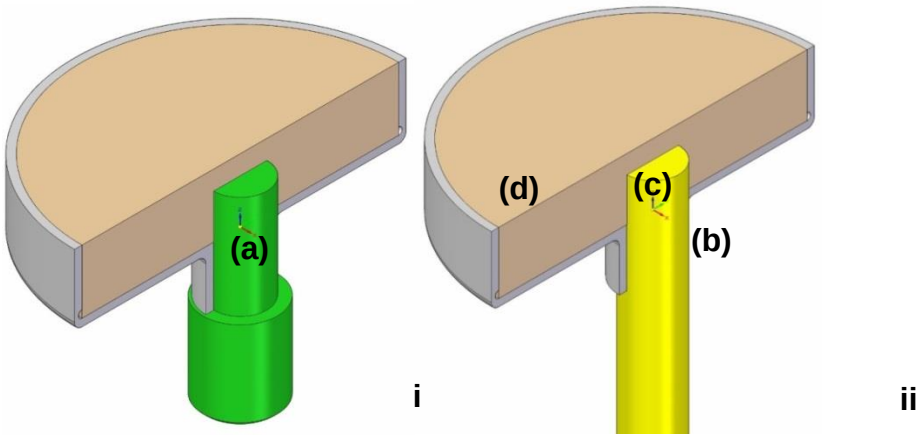

Figure 166: Explosive Casing i) with Detonator Cavity Forming Tool and ii) Detonator inserted

Figure 167 and Figure 168 show the two soil ejecta and near-field target charge positioning jigs and how they are used. These jigs were developed to ensure repeatable test set-up.

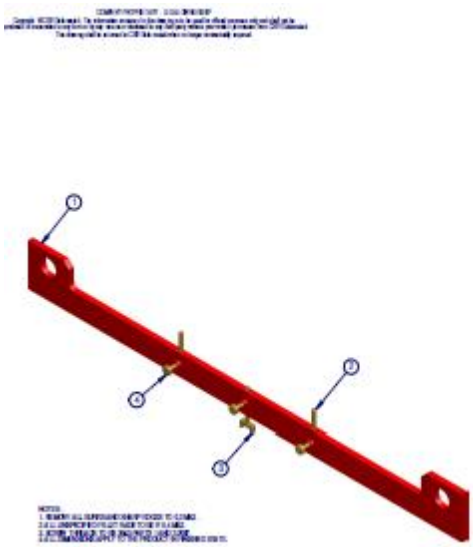

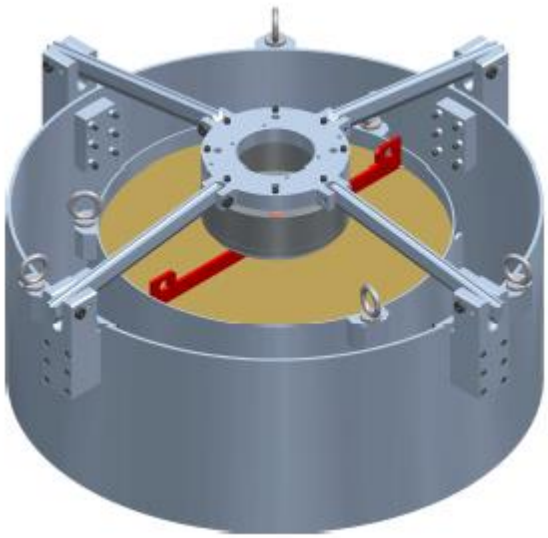

Figure 167: Soil Ejecta Positioning Jig

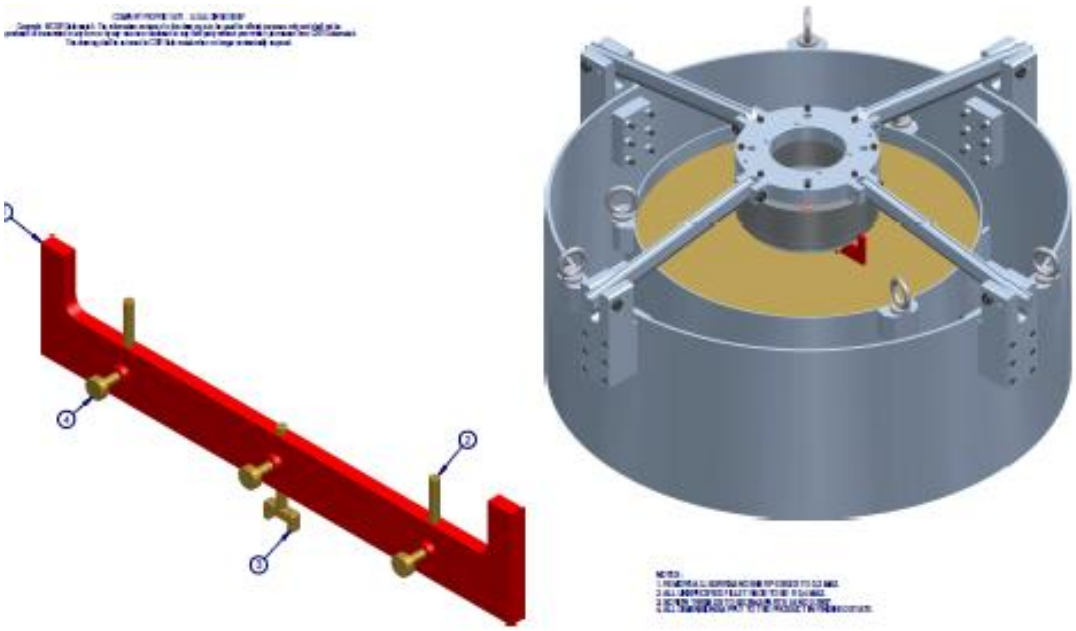

Figure 168: Near-Field Target-Positioning Jig

B.1.5 NIR Detector

The LS NIR sensor comprises four photodetector sensors. Sensors one to three are narrow band and centred at 870, 900 and 950 nm respectively, while senor four is broad band, covering the 450 to 1 150 nm wavelengths. The sensors all typically have rise times of between 10-20 ns. The values indicated for the narrow band are the peak wave length sensitivity but it should be noted that these sensors have a spectral bandwidth of around ±200 nm on either side of these peak values.

Table 16: NIR Sensors

Sensor No	Manufacturer	NIR Band Width Centre Band (nm)	Part Number	Photodiode Type
1	VISHAY	870	BPW96	Silicon NPN
2	VISHAY	900	BPW34FA	Silicon PIN

3	VISHAY	950	BPW34F	Silicon PIN
4	VISAHY	450-1150	BPV10F	Silicon PIN

B.2 Secondary Data Research Instruments

B.2.1 Cranfield Rig (McDonald 2013a)

Figure 169 (a) presents the Cranfield test rig that was used. The inverted and truncated V frame (a) is shown along with the square target plate (b) bolted in position with two force washers. The plastic soil bin (c) inside the steel bin (d) is shown at the bottom. Figure 169 (b) shows the underside of the target plate with the face-on forced sensor locations are at the centre (G1), 100 mm from the centre (G2) and 200 mm from the centre (G3). The method of operation is similar to that of the one-seventh scaled blast test rig in that the blast load impacts the target plate, pushing it upward against the force washers which are held in place with the V frame – this generates the force-time response of the target plate to the blast load.

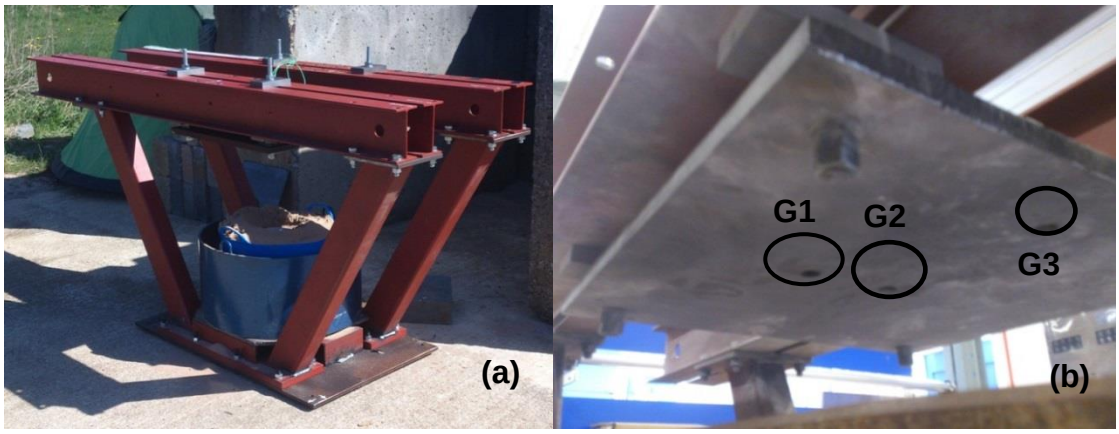

Figure 169: (a) Cranfield Blast Rig Assembly and (b) Target Plate with Face-on Force Sensors

The face-on force sensors use a force-washer that bears against the sensor plug inserted into the target face. There is sufficient clearance to ensure that the plug does not bind. The force is generated when the blast load acts against the sensor pin pushing against the force washer. The force response is related to the mass of the pin.

B.2.2 SIIMA (Snyman 2009)

Figure 170 shows the SIIMA test rig prepared for testing. The test rig is mounted on a concrete base (a) with a lined soil pit (b) in the centre. The height is adjusted by moving the rigid frame (c) up and down the two legs (d) and then locking the assembly when the correct height between the soil and the target box assembly (e) has been achieved. The target box assembly is pre-loaded against the frame, forming a vertically sprung pendulum. The force measurement is made through 16 load cells arranged in two banks of eight load cells on either side of the target box assembly frame attachment. The net force is obtained by subtracting the total upper load cell force from the lower load cell force.

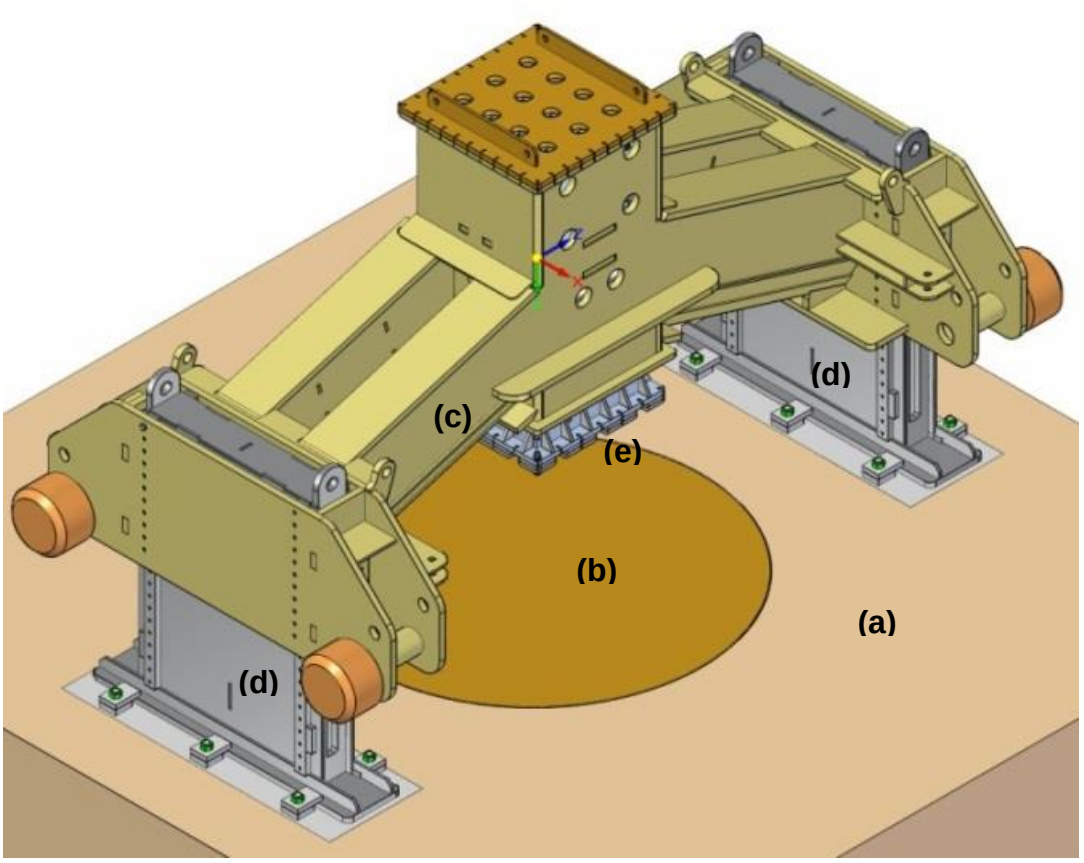

Figure 170: Scientifically Instrumented Impulse Measurement Apparatus (SIIMA)

Appendix C Soil

Table 17: Commissioning Tests of Measured Soil Parameters

Troxler (Bulk) Parameters				
Date	**Depth (mm)**	**Wet Density Kg/m^3**	**Dry Density Kg/m^3**	**% Moisture**
29/08/2014	**150**	1,660	1,528	8.7
	300	1,678	1,528	5.5
19/03/2015	**150**	1,637	1,572	4.1
	300	1,660	1,601	3.1
20/03/2015	**150**	1,663	1,549	7.4
	300	1,694	1,578	7.3
27/03/2015	**150**	1,541	1,436	7.3
	300	1,580	1,513	4.5
15/01/2016	**150**	1,660	1,583	4.8
	300	1,696	1,662	4.6

Appendix D Computational Model

Computational modelling is an exceptionally powerful tool that enables the researcher to model his experiment and obtain important first-order values of key parameters as well as to visualise the blast loading process. It can also be used to efficiently investigate specific phenomena and changes to set-up factors. The purpose was to develop additional modelling capability and to gain an engineering understanding of Autodyn as a computational modelling tool with regard to strengths and weakness, and to investigate near-field shallow-buried blast loading.

D.1 Modelling Plan

The initial focus of the computational modelling was the first series of one-seventh scale tests carried out using the small spacer and target available results. Based on these tests, a set of four near-field target models were developed in Ansys Autodyn®. The first three models investigated the effects of the D:H ratio on the side-on pressure, the blast front velocity and the force-time response of the target plate. The fourth model was exactly the same as previously with a 5:1 D:H ratio test charge, but with additional sensor (gauge) points.

These additional sensor points were gauge point 34 located at the midpoint between the soil surface and the target and in line with the outer edge of the target plate, and gauge point 35 located 100 mm above the soil and laterally on the edge of the modelling space. The purpose of gauge point 35 was to obtain predicted pressure and gas velocities from the blast products that are jetted out laterally by the target. This is a measurement point that could easily be applied in full-scale tests with relative safety of the equipment, thus providing data that could be related back to the blast load and transferred structural load. Gauge point 35 would also confirm whether the assumption of not having boundary flows was acceptable by determining the boundary flows and effects of reflections from this defined computational boundary.

In addition to the four near-field target models, a single ejecta model was run without a near-field target to provide data to compare with the ejecta tests carried out in 2015.

Table 18: One-Seventh Scale Computational Modelling Matrix

Model No	Test Charge PE4 (grams)	D:H Ratio	Soil	DOB mm	SOD mm
Base Line Target Plate (Small)					
1	20	5:1	Autodyn Sand	7.2	72
2	20	3:1	Autodyn Sand	7.2	72
3	20	2:1	Autodyn Sand	7.2	72
4	20	5:1	Autodyn Sand	7.2	72
6	20	5:1	Autodyn Sand	7.2	No target

D.2 Model Set-up

Figure 171 shows the quarter axisymmetric model implemented developed for the initial exploratory modelling. The image is zoomed in to show the graded grid as well as the location of the gauge points. As it is zoomed in, not all the gauge points are visible.

The model was executed as a 2D axisymmetric rendition of the near-field shallow-buried one-seventh scale test rig as assembled for the commissioning tests. Thus the small deflection jig target assembly was used with a target plate diameter of 290 mm. The final tests used a larger diameter plate of 360 mm and a thicker internal ring. The circular geometry used in the one-seventh scale test rig is ideally suited to axisymmetric modelling. Square targets require 3D modelling.

A graded grid with 6,500 2D cells centred on the explosive charge was used. Initial spacing was set at 1 mm in the vertical direction and 2 mm in the horizontal direction. The complete one-seventh test rig soil bin was modelled.

This was done to enable far-field measurements to be monitored to support any future decisions to reduce the model size. Typically the parameters reviewed were time of arrival of the blast wave, the overpressure and the size of the reflected boundary wave, etc. Although the grid was exceptionally coarse on the outer boundaries, it was considered sufficient for the purposes of this model.

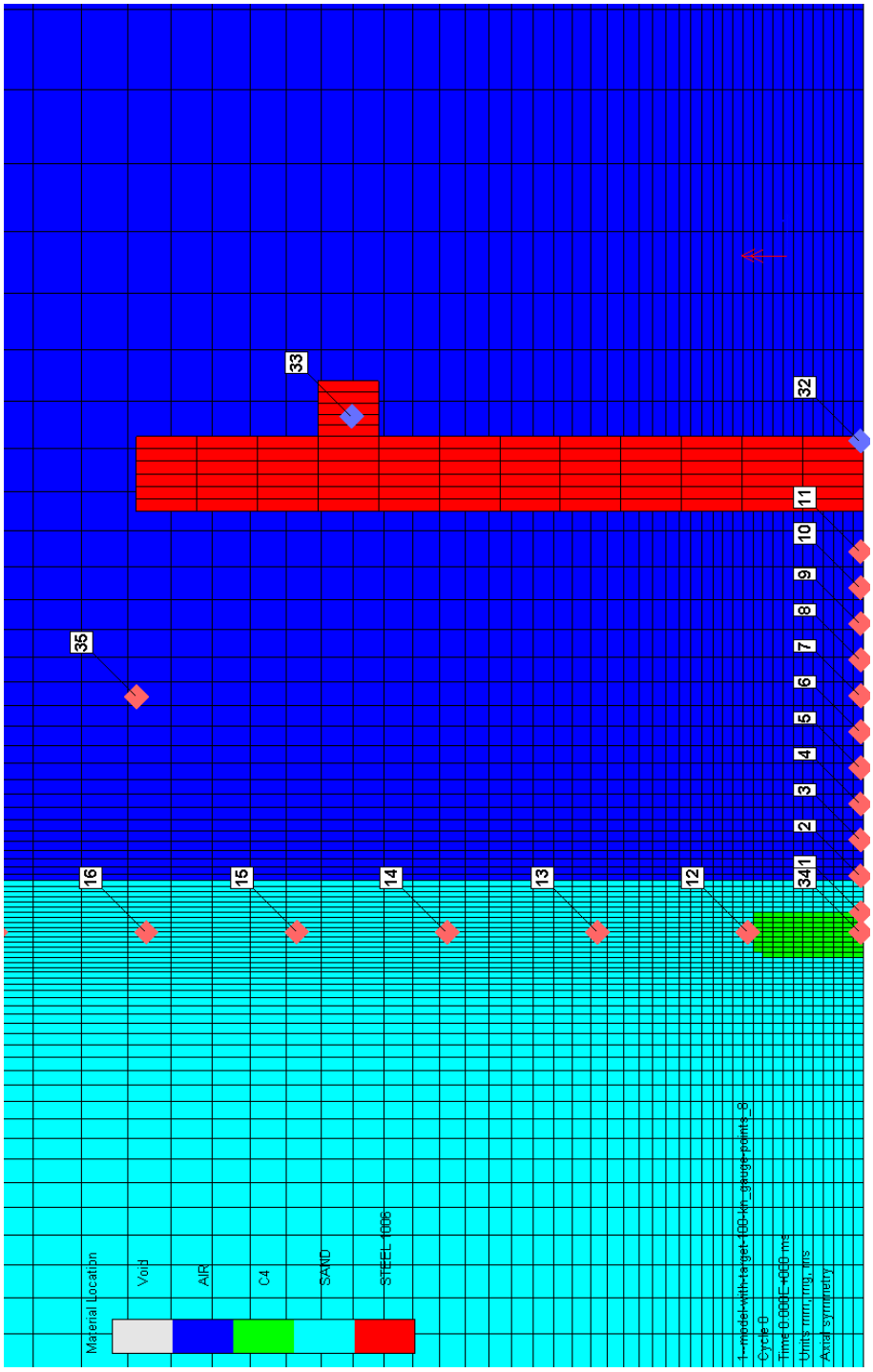

Figure 171: Model Grid and Gauge Points (Zoomed In)

The test volume modelled was 803 mm high and 650 mm wide. The charge was positioned with its centre at 500 mm from the bottom. This gave around 300 mm of air space above the charge. As the near-field target deflects the blast horizontally where there is around 650 mm of air space before the side boundary, this geometry was deemed suitable for this model. The steel sides of the soil bin were not modelled.

The target was modelled as a 15 mm thick target plate with a circular ring representing the deflection jig. Due to grid alignment issues, the ring diameter was made slightly larger to ensure nodal alignment with the target plate. The force washer was not modelled separately to keep the model simple. A gauge point was selected within the ring to provide the force-time output at approximately the same lateral geometric position as the force washers in the commissioning tests. Note that the grid was exceptionally coarse at this location; however, this was deemed acceptable as only the force-time output was required.

No boundary outflow was specified. The soil, explosive and air were modelled as Eulerian components (fixed grid) and the target was modelled as Lagrangian (deformable grid). Fluid structure interaction (FSI) for Euler/Lagrangian coupling used the standard Autodyn automatic (polygon-free) routine. From Figure 171 it can be seen that the requirements for the Euler/Lagrangian interaction zone to have at least two Euler cells for each Lagrangian (Ansys Inc. 2011) cell is only just met on the boundaries of the model. Again, for investigative purposes rather than absolute measurements, this is considered acceptable. The top point of the ring was made fixed.

The one-seventh scale test rig structure was not fully modelled to reduce complexity. This, combined with the restraining of the ring to simulate the fixing of the target in this model, results in a much more rigid model than in real life. Although not ideal, this is considered acceptable for exploratory modelling; however, this should be addressed in future models. Note that full modelling of the structure would be computationally expensive and possibly destabilise the model.

The material models used were those provided as standard in Autodyn. The target was mild steel. The explosive used was C4 as PE4 is not available in Autodyn. Although this is done as general practice, there is some concern as C4 has around 91% RDX with the rest binders and oil, whereas PE4 has around 88% RDX with the rest plasticisers (Cooper, Kurowski 1996). During the MABS conference the question was raised regarding the JWL parameters for PE4 by a Dr L. Schwer as all work seems to refer back to an Australian DSTO paper. The material model parameters used are listed in D.3.1.

Energy error was set at 10%. The explosive detonation was set to point with direct path options and placed at the bottom centre of the charge.

Eulerian gauge points were distributed vertically along the centre line between the soil and the target and laterally through the soil along the centre line of the charge for all models. For model 4, one gauge point was placed on the edge of the target plate in the middle between the soil and the target face (this is to emulate typical side-on pressure measurements taken in the past with larger test rigs) and another gauge point was placed on the lateral side boundary of the model space.

There were only two Lagrangian gauge points: one was in the centre rear of target plate and the other was in the centre of the pseudo force washer element.

For the ejecta model (model 6) there were only Eulerian gauge points, and these were selected as a rectangular grid ranging from the centre of the charge to 60 mm laterally and then upward for 400 mm. The gauges were equispaced 20 mm laterally and 10 mm vertically. It should be noted that Autodyn is limited to around 180 gauge points that can be selected for a single model.

D.3 Execution

The model was set up and refined until no energy errors occurred. The various models were run. The average solver time step was around 200 ns and data were captured every microsecond. On average a model ran for around 30–45 minutes after an average of 40,000 cycles. The results are presented and

discussed both with the actual test data and in their own sections where data that are not currently available from tests but have been obtained from the models (typically force and pressure morphology, pressure and pressure impulse, blast front velocity and crater dimensions) are compared in accordance with D:H ratio changes.

D.3.1 Autodyn® Material Model Parameters

D.3.2 Material Name – AIR

Equation of State	Ideal Gas
Reference density	1.22500E-03 (g/cm3)
Gamma	1.40000E+00 (none)
Adiabatic constant	0.00000E+00 (none)
Pressure shift	0.00000E+00 (kPa)
Reference temperature	2.88200E+02 (K)
Specific heat	7.17600E+02 (J/kgK)
Thermal conductivity	0.00000E+00 (J/mKs)
Strength	**None**
Failure	**None**
Erosion	**None**
Material Cut-offs	-
Maximum expansion	1.00000E-01 (none)
Minimum density factor	1.00000E-04 (none)
Minimum density factor (SPH)	2.00000E-01 (none)
Maximum density factor (SPH)	3.00000E+00 (none)
Minimum soundspeed	1.00000E-02 (m/s)
Maximum soundspeed (SPH)	1.01000E+20 (m/s)
Maximum temperature	1.01000E+20 (K)
Reference:	"Thermodynamic and Transport Properties of Fluids, SI Units", G. F. C. Rogers, Y. R. Mayhew

D.3.3 Material Name – C4

Equation of State	JWL
Reference density	1.60100E+00 (g/cm3)
Parameter A	6.09770E+08 (kPa)
Parameter B	1.29500E+07 (kPa)
Parameter R1	4.50000E+00 (none)
Parameter R2	1.40000E+00 (none)
Parameter W	2.50000E-01 (none)
C-J detonation velocity	8.19300E+03 (m/s)
C-J energy / unit volume	9.00000E+06 (kJ/m3)
C-J pressure	2.80000E+07 (kPa)
Burn-on compression fraction	0.00000E+00 (none)
Pre-burn bulk modulus	0.00000E+00 (kPa)
Adiabatic constant	0.00000E+00 (none)
Auto-convert to ideal gas	Yes
Additional options (Beta)	None
Strength	**None**
Failure	**None**
Erosion	**None**
Material Cutoffs	-
Maximum expansion	1.00000E-01 (none)
Minimum density factor	1.00000E-06 (none)
Minimum density factor (sph)	2.00000E-01 (none)
Maximum density factor (sph)	3.00000E+00 (none)
Minimum soundspeed	1.00000E-06 (m/s)
Maximum soundspeed (sph)	1.01000E+20 (m/s)
Maximum temperature	1.01000E+20 (K)
Reference:	"LLNL Explosives Handbook" Dobratz B. M. & Crawford P. C. UCRL-52997 Rev. 2 January 1985

D.3.4 Material Name – SAND

Equation of State	Compaction
Reference density	2.64100E+00 (g/cm^3)
Density #1	1.67400E+00 (g/cm^3)
Density #2	1.73950E+00 (g/ cm^3)
Density #3	1.87380E+00 (g/ cm^3)
Density #4	1.99700E+00 (g/ cm^3)
Density #5	2.14380E+00 (g/ cm^3)
Density #6	2.25000E+00 (g/ cm^3)
Density #7	2.38000E+00 (g/ cm^3)
Density #8	2.48500E+00 (g/ cm^3)
Density #9	2.58500E+00 (g/ cm^3)
Density #10	2.67130E+00 (g/ cm^3)
Pressure #1	0.00000E+00 (kPa)
Pressure #2	4.57700E+03 (kPa)
Pressure #3	1.49800E+04 (kPa)
Pressure #4	2.91510E+04 (kPa)
Pressure #5	5.91750E+04 (kPa)
Pressure #6	9.80980E+04 (kPa)
Pressure #7	1.79443E+05 (kPa)
Pressure #8	2.89443E+05 (kPa)
Pressure #9	4.50198E+05 (kPa)
Pressure #10	6.50660E+05 (kPa)
Unloading method	Linear
Density (Soundspeed) #1	1.67400E+00 (g/ cm^3)
Density (Soundspeed) #2	1.74560E+00 (g/ cm^3)
Density (Soundspeed) #3	2.08630E+00 (g/ cm^3)
Density (Soundspeed) #4	2.14680E+00 (g/ cm^3)
Density (Soundspeed) #5	2.30000E+00 (g/ cm^3)
Density (Soundspeed) #6	2.57200E+00 (g/ cm^3)

Equation of State	Compaction
Density (Soundspeed) #7	2.59800E+00 (g/ cm^3)
Density (Soundspeed) #8	2.63500E+00 (g/ cm^3)
Density (Soundspeed) #9	2.64100E+00 (g/ cm^3)
Density (Soundspeed) #10	2.80000E+00 (g/ cm^3)
Soundspeed #1	2.65200E+02 (m/s)
Soundspeed #2	8.52100E+02 (m/s)
Soundspeed #3	1.72170E+03 (m/s)
Soundspeed #4	1.87550E+03 (m/s)
Soundspeed #5	2.26480E+03 (m/s)
Soundspeed #6	2.95610E+03 (m/s)
Soundspeed #7	3.11220E+03 (m/s)
Soundspeed #8	4.60000E+03 (m/s)
Soundspeed #9	4.63400E+03 (m/s)
Soundspeed #10	4.63400E+03 (m/s)
Strength	**MO Granular**
Pressure (P-Y) #1	0.00000E+00 (kPa)
Pressure (P-Y) #2	3.40100E+03 (kPa)
Pressure (P-Y) #3	3.48980E+04 (kPa)
Pressure (P-Y) #4	1.01324E+05 (kPa)
Pressure (P-Y) #5	1.84650E+05 (kPa)
Pressure (P-Y) #6	5.00000E+05 (kPa)
Pressure (P-Y) #7	0.00000E+00 (kPa)
Pressure (P-Y) #8	0.00000E+00 (kPa)
Pressure (P-Y) #9	0.00000E+00 (kPa)
Pressure (P-Y) #10	0.00000E+00 (kPa)
Yield Stress (P-Y) #1	0.00000E+00 (kPa)
Yield Stress (P-Y) #2	4.23500E+03 (kPa)
Yield Stress (P-Y) #3	4.46950E+04 (kPa)
Yield Stress (P-Y) #4	1.24035E+05 (kPa)

Equation of State	Compaction
Yield Stress (P-Y) #5	2.26000E+05 (kPa)
Yield Stress (P-Y) #6	2.26000E+05 (kPa)
Yield Stress (P-Y) #7	0.00000E+00 (kPa)
Yield Stress (P-Y) #8	0.00000E+00 (kPa)
Yield Stress (P-Y) #9	0.00000E+00 (kPa)
Yield Stress (P-Y) #10	0.00000E+00 (kPa)
Density (D-Y) #1	1.67400E+00 (g/ cm^3)
Density (D-Y) #2	1.74570E+00 (g/ cm^3)
Density (D-Y) #3	2.08630E+00 (g/ cm^3)
Density (D-Y) #4	2.14680E+00 (g/cm^3)
Density (D-Y) #5	2.30000E+00 (g/cm^3)
Density (D-Y) #6	2.57200E+00 (g/cm^3)
Density (D-Y) #7	2.59800E+00 (g/cm^3)
Density (D-Y) #8	2.63500E+00 (g/cm^3)
Density (D-Y) #9	2.64100E+00 (g/cm3)
Density (D-Y) #10	2.80000E+00 (g/cm^3)
Yield Stress (D-Y) #1	0.00000E+00 (kPa)
Yield Stress (D-Y) #2	0.00000E+00 (kPa)
Yield Stress (D-Y) #3	0.00000E+00 (kPa)
Yield Stress (D-Y) #4	0.00000E+00 (kPa)
Yield Stress (D-Y) #5	0.00000E+00 (kPa)
Yield Stress (D-Y) #6	0.00000E+00 (kPa)
Yield Stress (D-Y) #7	0.00000E+00 (kPa)
Yield Stress (D-Y) #8	0.00000E+00 (kPa)
Yield Stress (D-Y) #9	0.00000E+00 (kPa)
Yield Stress (D-Y) #10	0.00000E+00 (kPa)
Density (D-G) #1	1.67400E+00 (g/cm^3)
Density (D-G) #2	1.74570E+00 (g/cm^3)
Density (D-G) #3	2.08630E+00 (g/cm^3)

Equation of State	Compaction
Density (D-G) #4	2.14680E+00 (g/cm^3)
Density (D-G) #5	2.30000E+00 (g/cm^3)
Density (D-G) #6	2.57200E+00 (g/cm^3)
Density (D-G) #7	2.59800E+00 (g/cm^3)
Density (D-G) #8	2.63500E+00 (g/cm^3)
Density (D-G) #9	2.64100E+00 (g/cm^3)
Density (D-G) #10	2.80000E+00 (g/cm^3)
Shear Modulus (D-G) #1	7.69000E+04 (kPa)
Shear Modulus (D-G) #2	8.69400E+05 (kPa)
Shear Modulus (D-G) #3	4.03170E+06 (kPa)
Shear Modulus (D-G) #4	4.90690E+06 (kPa)
Shear Modulus (D-G) #5	7.76900E+06 (kPa)
Shear Modulus (D-G) #6	1.48009E+07 (kPa)
Shear Modulus (D-G) #7	1.65710E+07 (kPa)
Shear Modulus (D-G) #8	3.67180E+07 (kPa)
Shear Modulus (D-G) #9	3.73470E+07 (kPa)
Shear Modulus (D-G) #10	3.73470E+07 (kPa)
Failure	**Hydro (Pmin)**
Hydro tensile limit	-1.00000E+00 (kPa)
Reheal	Yes
Crack softening	No
Stochastic failure	No
Erosion	**Geometric Strain**
Erosion strain	2.00000E+00 (none)
Type of geometric strain	Instantaneous
Material Cut-offs	-
Maximum expansion	1.00000E-01 (none)
Minimum density factor	1.00000E-04 (none)
Minimum density factor (sph)	2.00000E-01 (none)

Equation of State	Compaction
Maximum density factor (sph)	3.00000E+00 (none)
Minimum soundspeed	1.00000E-06 (m/s)
Maximum sound speed (sph)	1.01000E+20 (m/s)
Maximum temperature	1.01000E+20 (K)
Reference:	Laine L., Sandvik A."Derivation of mechanical properties for sand", 4th SILOS,CI-Premier LTD,p361–367

D.3.5 Material Name – STEEL 1006

Equation of State	Shock
Reference density	7.89600E+00 (g/cm^3)
Gruneisen coefficient	2.17000E+00 (none)
Parameter C1	4.56900E+03 (m/s)
Parameter S1	1.49000E+00 (none)
Parameter quadratic S2	0.00000E+00 (s/m)
Relative volume, VE/V0	0.00000E+00 (none)
Relative volume, VB/V0	0.00000E+00 (none)
Parameter C2	0.00000E+00 (m/s)
Parameter S2	0.00000E+00 (none)
Reference temperature	3.00000E+02 (K)
Specific heat	4.52000E+02 (J/kgK)
Thermal conductivity	0.00000E+00 (J/mKs)
Strength	**Johnson Cook**
Shear modulus	8.18000E+07 (kPa)
Yield stress	3.50000E+05 (kPa)
Hardening constant	2.75000E+05 (kPa)
Hardening exponent	3.60000E-01 (none)
Strain rate constant	2.20000E-02 (none)
Thermal softening exponent	1.00000E+00 (none)

Equation of State	Shock
Melting temperature	1.81100E+03 (K)
Ref. Strain Rate (/s)	1.00000E+00 (none)
Strain rate correction	1st Order
Failure	**None**
Erosion	**None**
Material Cutoffs	-
Maximum expansion	1.00000E-01 (none)
Minimum density factor	1.00000E-04 (none)
Minimum density factor (sph)	2.00000E-01 (none)
Maximum density factor (sph)	3.00000E+00 (none)
Minimum soundspeed	1.00000E-06 (m/s)
Maximum soundspeed (sph)	1.01000E+20 (m/s)
Maximum temperature	1.01000E+20 (K)
Reference:	LA-4167-MS. 1 May 1969. Selected Hugoniots: EOS 7th Int. Symp. Ballistics. Johnson & Cook

Appendix E Data

E.1 Research Data Summary Tables

Table 19: Total Research Data Summary

Test Data No.	Date	Test Key No.	Explosive	Mass (grams)	D:H	DOB (mm)	SOD (mm)
Ejecta Tests							
Commissioning Tests							
1	29/08/14	2-1002	PE4	20	2:1	7.2	221[4]
2	29/08/14	2-1004	PE4	20	2:1	7.2	205
3	29/08/14	2-1005	PE4	20	5:1	7.2	205
Final Tests							
4	26/03/15	9	PE4	19	2:1	7.2	200
5	27/03/15	10	PE4	19	2:1	7.2	200
6	27/03/15	11	PE4	19	2:1	7.2	200
7	27/03/15	12	PE4	19	2:1	7.2	200
8	26/03/15	8	PE4	19	3:1	7.2	200
9	27/03/15	15	PE4	19	3:1	7.2	200
10	27/03/15	13	PE4	19	5:1	7.2	200
11	27/03/15	14	PE4	19	5:1	7.2	200
Near and Intermediate Target Force Response							
Commissioning Tests							
12	14/06/13	Test 5	PE4	20	2:1	7.2	72
13	14/06/13	Test 6	PE4	20	2:1	7.2	72
14	14/06/13	Test 7	PE4	20	3:1	7.2	72
15	14/06/13	Test 9	PE4	20	5:1	7.2	72
16	14/06/13	Test 10	PE4	20	5:1	7.2	72
Final Tests							

[4] This is distance to the centre of the pressure-sensing element

Test Data No.	Date	Test Key No.	Explosive	Mass (grams)	D:H	DOB (mm)	SOD (mm)
Force Hammer Verification Tests							
17	14/01/16	Hammer Test 4	N/A	N/A	N/A	N/A	N/A
18	14/01/16	Hammer Test 5	N/A	N/A	N/A	N/A	N/A
19	14/01/16	Hammer Test 6	N/A	N/A	N/A	N/A	N/A
20	14/01/16	Hammer Test 7	N/A	N/A	N/A	N/A	N/A
21	14/01/16	Hammer Test 8	N/A	N/A	N/A	N/A	N/A
22	14/01/16	Hammer Test 9	N/A	N/A	N/A	N/A	N/A
23	14/01/16	Hammer Test 10	N/A	N/A	N/A	N/A	N/A
24	14/01/16	Hammer Test 11	N/A	N/A	N/A	N/A	N/A
Intermediate-Field Tests (Z=0.78-79 m/kg$^{1/3}$)							
25	15/01/16	2-1-1	PE4	19	5:1	7.2	200
26	15/01/16	2-1-2	PE4	19	5:1	7.2	200
27	15/01/16	2-1-3	PE4	19	5:1	7.2	200
28	18/01/16	2-1-4	PE4	19	3:1	7.2	200
29	15/01/16	2-2-1	PE4	19	3:1	7.2	200
30	15/01/16	2-2-2	PE4	19	3:1	7.2	200
31	15/01/16	2-2-3	PE4	19	3:1	7.2	200
32	18/01/16	2-2-4	PE4	19	2:1	7.2	200
33	18/01/16	2-3-1	PE4	19	2:1	7.2	200
34	18/01/16	2-3-2	PE4	19	5:1	7.2	200
35	18/01/16	2-3-3	PE4	19	3:1	7.2	200
36	18/01/16	2-3-4	PE4	19	2:1	7.2	200
37	19/01/16	3-1-1R	PE4	19	5:1	7.2	200
38	19/01/16	3-1-2	PE4	19	5:1	7.2	200
39	19/01/16	3-1-3	PE4	19	5:1	7.2	200
40	19/01/16	3-2-1	PE4	19	5:1	7.2	200
41	19/01/16	3-2-2	PE4	19	5:1	7.2	200

Test Data No.	Date	Test Key No.	Explosive	Mass (grams)	D:H	DOB (mm)	SOD (mm)
42	19/01/16	3-2-3	PE4	19	3:1	7.2	200
43	19/01/16	3-3-1	PE4	19	3:1	7.2	200
44	19/01/16	3-3-2	PE4	19	3:1	7.2	200
45	19/01/16	3-3-3	PE4	19	2:1	7.2	200
Near-Field Tests (Z=0.31 m/kg$^{1/3}$)							
46	19/01/16	4-1-1	PE4	19	2:1	7.2	72
47	19/01/16	4-1-2	PE4	19	2:1	7.2	72
Cranfield Rig Secondary Data Tests							
1	N/A	Test 1	PE4	160 gr[5]	N/A	100	360
2	N/A	Test 2	PE4	160 gr	N/A	100	360
3	N/A	Test 3	PE4	160 gr	N/A	100	230
4	N/A	Test 4	PE4	160 gr	N/A	100	230
5	N/A	Test 5	PE4	160 gr	N/A	100	100
6	N/A	Test 6	PE4	160 gr	N/A	50	230
SIIMA Secondary Data Tests							
7	N/A	Test 1	TNT	1,000	5:1	25	250
8	N/A	Test 2	TNT	1,000	5:1	25	250
9	N/A	Test 3	TNT	1,000	5:1	25	250
10	N/A	Test 4	TNT	1,000	5:1	25	250
11	N/A	Test 1	TNT	8,000	3:1	50	1,100
12	N/A	Test 2	TNT	8,000	3:1	50	1,100
13	N/A	Test 3	TNT	8,000	3:1	50	1,100
14	N/A	Test 4	TNT	8,000	3:1	50	1,100
15	N/A	Test 1	TNT	8,000	5:1	50	1,100
16	N/A	Test 2	TNT	8,000	5:1	50	1,100
17	N/A	Test 3	TNT	8,000	5:1	50	1,100

[5] Charge shape is spherical

Test Data No.	Date	Test Key No.	Explosive	Mass (grams)	D:H	DOB (mm)	SOD (mm)
18	N/A	Test 4	TNT	8,000	5:1	50	1,100
19	N/A	Test 1	TNT	8,000	5:1	50	1,300
20	N/A	Test 2	TNT	8,000	5:1	50	1,300
21	N/A	Test 3	TNT	8,000	5:1	50	1,300
22	N/A	Test 4	TNT	8,000	5:1	50	1,300

E.1.1 Research Data Measurement Summary

Table 20: Research Data Measurement Summary

No.	Date	Test Key No.	Measurement						
			Net Force	Side-On Pressure	Face-On Pressure	Deflection	High Speed Video	NIR	Crater
Ejecta Tests									
Commissioning Tests									
1	29/08/14	2-1002	N/A	x			x		x
2	29/08/14	2-1004	N/A	x			x		x
3	29/08/14	2-1005	N/A	x			x		x
Final Tests									
4	26/03/15	9	N/A	x			x		x
5	27/03/15	10	N/A	x			x		x
6	27/03/15	11	N/A	x			x		x
7	27/03/15	12	N/A	x			x		x
8	26/03/15	8	N/A	x			x		x
9	27/03/15	15	N/A	x			x		x
10	27/03/15	13	N/A	x			x		x
11	27/03/15	14	N/A	x			x		x
Near and Intermediate Target Force Response									
Commissioning Tests									

No.	Date	Test Key No.	Measurement						
			Net Force	Side-On Pressure	Face-On Pressure	Deflection	High Speed Video	NIR	Crater
12	14/06/13	Test 5	x			x			x
13	14/06/13	Test 6	x			x			x
14	14/06/13	Test 7	x			x			x
15	14/06/13	Test 9	x			x			x
16	14/06/13	Test 10	x			x			x
Force Hammer Verification Tests									
17	14/01/16	Hammer Test 4	x						x
18	14/01/16	Hammer Test 5	x						x
19	14/01/16	Hammer Test 6	x						x
20	14/01/16	Hammer Test 7	x						x
21	14/01/16	Hammer Test 8	x						x
22	14/01/16	Hammer Test 9	x						x
23	14/01/16	Hammer Test 10	x						x
24	14/01/16	Hammer Test 11	x						x
Intermediate-Field Tests (Z=0.78-79 m/kg$^{1/3}$)									
25	15/01/16	2-1-1	x			x	x	x	x
26	15/01/16	2-1-2	x	x		x	x	x	x
27	15/01/16	2-1-3	x	x		x	x	x	x
28	18/01/16	2-1-4	x	x			x	x	x
29	15/01/16	2-2-1	x	x		x	x	x	x
30	15/01/16	2-2-2	x	x		x	x	x	x
31	15/01/16	2-2-3	x			x	x	x	x

No.	Date	Test Key No.	Measurement						
			Net Force	Side-On Pressure	Face-On Pressure	Deflection	High Speed Video	NIR	Crater
32	18/01/16	2-2-4	x	x		x	x	x	x
33	18/01/16	2-3-1	x	x		x	x	x	x
34	18/01/16	2-3-2	x	x		x	x	x	x
35	18/01/16	2-3-3	x			x	x	x	x
36	18/01/16	2-3-4	x			x	x		x
37	19/01/16	3-1-1R	x			x	x		x
38	19/01/16	3-1-2	x		x	x	x	x	x
39	19/01/16	3-1-3	x	x	x	x	x		x
40	19/01/16	3-2-1	x	x	x	x	x	x	x
41	19/01/16	3-2-2	x	x	x	x	x	x	x
42	19/01/16	3-2-3	x	x	x		x	x	x
43	19/01/16	3-3-1	x	x	x	x	x	x	x
44	19/01/16	3-3-2	x	x	x	x	x		x
45	19/01/16	3-3-3	x	x	x	x	x		x
Near-Field Tests (Z=0.31 m/kg$^{1/3}$)									
46	19/01/16	4-1-1	x		x	x	x		x
47	19/01/16	4-1-2	x			x	x		x
Cranfield Rig Secondary Data Tests									
1	N/A	Test 1	x				x		
2	N/A	Test 2	x				x		
3	N/A	Test 3	x				x		
4	N/A	Test 4	x				x		
5	N/A	Test 5	x				x		
6	N/A	Test 6	x				x		
SIIMA Secondary Data Tests									
7	N/A	Test 1	x						

No.	Date	Test Key No.	Measurement						
			Net Force	Side-On Pressure	Face-On Pressure	Deflection	High Speed Video	NIR	Crater
8	N/A	Test 2	x						
9	N/A	Test 3	x						
10	N/A	Test 4	x						
11	N/A	Test 1	x						
12	N/A	Test 2	x						
13	N/A	Test 3	x						
14	N/A	Test 4	x						
15	N/A	Test 1	x						
16	N/A	Test 2	x						
17	N/A	Test 3	x						
18	N/A	Test 4	x						
19	N/A	Test 1	x						
20	N/A	Test 2	x						
21	N/A	Test 3	x						
22	N/A	Test 4	x						

Table 21: One-Seventh Scale Computational Modelling Matrix

Model No	Test Charge C4 (grams)	D:H Ratio	Soil	DOB mm	SOD mm
Base Line Target Plate (Small)					
1	20	5:1	Autodyn Sand	7.2	72
2	20	3:1	Autodyn Sand	7.2	72
3	20	2:1	Autodyn Sand	7.2	72
4	20	5:1	Autodyn Sand	7.2	72
6	20	5:1	Autodyn Sand	7.2	No target

E.1.2 Crater Results

Table 22: Crater Measurements

Test / Model	Primary Ø	Secondary Ø	Primary Depth	Secondary Depth
	mm	mm	mm	mm
Ejecta Test Results				
Soil Ejecta 2-1002.pnrf	673	277	148	80
Soil Ejecta 2-1004.pnrf	705	340	182	116
Soil Ejecta 2-1005.pnrf	653	329	166	88
One-Seventh (Target) Test Results				
One-Seventh Test 9	640	170	130	70
One-Seventh Test 10	670	175	130	85

E.1.3 Test Atmospheric Conditions

Table 23: Test Atmospheric Conditions

Date	Barometric Pressure (mBar)	Temperature (^{o}C)	RH (%)
29/08/2014	880.9	19	16.6
15/01/2016	877	29.1	49
18/01/2016	882.1	29.8	42.1
19/01/2016	881	33	881

E.1.4 Ejecta Model and Test Data Tables

Table 24: Ejecta Model Data Summary

Test	D:H	SOD (mm)	Peak Pressure Overall		Peak Pressure within 0.200 ms		Total +ve Phase
			MPa	ms	ms	MPa	ms
Autodyn Run 6 5-1 Ejecta	5:1	195	1.240	0.128	0.205	1.240	0.205
Autodyn Run 6 5-1 Ejecta Modified	5:1	195	1.187	0.127	0.207	1.187	0.207

Table 25: Ejecta Model Partitioned Side on Pressure Data Summary

Test	D:H	SOD (mm)	Total	Phase 1		Phase 2		Phase 3	
			ms	ms	%	ms	%	ms	
Autodyn Run 6 5-1 Ejecta (M 5:1)	5:1	195	0.205	0.134	66%	0.028	13%	0.043	21%
Autodyn Run 6 5-1 Ejecta_out Modified (MM 5:1)	5:1	195	0.207	0.134	65%	0.026	13%	0.047	23%

Table 26: Ejecta Model Specific Impulse Data Summary

Test	D:H	SOD (mm)	Peak Specific Impulse	Time to Peak Impulse
			Pa.s	ms
Autodyn Run 6 5-1 Ejecta	5:1	195	25	0.206
Autodyn Run 6 5-1 Ejecta Modified	5:1	195	38	0.207

Table 27: Ejecta Model Partitioned Specific Impulse Data Summary

Test	D:H	SOD (mm)	Phase 1 Impulse	Phase 2 Impulse	Phase 3 Impulse
			Pa.s	Pa.s	Pa.s
Model Results					
Autodyn Run 6 5-1 Ejecta	5:1	195	12	8	4
Autodyn Run 6 5-1 Ejecta Modified			19	14	5

E.1.5 Near-Field Target Model Data Tables

Table 28: Summary of Near-Field Target Model Total and Phased Pressure Durations (Visually Extracted)

D:H	DOB mm	SOD mm	Total	Phase 1		Phase 2		Phase 3	
			ms	ms		ms		ms	
1/7th Scale Model Results									
5:1	**7.2**	**72**	0.562	0.039	7%	0.111	20%	0.411	73%
3:1	**7.2**	**72**	0.438	0.033	7%	0.088	20%	0.317	72%
2:1	**7.2**	**72**	0.541	0.033	6%	0.080	15%	0.428	79%

Table 29: Summary of Near-Field Model Total and Phased Specific Impulse (Side-On Pressure) Results

D:H	DOB mm	SOD mm	Pressure Impulse	Phase 1		Phase 2		Phase 3	
			Total	Impulse		Impulse		Impulse	
			Pa.s	Pa.s		Pa.s		Pa.s	
1/7th Scale Near-Field Model Results									
5:1	**7.2**	**72**	935	116	12%	681	73%	138	15%
5:1	**7.2**	**72**	1,069	98	9%	676	63%	294	27%
5:1	**7.2**	**72**	1,184	100	8%	677	57%	406	34%

E.1.6 Free-field Blast Front and Ejecta Test Data

Table 30: Ejecta Blast Front Velocity (5:1 D:H)

Test	Blast Front Velocity at 72 mm				Blast Front Velocity at 195 mm			
	Front	Average/ SD	RHS	Average/ SD	Front	Average/ SD	RHS	Average/ SD
	m/s	m/s	m/s	m/s	m/s	m/s	m/s	m/s
1-1	2,194	1,674 445	2,161	1,599 402	1,555	1 196 239	1,837	1,415 415
1-2	1,983		1,632		1,219		1,671	
1-3	1,122		1,112		842		1,176	
1-4	1,162		1,194		1,061		714	
1-1R	1,909		1,898		1,303		1,679	
2-1	1,840	1,749 91	1,583	1,757 174	993	1 464 472	1,141	1,807 667
2-2	1,658		1,931		1,936		2,474	
3-2	1,493	1,733 264	1,249	1 804 397	1,093	1 327 228	968	1,456 374
3-3	1,607		2,153		1,636		1,875	
3-4	2,100		2,011		1,253		1,524	

Table 31: Ejecta Mass Calculated using Primary to Secondary Ratio

D:H	Primary Φ (mm)	Primary Depth (mm)	secondary Φ (mm)	Secondary Depth (mm)	Calculated Crater Soil Mass		Ratio
					Primary (kg)	Secondary (kg)	
5:1	646	158.2	350	54.4	20.2	8.4	42%
3:1	680	159.4	327	65.2	29.1	8.8	30%
2:1	672.5	142.5	331.25	63	27.1	8.7	32%

Table 32: Estimated Ejecta Mass

D:H	Ejecta Mass (kg)kg	Secondary/ Primary Ratio	Ejecta Mass (kg)	Estimated Crater Ejecta Mass	
				Primary (kg)	Secondary (kg)
5:1	12.96	42%	13.0	7.6	5.4
3:1	13.65	30%	13.7	9.5	4.1
2:1	12.46	32%	12.5	8.5	4.0

Table 33: Soil Ejecta Craters and Ejecta Mass

Data	Ejecta Mass (kg)	Primary Diameter (mm)	Primary Depth (mm)	Secondary Diameter (mm)	Secondary Depth (mm)	Estimated Ejecta Mass (kg)
Commissioning Tests						
One Test	-	653	166	329	88	-
Primary Research Tests						
Average	13	646	158	350	54	25
SD	2	5	13	18	10	2

Table 34: Free-field Side-On Peak Pressure Summary

Test	D:H	SOD	Peak Pressure Overall				Peak Pressure within 0.200 ms			
			Peak		Avg./SD		Peak		Avg./SD	
			MPa	MPa	ms	ms	MPa	ms	ms	ms
Model Results										
Autodyn Run 6 5-1 Ejecta	5:1	195	1.283		0.127		1.283		0.127	
Commissioning Tests										
Soil Ejecta 2-1005.pnrf	5:1	205	1.004		0.123		1.004		0.123	
Soil Ejecta 2-1002.pnrf	2:1	221	1.248	1.003	0.106	0.125	1.248	1.003	0.106	0.125
Soil Ejecta 2-1004.pnrf		205	0.759	0.245	0.144	0.019	0.759	0.245	0.144	0.019
Final Intermediate Ejecta Tests										
Soil Ejecta 2-1019-35_Copy	5:1	200	1.930	1.612	0.134	0.157	0.782	0.878	0.319	0.260
Soil Ejecta 2-1040		200	1.295	0.318	0.179	0.023	0.974	0.096	0.201	0.059
Soil Ejecta 2-1041	3:1	200	1.989	2.652	0.099	0.211	0.111	1.713	0.223	0.273
Soil Ejecta 2-1027.pnrf		200	3.316	0.664	0.323	0.112	3.316	1.602	0.323	0.050
Soil Ejecta 2-1028.pnrf	2:1	200	2.268	1.782	0.134	0.145	1.740	1.012	0.265	0.263
Soil Ejecta 2-1031		200	1.399	0.384	0.172	0.017	1.266	0.518	0.276	0.009
Soil Ejecta 2-1033		200	2.048		0.129		0.524		0.250	
Soil Ejecta 2-1016-34_Copy		200	1.413		0.144		0.520		0.262	

Table 35: Ejecta Side-On Peak Pressure (Commissioning Tests)

Test	D:H	SOD (mm)	Peak Pressure Overall				Peak Pressure within 0.200 ms			
			Peak		Avg./SD		Peak		Avg./SD	
			MPa	MPa	ms	ms	MPa	ms	ms	ms
Soil Ejecta 2-1005.pnrf	5:1	205	1.004	-	0.123	-	1.004	-	0.123	-
Soil Ejecta 2-1002.pnrf	2:1	221	1.248	1.003 0.245	0.106	0.125	1.248	1.003	0.106	0.125
Soil Ejecta 2-1004.pnrf		205	0.759		0.144	0.019	0.759	0.245	0.144	0.019

Table 36: Ejecta Side-On Peak Pressures (Finals Research Tests)

Test	D:H	SOD (mm)	Peak Pressure Overall				Peak Pressure within 0.200 ms			
			Peak		Avg./SD		Peak		Avg./SD	
			MPa	MPa	ms	ms	MPa	ms	ms	ms
Soil Ejecta 2-1019-35_Copy	5:1	200	1.930	1.612 0.318	0.134	0.157 0.023	0.782	0.878 0.096	0.319	0.260 0.059
Soil Ejecta 2-1040		200	1.295		0.179		0.974		0.201	
Soil Ejecta 2-1041	3:1	200	1.989	2.652 0.664	0.099	0.211 0.112	0.111	1.713 1.602	0.223	0.273 0.050
Soil Ejecta 2-1027.pnrf		200	3.316		0.323		3.316		0.323	
Soil Ejecta 2-1028.pnrf	2:1	200	2.268	1.782 0.384	0.134	0.145 0.017	1.740	1.012 0.518	0.265	0.263 0.009
Soil Ejecta 2-1031		200	1.399		0.172		1.266		0.276	
Soil Ejecta 2-1033		200	2.048		0.129		0.524		0.250	
Soil Ejecta 2-1016-34_Copy		200	1.413		0.144		0.520		0.262	

Table 37: Soil Ejecta Side-On Pressure Duration (All Tests)

Test	D:H	SOD (mm)	Total +ve Phase	Avg./SD
			ms	ms
Commissioning Tests				
Soil Ejecta 2-1005.pnrf	5:1	205	0.123	-
Soil Ejecta 2-1002.pnrf	2:1	221	0.114	0.121 0.007
Soil Ejecta 2-1004.pnrf		205	0.128	
Final Tests				
Soil Ejecta 2-1019-35_Copy	5:1	200	0.262	0.187 0.074
Soil Ejecta 2-1040			0.113	
Soil Ejecta 2-1041	3:1	200	0.151	0.387 0.236
Soil Ejecta 2-1027.pnrf			0.623	
Soil Ejecta 2-1028.pnrf	2:1	200	0.370	0.302 0.104
Soil Ejecta 2-1031			0.438	
Soil Ejecta 2-1033			0.201	
Soil Ejecta 2-1016-34_Copy			0.200	

Table 38: Soil Ejecta Side-On Pressure Partitioned Phase Durations

Test	D:H	SOD (mm)	Phase 1	Avg./ SD	Phase 2	Avg./ SD	Phase 3	Avg./ SD
			ms	ms	ms	ms	ms	ms
Commissioning Tests								
Soil Ejecta 2-1005.pnrf	5:1	205	0.009	-	0.047	-	0.067	-
Soil Ejecta 2-1002.pnrf	2:1	221	0.010	0.010 0.000	0.069	0.054 0.015	0.035	0.057 0.022
Soil Ejecta 2-1004.pnrf		205	0.010		0.039		0.079	
Final Tests								
Soil Ejecta 2-1019-35_Copy	5:1	200	0.006	0.014 0.008	0.049	0.052 0.003	0.207	0.121 0.086

Test	D:H	SOD (mm)	Phase 1	Avg./ SD	Phase 2	Avg./ SD	Phase 3	Avg./ SD
			ms	ms	ms	ms	ms	ms
Soil Ejecta 2-1040			0.022		0.056		0.035	
Soil Ejecta 2-1041	3:1	200	0.021	0.044	0.058	0.188	0.072	0.156
Soil Ejecta 2-1027.pnrf			0.068	0.023	0.317	0.129	0.239	0.083
Soil Ejecta 2-1028.pnrf	2:1	200	0.009	0.018	0.078	0.082	0.282	0.203
Soil Ejecta 2-1031			0.042		0.134		0.261	
Soil Ejecta 2-1033			0.008	0.014	0.062	0.031	0.131	0.070
Soil Ejecta 2-1016-34_Copy			0.011		0.054		0.135	

Table 39: Averaged Partitioned Ejecta Side-On Pressure Phase Duration Percentage Contribution

Test	D:H	SOD (mm)	Phase 1	Phase 2	Phase 3
Model Results					
Autodyn Run 6 5-1 Ejecta	5:1	195	58%	22%	21%
Autodyn Run 6 5-1 Ejecta Modified	5:1	195	65%	13%	23%
Commissioning Tests					
Soil Ejecta 2-1005.pnrf	5:1	205	7%	38%	55%
Soil Ejecta 2-1002.pnrf	2:1	221	8%	44%	47%
Soil Ejecta 2-1004.pnrf		205			
Final Tests					
Soil Ejecta 2-1019-35_Copy	5:1	200	8%	28%	65%
Soil Ejecta 2-1040					
Soil Ejecta 2-1041	3:1	200	11%	48%	40%

Test	D:H	SOD (mm)	Phase 1	Phase 2	Phase 3
Soil Ejecta 2-1027.pnrf					
Soil Ejecta 2-1028.pnrf	2:1	200	6%	27%	67%
Soil Ejecta 2-1031					
Soil Ejecta 2-1033					
Soil Ejecta 2-1016-34_Copy					

Table 40: Soil Ejecta Side-On Total Specific Impulse (All Tests)

Test	D:H	SOD (mm)	Specific Impulse		Time to Peak Impulse	
			Peak	Avg./SD	Total	Avg./SD
			Pa.s	Pa.s	ms	ms
Commissioning Tests						
Soil Ejecta 2-1005.pnrf	5:1	205	32	-	0.242	-
Soil Ejecta 2-1002.pnrf	2:1	221	34	27	0.215	0.241
Soil Ejecta 2-1004.pnrf		205	19	7	0.267	0.026
Final Tests						
Soil Ejecta 2-1019-35_Copy	5:1	200	110	75	0.393	0.334
Soil Ejecta 2-1040			41	34	0.274	0.060
Soil Ejecta 2-1041	3:1	200	53	516	0.244	0.506
Soil Ejecta 2-1027.pnrf			979	463	0.767	0.262
Soil Ejecta 2-1028.pnrf	2:1	200	295	165	0.493	0.429
Soil Ejecta 2-1031			205		0.559	
Soil Ejecta 2-1033			83	91	0.325	0.100
Soil Ejecta 2-1016-34_Copy			74		0.338	

Table 41: Partitioned Soil Ejecta Phase Specific Impulse (Commissioning Tests)

Test	D:H	SOD (mm)	Phase 1		Phase 2		Phase 3	
			Impulse	Avg./SD	Impulse	Avg./SD	Impulse	Avg./SD
			Pa.s	Pa.s	Pa.s	Pa.s	Pa.s	Pa.s
Commissioning Tests								
Soil Ejecta 2-1005.pnrf	5:1	205	5	-	11	-	15	-
Soil Ejecta 2-1002.pnrf	2:1	221	7	5 1	18	11 7	10	11
Soil Ejecta 2-1004.pnrf		205	4		4		12	1

Table 42: Partitioned Soil Ejecta Phase Specific Impulse (Final Research Tests)

Test	D:H	SOD (mm)	Phase 1		Phase 2		Phase 3	
			Impulse	Avg./SD	Impulse	Avg./SD	Impulse	Avg./SD
			Pa.s	Pa.s	Pa.s	Pa.s	Pa.s	Pa.s
Final Tests								
Soil Ejecta 2-1019-35_Copy	5:1	200	6	5 0.4	34	33 1.0	70	37 33
Soil Ejecta 2-1040		200	5		32		4	
Soil Ejecta 2-1041	3:1	200	17	51	30	326 295.9	6	138 132
Soil Ejecta 2-1027.pnrf		200	86	34.7	622		271	
Soil Ejecta 2-1028.pnrf	2:1	200	9	13 7	60	63 34	226	89 80
Soil Ejecta 2-1031		200	25		120		61	
Soil Ejecta 2-1033		200	10		41		32	
Soil Ejecta 2-1016-34_Copy		200	7		33		35	

Table 43: Partitioned Soil Ejecta Phase Specific Impulse Contribution

Test	D:H	SOD (mm)	Phase 1 Impulse		Phase 2 Impulse		Phase 3 impulse	
			Avg./ SD	Avg. %	Avg./ SD	Avg. %	Avg./ SD	Avg. %
			Pa.s		Pa.s		Pa.s	
Commissioning Tests								
Soil Ejecta 2-1005.pnrf	5:1	205	5	17%	11	34%	15	48%
Soil Ejecta 2 Tests	2:1	221	5 1	20%	11 7	40%	11 1	40%
		205						
Final Tests								

Test	D:H	SOD (mm)	Phase 1 Impulse		Phase 2 Impulse		Phase 3 impulse	
			Avg./ SD	Avg. %	Avg./ SD	Avg. %	Avg./ SD	Avg. %
			Pa.s		Pa.s		Pa.s	
Soil Ejecta 2 Tests	5:1	200	5 0.4	7%	33 1.0	43%	37 33	49%
Soil Ejecta 2 Tests	3:1	200	51 34.7	10%	326 295.9	63%	138 132	27%
Soil Ejecta 4 tests	2:1	200	13 7	8%	63 34	38%	89 80	54%

E.1.7 System Force Measurement Verification Data

Table 44: Peak Hammer vs. Net-Force Response

Test	Hammer	Avg. / SD	Net Force	Avg. / SD
	kN	kN	kN	kN
Hammer Test 4	20.5	17.17 2.52	11.44	10.29 2.03 (40%)
Hammer Test 5	17.4		12.97	
Hammer Test 6	16.2		7.83	
Hammer Test 7	18.4		7.67	
Hammer Test 8	14.2		11.14	
Hammer Test 9	13.2		10.48	
Hammer Test 10	16.7		8.08	
Hammer Test 11	20.7		12.70	

Table 45: Hammer vs.Net-Force Response Duration

Test	Hammer	Avg. / SD	Net Force	Avg. / SD
	ms	ms	ms	ms
Hammer Test 4	1.652	1.651 0.237 (8%)	1.628	1.513 0.146
Hammer Test 5	1.488		1.353	
Hammer Test 6	1.907		1.519	
Hammer Test 7	1.907		1.693	
Hammer Test 8	1.359		1.367	
Hammer Test 9	1.407		1.376	
Hammer Test 10	1.998		1.743	
Hammer Test 11	1.487		1.427	

Table 46: Hammer vs. Net Force Impulse

Test	Hammer	Avg. / SD	Net Force	Avg. / SD
	Ns	Ns	Ns	Ns
Hammer Test 4	10.7	9.14 1.08	8.3	7.48 0.83
Hammer Test 5	10.0		8.6	
Hammer Test 6	8.1		6.6	
Hammer Test 7	8.7		6.8	
Hammer Test 8	7.8		7.0	
Hammer Test 9	8.0		7.1	
Hammer Test 10	9.4		6.8	
Hammer Test 11	10.4		8.7	

E.1.8 Intermediate-Field Blast Data

Table 47: Peak Force and Positive Phase Duration

Test No.	D:H	DOB (mm)	SOD (mm)	Peak Force		Duration	
				kN	Avg. / SD	Total (ms)	Avg. / SD
Intermediate Field (Side-On Pressure)							
2-001	5:1	7.2	200	239.9	197.5 46.6	1.234	1.225 0.036
2-1-2	5:1	7.2	200	228.5		1.204	
2-1-3	5:1	7.2	200	200.9		1.183	
2-1-4	5:1	7.2	200	120.7		1.278	
2-2-1	3:1	7.2	200	165.9	140.2 23.3	1.100	1.185 0.060
2-2-2	3:1	7.2	200	160.2		1.177	
2-2-3	3:1	7.2	200	111.7		1.193	
2-2-4	3:1	7.2	200	123.2		1.270	
2-3-1	2:1	7.2	200	112.5	116.8 4.9	1.150	1.247 0.057
2-3-2	2:1	7.2	200	123.4		1.297	
2-3-3	2:1	7.2	200	111.8		1.260	
2-3-4	2:1	7.2	200	119.4		1.279	
Intermediate-Field (Face-On Pressure)							
3-1-001	5:1	7.2	200		- 192.1 43.9 (164.3)	-	0.818 0.065
3-1-R001	5:1	7.2	200	247.6		0.765	
3-1-002	5:1	7.2	200	140.3		0.909	
3-1-003	5:1	7.2	200	188.2		0.780	
3-2-001	3:1	7.2	200	178.4	191.1 17.7	0.805	0.816 0.010
3-2-002	3:1	7.2	200	216.1		0.813	
3-2-003	3:1	7.2	200	178.9		0.829	
3-3-001	2:1	7.2	200	197.3	184.2 17.0	0.797	0.799 0.003
3-3-002	2:1	7.2	200	195.0		0.798	
3-3-003	2:1	7.2	200	160.1		0.803	
Half-Scale GSS SOD 250 mm							

Test No.	D:H	DOB (mm)	SOD (mm)	Peak Force		Duration	
				kN	Avg. / SD	Total (ms)	Avg. / SD
Test 1	5:1	25	250	371.4	359 20	19.370	19.821 0.292
Test 2	5:1	25	250	327.5		19.763	
Test 3	5:1	25	250	380.4		20.026	
Test 4	5:1	25	250	355.2		20.124	
Half-Scale GSS SOD 350 mm							
Test 1	5:1	25	350	385.8	359 16	19.436	19.818 0.259
Test 2	5:1	25	350	347.1		19.722	
Test 3	5:1	25	350	353.2		20.056	
Test 4	5:1	25	350	349.3		20.056	
Full-Scale SOD 1 100 mm D:H 3:1							
Test 1	3:1	50	1 100	935.1	935 32	17.129	16.363 0.471
Test 2	3:1	50	1 100	981.9		16.174	
Test 3	3:1	50	1 100	892.7		15.855	
Test 4	3:1	50	1 100	931.9		16.294	
Full-Scale SOD 1 100 mm D:H 5:1							
Test 1	5:1	50	1 100	991.1	1 025 29	17.545	16.918 0.351
Test 2	5:1	50	1 100	1 038.2		16.818	
Test 3	5:1	50	1 100	1 055.3		16.467	
Test 4	5:1	50	1 100	1 051.1		16.939	
Test 5	5:1	50	1 100	987.8		16.819	
Full-Scale PE4 Flush Dry SOD 1 300 mm							
Test 1	2:1	Flush	1 300	554.7	555	15.118	15.118
Full-Scale PE4 Flush Wet							
Test 1	2:1	Flush	1 300	663.2	663	15.023	15.023
Full-Scale Oversaturated SOD 1 300 mm							
Test 1	5:1	50	1 300	1 387.9	1 388	16.344	16.344
NATO Soil 1							
Test 1	5:1	50	1 300	1 113.5	1 026	17.307	17.536

Test No.	D:H	DOB (mm)	SOD (mm)	Peak Force		Duration	
				kN	Avg. / SD	Total (ms)	Avg. / SD
Test 2	5:1	50	1 300	989.8	84	17.144	0.322
Test 3	5:1	50	1 300	1 094.9		17.758	
Test 4	5:1	50	1 300	905.9		17.934	
Commissioning Tests							
Test5	2:1	7.2	72	225.1	255.8 30.7	0.452	0.454 0.002
Test6	2:1	7.2	72	286.5		0.456	
Test7	3:1	7.2	72	238.0	238.0	0.424	0.424
Test9	5:1	7.2	72	175.6	213.0	0.456	0.430 0.027
Test10	5:1	7.2	72	250.4	37.4	0.403	
Shrivenham							
1-360_2	N/A	100	360	367.7	350.5 17.2	3.005	2.791 0.215
2-360_2	N/A	100	360	333.3		2.576	
3-230_2	N/A	100	230	595.5	611.2 121.7	3.474	3.586 0.111
4-230_2	N/A	100	230	626.8		3.697	
5-100_2	N/A	100	100	870.1	870.1	3.912	3.912
6-230-50	N/A	50	230	661.1	661.1	3.411	3.411

Table 48: Averaged Phase Duration

Test No.	D:H	DOB mm	SOD mm	Duration (ms)				
				Total	Avg. / SD	Phase 1	Phase 2	Phase 3
1/7th Scale Intermediate-Field (Side-On Probe)								
2-001	5:1	7.2	200	1.234	1.225 0.036	24%	22%	54%
2-1-2	5:1	7.2	200	1.204				
2-1-3	5:1	7.2	200	1.183				
2-1-4	5:1	7.2	200	1.278				
2-2-1	3:1	7.2	200	1.100	1.185 0.060	24%	27%	49%
2-2-2	3:1	7.2	200	1.177				

Test No.	D:H	DOB mm	SOD mm	Duration (ms)				
				Total	Avg. / SD	Phase 1	Phase 2	Phase 3
2-2-3	3:1	7.2	200	1.193				
2-2-4	3:1	7.2	200	1.270				
2-3-1	2:1	7.2	200	1.150	1.247 0.057	24%	29%	46%
2-3-2	2:1	7.2	200	1.297				
2-3-3	2:1	7.2	200	1.260				
2-3-4	2:1	7.2	200	1.279				
1/7th Scale Intermediate-Field (Side-On Probe)								
3-1-001	5:1	7.2	200	-	0.818 0.065	30%	29%	42%
3-1-R001	5:1	7.2	200	0.765				
3-1-002	5:1	7.2	200	0.909				
3-1-003	5:1	7.2	200	0.780				
3-2-001	3:1	7.2	200	0.805	0.816 0.010	38%	34%	29%
3-2-002	3:1	7.2	200	0.813				
3-2-003	3:1	7.2	200	0.829				
3-3-001	2:1	7.2	200	0.797	0.799 0.003	36%	36%	28%
3-3-002	2:1	7.2	200	0.798				
3-3-003	2:1	7.2	200	0.803				
Full-Scale SOD 1100								
Test 1 3:1	3:1	50	1,100	17.129	16.363 0.471	18%	39%	43%
Test 2 3:1	3:1	50	1,100	16.174				
Test 3 3:1	3:1	50	1,100	15.855				
Test 4 3:1	3:1	50	1,100	16.294				
Test 1 5:1	5:1	50	1,100	17.545	16.918	17%	36%	47%

Test No.	D:H	DOB mm	SOD mm	Duration (ms)				
				Total	Avg. / SD	Phase 1	Phase 2	Phase 3
Test 2 5:1	5:1	50	1,100	16.818	0.351			
Test 3 5:1	5:1	50	1,100	16.467				
Test 4 5:1	5:1	50	1,100	16.939				
Test 5 5:1	5:1	50	1,100	16.819				
Full-Scale PE4 SOD 1 300 mm								
Dry Soil	2:1	Flush	1, 300	15.118	15.118	16%	20%	64%
Wet soil	2:1	Flush	1, 300	15.023	15.023	15%	43%	43%
Full-Scale NATO Soil SOD 1 300 mm								
Test 1	5:1	50	1, 300	17.307	17.536 0.322	15%	24%	61%
Test 2	5:1	50	1, 300	17.144				
Test 3	5:1	50	1, 300	17.758				
Test 4	5:1	50	1, 300	17.934				
Full-Scale Oversaturated SOD 1 300 mm								
Test 1	5:1	50	1,300	16.344	16.344	12%	15%	73%
Shrivenham Scaled Tests (Deep-buried)								
1-360_2	N/A	100	360	3.005	2.791 0.215	56%	44%	-
2-360_2	N/A	100	360	2.576				
3-230_2	N/A	100	230	3.474	3.586 0.111	40%	35%	25%
4-230_2	N/A	100	230	3.697				
5-100_2	N/A	100	100	3.912	3.912	22%	28%	50%
6-230-50_2	N/A	50	230	3.411	3.411	45%	37%	18%

Table 49: Intermediate-Field Total and Phased Impulse

Test No.	D:H	DOB mm	SOD mm	Impulse		Phase 1		Phase 2		Phase 3	
				Total	Avg. / SD	Imp.	Avg. / SD	Imp.	Avg. / SD	Imp.	Avg. / SD
				Ns	Ns	Ns	Ns	Ns	Ns	Ns	Ns
1/7th Scale Intermediate Field(Side-On Pressure)											
2-001	5:1	7.2	200	36	38.5 1.8	22.3	22.1 0.4	11.6	8.5 2.6	2.0	7.8 4.1
2-1-2	5:1	7.2	200	39		22.7		10.2		6.2	
2-1-3	5:1	7.2	200	41		22.0		7.8		11.0	
2-1-4	5:1	7.2	200	38		21.5		4.6		12.3	
2-2-1	3:1	7.2	200	38	36.2 0.8	20.4	20.3 0.5	5.8	6.8 0.8	11.3	9.1 1.6
2-2-2	3:1	7.2	200	36		21.0		7.8		6.8	
2-2-3	3:1	7.2	200	36		20.4		7.2		8.6	
2-2-4	3:1	7.2	200	35		19.6		6.3		9.6	
2-3-1	2:1	7.2	200	36	33.6 1.7	20.1	19.0 0.8	6.9	5.8 0.7	8.6	8.8 0.5
2-3-2	2:1	7.2	200	34		19.1		5.7		9.2	
2-3-3	2:1	7.2	200	31		17.7		5.1		8.1	
2-3-4	2:1	7.2	200	34		19.3		5.4		9.3	
1/7th Scale Intermediate-Field (Face-On Pressure)											
3-1-001	5:1	7.2	200	-	46.8 5.8	-	26.6 5.9	-	5.6 0.7	-	14.4 0.6
3-1-R001	5:1	7.2	200	51		31.4		4.7		14.6	
3-1-002	5:1	7.2	200	39		18.3		6.3		13.6	
3-1-003	5:1	7.2	200	51		30.2		5.8		15.0	
3-2-001	3:1	7.2	200	38	38.5 1.0	25.2	24.9 1.0	1.5	2.6 0.9	10.8	11.1 0.2
3-2-002	3:1	7.2	200	40		25.9		2.6		11.3	
3-2-003	3:1	7.2	200	38		23.5		3.6		11.0	
3-3-001	2:1	7.2	200	36	36.4 0.7	22.9	22.6 0.7	3.3	3.2 1.0	10.0	10.6 1.1
3-3-002	2:1	7.2	200	37		23.3		1.9		12.1	
3-3-003	2:1	7.2	200	36		21.6		4.4		9.5	
Full-Scale PE4 SOD 1 300 mm											
Dry Soil	2:1	Flush	1,300	5,533	5,533	796	796	1,573	1,573	3,164	3,164

Test No.	D:H	DOB mm	SOD mm	Impulse		Phase 1		Phase 2		Phase 3	
				Total	Avg. / SD	Imp.	Avg. / SD	Imp.	Avg. / SD	Imp.	Avg. / SD
				Ns	Ns	Ns	Ns	Ns	Ns	Ns	Ns
Wet Soil	2:1	Flush	1,300	6,617	6,617	912	912	4,065	4,065	1,640	1,640
Full-Scale Oversaturated Soil SOD 1 300 mm											
Test 1	5:1	50	1,300	13,398	13,398	1,540	1,540	2,687	2,687	9,171	9,171
Full-Scale SOD 1 300 mm											
Test 1	5:1	50	1,300	11,761	12,263 362	1,705	1,596 101	4,357	4,110 582	5,698	6,556 619
Test 2	5:1	50	1,300	12,384		1,665		3,607		7,111	
Test 3	5:1	50	1,300	12,757		1,572		4,949		6,235	
Test 4	5:1	50	1,300	12,150		1,442		3,528		7,179	
Shrivenham 2/7th Scaled Tests (Deep-buried)											
1-360	N/A	100	360	529	515 14	335	295 40	194	217 23	-	-
2-360	N/A	100	360	501		255		240		-	
3-230	N/A	100	230	786	865 79	448	496 48	322	354 32	16	16 0.6
4-230	N/A	100	230	944		544		385		15	
5-100	N/A	100	100	891	891	250	250	489	489	153	153
6-230-50	N/A	50	230	833	833	414	414	432	432	-13	-13

Table 50: Total and Partitioned Phase Impulse and Percentage Contribution

D:H	DOB mm	SOD mm	Total	Phase 1		Phase 2		Phase 3	
			Avg./ SD Ns	Avg./ SD Ns	% of Total	Avg./ SD Ns	% of Total	Avg./ SD Ns	% of Total
Final 1/7th Scaled Tests Intermediate Field (Side-On Pressure)									
5:1	**7.2**	**200**	38.5 1.8	22.1 0.4	57%	8.5 2.6	22%	7.8 4.1	20%
3:1	**7.2**	**200**	36.2 0.8	20.3 0.5	56%	6.8 0.8	19%	9.1 1.6	25%
2:1	**7.2**	**200**	33.6 1.7	19.0 0.8	57%	5.8 0.7	17%	8.8 0.5	26%

D:H	DOB mm	SOD mm	Total	Phase 1		Phase 2		Phase 3	
			Avg./ SD Ns	Avg./ SD Ns	% of Total	Avg./ SD Ns	% of Total	Avg./ SD Ns	% of Total
Final 1/7th Scale Tests Intermediate Field (Face-On Pressure)									
5:1	**7.2**	**200**	46.8 5.8	26.6 5.9	57%	5.6 0.7	12%	14.4 0.6	31%
3:1	**7.2**	**200**	38.5 1.0	24.9 1.0	65%	2.6 0.9	7%	11.1 0.2	29%
2:1	**7.2**	**200**	36.4 0.7	22.6 0.7	62%	3.2 1.0	9%	10.6 1.1	29%

Table 51: Impulse Duration Phasing

D:H	DOB mm	SOD mm	Total Impulse Duration	Phase 1		Phase 2		Phase 3	
			ms	ms		ms		ms	
1/7th Scale Intermediate Field (Side-on Pressure) Tests									
5:1	**7.2**	**200**	1.225 0.036	0.296 0.048	24%	0.271 0.011	22%	0.658 0.029	54%
3:1	**7.2**	**200**	1.185 0.060	0.283 0.030	24%	0.324 0.034	27%	0.578 0.017	49%
2:1	**7.2**	**200**	1.247 0.057	0.302 0.016	24%	0.366 0.022	29%	0.579 0.044	46%
1/7th Scale Intermediate Field (Face-on Pressure) Tests									
5:1	**7.2**	**200**	0.818 0.065	0.243 0.026	30%	0.235 0.071	29%	0.340 0.109	42%
3:1	**7.2**	**200**	0.816 0.010	0.307 0.021	38%	0.275 0.008	34%	0.234 0.020	29%
2:1	**7.2**	**200**	0.799 0.003	0.290 0.012	36%	0.288 0.013	36%	0.221 0.013	28%

Table 52: Force Phase Duration Percentage of Total Duration

Test	D:H	DOB mm	SOD mm	Phase 1	Phase 2	Phase 3
Scaled Intermediate Field						
2-001	5:1	7.2	200	24%	22%	54%
2-2-1	3:1	7.2	200	24%	27%	49%
2-3-1	2:1	7.2	200	24%	29%	46%
3-1-001	5:1	7.2	200	30%	29%	42%
3-2-001	3:1	7.2	200	38%	34%	29%
3-3-001	2:1	7.2	200	36%	36%	28%
7-1-1	5:1	50	200	45%	29%	26%
7-1-2	5:1	100	200	54%	12%	35%
Shrivenham Scaled Near and Intermediate Field (Deep-buried)						
1-360_2	N/A	100	360	56%	44%	
3-230_2	N/A	100	230	40%	35%	25%
5-100_2	N/A	100	100	22%	28%	50%
6-230-50_2	N/A	50	230	45%	37%	18%
Full-Scale 1 100 mm SOD						
Full-Scale D:H 3:1	3:1	50	1,100	18%	39%	43%
Full-Scale D:H 5:1	5:1	50	1,100	17%	36%	47%
Full-Scale 1 300 mm SOD						
Full-Scale PE4 Dry	2:1	Flush	1,300	16%	20%	64%
Full-Scale PE4 Wet	2:1	Flush	1,300	15%	43%	43%
Full-Scale Oversaturated	5:1	50	1,300	12%	15%	73%
Full-Scale NATO Soil 1	5:1	50	1,300	15%	24%	61%

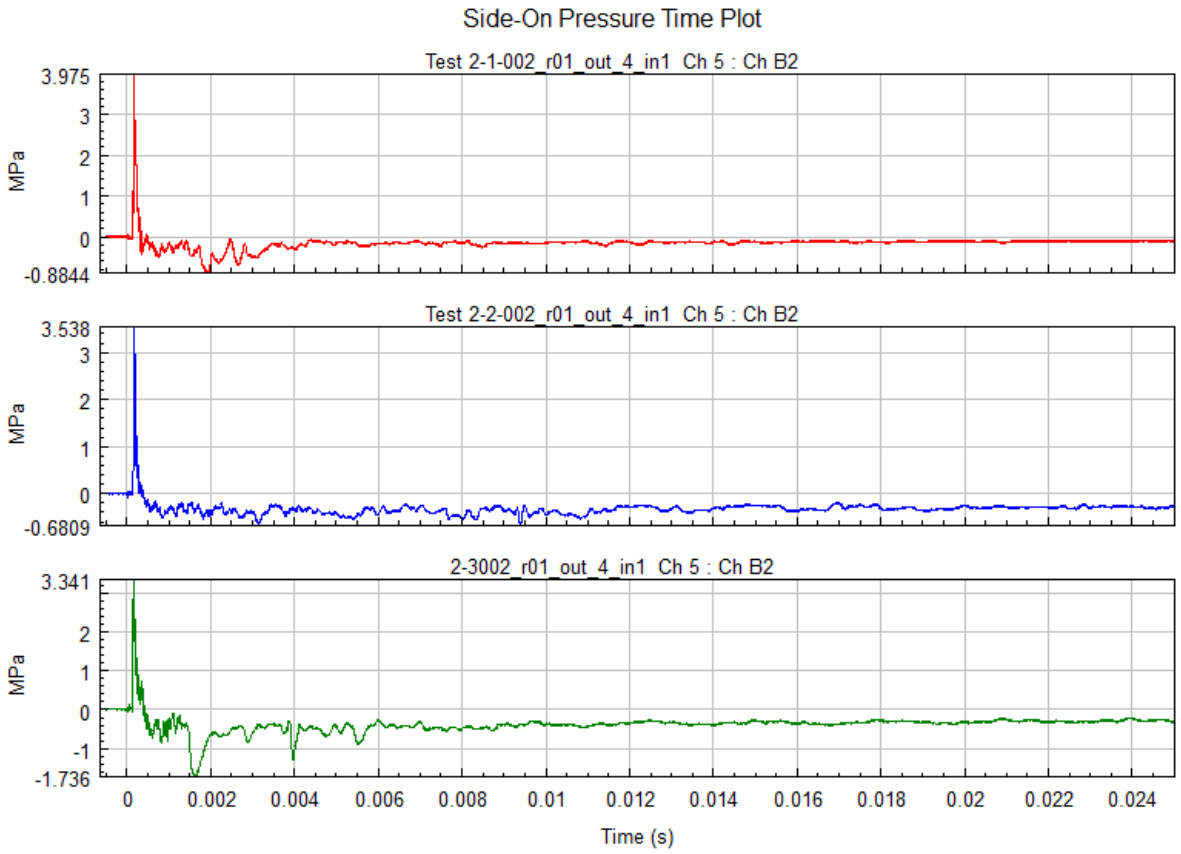

Figure 172: Intermediate-Field Side-On Pressure-Time Plots (D:H 5:1)

Table 53: Summary of Peak Intermediate Side-On Pressure and Duration

Test No.	Peak	Avg.	SD	Start	Avg	SD	Duration	Avg	SD
	MPa	MPa	MPa	ms	ms	ms	ms	ms	ms
2-1-1	8.54	4.8	2.2 (45%)	0.17	0.14	0.02 (15%)	0.15	0.17	0.02 (14%)
2-1-2	3.97			0.12			0.18		
2-1-3	3.03			0.12			0.14		
2-1-4	3.78			0.15			0.20		

Table 54: Intermediate-Field Target-Specific Impulse

D:H	DOB mm	SOD mm	Pressure Impulse	Phase 1		Phase 2		Phase 3	
			Total	Impulse		Impulse		Impulse	
			Pa	Pa		Pa		Pa	
1/7th Scale Final Tests Intermediate Field (Side-On Pressure)									
5:1	**7.2**	**200**	297 68	80 40	27%	197 68	66%	20 20	7%
3:1	**7.2**	**200**	253 84	74 23	29%	118 43	47%	61 20	24%
2:1	**7.2**	**200**	281 51	68 11	24%	183 52	65%	30 18	11%
1/7th Scale Near-Field (Face-On Pressure)									
5:1	**7.2**	**72**	4 536	2 872	63%	1,594	35%	70	2%
1/7th Scale Intermediate-Field (Side-On Pressure) Deep-buried									
5:1	**100**	**200**	104	2	2%	82	78%	21	20%

Table 55: Intermediate-Field Peak Pressure and Time to Peak

D:H	DOB mm	SOD mm	Peak Pressure	Time to Peak	Start	Duration
			MPa	Avg	ms	ms
1/7th Scale Intermediate-Field Side-On Pressure						
5:1	7.2	200	4.8 2.2	0.200 0.045	0.138 0.020	0.166 0.023
3:1	7.2	200	3.3 0.9	0.147 0.011	0.128 0.007	0.272 0.082
2:1	7.2	200	3.9 0.5	0.113 0.009	0.094 0.011	0.201 0.061

Table 56: Averaged Side-On Pressure Partitioned Phase Durations (Intermediate Target)

D:H	DOB mm	SOD mm	Total	Phase 1		Phase 2		Phase 3	
			ms	ms		ms		ms	
1/7th Scale Intermediate-Field Tests									
5:1	7.2	200	0.208 0.032	0.055 0.015	27%	0.091 0.011	43%	0.062 0.030	30%
3:1	7.2	200	0.300 0.081	0.036 0.009	12%	0.096 0.042	32%	0.168 0.046	56%
2:1	7.2	200	0.310 0.019	0.027 0.003	9%	0.123 0.039	40%	0.161 0.037	52%

E.1.9 Near-Field Blast Data

Table 57: Near-Field Craters

Test			Primary Diameter (mm)	Primary Depth (mm)	Secondary Diameter (mm)	Secondary Depth (mm)
DOB	SOD	Data				
Commissioning Tests						
7.2	72	Average	655	130	173	78
		SD	15	0	3	8
Primary Research Tests						
7.2	200	Average	671	152	354	66
		SD	45	20	30	3
7.2	200	Average	712	127	298	57
		SD	25	4	14	11
7.2	72	Average	700	159	299	63
		SD	31	21	20	3

Table 58: Peak force and Positive Phase Duration

Test No.	D:H	DOB (mm)	SOD (mm)	Peak Force		Duration	
				kN	Avg. / SD	Total (ms)	Avg. / SD
Near-Field							
4-1-001	5:1	7.2	72	206.1	271.6 65.56	0.895	0.871 0.024
4-1-002	5:1	7.2	72	337.2		0.847	
7-1-1	5:1	50	200	75.7	75.7	1.610	1.610
7-1-2	5:1	100	200	29.7	29.66	1.836	1.836
Half-Scale GSS SOD 250 mm							
Test 1	5:1	25	250	371.4	359 20	19.370	19.821 0.292
Test 2	5:1	25	250	327.5		19.763	
Test 3	5:1	25	250	380.4		20.026	
Test 4	5:1	25	250	355.2		20.124	
Commissioning Tests							
Test5	2:1	7.2	72	225.1	255.8 30.7	0.452	0.454 0.002
Test6	2:1	7.2	72	286.5		0.456	
Test7	3:1	7.2	72	238.0	238.0	0.424	0.424
Test9	5:1	7.2	72	175.6	213.0	0.456	0.430 0.027
Test10	5:1	7.2	72	250.4	37.4	0.403	
Shrivenham							
1-360_2	N/A	100	360	367.7	350.5 17.2	3.005	2.791 0.215
2-360_2	N/A	100	360	333.3		2.576	
3-230_2	N/A	100	230	595.5	611.2 121.7	3.474	3.586 0.111
4-230_2	N/A	100	230	626.8		3.697	
5-100_2	N/A	100	100	870.1	870.1	3.912	3.912
6-230-50	N/A	50	230	661.1	661.1	3.411	3.411

Table 59: Near-Field Force / Impulse Phase Duration

Test No.	D: H	DOB mm	SOD mm	Duration (ms)				
				Total	Avg. / SD	Phase 1	Phase 2	Phase 3
1/7th Scale Commissioning Tests (Near-Field)								
Test5	2:1	7.2	72	0.452	0.454	41%	37%	22%
Test6	2:1	7.2	72	0.456	0.002			
Test7	3:1	7.2	72	0.424	0.424	39%	19%	42%
Test9	5:1	7.2	72	0.456	0.430	50%	32%	18%
Test10	5:1	7.2	72	0.403	0.027			
1/7th Scale Final Tests (Near-Field)								
4-1-001	5:1	7.2	72	0.895	0.871 0.024	34%	30%	35%
4-1-002	5:1	7.2	72	0.847				
GSS Half-Scale SOD 250 mm								
Test 1	5:1	25	250	19.370	19.821 0.292	13%	20%	67%
Test 2	5:1	25	250	19.763				
Test 3	5:1	25	250	20.026				
Test 4	5:1	25	250	20.124				
Shrivenham Scaled Tests (Deep-Buried)								
1-360_2	N/A	100	360	3.005	2.791 0.215	56%	44%	-
2-360_2	N/A	100	360	2.576				
3-230_2	N/A	100	230	3.474	3.586 0.111	40%	35%	25%
4-230_2	N/A	100	230	3.697				
5-100_2	N/A	100	100	3.912	3.912	22%	28%	50%
6-230-50_2	N/A	50	230	3.411	3.411	45%	37%	18%

Table 60: Near-Field Total and Phased Impulse

Test No.	D:H	DOB mm	SOD mm	Impulse		Phase 1		Phase 2		Phase 3	
				Total	Avg. / SD	Imp.	Avg. / SD	Imp.	Avg. / SD	Imp.	Avg. / SD
				Ns	Ns	Ns	Ns	Ns	Ns	Ns	Ns
1/7th Scale Commissioning Tests (Near-field)											
Test 5	2:1	7.2	72	42	50 7.6	22.4	26 3.5	14.2	19 4.3	5.8	6 0.1
Test 6	2:1	7.2	72	58		29.4		22.8		5.5	
Test 7	3:1	7.2	72	30	30	13.6	14	5.1	5	11.7	12
Test 9	5:1	7.2	72	54	51 3.7	34.9	30 4.9	16.9	17 0.4	2.4 5.7	4 1.6
Test1 0	5:1	7.2	72	47		25.1		16.1			
1/7th Scale Near-Field											
4-1-001	5:1	7.2	72	68	70.9 2.6	27.6	32.8 5.2	26.8	24.1 2.7	14.0	14.0 0.0
4-1-002	5:1	7.2	72	73		38.1		21.4		14.0	
GSS Half-Scale SOD 250 mm											
Test 1	5:1	25	250	3 093	3 160 44	546	535	997	991 20	1 550	1 634 49
Test 2	5:1	25	250	3 172		518	11	984		1 671	
Test 3	5:1	25	250	3 215		540		1 018		1 657	
Test 4	5:1	25	250	3 160		537		963		1 659	
Full-Scale PE4 SOD 1 300 mm											
Dry Soil	2:1	Flush	1300	5 533	5 533	796	796	1 573	1 573	3 164	3 164
Wet Soil	2:1	Flush	1300	6 617	6 617	912	912	4 065	4 065	1 640	1 640
Full-Scale Oversaturated Soil SOD 1 300 mm											
Test 1	5:1	50	1300	13 398	13 398	1 540	1 540	2 687	2 687	9 171	9 171
Full-Scale SOD 1 300 mm											
Test 1	5:1	50	1300	11 761	12 263 362	1 705	1 596 101	4 357	4 110 582	5 698	6 556 619
Test 2	5:1	50	1300	12 384		1 665		3 607		7 111	
Test 3	5:1	50	1300	12 757		1 572		4 949		6 235	
Test 4	5:1	50	1300	12 150		1 442		3 528		7 179	

Test No.	D:H	DOB mm	SOD mm	Impulse		Phase 1		Phase 2		Phase 3	
				Total	Avg. / SD	Imp.	Avg. / SD	Imp.	Avg. / SD	Imp.	Avg. / SD
				Ns	Ns	Ns	Ns	Ns	Ns	Ns	Ns
Shrivenham 2/7th Scaled Tests (Deep-Buried)											
1-360	N/A	100	360	529	515 14	335	295 40	194	217 23	-	-
2-360	N/A	100	360	501		255		240		-	
3-230	N/A	100	230	786	865 79	448	496 48	322	354 32	16	16 0.6
4-230	N/A	100	230	944		544		385		15	
5-100	N/A	100	100	891	891	250	250	489	489	153	153
6-230-50	N/A	50	230	833	833	414	414	432	432	-13	-13

Table 61: Total and Partitioned Phase Impulse and Percentage Contribution

D:H	DOB mm	SOD mm	Total	Phase 1		Phase 2		Phase 3	
			Avg./ SD Ns	Avg./ SD Ns	% of Total	Avg./ SD Ns	% of Total	Avg./ SD Ns	% of Total
Commissioning Tests									
5:1	**7.2**	**72**	51 3.7	30 4.9	33%	17 0.4	33%	4 1.6	8%
3:1	**7.2**	**72**	30	14	17%	5	17%	12	38%
2:1	**7.2**	**72**	50 7.6	26 3.5	37%	19 4.3	37%	6 0.1	11%
Final 1/7th Tests Near-Field (Face-On Pressure)									
5:1	**7.2**	**72**	70.9 2.6	32.8 5.2	46%	24.1 2.7	34%	14.0 0.0	20%

Table 62: Near-Field Impulse Duration Phasing

D:H	DOB mm	SOD mm	Total Impulse Duration	Phase 1		Phase 2		Phase 3	
			ms	ms		ms		ms	
Commissioning Tests									
5:1	**7.2**	**72**	0.430 0.027	0.214 0.029	50%	0.139 0.004	32%	0.076 0.006	18%
3:1	**7.2**	**72**	0.424	0.163	39%	0.082	19%	0.178	42%
2:1	**7.2**	**72**	0.454 0.002	0.188 0.007	41%	0.167 0.012	37%	0.100 0.003	22%
1/7th Scale Near-Field (Face-On Pressure) Tests									
5:1	**7.2**	**72**	0.871 0.024	0.303 0.008	34%	0.266 0.001	30%	0.302 0.033	35%

Table 63: Near-Field Specific Impulse Summary

D:H	DOB mm	SOD mm	Pressure Impulse	Phase 1		Phase 2		Phase 3	
			Total	Impulse		Impulse		Impulse	
			Pa	Pa		Pa		Pa	
1/7th Scale Near-Field Model Results (Side-On)									
5:1	**7.2**	**72**	935	116	12%	681	73%	138	15%
5:1	**7.2**	**72**	1,069	98	9%	676	63%	294	27%
5:1	**7.2**	**72**	1,184	100	8%	677	57%	406	34%
1/7th Scale Near-Field Model Results (Face-On Pressure)									
5:1	**7.2**	**72**	4,536	2,872	63%	1,594	35%	70	2%

Table 64: Face-On Pressure Peak and Duration Summary

D:H	DOB mm	SOD mm	Peak Pressure	Time to Peak	Start	Duration
			MPa	Avg	ms	ms
1/7th Scale Intermediate Field Face-On Pressure						
5:1	7.2	200	173.8 56.5	0.175 0.001	0.152 0.012	0.023 0.011
3:1	7.2	200	94.0 47.1	0.128 0.011	0.098 0.007	0.194 0.02
2:1	7.2	200	73.3 31.5	0.117 0.029	0.097 0.022	0.318 0.185
1/7th Scale Near Field						
5:1	7.2	72	264.2		0.058	0.04

Table 65: 5:1 D:H Face-On Pressure results

Test No.	Peak	Avg.	SD	Start	Avg.	SD	Dura-tion	Avg.	SD
	MPa	MPa	MPa	ms	ms	ms	ms	ms	ms
3-1-2	117.26	173.8	56.5 (32%)	0.14	0.15	0.01 (8%)	0.03	0.02	0.01 (49%)
3-1-3	230.26			0.16			0.01		
4-1-1	264.21	-	-	0.06	-	-	0.04	-	-

E.1.10 Combined Test Point Data

Table 66: Pressure-Specific Impulse - All Test Points

D:H	DOB mm	SOD mm	Pressure Impulse	Phase 1		Phase 2		Phase 3	
			Total	Impulse		Impulse		Impulse	
			Pa	Pa		Pa		Pa	
1/7th Scale Near-Field Model Results									
5:1	**7.2**	**72**	935	116	12%	681	73%	138	15%
5:1	**7.2**	**72**	1,069	98	9%	676	63%	294	27%
5:1	**7.2**	**72**	1,184	100	8%	677	57%	406	34%
1/7th Scale Intermediate-field (Face-On Pressure)									
5:1	**7.2**	**200**	1,697 15	1,697 915	100%	-	-	-	-
3:1	**7.2**	**200**	2,605 499	405 266	16%	1 628 183	62%	573 273	22%
2:1	**7.2**	**200**	3,505 1,525	267 115	8%	2,165 1 008	62%	1,073 537	31%
1/7th Scale Near-Field (Face-On Pressure)									
5:1	**7.2**	**72**	4 ,36	2,872	63%	1,594	35%	70	2%

Table 67: Partitioned Pressure Phase Durations - All Test Points

D:H	DOB mm	SOD mm	Total	Phase 1		Phase 2		Phase 3	
			ms	ms		ms		ms	
1/7th Scale Intermediate Field (Face-On Pressure)									
5:1	**7.2**	**200**	-	-	-	-	-	-	-
3:1	**7.2**	**200**	0.337 0.008	0.023 0.011	7%	0.174 0.020	52%	0.139 0.017	41%
2:1	**7.2**	**200**	0.392 0.031	0.014 0.002	4%	0.191 0.032	49%	0.187 0.009	48%
1/7th Scale Near-Field (Face-On Pressure)									
5:1	**7.2**	**72**	0.348	0.026	7%	0.114	33%	0.208	60%

E.1.11 NIR Light Data

Table 68: Summary of NIR Light Traces Captured

Sensor 3	Sensor 4	Comments
2-2-1	-	Tail cut-off
2-2-2	2-2-2	Tail cut-off
2-3-2	2-3-2	Tail cut-off
2-2-4	2-2-4	-
3-1-001	-	-
3-1-R001	3-1-R001	-
3-2-001	3-2-001	-
3-2-002	-	-
3-2-003	3-2-003	-
3-3-002	3-3-002	-
3-3-003	3-3-003	-
4-1-001	4-1-001	-
4-1-002	4-1-002	-

Table 69: Partitioned Light Work Area and Percentage Contribution

D:H	DOB mm	SOD mm	Total		Phase 1		Phase 2		Phase 3	
			Normalised Area		Normalised Area		Normalised Area		Normalised Area	
Intermediate Field Side-On										
3:1	7.2	200	256.3	48.6	19%	207.7	81%	-	-	
3:1	7.2	200	156.7	17.7	11%	104.0	66%	35.0	22%	
2:1	7.2	200	194.0	34.6	18%	66.4	34%	93.0	48%	
Intermediate Face-On										
5:1	7.2	200	75.0	34.4	46%	40.1	53%	0.5	1%	
3:1	7.2	200	192.7	34.2	18%	58.1	30%	100.3	52%	
3:1	7.2	200	276.8	29.8	11%	74.5	27%	172.5	62%	
2:1	7.2	200	131.1	15.1	12%	116.0	88%	-	-	
2:1	7.2	200	149.8	15.5	10%	134.2	90%	-	-	
Near-Feld Face-On										

D:H	DOB mm	SOD mm	Total		Phase 1		Phase 2		Phase 3	
			Normalised Area		Normalised Area		Normalised Area		Normalised Area	
5:1	7.2	72	41.0	28.4	69%	12.6	31%		-	-
5:1	7.2	72	43.3	31.5	73%	11.8	27%		-	-

E.1.12 Measurement Assembly Displacement

Table 70: Measurement Head Deflection Area Summary

D:H	DOB	SOD	Peak Disp.	Max Area	Phase 1		Phase 1		Phase 3	
	mm	mm	mm	mm.s	mm.s		mm.s		mm.s	
1/7th Scale Intermediate-Field (Side-On Pressure)										
5:1	**7.2**	**200**	4.3 0.2	22.1 1.8	2.2 0.6	10%	8.8 2.5	40%	11.1 3.6	50%
3:1	**7.2**	**200**	3.9 0.2	23.3 2.2	1.9 0.3	8%	7.1 2.0	30%	14.3 3.5	62%
2:1	**7.2**	**200**	3.4 0.3	16.0 2.0	1.0 0.4	7%	8.3 0.8	52%	6.6 0.9	41%
1/7th Scale Intermediate-Field (Face-On Pressure)										
5:1	**7.2**	**200**	4.7 0.1	26.8 1.7	2.0 0.2	8%	5.2 0.9	20%	19.0 1.5	71%
3:1	**7.2**	**200**	3.8 0.2	23.2 0.4	1.4 0.2	6%	3.2 0.1	14%	18.5 0.6	80%
2:1	**7.2**	**200**	3.5 0.2	22.6 3.0	1.4 0.2	6%	3.5 0.8	15%	17.6 2.0	78%
1/7th Scale Near-Field (Face-On Pressure)										
5:1	**7.2**	**72**	5.9	40.0 1.0	0.9 0.4	2%	8.4 0.0	21%	30.7 1.3	77%
1/7th Scale Intermediate Deep-buried										
5:1	**50**	**200**	3.8	-	-	-	-	-	-	-
5:1	**100**	**200**	3.5	-	-	-	-	-	-	-

Table 71: Summary of Measurement Assembly Total and Phased Duration

D:H	DOB mm	SOD mm	Total Duration	Phase 1		Phase 2		Phase 3	
			ms	ms		ms		ms	
1/7th Scale Intermediate-Field (Side-On Pressure)									
5:1	**7.2**	**200**	8.7 0.5	2.2 0.4	25%	3.3 0.8	38%	3.2 1.2	36%
3:1	**7.2**	**200**	9.3 0.7	2.2 0.2	23%	2.9 0.7	32%	4.2 1.1	45%
2:1	**7.2**	**200**	7.9 0.3	1.7 0.4	21%	4.1 0.2	51%	2.2 0.1	28%
1/7th Scale Intermediate-Field (Face-On Pressure)									
5:1	**7.2**	**200**	9.1 0.6	2.1 0.1	23%	2.2 0.3	24%	4.8 0.3	53%
3:1	**7.2**	**200**	9.5 0.6	1.9 0.0	20%	1.7 0.1	18%	5.9 0.5	62%
2:1	**7.2**	**200**	9.5 0.4	1.8 0.1	19%	1.7 0.1	18%	6.0 0.2	63%
1/7th Scale Intermediate-Field (Face-On Pressure)									
5:1	**7.2**	**72**	10.0 0.4	1.2 0.2	12%	2.9 0.2	29%	5.9 0.4	59%
1/7th Scale Intermediate-Field (Side-On Pressure) Deep-buried									
5:1	**50**	**200**	-	-	-	-	-	-	-
5:1	**100**	**200**	-	-	-	-	-	-	-

E.2 Combined Test Data Plots One-Seventh Scale Tests

E.2.1 Computational Modelling

Note that the slight increase in the specific impulse of Phase Three is due to the manual extraction method used and is considered negligible for this work. The percentage contribution of each partitioned phase of the unmodified and modified model results remains similar.

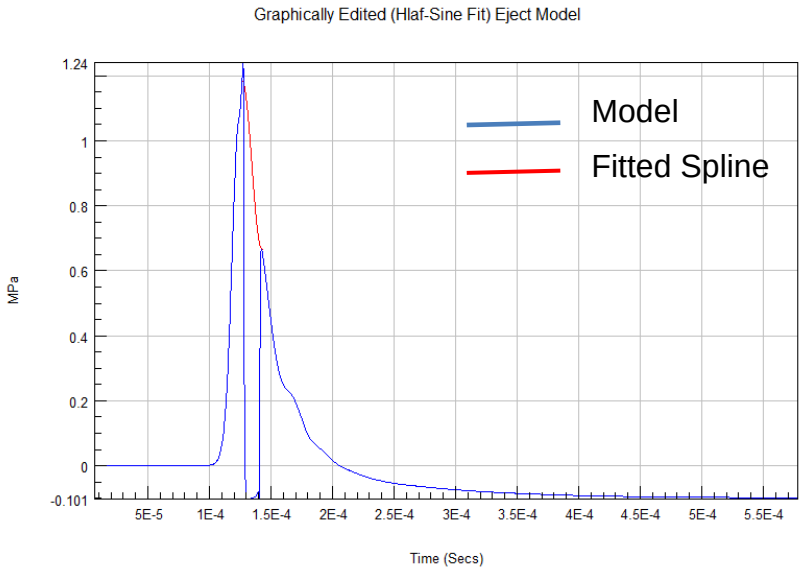

Figure 173: Modified Shallow-Buried Ejecta Pressure Plot

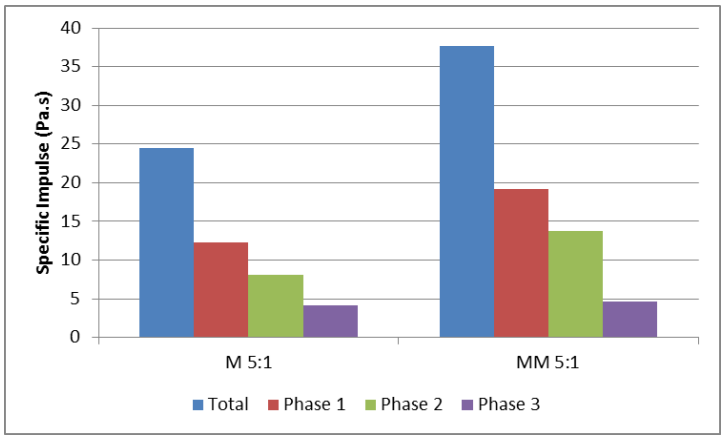

Figure 174: Ejecta Model Total and Phase-Specific Impulse

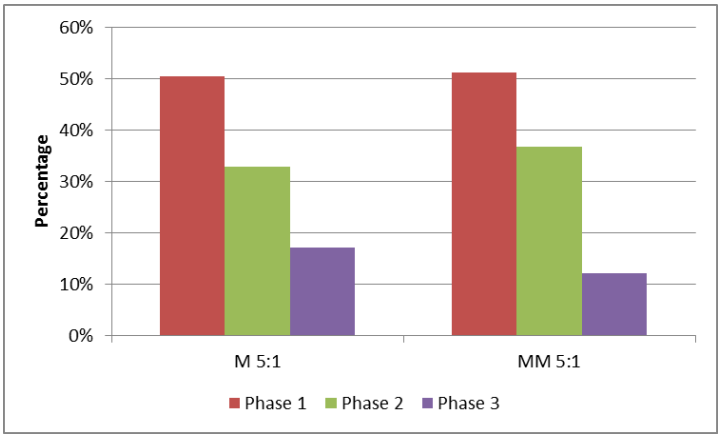

Figure 175: Ejecta Model Specific Impulse Contribution per Phase

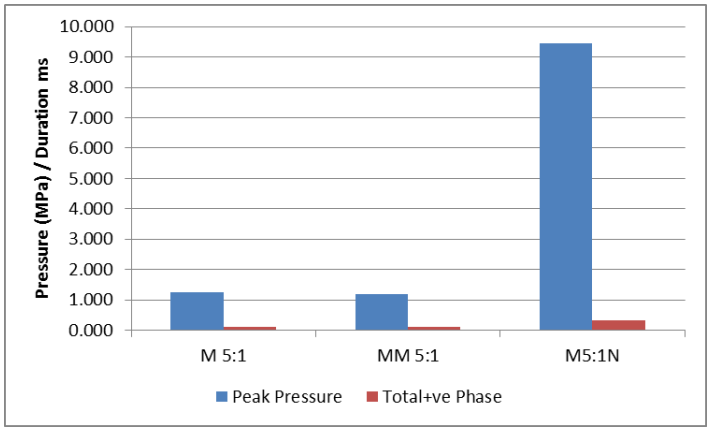

Figure 176: Ejecta Model Side-On Peak Pressure (No Target) Intermediate and Near-Field

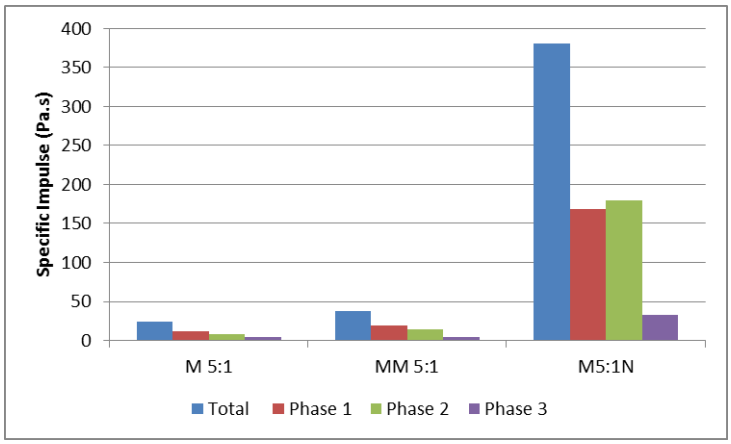

Figure 177: Partitioned Ejecta (No Target) Model Phased Specific Impulse

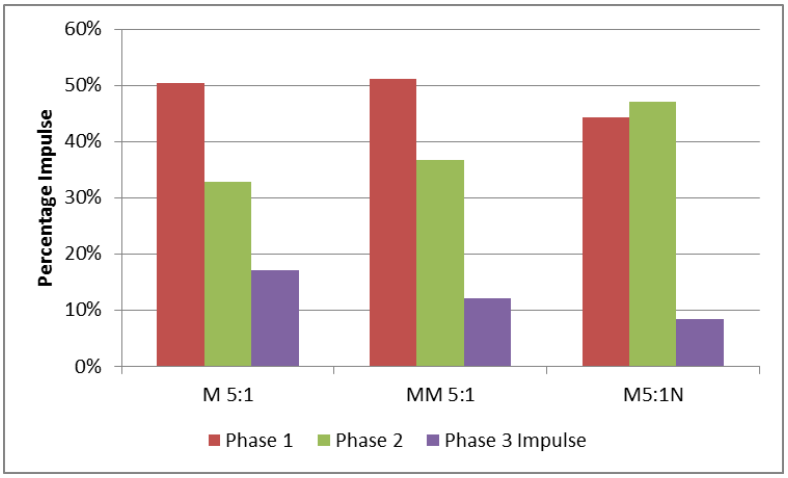

Figure 178: Partitioned Ejecta (No Target) Model Phased Specific Impulse Contribution

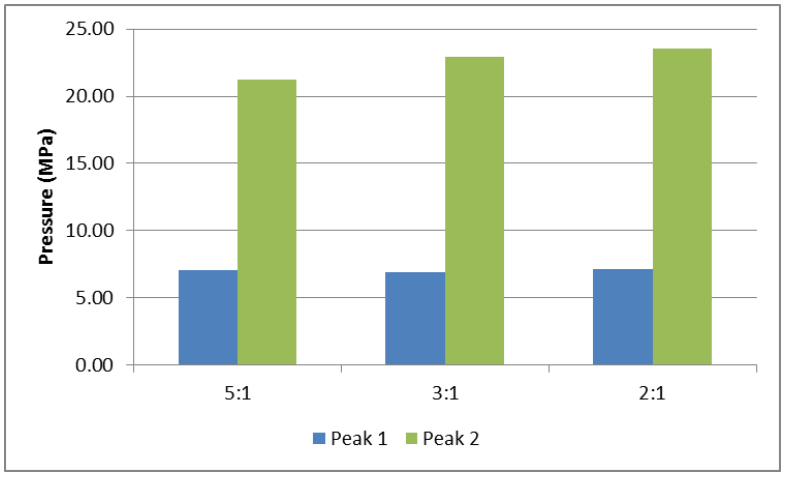

Figure 179: Near-Field Target Model Peak Pressures

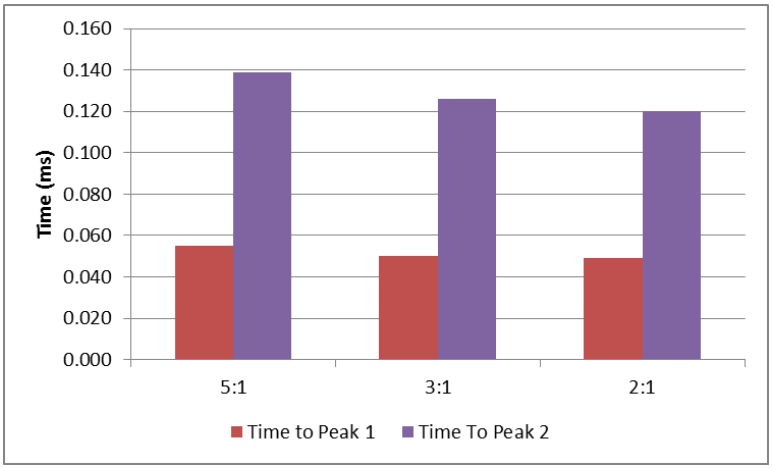

Figure 180: Near-Field Target Model Time to Peak

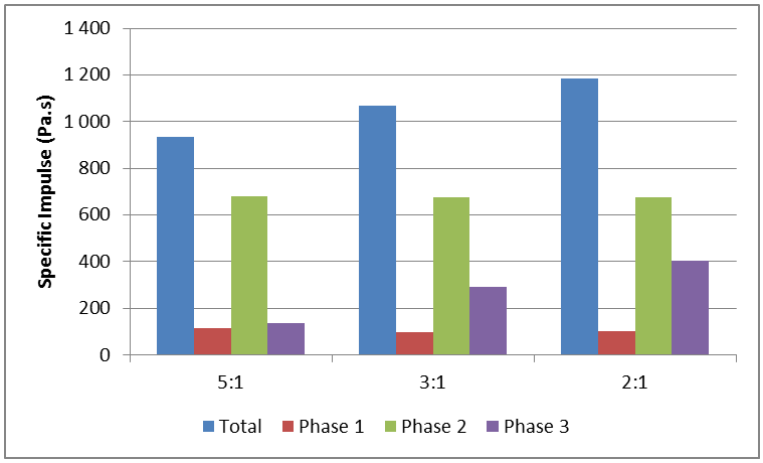

Figure 181: Near-Field Model Total and Phase-Specific Impulse

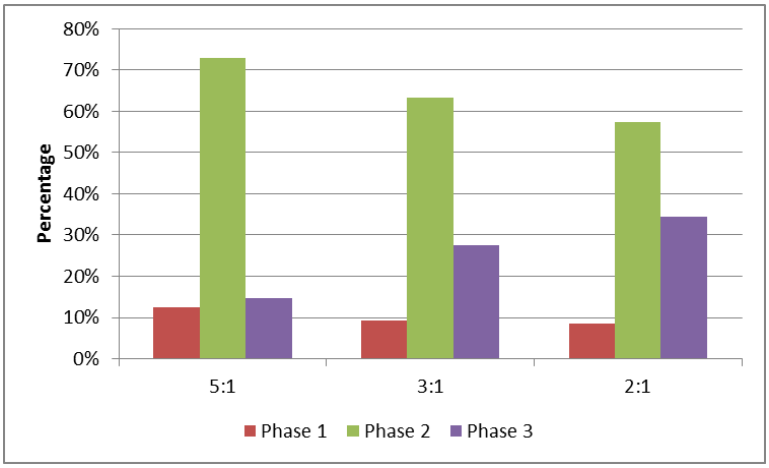

Figure 182: Near-Field Model Phase-Specific Impulse Contribution

E.2.2 Near-Field Blast Craters

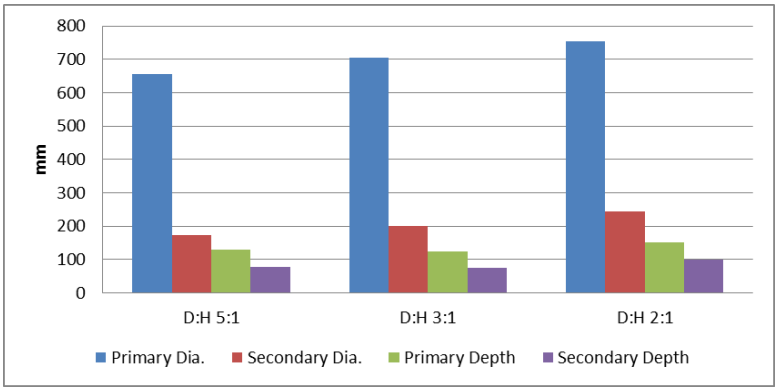

Figure 183: Average Commissioning Test Near-Field Blast Craters

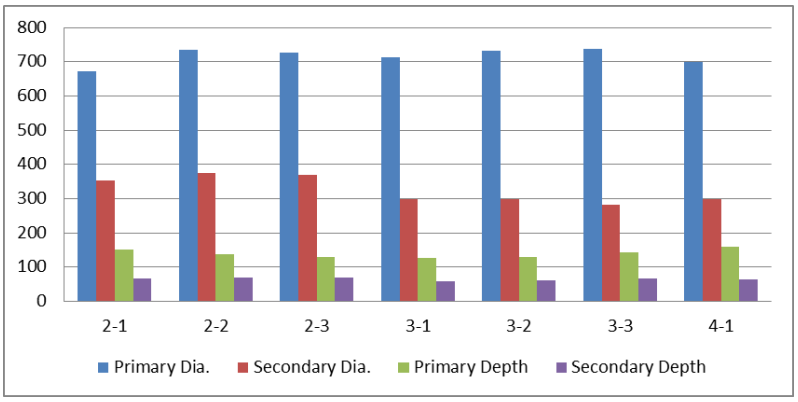

Figure 184: Crater Dimensions of Final Near-Field Tests

E.2.3 Side-On and Face –On Pressure

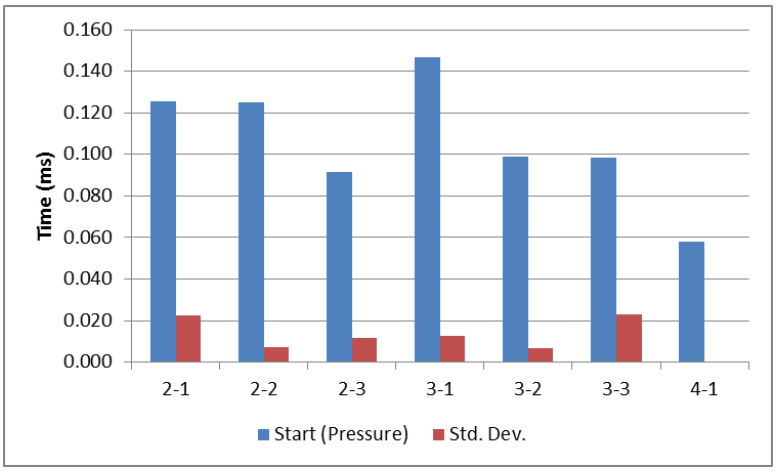

Figure 185: Pressure Trace Start Time

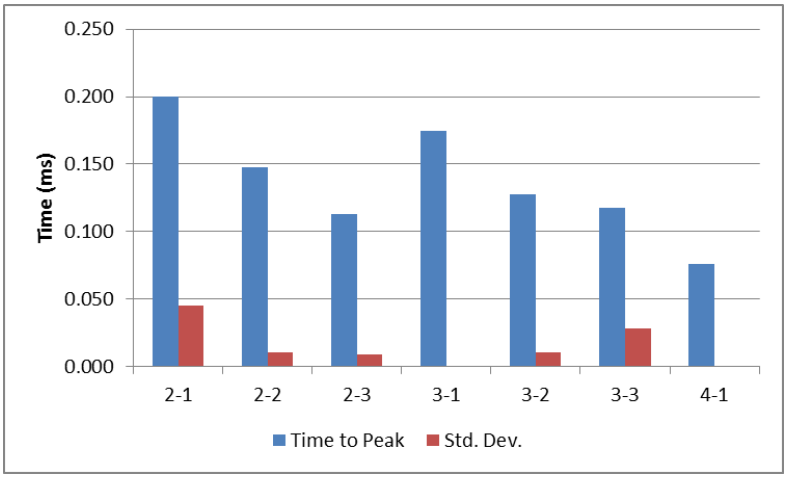

Figure 186: Time to Peak Pressure

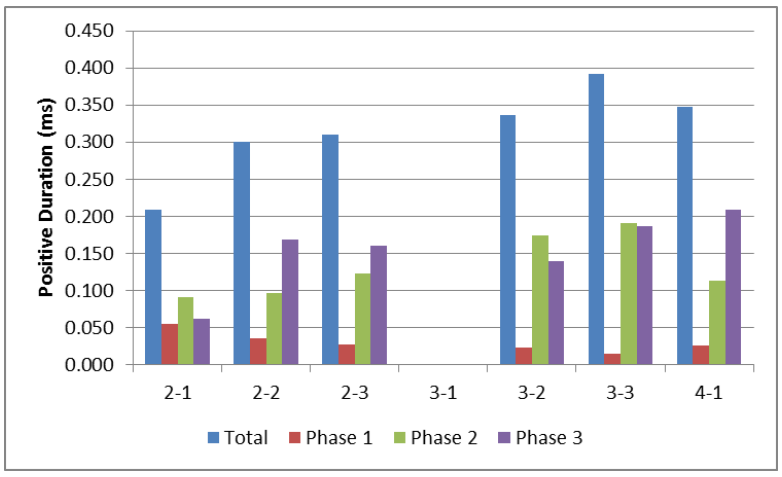

Figure 187: Averaged Pressure Positive Duration

E.2.4 Side-On and Face-On Specific Impulse

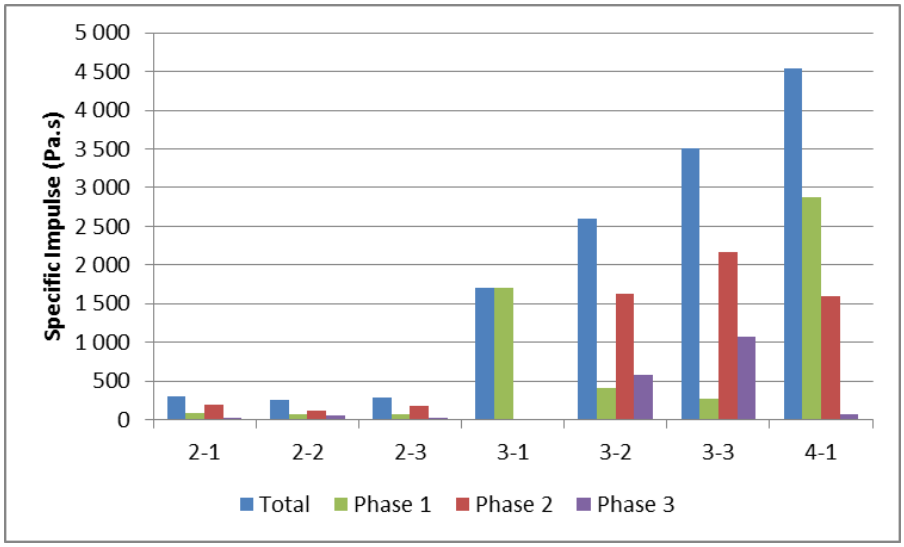

Figure 188: Averaged Specific Impulse

E.2.5 Target Response Net Force

E.2.6 Peak Force

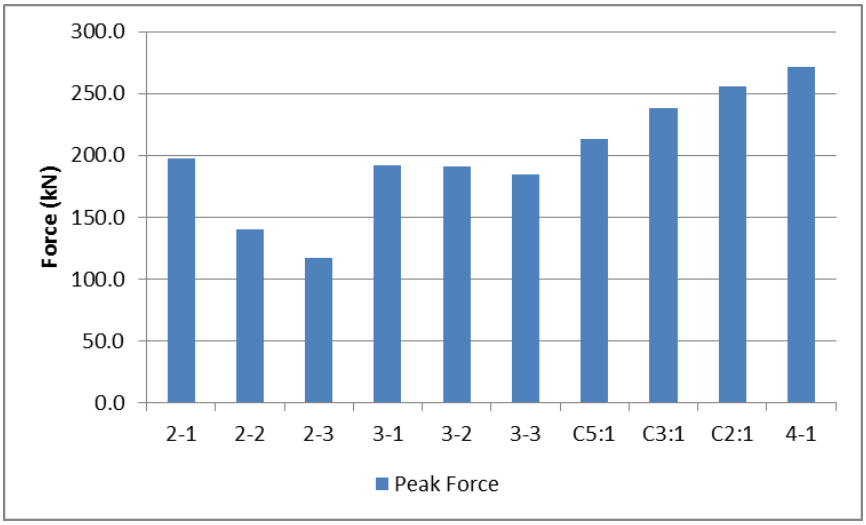

Figure 189: Peak Net Force

E.2.7 Phase Duration

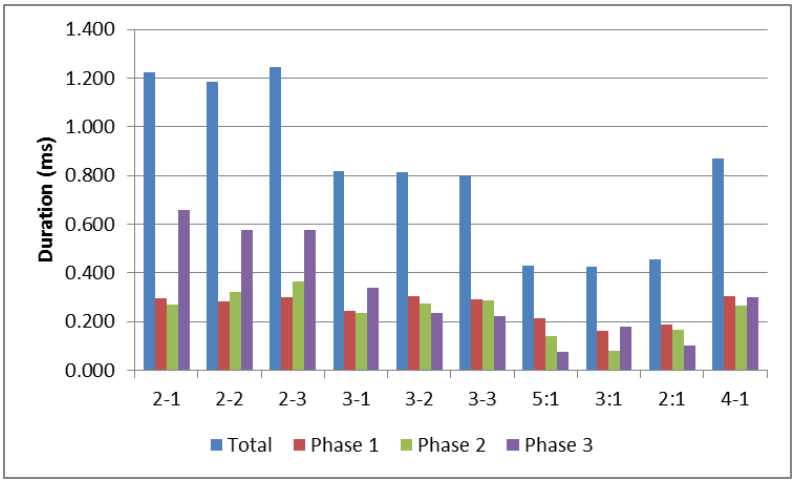

Figure 190: Total and Partitioned Phase Positive Net-Force Duration

E.2.8 Target Response Blast Impulse

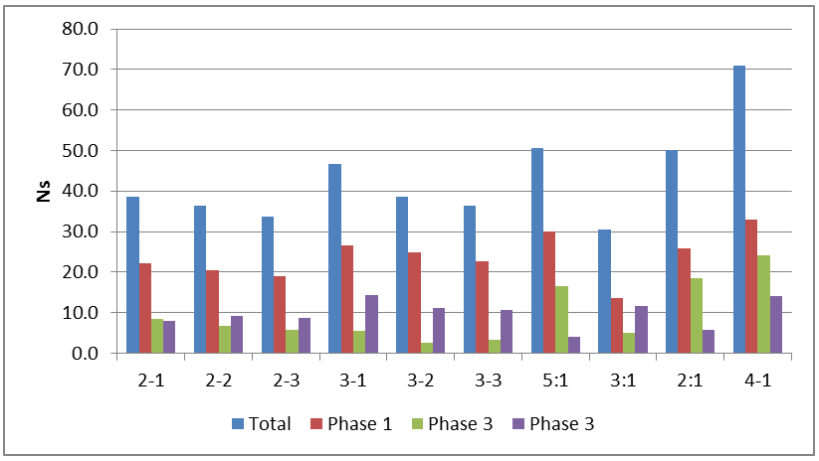

Figure 191: Averaged Partitioned Total and Phase Impulse

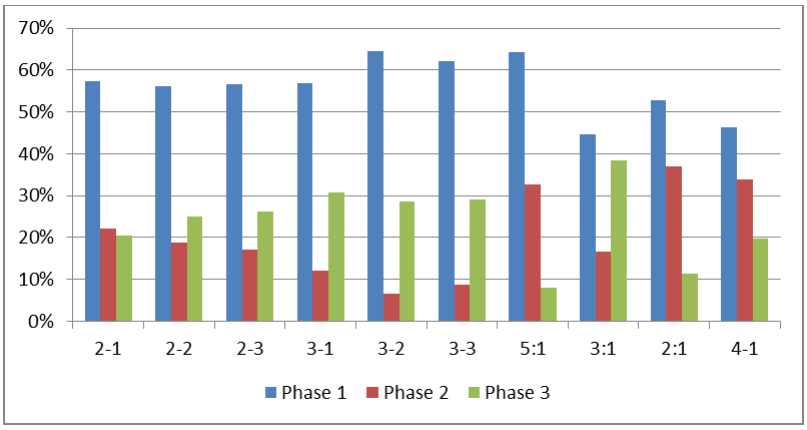

Figure 192: Average Partitioned Phase Impulse Contribution

E.3 Secondary Data

E.3.1 Shrivenham

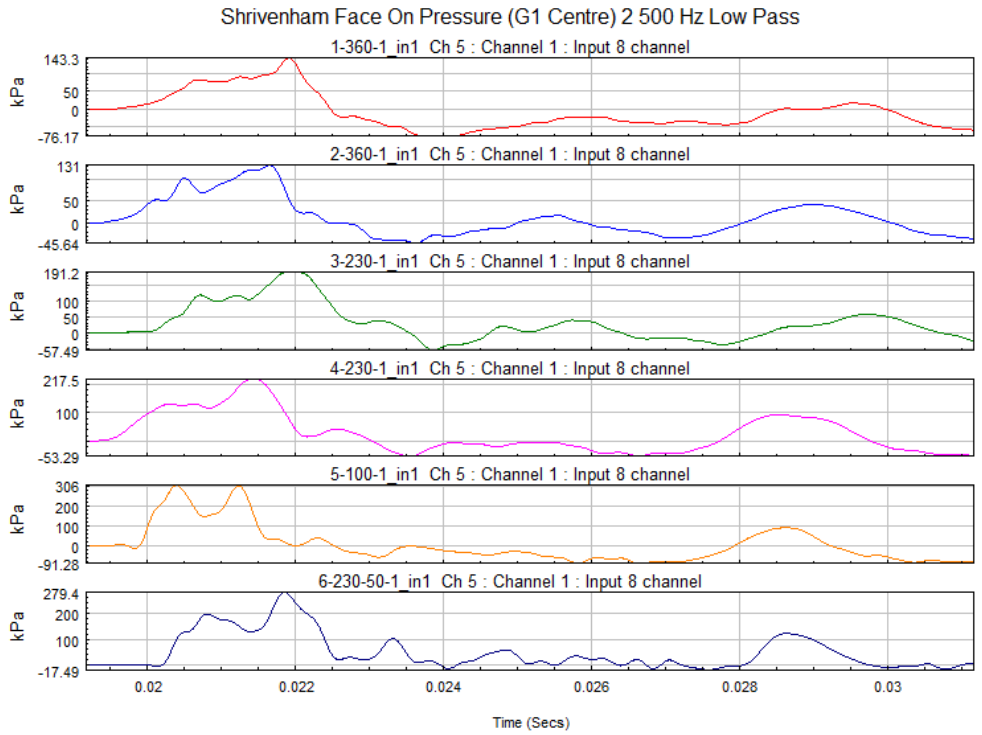

Figure 193: Cranfield Centre Target Face Force-Time Plot

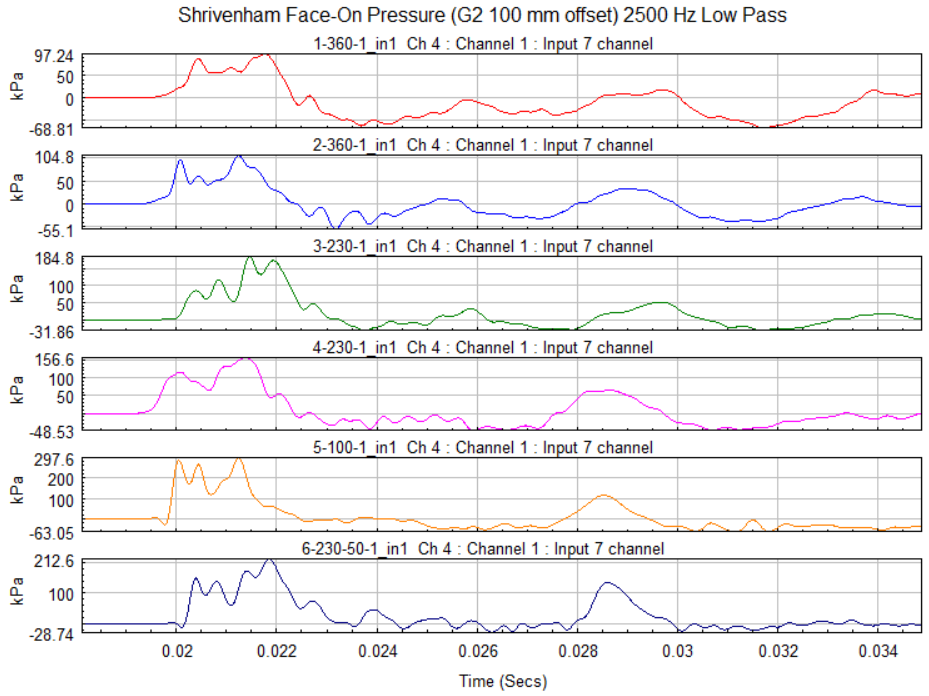

Figure 194: Cranfield Target Face-On Force-Time Plot 100 mm Offset

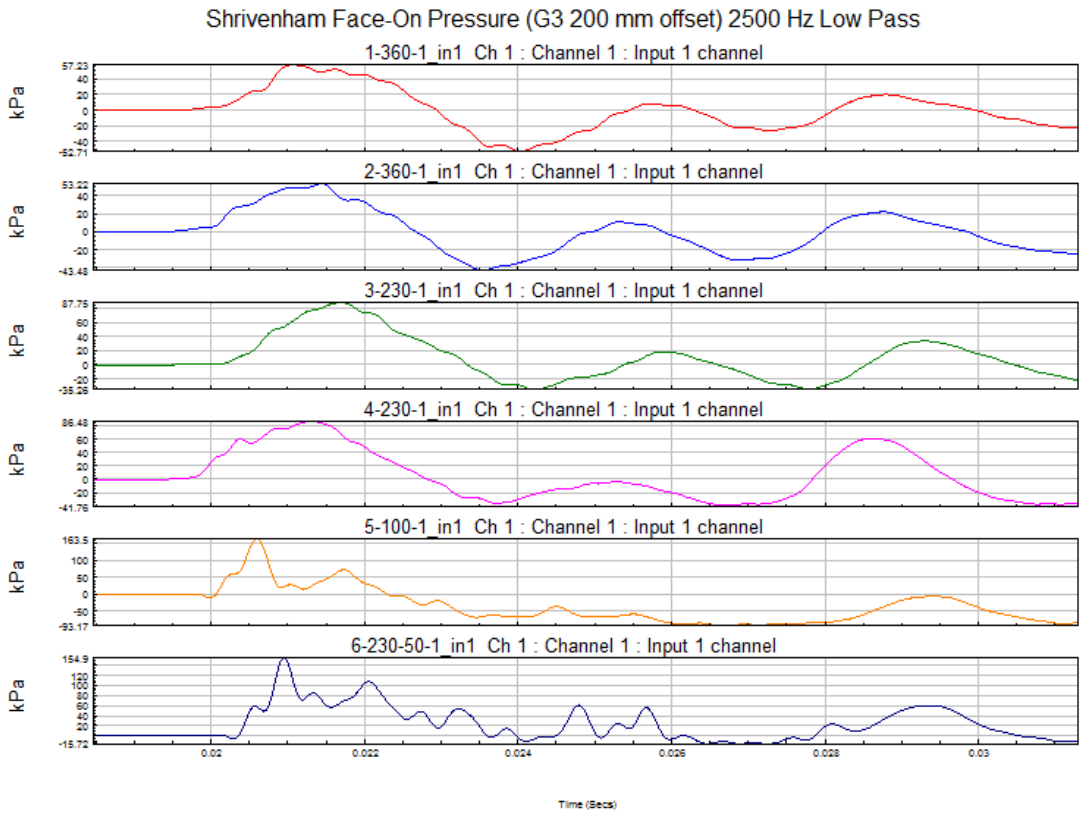

Figure 195: Cranfield Target Face-On Force-Time Plot 300 mm Offset

Table 72: Cranfield Blast Rig Total and Partitioned Phased Force Duration

Test No.	D:H	DOB (mm)	SOD (mm)	Duration							
				Total		Phase 1		Phase 2		Phase 3	
				ms	Avg. / SD	ms	Avg. / SD	ms	Avg. / SD	ms	Avg. / SD
1-360_2	N/A	100	360	3.005	2.791	1.845	1.574	1.161	1.216	-	-
2-360_2	N/A	100	360	2.576	0.215	1.304	0.270	1.272	0.056	-	
3-230_2	N/A	100	230	3.474	3.586	1.447	1.451	1.280	1.248	0.747	0.886
4-230_2	N/A	100	230	3.697	0.111	1.455	0.004	1.217	0.032	1.026	0.139
5-100_2	N/A	100	100	3.912	3.912	0.859	0.859	1.097	1.097	1.956	1.956
6-230-50	N/A	50	230	3.411	3.411	1.526	1.526	1.264	1.264	0.620	0.620

Table 73: (McDonald 2013b)Partitioned Phase Duration and Percentage Contribution

Test	DOB (mm)	SOD (mm)	Total	Phase 1		Phase 2		Phase 3	
			Avg. / SD (ms)	Avg. / SD (ms)	Percentage	Avg. / SD (ms)	Percentage	Avg. / SD (ms)	Percentage
1 and 2-360	100	360	2.791 0.215	1.574 0.270	56%	1.216 0.056	44%	-	-
2 and 3-230	100	230	3.586 0.111	1.451 0.004	40%	1.248 0.032	35%	0.886 0.139	25%
5-100_2	100	100	3.912	0.859	22%	1.097	28%	1.956	50%
6-230-50_2	50	230	3.411	1.526	45%	1.264	37%	0.620	18%

Table 74: Cranfield Blast Rig Peak Force

Test No.	D:H	DOB (mm)	SOD (mm)	Peak Force (kN)	Avg. / SD
1-360_2	N/A	100	360	367.7	350.5 17.2
2-360_2				333.3	
3-230_2	N/A	100	230	595.5	611.2 121.7
4-230_2				626.8	
5-100_2	N/A	100	100	870.1	870.1
6-230-50	N/A	50	230	661.1	661.1

Table 75: Peak Force and Positive Duration (McDonald 2013a)

Test No.	DOB (mm)	SOD (mm)	Peak Force (kN)	Duration (ms)
1 and 2 -360	100	360	351 17	1.943 0.218
2 and 3-230	100	230	611 121	3.172 0.135
5-100	100	100	870	2.740
6-230-50	50	230	661	3.363

Table 76: Summary of (McDonald) Partitioned Total and Phased Impulse

Test Name	DOB (mm)	SOD (mm)	Total	Phase 1		Phase 2		Phase 3	
			Avg./ SD (Ns)	Avg./ SD (Ns)	Percentage	Avg./ SD (Ns)	Percentage	Avg./ SD (Ns)	Percentage
1 and 2-360	100	360	515 14	295 40	57%	217 23	42%	-	-
2 and 3-230	100	230	865 79	496 48	57%	354 32	41%	16 0.645	2%
5-100	100	100	891	250	28%	489	55%	153	17%
6-230-50	50	230	833	414	50%	432	52%	-13	-2%

E.3.2 SIIMA

Table 77: Averaged SIIMA Peak Force and Positive Phase Duration

D:H	DOB	SOD	Peak Force Avg. / SD	Duration Avg. / SD
	mm	mm	kN	ms
½ Scale Tests				
5:1	25	250	359 20	19.821 0.292
Full-Scale Tests				
5:1	50	1300	1 026 84	17.536 0.322
5:1	50	1300	1 388	16.344

Table 78: Average Partitioned SIIMA Total and Phase Durations

D:H	DOB mm	SOD mm	Total Impulse Duration	Phase 1		Phase 2		Phase 3	
			ms	ms		ms		ms	
½Half-Scale Tests									
5:1	**25**	**250**	19.821 0.292	2.619 0.013	13%	4.005 0.182	20%	13.197 0.417	67%
Full-Scale Tests									
5:1	**50**	**1300**	17.536 0.322	2.584 0.134	15%	4.172 0.603	24%	10.780 0.457	61%

Table 79: SIIMA Total and Partitioned Phased Force Duration

Test No.	D:H	DOB (mm)	SOD (mm)	Duration							
				Total		Phase 1		Phase 2		Phase 3	
				ms	Avg. / SD	ms	Avg. / SD	ms	Avg. / SD	ms	Avg. / SD
Half-Scale GSS SOD 250 mm											
Test 1	5:1	25	250	19.370	19.821 0.292	2.604	2.619 0.013	4.124	4.005 0.182	12.642	13.197 0.417
Test 2				19.763		2.632		4.021		13.110	
Test 3				20.026		2.632		4.172		13.222	
Test 4				20.124		2.608		3.704		13.812	
Full-Scale SOD 1 300 mm											
Test 1	5:1	50	1300	17.307	17.536 0.322	2.635	2.584 0.134	4.315	4.172 0.603	10.357	10.780 0.457
Test 2				17.144		2.680		3.448		11.016	
Test 3				17.758		2.355		5.071		10.333	
Test 4				17.934		2.668		3.853		11.412	

Table 80: SIIMA Peak Force

Test No.	D:H	DOB (mm)	SOD (mm)	Peak Force (kN)	Avg. / SD
Half-Scale GSS SOD 250 mm					
Test 1	5:1	25	250	371.4	359 20
Test 2				327.5	
Test 3				380.4	
Test 4				355.2	
Full-Scale SOD 1 300 mm					
Test 1	5:1	50	1300	1 113.5	1 026 84
Test 2				989.8	
Test 3				1 094.9	
Test 4				905.9	

Table 81: Summary of SIIMA Tests Partitioned Total and Phased Impulse

D:H	DOB mm	SOD mm	Total	Phase 1		Phase 2		Phase 3	
			Avg. / SD Ns	Avg. / SD Ns	% of Total	Avg. / SD Ns	% of Total	Avg. / SD Ns	% of Total
½ Half-Scale Tests									
5:1	**25**	**250**	3,160 44	535 11	17%	991 20	31%	1,634 49	52%
Full-Scale Tests									
5:1	**50**	**1300**	12,263 362	1,596 101	13%	4,110 582	34%	6,556 619	53%

E.3.3 Scaling

Table 82: Summary Table of Full and Scaled Impulse for all Tests

Test	D:H	DOB mm	SOD mm	Scaled kN	Full kN	Scaled Ns	Full Ns
1/7th Scale Intermediate-Field Target							
Side-On Pressure Configuration							
2-1	5:1	7.2	200	197.5 46.6	9,677 2,281	38.5 1.8	13,220 86
2-2	3:1	7.2	200	140.2 23.3	6,872 1,141	36.3 0.8	12,453 38
2-3	2:1	7.2	200	116.8 4.9	5,723 238	33.6 1.7	1, 530 85
7-1-1	5:1	50	200	75.7	3,707	33.0	11,335
7-2-1	5:1	100	200	29.7	1,453	27.5	9,418
Face-on Pressure Configuration							
3-1	5:1	7.2	200	192.1 43.9	9,411 2,152	46.8 5.9	16,047 288
3-2	3:1	7.2	200	191.1 17.7	9,366 865	38.6 0.9	13,229 45
3-3	2:1	7.2	200	184.2 17.0	9,23 834	36.4 0.7	12,478 34
1/7th Scale Near-Field Target							
Commissioning Tests							
Test 5 and 6	2:1	7.2	72	255.8 30.7	12,532 1,504	50.1 7.6	17,178 2,613
Test 7	3:1	7.2	72	238.0	11,660	30.4	10,428
Test 9 and 10	5:1	7.2	72	213.0 37.4	10,439 1,833	50.6 3.7	17,342 1 279
Final 1/7th Scale Tests							
4-1	5:1	7.2	72	271.6 65.6	13,309 3,213	70.9 2.6	24,324 126
SIIMA							

Test	D:H	DOB mm	SOD mm	Scaled kN	Full kN	Scaled Ns	Full Ns
Half-Scale							
SIIMA Soil	5:1	25	250	358.6 20.1	1,435 80	3,160.2 43.8	25,281 350
Full-Scale							
NATO Soil	5:1	50	1300	20.9 1.7	1,026 84	35.8 1.1	12,263 362
Shrivenham							
1 and 2-360	N/A	100	360	350.5 17.2	4,212 206	515.0 14.2	21,456 592
3 and 4-230	N/A	100	230	611.2 15.6	7,345 188	864.9 78.8	36,038 3,285
5-100	N/A	100	100	870.1	10,458	891.2	37,132
6-230-50	N/A	50	230	661.1	7,945	833.4	34,726

Table 83: One Seventh-Scale Test Soil vs. NATO AEP Soil (NATO Standardization Agency (NSA) 31 August 2011)

Test Soil Granulometry		Up-Scaled Test Soil		AEP Soil		Up-Scaled SIIMA Soil		SIIMA Soil	
Sieve Size (mm)	% Passing	Sieve Size (mm)	% Passing	Sieve Size	% Passing	Sieve Size	% Passing	Sieve Size	% Passing
9.5	100	-	**-**	**-**	-	-	-	-	-
6.7	99.16	**46.9**	**-**	**-**	-	-	-	-	-
4.75	98	**33.25**	98	**37.5**	100	-	-	-	-
-	**-**	**-**	-	**19**	75.99	-	-	-	-
2	76.69	**14**	76.69	**13.2**	62.37	13.4	99	6.7	99
-	-	-	-	-	-	9.5	96	4.75	96
0.85	48.13	**5.95**	48.13	**6.7**	47.18	-	-	-	-
-	-	-	-	-	-	4.72	63	2.36	63
0.425	24.37	**2.975**	24.37	**2.36**	-	2.36	43	1.18	43

Test Soil Granulometry		Up-Scaled Test Soil		AEP Soil		Up-Scaled SIIMA Soil		SIIMA Soil	
Sieve Size (mm)	**% Passing**	**Sieve Size (mm)**	**% Passing**	**Sieve Size**	**% Passing**	**Sieve Size**	**% Passing**	**Sieve Size**	**% Passing**
0.25	14.57	**1.75**	14.57	**2**	27.9	1.2	32	0.6	32
0.15	8.94	**1.05**	8.94	**0.85**	27.9	0.6	21	0.3	21
0.075	5.82	**0.525**	5.82	**0.425**	18.9	0.3	11	0.15	11
-	-	**-**	-	**-**	-	0.17	7	0.075	7